# Carbonation mechanism of alkali-activated fly ash and slag materials

## In view of long-term performance predictions

Nedeljković, Marija

**DOI**
10.4233/uuid:97b9eabe-159e-43e1-8b35-edc61b1aa682

**Publication date**
2019

**Document Version**
Final published version

**Citation (APA)**
Nedeljković, M. (2019). *Carbonation mechanism of alkali-activated fly ash and slag materials: In view of long-term performance predictions*. [Dissertation (TU Delft), Delft University of Technology]. https://doi.org/10.4233/uuid:97b9eabe-159e-43e1-8b35-edc61b1aa682

# Carbonation mechanism of alkali-activated fly ash and slag materials

## -in view of long-term performance predictions

Marija Nedeljković

# CARBONATION MECHANISM OF ALKALI-ACTIVATED FLY ASH AND SLAG MATERIALS

-IN VIEW OF LONG-TERM PERFORMANCE PREDICTIONS

# CARBONATION MECHANISM OF ALKALI-ACTIVATED FLY ASH AND SLAG MATERIALS

-IN VIEW OF LONG-TERM PERFORMANCE PREDICTIONS

## Proefschrift

ter verkrijging van de graad van doctor
aan de Technische Universiteit Delft,
op gezag van de Rector Magnificus prof. dr. ir. T.H.J.J. van der Hagen;
voorzitter van het College voor Promoties,
in het openbaar te verdedigen op woensdag 27 februari 2019 om 15:00 uur

door

**Marija NEDELJKOVIĆ**

Civiel ingenieur,
Universiteit van Belgrado, Servië,
geboren te Lazarevac, Servië.

Dit proefschrift is goedgekeurd door de promotoren:

Prof. dr. ir. Klaas van Breugel
Dr. Guang Ye

Samenstelling promotiecommissie:

| | |
|---|---|
| Rector Magnificus, | voorzitter |
| Prof. dr. ir. Klaas van Breugel, | Technische Universiteit Delft, promotor |
| Dr. Guang Ye, | Technische Universiteit Delft, promotor |
| | |
| *Onafhankelijke leden:* | |
| Dr. Ivan Ignjatović, | University of Belgrade, Servië |
| Dr. Susan A. Bernal López, | University of Leeds, United Kingdom |
| Dr. Sieger R. van der Laan, | Tata Steel, Nederland |
| Prof. dr. Rob B. Polder, | Technische Universiteit Delft |
| Prof. dr. ir. Arjan Mol, | Technische Universiteit Delft |
| Prof. dr. ir. Erik Schlangen, | Technische Universiteit Delft, reservelid |

The work reported in this thesis is the M2i/STW project "Long-term performance of geopolymer concrete systems for production of environment friendly building materials - GeoCon 2" (code M2i: S81.1.13498b/code STW: 13361).







*Keywords:* carbonation, alkali activated materials, curing conditions, relative humidity, pore solution composition, $Na^+$ effective concentration, Na binding capacity, gel phases, $CO_2$ binding capacity, microstructure deterioration, porosity, modulus of elasticity, service life predictions

*Printed by:* Ipskamp Printing, The Netherlands

*Thesis format by:* Marija Nedeljković and Patrick Holthuizen

*Cover design by:* Marija Nedeljković and Yu Chen



ISBN 978-94-6384-020-0

An electronic version of this dissertation is available at
http://repository.tudelft.nl/.

*Mojoj porodici, učiteljima i budućim generacijama*

"Znanje, to su zlatne lestvice koje nas vode u nebesa;
znanje je svetlost koja osvetljava naš put kroz ovaj svet i vodi nas u život budućnosti,
pun neuvele slave."

"Knowledge is the golden ladder over which we climb to heaven;
knowledge is the light which illuminates our path through this life and leads to a future
life of everlasting glory."
Mihajlo Pupin

# ACKNOWLEDGMENTS

"Science is human and humans are never cool. Humans are full of emotion and tragedy". This quote by Victor Weisskopf perfectly describes a doctoral research. The Ph.D. research is full of emotions, questions, influences and it cannot be done in isolation. It moves you from something very empty to something absolutely wonderful. It requires an intense dedication to gaining knowledge, learning important lessons and receiving teachings that add to education and experience. Tremendous excitement, unwavering commitment and passion for doing Ph.D. research, that is what I owe to people who inspired and supported me during past years. Their diverse skills and visions helped moving across the boundaries and framing this thesis.

First of all, a very special gratitude goes to M2i and NWO-TTW for providing the funding for this research.

I would like to express my sincere gratitude to my promotor Prof. Klaas for his clear vision of the importance of science, education and research that boosted large motivation for improvement of this thesis. A fundamental characteristic of Prof. Klaas is to ask the right questions and challenge ideas. Therefore, the time with Prof. Klaas deserves a special name: 'andare a bottega'. This refers to an internship that the apprentice would complete in the master's studio in order to learn what could be uniquely transmitted in person and in that particular environment could then lead to making a unique artist of the apprentice. This is what I was becoming after leaving the master's studio: an artist in science with "onderbuikgevoel" for right answers.

Dr Ye. I would like to express my special thanks to my daily supervisor and promotor Dr Guang Ye who trusted I could do this wonderful Ph.D. project. He was there to expand my understanding about different things, to focus on long-term outcomes rather than on short-term, to support creative ideas and give room for independent decisions and my own opinion. I would certainly lose all that motivation to dig deeper, if I did not have to sweat and struggle my way through this research. Thank you for boosting the curiosity and passion for research and having high expectations for the project outcome. I am very much grateful for involving me in Geopolymer group, various projects, committees, workshops and supporting the idea of the internship in CRC. Xièxiè!

My gratitude goes to Sieger, who provided me with an opportunity to join his team as intern and who gave access to the research facilities in TATA STEEL. Without this precious support, it would not have been possible to conduct some of the most fundamental research in the thesis. I also thank you for regularly rejecting papers we wrote so far, thus inspiring me with the sharpest criticism, profound scientific thoughts and discussions. He kept challenging me to think 'independently' rather than thinking 'topically'! I would like to sincerely thank Enno, Frank, Stefan, Chris, Corrie, James for all stimulating discussions we have had during my internship. There was that amplification aspect in the research. Without you my microstructure characterization experiments would probably not have yielded as many beautiful results.

Besides my supervisors, I would like to thank the rest of my thesis committee: Dr. Susan Bernal, Dr. Ivan Ignjatovic, Prof. Rob Polder, Prof. Arjan Mol for reading the manuscript on a strict deadline, for their insightful comments, but also for the hard questions which incented me to widen my research from various perspectives.

Dr. Susan. If I have seen further it is because of your science. I was very, very lucky to have your pioneering carbonation studies when I have started with my own research and it's remarkable how much knowledge was already there. Nevertheless, I was very convinced and motivated from your findings that carbonation of AAMs is an important mechanism to be further studied. I am very much grateful for great heritage and your encouragement.

Erik. It was a lesson for someone aside to look how person can be engaged to his students. Hvala veliko for being supportive and having 'different' attitude! Most of all, thank you for giving me an opportunity not to leave Microlab. You took care of this Peter Pan, by maintaining my curiosity about concrete very high. To stop that concrete science would be an awfully big failure.

My forever interested, encouraging and always enthusiastic momak: Sale Milenković, my anchor, someone who hold me securely in heavy times. Unlimited thanks for having broad shoulders, continuous optimism and being extremely supportive for your deca. He guards my positive mood and spirit all the way to the end of this Ph.D. journey.
Momak, hvala od srca!

Oğuzhan. "The instruments are not rockets, use them, explore the things, be independent!" Yes, that was a lesson taken home. Thank you for the most wonderful course I have attended during Ph.D. journey. It was like a new world opened to me, the world of minerals and microscopy, which I was at last permitted to know in all details.
Teşekkürler!

Jeanette Visser. The best science always results from ectasies of logic. Heel veel bedankt for fundamentals of carbonation and alkali-silica gel formation. Thanks for all our discussions.

Steffen, Arno, Rob, Viktoria, have shown support for this Ph.D. project from the first presentation back in 2014. Their straightforward and always friendly approach is much appreciated.

I am very much grateful to Prof Dick Hordijk for his support and making possible the constructing of a geopolymer canoe together with students of U-Base from the Concrete structural department! This way, material has anticipated not only societal expectations with regard to sustainable research and innovation, but also involvement of students and learning about the possibilities and limitations of the developed geopolymer composite. At that time, many of us were moved to believe that this material is serving its purpose as a building material. All this would not happen without them, young people who strive and drive with their curiosity and people who recognize this and help them.

TU Delft Research Exhibition 2016 and 2017 enabled reinforcement of relevant stakeholders' realm and society awareness of innovative and sustainable geopolymer concrete. For this I wish to thank Susanne, Robbert, Dorien and Mark from TU Delft Valorisation Centre.

Thanks to TU Delft people who helped me find facilities and professional advice. I thank Ton (for all days I drive you crazy with endless casting and sawing of the concrete

samples, Tontje I am immensely grateful for all your kind words), Albert Bosman (for all manoeuvres and help in the Stevin lab), Ron and Ruud (for all XXL specifications), Jens and Ludo (for all perfect thin sections), Marco, Michele for allowing the use of FTIR room, Sander for hardness tests.

Arjan. Hartelijk bedankt, meneer, for lab experience before I was admitted to real research. The first microscopy and MIP experiments were an opportunity to find out whether I enjoy the challenges of the research and whether I have the fortitude to deal with all the failures. Thanks for all refreshing coffees, life and lab important lessons!

Thanks to John who helped me with multiple experiments. Without his help I would not get some of the most important conclusions in the thesis. You cheered my day with "Ja sam za ples" (Novi Fosili) and "Pozdrav svetu" we would sing together in the lab.

Knowing Maiko I never lacked an enthusiastic person whom I could ask for help at any time. He would appear as a rainbow and spoil me with all his positive energy whenever I was desperate. Thanks to Danielle, Nienke, Jari for all the hospitality and all enjoyable moments during our memorable summer parties at the famous Maikovic's garden.

I am very much grateful to Nynke (my special thanks for allowing Patrick to join the concrete nest), Iris, Claire, Anneke, meneer Jaap (for whom I would always be "mevrouw Nedel'ković", bedankt voor alle grapjes en glimlachen) for their unfailing support and assistance for managing my stay in Microlab.

Building a supportive learning culture around empowers growth and passion. An important group of people is geopolymer group. I would like to thank all people with whom I was working and who taught me about this material in various versions, Zhenming, Yibing, Kamel, Siyu Li, Shizhe, Boyu, Albina, Bahman, Yubo, Zainab, Silke, Xuhui. I wish to thank also to Yuwei Ma. Your thesis gave the basis for all that came after in my thesis. Thank you for that heritage. I would like to thank Kamel for support from the very start of this ambitious project. We did hundreds of experiments around mixture design development before we got something we were comfortable with. It was that fast iteration, getting the teams together and not try to design for perfection but design for further research. The end result was a variety of promising mixing ratios in terms of durability leading to ultimate use of geopolymer concrete in the real-life applications. Thank you for your constructive feedbacks, being accessible for discussion and helping to set goals. Furthermore, discussions with Yibing and Zhenming yielded many of conclusions in this work. I appreciate all the insights you shared with me. Bahman, I would like to thank you for giving me substantive feedback and useful tips on writing. I am extremely grateful for your support both academically and otherwise. Džejmi, thank you and your amazing family for friendship and introducing me to Chinese life and culture, which I deeply appreciate. Nobody could make my mood better than you!

Microlab and Microlab's people. What a cracking place to be with the people who inspire ideas, possibilities, innovation, changes! In this research community I made memories and friendships that I will remember for a lifetime. The four years were fully filled with sharing the knowledge, celebrating birthdays, welcoming Christmas, spending summers in laboratories, drinking in concrete nest, cooking, learning languages. I have learnt new world in the perfect environment. My concrete nest: Claudia (my chica with Latin charm), Stefan (my man) and your beloved persons Bianca and Fernando, who were there when things did not go as planned, who stuck around, and who lift me

up with all your energy and passion. Obrigado! Thanks also goes to: Bei, Bart, Yask, Jiayi, Yu Chen, Xuliang, Hao, Tianshi, Wenjuan, Yong, Hongzhi, Shi Xu, Yading, Henk, Desi, Renée, Kuba, Emanuelle, Gabriel. Some of colleagues have moved on to new endeavours before I finished Ph.D. Thank you Virginie Wiktor, Amir Tabaković, Hitham, Xu Ma, Balqis, Senot, Zhuqing Yu, Hua Dong, Farhad, Eirini, Martin, Peng Gao, Jose, Natalie, Lupita, Josepha, Xiaowei, Leyang, Damian.

I am indebted to the unflagging enthusiasm and dedication of Jeannette. Thank you for introducing not only me but also my family to Dutch festivities, Bloemencorso, famous Lisse and Boerderijdagen. Thank you for unforgetable cargo ship adventure and journey. I was impressed with your talks to captain about cathodic protection of the cargo ship, since the terms were not in my clearly limited engineering dictionary. Then, numerous experiences from the building sites which we could finally see from the sea side of the Copenhagen. Very important to highlight, your advices initiated my visits to the companies involved in the project. There it started all and it ended successfully. Hartelijk bedankt voor alles!

I was immensely lucky to have my Serbian predecessors at CITG who became very important to me during the last years. Luka, Mladena, Branko, Andrija and Aleksandra. As junior researchers, we need to see how the job is done by someone who has experience and enjoys doing it. Your enthusiasm inspired me as well as pushed the overall research forward. I thank Mladena who helped to foster many ideas in this work. Thanks for equipping me with the skills I was needed to successfully perform research, a readiness to accept failure, resilience, persistence, the ability to troubleshoot and a willingness to commit to very hard work. Branko, thanks for being always there and thanks for very constructive revisions, life important advice and support. On the top of all, thanks for making me feel as Luka's tetka. Luka, moj momak. Thanks for all smiles and being constant source of happiness and perfect moods. Andrija, thank you so much for taking care for me as for younger sister. All advice and critics improved my professional attitude toward the world generally. Thanks for always being cheerful about life. I would not imagine better older brothers than you and Branko! Aleksandra, thanks for all wedding plans and ideas you shared with me. I could not have a better wedding adviser!

My Serbs in Delft. It is the friends we meet along the way that help us appreciate the journey. Thank you for all birthdays parties, dinners, drinks, your trust for caring after my younger friends, for supporting virtual roommate: Jaca, Darko, Zoe, Teo, Uli, Steva Nadj-Perge, Marko, Ana, Višnja, Đurđa, Vukašin, Mira, Mare, Jova, Katarina,
Violeta, Dimitrije, Zvezdana, Uroš.

Ivan, Nikola, Jelena, Profesorka Sneška, Miša Stojanović. My ideas about geopolymers starting forming in my homeland, Serbia. Thank you for giving me opportunity to do research and master project on a strict deadline. I was really astonished by all calculations from Jelena and Nikola regarding chemistry and mixture design for the first geopolymers. Making geopolymers with setting time of only a few minutes and curing of the geopolymer concrete cubes in an oven at 80° degrees, was against all the theories I have learnt for traditional cement concrete. This blew my mind. How does this even exist? I would never imagine there is something to be made from by-products, all but not the concrete. I got unbelievably inspired by seeing this, and instead of shutting it down, I decided, let's take it seriously. I used every waking hour during my master project, try-

ing to learn about alkali activated materials, whatever it was. And after five months of hanging around with these people, the knowledge grew by 10 times. In another 4 years, it grew by 100 times. You make me love not per se this material, but more the science in all its shapes. Veliko hvala!

My maths professor, Toma Đuričić: I miss our short-lasting maths classes. Thanks for all maths competitions and best burek in Valjevo! Thanks for all Novak's tournaments you had to miss in order to teach me maths and prepare for becoming one day a Civil Engineer!

Moja razredna, Prof. Biljana Jovanović. Her enthusiasm, wise thoughts, work ethics and discipline, long discussions and advice matter the most for our academic performance. Thanks for creating perfect conditions to fall in love with literature, with different cultures and places. Reading books has provided me with a wonderful opportunity to reach the farthest destinations abroad and imagine the future of a scientist. Thanks generation '90s for our cheerful reunions!

Prof. Mirjana Daničić. Draga moja profesorka, I still owe you a big hug of gratitude! Without ever considering something in return, you would always be there to just do it and help with certificates of my annual evaluations. I am much grateful for all the kind words and support.

Prof. Mina Stanojević. I think it is all your responsibility for excellent international internships and interviews I have had. I could hardly talk English six years ago. Today, I succeed in expressing my opinions and writing this dissertation. That is how valuable your lessons were. Many thanks to you and Lila for all your sweetness, love and support.

Dragan Baškalović, my colleague and my great friend from the West. Dragan was my huge enthusiast and fan with regard to finishing Ph.D, which he would often refer to as a sport activity. Nothing could stop us from writing novels of strategies, events and plans from Vancouver to Delft and back. Thanks for all support and care during all Ph.D. tournaments.

I am also grateful to my family members and friends who have supported me along the way: moje kumice Duki and Kiki, Jole, Momir, Daša, Saška, Rade and Sneža, tetka Goca, teča Pera, Miloš, Sanja, tetka Zoka, teča Zoran, Cale, Rade, Vuja, ujko Dule Mirković, čika Mića, tetka Ceca, my Nedeljkovići from Moravci, Milica and Mladen, Ivana Milosavljević, Bobica, Vilma, Bernardeta, Milica Bugarčić, Jovana Mančić, Lidija, Mladjo, Miki, Mare, Milan, Saša, Dušica, Diana, Fanni, Souvik. Thanks for always being close by, despite the distance.

Several families have contributed to making me feel at home during my stay in the Netherlands: Tetka Anđelka and Cees, Brana and Janni, Andreja, Eline, Marco and Marcela, thanks for the warm welcome every time I come to Gouda and for great fun. Anđelka and Cees, thank you for being my second parents in the Netherlands and your care. I felt I am really that "daughter" which I cannot express my gratitude for accepting me as such.

My second family in the Netherlands, mamsie, papsie, Vincent, Christa, tante Marijke, for all the warm welcomes, Nederlands leren, and for your infinite support and enthusiasm throughout these three years. Thanks for having so much patience for all cancelled dinners and late comings. I will never forget our Sinterklaas and Christmas dinners and trips to Serbia. My Dutch friends: Mitchel, Anna, Sophie (mijn kleine prinses), Stef, Dave, Cansu, Danny, Linda, Roy, Dion, Kim, Baptiste, Frank Brands, Huibert, Marique,

Leon, Vanessa, Greet, Bert, Ada, I feel very honoured to get to know you and learn so much about Dutch culture.

I would like to thank my beloved, wonderful, cheerful, inspiring, unique Nedeljković family: mother Ankica, father Radiša, grandma Mica, grandpa Milenko, Pera, for their everlasting love and encouragement, for teaching me the importance of honesty, integrity and hard work in all that I do. There is nothing like the magic and inspiration that comes from the parents. I wish to thank my sister Milica (my passionated professor of Russian) and brother Ivan (my future colleague) for being my paranymphs, my best friends. It is like I would never fail while I would have you two and the same hold for life. Volim vas najviše na svetu!!!

Finally, my fiancé. It was a short step from interest in carbonation to the desire to act together, to decide to embark together on a journey of science and life between Serbia and the Netherlands! You deserve all the credits for pulling one of the journeys to the end. Thank you for your immense help in finishing this thesis (making it more beautiful than I wish to be) and allowing me to work on it day and night. It was a literal alignment of two minds into a shared consciousness. Thank you for tremendous criticism, neverending patience, tolerance, inspiration, silver lining, all happiness and love, Patrick!

*Marija Nedeljković*
*Delft, January 2019*

# CONTENTS

# 1

# INTRODUCTION

*"Divide each difficulty into as many parts as is feasible and necessary to resolve it."*

René Descartes

*This chapter presents the background of the research. The carbonation assessment of alkali-activated materials and barriers for their standardization are briefly summarised. The aim and objectives, scope of the research, methodology and outline of the thesis are given.*

1

## 1.1. RESEARCH BACKGROUND

CEMENT-BASED CONCRETE is used as a main material for infrastructures and buildings. Concrete structures have shown to be safe and durable, and this was one of the most important criteria for their design and use in the past. Nowadays, however, the sustainability requirements present the main challenge for concrete construction industry [1, 2]. More specifically, there are several aspects, which should be considered and improved in the current cement concrete production. Most important are high $CO_2$ emission and high energy consumption due to $CaCO_3$ calcination and clinker production [3–5]. Currently, the cement industry accounts for approximately 5-8.6 % of the global $CO_2$ emissions [1, 6, 7]. The regulations on the permissible level of emission of $CO_2$ make it necessary to innovate and improve the energy efficiency and provide environmentally friendly alternatives for cement industry. To fulfil sustainability criteria of reduced $CO_2$ emissions, low $CO_2$-emission cements are needed. Furthermore, production of waste from various industrial processes is a concern, as most of the waste cannot be landfilled and thus presents a burden for both its producer and the environment [8]. Replacement of ordinary Portland cement (OPC) by supplementary cementitious materials (SCMs) [9] is one of the possibilities to reduce the environmental impact of OPC production as shown in Figure 1.1.

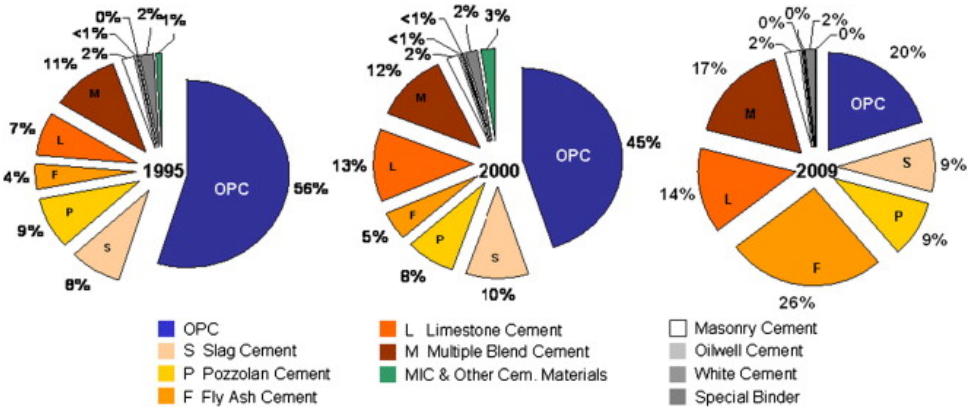


Figure 1.1: Cement types produced by Holcim 1995–2009 [5].

Commonly, SCMs are by-products from industrial processes, such as fly ash (FA) from coal-fired electricity production and ground granulated blast-furnace slag (GGBFS) from steel production [10]. The extent of replacement of OPC is limited by the composition and reactivity of the SCMs [9]. In fact, FA and GGBFS can completely replace OPC by taking advantage of alkali activation [4]. In this case, alkali activated materials (AAMs) or geopolymers are produced. AAMs is the broadest classification, encompassing any binder system derived by the reaction of an alkaline salt (alkali hydroxides, silicates, carbonates, sulfates, aluminates) with a solid silicate powder (GGBFS, FA, natural pozzolan or bottom ash) [11]. Geopolymers are a further subset of AAMs, an inorganic polymer cement synthesized via alkaline activation of aluminosilicate precursors (FA, kaoline,

metakaoline) [11, 12]. The term geopolymers was introduced by Davidovits in the period 1976-1979. Davidovits has defined geopolymers as a material that originates from inorganic polycondensation, called geopolymerization. Geopolymers[1] represent materials on the transition between glass and ceramics [13]. However, nowdays the usage of geopolymers is not limited only to ceramics but is considered to have a great potential to become a construction material in the building industry. In the Netherlands, the utilization of geopolymer concrete has been recommended by the CUR committee as one of the 7 high potential actions towards the Dutch initiatives on further lowering the $CO_2$ footprint of concrete [14].

Today a lot of research has been devoted to the development and characterization of AAMs [15–37] to promote their use because of their "green" nature. However, widespread use of AAMs in engineering practice and structural applications is limited by lack of standards and understanding of their long-term behaviour [11, 38, 39]. The use of alkali-activated concrete actually got its reputation from past applications (1980s and 1990s) as recognized only in several reports [40–42]. So far AAMs are increasingly used for non-structural applications. An effective strategy to increase the confidence in using AAMs for structural applications is to study their long-term performance.

In general, the deterioration mechanisms of concrete and their rate are controlled by the environment, the microstructure, the chemical stability and the fracture strength of the concrete [43, 44]. Deterioration of reinforced OPC-based concrete structures is often caused by the corrosion of reinforcing steel. Corrosion of reinforcing steel in concrete is mostly a result of chloride ingress and/or carbonation [45–47]. The assessment of the durability of OPC-based concrete is defined in the European Standard EN 206-1 [48], which describes durability in terms of minimum cement content, maximum water/cement ratio and minimum cover depth. This approach is inadequate for concrete structures made with alternative cements such as SCMs cements (blended systems of OPC, FA, GGBFS, silica fume, metakaolin, rice husk ash) or alkali-activated cements (FA, GGBFS, metakaolin, waste glass) due to their different reaction kinetics and microstructure features [41]. Major discussions regarding long-term performance of AAMs are focussed on their behaviour under carbonation, the general validity of the carbonation assessment methods and the prediction of their service-life in view of carbonation. For this reason, the research background of this thesis consists of three topics as stated next.

1. Defining an adequate methodology for testing carbonation of AAMs. RILEM TC 224-AAMs [49] addressed durability of AAMs as a main obstacle for their standardization. TC 224-AAMs puts an immense effort towards investigation and specification of reliable methods for durability testing with special attention to accelerated testing. The method for testing durability of alternative cement-based concretes is usually a standard approach valid for OPC-based concrete. For example, the standard approach to test the carbonation resistance of OPC-based concrete is determined by standard accelerated tests under relatively high $CO_2$-concentrations and fixed relative humidity (EN 13295:2004 [50]; Draft BS ISO/CD 1920-12 [51], EN 14630:2006 [52], RILEM CPC-18 [53], NORDTEST METHOD: NT Build 357 [54], Portuguese Standard LNEC E391 [55], French test method AFPC-

[1] The term alkali activated materials (AAMs) will be used throughout all thesis, instead of geopolymers.

AFREM [56]). These accelerated tests should be the basis for making a reliable prediction of the progress of carbonation in natural conditions. However, these standard accelerated tests do not contain recommendations on how the results of accelerated tests can be extrapolated to the natural conditions of carbonation. Furthermore, no recommendations are yet given to the researchers and engineers as a general approach for testing of AAMs.

2. Multiscale assessment of the carbonation mechanism of AAMs. For service-life predictions of AAMs in view of carbonation it is necessary, first, to understand the mechanism and define the parameters of critical influence on the carbonation rate. However, carbonation resistance of alkali-activated concretes is under debate for almost 20 years [19, 57–70]. The carbonation complexity of AAMs extends from atomistic scale to milimeter scale. The overal change is driven by multiple changes in the paste microstructure and microstructure between the paste and aggregates. The effect of carbonation on material properties (physical, chemical and mechanical), from multiscale point of view, has not been studied sufficiently to be considered in development of carbonation model or design of alkali activated concrete structures.

3. Limited number of case studies of long-term performance of alkali-activated concretes in the past. Limitations concern the type of environment (only limited number of case studies is known from a few decades ago in China, Ukraine, Russia [40]), the type of raw materials (Portland-blast furnace slag, slag and fly ash with unknown exact origin), the mixture design (type of aggregate, raw materials and alkaline activators, liquid-to-binder ratio) and the curing conditions (temperature, sealed/unsealed). The lack of data on long-term performance of alkali-activated concretes makes it challenging to support the predictive models of the service life of alkali activated concretes.

## 1.2. RESEARCH AIM AND OBJECTIVES

The above stated problems led to the definition of the research aim. The research aim concentrates to understanding the carbonation mechanism of alkali-activated materials and focuses on strategies to improve their performance in view of carbonation. To reach this research aim, the following objectives are made:

- to develop paste and concrete mixtures for carbonation study;
- to propose a methodology for investigation of pore solution composition and microstructure formation of alkali activated pastes;
- to propose a methodology (carbonation conditions, monitoring parameters, characterization techniques) to investigate the carbonation mechanism of alkali-activated pastes;
- to investigate the effects of carbonation on chemical properties ($CO_2$ binding capacity, pore solution composition, gel nanostructure, minerology of the reaction

products), physical properties (pore volume, pore size distribution) and mechanical properties (modulus of elasticity) of the pastes;

- to define the mechanism that drives the carbonation front in order to predict the long-term properties of alkali activated concrete due to carbonation;
- to recommend the curing conditions and alkali activated concrete mixtures for improved carbonation resistance in service.

## 1.3. RESEARCH SCOPE

In this research, two types of industrial by-products are used, GGBFS and low Ca- siliceous FA. Both, GGBFS and FA, are defined in EN 206 [48] as a type II addition in the production of concrete, as a pozzolanic or latent hydraulic additions. The NEN-EN 15167-1 specifies requirements for the chemical and physical properties as well as quality control procedures for GGBFS. NEN-EN 450-1 defines the same for FA. The GGBFS, FA and their blends are alkali activated with a mixture of sodium hydroxide and sodium silicate solutions. The experimental research considers the chemical and mineralogical characterization of the raw materials (GGBFS and FA), alkali-activated GGBFS and FA and carbonated alkali-activated GGBFS and FA pastes. The information with respect to the carbonation at the gel level (Level I) and paste level (Level II) has been used for carbonation study at the concrete level (Level III) (see Figure1.2).

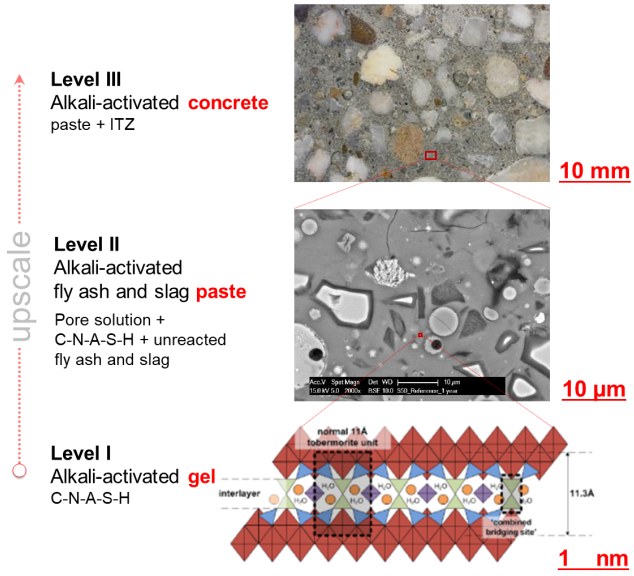


Figure 1.2: Three level concept.

In contrast to current literature, where usually gel is studied for carbonation mechanism, an other approach at the paste level is proposed in this thesis. This choice is

based on the chemical composition of raw materials and the tendency of alkali binding by the gel in alkali activated pastes. Moreover, the study comprised the carbonation of both: the pore solution carbonation and gel carbonation. Testing the pore solution at the paste level is also more important for understanding carbonation as shown by Sawada et al. [71] than at the concrete level. The pore solution analyses are specifically important for prediction of the carbonation rate. In addition, the influence of carbonation on the physical and mechanical properties at the paste level is the first step towards understanding the properties of carbonated concrete.

Finally, the understanding of the carbonation mechanism generated by this thesis is limited to the composition of the studied mixtures. However, the methodology for studying the carbonation mechanism, can be applied for any cementitious material.

## 1.4. RESEARCH METHODOLOGY

To understand the deterioration mechanism of alkali-activated materials due to carbonation, focus of this study will be on experimental testing of carbonation. Carbonation is studied in two systems: in the alkali-activated pastes and in the alkali-activated concretes. The pastes are designed with FA to GGBFS ratios by weight of 100:0, 70:30; 50:50, 30:70, 0:100.

First, chemical compositions of phases in the raw materials, i.e. GGBFS and FA, were assessed. Next, a PhAse Recognition and Characterization (PARC) software, extensively used for microstructure characterization of metallurgical slag produced in steelmaking [72, 73], was for the first time used to determine the spatial distribution (area/volume percentage) of the dominant reaction phases and chemical composition of AAMs as a function of different curing conditions. The phase characterization provided stoichiometry of the phases and the rate of gel formation, which were necessary for assessment of the carbonated alkali activated pastes.

To study the carbonation mechanism, pastes were ground to a powder to enable faster carbonation, with a focus on reactivity of $CO_2$ and maximum $CO_2$ uptake of different mixtures. In parallel, carbonation was studied in bulk alkali-activated pastes in terms of $CO_2$ reactivity and diffusivity, while capturing the effect of carbonation on the pore solution, pore structure and mechanical properties. Different exposure conditions were investigated: accelerated conditions and natural carbonation (indoor laboratory and outdoor sheltered) conditions. In this way, the thesis may shed light on the role of exposure conditions, such as relative humidity (RH) and $CO_2$ concentration on carbonation mechanism at the paste level.

For characterization of carbonated powdered pastes several techniques were used: Fourier transform infrared spectroscopy (FTIR), X-ray diffraction (XRD), Thermogravimetric (TG) analysis and Mass spectroscopy (MS) method. The gel molecular structure was investigated with FTIR. The products of carbonation were determined and quantified by XRD and Rietveld refinement method, respectively. The water content and $CO_2$ binding capacity of alkali activated pastes were measured with TG-MS.

Chemical changes of the bulk pastes along the carbonation path in natural exposure conditions were studied with PARC. The calculated results were validated with bulk analytical techniques such as X-ray fluorescence (XRF) and XRD. Element profiles (C, O,

Na, Mg, Si, Al, S, Ca) were derived for element spatial distributions along the carbonation depth. In addition, the depth positions of carbonation, oxidation and dissolution fronts were identified. This helped to investigate which mechanism drives the fronts. The effects of carbonation on the pore structure and modulus of elasticity were tested by nitrogen ($N_2$) adsorption, mercury intrusion porosimetry (MIP) and Nanoindentation method, respectively. The study on paste enabled comprehensive assessment of the local and bulk carbonation.

The alkali-activated concretes were also exposed to different environmental conditions, i.e. accelerated, natural laboratory indoor, natural outdoor sheltered conditions. The carbonation rate in all exposure conditions was monitored by measuring the carbonation depth using phenolphthalein indicator combined with Polarized optical microscopy.

Beside carbonation depth, pH measurements, microstructure and ITZ characterization, the compressive strength of alkali activated concretes was also monitored in natural outdoor conditions. The results are compared with results in cement-based concretes and discussed in view of their aim of predicting the service life of alkali-activated concrete.

## 1.5. THESIS OUTLINE

The thesis outline is given in the Figure 1.3. As discussed previously, the aim is to understand the carbonation mechanism at the micro-scale (paste) and to pass information to the meso-scale (concrete). The thesis is divided in four parts. The **PART I** presents the research background and existing results with respect to the carbonation of AAMs. This leads to the origin of the thesis frame. In **PART II**, development of the alkali-activated paste mixtures and their characterization was given as a basis for carbonation study. **PART III** explains carbonation mechanism and effects of carbonation on the micro properties of the alkali-activated pastes. **PART IV** is dedicated to the carbonation of alkali-activated concrete. The content of each chapter is summarized as follows:

Chapter 2 reviews the carbonation mechanism in OPC and alkali-activated materials in the context of available literature. The main differences regarding the pore solution and microstructure properties between these two groups of materials are recognized and addressed. The overview of the carbonation mechanisms, crucial factors, and carbonation modelling in OPC-based materials in contrast to AAMs, is given.

Chapter 3 presents the development of mixture design for alkali-activated FA and GGBFS pastes which are studied for carbonation mechanism. The effect of the mixture compositions on their workability and mechanical properties is presented. In addition, the reaction kinetics is studied for selected mixtures, which are further investigated in Chapter 4.

Chapter 4 deals with microstructure and pore structure characterization of the alkali-activated pastes prior their exposure to carbonation. The spatial distribution of the dominant reaction phases, their chemical composition and area/volume percentage were

determined. The microstructure characterization was done with PARC, $N_2$ and MIP.

Chapter 5 investigates the $CO_2$ binding capacity of alkali-activated pastes and provides basic understanding on the carbonation potential of studied mixtures. Cement-based pastes were also studied to provide a baseline for comparisons.

Chapter 6 evaluates the effect of the curing, exposure conditions and binder composition on the pore solution chemistry. The pore solution composition and pH of the carbonated pastes were studied with ICP-OES, in parallel with investigation of the chemical changes by FT-IR.

Chapter 7 evaluates the microstructure changes due to carbonation. Areas between the identified fronts (carbonation, oxidation, and dissolution fronts) were thoroughly studied with relation to the chemical composition of the phases, their spatial distribution and area/volume percentage. Element zonation (C, O, Na, Mg, Si, Al, S, Ca) provided the most distinct spatial distribution.

Chapter 8 evaluates the effect of carbonation on physical and micromechanical properties with MIP, $N_2$ and Nanoindentation, respectively. The changes of the chemical properties due to carbonation which are defined in Chapter 7, affected the physical and micromechanical properties, i.e. pore size distribution, pore volume and modulus of elasticity.

Chapter 9 presents a critical assessment of the carbonation mechanism in alkali-activated pastes, based on results from the previous chapters. The relationship between chemical, physical and mechanical changes due to carbonation is established. Carbonation degree, changes of the gel nanostructure, carbonation products and $CO_2$ binding capacity are discussed for pastes which were exposed in accelerated and natural carbonation conditions.

Chapter 10 presents the effects of the different carbonation conditions on the pH and compressive strength of alkali-activated concrete in comparison to cement based concretes (CEM I and CEM III/B). The influence of carbonation on ITZ is investigated in alkali activated concrete The results were interpreted using knowledge that was generated in the **PART III**. Service life predictions of alkali activated concrete with regard to carbonation are presented in Appendix B.

Chapter 11 concludes with the summary of the main findings and conclusions from **PART II, III, IV** regarding microstructure formation of the developed mixtures and the carbonation mechanism in the selected mixtures. Based on experimental evidences, the recommendations for structural application of alkali-activated concretes are given with respect to curing conditions and long-term performance due to carbonation. Furthermore, research perspectives for future studies are proposed.

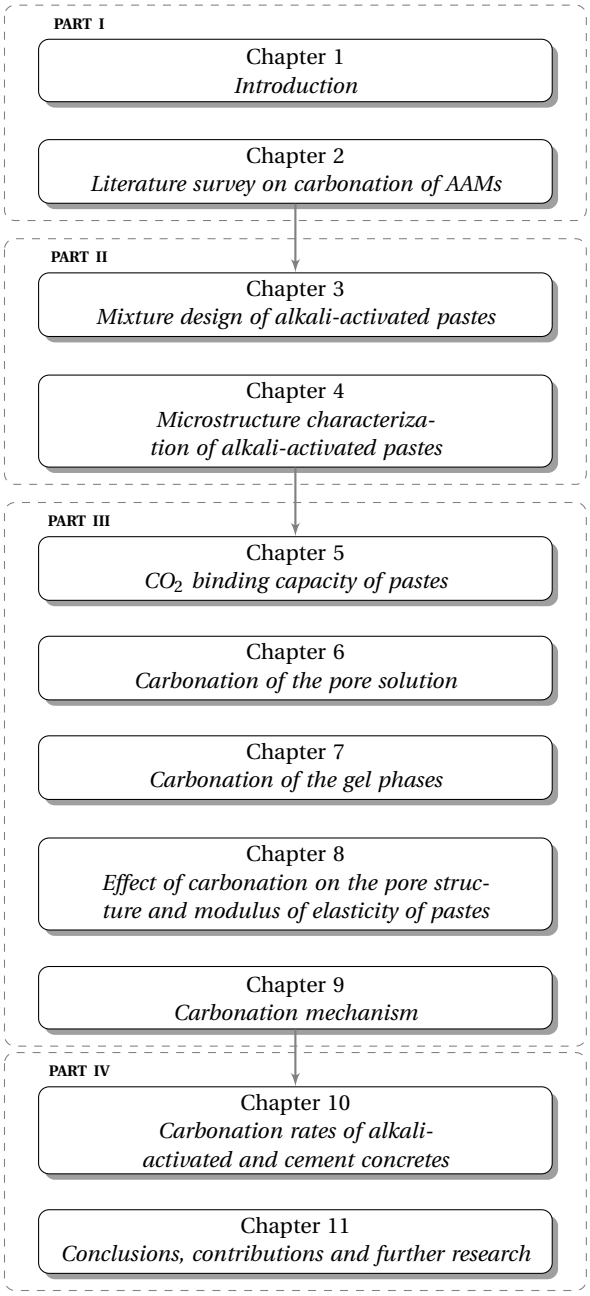


Figure 1.3: Thesis outline.

# 2

# LITERATURE SURVEY ON CARBONATION OF AAMS

*"No one wants to learn by mistakes, but we cannot learn enough from successes to go beyond the state of the art."*

Henry Petroski

*In this chapter, mixture designs for AAMs are first reviewed in relation to different properties of raw materials and alkaline activators. Then, carbonation mechanisms in OPC-based materials and AAMs are presented with respect to the current literature findings. This review focuses on the carbonation of the two main binder components, pore solution and gel phases (C-S-H, C-(N-)A-S-H), and the driving forces controlling the carbonation of these components. The effect of carbonation on the chemical, physical and mechanical properties of different materials is also reviewed. The existing predictive models for carbonation in OPC-based concrete are presented and questions regarding carbonation modelling in AAMs are addressed. Based on the current literature state of the art, the relevant issues regarding carbonation mechanism investigation are stated.*

## 2.1. ALKALI-ACTIVATED MATERIALS: MIXTURE DESIGN

THE DURABILITY of reinforced Ordinary Portland cement (OPC)-based concrete is related to the resistance of concrete to various degradation mechanisms (i.e. carbonation, chloride ingress, alkali-silica reaction, acid attack) that reduce its performance over time. The durability of alkali-activated materials (AAMs), similar to OPC-based materials, is mainly dependent on the microstructure features of the binder (e.g. phase assemblages and pore structure), which can be modified using different constituents and materials mixture designs. In the mixture design of AAMs, the most used raw materials are fly ash (FA), ground granulated blast furnace slag (GGBFS) and metakaolin. They react with alkaline solutions, including mostly alkali metal silicates and hydroxides, to form reaction products [74].
Parameters that are broadly studied for mixture design of alkali-activated systems are the properties of:

- raw materials (chemical composition [40], reactivity, surface area [57], particle size distribution [12] and loss on ignition) and
- alkaline activators (modulus and dosage of alkaline activator, pH of activator, viscosity of activator, water-to-binder ratio).

The critical parameters which dominate mixture design of AAMs are presented in the following sections.

### 2.1.1. RAW MATERIALS

#### 2.1.1.1. FLY ASH

FA is one of the most available resources for geopolymerization [75]. The chemical composition of FA defines this material as aluminoslilicate material. It was used for the very first time as starting material in mixture design of alkali activated binders by Glukhovsky in 1950s [24].

FA requirements for mixture design are presented in Table 2.1. A relatively high portion of silica ($SiO_2$), or the sum of $SiO_2$, alumina ($Al_2O_3$) and iron (III) oxide ($Fe_2O_3$), is needed to ensure that sufficient potentially reactive glassy material is present in FA. When FA with high CaO content is activated in an acidic or basic environment, the effect of a high calcium concentration typically leads to the acceleration of the rate of reaction. In a pozzolanic reaction between FA and $Ca(OH)_2$ or calcium silicate phases in OPC-based paste, the early reaction may be so rapid that it will be unsuitable for applications that require longer workability or setting time. Therefore, FA Class F (Table 2.1) is preferred in OPC-based materials and alkali activated binders due to the high content of amorphous aluminosilicate phases and low CaO content [76].

Loss on ignition (LOI) is a measure of unburnt carbon present in FA. It affects the quality of FA by increasing the water demand, increasing the fineness and reducing the pozzolanic activity. A maximum 5% of LOI is specified by EN 450-1 and 6% according to ASTM C618. A high level of $SO_3$ in cement-based concrete containing FA can lead to volume instability and thus loss of durability, due to formation of ettringite. Therefore EN 450-1 allows maximum 3% and ASTM C618 (2008) 5% of $SO_3$ in FA.

Fernandez-Jimenez et al. [77] observed that the fineness of FA has an important effect on the development of the strength of alkali activated systems. It was reported that, when the mean particle size was lower than 45 µm, strength increased remarkably, reaching 70 MPa after 1 day. Beside the mean particle size, Van Jaarsveld et al. [18] reported that the surface charge on the FA particle affects the initial setting properties of an alkali activated FA.

Table 2.1: Specifications for fly ash according to EN 450-1 and ASTM C618.

| | Low calcium fly ash | High calcium fly ash |
|---|---|---|
| Source | Bituminous coal and anthracite | Sub-bituminous (black lignite) and lignite |
| Type of binder | Pozzolana | Pozzolanic and hydraulic binder |
| EN 450-1 requirements | Class V<br>Silica fly ash | Class W<br>Calcareous fly ash |
| | $SiO_2 + Al_2O_3 + Fe_2O_3$ ≥70%<br>≤10% reactive CaO<br>≥25% reactive $SiO_2$<br>$SO_3$, max: 3,0%<br><5% LOI<br><1% free lime | ≥10% reactive CaO<br>≥25% reactive $SiO_2$ when CaO is 10-15%<br>If CaO >15% the compressive strength ≥10 MPa at 28 days (EN 197-1)<br><5% LOI |
| ASTM C 618 requirements | Class F | Class C |
| | $SiO_2 + Al_2O_3 + Fe_2O_3$ ≥70%<br>Free moisture, max 3,0%<br>LOI, max 6,0%<br>$SO_3$, max 5,0%<br>CaO, max: No limit<br>Amount retained when wet sieve on 45$\mu$m: max 34% | $SiO_2 + Al_2O_3 + Fe_2O_3$ ≥50%<br>Free moisture, max 3,0%<br>LOI, max 6,0%<br>$SO_3$, max 5,0%<br>CaO, max: No limit<br>(Note: CaO ≥10%<br>Amount retained when wet sieve on 45$\mu$m: max 34% |

#### 2.1.1.2. GROUND GRANULATED BLAST FURNACE SLAG

Due to its high reactivity GGBFS is the most suitable raw material for alkali activated cement. It has already been used in alkali-activated GGBFS-based concrete for structural applications worldwide [40]. The hydraulic activity of GGBFS can be measured in various ways. One of the method is by calculating the basicity coefficient which is calculated using wt% of oxides, Eq. 2.1:

$$K_b = \frac{CaO + MgO}{SiO_2 + Al_2O_3} \tag{2.1}$$

Based on the basicity coefficient, the GGBFS can be classified into three groups: acid ($K_b$<1), neutral ($K_b$=1), and basic ($K_b$>1). Neutral and basic GGBFS are preferred as starting materials for alkali activated binders. To ensure good hydration properties, the hydration modulus (HM), which is defined for GGBFS according to Eq. 2.2 and calculated

using wt% of oxides:

$$HM = \frac{CaO + MgO + Al_2O_3}{SiO_2} \tag{2.2}$$

should exceed 1.4 reported by Chang [78].



### 2.1.2. ALKALINE ACTIVATORS

#### 2.1.2.1. TYPE OF ACTIVATOR

Alkaline activation of raw materials (FA, GGBFS) is a chemical process of multiple steps. Alkaline activation can be attained by alkaline components as carbonates, hydroxides and silicates. Alkaline activator is mainly a compound from the element of the first and the second group in the periodic system of elements (Na, K, Ca). Positive ions ($Na^+$, $K^+$, $Ca^{2+}$) compensate the negative charge of Al that is present in the coordination 4 [79] in three-dimensional alumina-silicate network configurated of $SiO_4$ and $AlO_4$ tetrahedrons linked by oxygen bridges. The mechanism of alkaline activation starts with breaking of Si-O-Al bonds in a strong alkaline environment (pH value above 13) [74].

Glukhovsky [80] classified alkaline activators into six groups according to their chemical composition:

1. caustic alkalis: MOH
2. non-silicate weak acid salts: $M_2CO_3$, $M_2SO_4$, $M_3PO_4$, MF, etc.
3. silicates: $M_2O{\cdot}nSiO_2$
4. aluminates: $M_2O{\cdot}nAl_2O_3$
5. aluminosilicates $M_2O{\cdot}Al_2O_3{\cdot}(2\text{-}6)SiO_2$ and
6. non-silicate strong acid salts: $M_2SO_4$,

in which M stands for Na, K, 0.5 Ca.

For basic GGBFS alkaline activators from the first 3 groups can be used. For neutral and acid GGBFS, activators from the first and the third group ensure hardening in ambient conditions. Activators from group 2, in combination with activators from groups 1 or 3, can be used for neutral and acid GGBFS [81].

Despite the fact that NaOH, $Na_2SO_4$ and $Na_2CO_3$ are often used as activators [82, 83], the majority of studies have found that activation with sodium silicate or sodium silicate blended with NaOH gave the highest mechanical properties for both alkali-activated GGBFS and alkali activated FA systems. Different activators have different effects on properties of AAMs [17, 77]. Similarly, the type and concentration of activator may substantially influence the carbonation mechanism.

#### 2.1.2.2. MODULUS AND DOSAGE OF ALKALINE ACTIVATOR

The activator modulus is the mass ratio of the $SiO_2$ to the $Na_2O$ in the alkaline silicate activator. The dosage of activator in terms of % $Na_2O$ is defined as the ratio of the $Na_2O$ content of the alkaline activator to the mass of the binder. Wang et al. [57] found that both activator modulus and dosage of activator have a significant influence on the strength of alkali activated GGBFS-based mortars. In an activator containing sodium silicate or blended sodium silicate and sodium hydroxide, there is a competing effect between activator modulus and sodium dosage. Furthemore, the optimum activator

modulus of waterglass solution varies with the type of GGBFS, i.e. 0.75-1.25 for acid GGBFS, 0.9-1.3 for neutral GGBFS and 1.0-1.5 for basic GGBFS (see Figure 2.1).

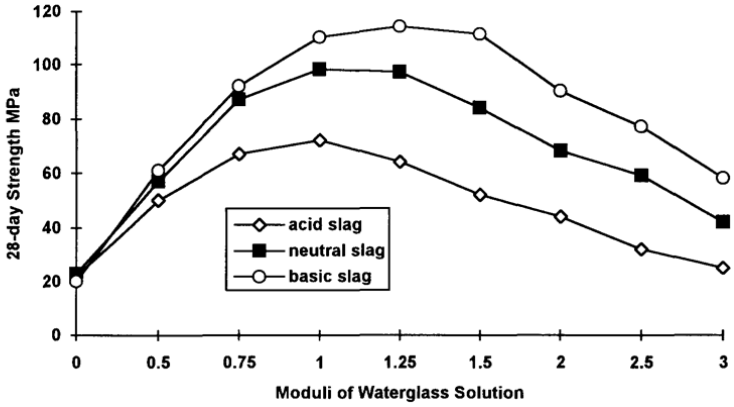


Figure 2.1: 28-days compressive strengths of alkali silicate-activated GGBFS mortars, cured at 20 °C, as a function of the modulus of the activating solution. The GGBFS had a fineness of 4500±300 $cm^2/g$, with an alkaline solution/GGBFS ratio of 0.41 and a sand/GGBFS ratio of 2.0, adopted from [57].

According to literature the $Na_2O$ dosage needed for alkali activated FA systems (5.3-15% by weight of binder) [77, 84, 85] is higher than that for the alkali activated GGBFS systems (3-6% by weight of binder) [31, 86]. According to Davidovits [15] geopolymerization requires highly alkaline solutions to dissolve the silicon and aluminium from the FA. Xu et al. [28] reported that the proportion of alkaline solution-to-alumino-silicate powder by mass should be approximately 0.33 to allow geopolymerization.

## 2.2. CARBONATION

Carbonation is one of the main causes of corrosion of the reinforcement in traditional OPC-based concrete. The carbonation reduces the pH of the concrete pore solution to values where passivation of reinforcing steel disappears [87]. The presence of oxygen and water promotes corrosion of the reinforcing steel. The corrosion products are more voluminous than the parent steel, causing tensile stresses in the concrete cover and subsequently, its cracking and spalling on a relatively short period (< 10 years after corrosion initiation). In period of 10 to 20 years, steel cross section loss may cause insufficient tensile capacity and thus may threat structural integrity and safety [88]. Therefore, carbonation is one of the most important deterioration mechanisms in predicting the long-term behaviour of OPC-based concrete [89–99]. It has also gained increasing attention in recent years in alkali-activated materials (AAMs) [39]. In order to use reinforced alkali-activated concrete for structural applications, the potential deterioration mechanisms must be understood. There is no method yet to evaluate adequate criteria for alkali-activated concrete service life prediction when carbonation is the dominant deterioration mechanism. Many standards with respect to durability testing have been

well established and widely applied to OPC concretes, but their applicability for AAMs remains to be addressed [100].

Carbonation of concrete is a continuous chemical reaction between $CO_2$ and the concrete components (see Figure 2.2). Its rate depends on the binder type and environmental conditions (RH, $CO_2$). Carbonation occurs in the paste and paste-aggregate interface, i.e. interfacial transition zone (ITZ) (Figure 2.2). More specifically, carbonation is affecting the pore solution (CASE I) and reaction products (CASE II), resulting in chemical, physical and mechanical changes of the microstructure (Figure 2.3).

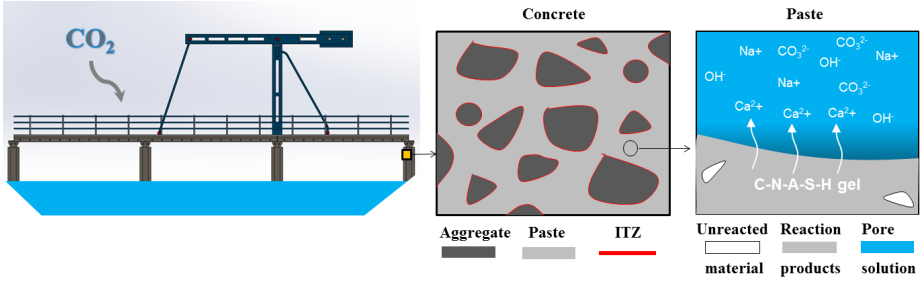


Figure 2.2: Illustration of concrete microstructure carbonation. Concrete consists of aggregates, paste and ITZ (middle). Paste consists of unreacted materials (FA and GGBFS), reaction products (gels) and pore solution (right). Carbonate ions are present in the pore solution, carbonation products are not shown. The gel will eventually dissolve when the pH drops due to carbonation of the pore solution as shown with white arrows (right).

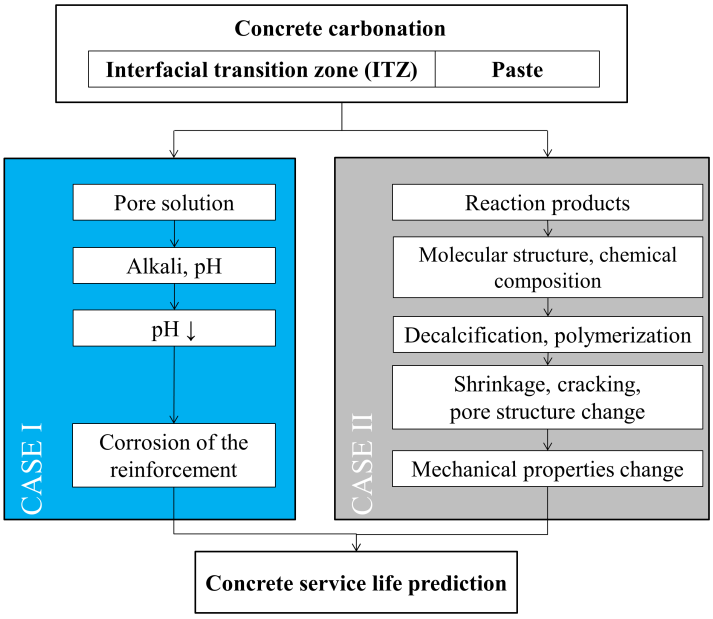


Figure 2.3: Concrete components involved in carbonation reactions.

In the following sections, the currently used prediction models for carbonation-induced corrosion and current state of understanding with existing knowledge gaps with respect to the carbonation mechanism in AAMs are reviewed. Furthermore, the carbonation mechanism in OPC-based materials and AAMs are compared. Experimental observations of various systems (alkali-activated GGBFS, FA and their blends) under different exposure conditions (RH, $CO_2$) are summarized. The carbonation resistance of each of the systems is discussed with respect to the pore solution and reaction products.



## 2.3. PREDICTIVE MODELS FOR CARBONATION RATE IN CONCRETE

### 2.3.1. OPC-BASED CONCRETES

The rate of carbonation is an important input for design of the concrete cover depth and the service life prediction of reinforced concrete structures because the initiation of reinforcement corrosion is usually considered as the end of service life of concrete infrastructure [101]. Comparing the cover depth with the carbonation depth will allow prediction of the time to corrosion of reinforcing steel in OPC-based concretes (see Figure 2.4). Currently used prediction models for carbonation-induced corrosion include a very basic square-root-time law derived from Fick's first law of diffusion and more accurate physical models considering the microstructural features and the carbonation of the different hydrated phases [102–106]. Furthermore, probabilistic engineering models take into account both concrete properties and environmental conditions. In practice a simple empirical model with a square root of time function is used to predict the carbonation depth (Eq. 2.3) for OPC-based concrete [90, 107, 108]. It assumes that carbonation occurs only at the carbonation front (Figure 2.4), which provides practical analytical solutions proportional to square root of time. Eq. 2.3 [109] includes a "penetrability and transport property":

$$X_c = \sqrt{\frac{2D_{CO_2}}{a} C_{CO_2} t} \tag{2.3}$$

where $X_c$ is the depth of carbonation (cm) of concrete at time t (s), $D_{CO_2}$ is $CO_2$ diffusion coefficient ($cm^2 s^{-1}$), $C_{CO_2}$ is atmospheric $CO_2$ concentration (g $cm^{-3}$), $a$ is the amount of $CO_2$ required to carbonate a unit volume of concrete, and t is the time.

The amount ($a$) of $CO_2$ absorbed per volume of carbonated concrete can be calculated according to Eq. 2.4 [94]. Pade and Guimaraes [94] assumed that 75% of the original CaO in the Portland cement (with 95% clinker content and an average CaO content of 65%) converts into calcium carbonates in carbonated concrete. For different cement types, the $CO_2$ binding capacity will be highly dependent on cement composition. For that reason, V.-L. Ta et al. had introduced the cement clinker content into Eq. 2.4 for different cements (for modified Eq. 2.4 see [99]).

$$a = 0.75 \times C \times CaO \times \frac{M_{CO_2}}{M_{CaO}} [kg m^{-3}] \tag{2.4}$$

where 0.75 is the fraction of CaO available for carbonation; C is the cement content

($kgm^{-3}$); CaO is the CaO content in cement; M the respective molar masses; ($CO_2$= 44 $gmol^{-1}$, CaO= 56 $gmol^{-1}$).

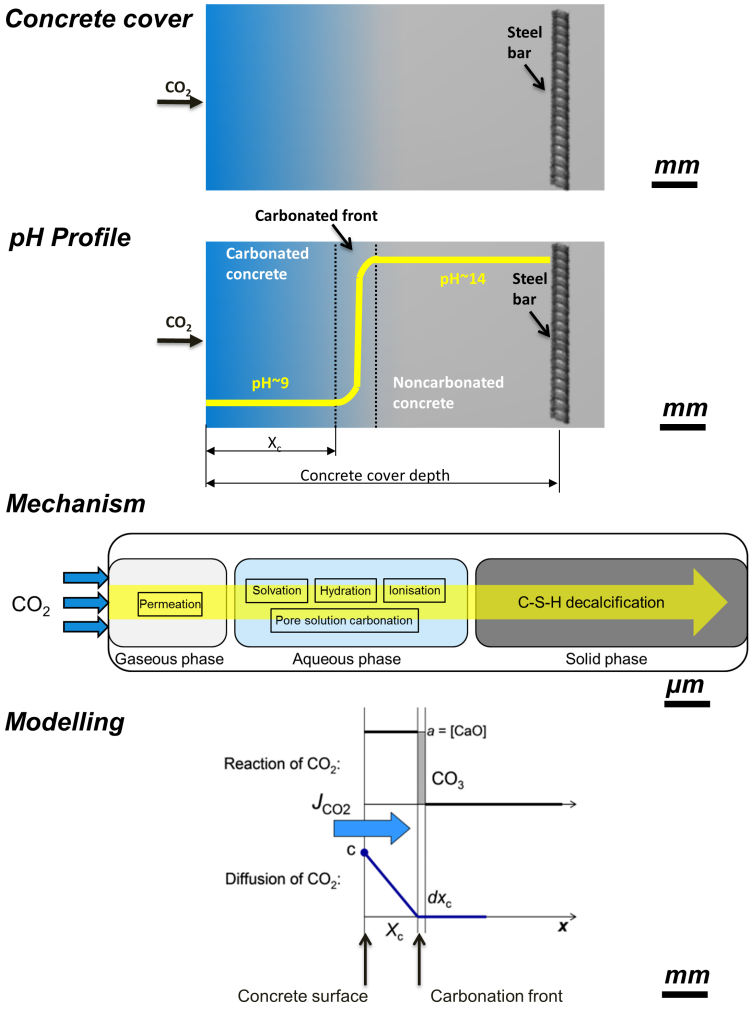


Figure 2.4: Schematic representation of the $CO_2$ diffusion, pH profile, mechanism and driving forces for carbonation in cement-based concrete.

Houst and Wittmann [110], Houst et al. [111], Saetta et al. [112], Steffens et al. [113] tuned their models in order to fit measured penetration curves for various boundary conditions and types of cements. On the other hand, the understanding of the overall process is done by Papadakis et al. [108]. They proposed the analytical solution for the propagation rate of the carbonation front considering the effective diffusivity of $CO_2$ in carbonated concrete and available CaO molar concentration of concrete. Tutti [114] used the moving-boundary methodology to model the carbonation of concrete.

He showed analytically that the interface between completely carbonated part and non-carbonated part behaves like $\sqrt{t}$ for sufficiently long time t. Existing carbonation models for OPC-based concrete are mainly based on the assumption that the reactants and products are present everywhere in a volume unit at all times. The models are based on linear or semi-linear systems of parabolic partial differential equations. Some of the models also consider the moisture state in unsaturated OPC-based concrete.

### 2.3.2. AAMS-CONCRETE

Bernal et al. [115] described the degree of accelerated carbonation (1.0± 0.2% v/v $CO_2$, temperature of 25± 2 °C, and RH=65± 5%) in the alkali-activated GGBFS concretes and OPC-based concrete samples (see Figure 2.5).

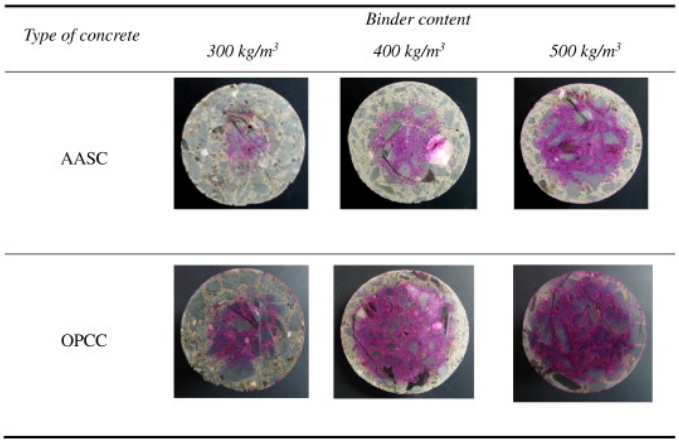


Figure 2.5: Transverse sections of carbonated concretes (OPC-concretes vs AAS-concretes) after 1000 h of exposure to a 1% v/v $CO_2$, with the carbonation depth determined with a phenolphthalein indicator. Samples are 76.2 mm in diameter [115]. The $Na_2O$ concentration of alkaline activator was 5 wt.%.

Authors [115] found lower carbonation depths for OPC-based concretes compared to alkali-activated GGBFS concretes. In addition, lower carbonation depths were measured in concretes with higher binder contents, regardless the type of binder. The known susceptibility of alkali-activated GGBFS binders to carbonation, which is generally ascribed to their higher alkali content, agrees with the fact that these samples show a higher extent of carbonation than OPC-based concrete samples irrespective of the water-to-cement ratio. The rate of carbonation correlates well with what would be expected from the tendencies in compressive strength, but less closely with the observed microstructure physical properties. This indicates that the binder chemistry is more critical to carbonation resistance than details of the pore structure. This observation suggests that the common assumption that carbonation is diffusion-controlled in OPC-based materials [102] may not apply in case of alkali-activated GGBFS. Figure 2.6, therefore, shows the results of fitting both diffusion-based and chemical reaction-based models to the carbonation data. The models were applied to the data using the assumption of cylindrical geometry of the

samples with no end effects (pseudo-infinite cylinders), which is appropriate given that the sample ends were sealed to prevent carbonate ingress from these surfaces. Figure 2.6 shows that the diffusion based model fits the 300 kg/m$^3$ data for the alkali-activated GGBFS concretes very well, but provides a poor description of the samples with higher binder content. On the contrary, the chemical reaction control model fits the 400 and 500 kg/m$^3$ data for both sample sets, but is unable to provide an adequate description of the 300 kg/m$^3$ data.

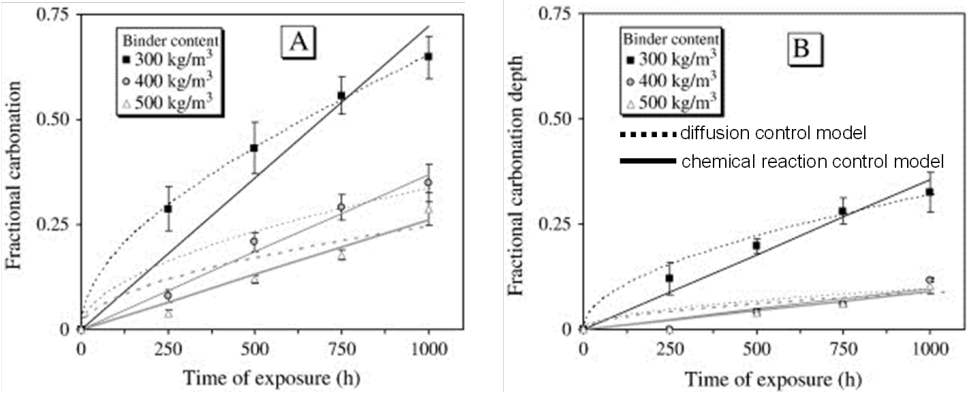


(a) alkali-activated GGBFS (b) Portland cement

Figure 2.6: Carbonation depth as function of the amount of binder of concretes for alkali-activated GGBFS and Portland cement. *Dashed lines* represent the best fit for the diffusion model to each data set, and *solid lines* are the best fit for the chemical reaction model. Error bars represent the standard deviation [115].

Beside literature, the RILEM Technical Committee for concrete with SCMs (TC 238-SCM) and AAMs (TC 224-AAM) have contributed to understanding carbonation of SCMs and AAMs. However, no recommendation for testing and modeling of carbonation of SCMs or AAMs-based systems is given, except for OPC-based concrete. Therefore, a special Technical Committee (TC 281-CCC) has been formed to address main questions with regard to the carbonation mechanism and prediction of concrete service life of SCMs and AAMs. Current understanding of carbonation mechanism in OPC and AAMs is presented next.

## 2.4. CURRENT UNDERSTANDING OF CARBONATION MECHANISMS IN OPC AND AAMS

### 2.4.1. CARBONATION RESISTANCE OF OPC

#### 2.4.1.1. CARBONATION OF THE PORE SOLUTION OF OPC

The first step in the carbonation process of OPC-based materials is pore solution carbonation. $CO_2$ molecules diffuse into concrete and dissolve in the pore water, forming carbonic acid ($H_2CO_3$) (reactions 2.5 and 2.6 ). Carbonic acid forms two salts: bicarbonates ($HCO_3^-$) and carbonates ($CO_3^{2-}$) (reactions 2.7 and 2.8 ). The bicarbonate ion ($HCO_3^-$)

is unstable in pore solution of high alkalinity (>13). Thus, it dissociates and forms additional carbonate ions ($CO_3^{2-}$). The carbonate ions then react with available alkali ($Na^+$, $K^+$, $Ca^{2+}$) in the pore solution, resulting in precipitation of alkaline carbonates ($Na_2CO_3$, $K_2CO_3$, $CaCO_3$).

$$CO_2(g) \rightarrow CO_2(aq) \tag{2.5}$$

$$CO_2(aq) + H_2O \rightarrow H_2CO_3 \tag{2.6}$$

$$H_2CO_3 \rightarrow HCO_3^- + H^+ \tag{2.7}$$

$$HCO_3^- \rightarrow CO_3^{2-} + H^+ \tag{2.8}$$

The main reaction occurring in pore solution of OPC-based paste after the formation of carbonic acid is the reaction of carbonic acid with $Ca(OH)_2$, resulting in precipitation of calcite ($CaCO_3$). Calcite has a higher specific volume than $Ca(OH)_2$ and hence fills up the pores. However, although the reaction with $Ca(OH)_2$ is the main reaction, there are reactions that occur earlier, such as carbonation of NaOH and KOH (reactions 2.9,2.10,2.11):

$$H_2CO_3 + 2NaOH \rightarrow Na_2CO_3 + 2H_2O \tag{2.9}$$

$$H_2CO_3 + 2KOH \rightarrow K_2CO_3 + 2H_2O \tag{2.10}$$

$$H_2CO_3 + Ca(OH)_2 \rightarrow CaCO_3 + 2H_2O \quad \text{associated with volume expansion} \tag{2.11}$$

The presence of alkaline carbonates in the pore solution is known to increase the solubility of $Ca(OH)_2$, as presented in reactions 2.12 and 2.13, which may then be carbonated in larger quantities.

$$Na_2CO_3 + Ca(OH)_2 \rightarrow CaCO_3 + NaOH \tag{2.12}$$

$$K_2CO_3 + Ca(OH)_2 \rightarrow CaCO_3 + 2KOH \tag{2.13}$$

The amount of soluble $Ca(OH)_2$ in the OPC paste is far greater than those of NaOH and KOH. For that reason, it is the governing factor for the alkalinity of the pore solution. As long as calcium ions are available, the formed sodium and potassium carbonates are unstable and reorganize with the dissolved $Ca(OH)_2$ to calcium carbonates, which crystallize into stable calcite and metastable aragonite [113].

The main consequences of carbonation of the pore solution in OPC is reduction of alkalinity and volume expansion (by precipitation of $CaCO_3$ in the pores), resulting in denser pore structure after carbonation.

#### 2.4.1.2. CARBONATION OF THE REACTION PRODUCTS OF OPC

Carbonation of C-S-H gel in hydrated OPC-based paste is a complex decalcification-polymerization process of the C-S-H and the formation of amorphous silica gel, see Eq. 2.14 [116]. This reaction does not affect the alkalinity of the pore solution [113], however, it induces the gel volume reduction:

$$C_xSH_y + \bar{C} \rightarrow xC\bar{C} + SH_t + (y-t)H \quad \text{associated with volume reduction} \tag{2.14}$$

where C, H, S, $\bar{C}$ are according to cement notations: C=CaO, H=$H_2O$, S=$SiO_2$, $\bar{C}$ =$CO_2$. The x, y, and t are the stoichiometric coefficients of Eq. 2.5 and they are not exactly defined. In particular, the amount of water inside the silica gel, $SH_t$, is unknown, as well as the exact type of calcium carbonate (x$C\bar{C}$) which is formed (calcite, vaterite or aragonite). Consequently, the change in the volume of solid phases is unknown and it explains the difficulty to quantify the evolution of porosity induced by C-S-H carbonation sufficiently accurate [116].

In OPC-based materials carbonation of several reaction products, such as C-S-H, $Ca(OH)_2$, ettringite, Afm and Aft determines the ultimate carbonation degree. Based on Eq. (2.14) the carbonation rate of C-S-H depends on the molecular structure of C-S-H, Ca/Si and $H_2O$/Si ratios. The molecular structure of C-S-H is shown in Figure 2.7. C-S-H has a layer structure. Ca has two positions in the C-S-H structure: Ca in the CaO sheet layer and Ca in the interlayer. Consequently, different energy is needed to remove Ca from these positions. The removal of Ca from the interlayer causes less changes of the structure than that from the CaO sheet layer (Figure 2.7). The C-S-H with higher Ca/Si ratio has better resistance to the carbonation [117].

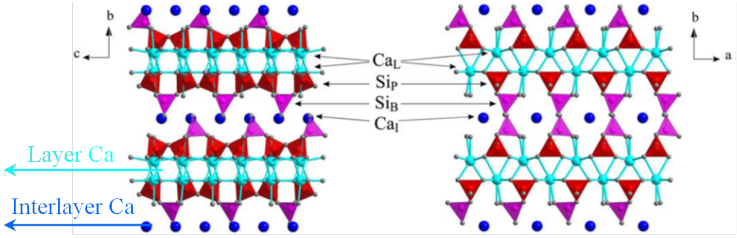


Figure 2.7: Two projections (right: along the $\vec{a}$-axis; left: along the $\vec{c}$-axis) of the tobermorite M structural model given by Hamid [118]; using the conventional $\vec{b}$ unique monoclinic axis. Label $Ca_L$ referes to layer calcium sites (light blue spheres), $Ca_I$ refers to interlayer calcium sites (blue spheres), $Si_P$ refers to paired silicon tetrahedra (red tetrahedra) and $Si_B$ refers to the bridging silicon tetrahedra (pink tetrahedra), adopted from [119].

## 2.4.2. CARBONATION RESISTANCE OF ALKALI-ACTIVATED SLAG (AAS)

### 2.4.2.1. CARBONATION OF THE PORE SOLUTION OF AAS

The pore solution in AAS is highly alkaline (pH>13) due to the presence of sodium, hydroxyl and potassium ions [57]. $Ca(OH)_2$ is usually not formed in sodium silicate-based activated GGBFS pastes. On the other hand, it can be found in NaOH-activated GGBFS paste [120]. The addition of alkalis stimulates the dissolution of the GGBFS and hence the formation of reaction products, mainly alkaline calcium aluminate silicate hydrates. Sodium and hydroxyl ions are supplied by the alkaline activator, while potassium and part of sodium originate from the GGBFS. These ions are partially incorporated in reaction products. Other ions accumulate in the pore solution and thus make calcium insoluble. Alkalis react instantly with $CO_2$ molecules that dissolve in the pore solution. Dissolution of both alkali and $CO_2$ requires water in the pores.

Thermodynamic simulations of Bernal et al. [62] show significant effect of $CO_2$ concentration on the pore solution composition. Figure 2.8 shows effect of 0.04 % v/v $CO_2$

on the pore solution composition, representative for natural carbonation conditions. The starting values for Ca and Mg concentrations in the initial system were fixed on 10 mmol/kg. Figure 2.9 shows effect of 4 % v/v $CO_2$ on the pore solution composition, where these conditions correspond to accelerated carbonation conditions. Depending on the NaOH concentration in solution, different products and their proportions can be observed in these two conditions. This suggests that correlation between natural and accelerated carbonation cannot be made for AAMs from the aspect of the pore solution carbonation.

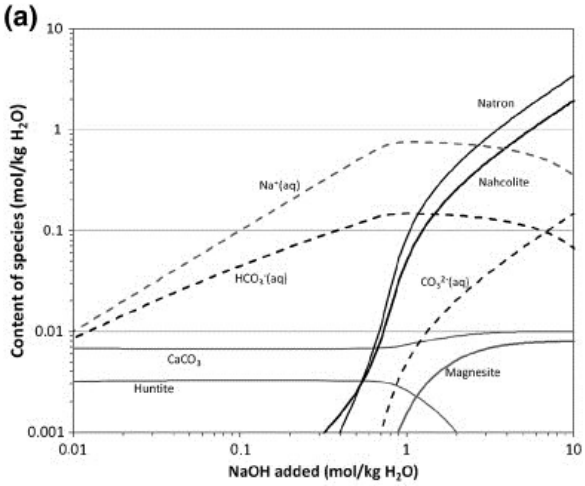


Figure 2.8: Calculated concentrations of key species present in or precipitated from simulated alkali-activated GGBFS pore solutions (10 mmol/kg Ca, 10 mmol/kg Mg) as a function of NaOH concentration, under natural carbonation (0.04% v/v $CO_2$). Dashed lines are dissolved species, solid grey lines are alkaline earth carbonates, and solid black lines are alkali metal carbonates. Adopted from [62].

According to Bernal [62] the accelerated carbonation of the pore solution leads to significantly larger pH reduction (two pH log units lower) compared to natural carbonation (Figure 2.10). The pH in case of natural carbonation remains above 10. The reason why the pH is so high, is that the $Na^+$ content remains constant regardless the partial pressure of $CO_2$ [61]. The significant reduction of the pH in accelerated conditions is attributed to a higher fraction of bicarbonate ions ($HCO_3^-$), which conditions are more acidic compared to carbonate ions ($CO_3^{2-}$) (Figure 2.10). This indicates that carbonation of the pore solution of AAS would not be a problem in service conditions. However, there are no experimental measurements to validate numerical predictions. Furthermore, in thermodynamic simulation of the pore solution the precipitation of metastable phases of calcium carbonates (vaterite and aragonite) was not taken into account. Similarly, the formation of gaylussite ($Na_2Ca(CO_3)_2{\cdot}5H_2O$ and pirssonite $Na_2Ca(CO_3)_2{\cdot}2(H_2O)$) was not observed in calculations. Thermodynamic simulations predicted only calcite ($CaCO_3$), huntite ($Mg_3Ca(CO_3)_4$) and magnesite ($MgCO_3$) to precipitate. In addition, due to lack of knowledge about the exact stochiometry of the gel phases that can precipitate in AAMs, an alternative method is needed to simulate the carbonation process that occurs at the

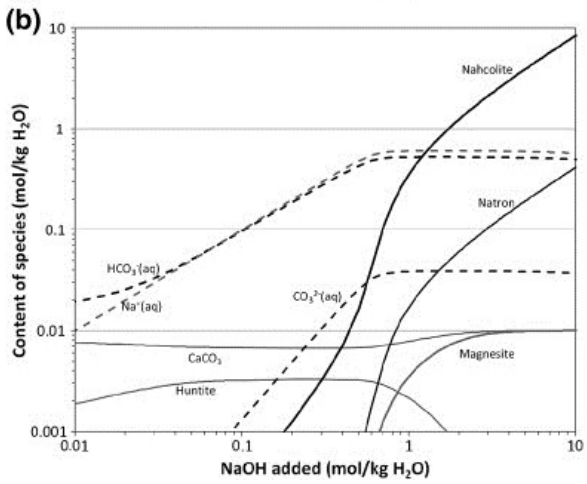


Figure 2.9: Calculated concentrations of key species present in or precipitated from simulated alkali-activated GGBFS pore solutions (10 mmol/kg Ca, 10 mmol/kg Mg) as a function of NaOH concentration, under accelerated carbonation (4% v/v $CO_2$) conditions. Dashed lines are dissolved species, solid grey lines are alkaline earth carbonates, and solid black lines are alkali metal carbonates, adopted from [62].

pore solution-gel interface. A thermodynamic equilibrium model may include the gel phases and not only describe in isolation the pore solution for an assumed Ca and Mg concentrations with variable NaOH contents.

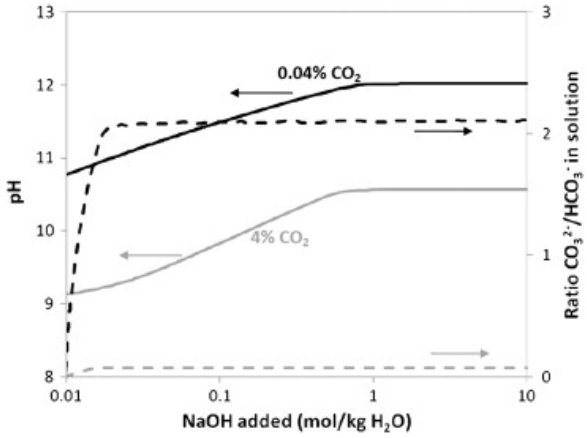


Figure 2.10: Plot of pH (solid lines) and carbonate/bicarbonate ratio (dashed lines) as a function of NaOH addition and $CO_2$ concentration, for simulated AAS pore solutions (10 mmol/kg Ca, 10 mmol/kg Mg). Black lines are at 0.04% v/v $CO_2$, and grey lines at 4% v/v $CO_2$, adopted from [62].

#### 2.4.2.2. CARBONATION OF THE REACTION PRODUCTS OF AAS

The molecular structure of reaction products of AAS mainly depends on the type of activator. Examples of this effect are shown in Figure 2.11. The use of waterglass leads to linear chains with occasional cross-linking in the gel molecular structure (see red dash circles, Figure 2.11) [121]. Bernal et al. [63] showed that carbonation of the reaction products of AAS mainly consists of decalcification of C-S-H type products.

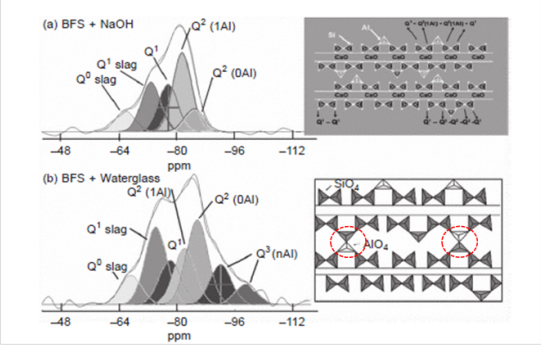


Figure 2.11: Structural model for an Al-containing C-S-H gel depending on the type of alkaline activator, adopted from [121]; (a) linear chains; (b) linear chains with occasional cross-linking, forming planes.

Bernal et al. [68] found that the MgO content in the raw GGBFS significantly influences the carbonation rate. Hydrotalcite-like phases (Mg-Al layered double hydroxides) have been found to increase the resistance of alkali-silicate activated GGBFS to carbonation by absorbing $CO_2$ in their structure. However, when GGBFS is blended with other precursors, such as systems based on alkali-activated GGBFS/FA or GGBFS/metakaolin [61, 63, 65], they exhibited lower resistance to accelerated carbonation compared to OPC-based materials or pure AAS.

When comparing the carbonation resistance of AAS concretes under natural and accelerated carbonation, Bernal et al. [65] showed that accelerated conditions did not replicate the carbonation rate under natural conditions. Lower carbonation depth was found for AAS concrete in natural carbonation performed for 7 years with RH varying between 70 and 76 % and temperature between 19 °C and 38 °C, than in accelerated conditions (1 % v/v $CO_2$). The authors found that the main products of natural carbonation of alkali activated GGBFS concrete are calcite and vaterite, derived from decalcification of the gel, along with sodium carbonates natron and trona associated with the carbonation of the pore solution [65]. The bicarbonate phase nahcolite, which is formed during accelerated carbonation, is not observed under natural conditions. A distinct carbonation front could not be observed in these specimens. Instead, it appeared that preferentially formed carbonated regions were identified in areas where microcracks were present. According to the literature [122], autogenous shrinkage or decalcification of the gel could be the cause of microcracking. It is not possible to conclude which mechanism is governing the microcracking, or if both are occurring simultaneously. Moreover, the influence of the pore structure of AAS bulk paste on the carbonation progress was barely discussed in the literature.

### 2.4.3. CARBONATION RESISTANCE OF ALKALI-ACTIVATED FLY ASH (AAFA)

#### 2.4.3.1. CARBONATION OF THE PORE SOLUTION OF AAFA

The alkali concentration in the pore solution of AAFA has been reported first by Lloyd et al. [123]. Regardless the calcium content in different AAFA pastes, i.e. low (5.6 wt.%) or high (19.11 wt.%), the pH of extracted pore solutions was higher than 13. However, authors did not provide the change of the pore solution composition due to carbonation.

Badar et al. [64] investigated corrosion of steel bars in low-Ca fly ash and high-Ca fly ash-based geopolymer concretes after 450 days of $CO_2$ exposure (5% v/v $CO_2$, 24±5°C and relative humidity 65±5%). After casting and 72 h curing at 80 °C, the concretes were subjected to accelerated carbonation. More aggressive corrosion took place in high-Ca fly ash-based geopolymer concrete under accelerated carbonation, compared to the low-Ca fly ash-based geopolymer concretes. Authors also reported that the use of phenolphthalein indicator for identification of carbonation front is not conclusive about the alkalinity of the concretes. Similar observations for some of the blended GGBFS-FA concretes were reported by Pasupathy et al. [69].

#### 2.4.3.2. CARBONATION OF THE REACTION PRODUCTS OF AAFA

The main reaction product in AAFA is an alkaline aluminosilicate gel (NASH) with a three-dimensional structure (considered to be a zeolite precursor) [124] (Figure 2.12). While the pore solution of AAFA is susceptible to carbonation, the NASH gel is found to be resistant to carbonation [63]. Bernal et al. [63] observed the formation of different sodium (bi)carbonates upon accelerated carbonation of low calcium fly ash geopolymer samples, depending on the $CO_2$ concentration. In these fly ash geopolymers, nanostructural changes of the N-A-S-H gel were not detected after $CO_2$ exposure. However, fully carbonated samples lost their load bearing capacity and could easily be destroyed by hand. Carbonation data for high calcium fly ash geopolymers have not been reported in open literature. Hence, the carbonation phenomenon in fly ash-based geopolymers needs to be clarified.

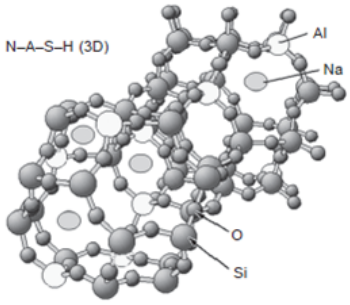


Figure 2.12: Plan view projection of the three-dimensional structure of a N-A-S-H gel, adopted from [41].

### 2.4.4. CARBONATION RESISTANCE OF BLENDED SLAG/FLY ASH (AASF)

#### 2.4.4.1. CARBONATION OF THE PORE SOLUTION OF AASF

Pasupathy et al. [69] reported carbonation resistance of a blended GGBFS-FA alkali-activated concrete in field conditions over a period of 8 years. The results indicated that the carbonation rate of alkali-activated concrete is highly dependent on the activator components of alkali-activated concrete. The main activator had equal molar amounts of Na and K in a 7 Molar solution. Alkali-activated concrete with 75% FA/ 25% GGBFS and additional $Na_2SiO_3$ activator (Type 1 concrete), showed a poor resistance against carbonation compared to OPC concrete. However, the performance of alkali-activated concrete with 70% FA/ 30% GGBFS and no additional $Na_2SiO_3$ activator (Type 2 concrete), was similar to OPC concrete. The pH of the Type 1 concrete ranges from about 10.07 at the surface to 11.25 at 50 mm depth. For Type 2 concrete the pH ranges from 9.68 to 11.38.

#### 2.4.4.2. CARBONATION OF THE REACTION PRODUCTS OF AASF

Bernal et al. [63] studied the effects of accelerated carbonation on AASF blends, containing two distinct types of gel: one of which resembles the C–A–S–H gel formed through alkali silicate activation of GGBFS, and the other of which N–A–S–H gel is formed through alkali silicate activation of FA. Under accelerated carbonation, each binder gel performs according to a similar mechanism as observed in the sole AAS or AAFA system. A crosslinked remnant silicate phase is derived from decalcification of the C–A–S–H gel, which coexists with the largely unaltered N–A–S–H gel resulting from activation of FA. Various alkali and alkali–earth carbonates were observed to precipitate. Bijen et al. [125] identified an acceleration of carbonation of NaOH-activated GGBFS and FA blends due to intensive microcracking of specimens during drying prior to $CO_2$ exposure. Bernal et al. [115] suggested that the interaction between carbonation and drying in alkali-activated concretes requires further investigation.

### 2.4.5. OPC VS AAMS CARBONATION: COMPARISON WITH RESPECT TO PORE SOLUTION AND REACTION PRODUCTS

Due to different reaction products (Table 2.2) and microstructures in AAMs compared to OPC-based materials or SCMs, the carbonation mechanisms are different as well. The rate and degree of carbonation depend on the pore solution chemistry and type of reaction products.

In the pore solution of OPC-based materials, $Ca(OH)_2$ is the main source of alkalinity. When the pore solution in OPC-based materials is carbonated, its pH decreases due to consumption of $Ca(OH)_2$, $Na^+$ and $K^+$ ions from the pore solution. On the other hand, alkalinity of the pore solution in AAMs is mainly provided by alkali that are supplied from alkaline activators ($Na^+$). Thus, due to different pore solution chemistry of OPC and AAMs, a different buffer mechanism for the pH of the pore solution in AAMs is expected. Since the buffer mechanism for the pH is still not clear in AAMs, the carbonation degree of the pore solution carbonation in AAMs is hard to determine.

Table 2.2: Reaction and carbonation products in OPC, OPC with SCMs and AAMs.

| Reaction products | | | | |
|---|---|---|---|---|
| | Cement based materials [41] | | Alkali-activated materials [41] | |
| | OPC | OPC with SCMs | Slag | Fly ash/ Metakaoline |
| Primary reaction products | C-S-H | C-A-S-H | C-(N)-A-S-H | N-A-S-H |
| Secondary reaction products | $Ca(OH)_2$<br>AFm (Calcium monosulfoaluminate)<br>Aft (calcium trisulfoaluminate hydrate, or ettringite)<br>Ettringite $Ca_6Al_2(SO_4)_3(OH)_{12} \cdot 26H_2O$) | $Ca(OH)_2$<br>AFm<br>AFt | Hydrotalcite (Mg-Al layered double hydroxide (LDH) phases) $[Mg_6Al_2CO_3(OH)_{16} \cdot 4H_2O]$<br>$C_4AH_{13}$<br>$CASH_8$ (stratlingite)<br>$C_4AcH_{11}$ (calcium monocarboaluminate hydrate) $C_8Ac_2H_{24}$ | Zeolites: hydroxy-sodalite, zeolite P, Chabazite-Na, zeolite Y, faujasite |
| Carbonation products | | | | |
| | Cement based materials [116] | | Alkali-activated materials [62] | |
| | OPC | OPC with SCMs | Slag | Fly ash/ Metakaoline |
| Pore solution carbonation | Calcium carbonate: Calcite | | Sodium carbonates:<br>Natron: $Na_2CO_3 \cdot 10H_2O$,<br>Trona: $Na_3H(CO_3)_2 \cdot 2H_2O$,<br>Thermonatrite: $Na_2CO_3 \cdot H_2O$,<br>Nahcolite: $NaHCO_3$<br>Natrite: $Na_2CO_3$<br>Sodium carbonate heptahydrate: $Na_2CO_3 \cdot 7H_2O$ | |
| Gel carbonation | Calcium carbonates: vaterite, aragonite, calcite silica gel/alumina silica gel, and water | | Calcium carbonates: vaterite, aragonite, calcite<br>Magnesium carbonates:<br>Huntite: $Mg_3Ca(CO_3)_4$<br>Dolomite: $CaMg(CO_3)_2$,<br>Hydrotalcite<br>Sodium carbonates:<br>Pirssonite: $Na_2Ca(CO_3)_2 \cdot 2H_2O$,<br>Gaylussite: $Na_2Ca(CO_3)_2 \cdot 5H_2O$,<br>Nyerereite: $Na_2Ca(CO_3)_2$<br>Sodium alumina silica gel, and water | - |
| $Ca(OH)_2$ | Calcite and water | | - | - |
| Calcium aluminate hydrate | Calcium carbonates, alumina gel, and water | | - | - |
| Hydrated ferrite phases | Calcium carbonates, ferrite phases, and water | | - | - |
| Ettringite | Calcium carbonates, gypsum, alumina gel, and water | | - | - |

Carbonation of the reaction products occurs when reaction products are not in equilibrium with the pore solution (due to decrease of pH, due to high solubility of certain phases, due to pore solution saturation with $CO_3^{2-}$ ions). In OPC-based materials carbonation of several reaction products, such as CSH, CH, ettringite, alumina ferric oxide monosulfate (Afm) determines the ultimate carbonation degree. Literature on the carbonation degree of the reaction products in AAMs is limited and large variations between available results exist. The products that are or can be formed due to carbonation of OPC, OPC with SCMs and AAMs are defined in Table 2.2.

## 2.5. PROBLEM DEFINITION OF CARBONATION IN AAMS

Carbonation studies for AAMs exhibit many discrepancies regarding the correlation between carbonation under natural and accelerated exposure conditions. Pore solution and pore structure change under natural carbonation are rarely studied. It appears that pore solution carbonation in alkali activated GGBFS would not be a problem in the service conditions (natural carbonation) according to the numerical predictions [62]. Nevertheless, experimental measurements are not available to validate numerical predictions. Furthermore, the change in the carbonate/bicarbonate phase equilibrium under accelerated exposure conditions also leads to a substantial reduction in the pH of the pore solution. This is unlikely to occur under natural carbonation [62]. Additionally, literature does not answer the questions what is the carbonation front like, how it behaves in time and which mechanism drives the carbonation front. Finally, there are no studies yet available for prediction of the service life of alkali activacted concrete for *structural* applications in view of carbonation. In addition, guidelines for design of alkali-activated concrete for its use in service where carbonation is dominant durability issue as determined for cement-based concrete by European Standard EN 206-1 [48] (type of environment, minimum binder content, maximum water-to-binder ratio, strength class), are not available.

Table 2.3 presents a summary of the findings from the literature with respect to AAMs carbonation. Further research on carbonation of AAMs is necessary, particularly with regard to the following aspects:

- adequate carbonation indicators,
- material scale for the carbonation mechanism (gel-paste-concrete),
- constituent materials and their mixture proportions,
- pore solution alkalinity quantification,
- $CO_2$ binding capacity,
- methodology for testing carbonation features,
- numerical prediction of the carbonation rate.

In this context, finding adequate test methods and testing at the right material scale are of high importance for understanding the carbonation mechanism in AAMs. Chem-

ical and physical characterization of the microstructure stands out as one of the most promising strategies to understand the complexity of the carbonation process.

Table 2.3: Summary of the findings from the literature with respect to AAMs carbonation.



| Subject | | Findings |
|---|---|---|
| Carbonation resistance of AAS | Pore solution | From numerical simulations: slight reduction of the pH under natural carbonation, significant reduction of the pH under accelerated carbonation, no experimental quantification of pH |
| | Reaction product | low resistance |
| Carbonation resistance of AAFA | Pore solution | slight reduction of the pH in the lower-Ca fly ash upon accelerated carbonation, significant reduction of the pH in the higher-Ca fly ash upon accelerated carbonation, no experimental data upon natural carbonation |
| | Reaction product | high resistance to carbonation |
| Carbonation resistance of AAMK | Pore solution | slight reduction of the pH upon accelerated carbonation, no experimental data upon natural carbonation |
| | Reaction product | high resistance to carbonation |
| Carbonation resistance of AASF-AASMK | Pore solution | no data |
| | Reaction product | low to moderate resistance |
| Standard | not yet established, accelerated carbonation tests do not represent behavior of AAMs exposed to natural carbonation with respect to alkalinity reduction and carbonation products, indicating different mechanisms in different environmental conditions | |
| Methodology | Phenolphthalein indicator is shown not to be fully suitable, more accurate method is needed to assess carbonation front in AAMs | |
| Effect of carbonation on the pH | not clear, or not available for some of the AAMs, the quantification is needed | |
| Effect of carbonation on the pore structure | not clear | |
| Effect of carbonation on the mechanical properties | not clear | |
| Predictive model | none | |

## 2.6. CONCLUDING REMARKS



Based on the presented state of the art with respect to AAMs carbonation, some of the most important conclusions can be drawn:

- The carbonation mechanism in AAMs is different from that of OPC-based materials. This hinders application of current codes of practice, designed for OPC-based materials, for testing carbonation of alkali activated concrete. Accordingly, the assessment of carbonation in AAMs should be different from that of OPC-based materials.
- The review shows a lack of information on the carbonation mechanism and carbonation effects on the microstructure properties in AAMs. It appears that discrepancies between natural and accelerated exposure conditions with respect to the carbonation mechanism is a major concern for reliable prediction of the carbonation rate in AAMs.
- Most of the literature studies were focussed on the carbonation of the reaction products. However, the effect of carbonation on long-term performance of AAMs cannot be assessed by studying carbonation of the reaction products and microstructure changes. The pore solution carbonation has to be considered as well.

Therefore, understanding the change of a whole system (pore solution and microstructure) due to carbonation and the initial variations of the microstructure with composition and exposure conditions is critical for making a predictive model for carbonation of AAMs. Further work is needed to extend the understanding of the carbonation mechanism of AAMs by including pore solution carbonation, $CO_2$ binding capacity, effect of the type of binder and effect of curing conditions.

# 3

# MIXTURE DESIGN OF ALKALI-ACTIVATED PASTES

*"Simplicity is not the goal. It is the by-product of a good idea and modest expectations."*

Paul Rand

*Understanding the carbonation mechanism is a prerequisite for an accurate prediction of the long-term behaviour of alkali activated materials (AAMs). It remains challenging as discussed in Chapter 2. In general, previous studies on the performance of AAMs under accelerated carbonation conditions do not encourage their use as binders with an adequate carbonation resistance. Hence, the fundamental knowledge of the complex carbonation mechanism is necessary in order to explain the changes of the chemical, physical and mechanical properties of binders due to carbonation. The durability of AAMs is mainly dependent on the microstructure features of the binder (e.g. phase assemblages and pore structure), which can be modified using different constituents and materials mixture designs. For that reason, this chapter focuses on the development of alkali-activated fly ash (FA) and ground granulated blast furnace slag (GGBFS) mixtures for carbonation mechanism investigation. Their properties such as workability and strength were tested in order to determine their suitability for making concretes. It is shown that fresh properties largely depend on the type of precursor (FA or GGBFS) and their proportions. The setting time of GGBFS-rich pastes was significantly reduced compared to FA-rich pastes. These pastes have also higher compressive strength than FA-rich pastes. Finally, it should be noted that this thesis focuses on understanding of the carbonation mechanism rather than development of the optimized mixtures designs.*

Parts of this chapter have been published in:
Nedeljković, M., Li, Z. and Ye, G. (2018) Setting, strength and autogenous shrinkage of alkali-activated fly ash and slag pastes: Effect of slag content, *Materials* [126]

## 3.1. INTRODUCTION

THE DURABILITY of AAMs is mainly dependent on the microstructure features of the binder (e.g. phase assemblages and pore structure), which can be modified using different constituents and materials mixture designs as demonstrated in Chapter 2. For that reason, this chapter focuses on the development of alkali-activated fly ash (FA) and ground granulated blast furnace slag (GGBFS) paste mixtures for carbonation mechanism investigation. Their properties, such as workability and strength, were tested in order to determine their suitability for making concretes. This chapter begins with characterization of raw materials, FA and GGBFS. Based on the review on the carbonation of AAMs in the literature (Chapter 2), FA and GGBFS are the most used by-products in the studies. Additionally, they are currently the most available in quantity in the Netherlands. Moreover, the chemical composition of different raw materials is known to influence their $CO_2$ binding capacity. Hence, special attention in this thesis is given to an assessment of the carbonation of the pastes with various chemical compositions. The alkaline activator for activation of FA and GGBFS was the same for all the paste mixtures. The influence of the GGBFS/FA ratio and liquid-to-binder (l/b) ratio on the workability, setting time, heat evolution and mechanical properties of the alkali activated pastes is studied and presented in the following sections.

## 3.2. MATERIALS AND PASTE MIXTURE DESIGN

### 3.2.1. RAW MATERIALS

The raw materials used in this study were GGBFS from ORCEM and FA from VLIEGASUNIE BV, the Netherlands. GGBFS had a specific gravity of 2900 kg/m$^3$, while FA had a specific gravity of 2440 kg/m$^3$. The chemical composition of the GGBFS and FA determined with X-ray fluorescence (XRF) is given in Table 3.1. XRF measurements were carried out with PANalytical's Epsilon 3XLE spectrometer equipped with a Rhodium X-ray source, the silicon-drift detector with 135 eV resolution at 5.9 keV/1000 cps. 2-3 grams of FA/GGBFS powder was poured in a 32 mm spectra cup fitted with a bottom of stretched 4 µm prolene film held with a concentric ring. Sulphur (S) was determined with Eltra Sulphur analyzer. Loss on ignition (LOI) was determined with LECO Thermogravimetric Analyser (TGA701). It consists of heating ("igniting") a sample from 25 °C to 1000 °C under an oxidising atmosphere using air with a constant heating rate of 10 °C/min. The negative LOI value in GGBFS is related to the oxidation of sulfur rich compounds in the GGBFS. The LOI of FA is related to the unburnt carbon.

The GGBFS has a higher proportion of CaO and MgO and lower proportions of $SiO_2$, $Al_2O_3$ and $Fe_2O_3$ compared to FA. The basicity coefficient (Kb = (CaO+MgO)/($SiO_2$+$Al_2O_3$)) for GGBFS is 0.98, which nearly complies with neutral type of GGBFS (Kb=1.0). The neutral GGBFS is preferred for alkali activation as shown by Chang [78]. The modulus according to a formula proposed in [78] (HM = (CaO+MgO+ $Al_2O_3$)/$SiO_2$) of GGBFS is 1.73. This is higher than the required value of 1.4 for good hydration properties of GGBFS [78]. The FA complies Class F FA (EN 450, ASTM C618) since it has low CaO content (≤ 10% reactive CaO, EN 450) and $SiO_2$ + $Al_2O_3$ + $Fe_2O_3$ ≥ 70%.

Table 3.1: Chemical composition of GGBFS and FA measured with XRF [%].

| | $SiO_2$ | $Al_2O_3$ | CaO | MgO | $Fe_2O_3$ | S | $Na_2O$ | $K_2O$ | $TiO_2$ | $P_2O_5$ | LOI |
|---|---|---|---|---|---|---|---|---|---|---|---|
| GGBFS | 35.5 | 13.5 | 39.8 | 8.0 | 0.64 | 1.0 | 0.4 | 0.53 | 1.0 | 0.009 | -1.3 |
| FA | 56.8 | 23.8 | 4.8 | 1.5 | 7.2 | 0.3 | 0.8 | 1.6 | 1.2 | 0.51 | 1.2 |

The particle shape of GGBFS and FA was studied with environmental scanning electron microscope in backscattered electron mode (ESEM-BSE), Philips-XL30-ESEM. The raw GGBFS particles have clear edges and angles as shown in Figure 3.1. This is due to inter-impacting and inter-rubbing between steel balls in the ball mill as GGBFS needs to be processed with a ball mill. On the other hand, raw FA particles consist of individual and agglomerated spheres of different size. Large quantity of FA spheres is hollow, known as cenospheres or floaters, which are very light and tend to float on water surface [10]. FA also contains small spherical particles within a large sphere, called pherospheres [10] as indicated by red arrows in Figure 3.1. The external surfaces of the solid and hollow spherical particles of low-CaO FA, as FA in this study, are generally smoother than those of high-CaO FA, which may have surface coatings of material rich in CaO [10].

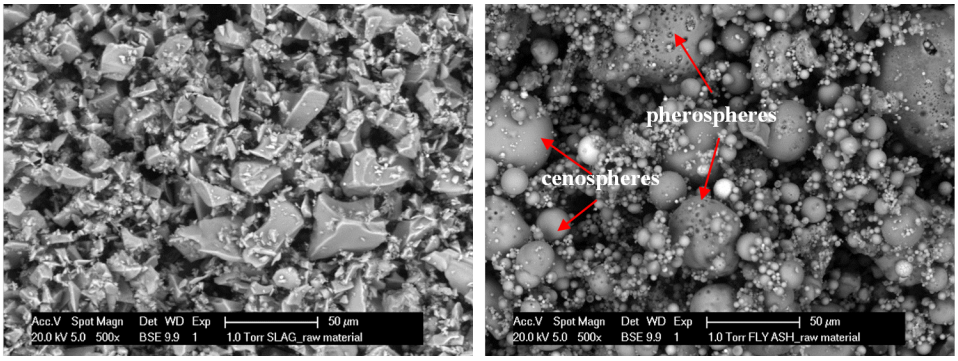


Figure 3.1: ESEM-BSE images of GGBFS (left) and FA (right) particles.

Figure 3.2 shows the particle size distributions of GGBFS and FA, which were measured with EyeTech Laser diffraction analyser, Ankersmid. An external ultrasonic bath was used for the deagglomeration of the particles, in order to increase the dispersion efficiency. The $d_{50}$, which represents the particle size of a cluster of particles, was 19 $\mu$m for GGBFS, while for FA, $d_{50}$ was 21 $\mu$m. For instance, for GGBFS, the $d_{50}$ means that 50% of the particles is larger than 19 $\mu$m, and 50% smaller than 19 $\mu$m. According to literature the dissolution of GGBFS is dominated by small particles. Particles > 20 $\mu$m react slowly, while particles < 2 $\mu$m react completely after 24 h in blended cements and in alkali-activated binders [127, 128].

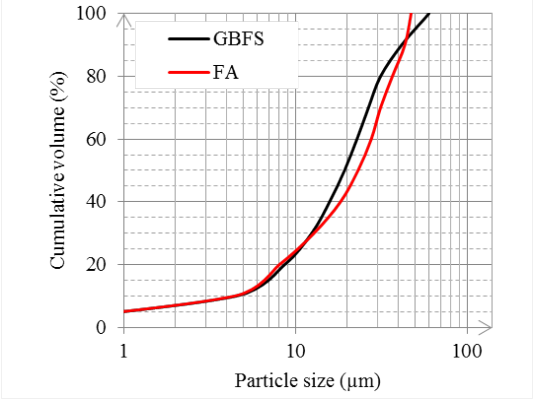


Figure 3.2: Particle size distributions of GGBFS and FA measured with Laser diffraction analyser.

The mineralogical composition of GGBFS and FA was studied with X-ray diffraction (XRD). XRD diffractograms of GGBFS and FA were acquired using a Philips PW 1830 powder X-ray diffractometer, with Cu K$\alpha$ (1.789Å) radiation, tube setting 40 kV and 40 mA, step size of 0.030°, rate of 2.0 seconds per step and 2 Theta range of 10-70°. Amorphous phase was dominant in GGBFS (see Figure 3.3). The presence of amorphous phase can be recognized by the broad hump centred around 31 2theta. In contrast to GGBFS, FA contained beside amorphous also crystalline phases such as mullite, quartz and hematite.

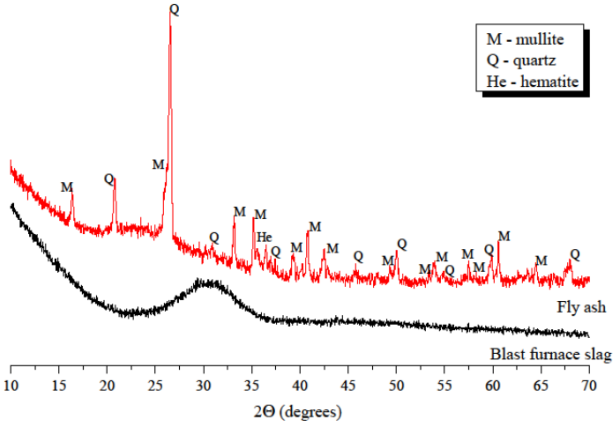


Figure 3.3: XRD diffractograms of GGBFS and FA.

### 3.2.2. ALKALINE ACTIVATOR

Alkaline activator was synthetized by mixing anhydrous pellets of sodium hydroxide with deionized water and sodium silicate solution in 1:1 weight proportion. 4M sodium hydroxide solution was used. The chemical composition of sodium silicate solution was: 27.5 wt. % $SiO_2$, 8.25 wt.% $Na_2O$, 64.25 wt.% $H_2O$. The actual alkaline activator com-

position was selected and modified based on the work of Marinković et al. [129]. The $Na_2O$ concentration of alkaline activator was reduced from 9.5 wt. % to 4.8 wt. %, and modulus (n=$SiO_2/Na_2O$) was reduced from 1.91 to 1.45. In contrast to the previous studies [129, 130], the $Na_2O$ concentration is reduced significantly for this study because of environmental reasons and high costs for the alkaline compounds. Furthermore, the composition of the alkaline activator was set according to recommendations from earlier studies [57, 131, 132]. Wang et al. [57] demonstrated that the sodium silicate solutions with moduli of 1-1.5 gave the best strengths regardless of curing conditions and type or fineness of GGBFS. The authors also suggested that the optimum $Na_2O$ concentration is likely to be within the range of 3.0-5.5% $Na_2O$ by the GGBFS weight [57, 132].



### 3.2.3. MIXTURE DESIGN

Challenges regarding casting, such as fast setting time and harsh workability, are well-known for alkali-activated GGBFS rich pastes [41]. This behaviour originates from the amorphous nature of GGBFS (Figure 3.3) and high $Na_2O$ wt.% concentration of the activator normally used for the activation of GGBFS [78, 133, 134]. In this study, the baseline for the carbonation study was to have a constant liquid-to-binder ratio (where 'liquid' is defined as the alkaline activator content and 'binder' is defined as the FA and/or GGBFS content), while the FA/GGBFS ratio is varied in the mixture design of the pastes. It has to be noted that mixtures might not have an optimized design for a specific FA/GGBFS ratio. An additional requirement was that all mixtures are suitable for casting. The mixtures include individual and blended systems. The individual systems were alkali-activated FA (S0) and alkali-activated GGBFS (S100). Blended systems were alkali-activated FA/GGBFS mixtures with the following ratios: 70:30, 50:50, 30:70, wt.%, named S30, S50 and S70, respectively. In addition to different FA/GGBFS proportions, the liquid-to-binder mass ratio was varied, as 0.4 and 0.5, to examine the effect of different liquid-to-binder ratios on the workability and setting time. All mixtures were designed with the alkaline activator composition defined in the section 3.2.2. Alkaline activator was prepared 24 hours prior to casting in order to cool down to ambient temperature. The synthesis of alkaline activator initially releases heat and 24 hours is needed for heat dissipation and dissolution of NaOH in the solution. The alkalinity (pH) of the activator was 14.4, as measured by pH meter 827 Metrohm. The detailed mixture design is given in Table 3.2. The early-age properties of alkali-activated pastes were compared with ordinary Portland cement (CEM I 42.5 N) paste.

Table 3.2: Mixture design with respect to 100 g of binder.

| Mixture | FA [% wt.] | GGBFS [% wt.] | CEM I [% wt.] | m($SiO_2$)/ m($Na_2O$) | m($Na_2O$)/ m(binder) | l/b (i) | l/b (ii) |
|---|---|---|---|---|---|---|---|
| S0 | 100 | 0 | | | | | |
| S30 | 70 | 30 | | | | | |
| S50 | 50 | 50 | - | 1.45 | 4.8 | 0.4 | 0.5 |
| S70 | 30 | 70 | | | | | |
| S100 | 0 | 100 | | | | | |
| CEM I | - | - | 100 | - | - | 0.4 | 0.5 |

## 3.3. EXPERIMENTAL PROGRAMME

### 3.3.1. WORKABILITY

Properties of fresh mixtures were determined by testing their workability and the setting time. The workability of mixtures was tested by the mini-slump spread test as recommended by Tan et al. [135]. The raw material was first premixed for 3 min prior to mixing with the alkaline activator. For each mini-slump test, 400 g of raw material was mixed with the alkaline activator in a glass cylindric container (diameter 10 cm and height 15 cm) for 2 min by hand. The fresh mixture was poured into a slump cone with a top inner diameter of 36 mm, a bottom inner diameter of 90 mm and height of 90 mm. The cone was placed in the centre of a square smooth glass plate. After filling it with the fresh mixture, the cone was lifted and the mixture subsided. The average spread of the mixture, as measured along the two diagonals and two median directions, was recorded.

### 3.3.2. SETTING TIME

With addition of alkaline activator to the raw materials (FA/GGBFS) the chemical reaction starts and the alkali-activated paste begins to stiffen accompanied by heat release. In cement-based pastes, the setting is a percolation process. In this process isolated or weakly bound particles are connected through the formation of reaction products so that solid paths are formed in the hardening pastes [136]. Hence, the setting of pastes will depend on factors that affect the connectivity between particles such as liquid-to-binder ratio (l/b) [137]. It is assumed that the same mechanism of setting is valid for alkali-activated pastes. However, different setting times are expected for alkali-activated pastes. The initial and final setting times of the alkali-activated pastes were measured using an automatic recording Vicat needle apparatus according to NEN-EN 196-3 [138]. In practice, the initial setting indicates the loss of workability and the beginning of the stiffening of the paste or concrete [139]. Setting time tests were conducted at 20 °C and 50% relative humidity (RH). Pastes were prepared according to the mixture design in Table 3.2 and cast in the same way as for the workability tests. The fresh mixtures were placed in the standard cone with geometry detailed in NEN-EN 196-3 [138]. According to the standard, the initial setting time is the time elapsed between “zero time” (the time when the alkaline activator is mixed with raw material) and the time at which the distance between the needle and the base-plate is 6 ± 3 mm. The final setting time is the elapsed time, measured between the “zero time” and the time when needle first penetrates only 0.5 mm into the paste.

### 3.3.3. CALORIMETRIC MEASUREMENTS

When FA and GGBFS are in contact with alkaline activator, FA and GGBFS react and consequently generate heat. Heat evolution is studied using isothermal conduction calorimetry in accordance with ASTM C1679 [140]. All raw materials were preconditioned at temperature of 20 °C to avoid any temperature difference with measurement temperature (20 °C). The mixtures were prepared by mixing raw material and alkaline activator externally. About 3 minutes later, the mixture is placed into the calorimeter (TAM-Air-314). Two samples were measured simultaneously per mixture. The amount of heat release was recorded and the cumulative heat was calculated up to one week.

### 3.3.4. MECHANICAL PROPERTIES

To investigate the effect of different FA/GGBFS and l/b ratios on the development of the mechanical properties of pastes, flexural and compressive strength were tested. A HOBART mixer was used for mixing 3 litres batch. After premixing raw material, alkaline activator was added at low speed mixing. Mixing continued at low speed for 1 min and for 2 min at high speed. The fresh mixtures were cast in steel prisms moulds (40×40×160 $mm^3$). The moulds were first covered with a thin layer of oil as a demoulding agent. Subsequently, filled prisms were covered with a thin plastic sheet. Samples were demoulded 24 h after casting and further cured unsealed in a fog room at 20 °C and RH 99 %.

First, the three-point flexural bending test was performed on 40×40×160 $mm^3$ specimens according to the NEN-EN-196-1 [141]. Three specimens were tested per age. Two halves of the specimen were then used for testing the compressive strength. The compressive strength was calculated as an average value of six samples. Then the standard deviations were calculated for each set of data.



## 3.4. RESULTS AND DISCUSSION

### 3.4.1. WORKABILITY

The flow of the fresh paste mixtures was reduced with increasing GGBFS content. Figure 3.4 shows the loss of workability for mixtures S70, S100 and CEM I with l/b=0.4 (indicated by red arrow). High specific surface area and high chemical activity of GGBFS require a larger amount of water than FA particles [10]. Hence, the workability and the setting time, as shown in the next section, decrease for GGBFS-rich pastes (see Figure 3.4 and Figure 3.7). With the increase of GGBFS, the liquid demand clearly increases in accordance with research of [10]. Therefore, in order to maintain good consistency of the mixture, the l/b ratio was changed to 0.5. The spread diameter increased for all pastes with l/b=0.5 compared to pastes with l/b=0.4.

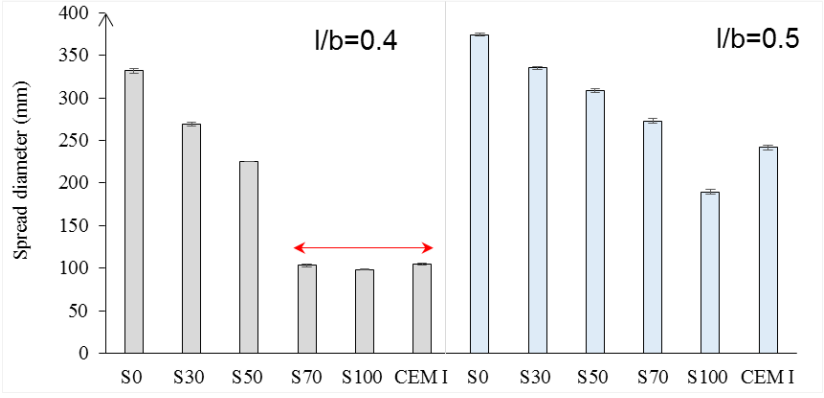


Figure 3.4: Mini-slump spread diameter of alkali-activated pastes and CEM I paste for l/b=0.4 (left), and l/b=0.5 (right).

In OPC-based pastes, the water content has a dominant role in controlling workability [10], as demonstrated for CEM I pastes (see Figures 3.5 (iii) and 3.6 (iii)). In contrast, for alkali-activated pastes not only the liquid-to-binder ratio, but also the particle shape has a significant influence on the spread diameter. The replacement of GGBFS by the same mass of FA improves the workability. The spherical shape and smooth glassy surface of FA particles (Figure 3.1) promote sliding of the particles. This reduces frictional forces between angular particles, which is known as "ball bearing effect" [142]. Furthermore, the addition of FA improved the flowability due to the packing effect. The packing density of the paste increases and the water retained inside the particle flocs decreases. This is again due to the spherical shape of FA, which minimizes the particle's surface to volume ratio, resulting in low fluid demand. A spherical shape, out of all 3D shapes, provides the minimum surface area for a given volume [143].

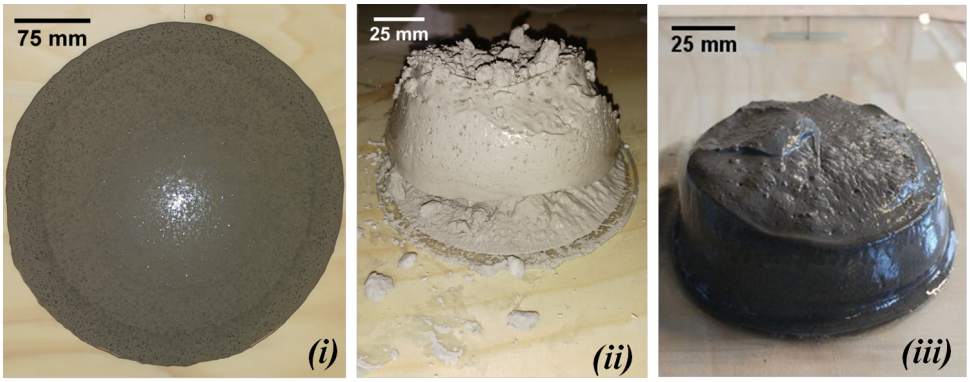


Figure 3.5: The mini-slump spread test for (i) S0 (alkali-activated FA paste), (ii) S100 (alkali-activated GGBFS paste), (iii) CEM I paste; l/b=0.4.

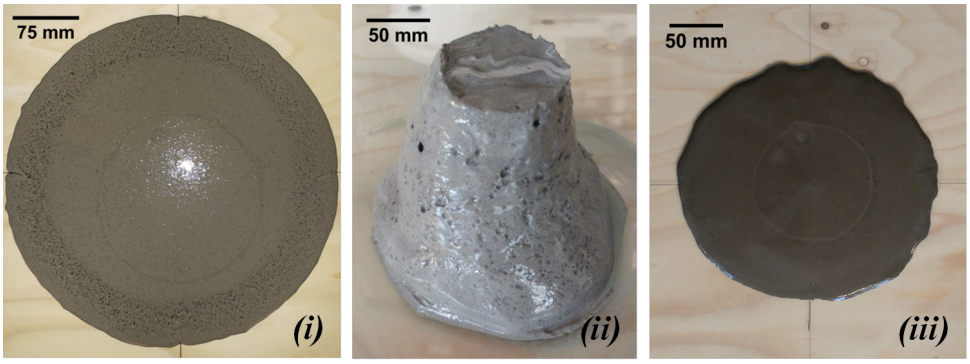


Figure 3.6: The mini-slump spread test for (i) S0 (alkali-activated FA paste), (ii) S100 (alkali-activated GGBFS paste), (iii) CEM I paste; l/b=0.5.

### 3.4.2. SETTING TIME

The influence of l/b ratio and GGBFS content on initial and final setting times of alkali activated pastes are illustrated in Figure 3.7. In OPC-based materials, setting is known as stiffening without significant development of compressive strength, which usually occurs within a few hours [144]. However, for alkali activated FA/GGBFS pastes it lasts 25-80 minutes (Figure 3.8). The setting time of alkali activated pastes is noticeably affected by the l/b ratio of the pastes and GGBFS content. Both initial and final setting time increased as the l/b ratio increased from 0.4 (Figure 3.7(a)) to 0.5 (Figure 3.7(b)). A negative linear relationship can be seen in Figure 3.8(b) between the final setting times and increase of GGBFS content. The alkali-activated FA (S0) paste has relatively long initial setting time due to slow rate of chemical reaction at low ambient temperature [145]. The initial setting time for alkali-activated FA (S0) paste with l/b=0.4 was 6 hours, while with l/b=0.5 it was 14 hours (not plotted in the Figure 3.7).



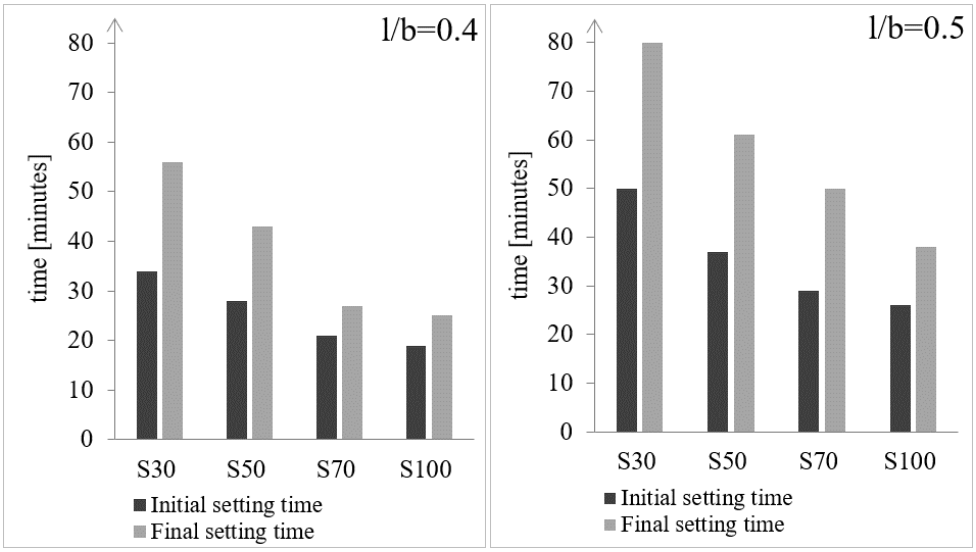


(a) Initial and final setting time of pastes with l/b=0.4. (b) Initial and final setting time of pastes with l/b=0.5.

Figure 3.7: Initial and final setting time of pastes with different l/b ratio. The setting time for S0 paste was not plotted due to very long initial setting times (for l/b=0.4 the initial setting time was 6h and for l/b=0.5 it was 14 h).

Both initial and final setting time decreased with an increase of GGBFS content, while all the final setting times were less than 80 minutes. Given that the surface area of GGBFS (2.54 $m^2/g$) is higher than of FA (1.73 $m^2/g$), the glass composition of the GBFS (lower in silica, less polymerized than FA glass) and the content of the amorphous phase in GGBFS (99 wt.%) is higher compared to FA (68 wt.%, Chapter 5, Figure 5.1), it is expected that when dissolution takes place the GGBFS will be more reactive than FA. In addition, the presence of soluble silica affects the reaction kinetics by enhancing the condensation process of dissolved GGBFS. This results in stiff paste mixtures S100 as demonstrated in

Figure 3.5ii and 3.6ii. Consequently, the apparent viscosity of the fresh pastes with more GGBFS is observed to be higher than that of pastes which contain more FA, leading to shorter setting time of GGBFS-rich pastes. This effect was demonstrated in the mixture even for smaller amount of GGBFS, i.e. below 30 wt.% GGBFS, as reported by Nath et al. [133].

To illustrate the effect of the liquid-to-binder ratio and binder composition on the setting time, final setting times for pastes S30 and S100 are compared. The final setting time was 25 and 40 minutes for pure alkali-activated GGBFS pastes (S100, l/b=0.4 and l/b=0.5), while the final setting time was 55 and 80 minutes for paste S30 with l/b=0.4 and l/b=0.5, respectively. Due to the use of high alkaline solutions (pH>14) the alkaline activation promotes the rapid precipitation of reaction products from the pore solution in GGBFS-rich pastes. The fine particle size distribution and high specific surface area of GGBFS, such as in the paste S100, accelerate the dissolution of GGBFS particles at high alkalinity, polycondensation of dissolved species and precipitation of reaction products, which have the 'thickening' effects on the pastes. Hence, the apparent viscosity increases and the fresh grouts become more viscous [146]. This promotes strength growth at early ages as will be demonstrated in section 3.4.4. The effect of GGBFS content on the initial setting time of the pastes (l/b=0.5) will be further examined in the next section by studying the rate of heat release. Similar to the results for workability of the alkali activated paste mixtures (see Figure 3.4), the results in Figure 3.7(b) for pastes with l/b=0.5 show that alkali activated paste mixtures can be used for carbonation study.

### 3.4.3. ISOTHERMAL HEAT RELEASE OF PASTES

The calorimetric heat release curves of alkali activated pastes are shown in Figure 3.9. Figure 3.8(a) shows the rate of heat release, while Figure 3.8(b) shows the cumulative heat release for alkali-activated FA/GGBFS pastes with l/b=0.5. The calorimetric curves for rate of heat release for all pastes have two characteristic peaks except for paste S0. Similar calorimetric curves are observed for GGBFS activated by sodium silicate solution [30]. The first peak is observed within the first few minutes of reaction. It corresponds to the wetting and partial dissolution of FA and GGBFS. The second broad peak occurs between 6.5 h and 17 h, which corresponds to the formation of reaction products [27]. The second peak did not appear for paste S0, meaning that none or very little amount of reaction products were formed in this paste. The main reason of the unreactivity of FA is most likely the composition of the amorphous phase being a glass too high in alumina and silica to react, despite being amorphous.

The rate of heat release shows how fast the dissolution of FA and GGBFS is (see Figure 3.8(a)). The rate varies among pastes. It is higher for GGBFS-rich pastes due to higher reactivity of GGBFS. Consequently, the cumulative heat release curves for alkali activated pastes indicate more heat release with increasing GGBFS content (Figure 3.8(b)). The setting times of the alkali activated mixtures agree well with calorimetry results. With increasing GGBFS content the setting time becomes shorter (Figure 3.7) due to fast formation of a large amount of reaction products in GGBFS-rich pastes (Figure 3.8(a)).

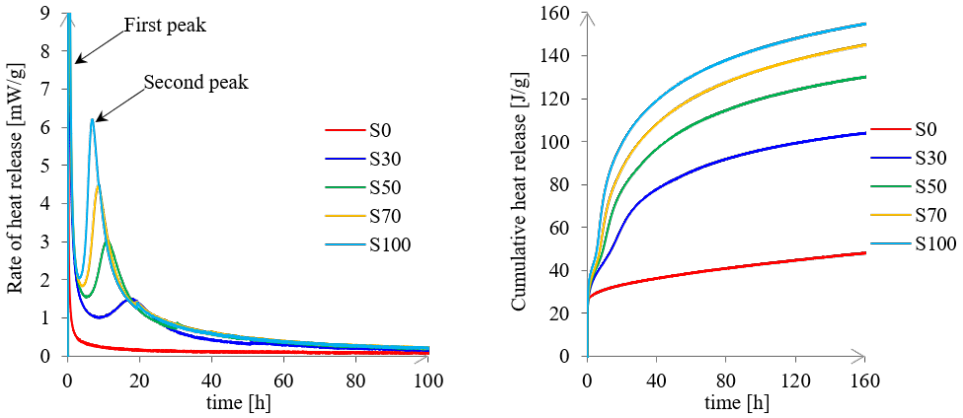


(a) Calorimetric curves for rate of heat release for alkali-activated pastes with l/b=0.5.

(b) Calorimetric curves for cumulative heat release for alkali-activated pastes with l/b=0.5.

Figure 3.8: Calorimetric curves for rate of heat release (a) and cumulative heat release (b) for alkali-activated pastes with l/b=0.5.

## 3.4.4. MECHANICAL PROPERTIES

### 3.4.4.1. COMPRESSIVE STRENGTH

**S100 paste**

Figure 3.9 shows the influence of the l/b ratio on compressive strength for paste S100. It can be seen that for both l/b ratios (0.4 and 0.5), compressive strength values are similar. The maximum compressive strength for paste S100 is obtained after 14 days (see Figure 3.9). An extended curing time in the fog room does not contribute to further increase of the compressive strength. In contrast, curing time for obtaining the maximum compressive strength in OPC-based paste is around 60 days (84.5 MPa), as reported by Chindaprasirt et al. [147]. The comparison is based on similar w/b ratio (0.35 for OPC-based paste and 0.38 for paste S100). Table 3.3 presents an overview of differences regarding gel properties in two pastes: S100 and OPC-based paste. The brittle behaviour and high compressive strength of alkali activated GGBFS-rich pastes is due to low porosity of GGBFS-rich pastes, supported by the porosimetry findings of Provis et al. [148] for the binders with the same GGBFS contents as studied in this work. In their investigation, the segmented porosities at 45 days of the pastes with GGBFS content of 50 wt.% or greater were significantly lower than those with a lower GGBFS content. Thomas et al. [149] reported that the specific surface area of the alkali activated GGBFS pastes is about 25% lower than that of OPC-based paste cured under the same conditions. Furthermore, molar volume calculations indicated that the atomic packing density is significantly higher in gel phases of alkali activated GGBFS paste than in OPC-based paste. Therefore, the presence of nanoparticulate building units in brittle materials gives superior mechanical strength with regard to the bulk material as shown by Knudsen [150].

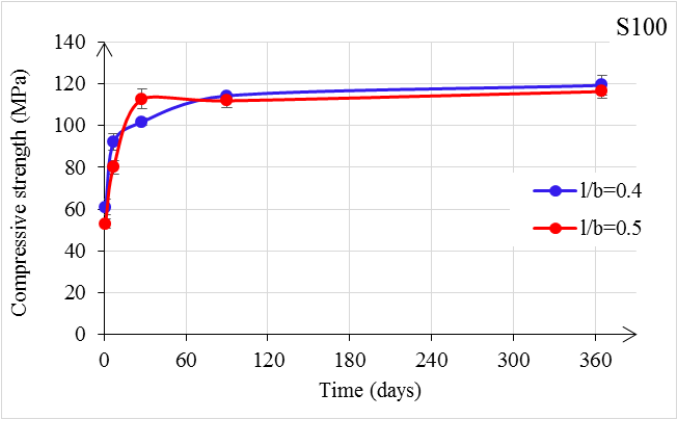


Figure 3.9: Compressive strength development for unsealed cured S100 paste.

Table 3.3: Properties of gel phases in alkali activated GGBFS paste and OPC-based paste.

| Property | Alkali activated GGBFS, w/GGBFS=0.38 | OPC [147], w/c=0.35 |
|---|---|---|
| Ca/Si | 0.84 | 1.4-1.6 |
| Gel morphology [151] | Foil-like | Fiber or honeycomb-like |
| Gel alkali binding capacity [152] | Moderate | Low |
| SANS specific surface area [149] | High | Low |
| Atomic packing density [149] | High | Low |
| Amorphous phase content at 28 d | 99 wt.% | 76.2 wt.% |
| Compressive strength at 28 d | 112.7 MPa | 77.6 MPa |
| Compressive strength at 60 d | 113.0 MPa (maximum) | 84.5 MPa (maximum) |

**FA/GGBFS blended pastes**

Figure 3.10 shows the influence of FA/GGBFS ratio on compressive strength development for pastes with l/b=0.4. The results of the compressive strength imply that the addition of a small amount of calcium into FA systems significantly improves their mechanical properties. By increasing GGBFS content, compressive strength increases during the first 90 days. After 1 year, the compressive strength is nearly the same for GGBFS-rich pastes: S70 and S100. A slight decrease of compressive strength for pastes S50 and S70 can be observed at ages > 90 days. However, the level of decrease of the compressive strength is within the band width of the standard deviation. It can also be seen from Figure 3.10 that strength development at 1 year is stagnated for GGBFS > 50 wt.%. This suggests that dissolution of raw materials between 90 days and 365 days was hindered. This is further confirmed in Chapter 6, by comparing the $Na^+$ concentration from the pore solution between 28 and 365 days. The $Na^+$ concentration was not changed for pastes S70 and S100, supporting the strength stagnation. The results for compressive strength of alkali activated pastes are in accordance with calorimetric response of pastes. Alkali activated FA-rich pastes have reduced cumulative heat release in the first 7 days, due to

slower reaction of FA in the pastes compared to GBFS in GBFS-rich pastes. The PARC measurements in Chapter 4 further showed very little consumption of FA in the paste evolution during one year. Consequently, FA-rich pastes have lower strength development.

**S0 paste**

For paste S0 (Figure 3.10), strength development was significantly limited by the low $Na_2O$ concentration of the alkaline activator and due to the applied curing conditions, which for all pastes were the same (unsealed curing conditions, 99% RH, 20 °C). Normally, FA requires much higher $Na_2O$ concentration and elevated curing temperatures (> 40 °C) in order to be dissolved [36]. This is consistent with very low heat release of paste S0, shown in Figure 3.8.



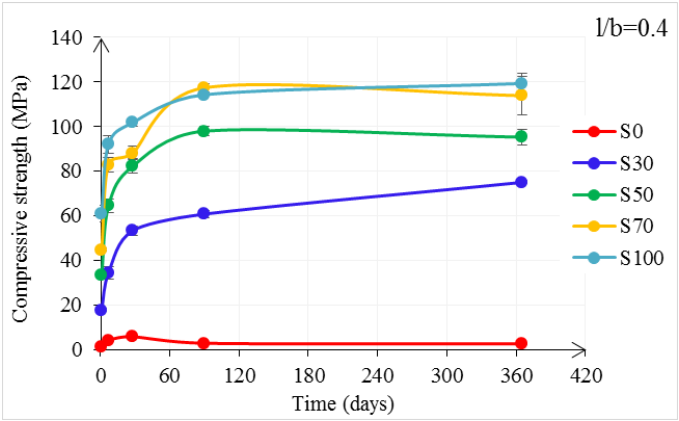


Figure 3.10: Compressive strength development for unsealed cured pastes with l/b=0.4.

Figure 3.11 presents compressive strength development for pastes with l/b=0.5. The compressive strength is slightly lower than for the pastes with l/b=0.4, suggesting that the increase of the l/b ratio does not significantly affect compressive strength development. The tendency of the strength development follows the tendency of the cumulative heat release curves for the first 7 days (Figure 3.8). Higher cumulative heat release of the GGBFS pastes indicated their high compressive strength compared to FA-rich pastes. In Figure 3.11, it can also be seen that with 70 wt.% GGBFS in the mixture, the compressive strength after 1 year reaches almost the same compressive strength as with 100 wt.% GGBFS. Compared to respective pastes with l/b 0.4, this time was 90 days. This implies that, indeed, pastes with l/b 0.4 have stagnation of the compressive strength in particular for paste S100, as indicated in Figures 3.9 and 3.10. The compressive strength development for pastes with l/b=0.5 (see Figure 3.11) shows that studied pastes have satisfactory strength. For these pastes, carbonation resistance will be investigated in following Chapters to show if the carbonation can affect the strength of these binders.

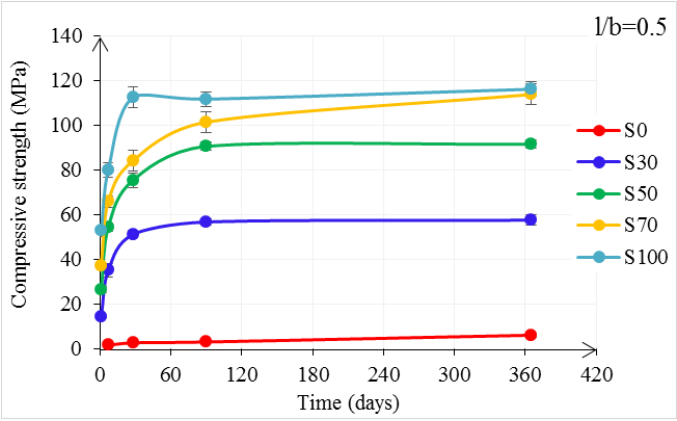


Figure 3.11: Compressive strength development for unsealed cured pastes with l/b=0.5.

### 3.4.4.2. FLEXURAL STRENGTH

Figure 3.12 shows the influence of l/b ratio on flexural strength development for paste S100. The flexural strength increases during the first 7 days, whereas it decreases at 28 days, for both l/b=0.4 and l/b=0.5. At later age, i.e. at 90 days, the flexural strength for l/b=0.4 increases, while for l/b=0.5 it has no further change. Between 90 and 365 days, it decreases to a minimum for l/b=0.4, while increases for l/b=0.5, resulting in a strength of 3.5 and 4.0 MPa, respectively.

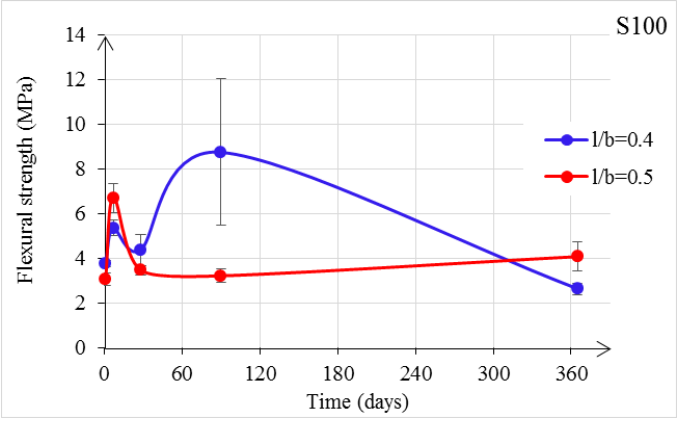


Figure 3.12: Flexural strength development for unsealed cured pastes with l/b=0.5.

Figure 3.13 shows the influence of FA/GGBFS ratio on flexural strength development for pastes with l/b=0.4. The flexural strength has similar behaviour for pastes S30, S50 and S100, while paste S0 and paste S70 showed a different behaviour. Similar to the compressive strength development, paste S0 has slow development of the flexural strength. For pastes with GGBFS, the scatter is significant and there is only increasing tendency

for paste S70. The flexural strength development for pastes with l/b=0.5 has different behaviour than for pastes with l/b=0.4 (see Figure 3.14). It increases for pastes S30, S50, S70, while it decreases only for paste S100. The scatter among different pastes with l/b=0.5 is less noticeable in comparison with that in pastes with l/b=0.4.

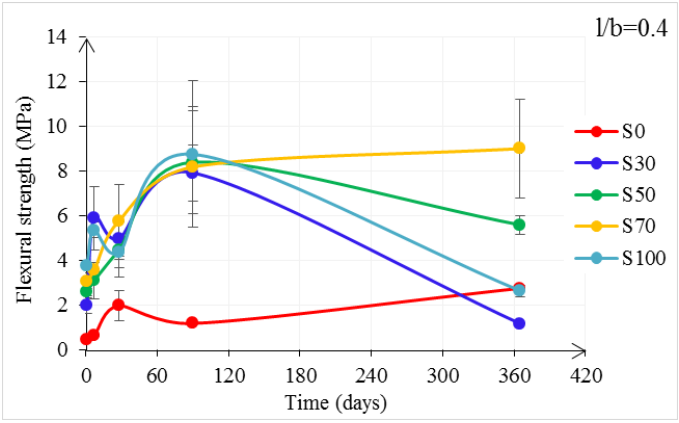


Figure 3.13: Flexural strength development for unsealed cured pastes with l/b=0.4.

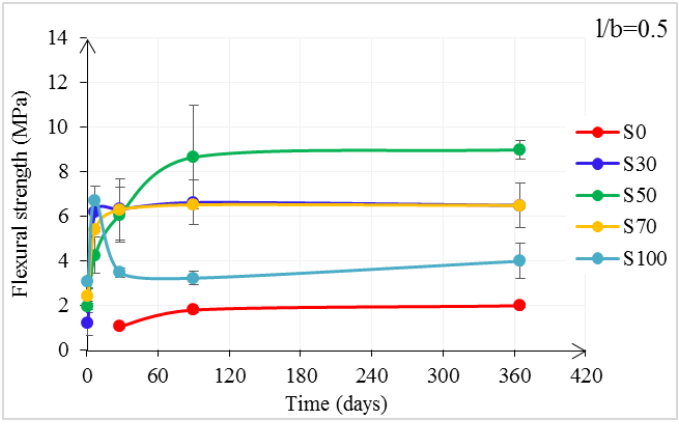


Figure 3.14: Flexural strength development for unsealed cured pastes with l/b=0.5.

Large deviations of flexural strength evolution appear in all alkali activated GGBFS pastes, specifically for lower l/b ratio (see Figure 3.13). The large scatter is mainly due to the development of microcracks, which were observed visually and microscopically. Microcracks were present at both surfaces of the sample (Figure 3.15), but also inside the sample. Li et al. [153] reported significant autogenous shrinkage of alkali activated FA/GGBFS pastes (S30, S50, S70, S100) during the first 7 days. Microcracks were consequently generated. This is also observed by Collins and Sanjayan [154], Ye et al. [152], Thomas et al. [149] and Hubler et al. [155]. Nevertheless, microcracks did not influ-

ence the compressive strength. The larger amount of reaction products, with elapse of time, resulted in higher compressive strength (see Figures 3.10 and 3.11). However, when the pastes were tested in bending, microcracks play a significant role. In particular, flexural fracture of pastes can be affected due to small defects such as surface drying shrinkage-induced microcracking compared to the mortar or even concrete, where these defects are normally reduced due to presence of aggregates and sample size. Moreover, the microcracks in GGBFS-rich pastes, if connected, can form preferential continuous pathways for mass transport and faster propagation of the carbonation front. For this reason, microcracks are expected to influence not only the flexural strength but also the carbonation.



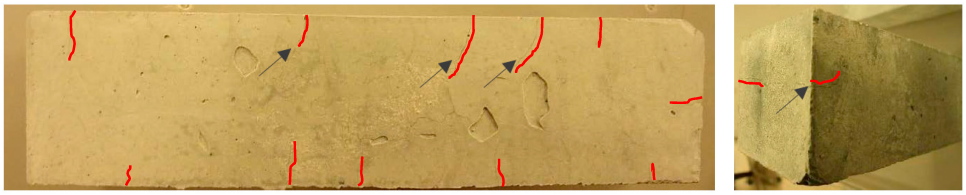

Figure 3.15: Visual observations of sample S100 surfaces. Samples were unsealed cured for 14 days (fog room, at 20°C 99% RH) and subsequently removed to laboratory conditions, at 20°C and 55 % RH. Arrows point to microcracks patterns, which are coloured in red. (The microcracks were the most present on the top surface, while on the other sides of samples their appearance was less).

Beside shrinkage induced microcracking, the "*defect density of unreacted material*" could also potentially be an explanation for observed flexural strength behaviour. The concept has been proposed by Duxson et al. [156] for metakaolin-based geopolymers with various Si/Al ratios. It is related to the gel transformation and densification during geopolymerization. It is believed that the *defect density* increases with an increase of amount of unreacted material (which is a potential reason for larger scatter of the results with l/b=0.4 compared to the results with l/b=0.5, since larger amount of unreacted material is assumed to be present in pastes with lower l/b ratio). Consequently, with an increased defect density, the number of potential pathways to failure increases accordingly. In addition, it was found that more labile species present in the pore solution and gel nanostructure of AAMs with lower $SiO_2/Na_2O$ ratio allow a greater degree of structural reorganization and densification of the gel units prior to hardening [156]. The structural ordering of these gel units, their interconnectivity and their morphological, physical and chemical changes over time play a critical role in understanding mechanical strength evolution. Further research is needed to investigate and quantify this behaviour in alkali activated FA/GGBFS materials.

## 3.5. CONCLUDING REMARKS

The aim of this chapter was to obtain mixtures with adequate workability, setting time and mechanical properties for carbonation study. Fresh properties and mechanical performance of the pastes have been studied for different l/b ratios, different FA/GGBFS ratios and a constant alkaline activator composition.

It is found that the FA/GGBFS ratio of the mixture significantly affects workability, setting time and mechanical properties of alkali activated pastes. Although FA and GGBFS vary in chemical composition and mineralogy, results showed that blended systems exhibit high reaction rates and high mechanical strength. In general, GGBFS-rich mixtures had shorter setting times due to high reactivity of GGBFS. Regarding the rate of heat evolution of the mixtures, the pure GGBFS (S100) has the highest rate of heat release, subsequently developing higher compressive strength than other mixtures. In contrast, none or very little amount of reaction products were formed in paste S0. The reason of the unreactivity of FA is the composition of the amorphous phase being a glass too high in alumina and silica to react in selected alkaline and curing conditions, despite being amorphous (as will be shown with PARC analysis in Chapter 4). To this end, carbonation mechanism is expected to be also dependent on the paste mixture composition.

Regarding the influence of l/b ratio on the investigated properties, it was found that mixtures with l/b=0.4 have faster initial setting time and stiffer consistency than mixtures with l/b=0.5. The l/b ratio does not significantly affect the compressive strength development. However, l/b=0.5 improved workability and provided longer initial setting time for the pastes, which is one of the main criterion for casting concrete batches (Chapter 10). Therefore, l/b=0.5 is used in mixture design for pastes and concretes in the following studies on carbonation.

With regard to the scatter in flexural strength of the pastes, it is assumed that shrinkage-induced microcracking and "*defect density of unreacted material*" are the main reasons for such behaviour. Further research is needed to confirm these mechanisms in alkali activated FA/GGBFS materials.

# 4

# MICROSTRUCTURE CHARACTERIZATION OF ALKALI-ACTIVATED PASTES

*"No design is possible until the materials with which you design are completely understood."*

Ludwig Mies van der Rohe

*The reaction products and pore structure are fundamental features of a material. Their correct characterization provides the basis for understanding of their evolution. This chapter presents the use of PhAse, Recognition and Characterization (PARC) software for determination of the spatial distribution of reaction products and their chemical composition in the microstructure of alkali activated pastes. The curing conditions can have a significant influence on the performance of alkali activated pastes under carbonation. For that reason, the effect of curing conditions, beside the effect of content of ground granulated blast furnace slag (GGBFS) on the gel formation, was studied. It was found that sealing of the samples resulted in formation of gel phases with a higher $Na^+$ uptake compared to the unsealed cured samples during first 28 days of reaction. The results showed that alkali activated pastes react at different rates with the dominant reaction products being Mg-rich gel (Ca-Mg-Na-Al-Si-H) around GGBFS particles and Ca-Na-Al-Si-H gel and Ca-Al-Si-H gel in the bulk paste. The characterization of physical properties, such as pore volume and pore size distribution, was performed with MIP and Nitrogen adsorption. Fly ash (FA) replacement level by GGBFS had significant effect on the pore structure evolution. The most prominent effect was observed in GGBFS rich pastes, where the porosity was reduced to 4 % when the amount of GGBFS used in the mixture increased up to 100 %. Increase of the GGBFS content decreases the total porosity by a factor of 10 (43.72% to 3.67%). Microstructure characterization of carbonated pastes will be presented in Chapter 7. The study on the effect of carbonation on the pore structure will be presented in Chapter 8.*

## 4.1. INTRODUCTION

THE MICROSTRUCTURE of AAMs, i.e. the reaction products and unreacted particles, their chemical composition, amounts and their distribution, make the fundamental link between the early age and long-term properties [157]. The chemical, physical and mechanical properties of microstructure depend on the chemical composition of the precursor materials [75, 158, 159], the type and concentration of the alkaline activator [77, 160] and the curing [19, 76].

The principal reaction product of alkali activated ground granulated blast furnace slag (GGBFS) is calcium (-sodium) aluminosilicate hydrate (C-(N-)A-S-H) gel [161, 162]. In alkali activated fly ash (FA) [163] sodium aluminosilicate hydrate gel (N-A-S-H) is the main reaction product. The changes of the microstructure and chemical composition of reaction products in AAMs over time have been the focus of many studies [32, 159, 164–166]. Despite numerous efforts on characterization of AAMs [32, 166, 167], rigorous definitions of the reaction products (N-A-S-H, C-A-S-H, C-(N-)A-S-H) do not yet exist. The presence of alkalis in the system even more complicates defining the reaction products. It is reported that alkalis can exist in several forms in AAMs, i.e. incorporated in C-S-H, physically adsorbed on the surface of reaction products and free in the pore solution [168].

The carbonation degree and the risk of reinforcement corrosion in alkali-activated concrete significantly depends on the $Na^+$ concentration in the pore solution. The use of highly alkaline activators for reaction of the FA and GGBFS provides a high concentration of $Na^+$ and leads to high pH levels in the pore solution of noncarbonated AAMs. Bernal et al. [62] showed that the Na content after natural and accelerated carbonation in alkali-activated concrete is sufficiently high to prevent corrosion of reinforcement. However, the potential leaching of $Na^+$ ions from the concrete, prior to (or during) the carbonation process, that can lead to a drop of the pH, has not been considered yet.

Beside the effect of the chemical composition of the precursor materials and activator concentration, understanding the link between curing conditions and microstructural properties of AAMs is of critical importance for the development of a durable material [122, 155]. Hubler et al. [155] have addressed this issue by showing that unsealed cured specimens can suffer from microcracking due to internal stresses caused by shrinkage, ultimately leading to a lower compressive strength compared to sealed cured specimens. Furthermore, it is found in this thesis (see Chapter 6, Figure 6.5) that the pore solution composition of sealed and unsealed cured samples is substantially different. Nevertheless, the effect of curing conditions on the composition of the reaction products, degree of reaction and microstructural features has not been investigated yet. Moreover, the effect of curing conditions on the carbonation mechanism in AAMs is unknown.

The main bulk characterization techniques in material science such as XRD, FT-IR, TG, NMR, SANS and in particular SEM-EDX, have been used extensively to test the chemical and spatial characteristics of materials [22, 162, 169, 170]. The SEM-EDX can be used for both local and bulk analyses. Both are important to interpret the behavior of multiphase materials. In general, bulk characterization with Spectral Imaging (SI) of the samples with SEM-EDX has not been utilized to its full potential because of the lack of techniques and algorithms for deriving phase compositions and distributions from SI

data sets. This is partially because of the fact that element overlays from SI are limited to combinations of maximum three elements if unique colour coding per phase is required. This is too restricted for analysis of multi-element materials like AAMs. With other algorithms, like Principle Component Analysis, principle components and phases do not necessarily coincide. Moreover, for microstructure characterization of alkali activated GGBFS/FA pastes, it is of great interest to estimate the relative contribution of FA and GGBFS to the degree of reaction, which is not possible with the current algorithms.

The aim of this chapter is to characterize raw materials (FA and GGBFS), unreacted FA and GGBFS and their reaction products in alkali activated pastes [72]. For that reason, an advanced characterization tool for multiphase materials overcoming the shortcomings of commercial SI-based phase recognition tools was used. Namely, PhAse Recognition and Characterization (PARC) software developed by Van Hoek et al. [72] was applied. PARC has been previously used for characterization of cultural heritage objects [171], dust characterization [172] and microstructure of metallurgical slag produced in steelmaking [72, 73]. With PARC, the effect of curing conditions and GGBFS content on the spatial distribution and compositional domains of the reaction products of alkali activated pastes is assessed. Two mixtures were chosen with the emphasis on the type of precursor, including a single system (alkali activated GGBFS, referred as S100) and a binary precursor system (alkali activated GGBFS+FA, with 50%-50% weight ratio referred as S50). The degree of reaction of FA and GGBFS was determined. Pore structure was also characterized.



## 4.2. MATERIALS AND METHODS

### 4.2.1. MATERIALS AND SAMPLE PREPARATION

Characterization of raw materials and mixture design are given in Chapter 3 (Table 3.1, Table 3.2). The precursors (FA, GGBFS) were dry-mixed for 2 minutes and then mixed with the activator. The pastes were cast in the polyethylene vials with a 35 mm diameter and 70 mm height and vibrated for 15-30 s on a vibrating table. The samples were stored in the closed vials for 24 h after casting. For unsealed cured conditions, samples were removed from the vials and cured afterwards in a curing room at room temperature and a relative humidity (RH) of ~99% for 28 days. On the other hand, sealed samples were kept in the vials in the curing room where unsealed samples were also cured. The samples were tested up to 1 year. The samples were characterized with PARC, XRF and XRD after certain periods of curing (1, 7, 28 days and 1 year). After a certain period of curing, the representative samples were gently crushed (from the sample surface) into small pieces with dimensions of approximately 1-2 $cm^3$ and immersed in isopropanol for one week, by which water is firstly replaced and then evaporated. Subsequently, samples were placed under vacuum at 25 °C for at least three weeks prior to testing. After this predrying, the samples were impregnated using a low viscosity epoxy resin and then polished down to ¼ $\mu$m. Before performing SEM-EDS, a carbon coating was applied to the polished sections of the samples. The pore structure was investigated with MIP and $N_2$ adsorption.

### 4.2.2. METHODS

#### 4.2.2.1. SCANNING ELECTRON MICROSCOPE/ ENERGY-DISPERSIVE X-RAY SPECTROSCOPY (SEM-EDX), PARC, IGOR

The characterization methodology is based on the following steps:

- Spectral Imaging (SI) of the samples with SEM-EDX,
- evaluating the SI images with PARC software to define phases, their area/volume percentages and spatial distribution,
- calculation of bulk chemical compositions of the phases and consistency check with bulk composition from XRF analysis.



A general description of each of these steps is given next.

**SEM-EDX**

To study the paste microstructure, a JEOL JSM-7001F FE-SEM, equipped with two EDX detectors (30 $mm^2$) and a Thermo-Noran System 7 EDX microanalysis system with NSS.3.3 software, was used.

The optimal microscope conditions for microanalysis were determined with Monte Carlo simulation in WinCasino v2.41 software (`www.gel.usherbrooke.ca/casino/index.html`) [167], using their experimental density (2.97 $g/cm^3$ for GGBFS and 2.6 $g/cm^3$ C-(N-)A-S-H gel) as an input parameter.

Based on several iterative experiments, 15 kV was chosen as an optimum beam accelerating voltage. Figure 4.1 shows the maximum penetration depth of the electron trajectories, ranging from 0.6 to 1.8 $\mu$m for GGBFS particles and from 1.0 to 2.5 $\mu$m for C-(N-)A-S-H gel. For backscattered electrons, the maximum sampling depth was about 30% of the interaction volume depth and its lateral dimension was close to the interaction volume depth. As electrons penetrate deeper, the lateral spread of the electron-solid interaction region increases. The lateral dimension of the interaction volume for cement-based materials is thought to be around 1-2 $\mu$m [173] which can be taken as the chemical spatial resolution for the SI.

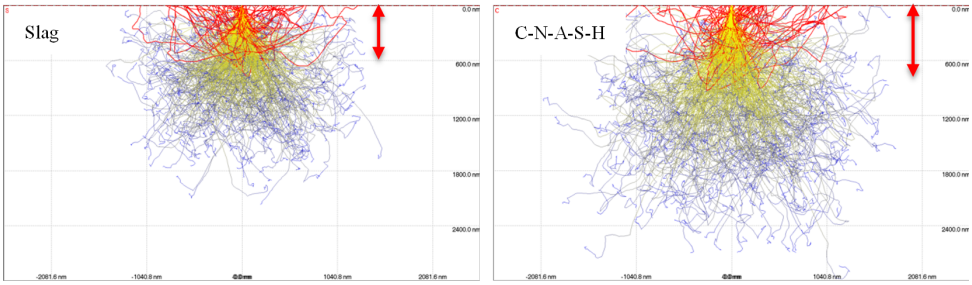


Figure 4.1: Monte Carlo simulation of the penetration of 1000 electrons accelerated at 15 kV in a beam of radius 10 nm into a GGBFS (left image) and C-(N-)A-S-H gel (right image). (The red trajectories are back-scattered electrons, which result from elastic scattering events. Inelastic scattering events cause a reduction of energy of the electrons until eventual disappearance in the specimen bulk. Yellow trajectories represents high energy and blue represents low energy trajectories.)

For the microscope the following settings were used: accelerating voltage 15 kV, beam current 3.4 nA, magnification 500× (equivalent to a field width of 256 microns) and a working distance (is distance between the pole piece and the specimen surface) of 11.5 mm. Video images were collected with a resolution of 1024×768 (pixel size equal 0.25 $\mu$m). For EDX data collection, the resolution of each SI dataset was 512×384 (pixel size equal 0.5 $\mu$m) with a total acquisition time of 3600 seconds. The microscope and EDX settings were kept constant for all the samples. An example of a stitched SEM-BSE image of nine fields is presented in Figure 4.2. The 3×3 matrix (00-22) is selected so that the phase distributions over a larger sample area can be determined. Finally, SEM-EDX analysis provides data on chemical composition across the large field of the sample by spectral imaging.



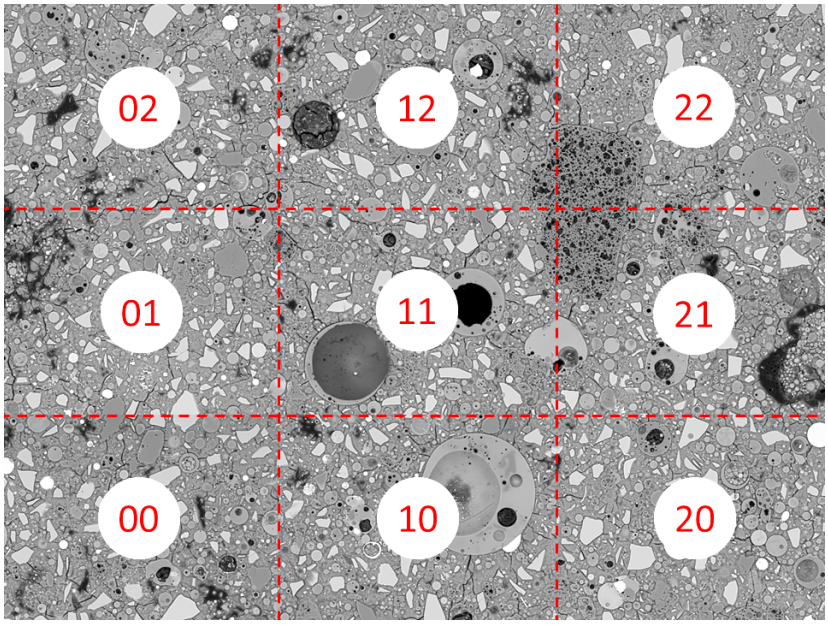


Figure 4.2: SEM-BSE image of the area of interest (3×3 matrix (fields are labelled 00-22), with an individual SI field comprising 512×384 pixels) for paste microstructure characterization. (Sample is paste S50, unsealed cured for 28 days). All 9 fields of the area were analysed under the same analytical conditions. Total field width equal 750 $\mu$m.

**PARC**

The PARC software was used to evaluate the SI data files. After loading the SI data file in the PARC software, from each individual pixel spectrum a user defined number of channels, covering the energy range of interest, is used for evaluation of the peak position and heights in each spectrum. The collected spectra are classified into empty-, embedding-, pure phase- and mixed spectra (e.g. from a phase boundary) based on detected peaks exceeding a user-defined threshold value. Empty spectra contain no peaks, embedding spectra only peaks from epoxy or conductive resin and all other spectra contain meaningful spectral information. The next step is grouping spectra with identical

peak combinations and designating these as PARC phases [72].

Using this procedure, all individual pixels are assigned to different phase groups. Once a particular setup (phase model) is defined, this model can be applied to multiple SI-datasets collected using the same analytical conditions.

Figure 4.3 presents an example of the PARC phase map of a SI dataset of the microstructure (sample is paste S50, unsealed cured for 28 days). The phase model obtained for the first field (00 field, see Figure 4.2), can be applied to other fields provided these were acquired under the same analytical conditions. If all the pixels in the new field are recognized with the first phase model, a next field can be processed. In case the second field contains pixels that are not recognized using the phase model, they will be assigned to new PARC phases and the PARC model will be updated accordingly. This continues until all pixels in all 9 fields are satisfactorily assigned (see Figure 4.2). When the final phase model is defined, the PARC phase area proportions and phase spectra results are exported. Spectra are processed using the NSS standardless analysis technique and PhiRhoZ correction software (correction software for average atomic number, absorption and fluorescence). An example of PARC legend of different phases (groups) is shown in Figure 4.3 (right) for the paste S50.



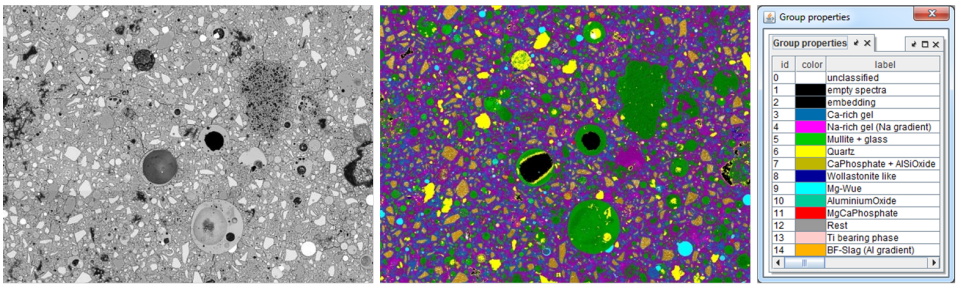


Figure 4.3: BSE image of the sample (left), and its corresponding PARC phase map (middle). PARC legend (right) of different phases (groups) defined for the paste S50 (unsealed cured for 28 days) for phase map of the middle image.

**IGOR**

In addition to PARC, IGOR PRO 7 was used for quantification of the mass percentage of each phase. IGOR is a statistical program with mathematical and image processing functions (www.wavemetrics.com) that is here used in combination with PARC to:

- combine the information obtained from multiple fields and obtain the measurement deviations,
- calculate average phase chemistry for one or multiple fields,
- calculate average/sum area % per phase for multiple fields,
- calculate sample bulk chemistry (mass balance) with densities of the unreacted FA and GGBFS (known) and reaction products (gel).

To convert the phase areas (obtained from PARC) to phase mass percentages, the density of each phase (gel and unreacted FA and GGBFS) are required. The gel density depends on the chemically bound water and gel porosity [120]. Therefore, to measure the gel density, the changes of gel porosity during the reaction should be known. This is obtained by measuring the nitrogen surface area, pore volume and capillary porosity of the sealed pastes with mercury intrusion porosimetry and Nitrogen adsorption tests [174]. Then, the density of gel is calculated based on density of bulk paste (obtained from MIP), the density of unreacted materials (known a priori) and the porosity of the bulk sample, as follows:

$$(\frac{m}{\rho})_{gel} = (\frac{m}{\rho})_{bulkpaste} - (\frac{m}{\rho})_{GGBFS} - (\frac{m}{\rho})_{FA} - V_{pore} \tag{4.1}$$

The calculated densities were then assigned to the gel phases in order to convert the PARC gel area measurements to phase proportions (wt.%). As also presented before, the density of the FA and GGBFS used in this study are 2.44 g/cm$^3$ and 2.97 g/cm$^3$, respectively. It should be noted that FA contains different minerals and each particle has different density, which are given in Table 4.2, Column 2 (see section 4.3.1.2). The gel calculated density varied between 1.7 g/cm$^3$ and 2.2 g/cm$^3$, depending on the mixture composition.



**Degree of reaction**

The degree of reaction of GGBFS and FA is calculated by comparing the volume fraction ($V_t$) of unreacted materials (GGBFS in paste S100 and GGBFS+FA in paste S50) with the volume fractions prior to the mixing of raw materials with alkaline activator (at time zero, $V_0$).

Based on the stereology principles [175], the area fraction of unreacted GGBFS and FA in a 2D image is equal to the 3D volume fraction. The area fractions of unreacted GGBFS and FA were obtained from multiple fields (the representative fields for each curing time are shown in Figure 4.20a-fii and Figure 4.25a-fii) in PARC analysis. The degree of reaction of GGBFS or GGBFS and FA is then calculated as:

$$\alpha(t) = (1 - \frac{V_t}{V_0}) \cdot 100\% \tag{4.2}$$

Volume fractions of GGBFS and alkaline activator at the time zero ($V_0$) in paste S100 were determined from the initial liquid-to-binder ratio. The volume of the activator mixed with 1 kg of GGBFS was calculated as 0.4 l (activator density was measured as 1.25 g/cm$^3$ and 0.5 kg of activator was added). Using the GGBFS density (2.97 g/cm$^3$), 1 kg GGBFS corresponds to 0.337 l. Hence, the volume fraction of GGBFS at time zero ($V_0$) for paste S100 was 45.73%. For the paste S50, similar calculations were made, considering the density of FA (2.44 g/cm$^3$) and GGBFS. The volume fractions of GGBFS and FA at the time zero ($V_0$) for paste S50, were 22% for GGBFS and 26% for FA.

#### 4.2.2.2. X-RAY FLUORESCENCE

X-ray fluorescence (XRF) measurements were carried out using Panalytical AXIOS Max Advanced XRF spectrometer. The tested paste samples were ground to powder and subsequently pressed under high pressure (20 tonnes) into a tablet to obtain homogeneous sample surface for measurements.

#### 4.2.2.3. X-RAY DIFFRACTION

XRD measurements were performed on powered samples. A few grams (3-5 g) of samples were ground to below a fineness of 15 $\mu$m, with an internal standard of 10 wt. % added metallic silicon. Both the sample and the internal standard were premixed and ground for 20 minutes under cycloxhexan (~7 ml) using sintered corundum grinding elements with a McCrone micronizer mill. Afterwards, the slurry was poured into a ceramic dish and transferred to an oven. The slurry was kept for a few minutes at 65 °C in the oven. Subsequently the dried powder was pressed in a bottom-loaded XRD holder and prepared for XRD measurement. XRD diffractograms were acquired from 10° to 130° 2-theta with a Bruker D4 diffractometer using Co-K$\alpha$ radiation and a Lynxeye position-sensitive detector. The Bruker Topas software was used to perform Rietveld quantification of the phases. The Rietveld fitting error obtained on the amorphous phase in the samples, showed high-precision with general statistical errors less than 1.0 % absolute.

4

#### 4.2.2.4. PORE STRUCTURE CHARACTERIZATION

$CO_2$ diffusion is largely dependent on the pore structure properties, i.e. total porosity, pore size distribution and pore connectivity of alkali activated pastes. The pastes can contain capillary pores and gel pores through which $CO_2$ can diffuse. The capillary pores are initially liquid-filled space. With evolution of FA and GGBFS dissolution, the volume of capillary pores is reduced due to formation of new reaction products. Hence, capillary pores are refined with elapse of time and their size ranges from few nanometers to few micrometers. The capillary pores can be connected or disconnected. The gel pores are pores of gel phases and their size is a few nanometers. The gel pores are connected pores. The characterization of the pore structure is essential to clarify the $CO_2$ transport path in alkali activated pastes. For characterization of the pore structure two techniques will be used, mercury intrusion porosimetry (MIP) and nitrogen adsorption. With MIP, pore size from few nanometers to hundreds of micrometers can be determined. Nitrogen adsorption can only assess the nanometer pores. The combination of the two techniques provides comprehensive assessment of the pore structure since both capillary and gel pores are often present in the pastes.

**Mercury intrusion porosimetry**

MIP measurements were performed with a Micrometrics PoreSizer® 9500. The maximum pressure of this device is 210 MPa, which corresponds to a minimum pore diameter of about 7 nm based on a cylindrical pore model. The measurements were carried out in two stages. The first stage was at low-pressure: from 0 to 0.14 MPa. The second stage was at high pressure running from 0.14 to 210 MPa, as an end of intrusion. Then extrusion starts with decreasing the pressure to 0.14 MPa. Figure 4.4 shows typical MIP cumulative curves.

For sample preparation the procedure as described for SEM-EDX analysis was used. Assuming the cylindric pore shape, the diameter of pores intruded by mercury can be calculated using Washburn's equation 4.3 [176]:

$$D = \frac{-4\gamma cos\theta}{P} \tag{4.3}$$

where D is the pore diameter, $\gamma$ is the surface tension of the mercury (0.485 N/m at 25°C), $\theta$ contact angle between mercury and paste (140°), P is the applied pressure to the mercury.

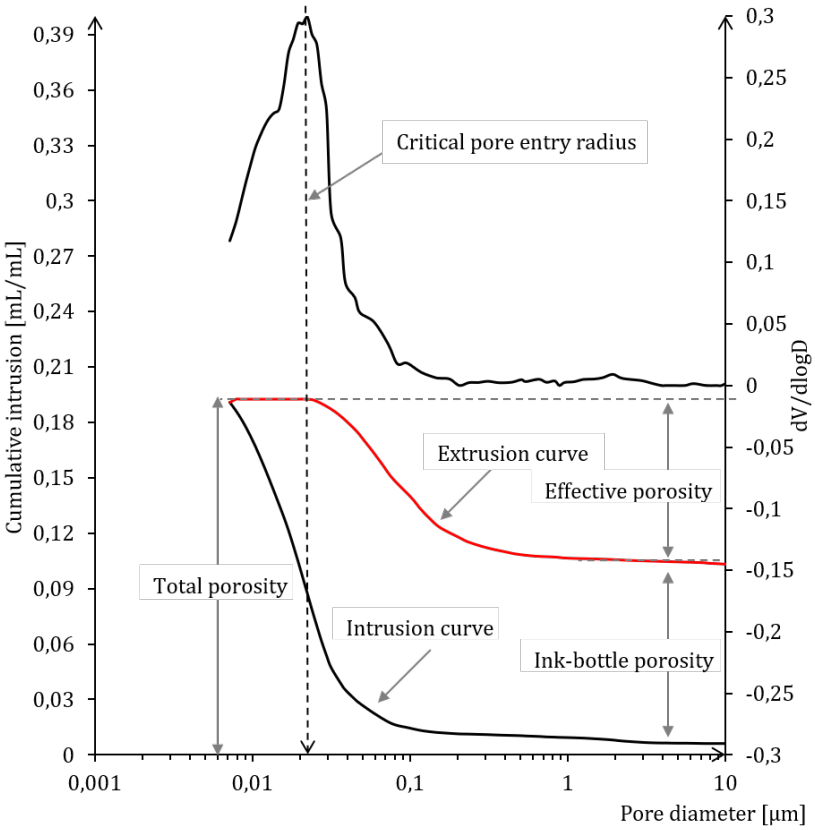


Figure 4.4: Example of the intrusion and extrusion MIP curves obtained for CEM III/B paste (maximum MIP pressure of 210 MPa, CEM III/B paste with w/b=0.5 cured for 56 days). Extrusion curve illustrates ink-bottle pores where the mercury remains trapped in the sample. The characteristic features of MIP cumulative curves are the total percolated pore volume, the effective porosity, the ink-bottle porosity and the critical pore entry diameter.

The main properties of the pore structure of pastes which can be determined from cumulative MIP curves (Figure 4.4) are:

- Total porosity. The total accessible pore volume (interconnected pores) divided by the bulk volume of the sample. It should be noted that the MIP does not measure the total pore volume of the paste. The total pore volume of the paste consists of continuous pores, continuous pores with ink-bottle pores (mercury cannot be extruded from the ink-bottle pores), isolated pores and pores with diameter smaller than 2 nm (Figure 4.5) [177].

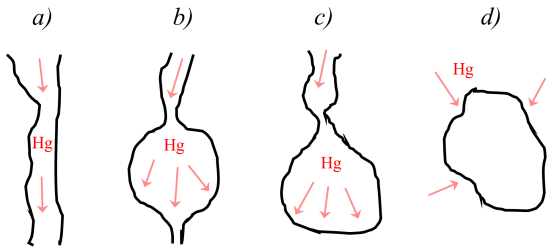


Figure 4.5: Illustration of capillary pore geometry: a) continuous pore, b) continuous pore with ink-bottle, c) dead-end pore with ink-bottle, d) isolated pore, adapted from [177].



- Effective porosity. It is determined from the volume of mercury intruded at the maximum applied pressure in the second intrusion divided by the bulk volume of the sample.
- Ink-bottle porosity. It represents the volume of mercury that remains in the pores after extrusion (Figure 4.6). It can be calculated by subtracting the effective porosity from the total porosity.

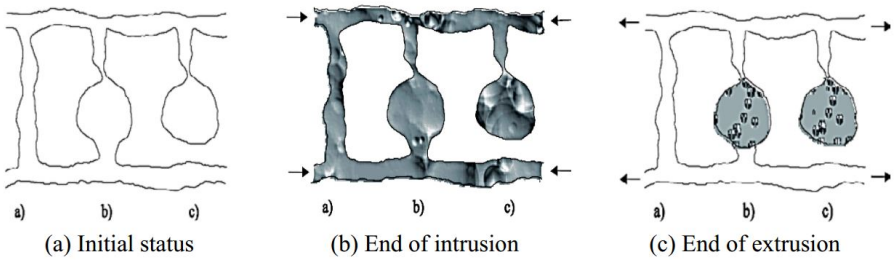


(a) Initial status (b) End of intrusion (c) End of extrusion

Figure 4.6: Illustration of ink-bottle effect (Arrows indicate the flow direction of mercury). Adopted from [177].

- Pore connectivity. Pore network connectivity affects the transport of $CO_2$ and hence plays an important role in determination of the rate of carbonation. It can be calculated as a ratio of the effective porosity over the total porosity.
- The critical (threshold) pore entry diameter. It is defined mathematically by the inflection point of the main intrusion step [173]. The diameter greater than that of the critical pore entry cannot form a connected path through the sample [177].

The total pore volume, pore size distribution measurements and the interconnectivity of pores are critical for understanding the $CO_2$ diffusion in alkali-activated pastes. If the isolated capillary pores are dominant in the microstructure, the mercury will not be intruded. For that reason, isolated capillary pores are assumed not to contribute to the transport properties ($CO_2$ diffusion).

**Nitrogen adsorption**

In absence of capillary pores, connected gel pores (with size larger than 2 nm) become the transport path for $CO_2$ in the microstructure. In those cases, characterization of the gel pore structure is essential. Adsorption and desorption isotherms can be used to study the gel porosity (in this study at an age of 28 days and at later ages). Condensation of the adsorbate in pores occurs as a function of the pore size. Isotherms are determined experimentally being usually depicted as the amount adsorbed gas ($Q_i$) versus the relative pressure ($P/P_0$) of the gas. According to IUPAC [178], adsorption isotherms are classified into six different types. The type of isotherm depends on the nature of the adsorbate gas and the material [173]. Isotherms of type IV are typical for mesoporous materials, such as alkali activated pastes. In this study, $N_2$ adsorption was used to determine the size distribution of pores in the range of 2-37 nm. The $N_2$ adsorption tests were conducted by using Gemini VII 2390 with a relative pressure ($P/P_0$) range from 0.05 to 0.99. The relative pressure is defined as equilibrium vapor pressure divided by the saturation vapor pressure. Approximately 1 gram of sample was used for the analysis.

The interpretation of the $N_2$ isotherms is based on the mathematical models including the equations of Brunauer-Emmet-Teller (BET) or Barrett-Joyner-Halenda (BJH). The BET theory is based on the multilayer adsorption of gas molecules onto the adsorbent. The pore size distributions can be determined from the adsorption or desorption curves. It is assumed that all pores are filled with $N_2$ (Figure 4.7).

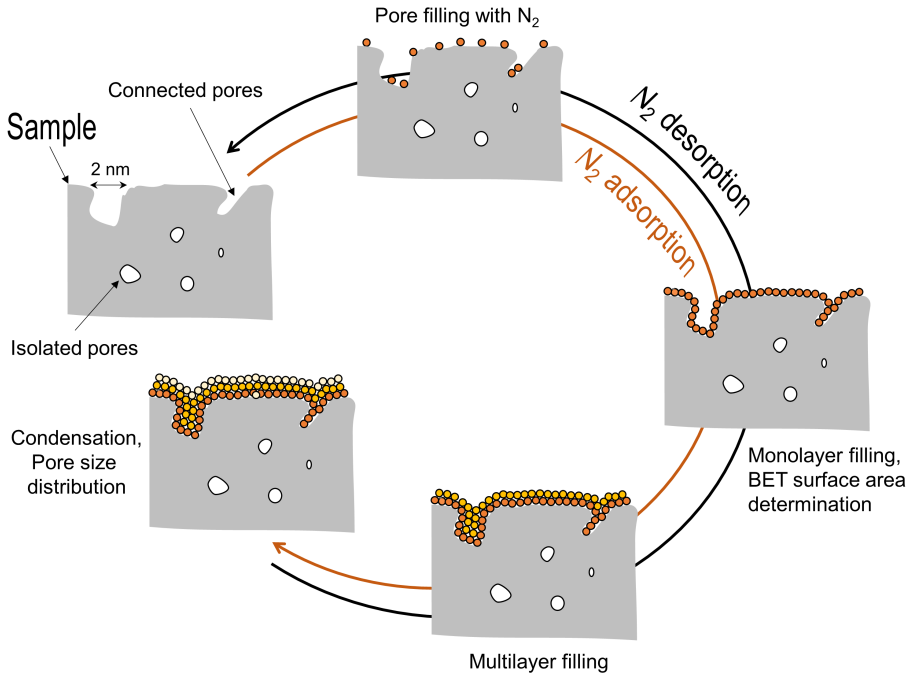


Figure 4.7: Illustration of $N_2$ adsorption and desorption processes on the internal accessible surface area of the pastes.

The mean pore diameter (d) can be calculated assuming a cylindrical pore shape [179]:

$$d = \frac{4V}{S_{BET}} \tag{4.4}$$

where $S_{BET}$ is the BET surface area and V is the pore volume determined from the adsorption isotherm. From the isotherm data using the BET method [180] surface areas can be determined according to Equation 4.5.

$$S_{BET} = \frac{N_A V_m A_n}{V_o} \tag{4.5}$$

where $N_A$ is the Avogadro constant $6.02214076 \times 10^{23}$ $mol^{-1}$, $V_m$ is the amount of gas needed to cover the surface with a monolayer, $A_N$ is the surface area occupied by a single adsorbed gas molecule ($16.2 \times 10^{-20}$ $m^2$) and $V_o$ is the molar volume of gas.

In comparison to the MIP method, the Nitrogen adsorption method is less destructive for the pore structure characterization in terms of the preparation procedure and testing conditions (RH, pressure, temperature). For instance, pore characterization of silicate gel (by-product of carbonation reactions in pastes) with MIP under pressure, the gel structure might collapse and results would be meaningless. Alternatively, filling pores with liquid nitrogen is far less destructive [181]. Therefore, it is very important to have information on the pore structure analysis from both, MIP and Nitrogen adsorption techniques.

## 4.3. RESULTS AND DISCUSSION

### 4.3.1. CHARACTERIZATION OF RAW MATERIALS WITH PARC

#### 4.3.1.1. RAW GGBFS

The representative BSE image of raw GGBFS was divided into nine fields as shown in Figure 4.8. Subsequently, a data set from each SI image field was selected and imported into PARC for the preliminary phase characterization according to the procedure described in 4.2.2.1.

The phases containing (up to) seven X-ray peaks (each peak corresponding to an element) which exceed the selected threshold value as shown in Figure 4.9. Here, the user-defined threshold (minimum energy cutoff) was selected as 0.9 keV. The low energy cut-off at 0.9 keV was selected to exclude O and C which are present in all spectra, and the L lines of transition metals. The sum EDX spectrum of GGBFS pixels is presented in Figure 4.9.

Figure 4.10 shows the large-area PARC phase map of the raw GGBFS and its corresponding phase legend where the GGBFS particles are coded as purple.

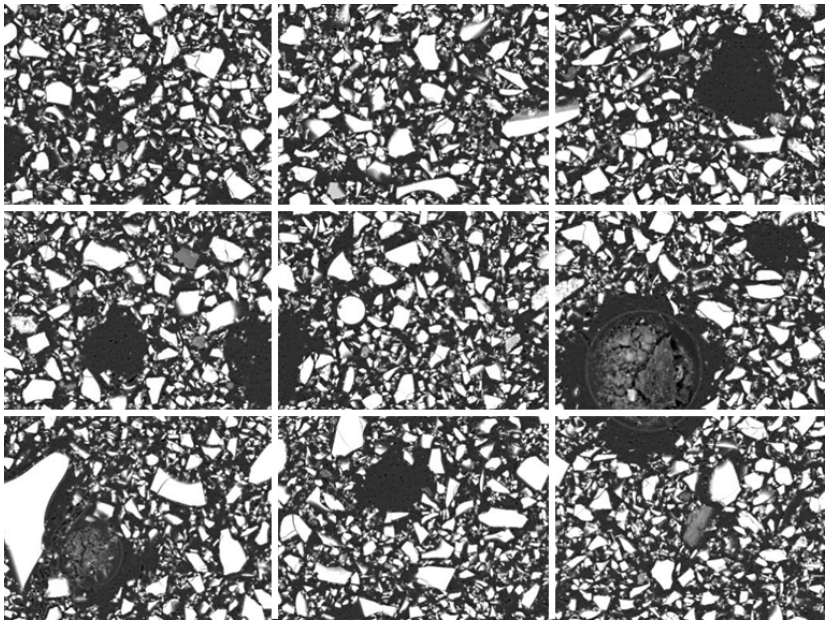

Figure 4.8: Large area BSE image of a polished section of an epoxy impregnated unreacted GGBFS (the number of acquired fields was 9). The image width is 750 $\mu$m.

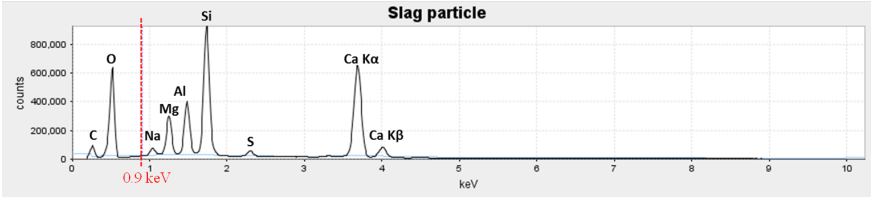


Figure 4.9: PARC sum spectrum for GGBFS particle (purple coloured in the PARC map, Figure 4.10) indicating the presence of Na, Mg, Al, Si, S, Ca by their characteristic X-ray lines.

The compositional domain of GGBFS particles, which was obtained with IGOR, is presented in Table 4.1. Comparison of the GGBFS bulk composition obtained from XRF (see Chapter 3, Table 3.1) and PARC (see Table 4.1), shows close correspondence as well as deviations that can be explained by Fe-metal droplets (yellow circled in Figure 4.10) and $Al_2O_3$ grains (white circled in Figure 4.10) included in the slag samples. These are naturally occurring contaminants in GGBFS.

Table 4.1: Chemical composition of GGBFS measured with PARC (wt.%).

| | $SiO_2$ | $Al_2O_3$ | CaO | MgO | $Fe_2O_3$ | $SO_3$ | $Na_2O$ | $K_2O$ | $TiO_2$ | $P_2O_5$ | MnO |
|---|---|---|---|---|---|---|---|---|---|---|---|
| GGBFS | 35.48 | 13.09 | 38.11 | 8.14 | 0.19 | 2.53 | 0.45 | 0.35 | 1.12 | 0.22 | 0.32 |

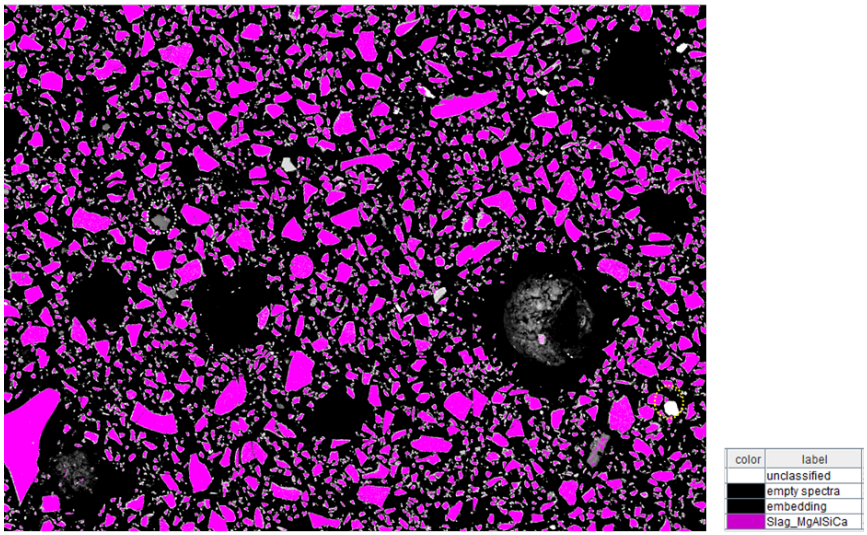


Figure 4.10: Large-area PARC phase map of the unreacted GGBFS (left) (image width: 750 $\mu$m), legend of group phases identified in the unreacted GGBFS (right).

#### 4.3.1.2. RAW FA

Since FA is more heterogenous than GGBFS, its representative area was divided into 12 fields (Figure 4.11).

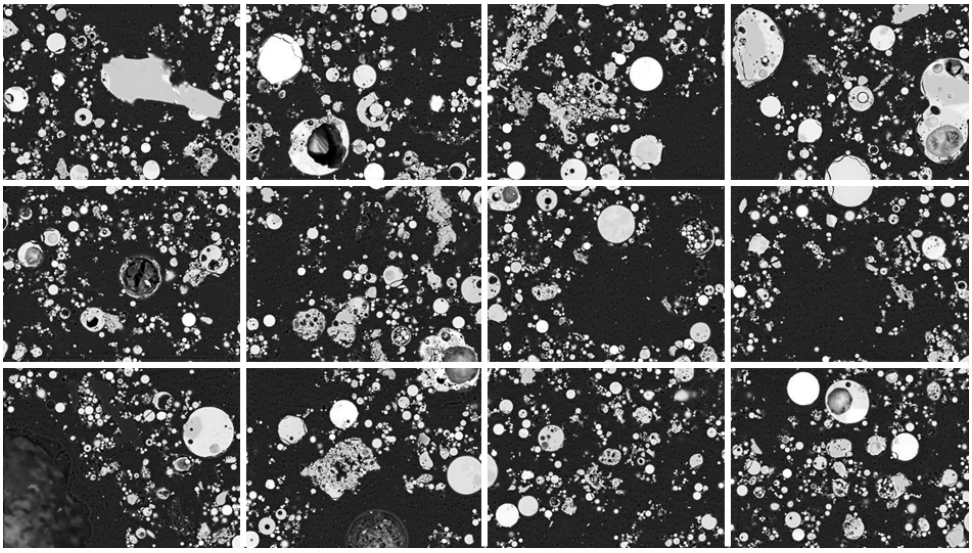

Figure 4.11: BSE image of large-area of a polished section of an epoxy impregnated unreacted FA (the number of acquired fields was 12) (the image width is 1000 $\mu$m).

The EDX spectra for the AlSi and quartz are presented in Figure 4.12 and Figure 4.13. These two phases are the major phases in FA mineralogical composition (see Chapter 5, Figure 5.1). Again, the procedure followed for construction of the phase map was as explained in Section 4.2.2.1. This procedure generated the phase map presented in Figure 4.14 for the BSE image shown in Figure 4.11.

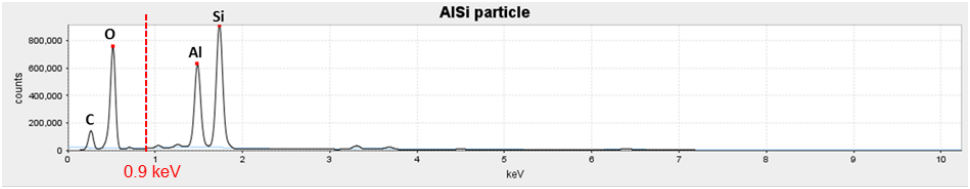


Figure 4.12: PARC sum spectrum for AlSi particle (blue coloured in the composite map, Figure 4.14) indicating the presence of O, Al, Si by their characteristic X-ray lines.

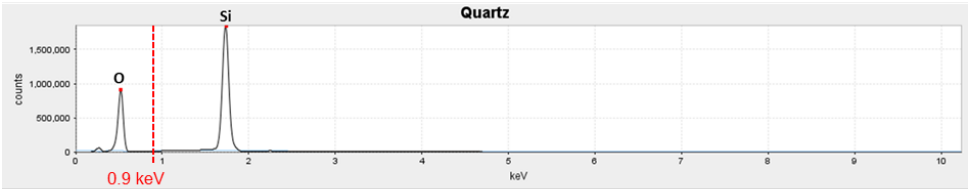


Figure 4.13: PARC sum spectrum for Quartz ($SiO_2$, yellow coloured in the composite map, Figure 4.14), indicating the presence of O and Si by their characteristic X-ray lines.

The distribution of the identified phases in FA particles, Figure 4.14, shows that the main phases are mullite and AlSi glass (blue colour, denoted as AlSi in the legend), which significantly varied in surface area, and quartz (yellow colour) with the corresponding spectra shown in Figure 4.12 and Figure 4.13. Hematite (red colour), Na-, P-, Ti-, Ca-, Mg-alumina silicates and some impurities, such as calcite and dolomite, were also identified. The corresponding phase compositions and their proportions are presented in Table 4.2. The bulk composition of FA obtained with PARC is presented in Table 4.3. It can be seen that PARC data (Table 4.3) agree well with XRF data as far as this FA bulk composition is concerned (Chapter 3, Table 3.1). Furthermore, PARC reproduces very well the quartz and hematite fractions (see Table 4.2) obtained with Rietveld method (see Chapter 5, Figure 5.1).

Figure 4.11 and Figure 4.14 also show how phases can be differently enclosed. For instance, quartz phase (yellow, Figure 4.14) is embedded in the AlSi phase (blue, Figure 4.14). A similar disctinction was also made by Rickard et al. [182], who observed that quartz can be present as a discrete particle (larger crystallite size (>100 nm)) or within FA spheres (smaller crystallite size (<100 nm)). This means that a single particle can contain phases with different glass composition and, therefore, different reactivities of each glassy phase within particle can be expected, as shown in literature [21, 183, 184].

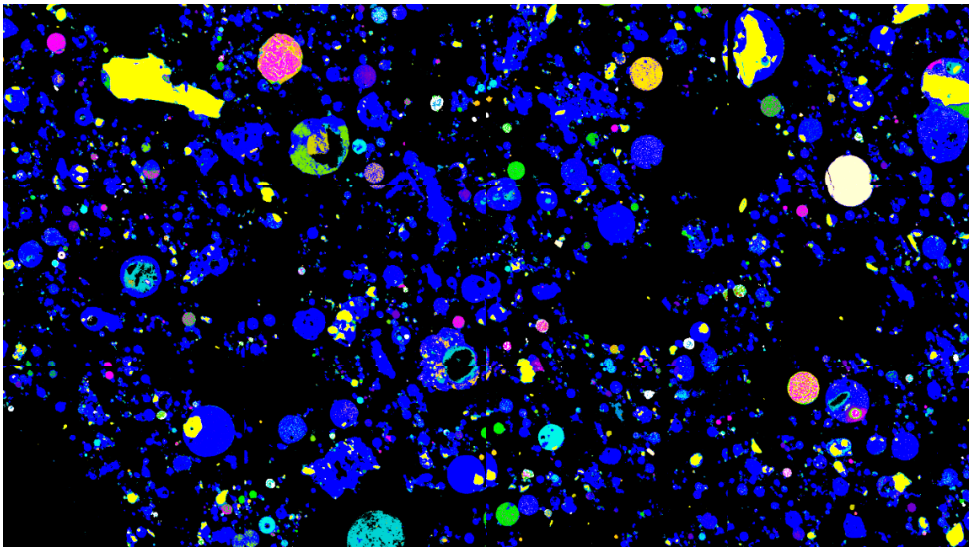

Figure 4.14: Large-area PARC phase image with individual phases in unreacted FA (width 1000 $\mu$m).

Table 4.2: Chemical composition of phase domains of FA particles obtained with PARC (% wt.).

| | Density [g/cm$^3$] | Weight [% wt.] | $Na_2O$ | MgO | $Al_2O_3$ | $SiO_2$ | $P_2O_5$ | $SO_3$ | $K_2O$ | CaO | $TiO_2$ | MnO | $Fe_2O_3$ |
|---|---|---|---|---|---|---|---|---|---|---|---|---|---|
| Quartz | 2.62 | 8.50 | 0.31 | 0.09 | 0.09 | 98.35 | 0.14 | 0.63 | 0.00 | 0.00 | 0.00 | 0.00 | 0.39 |
| Hematite | 5.74 | 0.97 | 0.33 | 0.46 | 0.76 | 3.04 | 0.00 | 0.00 | 0.20 | 0.59 | 0.00 | 0.36 | 94.27 |
| AlSi | 2.44 | 74.21 | 0.88 | 0.64 | 31.51 | 58.67 | 0.48 | 0.26 | 1.74 | 0.87 | 1.11 | 0.03 | 6.37 |
| NaAlSi | 2.44 | 1.91 | 5.36 | 0.78 | 25.58 | 61.24 | 0.57 | 0.16 | 2.03 | 0.60 | 0.58 | 0.20 | 2.90 |
| KAlSi | 2.44 | 1.51 | 1.07 | 0.20 | 19.82 | 66.40 | 0.31 | 0.20 | 10.45 | 0.30 | 0.30 | 0.03 | 0.95 |
| CaAlSi | 2.44 | 2.51 | 0.00 | 0.37 | 35.18 | 41.74 | 0.70 | 0.15 | 0.00 | 17.45 | 0.56 | 0.00 | 3.85 |
| MgAlSi | 2.44 | 1.99 | 1.07 | 9.44 | 20.28 | 57.13 | 0.78 | 0.14 | 1.22 | 1.25 | 0.61 | 0.16 | 7.94 |
| FeAlSi | 2.44 | 0.92 | 0.56 | 1.04 | 14.60 | 39.80 | 0.23 | 0.05 | 0.98 | 0.71 | 1.12 | 0.05 | 40.85 |
| TiAlSi | 2.44 | 0.86 | 1.27 | 1.22 | 29.71 | 43.39 | 0.00 | 0.00 | 1.51 | 2.77 | 14.45 | 1.24 | 4.45 |
| CaMgAlSi | 2.44 | 1.27 | 0.14 | 8.24 | 20.64 | 39.17 | 2.34 | 0.00 | 0.02 | 21.03 | 0.53 | 0.11 | 7.78 |
| MgFe | 2.44 | 1.47 | 0.01 | 6.67 | 1.86 | 0.57 | 0.04 | 0.03 | 0.01 | 0.39 | 0.11 | 0.81 | 89.51 |
| P | 2.44 | 0.93 | 0.00 | 6.09 | 11.6 | 17.14 | 24.01 | 0.07 | 0.30 | 36.60 | 0.88 | 0.00 | 3.31 |
| Calcite | 2.71 | 0.29 | 0.00 | 0.00 | 0.82 | 0.43 | 1.54 | 2.33 | 0.00 | 94.38 | 0.00 | 0.00 | 0.49 |
| Dolomite | 2.87 | 0.12 | 0.00 | 32.17 | 1.30 | 2.09 | 0.97 | 3.75 | 0.07 | 57.65 | 0.09 | 0.14 | 1.78 |
| $Al_2O_3$ | 4.00 | 0.54 | 0.08 | 0.00 | 91.84 | 5.37 | 0.45 | 0.02 | 0.07 | 0.31 | 1.02 | 0.02 | 0.84 |

Table 4.3: Chemical composition of FA obtained with PARC (wt.%).

| | $SiO_2$ | $Al_2O_3$ | CaO | MgO | $Fe_2O_3$ | $SO_3$ | $Na_2O$ | $K_2O$ | $TiO_2$ | $P_2O_5$ | MnO |
|---|---|---|---|---|---|---|---|---|---|---|---|
| FA | 60.46 | 24.99 | 2.21 | 1.13 | 6.02 | 0.38 | 1.05 | 1.70 | 1.41 | 0.59 | 0.06 |

#### 4.3.1.3. OBSERVATION OF MICROSTRUCTURE OF ALKALI-ACTIVATED FA/GGBFS PASTES

Backscattered electron imaging was performed at 28 days to characterize the microstructure morphology before carbonation of alkali-activated FA (S0), GGBFS (S100) and their blends (S30, S50, S70). Paste CEM I was also made as a baseline for comparison between cement and alkali-activated pastes (Figure 4.15). The water-to-binder ratio of CEM I paste was 0.5. All pastes were unsealed cured for 28 days.

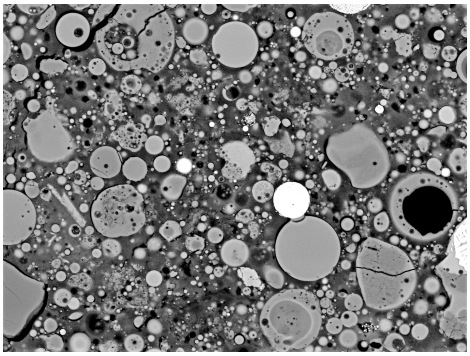

(a) S0 (100% FA), 28 days

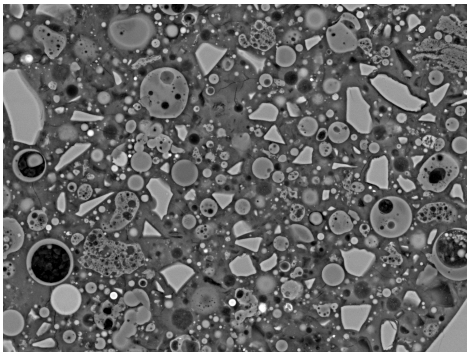

(b) S30, 28 days

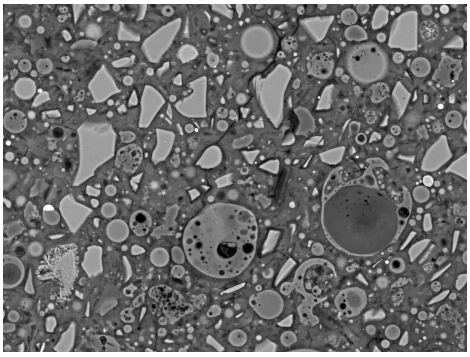

(c) S50, 28 days

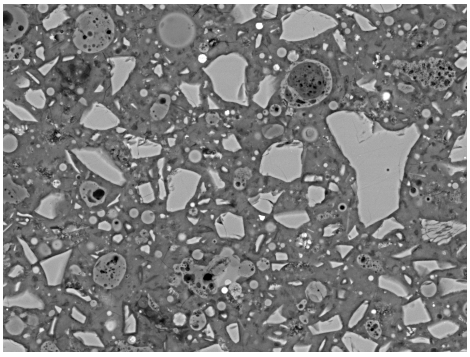

(d) S70, 28 days

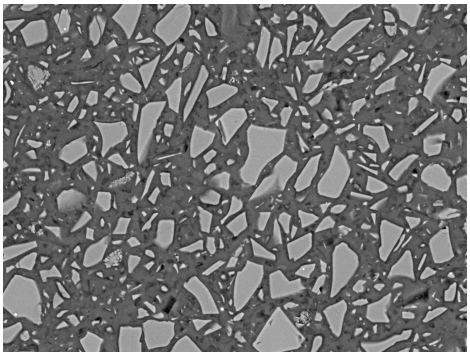

(e) S100 (100% GGBFS), 28 days

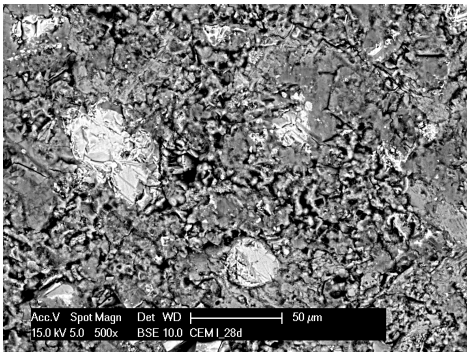


(f) CEM I, 28 days

Figure 4.15: ESEM-BSE images of alkali-activated pastes and paste CEM I at 28 days. For all images, the field size was 250 $\mu$m × 170 $\mu$m.

The SEM-BSE image for paste S0 shows a highly heterogeneous microstructure with different sizes of unreacted FA particles (see Figure 4.15a). It can be noted that pores are present in the gel around unreacted particles or they originate from porous spherical

shells where activator was diffusing during the activation. The porous microstructure of paste S0 is consistent with the limited mechanical strength (Chapter 3, Figure 3.14).

With the presence of GGBFS, the microstructure appeared to be refined (S30, S50, S70, S100), see Figure 4.15b-e. The GGBFS particles are embedded in the gel phases or they surround FA particles. The dissolution processes of FA and GGBFS is different due to their different chemical composition, reactivity and surface area. Simultaneous dissolution of both FA and GGBFS mainly results in gel composed of Ca-Mg-Na-Al-Si-H (see Figures 4.16 and 4.17). Distribution and amount of this gel in the microstructure depends on the type of activator and curing conditions which will be further investigated in Section 4.3.2. Microstructures of pastes S50, S70 and S100 appear denser than pastes S0, S30 and CEM I, as will be further supported with MIP measurements of the pore structure in Section 4.3.3. Compared to CEM I paste (see Figure 4.15f), alkali-activated pastes have a significantly lower capillary porosity at 28 days. The microstructure of paste CEM I is more coarse. Clinker particles are surrounded with reaction products (calcium hydroxide and calcium silicate hydrate gel), while relatively large capillary pores remain.

The amounts of Al, Si, Ca, Mg in atomic-% within the binder regions (excluding unreacted FA and GGBFS) were obtained from EDX spectra. The effect of FA/GGBFS ratios on gel chemistry is shown by CaO-$SiO_2$-$Al_2O_3$ and CaO-$Al_2O_3$-MgO ternary diagrams (Figures 4.16 and 4.17). Calcium, aluminium, silicon and magnesium contents in the samples were renormalized to 100% on an oxide basis, excluding all other elements present in the samples.

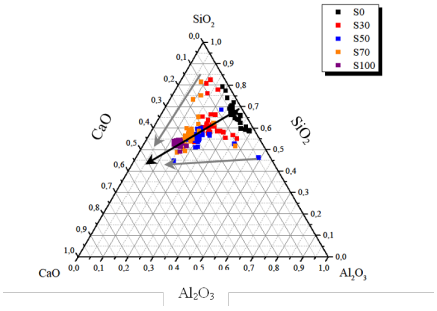


Figure 4.16: Ternary diagram of CaO-$Al_2O_3$-$SiO_2$ as a function of GGBFS replacement level.

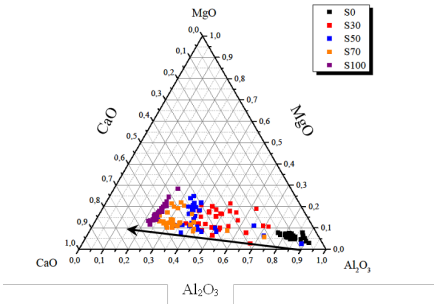


Figure 4.17: Ternary diagram of CaO-$Al_2O_3$-MgO as a function of GGBFS replacement level.

The main reaction products in alkali activated FA paste (S0) consist of $Al_2O_3$ and $SiO_2$ as can be seen from the plotted points in the ternary diagram (Figure 4.16), where the CaO content is close to zero. The main reaction product in alkali activated pastes that contain GGBFS is Ca-Na-Al-Si-H gel with modifications in chemical composition of oxides across the different GGBFS/FA pastes. The $Al_2O_3$ content [0.1-0.4] and $SiO_2$ content [0.6-0.9] of the pastes suggest that all gels are strikingly different in composition for different FA/GGBFS ratios (Figure 4.16).

On the other hand, the CaO content [0.15-0.35] increases with increasing GGBFS content in the mixtures, which clearly indicates the change in gel composition as a function of CaO content (Figure 4.16). The pastes with 50, 70 and 100 % wt. GGBFS exhibit

a uniform composition of the gel, with all points closely clustered as shown in Figure 4.16.The dispersion of MgO can be observed from Figure 4.17. Mg is not only in the Ca-Mg-Na-Al-Si-H gel surrounding the GGBFS particles, but also in Ca-Na-Al-Si-H gel as can be seen from the relation between CaO, $Al_2O_3$ and MgO in the ternary diagram of Figure 4.17 and from the spectra in Figure 4.19. The spatial distribution of MgO, but also other elements, are studied with PARC in the next sections. The proportions and chemical domains of different reaction products are investigated for two mixtures as a function of curing conditions and GGBFS content in single (GGBFS, referred as S100) and binary (FA+GGBFS with 50%-50% mix ratio referred as S50) alkali-activated pastes. Their characterization provides the basis for understanding the microstructure evolution and later the effects of carbonation on the microstructure.

## 4.3.2. CHARACTERIZATION OF ALKALI-ACTIVATED PASTES WITH PARC



### 4.3.2.1. GGBFS PASTE (S100)

The first step is to distinguish the unreacted GGBFS particles and the reaction products. However, this is not an easy task due to the similarity of the chemical compositions of these phases. It is therefore necessary to subdivide the groups with identical combination of elements into different subgroups corresponding to different phases based on the elemental proportions. This can be done in PARC by interactively selecting data regions in bivariate histogram plots or density plots of channel intensities [72] and looking for distinct populations.

The correlation between Mg and Al+Si+Ca content is used for distinguishing the phases. As an example, Figure 4.18a shows regions identified for unreacted GGBFS particle and the reaction products of Ca-Na-Al-Si-H gel and Ca-Mg-Na-Al-Si-H gel of the sealed 28 days cured S100 paste. These regions are used for mapping the phases in the BSE images. In Figure 4.18d the identified GGBFS particle ((b) purple phase) and Ca-Mg-Na-Al-Si-H gel ((c) cyan phase) are presented. The complete map of phases in 28 days sealed cured specimens (with the three main phases of Slag particles, Ca-Na-Al-Si-H gel, Ca-Mg-Na-Al-Si-H gel with chemical compositions in Figure 4.19) is shown in Figure 4.18e.

The phase distributions of the paste S100 as a function of curing time and curing conditions are visualized in Figure 4.20. Backscattered electron images of polished sections are shown in Figure 4.20i. The corresponding PARC maps are presented in Figure 4.20ii. The compositional domains of the three identified phases (Ca-Na-Al-Si-H, Ca-Mg-Na-Al-Si-H, Ca-Al-Si-H) are presented in Table 4.4.It can be observed that the major changes in time are in Na/Si, Mg/Si, Ca/Si element ratios.

The Ca/Si ratio in Ca-Na-Al-Si-H gel of sealed S100 pastes at 1 day is 0.61. From 7 to 28 days this value increases to 0.84. A similar Ca/Si atomic ratios were also observed in the reaction products of alkali activated slag by Ben Haha et al. [120]. After 28 days, the Ca/Si ratio of NaAlSiCa gel did not change significantly (at 1 year Ca/Si is 0.85, Table 4.5).

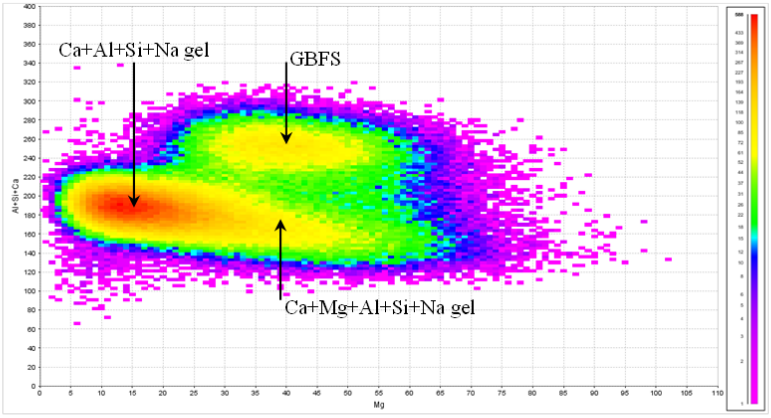


(a) Density plot of Mg and (Al+Si+Ca) to extract groups of pixels for Ca-Al-Si-Na gel, Ca-Mg-Na-Al-Si gel and slag particle, in 28 days sealed cured paste S100.

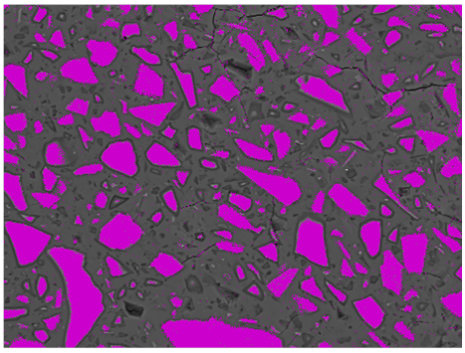

*(b) BSE image with selected pixels from desity plot in highlighted red. GBFS particles. Image width=250 µm*

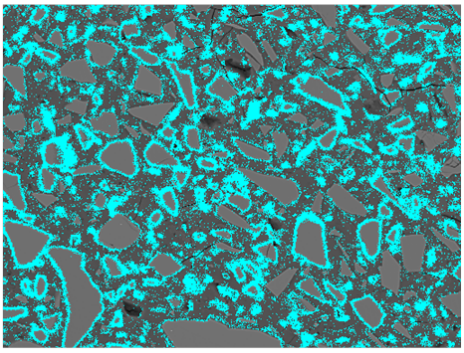

*(c) BSE image with not selected pixels from desity plot in highlighted red. NaMgAlSiCa gel*

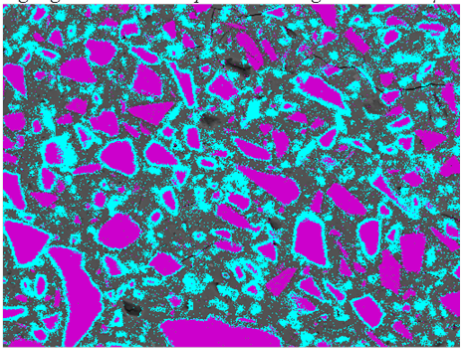

*(d) BSE image corresponds to (b) purple and (c) cyan, the thickness of the NaMgAlSiCa gel rim is 0.5-1 µm*

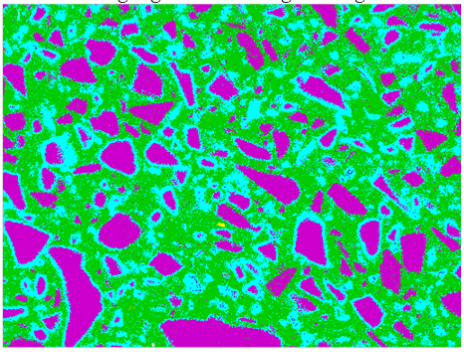

*(e) Complete map, GBFS particles+NaMgAlSiCa gel+ NaAlSiCa gel*


Figure 4.18: SEM-BSE images of the S100 microstructure (sealed cured paste for 28 days), the chemical domains of different phases.

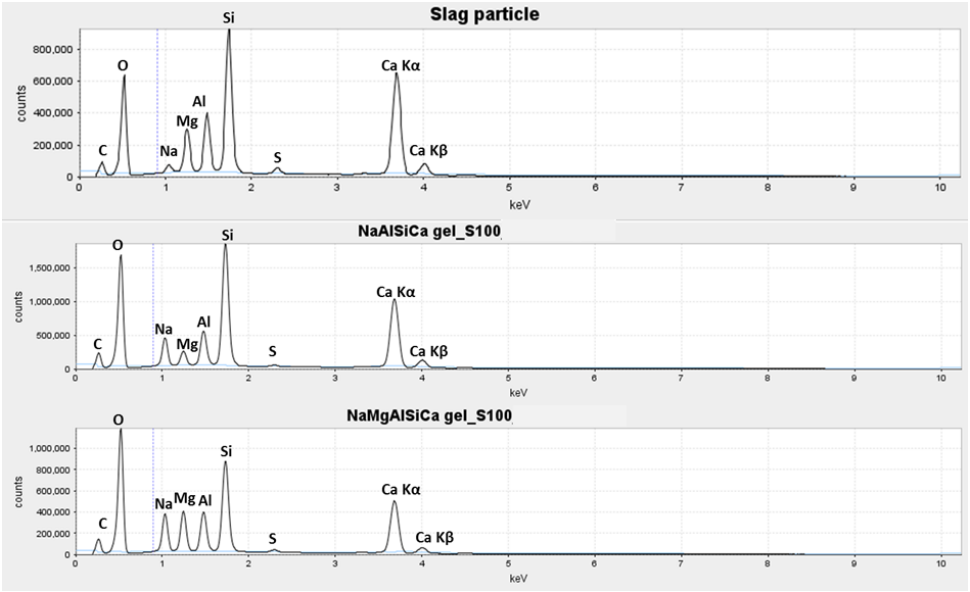


Figure 4.19: PARC sum spectra for chemical domains of slag particle, NaAlSiCa gel and NaMgAlSiCa gel in paste S100.

The fact that Ca/Si does not change after 28 days is an evidence of limited GGBFS dissolution in studied conditions. As long as activator and water are present there is a condition for GGBFS dissolution. At 1 year, it was still possible to extract pore solution from paste (and test for composition, Table 6.5), which proved that both activator and water are present, however, strength and Ca/Si did not change. Based on this, either the gel reached equilibrium with the remaining GGBFS or there is no available space for reaction products precipitation, since porosity of S100 is much lower compared to paste S50 (Table 4.10).

Simultaneously, in the boundary of GGBFS particle a transitional phase develops (Ca-Mg-Na-Al-Si-H gel), which also did not change significantly between 28 days and 1 year. Meanwhile, the Ca/Si ratio of Ca-Na-Al-Si-H gel in unsealed S100 pastes was 0.61 at 1 day and increased to 0.69 (a lower value than that of sealed cured samples) from 7 to 28 days.

The Al/Si ratio is significantly higher in Ca-Mg-Na-Al-Si-H gel (0.36-0.52) than in Ca-Na-Al-Si-H gel (0.25-0.27) in sealed S100 paste. The reason is that Al, similar to Mg, stays rather in the rims of the GGBFS particles (see Figure 4.21) than in the outer gel. The measured Al/Si ratios (0.25-0.27) of Ca-Na-Al-Si-H gel in sealed cured samples were consistent with literature [26, 185, 186]. The Al/Si ratio increases over time in sealed conditions until 28 days, after which no changes are observed until 1 year. The Al/Si ratio values of unsealed cured samples were comparable to that of sealed cured samples.

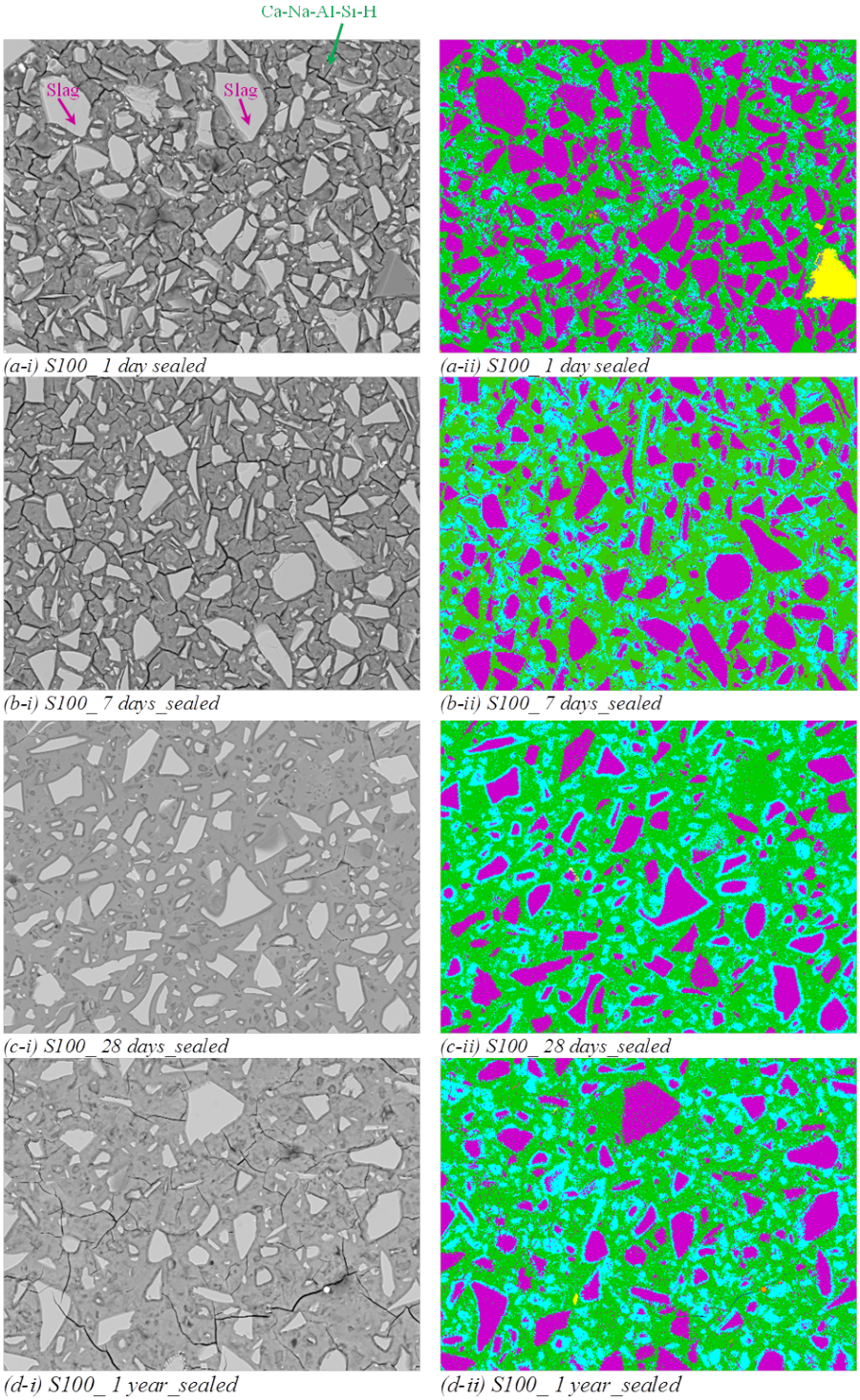


Figure 4.20: SEM-BSE images (i) of the microstructure of paste S100 at different curing periods, with mapped chemical domains of different phases (ii).

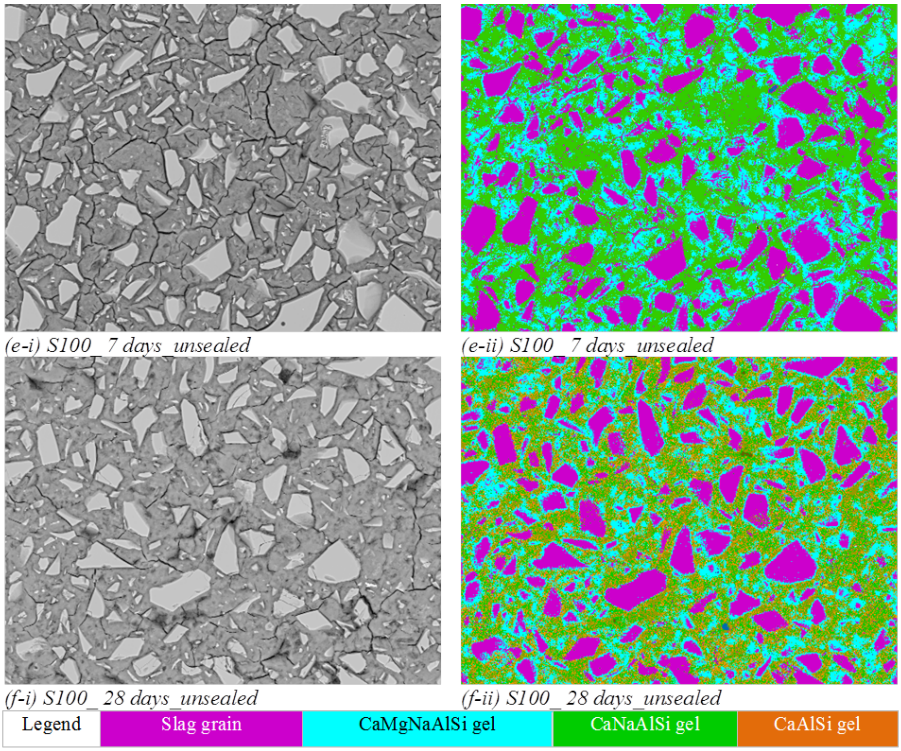


Figure 4.20: SEM-BSE images (i) of the microstructure of paste S100 at different curing periods, with mapped chemical domains of different phases (ii).

Table 4.4: Atomic ratios in the reaction products by PARC analysis in pastes S100.

| Paste S100 | | | | | | | | | | | |
|---|---|---|---|---|---|---|---|---|---|---|---|
| Reaction Products | Ca-Na-Al-Si-H | | | | Ca-Mg-Na-Al-Si-H | | | | Ca-Al-Si-H | | |
| Atomic ratio | Na/Si | Mg/Si | Al/Si | Ca/Si | Na/Si | Mg/Si | Al/Si | Ca/Si | Na/Si | Al/Si | Ca/Si |
| Standard Deviation | ±0.003 | ±0.001 | ±0.003 | ±0.016 | ±0.020 | ±0.017 | ±0.002 | ±0.025 | ±0.007 | ±0.006 | ±0.027 |
| | | | | | | | | | | | |
| 1 day sealed | 0.37 | 0.11 | 0.25 | 0.61 | 0.43 | 0.34 | 0.36 | 0.45 | - | - | - |
| 7 days sealed | 0.37 | 0.11 | 0.27 | 0.64 | 0.31 | 0.53 | 0.46 | 0.66 | - | - | - |
| 28 days sealed | 0.33 | 0.10 | 0.26 | 0.84 | 0.31 | 0.66 | 0.52 | 0.84 | - | - | - |
| 1 year sealed | 0.29 | 0.10 | 0.24 | 0.85 | 0.25 | 0.69 | 0.51 | 0.83 | - | - | - |
| 7 days unsealed | 0.32 | 0.10 | 0.26 | 0.60 | 0.27 | 0.49 | 0.44 | 0.61 | - | - | - |
| 28 days unsealed | 0.12 | 0.11 | 0.25 | 0.69 | 0.08 | 0.41 | 0.40 | 0.73 | 0.06 | 0.18 | 0.71 |

Table 4.5: Atomic ratios in the reaction products by PARC analysis in pastes S50.

| Paste S50 | | | | | | | | | | | |
|---|---|---|---|---|---|---|---|---|---|---|---|
| Reaction Products | Ca-Na-Al-Si-H | | | | Ca-Mg-Na-Al-Si-H | | | | Ca-Al-Si-H | | |
| Atomic ratio | Na/Si | Mg/Si | Al/Si | Ca/Si | Na/Si | Mg/Si | Al/Si | Ca/Si | Na/Si | Al/Si | Ca/Si |
| Standard Deviation | ±0.002 | ±0.002 | ±0.002 | ±0.007 | ±0.033 | ±0.027 | ±0.011 | ±0.024 | ±0.001 | ±0.002 | ±0.002 |
| | | | | | | | | | | | |
| 1 day sealed | 0.33 | 0.10 | 0.26 | 0.30 | 0.35 | 0.29 | 0.32 | 0.28 | 0.19 | 0.30 | 0.37 |
| 7 days sealed | 0.35 | 0.08 | 0.29 | 0.34 | 0.41 | 0.37 | 0.45 | 0.41 | 0.19 | 0.35 | 0.47 |
| 28 days sealed | 0.30 | 0.09 | 0.31 | 0.49 | 0.33 | 0.30 | 0.37 | 0.49 | 0.18 | 0.36 | 0.46 |
| 1 year sealed | 0.40 | 0.05 | 0.30 | 0.50 | 0.47 | 0.37 | 0.38 | 0.51 | 0.11 | 0.55 | 0.35 |
| 7 days unsealed | 0.30 | 0.08 | 0.28 | 0.33 | 0.41 | 0.29 | 0.43 | 0.31 | 0.16 | 0.29 | 0.38 |
| 28 days unsealed | 0.25 | 0.09 | 0.30 | 0.48 | 0.26 | 0.28 | 0.35 | 0.47 | 0.14 | 0.31 | 0.49 |

The BSE images can also be used for investigating the evolution of gel chemistry around the reacted GGBFS particles. As an example, the BSE image of an GGBFS particle (2 years of cured S100 paste) and the corresponding EDX linescan-profile at section A-D are shown in Figure 4.21. In the GGBFS particle boundary a transition zone is established for a Ca-Mg-Na-Al-Si-H gel. It can be observed that going farther from the boundary of the GGBFS particle, Mg drops substantially. Ca dissolves from the particles and it enriches the outer gel. This leaves a Mg enriched Ca-Mg-Na-Al-Si-H gel in the boundary of GGBFS particle (A-B, C-D), similar to slag cement paste [187]. To illustrate Mg spatial distribution compared to other major elements in paste S100, X-ray element maps were produced showing element zonation in noncarbonated paste S100 (2 years of exposure), at 8000 times magnification (see Figure A.1, Appendix A). Although it was expected that Mg would form hydrotalcite or maxnerite phases as it has been reported by Myers et al. [188], clear formation of these phases were not found neither with XRD, nor TG-MS analyses in this thesis (Chapters 5 and 7) and [189]. For that reason, an assumption is made that Mg is either forming Mg-Al-Si-H gel or it is in a form of poorly crystalline hydrotalcite, both highly intergrown with Ca-Na-Al-Si-H gel. This is a reasonable assumption considering the element mapping results (Figure A1, Appendix A), where Mg was highly concentrated in the GGBFS rim compared to the matrix, consistent with PARC measurements. If there are Mg-containing phases formed in the paste S100, then they are only concentrated in this narrow rim, which makes it difficult to identify using the bulk sample. The difference of gel greyscale level in BSE image (see Figure 4.21) between the GGBFS particle boundary (A-B, C-D) and far from that boundary, is attributed to the different nanoporosities of these two regions, indicated higher nanoporosity of Ca-Mg-Na-Al-Si-H gel than that of Ca-Na-Al-Si-H gel.

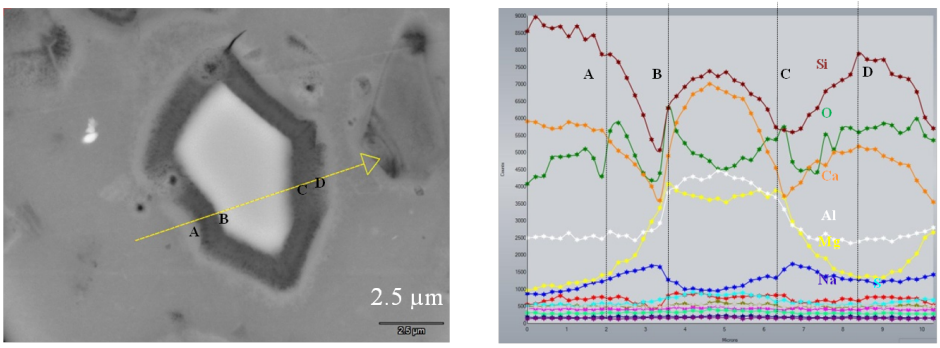


Figure 4.21: The BSE image of microstructure around reacted GGBFS particle and corresponding EDX linescan-profiles for the constituent elements of the paste S100 after 1 year of reaction.

It can also be seen that the Al distribution is similar to that of Mg. On the other hand, the distributions of Ca and Si are very similar. Ca and Si are precipitating further from the rim of GGBFS particle. Na also has been found in higher amount around rims of GGBFS particles.

The Na/Si ratio strongly depends on the curing conditions. As will be shown in Chapter 6, the significant effect of $Na^+$ loss on the pore solution composition of unsealed pastes was seen. The results presented in this chapter show that the effect of $Na^+$ loss is not limited to the pore solution composition of the unsealed pastes, but can also significantly affect the chemical composition of the reaction products (see 7 days and 28 days results in Table 4.4). This is supported by density plots of Na versus Mg+Al+Si+Ca (see Figure 4.22) of sealed and unsealed samples. Na is lower in the gel of unsealed cured samples compared to the sealed samples. On the other hand, the Ca/Si ratio increases from age of 1 day to 28 days, regardless of curing method (Table 4.4). This implies that the dissolution of GGBFS continues in this period.



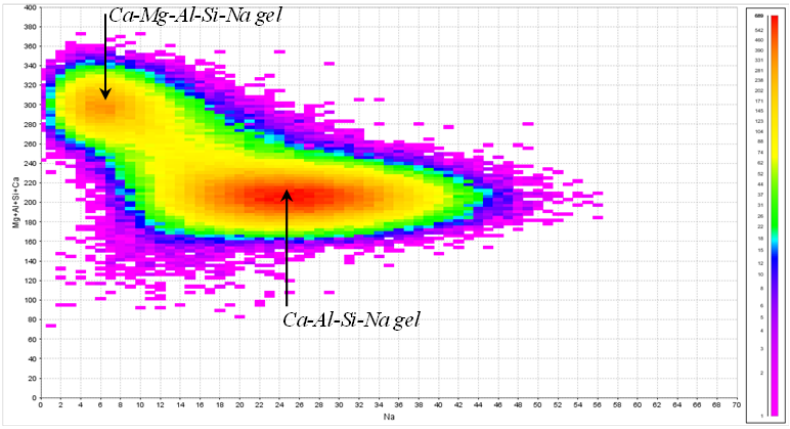


*(a) Density plot of Na and (Mg+Al+Si+Ca) to extract groups of pixels for Ca-Al-Si-Na gel and Ca-Mg-Al-Si-Na gel in 28 days sealed cured paste S100.*

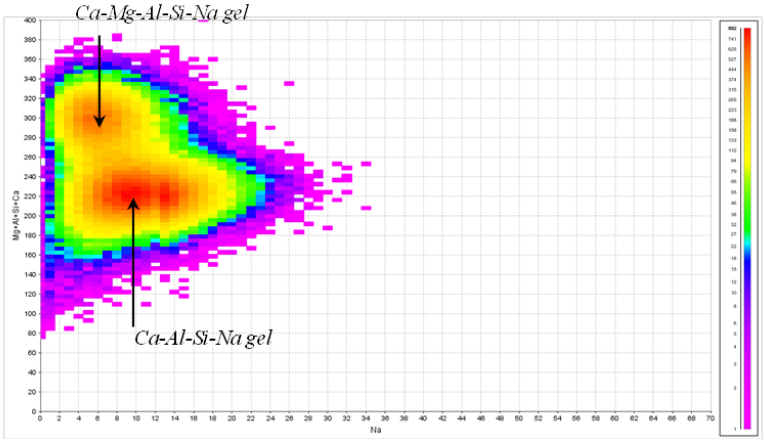


*(a) Density plot of Na and (Mg+Al+Si+Ca) to extract groups of pixels for Ca-Al-Si-Na gel and Ca-Mg-Al-Si-Na gel in 28 days unsealed cured paste S100.*

Figure 4.22: Density plot of Na and (Mg+Al+Si+Ca) to extract groups of pixels for Ca-Al-Si-Na gel and Ca-Mg-Al-Si-Na gel in 28 days sealed cured paste S100 (a) and 28 days unsealed cured paste S100 (b).

The evolution of the phase proportions of paste S100 is presented in Figure 4.23. Comparison of the phase proportions of sealed cured samples at 28 days and 1 year shows that there is no further reaction of GGBFS. This is supported with the similar Ca/Si ratio observed at 28 days and 1 year of curing (see Table 4.4). This suggests that the degree of reaction of GGBFS is limited and reaches its maximum in the first 28 days for the studied conditions. In unsealed cured specimens, a Ca-Al-Si-H (orange coded) phase is found at 28 days (see Figure 4.20), with a lower Na uptake in the gel compared to the sealed cured paste (see Table 4.4). This gel transformation is attributed to the loss of $Na^+$ in unsealed curing conditions which is explained in Chapter 6, section 6.3.1.1. This phase, Ca-Al-Si-H (orange coded), was not observed in sealed cured specimens even until 1 year of curing.



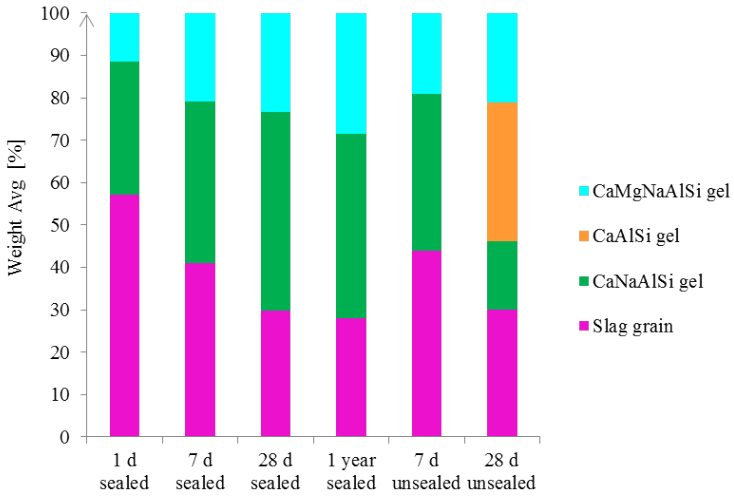


Figure 4.23: The effect of curing conditions (unsealed and sealed) on the evolution of the phases and their weight proportions in pastes S100.

#### 4.3.2.2. BINARY GGBFS-FA PASTE (S50)

The sum spectra of three gels (Ca-Na-Al-Si-H, Ca-Mg-Na-Al-Si-H and Ca-Al-Si-H) observed in paste S50 are depicted in Figure 4.24. The distribution of the main reaction products are also visualized in Figure 4.25. Backscattered electron images of polished sections are shown in Figure 4.25i with the corresponding PARC maps presented in Figure 4.25ii.

It can be observed that, at early age, the reaction products appear to be very heterogeneous (Figure 4.25a, b, c, e, f-ii) and less heterogeneous at later ages of reaction (Figure 4.25 d-ii). The composition of the reaction products in paste S50 determined with PARC is presented in Table 4.5. The Ca/Si ratio of the gel Ca-Na-Al-Si-H decreases by a factor two in paste S50 compared to paste S100, which is proportional to the GGBFS content. Besides the differences in Na, Mg and Ca, substantial differences in the amount of different reaction products can be seen between pastes S50 and S100 (Figure 4.23 vs Figure 4.26).

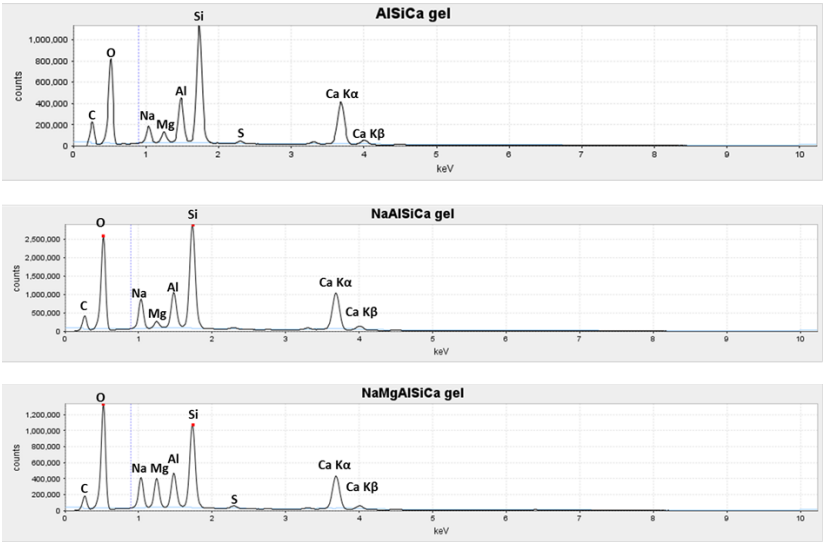


Figure 4.24: PARC sum spectrum from chemical domain of AlSiCa gel, NaAlSiCa gel, NaMgAlSiCa gel in S50.

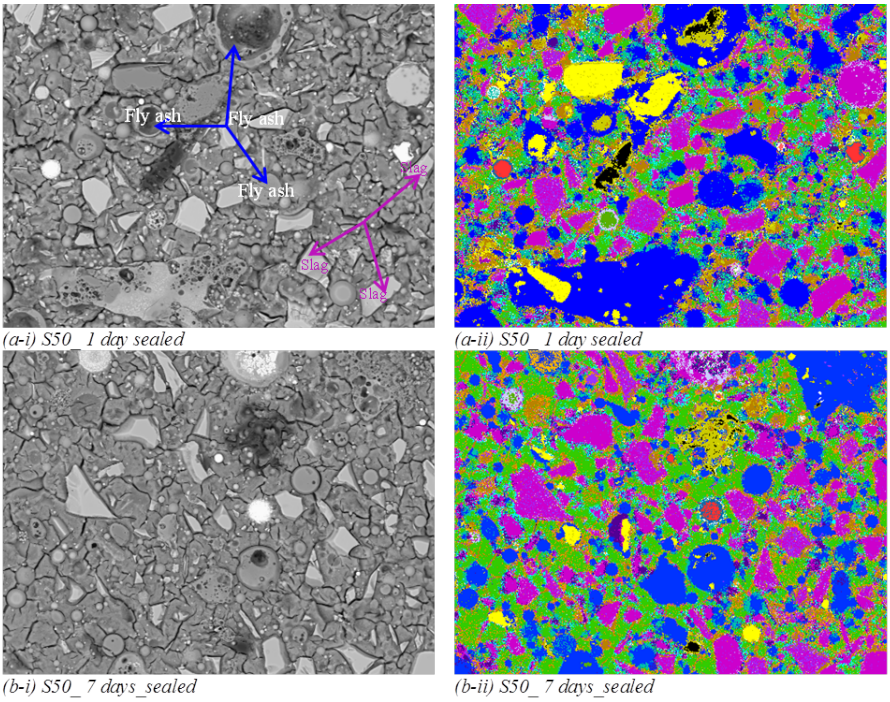


*(a-i) S50_ 1 day sealed* *(a-ii) S50_ 1 day sealed*

*(b-i) S50_ 7 days_sealed* *(b-ii) S50_ 7 days_sealed*

Figure 4.25: SEM-BSE images (i) of the microstructure of paste S50 at different curing periods, with mapped chemical domains of different phases (ii).

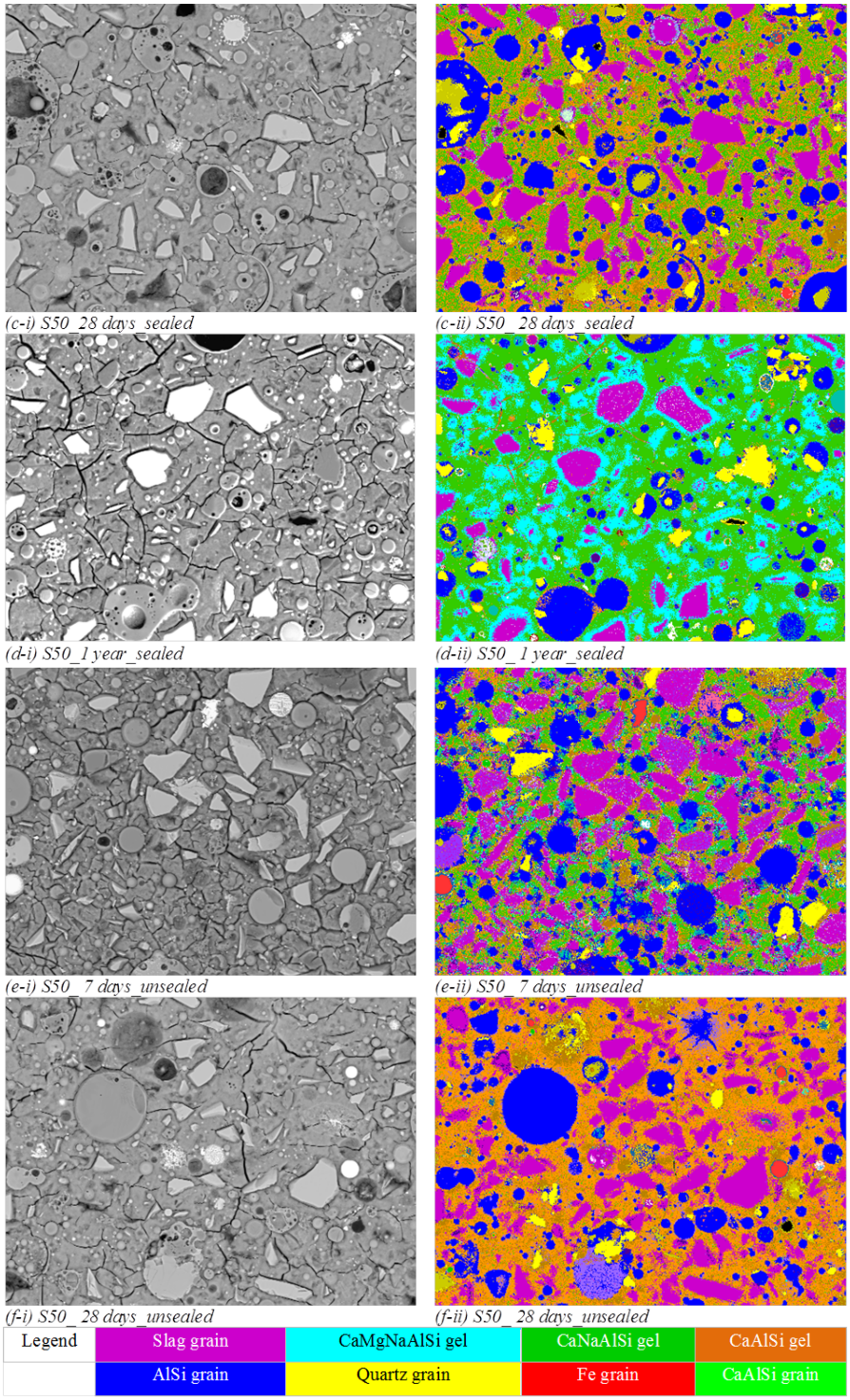


Figure 4.25: SEM-BSE images (i) of the microstructure of paste S50 at different curing periods, with mapped chemical domains of different phases (ii).

Figure 4.26 shows the effect of curing time (1 day, 7 days, 28 days, 1 year) and curing conditions (unsealed and sealed) on the evolution of the reaction products and their proportions in pastes S50. It can be seen that a significant transformation of the reaction products has occurred during the considered times of curing. The amount of Ca-Al-Si-H gel after 28 days is significantly higher in unsealed cured samples compared to sealed cured samples, which indicates that Na uptake in the gel in unsealed cured samples was clearly limited. This is due to $Na^+$ leaching from these samples, as previously mentioned.

It seems that while the GGBFS dissolution has the main contribution to reactions at early ages, FA particles (glassy AlSi grains) react at later ages. The presence of FA in the paste S50 leads to a higher Al content and consequently formation of Ca-Al-Si-H gel (Table 4.5). This is in contrast to paste S100, where Al is mainly incorporated in Ca-Mg-Na-Al-Si-H (Table 4.4). Table 4.5 also shows that, similar to paste S100, the Na content varies significantly depending on the curing conditions in the paste S50. However, the Na content in sealed cured pastes S50 (see Table 4.5) is constant during the entire curing regime, while for pastes S100, Na decreases with elapse of curing time (see Table 4.4). This may suggest a lower Na binding capacity of pastes S100 with GGBFS as single precursor.



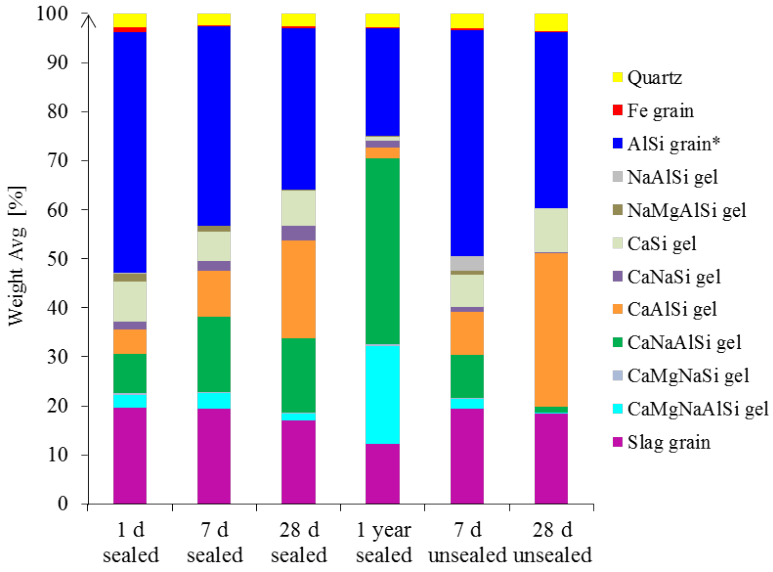


Figure 4.26: The effect of curing conditions (unsealed and sealed) on the evolution of the phases and their weight proportions in pastes S50. Note that AlSi grain* consists of AlSi grain, NaAlSi grain, KAlSi grain, CaAlSi grain, MgAlSi grain, FeAlSi grain, TiAlSi grain, PAlSi grain, CaMgAlSi grain.

The Na binding capacity of FA/GGBFS paste (S50) can be enhanced due to the presence of FA. Namely, the silanol groups are the main adsorbing sites for alkalis. The lower the Ca/(Al+Si) is, the higher the number of silanol groups in the gel will be. This implies that more alkalies will be incorporated in Ca-Na-Al-Si-H with lower Ca/(Al+Si) ratio, such as in pastes S50, that have a lower CaO content and a higher $SiO_2$ content than paste S100.

#### 4.3.2.3. DEGREE OF REACTION

In both sealed and unsealed S100 pastes, degree of GGBFS reaction (see Figure 4.28) is comparable with the one reported by Brough et al. [30]. The alkaline activation of GGBFS results in formation of a significant amount of reaction products around the GGBFS particles, as can be observed from Figure 4.20 a-i. Although the final reaction degree was nearly the same in sealed and unsealed conditions, the composition of reaction products is different (Table 4.4).

In paste S50, GGBFS has a larger reaction degree at 1 day but smaller at 28 days. This is most likely because only the GGBFS contributes to the reaction degree at 1 day. In paste S50, the reaction degree of GFBS is increased until the end of the tests. This is in contrast to the paste S100 in which the reaction degree did not increase after 28 days. In paste S50, FA has a very low reaction degree, which reaches only 30% after 1 year in sealed conditions. Due to the very low reactivity of AlSi grains, the boundary layer is not formed around these grains (see Figure 4.25). In paste S50, FA (glassy AlSi particles) are embedded in a "homogeneous" Ca-Na-Al-Si-H gel (see Figure 4.27, green colour). This gel is denser than the gel in the transitional zone (Ca-Mg-Na-Al-Si-H gel, cyan colour, schematized in Figure 4.27). This transitional zone is marked by strong compositional gradients between the GGBFS and the "green" gel which was shown in Figure 4.21. Since the Ca-Mg-Na-Al-Si-H gel is more porous than Ca-Na-Al-Si-H gel (see Figure 4.21), GGBFS dissolution is allowed further with time.

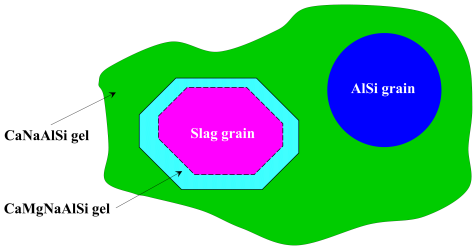


Figure 4.27: Schematic representation of the coating (surrounding) of AlSi grain in paste S50 (Ca-Na-Al-Si-H gel), and the coating of slag grain (Ca-Mg-Na-Al-Si-H gel) in paste S50.

Also, the reaction degree of sealed and unsealed conditions is different (that is in contrast to observations made for GGBFS in paste S100), probably due to different Na-binding capacities of FA and GGBFS in paste S50 compared to that of only GGBFS in paste S100. Furthermore, the low alkaline conditions and ambient curing temperature used in this study (when compared to literature [13, 77]) are also possible reasons for a moderate degree of FA reaction in pastes S50 at 7 days and 28 days. The degree of reacton

of FA in unsealed conditions seem to be smaller than in sealed condition. The degree of reaction of FA is mainly dependent on the reactivity of AlSi-grains. Due to crystalline nature, quartz and Fe-grain do not contribute to FA reactivity (Figure 4.26).

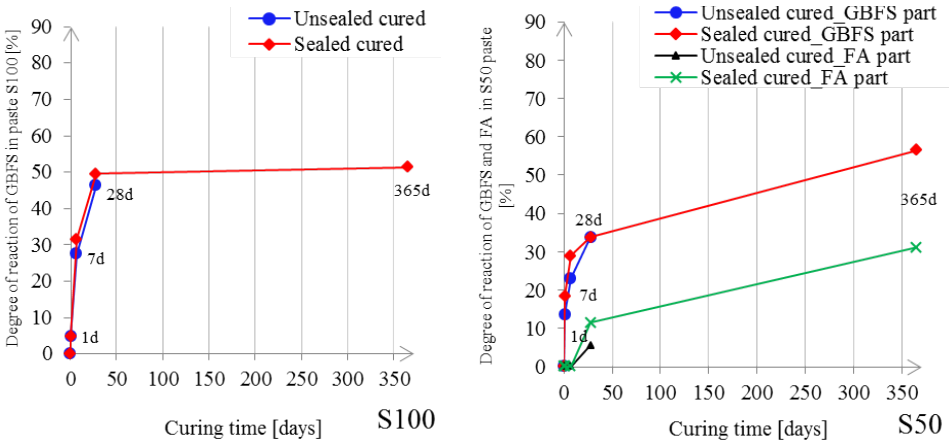


Figure 4.28: Degree of reaction of paste S100 (left) and paste S50 (right).

#### 4.3.2.4. BULK CHEMISTRY

The bulk compositions inferred from XRF analyses are shown in Table 4.6 and Table 4.7 for the S100 and S50 pastes, respectively. No specific change of weight fractions of MgO, $Al_2O_3$, $SiO_2$, $SO_3$, $K_2O$, CaO with the change of curing time or curing conditions in both pastes can be observed. There is also no significant difference between these weight fractions in the sealed and unsealed specimens. Meanwhile, a lower amount of $Na_2O$ is observed in unsealed samples. The results also show that the $Na_2O$ content is similar in sealed cured samples at all curing ages, while it is decreasing in unsealed cured samples with elapse of time. It is important to note that the consistency of XRF results with PARC regarding the $Na_2O$ content (Tables 4.6, 4.7, 4.8, 4.9) confirms the reliability of these observations.

The lower amount of $Na_2O$ content in the unsealed cured samples (in both S50 and S100) at 28 days can be explained by the fact that the pore solution is not in equilibrium with the RH of the curing room atmosphere in these specimens from day 1 (see Chapter 6, section 6.3.1.1). Due to a RH gradient between the sample and curing room atmosphere, condensation of water on the samples causes dilution of the pore fluid. Consequently, the initial equilibrium between the pore fluid and the gel cannot be maintained. This causes the gel to re-equilibrate by releasing $Na^+$ into the pore fluid until the pore fluid becomes in equilibrium with the outside RH. It is interesting that the $Na_2O$ content and its changes are similar in both S50 and S100 pastes, that is because the same RH was imposed on samples. The rest of the oxides have different fractions in S50 and S100, which is consistent with the level of GGBFS replacement.

Finally, it can be seen that the bulk composition of the samples (S50 and S100) stays constant in both analyses, XRF (Table 4.6 and Table 4.7) and PARC (Table 4.8 and Table 4.9), while the phase proportions change with time (see Figure 4.23 and Figure 4.26).

Table 4.6: Bulk chemistry obtained with XRF for the pastes S100.

| S100 | 1d sealed | 7d sealed | 28d sealed | 1 year sealed | 7d unsealed | 28d unsealed |
|---|---|---|---|---|---|---|
| $Na_2O$ | 4.48 | 4.80 | 4.45 | 5.12 | 3.96 | 2.76 |
| MgO | 6.00 | 6.11 | 5.89 | 6.71 | 6.29 | 6.02 |
| $Al_2O_3$ | 10.09 | 10.35 | 9.98 | 10.02 | 10.59 | 10.32 |
| $SiO_2$ | 33.90 | 34.70 | 33.71 | 36.42 | 35.44 | 34.58 |
| $P_2O_5$ | 0.00 | 0.00 | 0.00 | 0.00 | 0.00 | 0.00 |
| S | 1.44 | 1.44 | 1.43 | 1.60 | 1.32 | 1.20 |
| $K_2O$ | 0.42 | 0.41 | 0.42 | 0.33 | 0.40 | 0.38 |
| CaO | 40.53 | 39.62 | 41.24 | 37.40 | 39.29 | 41.76 |
| $TiO_2$ | 1.39 | 1.22 | 1.40 | 1.17 | 1.31 | 1.43 |
| MnO | 0.36 | 0.31 | 0.35 | 0.32 | 0.33 | 0.38 |
| $Fe_2O_3$ | 0.69 | 0.66 | 0.68 | 0.61 | 0.66 | 0.67 |



Table 4.7: Bulk chemistry obtained with XRF for the pastes S50.

| S50 | 1d sealed | 7d sealed | 28d sealed | 1 year sealed | 7d unsealed | 28d unsealed |
|---|---|---|---|---|---|---|
| $Na_2O$ | 5.09 | 5.12 | 4.46 | 4.56 | 4.78 | 3.88 |
| MgO | 3.87 | 4.07 | 3.78 | 4.16 | 4.21 | 4.50 |
| $Al_2O_3$ | 15.42 | 15.08 | 13.71 | 14.41 | 15.36 | 15.49 |
| $SiO_2$ | 43.27 | 43.38 | 41.00 | 45.74 | 44.12 | 44.83 |
| $P_2O_5$ | 0.31 | 0.32 | 0.30 | 0.23 | 0.32 | 0.34 |
| S | 1.07 | 1.10 | 1.17 | 1.12 | 1.00 | 0.96 |
| $K_2O$ | 0.85 | 0.86 | 0.93 | 0.81 | 0.82 | 0.80 |
| CaO | 22.50 | 22.92 | 25.89 | 22.58 | 22.39 | 22.47 |
| $TiO_2$ | 1.34 | 1.36 | 1.59 | 1.30 | 1.26 | 1.34 |
| MnO | 0.20 | 0.21 | 0.26 | 0.21 | 0.20 | 0.21 |
| $Fe_2O_3$ | 4.94 | 4.82 | 6.03 | 4.73 | 4.65 | 4.58 |

Table 4.8: Bulk chemistry obtained with PARC for the pastes S100.

| S100 | 1d sealed | 7d sealed | 28d sealed | 1 year sealed | 7d unsealed | 28d unsealed |
|---|---|---|---|---|---|---|
| $Na_2O$ | 4.71 | 4.92 | 4.90 | 4.35 | 4.32 | 1.77 |
| MgO | 7.03 | 7.10 | 6.892 | 7.17 | 7.15 | 6.68 |
| $Al_2O_3$ | 12.09 | 12.06 | 11.51 | 10.84 | 12.26 | 11.60 |
| $SiO_2$ | 30.04 | 31.03 | 33.62 | 33.87 | 31.06 | 33.49 |
| $P_2O_5$ | 0.32 | 0.30 | 0.24 | 0.24 | 0.31 | 0.31 |
| $SO_3$ | 1.68 | 1.95 | 1.72 | 1.66 | 1.60 | 1.24 |
| $K_2O$ | 0.54 | 0.47 | 0.36 | 0.31 | 0.48 | 0.34 |
| CaO | 41.09 | 40.44 | 39.22 | 39.80 | 41.23 | 42.95 |
| $TiO_2$ | 1.01 | 0.99 | 1.02 | 1.01 | 1.03 | 1.03 |
| MnO | 0.29 | 0.29 | 0.29 | 0.29 | 0.30 | 0.28 |
| $Fe_2O_3$ | 0.40 | 0.44 | 0.31 | 0.48 | 0.25 | 0.33 |

Table 4.9: Bulk chemistry obtained with PARC for the pastes S50.

| S100 | 1d sealed | 7d sealed | 28d sealed | 1 year sealed | 7d unsealed | 28d unsealed |
|---|---|---|---|---|---|---|
| $Na_2O$ | 4.26 | 4.54 | 4.13 | 6.49 | 3.61 | 2.55 |
| MgO | 4.83 | 5.13 | 4.51 | 4.42 | 5.26 | 4.84 |
| $Al_2O_3$ | 16.46 | 17.41 | 17.06 | 15.21 | 16.87 | 16.30 |
| $SiO_2$ | 42.8 | 42.55 | 40.30 | 44.23 | 43.22 | 43.21 |
| $P_2O_5$ | 0.61 | 0.61 | 0.55 | 0.55 | 0.61 | 0.55 |
| $SO_3$ | 1.22 | 1.40 | 1.85 | 1.71 | 1.46 | 1.62 |
| $K_2O$ | 1.09 | 1.05 | 1.00 | 0.98 | 1.03 | 0.84 |
| CaO | 23.77 | 23.44 | 26.83 | 22.69 | 23.80 | 26.73 |
| $TiO_2$ | 0.94 | 1.03 | 0.91 | 0.98 | 1.05 | 0.91 |
| MnO | 0.21 | 0.19 | 0.17 | 0.23 | 0.21 | 0.20 |
| $Fe_2O_3$ | 3.71 | 2.39 | 2.44 | 2.61 | 2.90 | 2.24 |

4

#### 4.3.2.5. PHASE MINEROLOGY

XRD tests were only performed on S50 paste that has 50 wt. % of FA and hence contains crystalline phases. These phases are quantified with XRD-Rietveld analysis. Quantification of the reaction products with XRD was not possible for the S100 paste due to its amorphous nature. However, PARC showed to be a very useful technique in separating reacted and unreacted phases and also enabled calculation of the degree of reaction of the S100 samples (Figure 4.28). Figure 4.29 shows the obtained XRD diffractograms as a function of curing time and curing conditions. The broad humps beneath the peaks of the crystalline phases of XRD diffractograms indicate the presence of amorphous phase (see Figure 4.29), which is quantified in Figure 4.30. This hump becomes more pronounced with the presence of the nanocrystalline phase such as Ca-Na-Al-Si-H (around 34 2 Theta), that is the main reaction product of the studied alkali activated pastes. This hump is most visible in the XRD diffractogram for 1 year sealed cured sample.

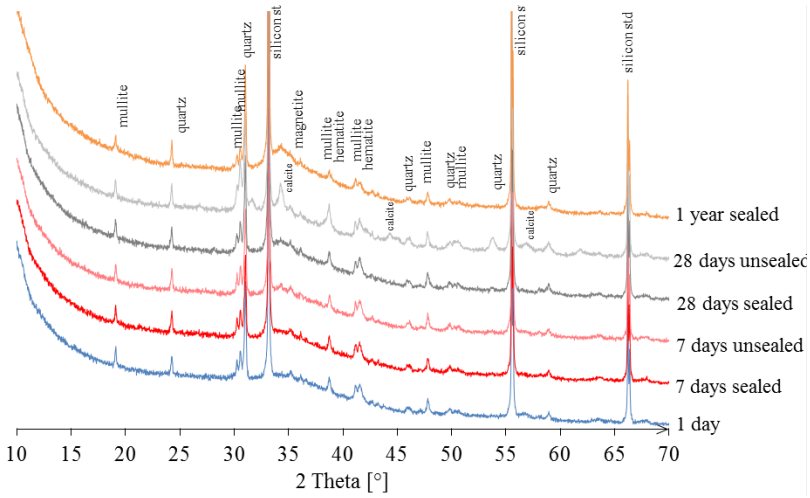


Figure 4.29: XRD diffractograms with respect to the phases in paste S50 for sealed and unsealed curing conditions.

Figure 4.30 shows that curing conditions affect the mineralogical composition and the content of the phases in the samples S50. The amorphous phase content of the sealed cured pastes is similar at 1, 7 and 28 days but it is increased after 1 year. While the amount of quartz in the specimens is almost constant during 1 year of reaction (see Figure 4.30), mullite seems to be decreasing after 28 days. The amount of quartz determined with QXRD is similar to results obtained for quartz with PARC (see Figure 4.26). A decrease in the amorphous content can also be observed in unsealed cured samples, which is due to the formation of calcite (see Figure 4.30). The calcite content increases in the unsealed cured samples with curing age. The calcite was formed due to superficial carbonation of the unsealed cured samples as described in Chapter 6, section 6.3.1.3.



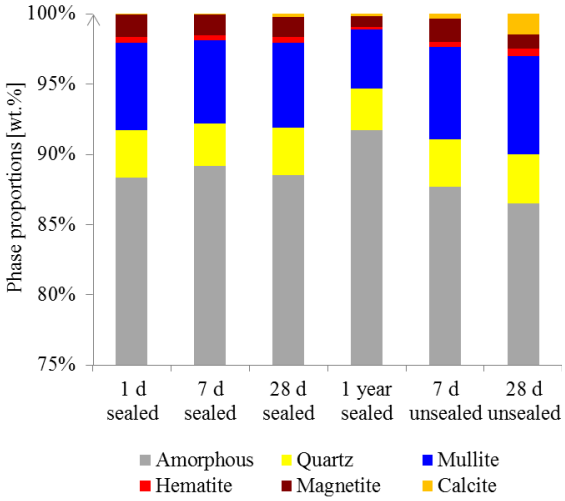


Figure 4.30: Quantitative phase analysis with Rietveld method for paste S50 as a function of time and curing conditions.

### 4.3.3. PORE STRUCTURE OF ALKALI ACTIVATED PASTES DETERMINED WITH MIP

The porosity of alkali activated FA (S0), GGBFS (S100) and blended FA/GGBFS pastes (S30, S50, S70) at 28 days was measured first with MIP. The mean pore diameter (0.13 $\mu$m) was only determined for alkali activated FA paste. For the pastes containing GGBFS the mean pore size was not accessible with MIP. It was determined with $N_2$ adsorption. The characteristic size of capillary pores and the shape of cumulative MIP curves generally observed in cement paste are not observed in alkali activated pastes (see Figure 4.31), with exception of paste S0. Paste S0 has a high porosity and large pore size distribution because of the two reasons. The first is the use of lower alkaline concentration for dissolution of the FA used in this study than generally described in literature [36]. The second is the use of ambient curing conditions instead of curing at elevated temperature usually applied for curing of alkali activated FA-based systems [129]. The MIP results are in agreement with SEM observations. A number of cavities was observed in paste S0 with a large amount of unreacted FA particles (see Figure 4.15).

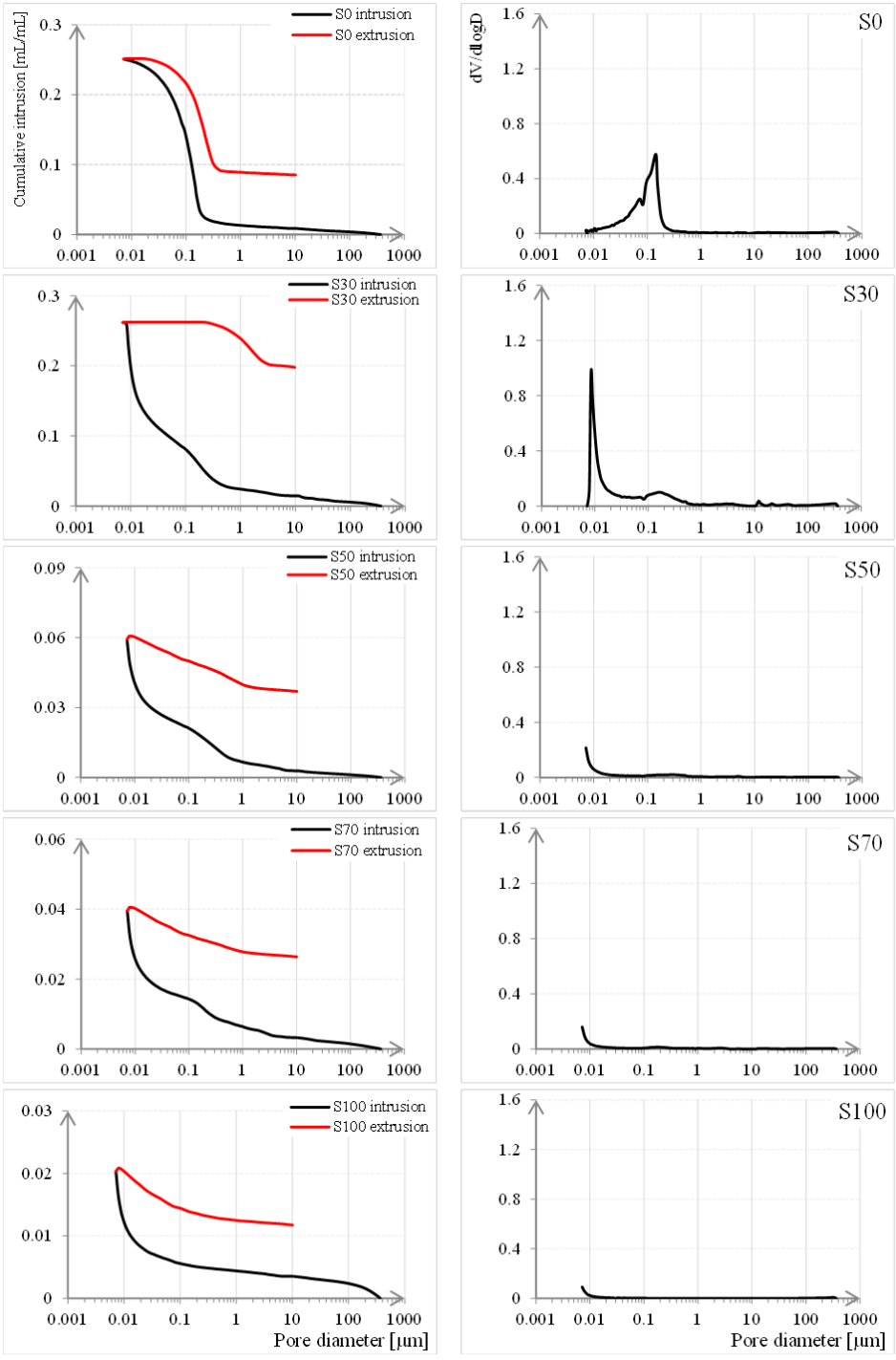


Figure 4.31: Pore size distribution and differential curves of pastes at 28 days determined with MIP.

When GGBFS is used, smaller pore sizes are found, which is consistent with observations described in literature [148]. The dense microstructure is assigned to the large amount of reacted GGBFS and higher space-filling capacity by Ca-Na-Al-Si-H gel than by Na-Al-Si-H gel. The Na-Al-Si-H type gels (gel type in paste S0) do not chemically bind water and therefore do not provide the same degree of pore network obstruction as Ca-Na-Al-Si-H gel [148]. BSE images (Figure 4.16) and MIP results (Table 4.10, Figure 4.31) showed that capillary pores are absent for mixtures S50, S70 and S100. This is in line with the study of Lloyd et al. [190] and it implies slower rate of ions transport thought the pore structure for GGBFS-rich pastes which will be further studied in Chapter 8.

Table 4.10: Pore structure properties of pastes at 28 days characterized with MIP (> 7nm).

| Mixtures | Mean pore diameter [$\mu$m] | Total porosity [%] |
|---|---|---|
| S0 | 0.13 | 43.72 |
| S30 | 0.08 | 26.04 |
| S50 | - | 9.40 |
| S70 | - | 6.54 |
| S100 | - | 3.57 |

The difference in total porosity at 28 days of pastes S30 and S50 was significant (see Table 4.10), implying that the amount of reaction products in paste S50 is significantly higher than in paste S30. It should be noted that the total porosity of pastes S50, S70, S100 may be higher than measured with MIP because the mercury could not be intruded into very fine pores (<7 nm) which are present in high GGBFS-based alkali activated binders [190]. Therefore, the pore structure was further studied with Nitrogen adsorption (next section).

### 4.3.4. PORE STRUCTURE OF ALKALI ACTIVATED PASTES DETERMINED WITH $N_2$ ADSORPTION

$N_2$ adsorption identifies sizes of the pores that are beyond the detection range of the mercury intrusion method. By coupling $N_2$ adsorption with MIP it covers the entire pore size range. Before considering the pore size distribution, adsorption isotherms should be considered first. Figure 4.32 shows $N_2$ adsorption isotherms of the studied alkali-activated pastes. The shape of a $N_2$ adsorption isotherm can be used for determining whether the pores present in the sample are micropores (below 2 nm), mesopores (between 2 and 50 nm) or macropores (above 50 nm) [191]. Comparing the quantities of adsorbed $N_2$ of different alkali-activated pastes indicates a higher gel porosity for pastes S50, S70 and S100 than for pastes S0 and S30. For the pastes S50, S70 and S100, the dependence between the adsorbed $N_2$ and relative pressure is found to be linear. The straight line extrapolates to a non-zero positive intercept on the ordinate. This intercept shows the volume of micropores in which adsorption takes place by the pore volume-filling mechanism [192]. The isotherms are typical for microporous to mesoporous materials [192].

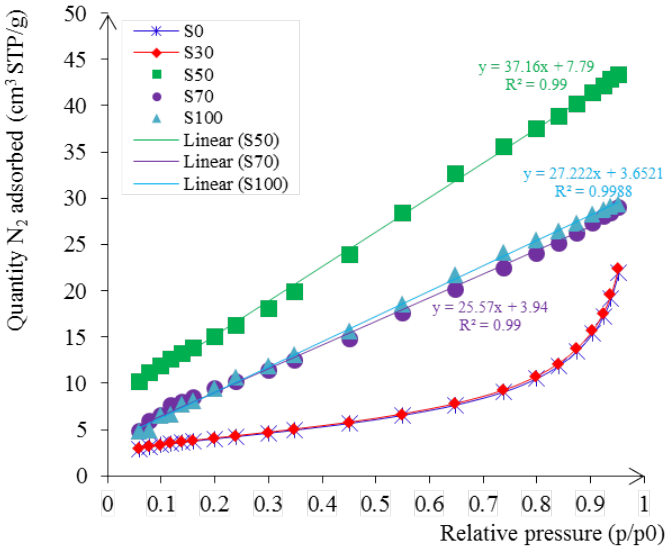


Figure 4.32: $N_2$ adsorption isotherms for alkali-activated pastes at 28 days. The $N_2$ adsorption isotherms were fitted for pastes S50, S70 and S100. $R^2$ is the correlation coefficient from the least-squares linear fits.
The amount of adsorbed $N_2$ [mmol/g] is recalculated into volume at STP (STP = Standard Temperature and Pressure), [$cm^3$ STP/g].

Figure 4.33 shows pore size distributions of alkali activated pastes measured with $N_2$ adsorption. The critical pore sizes around 4 nm were identified for S50 and S70 pastes. The peaks for gel pores in S0 and S30 samples were not detected in Figure 4.33 (right). This is consistent with the findings of Ma et al. [193], where for a given alkaline activator composition ($SiO_2$:$Na_2O$=0.5:1.5) the similar curves were observed. By increasing the GGBFS content pores became refined and capillary pores could not be observed anymore. Such a low porosity is also found in ultra-high performance cement-based composites containing silica fume [194]. Samples S50, S70 and S100 at age of 28 days are remarkably free of mercury intrusion (see Figure 4.31), indicating that the pores are smaller than 7 nm, consistent with $N_2$ adsorption results (see Figure 4.33). This has two implications for $CO_2$ diffusion of the studied pastes:

1. in alkali activated FA/GGBFS pastes (S50, S70, S100), the largest volume of the pores at 28 days is observed at the level of gel pores. This means that the gel pores will be the main transport path for $CO_2$, assuming that these pores are connected and partially filed with water. The saturation degree will be measured in Chapter 6, section 6.3.1.1.

2. in alkali activated FA/GGBFS pastes (S0, S30), the characteristic peak for gel pores cannot be distinguished from the measured range. However, it is certain that the pores are all larger than 37 nm in these two pastes, according to MIP results, Figure 4.31.

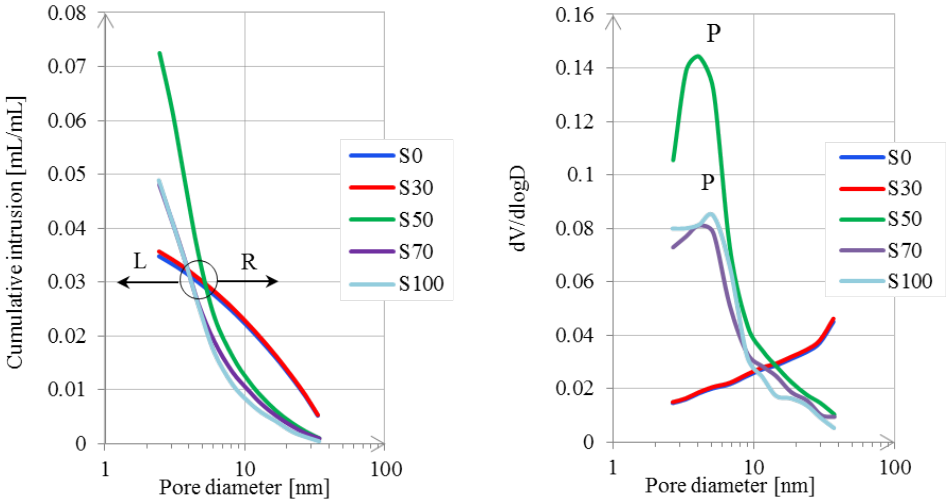


Figure 4.33: Pore size distribution (left) and differential curves (right) of alkali-activated pastes at 28 days determined with $N_2$ adsorption. In the left graph, curves for the pastes S50, S70 and S100 show higher pore volume, contributed by the large dissolution of GGBFS and subsequent gel formation. Right of the indicated circle pore volume of pastes S0 and S30 surpasses the ones for the other three pastes. In the right graph, P corresponds to threshold gel pore diameter in pastes S50, S70 and S100.

## 4.4. CONCLUDING REMARKS

In this chapter the characterization of the microstructure, including chemistry of reaction products and pore structure properties of the alkali-activated pastes prior to carbonation, is performed. In particular, the effect of curing conditions and GGBFS content on the microstructure evolution of alkali-activated FA/GGBFS pastes were investigated. This was achieved by using the PhAse, Recognition and Characterization (PARC) software for the first time. It can be concluded that:

- PARC: The pastes reacted at different rates. Dominant phases were Mg-rich gel around GGBFS particles, i.e. Ca-Mg-Na-Al-Si-H. Phases at larger distance from the GGBFS and FA particles consisted mainly of Ca-Na-Al-Si-H. The next chapter investigates carbonation of the gel phases in alkali-activated pastes.
  - Curing conditions have significant influence on the chemical composition of the phases of the microstructure of alkali-activated pastes. This effect is most dominant after 28 days of curing, while at 7 days no significant difference was found between sealed and unsealed pastes. The different chemical composition is due to $Na^+$ loss from the samples which were cured unsealed. Instead of Ca-Na-Al-Si-H gel, Ca-Al-Si-H gel is formed in these samples. The sealing of the samples resulted in a higher $Na^+$ content in the Ca-Na-Al-Si-H gel. The effect of curing conditions was larger in paste S50 than in paste S100. The main changes concerned the chemical composition of the gel phases and their proportions. Apart from the chemical modifications of the gel phases,

mineralogy of paste S50 was also dependent on the curing conditions. Consequently, the carbonation degree is expected to be different for sealed and unsealed cured samples.

- GGBFS content. The three main phases in paste S100 after 28 days of sealed curing were distinguished: unreacted slag particles, Ca-Na-Al-Si-H gel and Ca-Mg-Na-Al-Si-H gel. The Ca/Si ratio of the Ca-Na-Al-Si-H gel decreases by a factor two in paste S50 compared to paste S100, proportionally to the GGBFS content. Paste S50 has more phases than paste S100 (Figure 4.23 vs Figure 4.26). Besides amorphous phase (unreacted GGBFS and FA, and gel phases), paste S50 contains quartz, mullite, hematite and magnetite, which can not be carbonated. Therefore, paste S50 has a lower amount of phases that can be carbonated, which suggests lower degree of carbonation compared to paste S100.



- MIP and $N_2$: The replacement level of FA by GGBFS had a significant effect on the pore structure evolution. For instance, the most prominent effect was observed in GGBFS rich pastes, where porosity was reduced to 4% when the content of GGBFS used in the mixture increased up to 100%. Increase of the GGBFS content decreases the total porosity by a factor of 10 (43.72% to 3.67%). Furthermore, an increase of the GGBFS content refines the pore size distribution and pastes consist generally of gel pores. This indicates low permeable alkali-activated pastes with GGBFS, which suggests a slow $CO_2$ diffusion in these pastes.

# 5

# $CO_2$ BINDING CAPACITY OF PASTES

*"When you want to know how things really work, study them when they're coming apart."*

William Gibson

*Quantification of the $CO_2$ binding capacity of ordinary Portland cement (OPC)-based concrete is of high importance for its carbonation potential and service life predictions. Such information is still not obtained for alkali activated materials (AAMs). To address this gap, this chapter evaluates the $CO_2$ binding capacity of alkali activated fly ash (FA) and ground granulated blast furnace slag (GGBFS) pastes. To accelerate the process, the pastes were ground to powder. Five mixtures with different FA/GGBFS ratio are considered. The results showed that the alkali-activated pastes have a lower $CO_2$ binding capacity in comparison to OPC-based pastes. Furthermore, alkali-activated pastes have similar $CO_2$ binding capacity regardless of the FA/GGBFS ratio. It was observed that the silicate functional groups corresponding to the reaction products in the pastes were progressively changing during the first 7 days, after which only carbonate groups changed. It was also found that the $CO_2$ bound in the alkali-activated pastes occurs to a substantial extent in amorphous form. The information on reactivity of $CO_2$ and maximum $CO_2$ binding capacity of ground pastes will be used in Chapter 7 for comparing with the $CO_2$ binding capacity of bulk alkali activated pastes.*

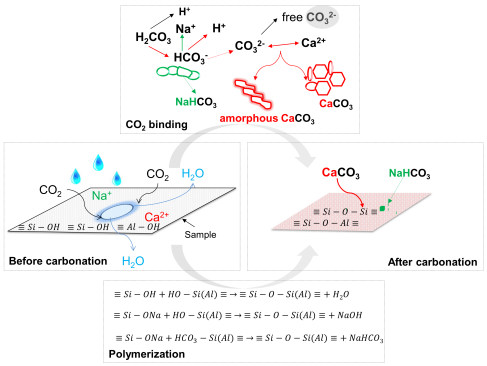


Parts of this chapter have been published in:
Nedeljkovic, M., Ghiassi, B., Melzer, S., Kooij, C., van der Laan, S., Ye, G. (2018) $CO_2$ binding capacity of alkali-activated fly ash and slag pastes, Ceramics International [195]

## 5.1. INTRODUCTION

AS DISCUSSED in Chapter 2, an accurate quantification of the $CO_2$ binding capacity (i.e. the amount of $CO_2$ bound per weight) of alkali activated materials (AAMs) is of critical importance for determination of their carbonation degree and service life predictions of alkali activated concrete structures. However, the $CO_2$ binding capacity of AAMs has not been experimentally determined previously and needs further attention.

In AAMs the $CO_2$ binding capacity is expected to be different from that of OPC-based concrete due to their differences in constituting phases and pore structure [196]. While the main reaction products in OPC-based materials are portlandite and C-S-H, different alkaline gel phases are formed in AAMs. These include sodium aluminosilicate hydrate (Na-Al-Si-H) [167, 196, 197], calcium aluminosilicate hydrate (Ca-Al-Si-H), calcium sodium aluminosilicate hydrate (Ca-Na-Al-Si-H) and calcium magnesium sodium aluminosilicate hydrate (Ca-Mg-Na-Al-Si-H) as shown in Chapter 4, section 4.3.2.1. This suggests that the $CO_2$ binding capacity of AAMs, in contrast to OPC-based materials, is not only a function of the reactive CaO content. It is also influenced by the $Na_2O$ content consumed during the precursors (e.g. FA and GGBFS) dissolution.



Hence, this chapter focusses on reactivity of $CO_2$, the quantification of the $CO_2$ binding capacity and carbonation products of alkali activated FA and GGBFS pastes in comparison to OPC-based pastes. To accelerate the carbonation process, the pastes were ground to powder after 28 days of sealed curing. The mechanism and degree of carbonation were investigated through a complementary set of analytical methods, including TG-DTG-MS, FT-IR, XRD/QXRD. The TG-DTG-MS was used for quantification of the $CO_2$ binding capacity. The FT-IR analysis was performed to investigate the alterations of the molecular structure of the gel after accelerated carbonation and to detect the carbonate bands in powders as a basis for determining the presence of carbonation products. The XRD and quantitative XRD (QXRD) were used for phase identification and quantification of the carbonation products in carbonated powders, respectively.

The information on reactivity of $CO_2$ and $CO_2$ binding capacity of ground pastes will be used for comparison with $CO_2$ binding capacity of bulk alkali activated pastes in Chapter 7.

## 5.2. MATERIALS AND METHODS

### 5.2.1. MATERIALS AND SAMPLE PREPARATION

In addition to FA and GGBFS, also Ordinary Portland Cement (OPC) (CEM I 42.5 N) and blends of OPC and GGBFS (CEM III/B 42.5 N) were used. These cements are in compliance with Dutch standard NEN-EN 197-1:2011. The chemical composition of CEM I and CEM III/B was determined with X-ray Fluorescence (XRF) (Table 5.1). The chemical composition of FA and GGBFS was reported in Chapter 3 (Table 3.1).

X-ray diffraction is used to study the minerology of raw materials. Figure 5.1 shows results of quantitative phase analysis performed by Rietveld method for GGBFS, FA, CEM I and CEM III/B. Figure 5.1 shows that GGBFS is fully amorphous, while FA is composed of amorphous and crystalline phases (such as quartz, mullite, magnetite and hematite). CEM I and CEM III/B have different mineral composition. The CEM I consists of tri-

Table 5.1: Chemical composition of CEM I (42.5 N) and CEM III/B (42.5 N) measured with XRF [%].

| | $SiO_2$ | $Al_2O_3$ | CaO | MgO | $Fe_2O_3$ | S | $Na_2O$ | $K_2O$ | $TiO_2$ | $P_2O_5$ | LOI |
|---|---|---|---|---|---|---|---|---|---|---|---|
| CEM I | 19.6 | 4.8 | 62.6 | 1.8 | 3.0 | 1.4 | 0.4 | 0.6 | 0.3 | 0.2 | 2.8 |
| CEM III/B | 30.0 | 11.0 | 45.0 | 7.0 | 1.3 | 1.9 | 0.4 | 0.5 | 0.9 | 0.6 | 0.1 |

calcium silicate ($C_3S$), dicalcium silicate ($C_2S$), tricalcium aluminate ($C_3A$), tetracalcium aluminate ferrite ($C_4AF$) and small amounts of minor constituents like anhydrite ($CaSO_4$), calcite ($CaCO_3$), periclase, gypsum and quartz. The XRD diffractogram of CEM III/B shows that it is predominantly amorphous.

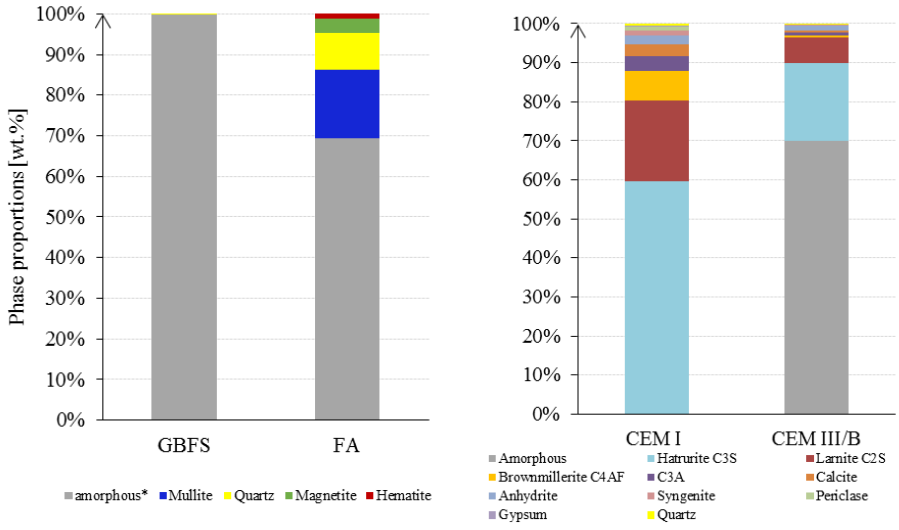


Figure 5.1: Quantitative phase analysis by Rietveld method for raw materials: GGBFS, FA, CEM I and CEM III/B.

The alkaline activator was prepared as explained in Chapter 3, Section 3.2.2. For each paste, the liquid-to-binder mass ratio was 0.5. The pastes were produced with the following FA/GGBFS ratios of 100:0, 70:30, 50:50, 30:70, 0:100 wt.%, named S0, S30, S50, S70, S100, respectively. Cement pastes were made with water-to-binder ratio 0.5. The pastes were cast in polyethylene vials, with 35 mm diameter and 70 mm height, and vibrated for 15-30 s on a vibrating table. The pastes were all sealed cured during the first 28 days. One set of samples was sealed cured for 180 days and it will be referred to as "reference materials". Figure 5.2 shows typical cylindric paste sample after 28 days of sealed curing.

### 5.2.2. ACCELERATED CARBONATION CONDITIONS

The accelerated carbonation was performed in the $CO_2$ chamber, Figure 5.2, where the $CO_2$ concentration, temperature and relative humidity are controlled. The $CO_2$ concentration was kept constant at 1% by volume. The temperature in the chamber was fixed

at 20°C and a relative humidity at 60%, which are the optimal conditions for fast carbonation [198].

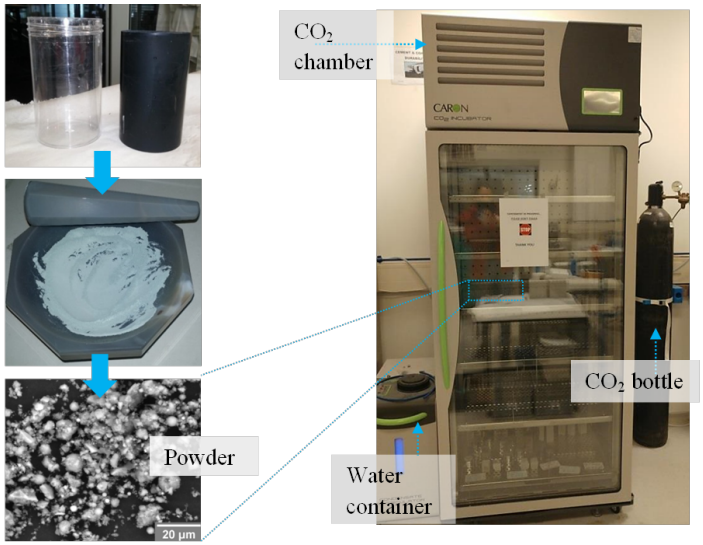


Figure 5.2: Left: Bulk sample after demoulding (up), ground sample (middle), SEM-BSE image of the powder (down). Right: Set-up for accelerated carbonation (Caron Reach-in CO2 Incubator 7400-33-3.

### 5.2.3. EXPERIMENTAL PROGRAMME

After 28 days of curing, the cylindric samples were demoulded and ground to a powder (see Figure 5.2). The powder was obtained from the sides of the paste cylinders using a diamond drilling tool and then it was placed in the $CO_2$ chamber. By dusting, the powder was evenly distributed over a paper before exposure in the $CO_2$ chamber. The average particle size of the powder was 75 $\mu$m, still allowing full carbonation on a practical timescale [61]. The mechanism and degree of the carbonation were investigated through a complementary set of analytical methods, including TG-DTG-MS, FT-IR, XRD/QXRD. The TG-DTG-MS allowed quantification of the $CO_2$ binding capacity. The FT-IR analysis was performed to investigate the alterations of the gel molecular structure after accelerated carbonation and to detect the carbonates in powders as a basis for determining the presence of carbonation products. The XRD and QXRD were used for identification of the carbonation products and their quantification in carbonated powders. It should be noted that the powders were analyzed with TG-DTG-MS, FT-IR and XRD, immediately after the exposure period without any pre-drying. Therefore, the results include also the effect of moisture in the samples. However, small amounts of moisture do not affect quantification of the $CaCO_3$. The sample materials that were not exposed to carbonation are referred to “reference materials” or “0 h carbonation”, hereafter.

#### 5.2.3.1. TG-DTG-MS

The TG-DTG-MS method was used to quantify the binding capacity of $CO_2$ by the powders. The TG-DTG-MS tests were performed at 0 h, 28 days, 180 days. The measurements were performed on the samples shortly after collecting them from the carbonation chamber.

Netzsch STA 449 F3 Jupiter coupled with a mass spectrometer Netzsch QMS 403 C was used to identify the $H_2O$ and $CO_2$ emissions for each temperature range. Samples of approximately 35 mg were placed in an alumina crucible and exposed under an inert atmosphere of argon and increasing temperatures ranging from 40 °C to 1100 °C at a heating rate of 10 °C/min. A blank curve, obtained under the same conditions with the same empty alumina crucible, was systematically subtracted. The Mass Spectrometer (MS) was coupled to the TG to allow separation of concurrent mass loss from $H_2O$ and $CO_2$ release. The response of a sample with unknown concentration of $CO_2$ was compared to the response of a standard sample with known concentration under identical analytical conditions. Calcite was defined as the standard for calibration of the mass loss upon heating (Figure 5.3). Calibration of the Mass Spectrometer response to the $CO_2$ release from this standard compound allowed quantification of the $CO_2$ release from more complex powders, that besides calcium carbonates also contain other compounds as reaction products. The peak integral, i.e. the area under the MS $CO_2$ curve, was quantified using OriginPro 9 software for each paste.



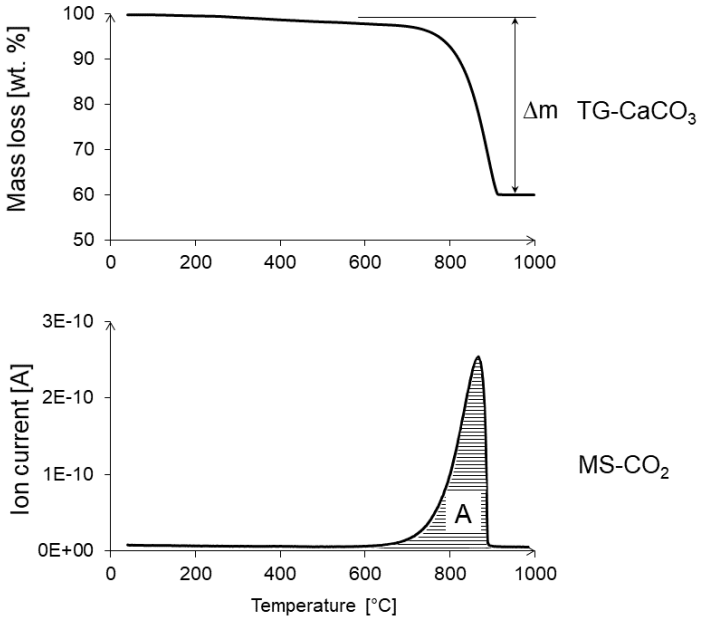


Figure 5.3: Mass loss (wt.%) due to decomposition of $CaCO_3$ (TG) and $CO_2$ peak area definition (MS-$CO_2$).

#### 5.2.3.2. FT-IR

The alteration of the molecular structure of the gel under accelerated carbonation was investigated with FT-IR. The silicate (Si-O-T, T=Si, Al) and carbonate groups ($CO_3^{2-}$) were characterized in powdered pastes at different time intervals: 0h, 0.5h, 1h, 3h, 6h, 12h, 24h, 48h, 7 days, 14 days, 28 days, 180 days. Around 35 mg of powder of each paste was collected and subsequently measured using attenuated total reflectance Fourier transformed infrared (ATR-FTIR). Spectra were acquired with PerkinElmer Spectrum 100, over the wavelength range of 4000 (2000) $cm^{-1}$ to 600 $cm^{-1}$ with a resolution of 4 $cm^{-1}$. A total of 16 scans were collected per measurement.

#### 5.2.3.3. XRD-QXRD

Powders for XRD measurements were collected from reference samples (no $CO_2$, 180 days of sealed curing) and at 180 days of carbonation. XRD-QXRD analyses were performed as explained in Chapter 4, Section 4.2.2.3.

## 5.3. RESULTS

### 5.3.1. QUANTIFICATION OF $CO_2$ BINDING CAPACITY

Figure 5.4 shows the DTG curves along with identified temperature ranges of the dehydration and decarbonation of the phases in noncarbonated and carbonated cement and alkali-activated paste powders. Figure 5.4 shows results for sealed cured, 180 days old pastes. In the reference CEM I and CEM III/B pastes, two peaks can be observed. The first peak at 50-200 °C temperature range is associated with the evaporation of free water and decomposition of hydrates. The second peak, at 450 °C, is assigned to dehydration of portlandite [173]. In contrast, in alkali-activated pastes, only one peak at temperature range of 50-200 °C is found, that is common for the dehydration of the gel phases (N-A-S-H, C-(N-)A-S-H) [63]. This clearly shows the absence of portlandite in alkali activated pastes.

The DTG curves of powders carbonated for 180 days showed a peak below 200 °C (Figure 5.4). Additionally, it can be observed that the portlandite is still remaining in the carbonated paste CEM I, whereas it has completely disappeared in the CEM III/B paste (Figure 5.4). The broad peaks in the temperature range of 250-950 °C correspond to release of $CO_2$ from different metastable to stable carbonates. The relative intensities of these peaks change with the GGBFS content in alkali activated pastes and become dominant with increasing the amount of GGBFS.

The MS $CO_2$ curves of the reference (0 h) and carbonated (28 days and 180 days) pastes are plotted in Figure 5.5. The carbonate types present in the samples can be identified from the temperature ranges in which the $CO_2$ is released as follows:

- carbonates from the aqueous solution with lower temperature release between 100 °C and 180 °C, such as sodium bicarbonates/carbonates;
- amorphous carbonates with higher release temperatures between 245 °C and 645 °C;
- crystalline carbonates detected with XRD with known temperature release between 645 °C and 745 °C.

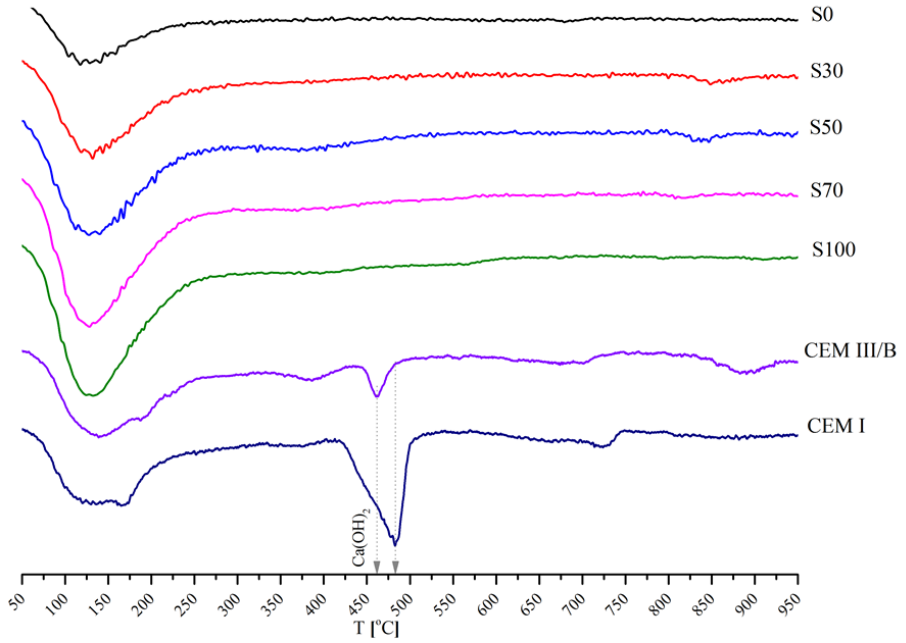


(a) DTG curves for reference (noncarbonated) powders (after 180 days of sealed curing).

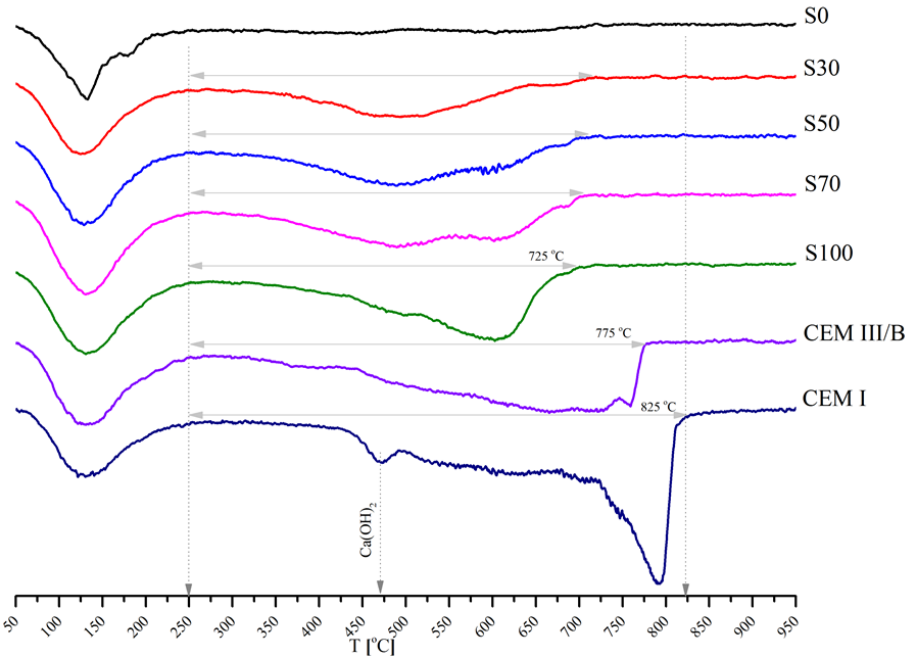


(b) DTG curves for carbonated powders (after 180 days of carbonation).

Figure 5.4: DTG curves

The quantity of each carbonate type can also be estimated from the area under the MS $CO_2$ curves in each of these temperature ranges. The TG-DTG-MS spectra show a minor release of $CO_2$ at around 100 °C and the major release at temperatures above 300 °C in all paste types. It also seems that a premature carbonation (at t=0 h) has taken place in most of the pastes during the grinding of the pastes. Another interesting observation is that the $CO_2$ release ends at 650-700 °C in alkali activated pastes that is lower than the maximum release temperature in cement-based pastes (750 °C).

In alkali activated pastes (except S0), a small but distinct $CO_2$ release peak is observed at 675 °C only in 180 days carbonated samples. In the temperature range of 300 °C to 650 °C, all carbonated pastes show multiple release peaks. These peaks are clearly observable at 500 °C and at 600 °C in alkali activated pastes. In blended pastes (i.e. S30, S50 and S70), there is a significant difference between the peaks at 500 °C in 28 days and 180 days carbonated samples, but the peaks at 600 °C do not show significant differences. Interestingly, this peak (at 600 °C) is almost absent in the paste S30. Additionally, paste S0 shows a distinct $CO_2$ emission at 140 °C that can be attributed to the nahcolite decarbonation as also observed in XRD analyses (Figure 5.11) and previously reported data in the literature [63]. These results show that depending on the type of pastes various forms of carbonates are formed under accelerated carbonation tests.



In general, the total $CO_2$ release has increased from 28 days to 180 days in alkali activated blended pastes, showing that carbonation has been progressing during this period. This is similar to CEM I and CEM III/B pastes in which the released $CO_2$ between 28 days and 180 days significantly increased in the temperature range of 550 °C to 800 °C. On the contrary, S0 paste hardly binds any $CO_2$ and S100 paste shows little difference between the $CO_2$ release of 28 and 180 days of carbonation.

It is known that $CaCO_3$ can precipitate from aqueous solution in various metastable forms [199, 200], while $CO_2$ is likely to be present as adsorbed $CO_2$ or carbonate/bicarbonate ions in solution (such as $CO_3^{2-}$ or $HCO_3^{2-}$) [201]. The simultaneous presence of amorphous $CaCO_3$, metastable $CaCO_3$ (vaterite and aragonite) and calcite in the carbonated powder makes it difficult to carry out a rigorous separation of temperature ranges for their decomposition. However, this does not affect calculations made for determination of the total bound $CO_2$.

The calculations of bound $CO_2$ show that, on average, 10-36 % $CO_2$ by mass of pastes was bound after 180 days through formation of Ca- and/or Na- carbonates (Table 5.2). It can be observed that the identified $CaCO_3$ is mainly crystalline in S100 paste, while it is mainly amorphous in all other alkali-activated pastes. It also seems that the alkali activated pastes take up similar amounts of $CO_2$ after 180 days of exposure.

Pastes S70 and S100, although having a higher CaO content in their chemical composition (Chapter 3, Table 3.1), have a lower bound $CO_2$ compared to other pastes. This may seem contradictory to the XRD results (Figure 5.12), but it should be noted that the total amount of crystalline $CaCO_3$, determined with QXRD, underestimates the $CO_2$ amount quantified by thermal analysis. This can be the reason for the observed difference between the TG-DTG-MS and QXRD results as various forms of $CO_2$ appeared in the samples, including adsorbed $CO_2$ in the C-(N-)A-S-H gel and pore solutions, amorphous $CaCO_3$ (that all cannot be detected with XRD), as well as chemically bound $CO_2$ in crystalline phases $NaHCO_3$ and $CaCO_3$ polymorphs.

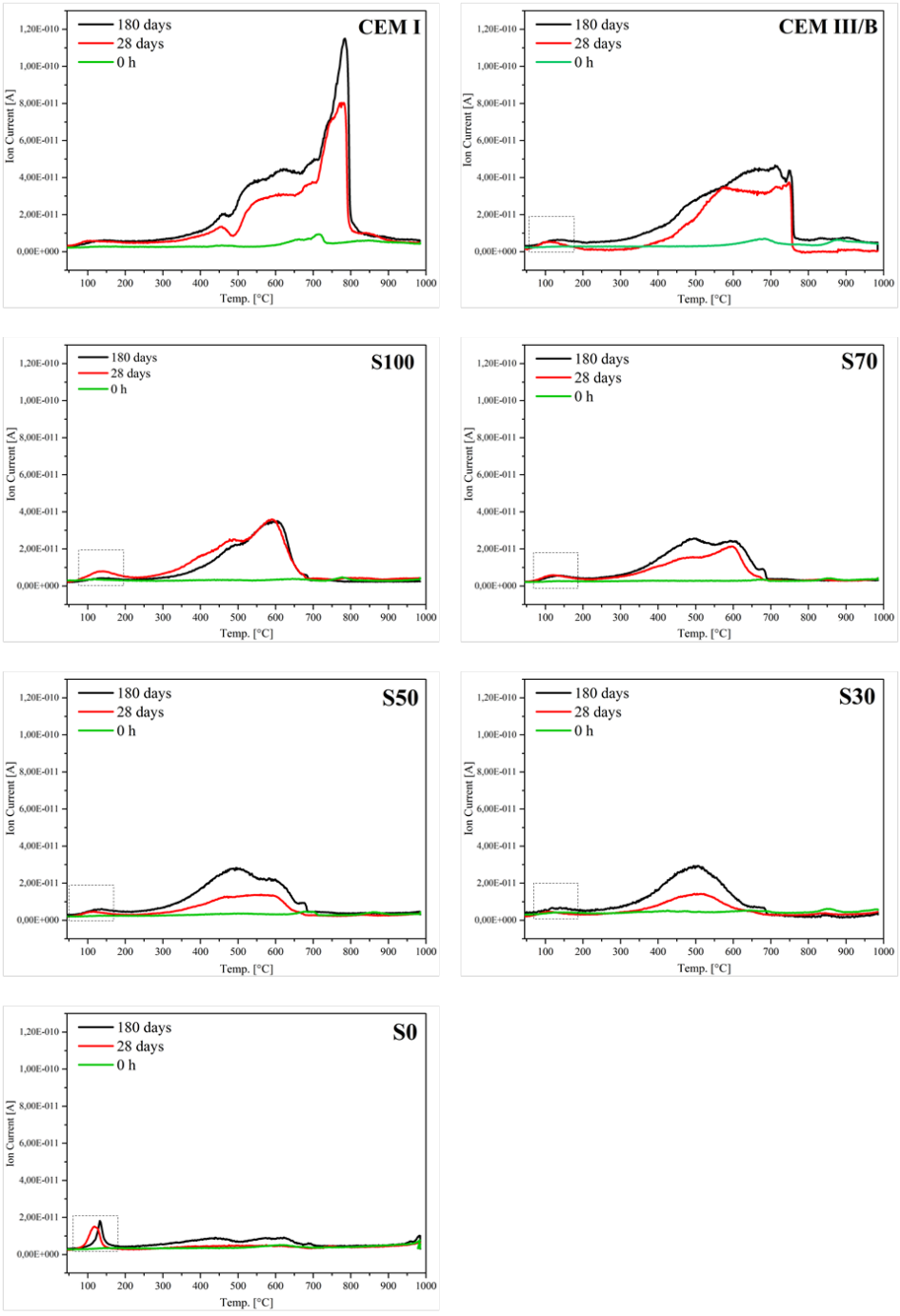


Figure 5.5: MS $CO_2$ curves of reference paste powders (samples before carbonation, 0 h, green lines), MS $CO_2$ curves of paste powders obtained after 28 days of continuous carbonation (red lines), MS $CO_2$ curves of paste powders obtained after 180 days of continuous carbonation (black lines), (exposure conditions: 1% v/v $CO_2$, 20 °C, 60 %RH).

The variation of temperatures at which these carbonates are decomposed from the pastes, stems from the differences in the gel's chemical and molecular structure in these pastes. The carbonation of gel phases with different Ca/Si ratio, i.e. with different intrinsic atomic ordering of calcium (alumino) silicate hydrates, will certainly lead to structurally different types of carbonates, as will be shown in Section 5.3.3.

### 5.3.2. MOLECULAR ANALYSIS OF THE FUNCTIONAL GROUPS

The FT-IR technique was used to monitor the changes of the reaction products during carbonation. This information is important for comprehensive understanding of the gel carbonation at molecular level. Three major functional groups are distinguished:

- water ($H_2O$ and OH) region;
- Si–O–Si (Al) region;
- carbonate (O-C-O) region.



The FT-IR spectra and the characteristic frequencies of pure Na-carbonates and Ca-carbonates obtained from [202, 203] are shown in Figures 5.6 and 5.7. These spectra were used to differentiate carbonate phases in carbonated alkali activated pastes. All the samples were cured for 28 days under sealed conditions before they were carbonated. The FT-IR spectra of reference and carbonated pastes are compared in Figure 5.9. A separate presentation of the reference spectra (after 180 days of sealed curing) and spectra of pastes at 180 days of carbonation is made in Figure 5.10 for clarity of analysis.

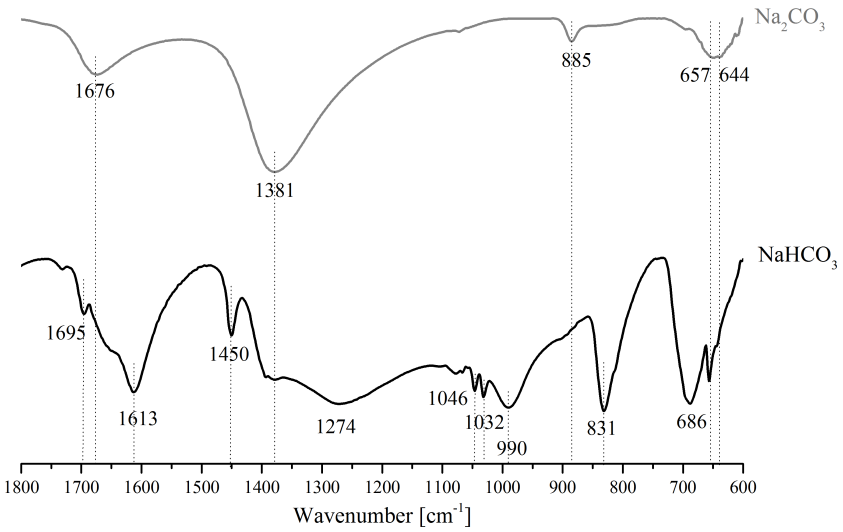


Figure 5.6: FT-IR spectra and characteristic frequencies of Na-carbonates [$cm^{-1}$].

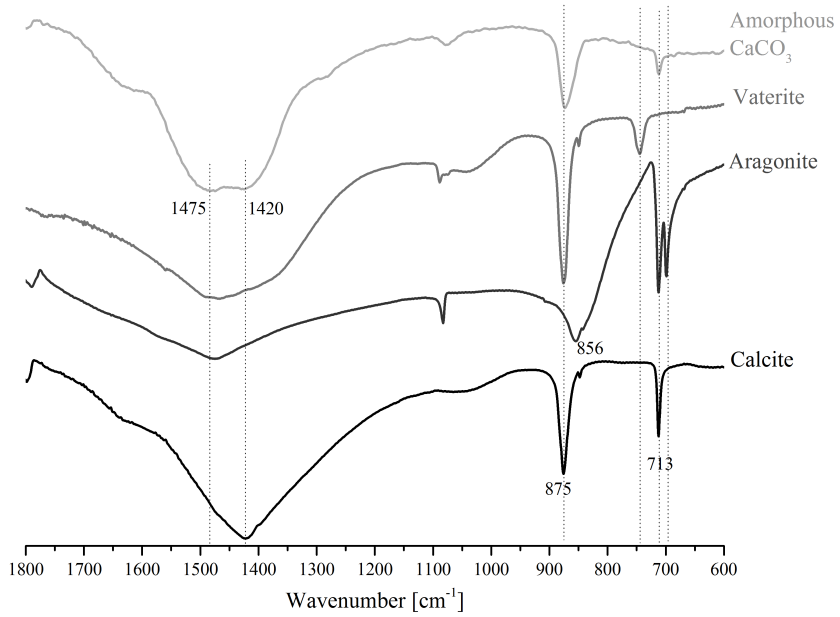


Figure 5.7: FT-IR spectra and characteristic frequencies of Ca-carbonates [$cm^{-1}$] obtained from [203].

#### 5.3.2.1. WATER ($H_2O$ AND OH) REGION

The presence of $H_2O$ is detected by two characteristic absorption bands in the 3700-2500 $cm^{-1}$ region (corresponding to the stretching and deformation modes of $OH^-$) and in the 1640 $cm^{-1}$ region (associated with bending vibration mode of $H_2O$) that is in agreement with those reported in the literature [204]. The important difference between the reference cement-based and alkali-activated paste powders (0 h, Figure 5.9) is found in the region of the $OH^-$ group (3700-2500 $cm^{-1}$ region). In the cement paste powders (CEM I and CEM III/B) this band at 3642 $cm^{-1}$ is assigned to $OH^-$ group of portlandite. This shows the absence of portlandite as also shown by the TG-DTG-MS spectra (Figure 5.4).

The intensity of the $OH^-$ group band related to portlandite at 3642 $cm^{-1}$ in pastes CEM I and CEM III/B is gradually decreased (0-28 days of carbonation, Figure 5.9) until it completely disappeared after 180 days of accelerated carbonation (Figure 5.10). Carbonation, in general, leads to reduction of water-related bands, at 3700-2500 $cm^{-1}$ and 1640 $cm^{-1}$, in all the pastes (Figure 5.10). This is in agreement with the reduced release of water in DTG curves (Figure 5.4). This reduction is most significant for the alkali-activated pastes.

#### 5.3.2.2. SI–O–SI (AL) REGION

Positions of silicate groups (symmetric stretching bands ~950 $cm^{-1}$, Si-O-T (with T=Si,Al)) in FT-IR spectra indicate different gel molecular structures for the alkali-activated pastes compared to cement-based pastes (most deviant for S0 and cement-based pastes, the latter with a double peak at 1120 $cm^{-1}$ and ~950 $cm^{-1}$, Figure 5.10). Depending on the connectivity of silicon sites in silicate glasses as visualized in Figure 5.8, the $SiQ^4$ unit has

an IR absorption band centered around 1200 $cm^{-1}$, the $SiQ^3$ unit around 1100 $cm^{-1}$, the $SiQ^2$ unit around 950 $cm^{-1}$, the $SiQ^1$ unit around 900 $cm^{-1}$ and the $SiQ^0$ unit around 850 $cm^{-1}$ [205].

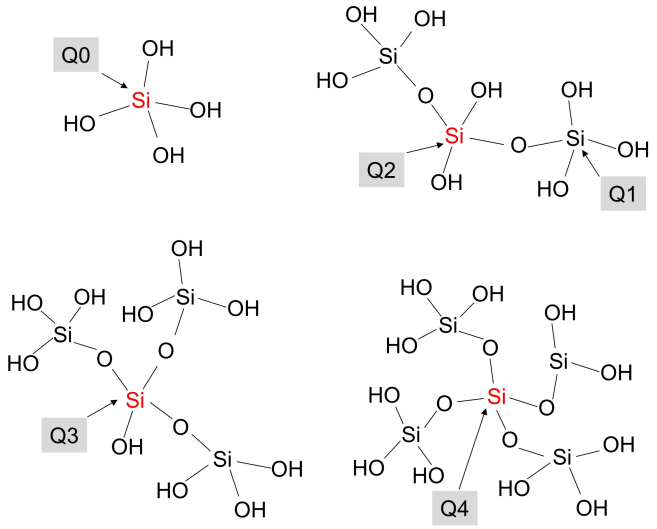


Figure 5.8: Connectivity of silicon sites in silicate glasses.

Regardless of the type of the paste, the IR absorption band implies that the $SiQ^2$ was the main unit in the gel structure of the studied pastes before carbonation. The Si-O-T stretching band appears at approximately 1015 $cm^{-1}$ for the carbonated powders containing GGBFS, while the same band in the reference powders (noncarbonated) appears around 950 $cm^{-1}$ (Figure 5.10). This shift is caused by gradual polymerization of the orthosilicate units ($SiO_4{}^{4-}$) in the gel phases of cement and GGBFS pastes, i.e., the C-S-H, C-(N-)A-S-H gels, yielding $Q^2$ and $Q^3$ silicate units (Figure 5.10). Meanwhile, as the FA-rich pastes are predominantly amorphous aluminosilicate materials, they likely consist of both Si-OH and Al-OH groups and can be, therefore, subjected to polymerization of Si-O-Al [206]. The extraction of the network modifyers (Ca, Na) from the gel interlayers as a result of carbonation leads to an excess of negative charge which is subsequently eliminated by adsorption of the cations (mostly $Na^+$) from the pore water. A similar process also occurs in carbonated OPC-based pastes as reported by Anstice et al. [207].

The carbonation process is described with chemical reactions 5.1-5.3, where a, b, c, d, e, and f are the stoichiometric coefficients for the respective oxide components CaO, $Na_2O$, $Al_2O_3$, $SiO_2$ and $H_2O$. The coefficients are different for each of the studied mixtures.

Formation of carbonate ions:

$$CO_2(aq) + H_2O \rightarrow H_2CO_3 \rightarrow HCO_3^- + H^+ \rightarrow CO_3^{2-} + 2H^+ \tag{5.1}$$

Formation of sodium carbonates:

$$H_2CO_3 + 2NaOH \rightarrow Na_2CO_3 + 2H_2O \tag{5.2}$$

Formation of calcium carbonates:

$$aNa_2CO_3 + (CaO)a(Na_2O)b(Al_2O_3)c(SiO_2)d(H_2O)e \rightarrow$$
$$aCaCO_3 + (Na_2O)b(Al_2O_3)c(SiO_2)d(H_2O)f + 2aNaOH + (e-f)H_2O \tag{5.3}$$

When no cations are available to preserve charge equilibrium, neighbouring groups Si-OH, Si-ONa, Al-OH or Al-ONa condense and merge to Si-O-Si or Si-O-Al gel. The reactions taking place during the process are considered in 5.4-5.6.

Formation of Si-O-Si or Si-O-Al gel:

$$\equiv Si-OH + HO-Si(Al) \equiv \rightarrow \equiv Si-O-Si(Al) \equiv + H_2O \tag{5.4}$$

$$\equiv Si-ONa + HO-Si(Al) \equiv \rightarrow \equiv Si-O-Si(Al) \equiv + NaOH \tag{5.5}$$

$$\equiv Si-ONa + HCO_3-Si(Al) \equiv \rightarrow \equiv Si-O-Si(Al) \equiv + NaHCO_3 \tag{5.6}$$

The peak intensities of silicate functional groups in pastes did not undergo further change after 7 days of accelerated carbonation (Figure 5.9). Based on the FT-IR time-series measurements (see Figure 5.9), it appears that most of the pastes have been fully carbonated after 7 days of exposure in the carbonation chamber. The results suggest that the carbonation of a C-(N)-A-S-H type gel might take place in two stages:

- decalcification of the gel toward formation of a N-A-S-H, followed by
- de-alkalinisation of the metastable N-A-S-H gel and final formation of an aluminosilicate type gel, whose structure is similar to the decalcified binding product.

Both silicate and carbonate changes are least apparent for the S0 paste. This suggests that the gel in this paste did not carbonate as earlier found by the TG-DTG-MS results. The $CO_2$ was mainly present as adsorbed on the N-A-S-H gel or in aqueous solution. This, also, is consistent with a study of Bernal et al. [63].

The silicate band in paste CEM I (950 $cm^{-1}$ →1075 $cm^{-1}$) shifts more compared to silicate band in paste CEM III/B (960 $cm^{-1}$→1021 $cm^{-1}$) and alkali-activated pastes after carbonation (950 $cm^{-1}$→1015 $cm^{-1}$). The magnitude of this shift is indicative of the polymerization degree [208]. In this study this effect is lower for alkali-activated pastes (65 $cm^{-1}$) and paste CEM III/B (75 $cm^{-1}$), compared to carbonated paste CEM I (125 $cm^{-1}$). Comparing the magnitude of Si-T shift from this study with that of reported by Li et al. [209] and of Palacios et al. [59], it can be deduced that carbonated alkali-activated slag can polymerize even further after carbonation (1031 $cm^{-1}$) than observed in this study (1015 $cm^{-1}$). Concerning the $CO_2$ concentration used in this study (1% v/v $CO_2$) and from [209] (20% v/v $CO_2$) and [59] (100% v/v $CO_2$) it can be concluded that the degree of gel polymerization increases with the $CO_2$ concentration, in agreement with the findings of Castellote et al. [210].

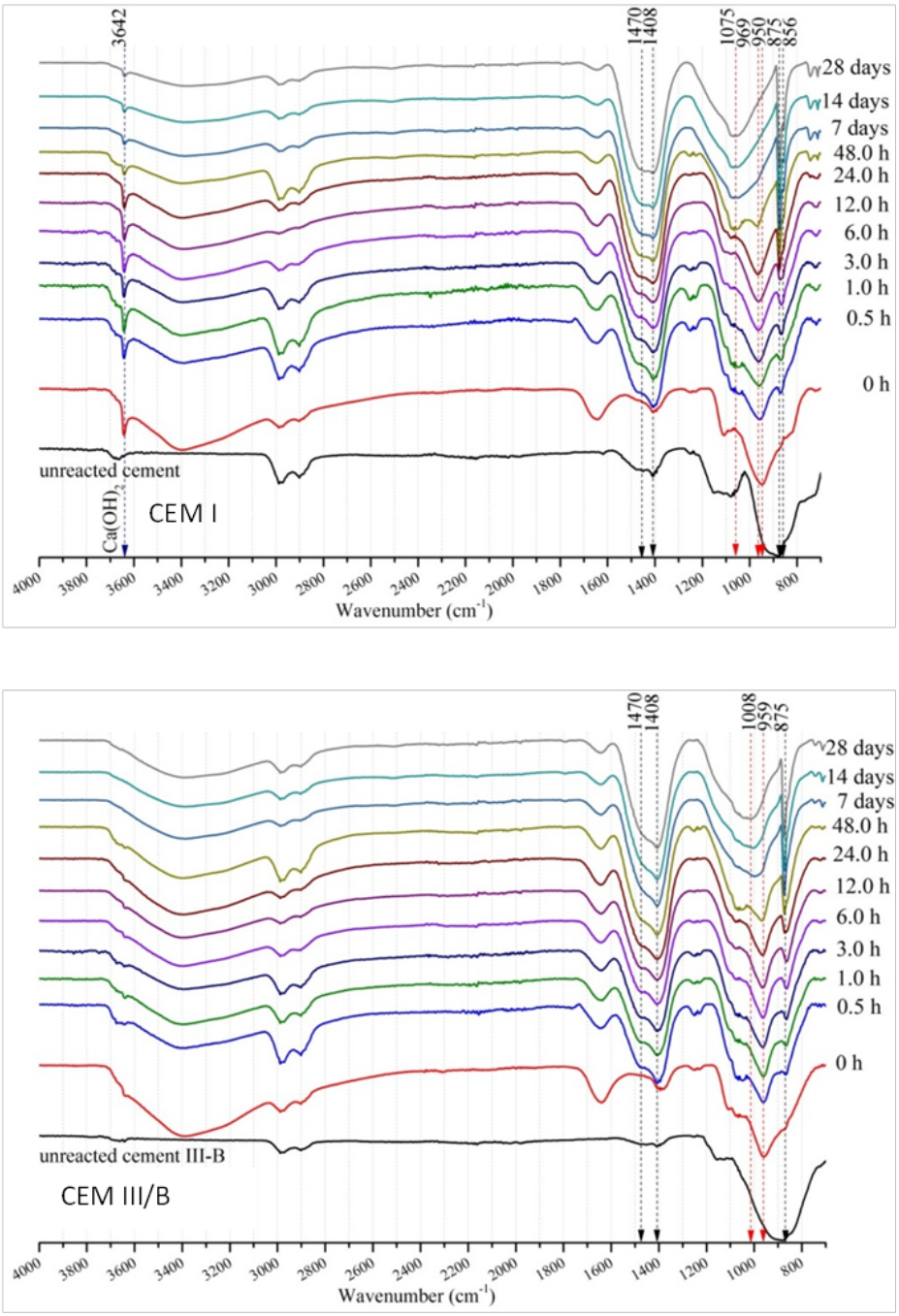


Figure 5.9: FT-IR spectra of cement pastes (CEM I and CEM III/B) and alkali-activated FA/GGBFS pastes from time zero of exposure until 28 days (exposure conditions: 1% $CO_2$, 60 %RH).

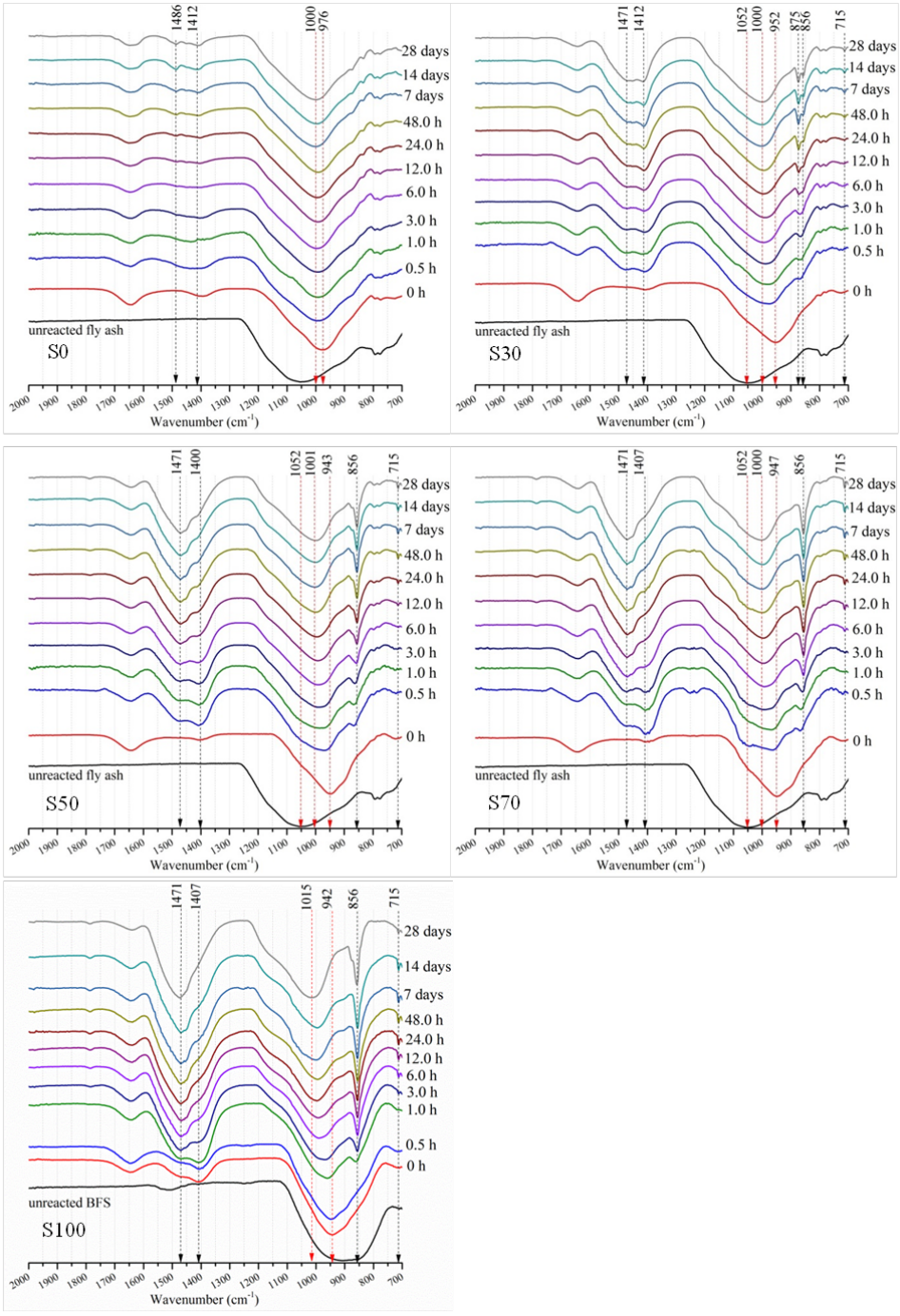


Figure 5.9: FT-IR spectra of cement pastes (CEM I and CEM III/B) and alkali-activated FA/GGBFS pastes from time zero of exposure until 28 days (exposure conditions: 1% $CO_2$, 60 %RH).

#### 5.3.2.3. CARBONATE (O-C-O) REGION

The FT-IR spectra of carbonated pastes show third type of bands, i.e. the carbonate bands. Three types of carbonate bands can be observed: strong broad band at 1408-1470 $cm^{-1}$ due to the asymmetric stretching of $CO_3^{2-}$ ($v^3$), narrow band at 875-856 $cm^{-1}$ representing the bending ($v^2$) of $CO_3^{2-}$, and the band at 713 $cm^{-1}$ in-plane bending ($v^4$) of $CO_3^{2-}$. Most of these bands correspond to characteristic bands of amorphous $CaCO_3$, vaterite, aragonite and calcite, as it can be deduced by comparison to the FT-IR spectra of their pure chemical compounds (Figure 5.7).

After first 0.5h of $CO_2$ exposure, the $CO_2$ uptake was recorded through appearance of carbonate bands at 1400-1500 $cm^{-1}$. This implies that the carbonation rate for powdered paste samples is initially controlled by the sorption of $CO_2$ at surface sites rather than by the rate of chemical reaction at the surface. This is consistent with the study of Reardon et al. [211] for carbonation of cement powder paste under high $CO_2$ pressure.

Figure 5.9 shows that the $CO_2$ uptake is more pronounced in cement-based pastes than in alkali-activated pastes. This can be seen from the increase of the intensity of the bands at 1400-1500 $cm^{-1}$ region after 0.5 h. This is mainly due to higher CaO content in the cement-based pastes and hence higher affinity of cement-based pastes to adsorb $CO_2$. Hence the influence of composition of starting gel phases in the pastes on the $CO_2$ uptake is considerable. The rate of $CO_2$ uptake with progress of carbonation from 7 days to 28 days was slower than in the first 7 days with an initial rapid $CO_2$ uptake. Although FT-IR spectra show an intermediate $CO_2$ uptake between 7 and 28 days, the $CO_2$ uptake varied between pastes in period of 28 to 180 days (Figure 5.9). It can be seen that in S50, S70 and S100 pastes in region 1400-1500 $cm^{-1}$ the right shoulder around 1400 $cm^{-1}$ disappears with elapse of carbonation time and that the left shoulder close to 1500 $cm^{-1}$ became larger after 7 days of exposure, even more pronounced in the GGBFS-rich pastes. It is assumed that in the first few hours of carbonation $CO_2$ is combined with gel phases, whereas in later ages, between 48 hours and 28 days, $CO_2$ is gradually released and forms aragonite (pastes S50, S70, S100). The aragonite is identified based on pure aragonite FTIR spectra in Figure 5.7 and QXRD results in Figure 5.13. The formation of aragonite was concurrent with the presence of amorphous silica in the samples as also observed in previous study [212].

Rafai et al. [213] reported similar $CO_2$ transformation during early carbonation of cement-based concrete. Using stable isotope 18O and 13C, authors found that the initial $CaCO_3$ has a distinct isotope composition, and a large quantity of $CO_2$ was combined with C-S-H gel. The $CO_2$ was then gradually released and produced another $CaCO_3$, which was characterized by a much larger 18O content than the initial $CaCO_3$. Similarly, Black et al. [212] reported the amorphous calcium carbonate as the first carbonation product from studies of the C-S-H carbonation at a longer time scale, formed presumably by the physical adsorption of $CO_2$ on the C-S-H gel surface. The subsequent formation of crystalline $CaCO_3$ polymorphs depended upon the Ca concentration and Ca availability in the surface layers as seen in this study. Different crystalline forms of the same compound ($CaCO_3$) exhibit slightly different IR spectra (spectra between vaterite, aragonite, calcite), the so-called polymorphism effect [214]. This is reflected in the FT-IR spectra for most of the studied pastes.

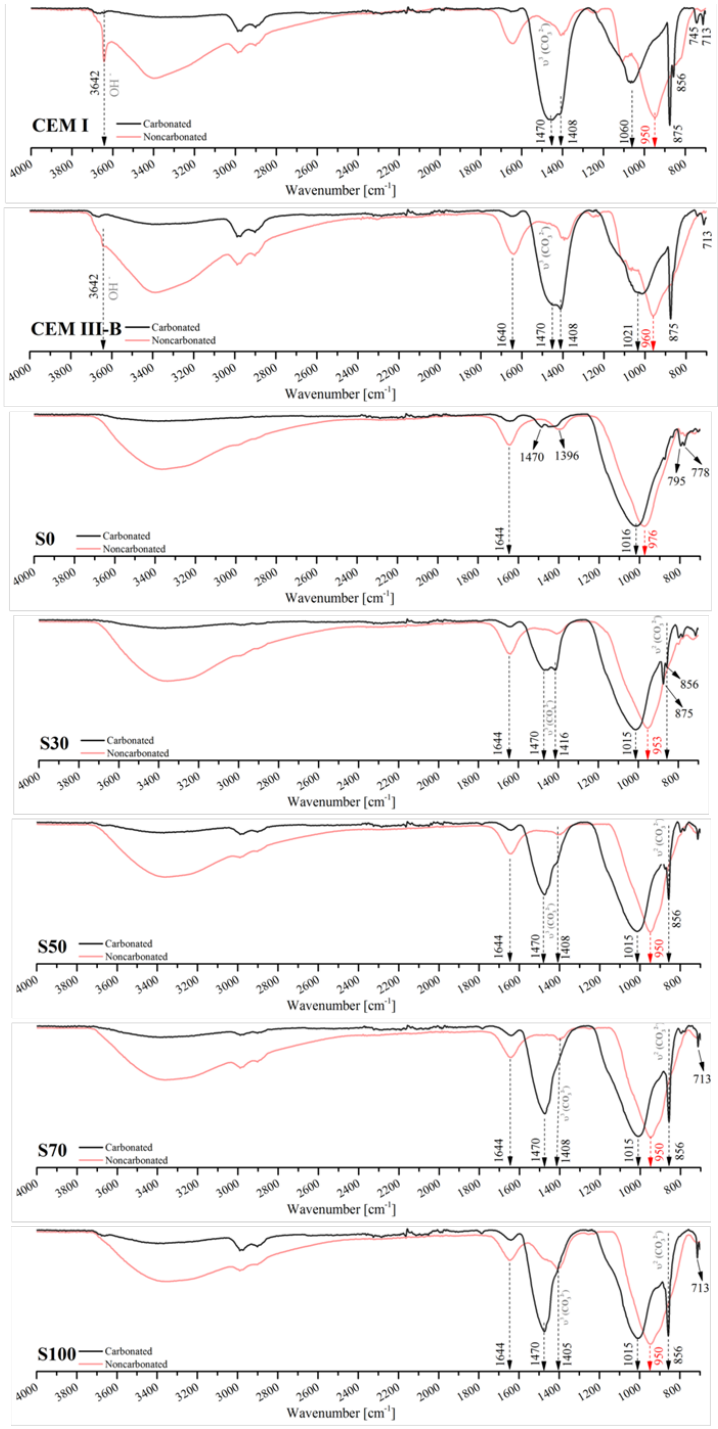


Figure 5.10: Comparison of reference FT-IR spectra and after 28 days and 180 days of carbonation (1% v/v $CO_2$, 60 % RH), for cement and alkali-activated pastes.

While S0 paste shows hardly any carbonate bands, the intensity of the broad 1400-1500 $cm^{-1}$ bands increased with GGBFS content (from S30 to S100 paste). Pastes S30, S50, S70 and S100 contain a sharp carbonate peak at 856 $cm^{-1}$ and only S30 has a second sharp peak at 875 $cm^{-1}$. Additionally, the broad, unsplit band in the range 1400-1500 $cm^{-1}$ represents amorphous $CaCO_3$ [203] and it is characteristic of the sample S30. This observation is in agreement with the decomposition of amorphous phase of the sample S30 demonstrated by the mass spectrometry analysis (Figure 5.5). In contrast, FT-IR spectra of the carbonated samples S50, S70, S100 (Figure 5.10) contain well-resolved $v^3$ doublets with maximum at 1470 $cm^{-1}$, corresponding to aragonite [203], as confirmed with XRD analysis (Figure 5.13). The cement-based pastes contain also three $CaCO_3$ polymorphs, vaterite, aragonite, and calcite.

The calcite band in cement pastes at 875 $cm^{-1}$, overlaps with the vaterite band according to the frequency ranges for vaterite and calcite carbonate groups in Figure 5.7. To further examine the presence of different $CaCO_3$ and their proportions, and also of Na-carbonates since the appearance of Na-carbonates in FT-IR spectra is not clear, XRD analysis is followed in the next section.

5

### 5.3.3. CRYSTALLINE CARBONATION PRODUCTS

To confirm the transformation of gel phases to various types of metastable (vaterite, aragonite) and stable $CaCO_3$, phase identification and quantitative analysis with XRD/QXRD were performed to complement the FT-IR identifications in Section 5.3.2. Figure 5.11 shows XRD diffractograms of CEM I and CEM III/B pastes along with identified and quantified carbonation products for carbonated cement-based paste powders after 180 days of carbonation. It can be seen that the amorphous phase is dominant and its content is significantly higher in CEM III/B than in CEM I paste. The presence of remaining portlandite in the carbonated powder of CEM I paste and its absence in CEM III/B is clear. This residual portlandite in paste CEM I was also found in TG-DTG analyses. Hydrotalcite was found in paste CEM III/B, resulting from the high MgO content in this paste compared to paste CEM I, where MgO is very low. Regarding the carbonation products, vaterite, aragonite and calcite were found in paste CEM III/B, while only aragonite was found in paste CEM I.

Figure 5.12 shows XRD diffractograms along with identified carbonation products for reference alkali-activated pastes (noncarbonated powders) and for carbonated powders after 180 days of carbonation. Similar to paste CEM III/B, also in alkali-activated pastes S0→S100 the amorphous phase is dominant (Figure 5.13). The pastes containing FA showed peaks for quartz, mullite, hematite and magnetite. Comparison of the XRD diffractograms of noncarbonated and carbonated pastes shows several additional peaks formed in the carbonated samples (Figure 5.12). These peaks showed that nahcolite is a carbonation product in paste S0 as also found by Bernal et al. [7].

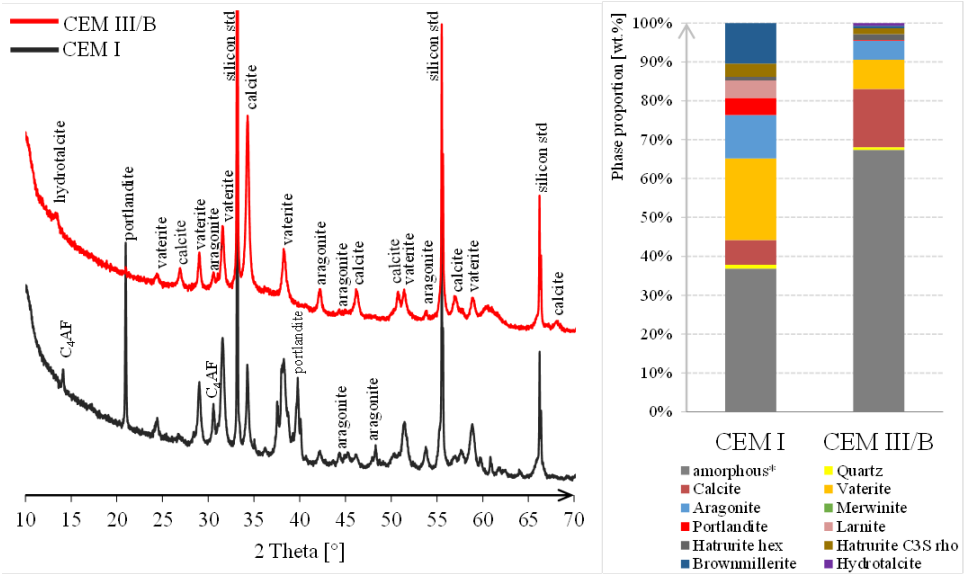


Figure 5.11: XRD diffractograms with respect to the phases in: CEM I and CEM III/B carbonated powders (left), quantitative phase analysis by Rietveld method for cement paste carbonated powders after 180 days carbonation (right).

Aragonite was a dominant carbonation product in S50, S70 and S100, but this was not the case for paste S30 as also observed in FT-IR spectra (Figure 5.9). In paste S30, the amount of calcite was found to be higher than aragonite. It is known that the resulting $CaCO_3$ polymorph depends on the conditions of carbonation such as relative humidity, temperature, $CO_2$ concentration as well as type of cement [215], but also on the environmental conditions (RH, % $CO_2$) during preparation of the powder. It should be noted that these factors can also affect the quantitative phase analysis by Rietveld method and can be a reason for such a high amount of calcite observed in the paste S30, compared to the other pastes. In Figure 5.5 (MS $CO_2$), paste S30 has a range of amorphous calcium carbonates, which cannot be identified with XRD. In addition, the small peak around 675 °C appears in paste S30 (Figure 5.5), suggesting decomposition of other form of $CaCO_3$ than amorphous. It is believed that this peak is related to the decomposition of calcite, as low crystalline calcite with high dispersity is thermally less stable and preferentially decomposes within the temperature range of 680-775 °C [103].

Generally, the amount of carbonates increases with increasing GGBFS content in the pastes, but still alkali-activated pastes have lower carbonate amounts compared to pastes CEM I and CEM III/B (Table 5.2, QXRD results). As for carbonate phases in cement-based pastes, higher proportion of vaterite in CEM I paste than in paste CEM III/B is believed to be a consequence of initially higher portlandite content in CEM I paste and due to similarities in the portlandite and vaterite symmetries [216] and their (positive) surface charge [217] as observed by Black et al. [212].

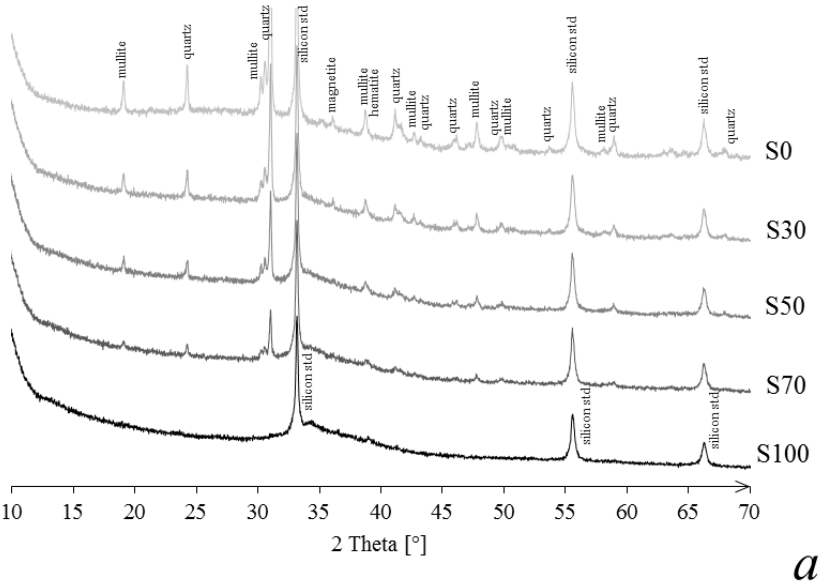


(a) reference noncarbonated powders

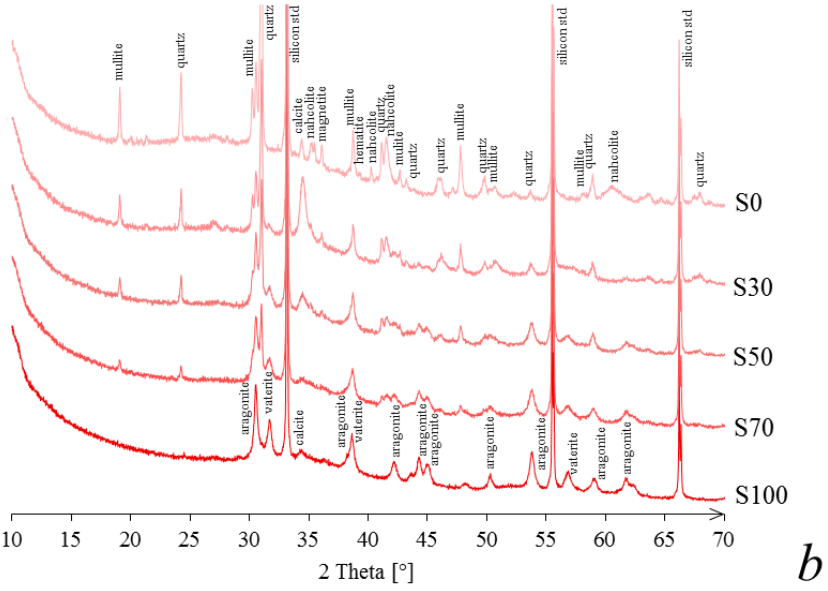


(b) carbonated powders after 180 days carbonation

Figure 5.12: XRD diffractograms with respect to the phases in alkali-activated FA and GGBFS

In order to compare the tendencies of pastes to bind the $CO_2$, quantification of $CO_2$ binding capacity was done with two analyses, TG-DTG-MS and QXRD. Quantitative phase

analysis by Rietveld method gives the $CO_2$ that is bound in the crystalline phases only. It can be seen that the largest portion of well crystallized carbonates is found for cement-based pastes. Regarding the disagreement between values for $CO_2$ binding capacity measured with TG-DTG-MS and QXRD (Table 5.2), it is clear that the TG-DTG-MS gives the highest values for $CO_2$ binding capacity because $CO_2$ is contained in crystalline and amorphous phases, the latter not detected in XRD. The TG-MS values are also supported by FT-IR characterization of the early carbonation of the pastes, where it was evidenced that initially amorphous carbonates were formed. These metastable carbonates under the accelerated carbonation conditions were gradually converted into the more stable aragonite. However, not all the metastable carbonates were completely converted as shown by TG-DTG-MS results (Figure 5.5).

The difference between the $CO_2$ binding capacity values measured with TG-DTG-MS and QXRD at 180 days, gives the amount of the $CO_2$ which is in amorphous form. The $CO_2$ binding capacity can be calculated from the chemical composition of the paste based on the (earth) alkaline content of each paste and assuming the stoichiometry of bonding (namely CaO-$CO_2$, MgO-$CO_2$, NaOH-$CO_2$, KOH-$CO_2$). The calculated $CO_2$ binding capacities for the pastes are given in Table 5.2. The actual amount of $CO_2$ bound (TG-DTG-MS) was found to be less than the theoretical in all alkali-activated pastes. If the MgO, $Na_2O$ and $K_2O$ would be not accounted in calculation of theoretical $CO_2$ capacity, this difference would be much lower.



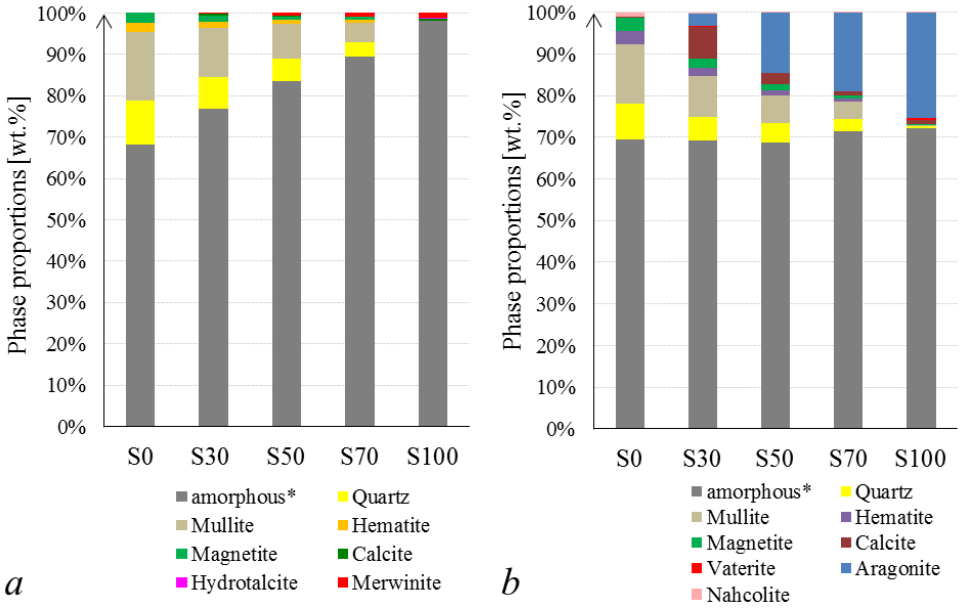


(a) alkali-activated FA and GGBFS reference noncarbonated powders

(b) alkali-activated FA and GGBFS carbonated powders after 180 days carbonation

Figure 5.13: Quantitative phase analysis by Rietveld method

Table 5.2: The measured $CO_2$ binding capacity of carbonated powders compared to the theoretical $CO_2$ binding capacity of water-free paste (expressed as values normalized to 100%).

| | $CO_2$ binding capacity | | |
|---|---|---|---|
| | Theoretical[a] | QXRD[b] (180 days) | TG-DTG-MS[c] (180 days) |
| | [wt.%] | [wt.%] | [wt.%] |
| S0 | 11.36 | 0.70 | 5.30 |
| S30 | 17.33 | 5.04 | 14.68 |
| S50 | 21.59 | 7.66 | 16.09 |
| S70 | 24.05 | 8.82 | 15.00 |
| S100 | 28.34 | 11.88 | 14.36 |
| CEM I | 32.03 | 17.16 | 35.95 |
| CEM III/B | 27.26 | 12.32 | 26.87 |

[a] The theoretical $CO_2$ binding capacity is the sum of the individual (earth) alkaline oxide $CO_2$ binding capacities (the amount of $CO_2$ bound as $CaCO_3$, $MgCO_3$, $NaHCO_3$, $KHCO_3$), calculated as shown in equation: % $CO_2$ = 0.785(% CaO - 0.56% $CaCO_3$ - 0.7% $SO_3$) + 1.091% MgO + 1.42% $Na_2O$ + 0.94% $K_2O$ of [218]. The weight percent of oxides [%] was used from Table 3.1 and Table 5.1. It should be noted that $Na_2O$ weight was accounted from both the raw material and from alkaline activator for the calculation of the theoretical $CO_2$ binding capacity in alkali activated pastes.
[b] $CO_2$ binding capacity from the quantitative phase analysis by Rietveld method for paste carbonated powders after 180 days of carbonation (Figure 5.12 and Figure 5.13), i.e. the amount of $CO_2$ bound as crystalline $CaCO_3$ and $NaHCO_3$, which were detected with XRD analysis.
[c] $CO_2$ binding capacity from Figure 5.5, quantified with TG-DTG-MS method from the powders after 180 days of carbonation, i.e. the amount of $CO_2$ bound as amorphous and crystalline $CaCO_3$ and $NaHCO_3$, which were detected from the TG-DTG-MS analysis.



### 5.3.4. DISCUSSION

Carbonation is the most common reason of the concrete deterioration under environmental conditions [47]. It induces chemical and physical changes to the cement paste properties that further influence its long-term performance. In this Chapter the $CO_2$ binding capacity, carbonate phases and the dynamic of gel changes under accelerated carbonation have been studied in both cement pastes and blended FA-GGBFS alkali-activated pastes.

The results showed that with increase of the GGBFS content in alkali activated pastes, the proportion of crystalline $CaCO_3$ increases. In addition, while calcite decreases, aragonite increases. For all alkali activated pastes (excluding S0) the total amount of $CO_2$ bound after 180 days is similar. Since crystalline Na-(bi)carbonates play a minor to no role according to TG-MS results (Figure 5.5) and XRD results (Figure 5.13), the $CO_2$ binding capacity is mainly dependent on the CaO content in the raw materials of the samples (the main carbonation products were identified as vaterite, aragonite and calcite). The near or full $CO_2$ binding capacity of water-free paste as theoretically calculated, is achieved for pastes CEM I and CEM III/B, as shown in Table 5.2.

In contrast to alkali activated pastes, cement based pastes reach a much higher (equilibrium) $CO_2$ binding for well exposed grains. That is 101-112% of theoretical capacity of which on average 47% is in the form of crystalline carbonates and the rest is in amorphous form. This clearly indicates that there is a reduced potential for the $CO_2$ binding to

take place over the service life of alkali-activated materials compared to cement-based materials. Furthermore, it is important to consider the effect of $CO_2$ binding capacity on the mechanical and permeability properties for cements with different chemistries varies. For instance, in pure OPC systems carbonation leads to pore structure refinement and increase in mechanical strength, while in blended OPC cements and alkali-activated systems, the opposite effect is observed [219], [61].

Based on FT-IR results, the aluminosilicate gel after carbonation was characterised by a degree of polymerisation higher than the original C-S-H/C-N-A-S-H gel. Aluminosilicate gel may capture substantial Na in the structure as shown by the reactions 5.5 and 5.6, that does not allow formation of Na-carbonates. This is consistent with XRD results, where it was shown that Na-carbonates (nahcolite) content is too low and at the level of measurement error.

The preservation of $OH^-$ and $Na^+$ ions in the pore solution or in the gel of the alkali activated pastes during carbonation would reduce the risk of pore solution neutralization which is important for preserving the passivity of the reinforcement oxide layer in alkali-activated concrete. However, the gel deterioration due to carbonation that leads to Ca leaching and polymerization of remaining aluminosilicate units certainly affects the overall microstructure and have negative effects on the micromechanical properties of the alkali-activated pastes as exemplified in Chapter 8.

Since modeling of carbonation is associated with chemical reactions and $CO_2$ diffusion, $CO_2$ binding capacity of alkali activated pastes is very important input in such models. Apart from the $CO_2$ binding capacity, the future models will strongly benefit from improved understanding of nucleation of different carbonates as shown by FT-IR study.



## 5.4. CONCLUDING REMARKS

The aim of this chapter was to investigate the $CO_2$ binding capacity and mineralogical changes of alkali-activated and cement pastes under accelerated carbonation conditions. All the samples were cured for 28 days under sealed conditions before they were carbonated. To accelerate the process, the pastes were crushed and ground to powder. Based on the results presented in the chapter, following conclusions can be drawn:

- Carbonation causes polymerization of the alumina-silicate network of the C-N-A-S-H gel in alkali activated FA/GGBFS pastes. In cement-based pastes carbonation induces polymerization of C-S-H and loss of CH.
- $CO_2$ binding capacity is much higher in CEM I and CEM III/B pastes than in alkali activated pastes, due to their higher CaO content.
- With increase of the GGBFS content in the alkali activated pastes, the proportion of crystalline $CaCO_3$ increases, calcite decreases and aragonite increases after 180 days of exposure to accelerated carbonation.

- In all the alkali activated pastes studied here (excluding S0) the total amount of $CO_2$ bound after 180 days is similar. Since crystalline Na-(bi)carbonates play a minor to no role according to TG-MS results (Figure 5.5) and XRD results (Figure 5.13), the $CO_2$ binding capacity is mainly dependent on the CaO content in the raw materials of the samples. The near or full $CO_2$ binding capacity of water-free paste as theoretically calculated, is achieved for pastes CEM I and CEM III/B, as shown in Table 5.2. In contrast to alkali activated pastes, cement based pastes reach a much higher (equilibrium) $CO_2$ binding for well exposed grains. That is 101-112% of theoretical capacity of which on average 47% is in the form of crystalline carbonates and the rest is in amorphous form.

- Time-series FT-IR measurements showed that spectral changes related to the silicate polymerization of the decalcified gels were more significant in cement-based pastes. This means that the microstructure of the aluminosilicate gel structure was more affected in the cement-based pastes than in the alkali activated pastes. These changes of silicate positions were predominant in the first 7 days. Although, the changes in carbonates continued up to 180 days. This shows that the transformation of carbonates from initially amorphous $CO_2$ to eventually crystalline compounds is a slow process that naturally occurs without any additional $CO_2$ binding.

- Effect of the longer exposure time (28 vs 180 days) was shown to be significant for $CO_2$ binding in cement-based and FA-rich (S30) alkali activated pastes.

- $CO_2$ binding capacity and understanding of nucleation of different carbonates are important factors for modeling the carbonation of alkali activated FA/GGBFS materials.

# 6

# CARBONATION OF THE PORE SOLUTION

*"Water is the driving force of all nature."*

Leonardo da Vinci

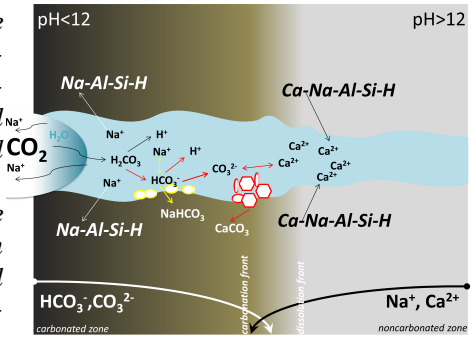


*When hardened alkali activated paste is exposed to environment, carbonation of the paste takes place. Initially, carbon dioxide gas molecules dissolve in the pore solution of the pastes, which results in additional carbonation reactions and physicochemical changes of the material.*
*This chapter focusses on the effect of the carbonation reactions on the pore solution chemistry in alkali-activated fly ash (FA) and ground granulated blast furnace slag (GGBFS) pastes. In particular, the effect of three parameters on the propagation rate of the carbonation front was studied: GGBFS content, different types of curing conditions and exposure conditions. Inductively coupled plasma optical emission spectrometry (ICP-OES) is used for detection of elements in the pore solutions of the studied mixtures. Furthermore, the pH of the pastes is measured. The carbonation depths are recorded periodically to determine the kinetics of the carbonation process. The substantial decrease of $[Na^+]$ in the pore solution in unsealed cured samples resulted in a faster propagation rate of the carbonation front in these specimens. Furthermore, the pH was lower in carbonated unsealed cured samples compared to the carbonated sealed cured samples. The replacement of FA by GGBFS in the pastes significantly improves their carbonation resistance. The potential risks with respect to carbonation of the pore solution are also identified and discussed.*

Parts of this chapter have been published in:
Nedeljkovic, M., Ghiassi, B., van der Laan, S., Li, Z., Ye, G. Effect of curing conditions on the pore solution and carbonation resistance of alkali-activated fly ash and slag pastes, 116, pages 146-158, 2019, Cement and Concrete research [220]

## 6.1. INTRODUCTION

THE CARBONATION in alkali activated materials (AAMs) is strongly influenced by the type of precursor (FA, GGBFS, metakaoline) [63, 68], the nature and dosage of the alkaline activator [209], the curing conditions and the exposure conditions [198]. The effect of these parameters on the carbonation resistance of AAMs has been extensively studied in accelerated carbonation conditions [61, 68, 160, 209], but has received little attention in the case of natural carbonation conditions. Furthermore, the role of curing conditions on the carbonation resistance has not been studied yet. The use of highly alkaline activators for reactions of FA and GGBFS, provides a high amount of $Na^+$ and $OH^-$ ions leading to high pH levels in the pore solution of noncarbonated AAMs. It has been shown that this may ensure a sufficiently high $Na^+$ concentration after natural and accelerated carbonation to prevent corrosion of reinforcement in AAMs [62]. However, it is not clear if the susceptibility of AAMs to leaching of $Na^+$ ions prior to, or during, the carbonation process can lead to a significant decrease of pH [123, 221, 222].

Hence, the aim of this chapter is to investigate the effect of carbonation on the pore solution chemistry and alkalinity of alkali-activated FA/GGBFS pastes. Firstly, the pore solution and pH of noncarbonated pastes are characterized in relation to different curing conditions. Secondly, the effect of curing conditions on the propagation rate of the carbonation front under accelerated conditions is tested. Finally, the effect of different exposure conditions, natural and accelerated conditions, on the evolution of the pH of the pore solution and the carbonation depth was studied.



## 6.2. MATERIALS AND METHODS

### 6.2.1. MATERIALS AND SAMPLE PREPARATION

The material and mixture compositions were shown in Chapter 5. Pastes were cast in two types of polyethylene vials, (A) with 35 mm diameter and 70 mm height and (B) with 54 mm diameter and 100 mm height and vibrated for 15-30 s on a vibrating table. The samples denoted as (A) were used for leaching measurements, pore solution extraction and RH measurements, while samples (B) were used for mass loss, carbonation depth and pH measurements. The samples were stored in closed vials (A, B) for 24 h after casting. For unsealed curing conditions, samples were removed from the vials and afterwards cured in a curing room at room temperature and a RH of ~ 99% for 28 days. The sealed samples were kept in the vials in the same curing room of unsealed samples until the testing.

### 6.2.2. EXPERIMENTAL PROGRAMME

Figure 6.1 shows an overview of the test programme followed to investigate the effect of curing and exposure conditions on the properties of alkali-activated FA/GGBFS pastes. First mass loss, internal relative humidity (RH), pore solution composition and pH are studied for curing under both sealed and unsealed conditions. Additionally, $Na^+$ loss was monitored for unsealed cured samples during the first 28 days of curing. The sealed cured samples were unsealed after 28 days of curing when all the samples were placed in the laboratory conditions at 55-60% RH (0.04% v/v $CO_2$, 20°C) for additional 28 days

(preconditioning of the samples prior to carbonation). This preconditioning was intended to equilibrate the internal RH of the samples with the environment before performing the carbonation tests. One set of unsealed samples was left in the curing room for additional 28 days, to provide insight into the further leaching after the first 28 days of curing. During carbonation exposure, the carbonation depth was monitored in both sealed and unsealed cured samples.

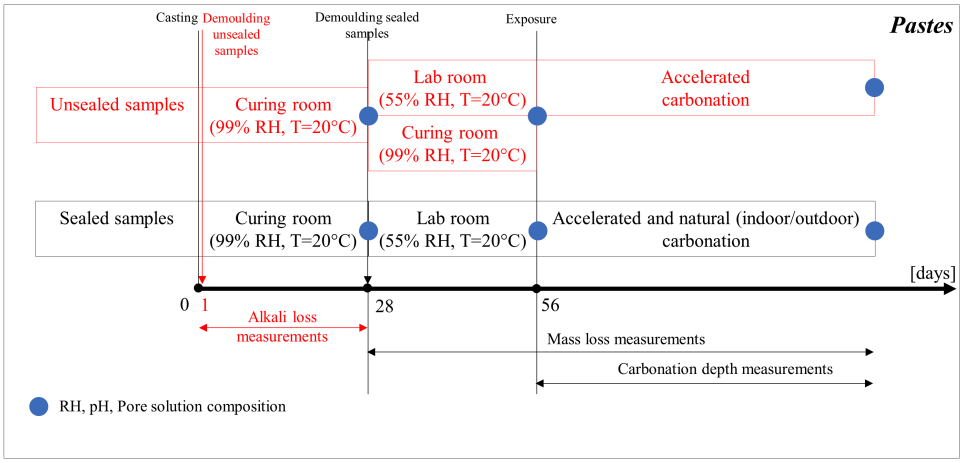


Figure 6.1: Schematic representation of the test programme.

#### 6.2.2.1. RH MEASUREMENTS

Free water in the pore structure of the pastes is critical for the carbonation progress. In order to ensure that the internal relative humidity of the pastes is in equilibrium with the RH of the exposure site, the internal RH of the pastes was measured after 1 day (before demoulding of the samples), after 28 days of curing and after 28 days of preconditioning (a total of 56 days). The procedure for internal RH measurements follows Huang et al. [223]. The internal RH of bulk pastes (A) was measured by Rotronic HygroLab C1 equipped with two HC2-AW RH station probes with an accuracy ±1% RH. The RH probes were calibrated using saturated salt solutions with known constant RH in the range of 65-95%. The samples were cut in thin slices of less than 7 mm, so in the sample holder there were a few slices of one sample. The sample slices were then put in two plastic containers in the measuring chambers. Samples and atmosphere equilibrated in 3-5 hours. The measured RH represents the average of the internal RH and it is not related to RH of a specific depth of the samples.

#### 6.2.2.2. MASS LOSS MEASUREMENTS

Mass loss measurements were used to assure that a preconditioning period of 28 days prior exposure of samples to accelerated carbonation is sufficient. The mass loss after 28 days of curing of the sealed and unsealed pastes was monitored in the laboratory conditions (55% RH, 20°C) until constant mass was reached. The mass of samples was measured after the samples were removed from the curing room. It was observed that at

the age of 56 days the difference between two measurements was less than 0.01 g. Based on this observation, the samples were preconditioned for 28 days before carbonation exposure (curing of 28 days and preconditioning of 28 days), as indicated in Figure 6.1. The evaporable water in the pastes was also determined (at specific periods) by measuring the weight loss per gram of the samples during their exposure to 105 °C in an oven (Jouan oven Type E455 EL), until reaching a constant weight.

#### 6.2.2.3. PORE SOLUTION AND pH MEASUREMENTS

Procedure for pore solution extraction from alkali-activated FA/GGBFS pastes is adopted from [224]. The pore solutions were pressed out from the pastes (type A sample size with 35 mm diameter and 70 mm height) with a high-pressure apparatus MacBen-type. The device has an oil-hydraulic end-load capacity of 5000 kN and the cylinder assembly with an inner diameter of 34 mm and a height of 115 mm fitting the size of the paste cylinders (A). Pressures of up to 750 MPa were used to extract the pore fluid. The fluid was extracted through a drain channel and collected in a syringe with almost no exposure to the atmosphere. Around 0.5 to 5 ml of pore solution could be collected for each sample depending on the type of the paste and the curing age. The pressed-out pore solutions were filtered using Whatman 41 filter paper and half of each solution was diluted using nitric acid (0.2 vol.%). Inductively coupled plasma optical emission spectrometry (ICP-OES) was used for chemical analysis of the pore solution composition. Chemical analyses of diluted solutions were carried out with a Perkin Elmer Optima 5300 DV apparatus.



The pH was measured on the non-diluted solutions. The non-diluted solutions of the samples cured for 28 days and 56 days were left for measurement of $OH^-$ concentration by titration against HCl acid. While pore fluid extraction from the original samples was successful, the direct extraction from carbonated samples was not possible due to both the low relative humidity during the carbonation process and the small amount of the sample material. Therefore, the pH measurements were carried out on the powder suspension, similar to [225]. The suspension was obtained by equilibrating 1 g of powdered sample with 10 ml of de-ionized water during 15 minutes at ambient temperature while stirring with a magnetic bar. Subsequently, the pH of the suspension was measured with a pH meter 827 Metrohm. The powders were obtained from the outer surface of the samples within a thickness of 1 mm. These pore solutions from suspensions were used as a substitute for pressed-out fluids to compare non-carbonated samples with 500 days curing (as reference) with samples carbonated for 500 days.

#### 6.2.2.4. ALKALI LOSS MEASUREMENTS PRIOR TO $CO_2$ EXPOSURE

It was noticed from measurements of the pore solution composition that unsealed curing is associated with a leaching process induced by the RH of curing room in which mainly $Na^+$ loss from the paste body occurs. A common curing set-up was used for alkali loss measurements to confirm $Na^+$ loss. The test set-up is shown in Figure 6.2. The specimens (sealed and unsealed) after 1 day of casting, were placed in the curing room with 99% RH and 20 °C. Moisture condensed on the surface of the specimens was collected in plastic containers that were placed under the specimens. After 1, 4, 7, 21, 28 days, the liquid from the plastic containers was collected to analyze the $[Na^+]$ in the leached solutions. The collected liquid was filtered using Whatman 41 filter paper. Afterwards, the

liquid was diluted using nitric acid (0.2 vol.%). Chemical analyses of the diluted liquids were carried out with a Perkin Elmer Optima 5300 DV apparatus.

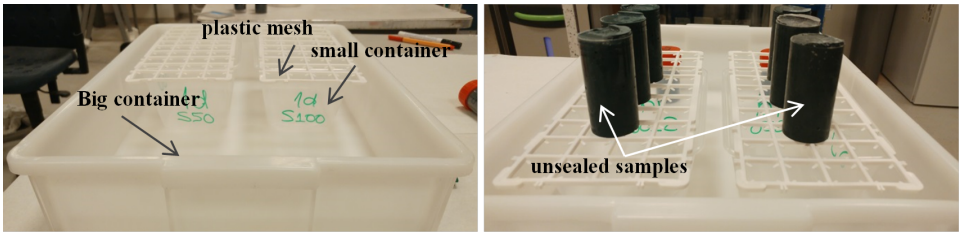


Figure 6.2: Set up for alkali loss measurements.

#### 6.2.2.5. ESEM-EDX

Investigation of the morphology and element content of the deposits found on the surface of the unsealed cured samples and in the small plastic containers (Figure 6.2) was done with the Philips-XL30-ESEM microscope, equipped with NSS.3.3. The deposit was collected from the sample surface with a brush, while the liquid drop of the deposit was collected from the small plastic container. For scanning electron microscope/energy-dispersive X-ray (SEM-EDX) analysis, deposits were placed onto carbon-coated sticky stubs and directly observed under the ESEM-BSE mode.

#### 6.2.2.6. CARBONATION SITES AND EXPOSURE CONDITIONS

Paste samples have been exposed to three different test sites for a period of one year. An overview of the exposure sites is given in Figure 6.3. The description of the exposure conditions is given in Table 6.1. Three exposure conditions were studied: accelerated carbonation, natural indoor (laboratory) carbonation and natural outdoor (unsheltered) carbonation.

The accelerated carbonation was performed in a $CO_2$ chamber (Figure 6.3 (1)) where $CO_2$ concentration, temperature and relative humidity were controlled simultaneously. The $CO_2$ concentration was 1% v/v. The $CO_2$ of 1% v/v was chosen since it was reported by Bernal et al. [63] that conducting accelerated carbonation using $CO_2$ concentrations beyond $CO_2$ ~1% v/v will not accurately replicate the carbonation mechanisms observed in practice. The inlet flow of $CO_2$ was kept constant at the rate of 100 $cm^3$/min. The temperature in the chamber has been regulated at 20°C and a relative humidity at 60%.

The carbonation of pastes under natural indoor conditions was performed in the laboratory at the concentration of $CO_2$, which is about 0.03–0.04% by volume, RH at 55%, and temperature at 20°C (Figure 6.3 (2)).

The natural outdoor carbonation of pastes took place in the unsheltered environment (Figure 6.3 (3)). The local measurements of $CO_2$ concentration, RH and temperature were provided by the Dutch national weather service (Royal Netherlands Meteorological Institute (KNMI)).

Table 6.1: Exposure conditions.

| | Natural laboratory [source: RH sensor] | Natural outdoor [source: KNMI, Utrecht] | Accelerated carbonation |
|---|---|---|---|
| $CO_2$ concentration | 0.04% v/v | 0.04% v/v | 1.00% v/v |
| Relative humidity | 55% | 80-98% | 60% |
| Temperature | 20 °C | 0-20 °C | 20 °C |

*The $CO_2$ concentration, the average temperature (in Celsius) and the average relative humidity (in %) in outdoor conditions are shown in additions to Table 6.1.

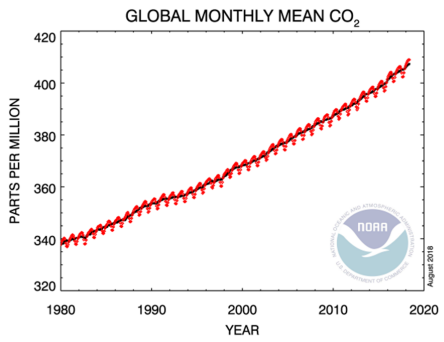


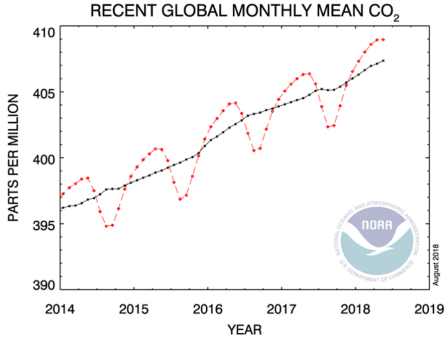


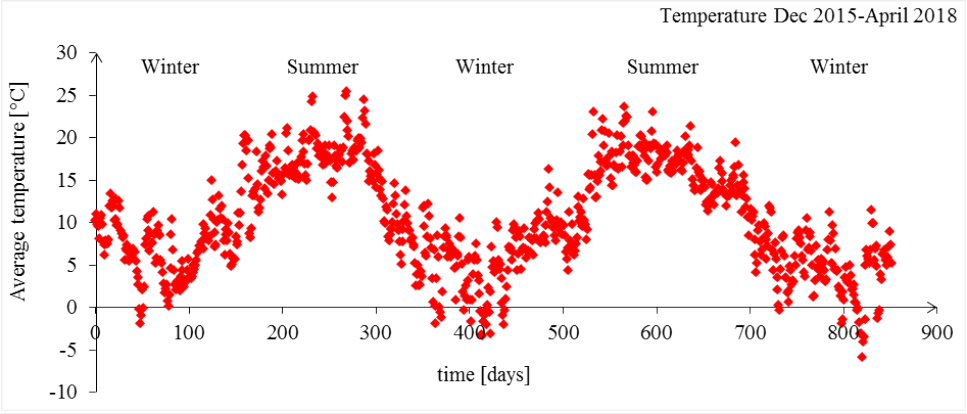


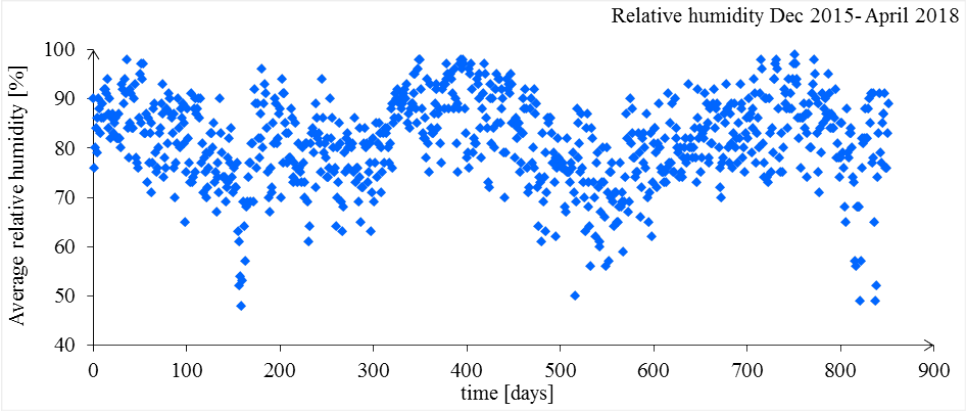

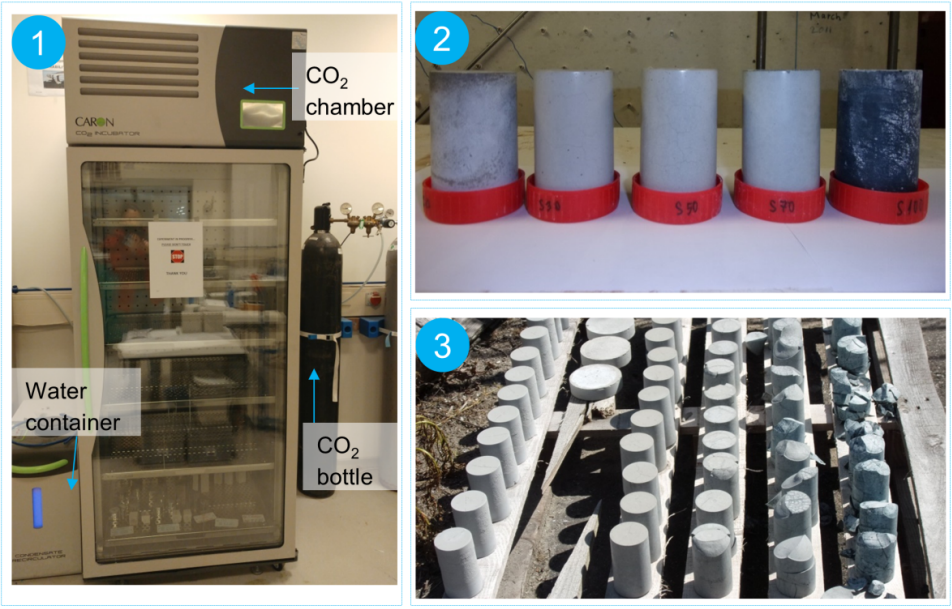


Figure 6.3: Exposure sites: (1) $CO_2$ chamber for accelerated carbonation, (2) natural indoor conditions, (3) natural outdoor conditions.



#### 6.2.2.7. CARBONATION DEPTH MEASUREMENTS

Carbonation started 56 days after curing and preconditioning. The carbonation depth was measured with phenolphthalein, according to the standard EN 13295:2004[50]. The cylinders were split and the fresh surface was sprayed with a 1 wt. % phenolphthalein solution (comprising 1 g of phenolphthalein in a solution of 70 ml ethanol and 30 ml demineralized water). The recorded carbonation depths are the average of measurements at 10 locations on the sample.

## 6.3. RESULTS AND DISCUSSION

### 6.3.1. EFFECT OF CURING CONDITIONS

#### 6.3.1.1. MASS LOSS AND INTERNAL RH

**Mass loss**

The changes of the mass of the specimens with time are presented in Figure 6.4 and Figure 6.5. The total mass percentage of water loss in the pastes due to drying after 28 days storage in the laboratory conditions (55% RH and 20 °C) is presented in Table 6.2.

In general, the amount of evaporable water for the unsealed cured samples is higher compared to the sealed ones. The amount of evaporable water between conditions of 99% RH and 28 days curing and subsequent 55% RH exposure until 56 days is the highest in paste S0 and the lowest in paste S100. In alkali-activated FA materials, a much higher $Na_2O$ concentration and curing temperatures (> 40 °C) are required for a com-

plete dissolution of FA [193]. In the present study, due to the low $Na_2O$ concentration of the alkaline activator and the applied curing conditions (ambient temperature), paste S0 has a limited degree of reaction. This is supported by the low strength development (see Chapter 3, Figure 3.13).

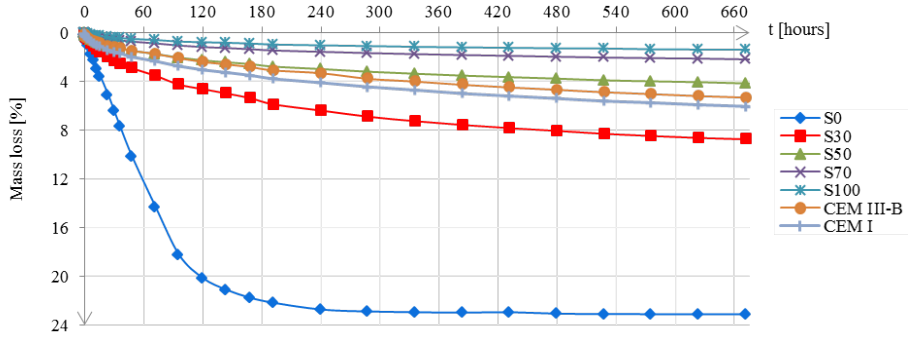


Figure 6.4: Unsealed samples first 28 days; mass loss measured from 28 days in laboratory conditions (55% RH, 20°C).

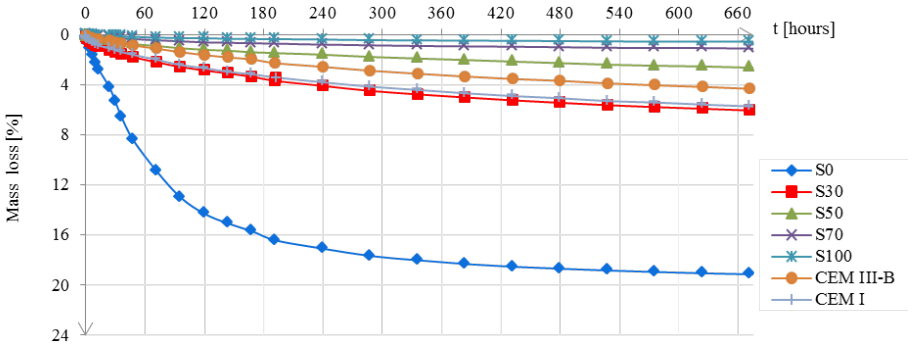


Figure 6.5: Sealed samples first 28 days; mass loss measured from 28 days in laboratory conditions (55% RH, 20°C).

This low reaction degree implies the existence of free water in the pores as experimentally measured here (see Figure 6.4 and Figure 6.5). On the other hand, based on the measurements of the evaporable water content at 105°C, it can be seen that with increasing GGBFS content more evaporable water is measured at 105°C than is lost in the curing step at 55% RH. This suggests that GGBFS-rich pastes have more chemically bound water than FA-rich pastes. Another effect that can be observed is that with increasing GGBFS the total free water (sum of evaporated at 55% RH + mass loss at 105°C) decreases, implying that some water must become structurally bound in the samples.

The mechanisms affecting the transport of free water in unsealed cured samples are illustrated in Figure 6.6a. The loss of alkalis in case of unsealed samples exposed to 99% RH is due to several counter-affecting phenomena (Figure 6.6b).

Table 6.2: Water loss (in mass percentage) and internal RH of the pastes*.

| | Sample mass [g] | | Water loss [wt.%] | | | | | | Internal RH [%] | | | | |
|---|---|---|---|---|---|---|---|---|---|---|---|---|---|
| | At age of 28d | | Stored in lab RH 55% conditions from age of 28d to 56d | | Heating at 105°C (at 56d) | | Total water loss | | 1d ** | 28d | | 56d | |
| | sealed | unsealed | sealed | unsealed | sealed | unsealed | sealed | unsealed | sealed | sealed | unsealed | sealed | unsealed |
| S0 | 349.5 | 359.8 | 19.13 | 23.15 | 5.05 | 3.08 | 24.18 | 26.23 | >95.00 | >95.00 | >95.00 | 64.1 | 64.3 |
| S30 | 376.6 | 379.4 | 6.05 | 8.78 | 14.45 | 13.87 | 20.50 | 22.65 | >95.00 | >95.00 | >95.00 | 64.6 | 65.0 |
| S50 | 382.0 | 381.7 | 2.63 | 4.20 | 16.90 | 17.00 | 19.53 | 21.20 | 91.88 | 90.30 | 94.00 | 64.1 | 65.0 |
| S70 | 401.0 | 397.4 | 1.10 | 2.22 | 17.81 | 17.80 | 18.91 | 20.02 | 88.12 | 80.80 | 80.00 | 63.8 | 64.0 |
| S100 | 413.0 | 413.9 | 0.55 | 1.42 | 16.73 | 17.12 | 17.28 | 18.54 | 87.07 | 71.50 | 73.00 | 62.3 | 62.0 |
| CEM III/B | 365.0 | 358.2 | 4.32 | 5.36 | 19.96 | 20.39 | 24.28 | 25.75 | >95.00 | >95.00 | >95.00 | 78.9 | 80.0 |
| CEM I | 353.0 | 342.9 | 5.72 | 6.08 | 22.00 | 22.10 | 27.72 | 28.18 | >95.00 | >95.00 | >95.00 | 70.4 | 73.0 |

* 'Sealed' are the samples that were cured in sealed conditions first 28 days and then demoulded and exposed to lab conditions until 56 days.
'Unsealed' are the samples that were cured in 20°C, ~99 % RH conditions during the first 28 days and further exposed to lab conditions until 56 days.
** The 1d internal RH presents the time zero when the samples were removed from moulds to curing room (all samples were kept in moulds for 1 day before curing in the fog room). The RH of the activation solution (NaOH+WG) before mixing with raw FA and GGBFS was 92.03%.

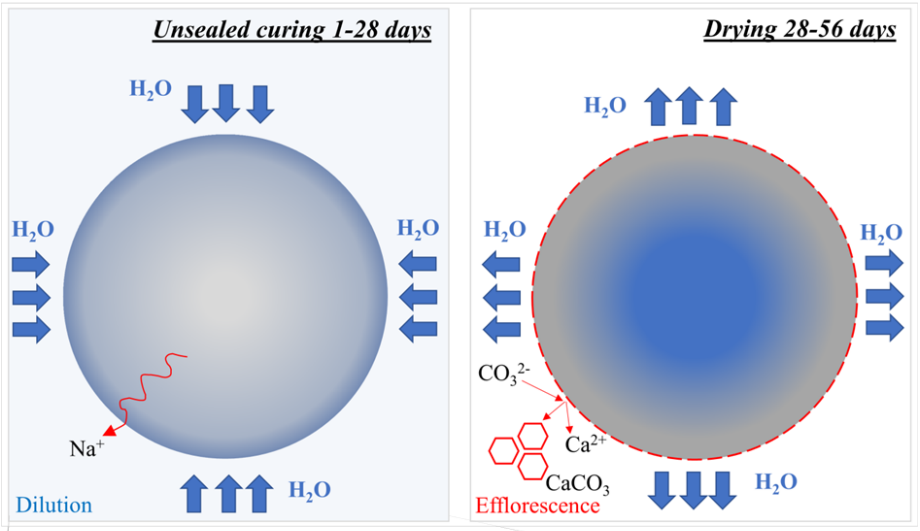


(a) Illustration of the water transport during the unsealed curing (1-28 days) and drying of the pastes (28-56 days).

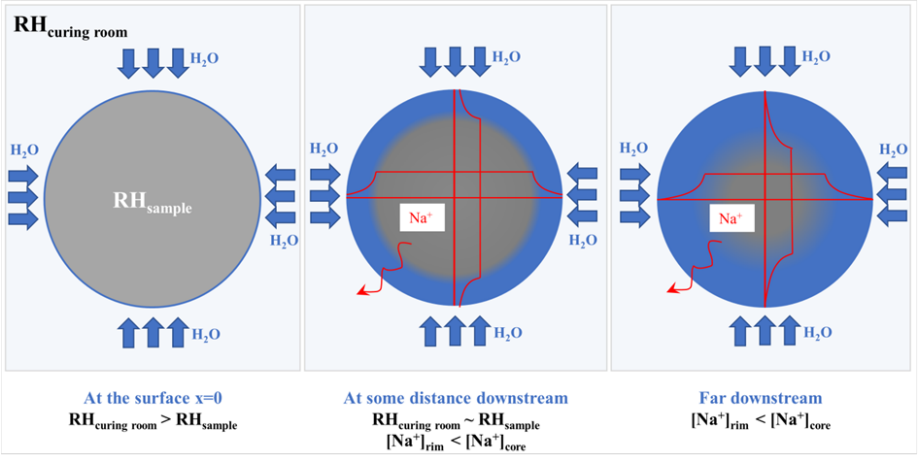


(b) Illustration of the boundary conditions during the water transport and $Na^+$ loss in the unsealed curing conditions of the pastes (1-28 days):

- left: day 1, demoulding of the samples and subsequent exposure of the samples to 99% RH;
- middle: advective movement of $Na^+$ by dilution of the pore solution at the surface of the samples followed by diffusive movement of $Na^+$;
- right: diffusive movement of $Na^+$ from the interior towards the surface of the samples.

Figure 6.6: (a) Illustration of the water transport during the unsealed curing (1-28 days) and drying of the pastes (28-56 days); (b) illustration of the boundary conditions during the water transport and $Na^+$ loss in the unsealed curing conditions of the pastes (1-28 days).

The RH of the activation solution (NaOH+waterglass) before mixing with raw FA and GGBFS was 92.03%, while the RH of the pastes S30, S50, S70 and S100 at 1 day (when 99% RH curing initiated) was 95.86%, 91.88%, 88.12%, 86.98%, respectively (see Table 6.2). This difference in the RH of the environment and the specimen causes a capillary flow from the surface to the interior of the samples and, therefore, an inward movement of the ions (advection). Meanwhile, condensation of water on the surface of the samples leads to dilution of the ions at the surface compared to the interior of the specimens. This causes a diffusive movement of ions from the interior towards the surface of the sample. There is, therefore, a clear competition between both phenomena. Based on the observed $[Na^+]$ difference in the pore solution in sealed and unsealed curing conditions (see Table 6.3), the second mechanism is dominant in the studied samples. Both advection and diffusion are governed by the microstructure of the paste and, for that reason, the alkali loss between the studied alkali activated pastes is different (see Figure 6.11).

On the other hand, when samples are moved from the curing room subsequent drying of the surface causes efflorescence (see Figure 6.6a, drying 28-56 days). The product of efflorescence is calcite as will be shown in Figure 6.10a. Calcite was formed already in the curing room on the wet outer surface of the samples. In the high pH fluid, $CO_2$ will be present as $CO_3^{2-}$ and together with $Ca^{2+}$ it forms calcite. The calcium carbonate efflorescence is promoted even at smaller amounts of alkali dissolved in the aqueous film, such as in cement based pastes [226], compared to alkali activated pastes.



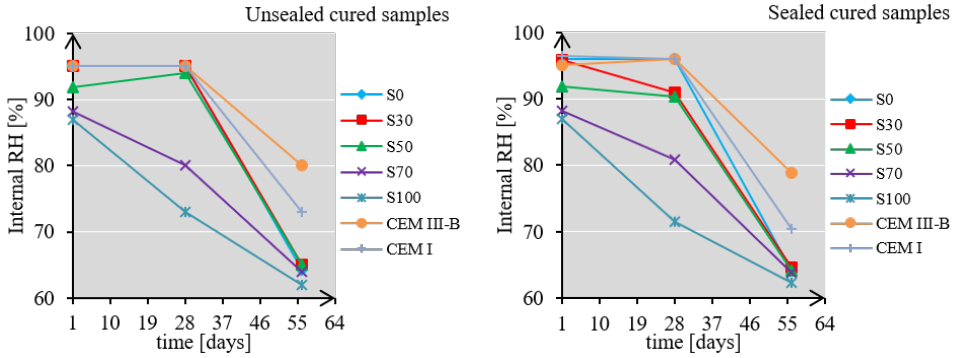


(a) Samples were kept one day in a mould. Then demoulded and cured unsealed in fog room (at 20°C, 99% RH) until 28 days. After 28 days, samples were removed from fog room and preconditioned in the laboratory conditions (at 20°C, 55% RH) for additional 28 days.

(b) Samples were kept sealed for 28 days. After 28 days, samples were demoulded and preconditioned in the laboratory conditions (at 20°C, 55% RH) for additional 28 days.

Figure 6.7: Measured internal RH for unsealed (A) and sealed (B) cured samples after 1 day, 28 days and 56 days.

Note that standard solution for calibration of machine for RH measurements was 95% RH. Therefore, RH of samples could be measured up to 95%. It should be bear in mind, that some of the samples have higher internal RH than 95% at 1 day and 28 days.

**Internal RH**

The internal RH of the pastes was also measured at the age of 28 days (before storage in the laboratory conditions) and at the age of 56 days (after 28 days of storage in the laboratory conditions) as shown in Table 6.2 and Figure 6.7. The RH of the unsealed samples is generally higher than that of the sealed samples, which is consistent with the pore fluids being more diluted in the unsealed samples, thus having a higher water activity. The results, presented in Table 6.2, show that the internal RH of the pastes at 28 days decreases with increasing GGBFS content (from paste S0 to S100). This phenomenon can be attributed to the self-desiccation in these mixtures [153] and it has a similar effect on the sealed and unsealed samples. The RH of the samples after 56 days show that the samples have not reached the equilibrium condition with the environment yet. The internal RH of alkali-activated pastes is around 62-65% RH at this age. As the accelerated carbonation tests are performed at 60% RH, it is expected that the RH of the samples was equilibrated with the RH of the exposure site in a short time after the start of the experiment. The pastes CEM I and CEM III/B showed a higher internal RH compared to alkali-activated pastes showing that drying is slower in these materials. The internal RH of CEM I paste with water-to-cement ratio 0.5 at 28 days is in agreement with literature [227].

#### 6.3.1.2. pH AND COMPOSITION OF THE PORE SOLUTION

The pore solution analysis was performed on both groups (sealed and unsealed) of samples after 28 and 56 days curing before exposure to carbonation. Additionally, the pore solution analyses were performed after 1 year only for sealed cured samples. These analyses enabled the quantification of the concentration of the main ions ($Na^+$, $K^+$, $Ca^{2+}$, $S^{2-}$) in the pore solution and measurement of the pH. Results of pH and composition of the pore solution are presented in Table 6.3, Table 6.4 and Table 6.5.

Table 6.3: pH values and main element composition of pastes pore solutions analyzed with ICP-OES (28 days). The pore solutions were extracted with high pressure method.

| | | pH | [Na] | [K] | [Ca] | [S] | Porosity |
|---|---|---|---|---|---|---|---|
| Curing room (99% RH) | | [-] | [mmol/L] | [mmol/L] | [mmol/L] | [mmol/L] | [%] [174] |
| S0 | Sealed | 13.40 | 1336 | 20 | 21.73 | 298 | - |
| | Unsealed | 13.02 | 101 | 4 | 33.08 | <1.5 | 43.71 |
| S30 | Sealed | 13.45 | 1004 | 23 | 19.40 | 375 | - |
| | Unsealed | 13.16 | 150 | 3 | 8.63 | 51 | 26.04 |
| S50 | Sealed | 13.70 | 1078 | 26 | 8.48 | 292 | - |
| | Unsealed | 13.30 | 211 | 4 | 3.35 | 79 | 9.4 |
| S70 | Sealed | 13.80 | 1116 | 27 | 23.10 | 378 | - |
| | Unsealed | 13.40 | 326 | 7 | 10.23 | 172 | 6.54 |
| S100 | Sealed | 14.00 | 1556 | 36 | 29.50 | 573 | - |
| | Unsealed | 13.60 | 551 | 11 | 19.63 | 326 | 3.57 |
| CEM III/B | Sealed | 13.08 | 61 | 58 | 44.08 | - | - |
| | Unsealed | 13.00 | 56 | 45 | 12.80 | 5 | 48.87 |
| CEM I | Sealed | 13.62 | 193 | 230 | 39.28 | - | - |
| | Unsealed | 13.28 | 105 | 85 | 4.75 | <1.5 | 46.48 |

Table 6.4: pH values and main element composition of pastes pore solutions analyzed with ICP-OES (56 days). The pore solutions were extracted with high pressure method.

| | | pH [-] | [Na] [mmol/L] | [K] [mmol/L] | [Ca] [mmol/L] | [S] [mmol/L] |
|---|---|---|---|---|---|---|
| S0 | Sealed * | | | | | |
| | Unsealed L ** | | | | | |
| | Unsealed C *** | 12.90 | 29 | 1 | 3.80 | |
| S30 | Sealed * | | | | | |
| | Unsealed L ** | | | | | |
| | Unsealed C *** | 13.00 | 106 | 2 | 3.15 | |
| S50 | Sealed * | 13.72 | 1233 | 18 | 10.85 | |
| | Unsealed L ** | 13.58 | 424 | 6 | 54.68 | |
| | Unsealed C *** | 13.25 | 187 | 4 | 3.45 | |
| S70 | Sealed * | 13.80 | 1363 | 32 | 29.55 | 0.42 |
| | Unsealed L ** | 31.60 | 426 | 6 | 3.50 | 0.26 |
| | Unsealed C *** | 13.34 | 368 | 6 | 5.58 | |
| S100 | Sealed * | 14.00 | 1544 | 36 | 5.73 | 0.55 |
| | Unsealed L ** | 13.60 | 557 | 10 | 12.88 | 0.32 |
| | Unsealed C *** | 13.53 | 463 | 10 | 2.65 | |
| CEM III/B | Sealed * | | | | | |
| | Unsealed L ** | | | | | |
| | Unsealed C *** | 13.05 | 59 | 53 | 1.95 | |
| CEM I | Sealed * | | | | | |
| | Unsealed L ** | | | | | |
| | Unsealed C *** | 13.29 | 116.13 | 79 | 15.58 | |

* Samples that were sealed cured for 28 days, demoulded at 28 days and further kept in unsealed laboratory conditions (55% RH) until 56 days.
** Samples that were unsealed cured for 28 days, and further kept in unsealed laboratory conditions (55% RH) until 56 days.
***Samples that were unsealed cured for 28 days, and further kept in unsealed curing conditions (99% RH) until 56 days.

Table 6.5: pH values and main element composition of pastes pore solutions analyzed with ICP-OES (1 year sealed, reference, noncarbonated samples). The pore solutions were extracted with high pressure method.

| | | pH [-] | [Na] [mmol/L] | [K] [mmol/L] | [Ca] [mmol/L] | [Mg] [mmol/L] | [Si] [mmol/L] | [Al] [mmol/L] |
|---|---|---|---|---|---|---|---|---|
| S0 | Sealed | 11.99 | Not measured | | | | | |
| S30 | | 12.07 | 741.09 | 22.67 | 8.13 | 1.88 | 27.79 | 7.07 |
| S50 | | 12.10 | 715.30 | 28.23 | 1.83 | 0.36 | 16.11 | 5.19 |
| S70 | | 12.48 | 1249.39 | 48.08 | 5.53 | 1.33 | 16.89 | 11.48 |
| S100 | | 12.63 | 1570.22 | 43.25 | 31.28 | 7.86 | 35.82 | 18.41 |

Figure 6.8 shows that the pH of all sealed alkali-activated pastes is in the range of 13.5 to 14.0 at 28 days of curing, as expected. This value is lower in unsealed pastes (but still higher than 13.0), which is due to Na-hydroxide loss from these specimens as shown in Section 6.3.1.3. Additionally, no specific change of pH is observed at 56 days of curing compared to 28 days (Figure 6.8b). A similar effect is also observed in CEM I pastes. The pH in the sealed samples is always higher than in unsealed pastes. This difference is smaller in CEM III/B pastes (Figure 6.8a).

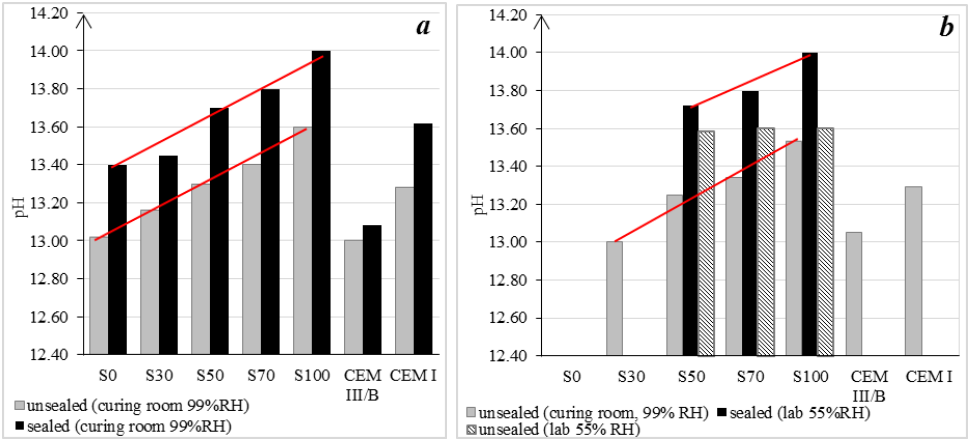


(a) 28 days (b) 56 days

Figure 6.8: The effect of sealing on the pH in the pore solution of the pastes at 28 days (a) and 56 days (b).

Table 6.5 shows that the pH of all pastes after 1 year of sealed curing is lower than the pH of pastes at 28 days (Table 6.3) and 56 days (Table 6.4). Since the formation of the reaction products is a continuous process, the $OH^-$ consumption is too, as long as the pore solution is available. Therefore, the main reason for pH drop of the pore solution of sealed cured samples after 1 year, is the continuous evolution of the gel phases.

The $[Na^+]$ in the alkaline activator before mixing with raw materials was 4026 mmol/L. After 28 days curing in sealed conditions, it can be seen that this value, in pastes (S0-S100), is reduced to the range of 1004 mmol/L to 1556 mmol/L (Figure 6.9a). It is clear that a part of Na+ is taken up by reaction products during the formation of the reaction products of FA and GGBFS pastes, while the other part of Na+ is present in the pore solution (or leached in the unsealed cured samples).

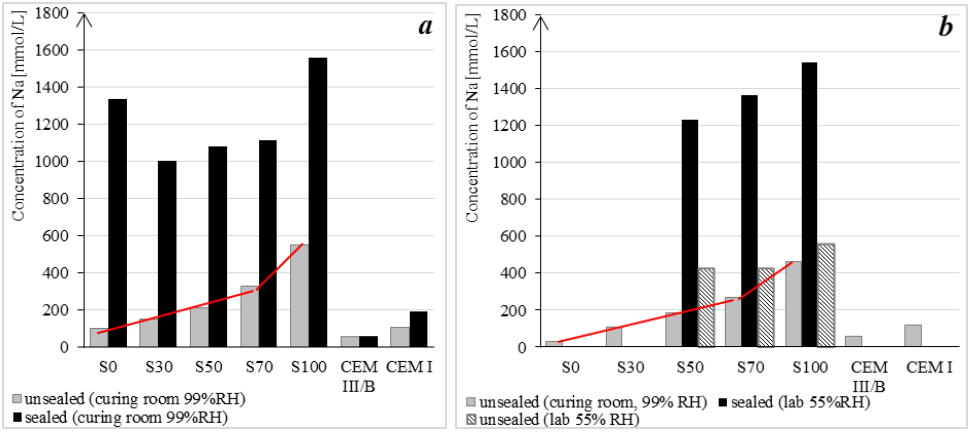


(a) 28 days (b) 56 days

Figure 6.9: The effect of sealing on the $Na^+$ content in the pore solution of the pastes at 28 days (a) and 56 days (b).

The effect of the FA/GGBFS ratio on the $[Na^+]$ in the pore solution is not clear at 28 days. The pastes S0 (100% FA) and S100 (100% GGBFS) have the highest $[Na^+]$, while in pastes S30, S50 and S70 the $[Na^+]$ increases with increasing the content of GGBFS. On the other hand, the $[K^+]$ always increases with increasing GGBFS content (see Table 6.3). A relatively high $[S^{2-}]$ is found in the pore solutions with no specific correlation with the FA/GGBFS ratio. Compared to CEM I and CEM III/B pastes, the pore solution in alkali-activated pastes contains a significantly higher amount of $Na^+$, but a comparable $[K^+]$.

In contrast to CEM I and CEM III/B pastes, the $[Na^+]$ of pore solutions of unsealed alkali activated pastes is still decreasing in all the pastes until 56 days in the curing room (Table 6.4). This decrease is higher in pastes with higher percentage of FA. This can be explained by the higher porosity of FA-rich specimens compared to GGBFS-rich ones, measured at 28 days (S0>S30>S50>S70>S100) (see Table 6.3). It can be also observed that the $[Na^+]$ of the pore solutions of unsealed samples in laboratory conditions is higher than in the unsealed samples in curing room (see Figure 6.9b). This was expected, as the high relative humidity in the curing room promotes the loss of $Na^+$ in these specimens as explained in Section 6.3.1.1.

Table 6.5 shows that the $[Na^+]$ in sealed cured samples after 1 year is lower in pastes S30 and S50 compared to the values at 28 days or 56 days (see Table 6.3 and Table 6.4). On the other hand, the $[Na^+]$ is not significantly changed in pastes S70 and S100 for curing period of 1 year compared to 28 days or 56 days. This is likely due to a higher Na-binding capacity of gel phases in pastes with high FA content. This is consistent with the PARC results (Chapter 4), where a higher Na/Si ratio is obtained in paste S50 (Na/Si=0.4) compared to paste S100 (Na/Si=0.29) after 1 year of sealed curing.

A comparison between $[Na^+]$, $[K^+]$, $[Ca^{2+}]$ and $[S^{2-}]$ in all samples clearly shows a significant effect of curing on the pore solution chemistry. A significant drop of ion con-

centration can be observed in the pore solution in the unsealed pastes. Figure 6.9 shows the difference between $[Na^+]$ in these specimens at 28 days and 56 days, respectively. It can be seen that these values are significantly lower in unsealed alkali-activated pastes, but still remain at a higher level compared to CEM I and CEM III/B pastes. The effect of leaching on the $[Na^+]$ in cement-based pastes is also significant, but seems negligible in CEM III-B pastes. Alkali activated pastes, in direct contact with water during unsealed curing, show $Na^+$ leaching. There is, therefore, a competition between the $Na^+$ consumption for the reaction of FA and GGBFS and the $Na^+$ loss due to leaching.

#### 6.3.1.3. ALKALI LOSS

The alkali content in the pore solution can vary depending on the curing conditions, as shown in Section 6.3.1.2. Significant alkali loss was observed for unsealed cured samples. The mechanism for alkali loss was explained in Section 6.3.1.1. The main role of the alkalis is to provide the right environment for dissolution of the FA and GGBFS. In addition, the alkalis content in the pore solution of AAMs is highly important as they are the main buffer for alkalinity during carbonation. Beside alkalis (Na), calcium ions may also contribute to maintaining a high pH of the pore solution. This is supported by the findings from Chapter 5, where it was shown that not all the CaO was consumed by carbonation of studied alkali activated pastes (see Table 5.2). This implies that, after NaOH carbonation, the remaining CaO can act as a buffering agent for the pH of the pore solution.

Beside alkali loss, the efflorescence occurred in all samples cured in unsealed conditions, except for pastes CEM I, CEM III/B and S0 as was observed when they were moved from the fog room to the laboratory environment (55-60% RH). The beneficial effects of soluble silicate and GGBFS addition to mitigate or delay efflorescence [228] cannot be supported nor rejected by the current study. The presence of water with water-soluble salts and exposure to moisture gradients or wet/dry cycles are main conditions for efflorescence. Evaporation of aqueous salt solution may occur at the surface or in regions near the surface when a moisture gradient between the ambient atmosphere and the material exists. This resulted in the appearance of efflorescence on the surface of the unsealed cured specimens with GGBFS (see Figure 6.10a). The efflorescence powder was collected carefully from the sample's surfaces for further chemical analysis.

SEM-EDX analysis showed that the product of efflorescence was calcite ($CaCO_3$), with the particle size of about 10-20 $\mu$m (Figure 6.10b). Similar morphology was also observed in the study by García-Carmona et al. [200], where the calcite particles were obtained by carbonation of slaked lime in a semicontinuous process. The $CaCO_3$ formation in this study resulted from $Ca^{2+}$ and $OH^-$ carbonation when the $CO_2$ and $H_2O$ are simultaneously present and when the solubility of calcite is exceeded. The $Ca^{2+}$ and $OH^-$ ion pair from solution is transported towards the surface of the hardened paste where it reacts away to carbonate at the cylinder surface. Since the precipitation takes $Ca^{2+}$ out of solution, it is replenished by diffusion through the fluid and re-equilibration (Ca-release) from the gel. The final result of the subsequent steps through which the carbonates are formed can be described by the following reaction similar to [144]:

$$CO_2(aq) + Ca^{2+}(aq) + 2OH^-(aq) \rightarrow CaCO_3 + H_2O \tag{6.1}$$

Meanwhile, the deposits from the plastic container in which the moisture from the surface of the specimen S100 was collected after 1 day of unsealed curing, were also analyzed. The carbon together with oxygen, sodium, calcium and traces of aluminium, silicon, sulfur and potassium were detected as demonstrated by the EDX spectrum (Figure 6.10c). The anhedral crystals (Figure 6.10c) are identified as gaylussite ($Na_2Ca(CO_3)_2 \cdot 5H_2O$). They are formed mostly of Na and Ca (EDX spectrum, Figure 6.10c), similar to the gaylussite identification by Jones et al. [229]. The mechanism of the Na, Ca-carbonate formation can be described by the following reactions:

$$CO_2(g) + 2OH^-(aq) \rightarrow CO_3^{2-}(aq) + H_2O \tag{6.2}$$

$$2CO_3^{2-}(aq) + 2Na^+(aq) + Ca^{2+}(aq) + 5H_2O \rightarrow Na_2Ca(CO_3)_2 \cdot 5H_2O \tag{6.3}$$

The ICP-OES results for $Na^+$ from alkali loss experiments of the pastes S50 and S100 are presented in Figure 6.11. It should be noted that this figure shows the cumulative amount of the $Na^+$ in the solutions collected in the plastic containers and for each stage the new measured absolute amount of Na was added to the previous. The containers were removed for the $Na^+$ measurement and a new empty container was placed for the collection of the fluid in the next time segment to avoid saturation of the solutions with the solids precipitating in the containers as shown in Figure 6.10a, c. The results clearly show the continuous loss of Na from the samples with time. It seems that the highest amount of alkali loss occurred between 7 and 28 days. The leached Na amount is lower in specimen with higher GGBFS content (Figure 6.11). The higher alkali loss in pastes S50 compared to pastes S100 is due to a more porous microstructure of paste S50 compared to paste S100 as shown in Table 6.3, column 8. This facilitates the Na-leaching process. Water from the curing atmosphere can more readily enter the gel and become self-expelled in paste S50 compared to paste S100. The absolute mass of leached $Na^+$ was measured from the total solution volume, which was collected in the plastic container during 28 days of unsealed curing of the samples S50 and S100. It is found that 0.8 g and 0.65 g of $Na^+$ was leached from the samples S50 and S100, respectively. The absolute amount of Na, initially used for the activation, was 4.62 g. This implies that 17.3% and 14% of this initial Na amount was leached from the samples S50 and S100, respectively. It should be noted that the ICP-OES analysis enabled the quantification of $[Na^+]$ in solution but not of the $[Na^+]$ which had already reacted with carbonate ions forming a solid during alkali loss as found from SEM-EDX analysis (Figure 6.10c). This implies that a higher amount of Na was expelled than measured in the experiments.


(a) Pastes S100 at 56 days (left, (1)-unsealed cured sample, (2)-sealed cured sample), the plastic container in which the fluid, condensed on the surface of the specimen S100, was collected after 4 days of unsealed curing (right).

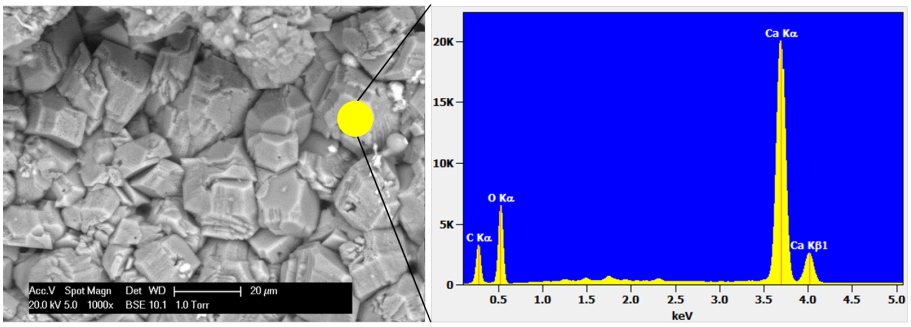


(b) ESEM-BSE image and EDX spectrum of the deposit from the surface of the cylindric sample labelled as (1) shown in Figure 6.10a.

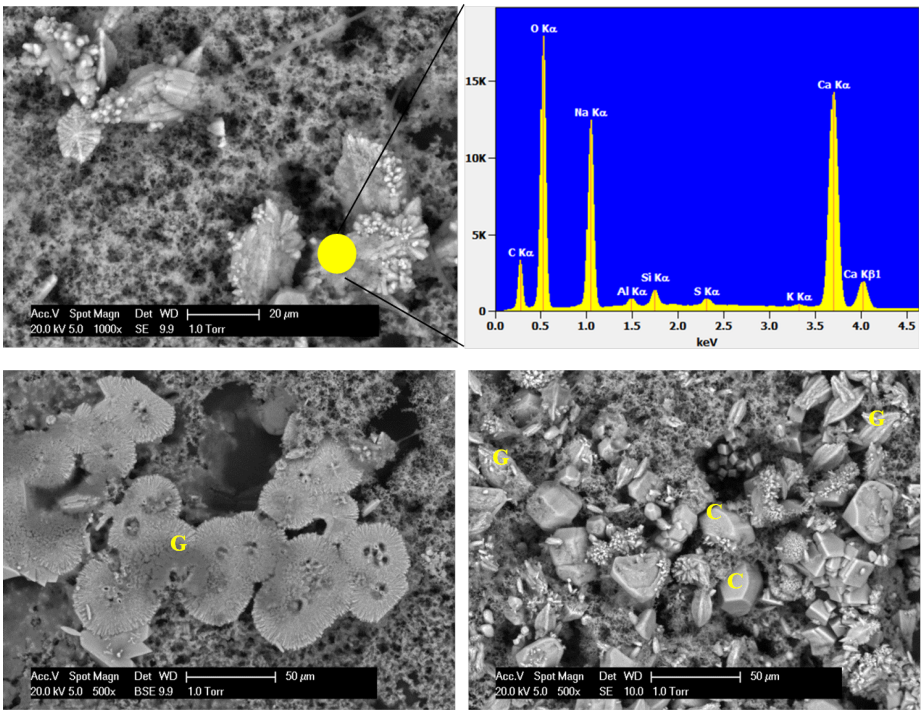


(c) ESEM-BSE images and EDX spectrum of the deposit from the plastic container shown in Figure 6.10a (Gaylussite-G, Calcite-C).

Figure 6.10: ESEM-EDX analyses of the leaching products

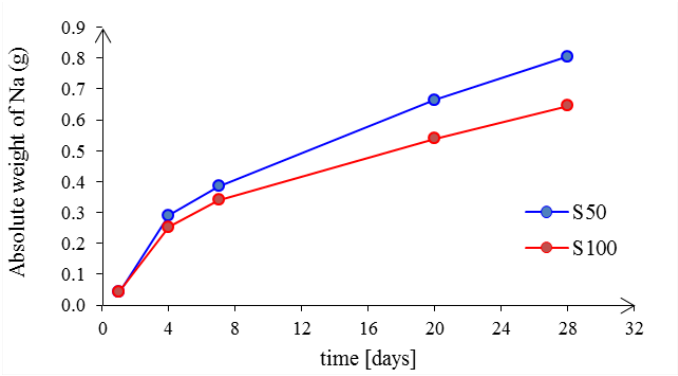


Figure 6.11: Cumulative Na leached from the unsealed pastes (S50 and S100) during 28 days of curing in 99% RH.

## 6.3.2. EFFECT OF EXPOSURE CONDITIONS

### 6.3.2.1. CARBONATION DEPTH: ACCELERATED CARBONATION

The carbonation depths were measured for both sealed and unsealed cured samples and the results are presented in Figure 6.12.

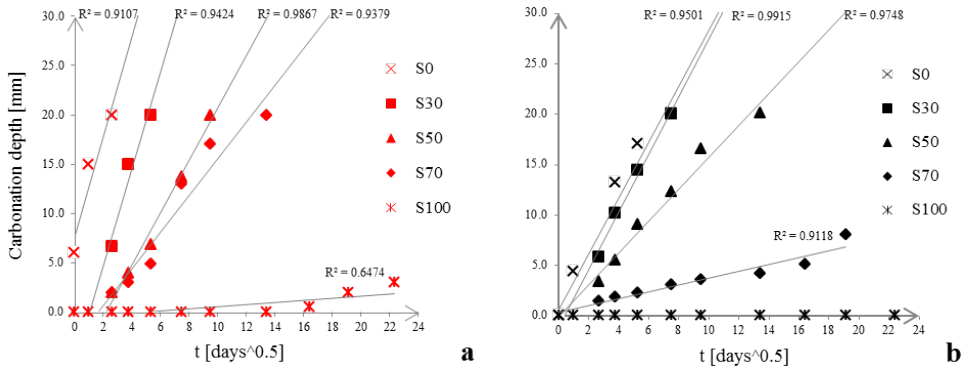


(a) unsealed cured samples

(b) sealed cured samples

Figure 6.12: Carbonation rate for the unsealed cured samples (a), and for the sealed cured samples (b). $R^2$ is the correlation coefficients from the least-squares linear fits.

Carbonation of the pore solution was observed in the pastes S0, S30, S50 even after 1 day of exposure. It can be seen that in general the propagation rate of carbonation front is faster in the unsealed cured samples. The reason is that $Na^+$ leaching in unsealed samples leads to modification of composition of reaction products and the degree of reaction (compared to sealed cured samples), all of which have a strong influence on the carbonation resistance. These results are indirectly supported by the previous study of the author where it was shown that paste S100 has a different compressive strength development in sealed and unsealed curing conditions [189].

It can also be observed that, in unsealed samples, carbonation depth lines do not pass through the origin. While a positive intercept as a result of early carbonation of the paste during curing and preconditioning period can be observed in the paste S0, the other pastes show delayed carbonation. The latest is related to the paste S100 in which the carbonation was only detected after t=180 days of exposure. On the other hand, in sealed samples, all the curves pass through the origin besides the paste S100 in which carbonation was not observed. It can also be seen that the propagation rate of carbonation front (slope of the curves) significantly decreased with increasing GGBFS content.

The carbonation depth seems to be linearly proportional to the square root of time (Figure 6.12), that is similar to cement-based materials [106]. This relation is usually described by the Fick's $1^{st}$ law of diffusion, whereas the slope of these curves corresponds to the diffusivity constant or carbonation coefficient K ($x=K\cdot t^{0.5}$, where x, carbonation depth; t, time in days). It should be noted that here Fick's $1^{st}$ law of diffusion describes the reactive transport in a porous medium and not the pure $CO_2$ diffusion.

The role of curing conditions on the carbonation coefficient K is clear in Figure 6.13. This shows the importance of calcium from GGBFS and shows when the system is rich in GGBFS, alkalis play a less important role in carbonation resistance of the samples in the studied carbonation conditions.



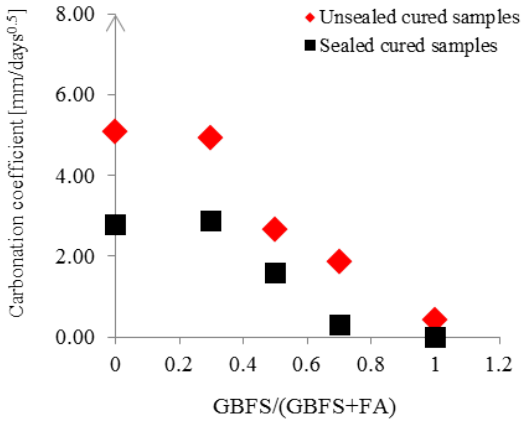


Figure 6.13: The relationship between carbonation coefficients (K) and GGBFS content for the unsealed and sealed cured samples. The carbonation coefficients are calculated using the data in Figure 6.12, from linear fits of the carbonation depths as a function of the square root of time ($x=K\cdot t^{0.5}$).

#### 6.3.2.2. CARBONATION DEPTH: NATURAL VS ACCELERATED CARBONATION

The carbonation depth was measured in accelerated conditions as well as in natural indoor and outdoor conditions (see Figure 6.3). The measurements taken at 1 year of exposure are shown in Figure 6.14. A substantial difference can be seen between carbonation depths in accelerated and natural conditions as function of binder composition. The carbonation depths in samples with high FA content (GGBFS/(GGBFS+FA)= 0, 0.3, 0.5) were higher than in samples with high GGBFS content (GGBFS/(GGBFS+FA)= 0.7, 1.0), for both accelerated and natural exposure conditions.

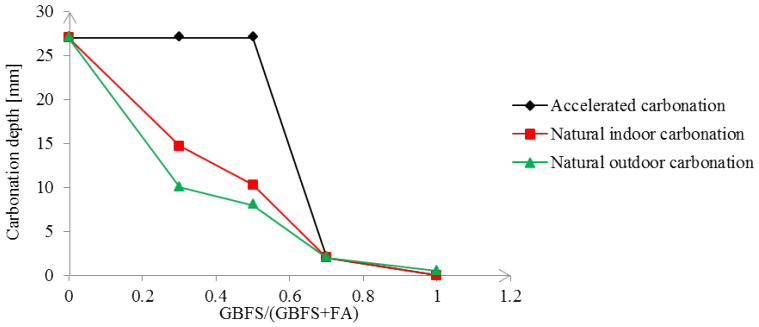


Figure 6.14: Carbonation depth of alkali activated pastes after 1 year of exposure under different conditions.

Table 6.6: Summary of different properties of studied samples under carbonation (specimens were cylindrical with 54 mm diameter and 100 mm height). All samples were first sealed cured for 28 days. Subsequently, samples were unsealed after 28 days of curing when all the samples were placed in the laboratory conditions at 55-60% RH (0.04% v/v $CO_2$, 20 °C) for additional 28 days (preconditioning of the samples prior to carbonation).

| **Accelerated carbonation conditions (1% v/v $CO_2$, 60% RH, 20 °C, 500 days)** | | | |
|---|---|---|---|
| Mixture | Cracking (microscopic observation) | Carbonation depth [mm] (studied depth = 27 mm) | pH at the carbonated layer |
| S0 | not observed | 27 | 10.10 |
| S30 | observed prior exposure (surface microcracking) and magnified after carbonation; larger spacing between microcracks | 27 | 10.50 |
| S50 | observed prior exposure and magnified after carbonation larger spacing between cracks | 27 | 10.89 |
| S70 | observed slower development microcracks smaller spacing between cracks | 1-3 | 12.56 |
| S100 | observed slower development of microcracks smaller spacing between cracks | 0 | 12.61 |
| **Natural indoor laboratory conditions (0,04% v/v $CO_2$, 50-60% RH, 20 °C, 1 year)** | | | |
| Mixture | Cracking (microscopic observation) | Carbonation depth [mm] Studied depth = 27 mm | pH at the carbonated layer |
| S0 | Not observed | 27 | 10.64 |
| S30 | slower development of microcracks | 14.7 | 10.96 |
| S50 | slower development of microcracks | 10.3 | 10.96 |
| S70 | slower development of microcracks | 1-2 | 11.54 |
| S100 | None | 0 | 12.42 |
| **Natural outdoor unsheltered conditions (0,04% v/v $CO_2$, 80-98% RH, 0-20 °C, 1 year** | | | |
| Mixture | Cracking (microscopic observation) | Carbonation depth [mm] Studied depth = 27 mm | pH at the carbonated layer |
| S0 | Not observed | 27 | 11.11 |
| S30 | Samples were severely cracked | 7-10 | 11.34 |
| S50 | Samples were severely cracked | 5-8 | 11.95 |
| S70 | Samples were severely cracked | 2-8 | 11.81 |
| S100 | Samples were severely cracked | 1-2 | 12.18 |

The low carbonation depth in high GGBFS pastes suggests that the GGBFS content plays a significant role in the carbonation process. It seems that 50 wt. % GGBFS is a threshold GGBFS content. In pastes with lower GGBFS content than this threshold value, the carbonation resistance is significantly lower. The difference in carbonation depth measured in pastes exposed to natural indoor and natural outdoor conditions, could be explained by comparing the different RH in those two exposure conditions. The high RH (80-95%) in natural outdoor unsheltered environment (Table 6.2), resulted in slower $CO_2$ diffusion into the pastes. In contrast, the moderate RH (55%) in natural indoor conditions enabled faster $CO_2$ diffusion assuming that the samples are partially saturated. As earlier discussed, this $CO_2$ diffusion rate is also dependent on GGBFS content (Section 6.3.2.2). In Table 6.6, it can also be seen that samples in natural outdoor conditions were severely cracked, except for sample S0. The weathering conditions, which include cycles of wet and dry conditions (see additions to Table 6.1 for RH changes), resulted in cracking of the samples. The cracking path, unless saturated with water, is considered as one of the main path for carbonation in the pastes, except sample S0.

#### 6.3.2.3. pH OF THE PORE SOLUTION: ACCELERATED CARBONATION

The pH of the suspensions of the 500 days sealed cured reference and 500 days carbonated samples are presented in Figure 6.15.



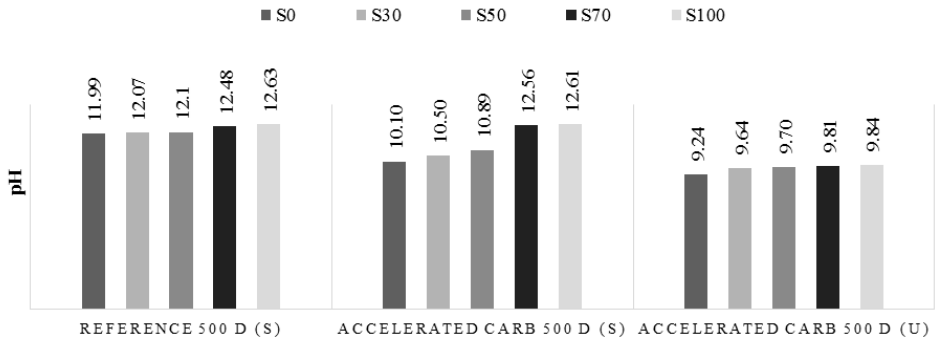


Figure 6.15: pH of suspensions of alkali-activated pastes as a function of GGBFS content in the paste and curing conditions:

- sealed cured pastes for 500 days (noncarbonated, reference),
- S: samples which were sealed cured for 28 days, preconditioned for 28 days and exposed to accelerated carbonation up to 500 days,
- U: samples which were unsealed cured for 28 days at curing conditions 20°C and 99% RH, preconditioned for 28 days and exposed to accelerated carbonation up to 500 days.

At a first glance, it is clear that the pH of the noncarbonated sealed cured pastes decreased from 13.40 ~ 14.00 at 28 days (see Table 6.3) to 11.99 ~ 12.63 at 500 days (see Figure 6.15). This reduction can be attributed to the consumption of $Na^+$ and $OH^-$ with the continuous gel formation, as schematically presented in Figure 6.16. A major part of $Na^+$ and $OH^-$ is consumed for breaking up the alumino-silicate network of the FA

glass (during gel formation). In contrast, breaking up the GGBFS glass requires a lower amount of alkalis. For this reason, the reduction of pH is higher in FA-rich pastes compared to GGFBS-rich pastes. A similar change of pH after 1 year of sealed curing was also reported by Pouhet and Cyr [230] for alkali activated metakaoline and by Zuo et al. [231] for alkali activated GGBFS.

As schematically shown in Figure 6.16, a larger reduction of pH is expected in the unsealed cured samples due to the leaching of $Na^+$ from the pore solution. In contrast, the pH buffering agent in cement-based materials (that is calcium from $Ca(OH)_2$ and C-S-H) increases until reaching the maximum degree of hydration and then it remains constant through time. This ensures a longer passivation of the reinforcing steel surface when carbonation starts in cement-based materials [232] compared to alkali activated pastes.

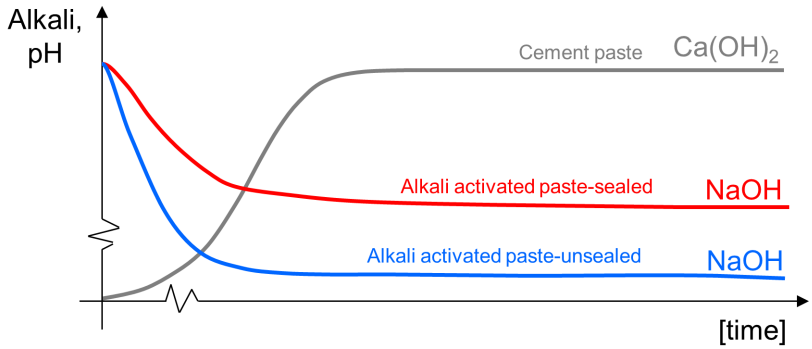


Figure 6.16: Schematic illustration of the content of alkali sources in cement paste (grey line, alkali source: $Ca(OH)_2$) versus alkali activated paste, sealed (red line, alkali source: NaOH) and unsealed cured (blue line, alkali source: NaOH) during the hydration process.

In carbonated sealed-cured alkali activated pastes, a clear reduction of pH is observed in S0, S30 and S50 samples (for example this value is reduced from 11.99 to 10.10 in paste S0). Meanwhile, the change of pH is negligible in the pastes with high GGBFS contents (S70 and S100). In S100, this was expected because the paste was not carbonated. In paste S70, however, a reduction of pH was expected. As the carbonation occurred only in the microcracks of the sample S70, the carbonation front was not uniform and thin. The obtained powders were, therefore, a mix of carbonated and noncarbonated parts that led to a high pH. The role of $Na^+$ consumption is also insignificant in this paste due to the small portion of FA.

In unsealed samples, the reduction of pH after carbonation is much more than that of the sealed cured samples. The pH of carbonated unsealed pastes reaches a value of 9.24 in S0 and a value of 9.84 in S100. Note that all these pH values are related to the strongly carbonated outer surface material (for pastes S0, S30 and S50). This larger pH reduction is the result of three concurrent mechanisms: continuous FA and GGBFS dissolution, $Na^+$ leaching, and carbonation of NaOH in the pore solution. Carbonation of NaOH is followed by dissolution of the calcium from the Ca-Na-Al-Si-H gel, which acts as a pH buffering agent. In samples with lower GGBFS content, the amount of available

calcium is less and thus the buffering capacity is less. Therefore, the pH of these samples after carbonation shows a larger reduction. It is assumed that for the GGBFS containing pastes a combination of $CaCO_3$ and gel phases with remaining $Na^+$ buffers the pH above 9. On the other hand, it is likely that for carbonated paste S0 the NASH gel and remaining $Na^+$ buffer the pH. The obtained pH values in all carbonated unsealed cured samples are lower than the pH values predicted by Bernal et al. [62] for the same NaOH content and $CO_2$ concentration.

It is clear that the pH decreases faster in carbonated alkali activated pastes compared to cement-based pastes. The combination of a low [$Na^+$] with an eventual $Na^+$ loss in unsealed curing conditions, leads to a lower pH. This could accelerate corrosion of reinforcing steel in carbonated samples unless the concentration of alkalis in the pore solution remains high at both early and later ages. This latter can be achieved when appropriate curing conditions are followed and the permeability of the material is sufficiently low. The obtained pH values in carbonated unsealed samples (see Figure 6.15) are very low and near the limit of depassivation of the steel [47]. It should, however, be noted that these results are obtained from alkali activated *pastes*. The effect of carbonation on the pore solution of alkali activated *concrete* will be presented in Chapter 10.

#### 6.3.2.4. pH OF THE PORE SOLUTION: NATURAL VS ACCELERATED CARBONATION

It has already been reported in literature that the sodium carbonates precipitate in carbonated and highly concentrated NaOH solution [62]. The amount of physically absorbed $CO_2$ is estimated at approximately 16.6 g $CO_2$/L of solution at ambient condition [230]. In this study, direct accelerated carbonation of the pore solution was performed in order to determine carbonation products. The pore solutions were extracted from the sealed cured pastes at 28 days of curing prior to carbonation. Figure 6.17 shows FT-IR spectra of synthesized chemical compounds, $Na_2CO_3$ and $NaHCO_3$. Besides, Figure 6.17 also shows the FT-IR spectra of the carbonated pore solutions of paste S0. It is clear that the sodium carbonates (mainly $NaHCO_3$) (Figure 6.17), were the main carbonation products of the pore solution carbonation consistent with the literature [230]. The carbonation of the pore solution of other pastes was also performed, however, results are not shown, since similar spectra were obtained as for paste S0.

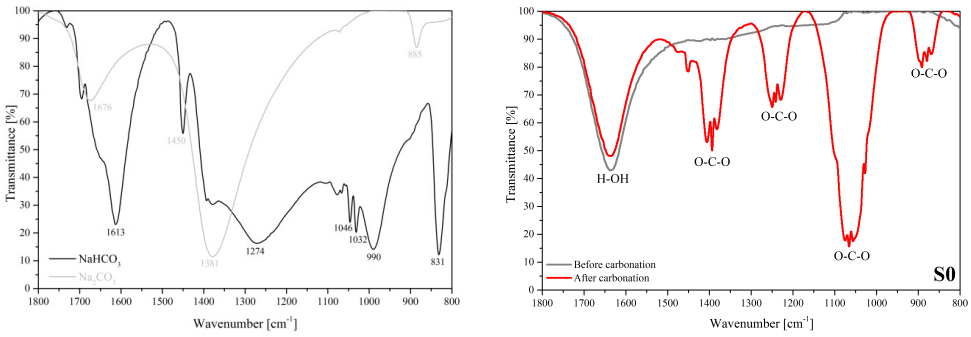


Figure 6.17: FT-IR spectra of synthesized chemical compounds $NaHCO_3$ and $Na_2CO_3$ (left). FT-IR spectra of pore solution of paste S0, before and after carbonation (right).

The effect of exposure conditions on the pH of the pore solution of alkali activated pastes is presented in Figure 6.18 b, c, d. All pastes were sealed cured before exposure to carbonation.

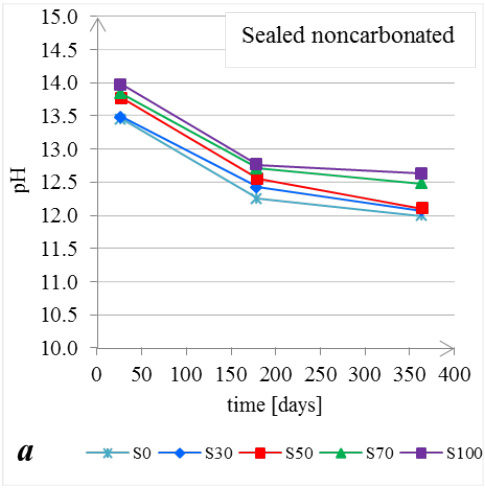


(a) noncarbonated (28 days, 180 days and 365 days)

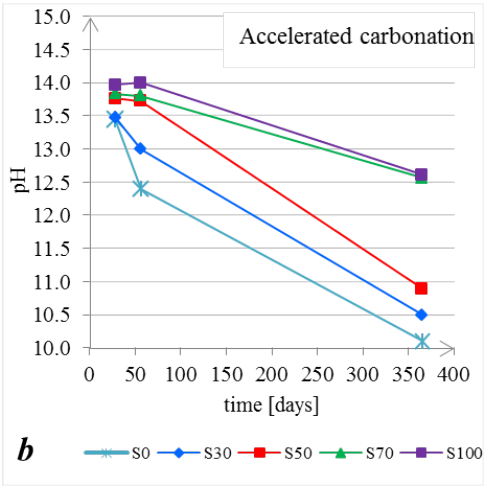


(b) exposed to accelerated carbonation

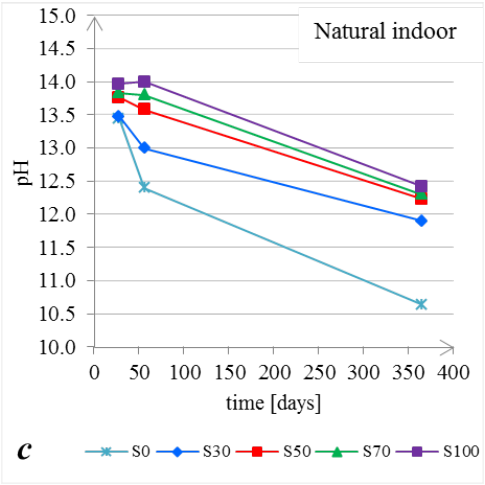


(c) exposed to natural indoor carbonation

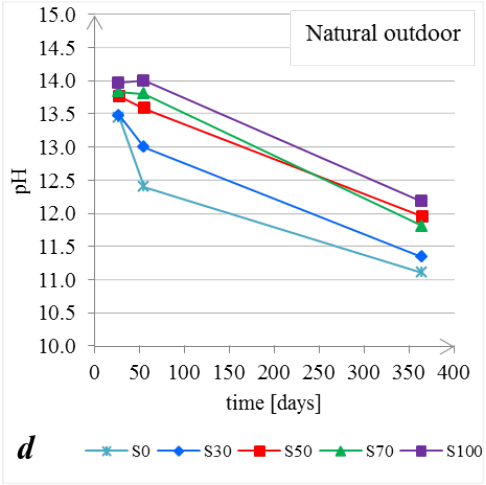


(d) exposed to natural outdoor carbonation.

Figure 6.18: pH of the pore solutions of alkali-activated pastes
Note that all samples before carbonation were sealed cured.

In Figure 6.18a the pH values of reference samples are shown which were sealed cured for 28 days, 180 days and 1 year. Irrespective of the GGBFS content in the pastes, the pH at 28 days of the pore solutions for all five mixtures is beyond 13. The pH beyond 13 had been reported earlier [31], even after shorter period of time, i.e. 3h, 24h, 48h to

7d for alkali activated GGBFS, either activated with sodium silicate or sodium hydroxide. According to these findings, the pH of pore solutions undergoes slight variations with the reaction time compared to original alkaline solution. In the period between 28 days and 180 days of continuous formation of the gel phases, the pH decreased, while this decrease of the slope between 180 and 365 days was moderate (see Figure 6.18a). After 1 year of sealed curing, pH of all pastes was beyond 12.

The pH level for pastes S70 and S100 was similar for all exposure conditions (Figure 6.18b, c, d) including reference samples (Figure 6.18a). This is consistent with measured carbonation depths in these pastes (Figure 6.14), which were less than 2 mm regardless the exposure conditions. The high pH values suggested strong alkaline media under all exposures after 1 year, indicating slightly carbonated or noncarbonated pore solution of pastes. Similar to S70 and S100 pastes, the pH of paste S50 is maintained above pH 12 in natural indoor and natural outdoor conditions.

In Figure 6.18b the pH for pastes S0, S30, S50 exposed to accelerated carbonation is lower than in pastes cured under sealed conditions (Figure 6.18a). The highest drop can be seen in paste S0, from pH 13.5 to pH 10. This drop is lower under natural outdoor and natural indoor conditions, respectively. For samples S30 and S50, the pH of the carbonated depth was beyond 11, most likely due to free alkali which remained in the carbonated pore solution.



#### 6.3.2.5. RELATIONSHIP BETWEEN $Na^+$ IN THE PORE SOLUTION AND NA-BINDING BY THE GEL

In the noncarbonated specimens, calcium sodium aluminosilicate hydrate (Ca-Na-Al-Si-H) gel is the main gel phase in alkali activated GGBFS containing pastes (Chapter 4, Figure 4.25, Table 4.4). According to Hong and Glasser [233], Ca-Na-Al-Si-H can adsorb large amount of alkalis, up to 20% of the Na or K content that was added [233, 234]. Furthermore, in alkaline activation of aluminosilicate precursors, cations (Na, K) neutralise the electrical charge which is produced when $SiO_4$ tetrahedron is replaced by $AlO_4^-$ tetrahedron [41]. Additionally, the comparison of alkali binding between synthetic gel and gel in "real" pastes must be considered. The gel in "real" cement pastes is C-S-H, where the silicon may be substituted by Al. Hong and Glasser [233] assumed, by analogy with zeolites, that this will increase the acidity of Si-O and Si-OH and, therefore, the strength of alkali binding [233]. For this reason, it is believed that the gel phases in pastes will have higher $Na^+$ binding capacity than pure synthesized gel phases. In hardened alkali activated pastes, as studied here, $Na^+$ can be present in the pore solution and adsorbed by the gel phases such as by the Ca-Na-Al-Si-H type gel.

In Figure 6.18 the evolution of the pH indicates that the formation of the gel phases has reduced the pH of the alkali activated pastes S30, S50 and S70 during 1 year of sealed curing. In Figure 6.19 the evolution of $[Na^+]$ indicates that the formation of the gel phases reduces the $[Na^+]$ of the pore solution of the pastes S30, S50 and S70 during 1 year. This explains the pH reduction, shown in Figure 6.18. The pH reduction took place due to the $[OH^-]$ and $[Na^+]$ reductions in the pore solution, since $[OH^-]$ and $[Na^+]$ were consumed for the formation of the gel phases.

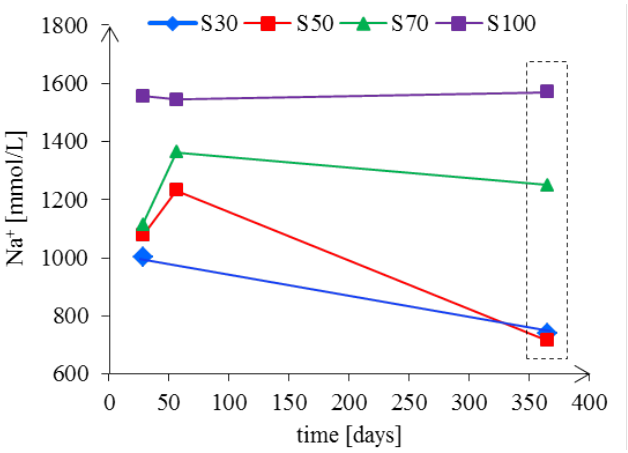


Figure 6.19: $Na^+$ in the pore solution of the sealed cured alkali activated FA/GGBFS pastes at 28, 56 and 365 days.

Figure 6.20 shows the relationship between $[Na^+]$ in the pore solution and $Na^+$ absorbed by the gel phases for two pastes, S50 and S100. Different types of $Na^+$ binding isotherms have been obtained. In paste S50, $[Na^+]$ decreased in the pore solution between 28 days and 1 year, while Na/Si in the gel increased between 28 days and 1 year. On the other hand, no significant change was observed regarding $Na^+$ amount for paste S100. This observation is consistent with Na/Si change in the gel composition between 28 days and 1 year for paste S100 (see Figure 6.20, S50, S100, dash lines).

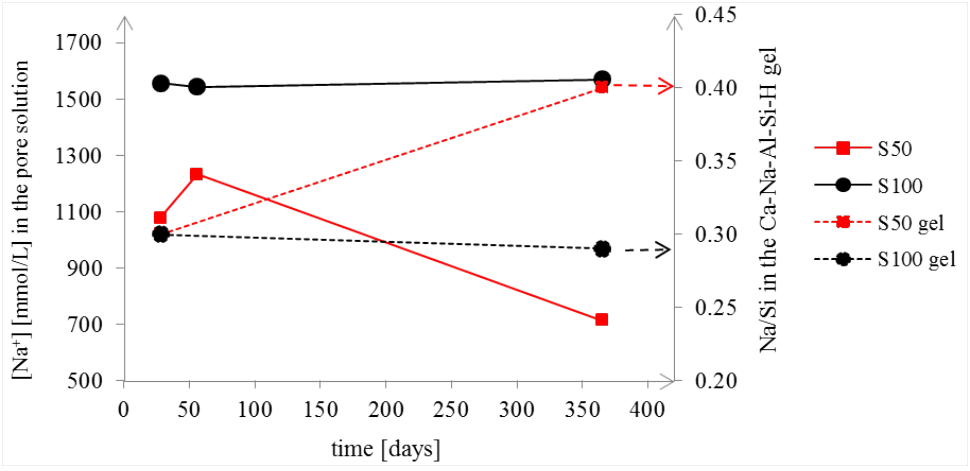


Figure 6.20:
- $[Na^+]$ in the pore solution in pastes S50 (solid red line) and S100 (solid black line), data obtained from Table 6.3, 6.4 and 6.5, and
- $Na^+$ adsorbed by the gel phases such as by the C-(N)-A-S-H type gel in pastes S50 (dash red line) and S100 (dash black line), data obtained from Table 4.3, Chapter 4.

The results from this study are in accordance with a previous study regarding $Na^+$ uptake by gel phases [235]. In that study, the silanol groups were the main adsorbing sites for alkalis. The lower the Ca/Si ratio, the higher the amount of silanol groups in the gel. This further implies that more alkalis will be incorporated in C-(N-)A-S-H with lower Ca/Si ratio as shown by thermodynamic modelling [235] (see Figure 6.21). The Na/Si ratios found in this study (see Figure 6.20) were consistent with Na/Si values shown in Figure 6.21. This shows that samples with high GGBFS content will have lower $Na^+$ uptake by the gel phases. This is in accordance with results in Figure 6.20, where it can be seen that the uptake of $Na^+$ by the gel phases increases as the Ca/Si ratio decreases. This is in agreement with a higher $[Na^+]$ present in the pore solution of GGBFS-rich pastes compared to FA-rich pastes prepared with the same initial amount of alkaline activator (S30<S50<S70<S100), see Figure 6.19. Higher $[Na^+]$ in the pore solution provides higher alkalinity to both noncarbonated and carbonated GGBFS-rich pastes, as shown in Figure 6.18. This suggest great importance of binder type on the alkalinity of the pore solution.

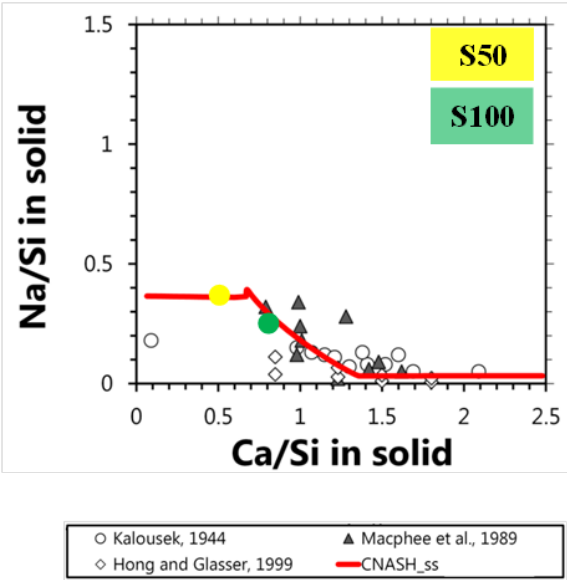


Figure 6.21: Comparison of the simulation results (25 °C, 1 bar, 0.25 M NaOH/solids mass ratio = 50) using the thermodynamic model developed (CNASHss, bold red traces) to published solubility data in the CaO-$Na_2O$-$SiO_2$-$H_2O$ system at alkali concentrations 0.1 M ≤ [NaOH] ≤ 0.3 M (Hong and Glasser, 1999 [233]; Kalousek, 1944 [236]; Macphee et al., 1989 [151]). mM = mmol/L. Adopted from [235].

## 6.4. CONCLUDING REMARKS

The aim of this chapter was to study the carbonation of the pore solution of alkali activated pastes. The influence of mixture compositions and curing conditions on the propagation of the carbonation front and on the pH of the pore solution was evaluated for different exposure conditions. The following conclusions can be drawn:

- An alkali leaching mechanism was observed in the unsealed cured specimens. This is most likely the result of several counter-affecting mechanisms. The RH difference between the environment and the specimen causes a capillary flow from the surface to the interior of the samples and, therefore, an inward movement of the ions (advection). Meanwhile, condensation of water on the surface of the samples leads to dilution of the ions at the surface compared to the interior of the specimens. This causes a diffusive movement of ions from the interior towards the surface of the samples. Here, the diffusive outward movement of ions governed the inward advective water movement that in total led to a loss of the alkali from the pore solution.

- A higher reduction of pH was seen in pastes containing 0, 30, 50 wt.% GGBFS in comparison to pastes containing 70 and 100 wt.% GGBFS. The main reason is larger consumption of $Na^+$ and $OH^-$ during FA dissolution in pastes containing a large content of FA. The binding of $Na^+$ by the gel phases of the alkali activated paste reduces the effective $[Na^+]$ in the pore solution and hence the pH of the pore solution. The process continued up to 1 year. The GGBFS-rich pastes have a lower $Na^+$-binding capacity, hence there is a higher $[Na^+]$ in the pore solution. This ensures a larger alkalinity buffer of the pore solution once the carbonation occurs in GGBFS-rich pastes.

- Alkali leaching led to a faster propagation rate of carbonation front in unsealed samples. The replacement of FA by GGBFS significantly improved the carbonation resistance, independent from the curing condition.

- There are two reasons of pH decrease at long-term:

  – the pH of alkali activated pastes decreased due to ongoing gel formation (from pH 13.40–14.00 after 28 days of sealed curing to the pH 11.99-12.63 after 500 days (see Figure 6.18)).

  – the pH decreased due to carbonation of the alkalis in the pore solution of the pastes.

  As can be seen, curing may affect the long-term performance of AAMs not only in view of carbonation, but also in view of gel formation at later ages. The availability of alkalis is a first preventive measure for obtaining satisfactory carbonation resistance of AAMs.

- Regarding changes in pH of samples exposed to the natural and accelerated conditions, it was shown that a lower pH is measured in the accelerated conditions of carbonation. However, under studied conditions (1% v/v $CO_2$) the accelerated carbonation seems not to reduce the pH for any paste from 100% FA to 100% GGBFS to a level that might cause depassivation of the reinforcing steel (pH~9.0).

From presented results in this chapter, it is clear that an early age $Na^+$ loss has significant effect on chemistry of the pore solution of unsealed cured samples (external RH 99%) and hence on the carbonation rate. Due to the susceptibility of the mixtures to an early age loss of $Na^+$, sealed curing conditions are recommended for practice. This is in contrast to the traditional curing of OPC-based concretes. Curing under water favours cement hydration, especially in the external layer of the OPC-based concrete specimens.

In practice, curing agents, such as commercially available products, can be applied at the outer surface of alkali-activated concrete. This would prevent an early age loss of $Na^+$ from outer layers of alkali activated concrete. This is relevant only for structural applications of alkali activated concrete in environments where average RH is ≥ 85%. This RH, with a demoulding at the age of 24 h, can be considered as the most representative of the building sites in the Netherlands (outdoor RH is on average ~90%, Table 6.1). In contrast, $Na^+$ loss may not to be an issue in conditions of moderate RH (~60-75%).

# 7

# CARBONATION OF THE GEL PHASES

*"By the help of microscopes, there is nothing so small, as to escape our inquiry; hence there is a new visible world discovered to the understanding."*

Robert Hooke

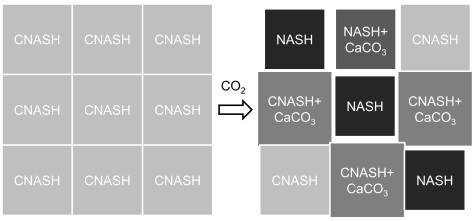


*As a consequence of the pore solution carbonation in alkali activated pastes, alkalinity became reduced as shown in Chapter 6. Due to changes of the pore solution alkalinity, the stability of solid phases in the microstructure is unknown. The reduction of alkalinity usually increases the solubility of gel phases in OPC-based materials. To investigate the carbonation of the gel phases of alkali activated pastes, several techniques were adopted. Scanning electron microscope/energy-dispersive X-ray (SEM-EDX) was used for element zonation along the carbonation depth. Fourier transformed infrared spectroscopy (FT-IR) technique was used to investigate changes of the gel molecular structure. The carbonation products and $CO_2$ binding capacity were analysed with X-ray diffraction (XRD) and thermogravimetric analysis coupled with mass spectroscopy (TG-MS). The changes of the gel phases were obtained with PhAse Recognition and Characterization (PARC). It was shown that the carbonation mechanism involves element changes, mainly of calcium and sulfur. Furthermore, the spatial distribution and chemical composition of the gel phases were also changed due to gel decalcification. The carbonation products were mainly calcium carbonates. They were intergrown with the gel phases. The changes of the element distribution and gel phases resulted in overall microstructure change. The microstructure deterioration was substantially lower in pastes with high slag content.*

Parts of this chapter have been published in:
Nedeljkovic et al. (2017) New test method for assessing the carbonation front in alkali-activated fly ash and slag binders: microscopic complementary techniques, Key engineering materials
Nedeljkovic et al. (2018) Element zonation in carbonated alkali-activated slag paste. Conference in honor of centennial of laboratory of construction materials, Lausanne, Switzerland

## 7.1. INTRODUCTION

In ordinary Portland cement (OPC)-based concrete highly alkaline pore water is formed in the pH range 13-14 after 0.5 to 1 day of cement hydration [237, 238]. The high alkalinity of pore water ensures the stability of the reaction products in the paste. Furthermore, it forms a passivation layer around reinforcing steel in concrete. Carbonation of OPC-based concrete, however, results in reduction of initially high alkalinity of the pore water of the concrete cover to pH below 9 [47]. A reduction of pH breaks down the passivation layer around the reinforcing steel, leading to its corrosion in concrete. In Chapter 6 it was shown that pH of alkali-activated pastes decreases due to carbonation, similar to OPC-based materials. However, the measured pH of alkali activated pastes did not reach the value below pH 9. It is expected that the reduction of pH in carbonated alkali activated pastes affects the stability of the gel phases and further affects the microstructure. As schematically shown in Figure 7.1, $CO_2$ diffuses gradually into the sound microstructure due to concentration gradient. After a certain period, the carbonation front is formed (red line). The carbonation front separates the whole section into three different zones:

- carbonated microstructure,
- partially carbonated microstructure (carbonation front),
- noncarbonated sound microstructure.

In each of the zones in the middle part of Figure 7.1, the behaviour of elements and gel phases are assumed to be different under the $CO_2$ concentration gradient. For that reason, several aspects are investigated in this chapter with the following sequence:

- element changes,
- distribution, identification and quantification of carbonation products,
- gel molecular structure change of carbonated pastes,
- distribution and chemical composition of the gel phases,
- microstructure deterioration.

Several testing methods have been used to accomplish these objectives. The FE-SEM-EDX were used for extraction of element profiles. Optical microscopy was adopted to characterize carbonation products and their distribution in carbonated pastes. The identification and quantification of carbonation products and $CO_2$ binding capacity were obtained with XRD/QXRD and TG-MS. FT-IR method was followed to investigate changes of the gel molecular structure. The chemical changes of the gel phases were obtained with SEM-EDX and PARC. These methods are further discussed in the following sections.

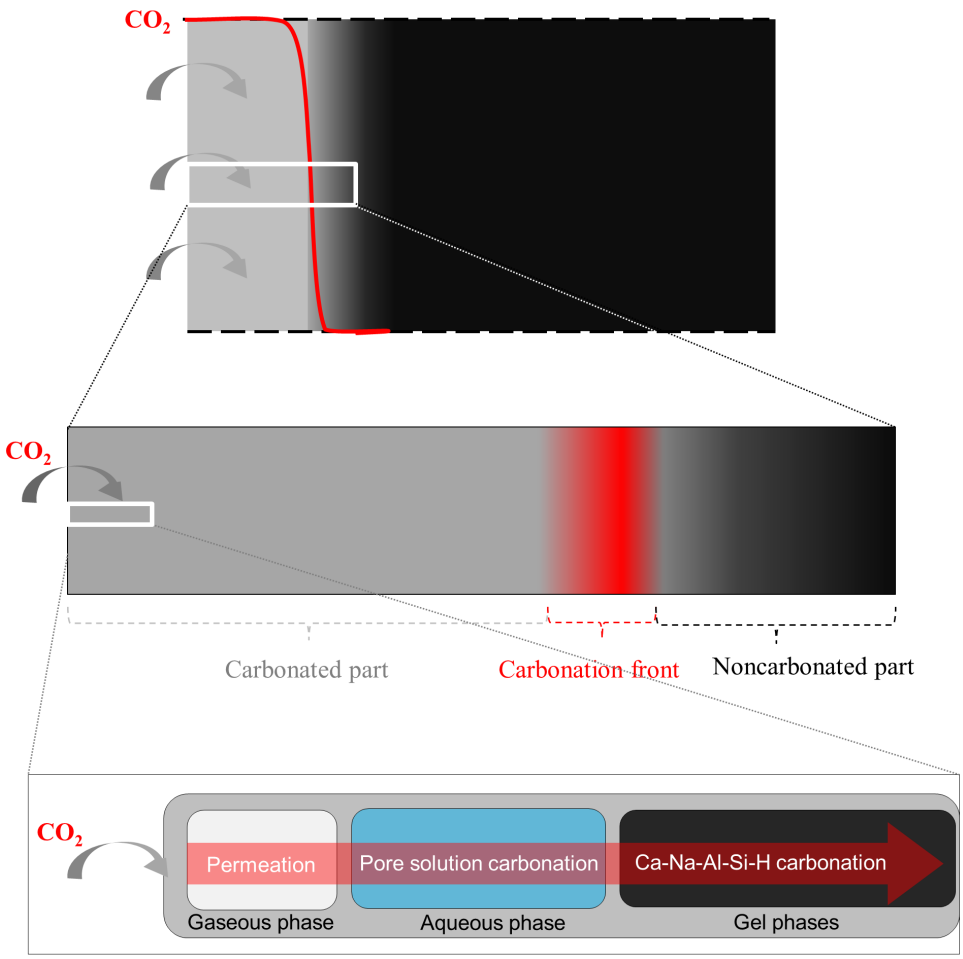


Figure 7.1: Top: diffusion of $CO_2$ in the sample microstructure. Middle: distinction between carbonated part, carbonation front and noncarbonated part. Bottom: overview of the carbonation mechanism.

## 7.2. MATERIALS AND METHODS

### 7.2.1. MATERIALS AND SAMPLE PREPARATION

The chemical compositions of the precursors FA and GGBFS and mixture design are given in Chapter 3. Since in Chapter 6 it was shown that sealed curing conditions prevent alkali loss and premature carbonation of the pastes, samples were cured sealed for the first 28 days. After 28 days of sealed curing, samples were removed from the cylinder moulds for preconditioning (additional 28 days at 55% RH, ambient temperature). After preconditioning the samples were exposed to different carbonation conditions. There is an exception for alkali-activated slag paste (S100) considering the curing method. In Chapter 6 it was found that paste S100 was carbonated only when it was cured unsealed.

Hence, it was decided to study the carbonation mechanism in paste S100 exposed to natural laboratory conditions (0.04% v/v $CO_2$ at 20°C, and 55% RH) for 2 years. The reference paste samples were kept in sealed conditions for 1 year.

Exposure sites and conditions were explained in Chapter 6. The exposure sites are given in Figure 6.3 and the exposure conditions are listed in Table 6.1.

### 7.2.2. METHODS

To determine the effect of carbonation on the microstructure for different binder composition and exposure conditions, several parameters were selected for investigation: element changes, the molecular change of the gel phases and their distribution, carbonation products (distribution, type and quantity) and microstructure changes.

#### 7.2.2.1. OPTICAL MICROSCOPY AND FE-SEM-EDX

The microstructure of pastes was characterized with an Optical Microscope (Zeiss AxioImager, transmitted light) and a Field Emission Scanning Electron Microscope (FE-SEM) (JEOL JSM7001F, with operating conditions of 15 kV and 6 nA). The paste samples were epoxy impregnated, polished and carbon coated. Optical images were made before the samples were carbon coated for FE-SEM analysis. Element changes were studied with energy dispersive X-ray spectroscopy (EDX, dual SDD and NSS 3.3). Extraction of the element profiles was performed by segmentation (the process of partitioning a digital image into sets of pixels) of the profile brightness intensity of element maps, which is related to the number of the counts collected with the EDX detector. The use of element concentrations based on averaged brightness intensities of element maps instead of widely used quantitative EDX analysis has three reasons:

- EDX analysis are standardless and normalized to 100% (unless analyses are calibrated with standards, which is rare),
- density differences caused by porosity or from $CO_2$ addition remain unnoticed by quantitative EDX analysis, except by deviant ZAF (correction software for average atomic number, absorption and fluorescence) correction effects they cause,
- absolute amount of element characteristic X-rays per volume area is faithfully represented in element maps, showing effects of material loss and carbonation in lowered intensities.

For quasi-local averaging, the EDX map was cut in 250 pixels blocks (~ 250×820 $\mu m^2$) and average intensity was measured per block (1, ..., n) using Axiovision 4.8 software (Zeiss), as illustrated in Figure 7.2. The unreacted GGBFS and FA particles, voids and microcracks were eliminated by image segmentation and only counts from the reacting part (gel) were used for EDX profiling. The examined length was 9.5 mm long and 0.82 mm wide.

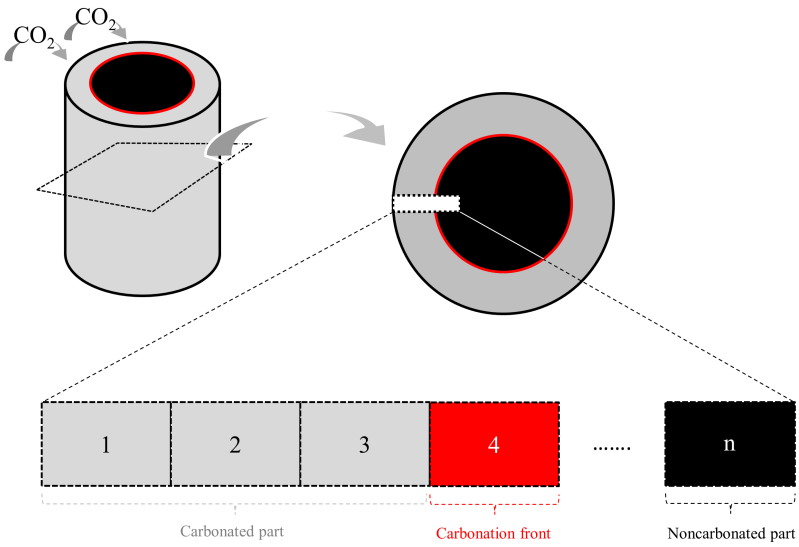


Figure 7.2: Top: schematic representation of the cylindrical paste specimen and core sample crosscutting with characteristic carbonation front. Bottom: the segmentation of the paste "ribbon" for element zonation. Distinction is made between carbonated part (1+2+3), carbonation front (4) and noncarbonated part (n).

#### 7.2.2.2. POLARIZED LIGHT MICROSCOPE (PLM)

The carbonation front was assessed under polarized light microscope (PLM). For this purpose, thin sections were prepared by sawing small prisms from the samples. The dimensions of the prisms were 50 mm × 30 mm, with a thickness of about 10 mm. The sawn prisms were impregnated under vacuum with an epoxy resin containing a fluorescent dye. The thickness of the final thin section samples was around 30 $\mu$m to ensure sufficient light transmission for optical microscopic examination of the carbonation front and carbonates.

#### 7.2.2.3. XRD, TG-MS AND FT-IR

The samples were tested for identification and quantification of carbonation products (XRD/QXRD), $CO_2$ binding capacity (TG-MS) and gel molecular structure change of carbonated pastes (FT-IR) according to the procedures as explained in Chapter 5.

#### 7.2.2.4. PARC

The samples were tested for distribution and chemical composition of the gel phases and microstructure deterioration according to the procedures as explained in Chapter 4.

## 7.3. RESULTS AND DISCUSSIONS

### 7.3.1. ELEMENT ZONATION

#### 7.3.1.1. PASTE S50

In OPC-based materials the propagation rate of the carbonation front is mainly controlled by diffusion of $CO_2$ into the pore system, with a $CO_2$ concentration gradient as

a driving force [215]. It is assumed that the same mechanism governs carbonation in AAMs. As soon as $CO_2$ dissolves in the pore solution of the pastes, it forms a $CO_2$ concentration gradient between two areas of the material, one which is noncarbonated and one which is carbonated. Subsequently, the $CO_2$ concentration gradient causes the changes of the sound part. The whole system (pore solution and solid phases) needs a long time before the equilibrium between the components is again obtained. In this section, the locations and shapes of the carbonation and dissolution front are investigated.

The element zonation is used for identification of the fronts. Pastes S30, S50 and S70 were examined after 1 year of natural laboratory carbonation. All the samples showed similar type of zonation around the carbonation front. For that reason, the zonation is demonstrated only for sample S50.

First, the microscopic investigation of paste S50 was done with optical polarization (a) and fluorescent light microscope (b) in Figure 7.3. The colour difference enabled distinction between the carbonated and noncarbonated area. Microcracks, voids and pores were filled with epoxy resulting in higher intensities of fluorescent light in the carbonated area labelled as "2" compared to noncarbonated core of the sample labelled as "1". The presence of microcracks was more pronounced for the carbonated than for the noncarbonated part. This proves that carbonation reduces the density of the sample. Furthermore, the pore structure characterization of the carbonated and noncarbonated part will be presented in Chapter 8.

The zone between part "1" (noncarbonated) and part "2" (carbonated) was mapped. The changes of the individual elements were then distinguished.



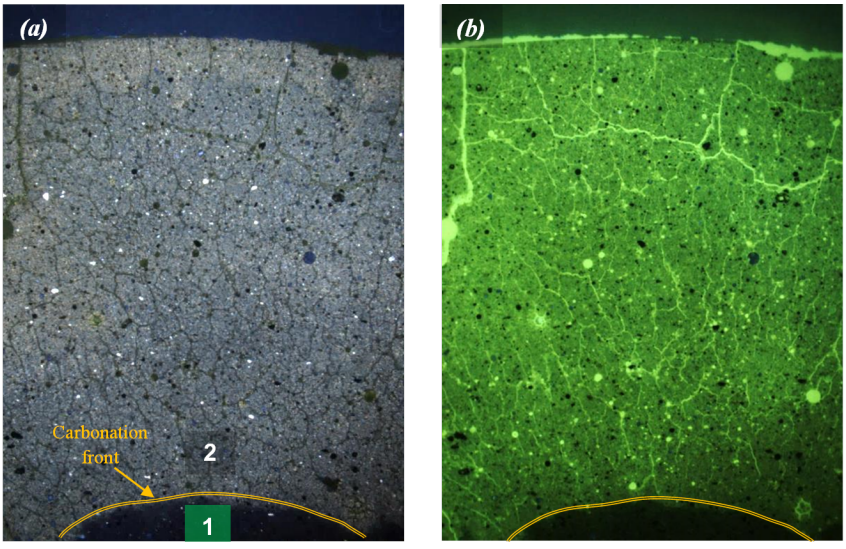


Figure 7.3: Photo of paste S50 thin section under a) polarization, and b) fluorescent light at 40 times magnification. Carbonation depth (from the sample top surface to the carbonation front) is 10.3 mm (nat lab carbonation). (1) is the symbol for noncarbonated core of the sample, (2) is carbonated part.

Figure 7.4 shows the element maps for calcium, silicium, sodium and sulfur as a

function of depth from the carbonated part "2" toward the noncarbonated part "1". Based on BSE image and carbon profile, the carbonation front was identified. Figure 7.5 shows element changes as a function of the depth from the exposed surface. Based on element maps (Figure 7.4) and element fluctuations (Figure 7.5) several fronts can be distinguished (Figure 7.5):

- dissolution front: here the pH starts to drop from 12.6 to lower values (see Figure 6.18, Chapter 6). The Ca map shows lower intensity in this area as shown in Figure 7.4;
- carbonation front: here the pore solution starts to hit its saturation limit for $CaCO_3$, left area in Ca map in Figure 7.4;
- desulfurization front (see Figure 7.5): here the redox potential ($E_h$) of the pore solution begins to be buffered by oxide from outside atmosphere.

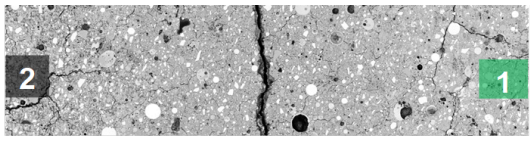


(a) BSE image

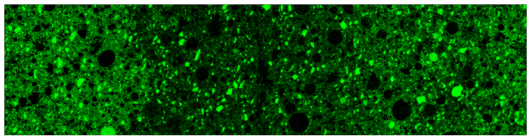

(b) Ca element map

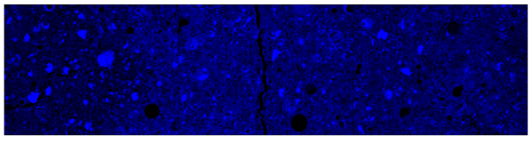

(c) Si element map

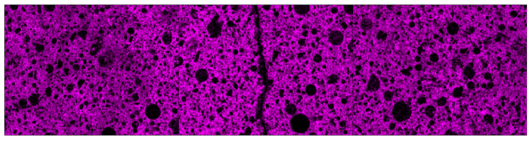

(d) Na element map

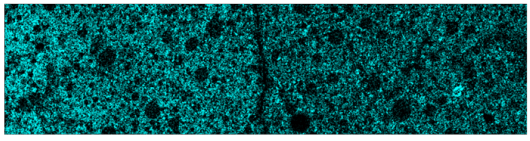

(e) S element map

Figure 7.4: Carbonation of S50 paste (ribbon shown in Figure 7.2) at the location of the carbonation front at 1 year. BSE image (a) and element maps (b-f). Ribbon length 1500 $\mu$m.

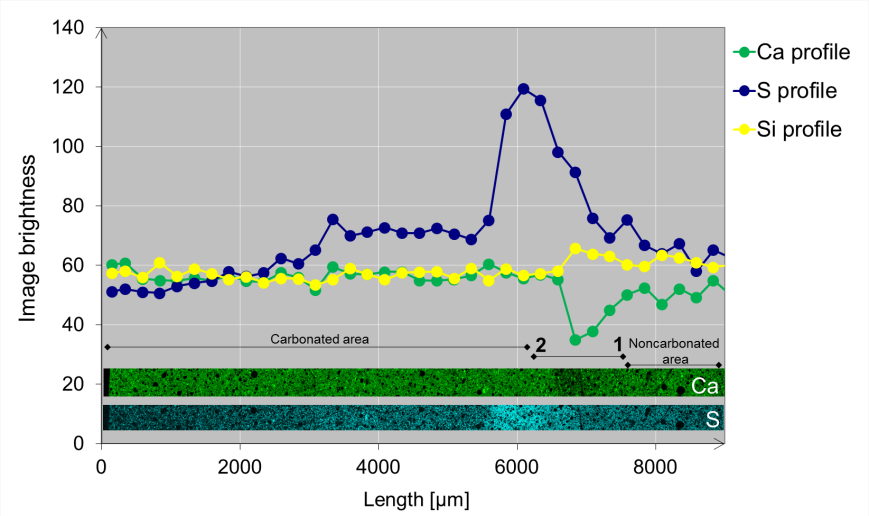


Figure 7.5: Averaged brightness profiles of the extracted EDS element maps along the ribbon of S50 paste as described in Figure 7.2. One pixel is 1 $\mu$m.

**Calcium profile**

A remarkable observation in Figure 7.5 is that calcium was not carbonated in-situ. This implies that the actual calcium concentration changes at each spot. The gel dissolution (i.e. calcium loss) takes place at the point where carbon is reduced (see Figure 7.5). Namely, the gel of the noncarbonated part is affected by the $CO_2$ concentration gradient by change of the pH. The pH is believed to change gradually across the dissolution part (see Figure 7.6, from pH > 12 to pH ≤ 10). Accordingly, calcium is leached gradually (see calcium profile in Figure 7.5 and microstructure changes in Figure 7.7) to the pore solution in the dissolution part, where it exists together with carbonate ions. When saturation of the pore solution with calcium and carbonate ions reaches a critical level, $CaCO_3$ precipitates at the carbonation front. Consequently, the pore solution is locally buffered and the local composition does not change.

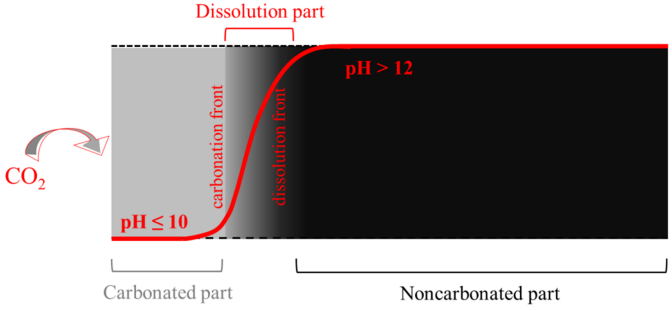


Figure 7.6: pH change under carbonation in alkali activated paste.

**Sulfur profile**

The profile of sulfur is different from the profiles of other elements. Sulfur has a major peak left to carbonation front (see Figure 7.5). The peak is remarkably wide. Sulfur precipitates in both the carbonation part and dissolution part. It seems that sulfur is accumulating in the dissolution part due to change of pore solution alkalinity as illustrated in Figure 7.6. It increases at the carbonation front, where the pore solution is saturated with calcium and carbonate ions, whereas no accumulation of sulfur is observed in the noncarbonated area. Sulfur profile can be explained by considering the relationship of redox potential $E_h$ and pH for sulfur species when the pH of the systems is changing from a very high pH 12.6 to pH 10.6. It is known that $S^{2-}$ is stabilized at pH > 12.9. Below this pH value, $HS^-$ formation and the eventual oxidation of the sulphur species to $SO_4{}^{2-}$ are favoured [239]. For that reason, a higher pH of the pore solution is expected to retard the oxidation of sulphides and the lower pH of the pore solution to accelerate this process, consistent with literature [240, 241].

**Silicium profile**

There is a slight tendency for silicium to increase in the region of the dissolution front. On the other hand, silicium is lower for both the noncarbonated part and the carbonated part. It is likely that the local intensity of silicium increases in the dissolution part because of silicate gel polymerization.

**Observation of the dissolution front**

Figure 7.7, in addition to Figure 7.5, shows that the gel dissolution front was gradual. The gel dissolution occurs by lowering of the pH due to the presence of carbonate ions in the pore solution. By dissolution of the gel, the gel porosity is also changing.

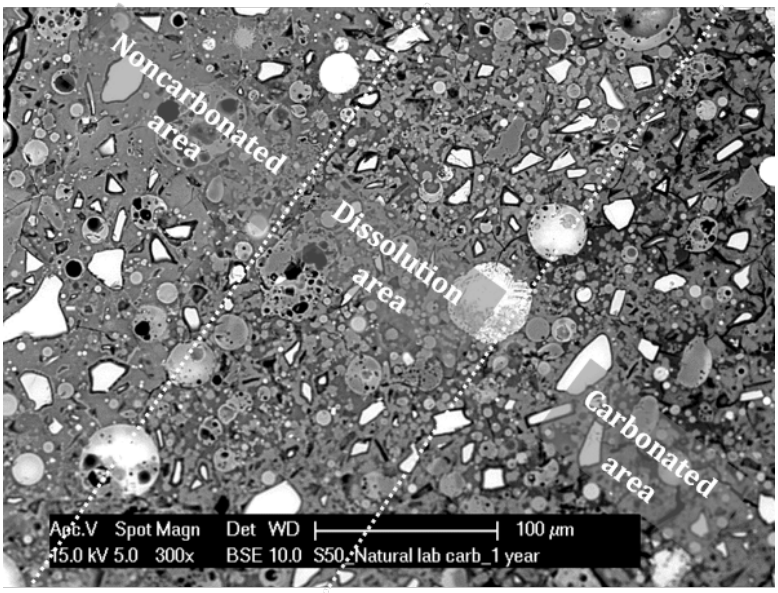


Figure 7.7: SEM image of paste S50 showing dissolution area between carbonated and noncarbonated areas. The location is selected based on BSE image in Figure 7.4.

This provides the pathway for transport of more ions over the dissolution area (see Figure 7.7). Given Figure 7.5 and Figure 7.7, it can be said that the dissolution front and the carbonation front do not exactly coincide. Gel dissolution and the precipitation of the carbonates proceed at the same speed and the dissolution of the gel occurs before precipitation of the carbonates. For precipitation of carbonates, the pore solution needs to be saturated with carbonate ions, but also that calcium ions are present. This occurs when a sufficient amount of $CO_2$ molecules is dissolved and supplied to the reaction site. For that reason, $CO_2$ diffusion is the rate-limiting step of the carbonation mechanism of alkali activated paste S50.

#### 7.3.1.2. PASTE S100

The mosaic of unsealed cured paste S100 after 2 years of exposure is shown in Figure 7.8. Red lines indicate the position of the EDS-mapped area ("ribbon" in Figure 7.10). Carbonation did not occur after 2 years in sealed cured paste (first 28 days sealing, and then paste samples were unmoulded and kept 2 years in laboratory conditions), whereas it did occur in unsealed cured paste S100.

The gel in paste S100 was carbonated only near the surface to 2.2 mm depths after 2 years, followed by the oxidized and noncarbonated areas. The noncarbonated and carbonated microstructures are shown in Figure 7.9. The volume proportion of the angular GGBFS particles seems clearly higher in the carbonated area. The difference is attributed to processes which subsequently occurred during the 2 years of exposure, such as leaching of Na in the curing period (first 28 days), drying after samples were moved from the curing room to laboratory conditions and natural carbonation. $Na^+$ leaching during curing and subsequent ingress of $CO_2$ changed the near surface area of the sample, such that the dissolution of GGBFS grains in that area was restricted compared to the core of the sample.

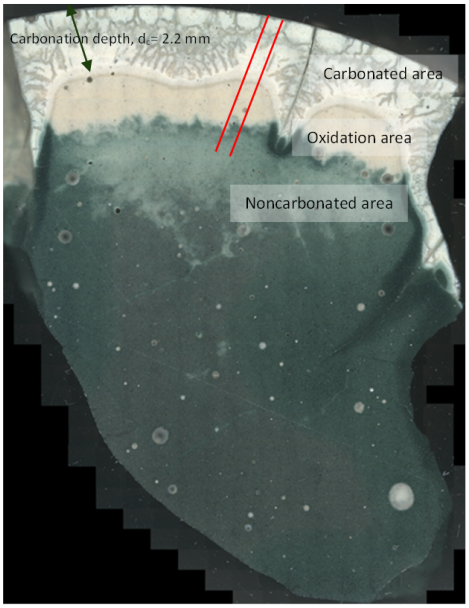


Figure 7.8: Mosaic of unsealed cured paste S100 after 2 years of exposure to natural laboratory carbonation determined with Optical Microscope. The red lines indicate location of the extracted maps.

The microcracks visible in the noncarbonated microstructure are due to sample preparation (Figure 7.9), although in Figure 7.8 under high magnification they were not present (not shown here). Carbonation was sporadic, as can be seen in Figure 7.9. Depending on the local gel structure, i.e. Ca/Si ratio and gel porosity, carbonation will be enhanced by microcracks as demonstrated in Figure 7.8, where carbonation follows the microcrack paths. The oxidation area had less apparent microcracks. However, those observed seemed induced by drying.

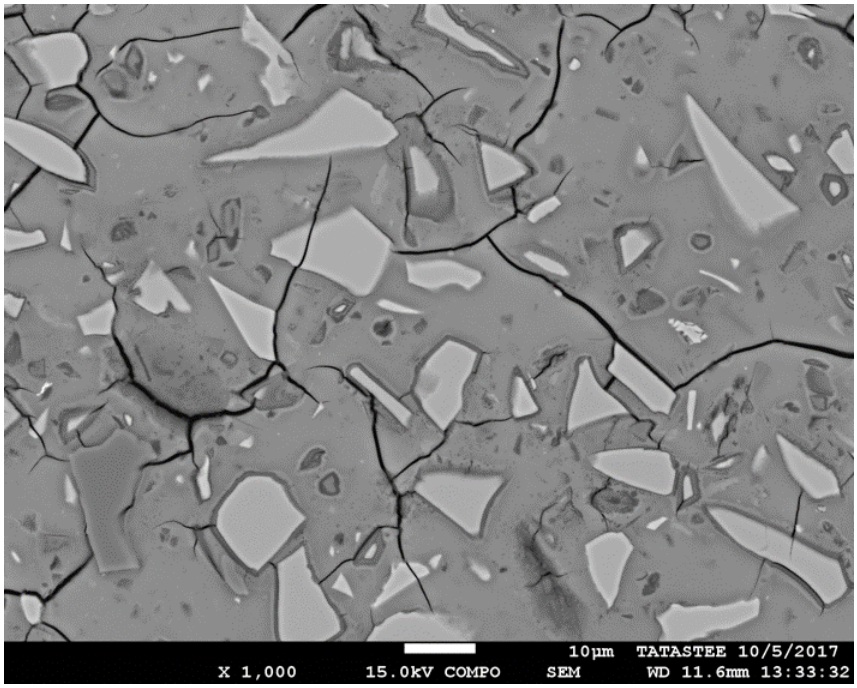


(a) reference noncarbonated S100 paste at 1000 times magnification

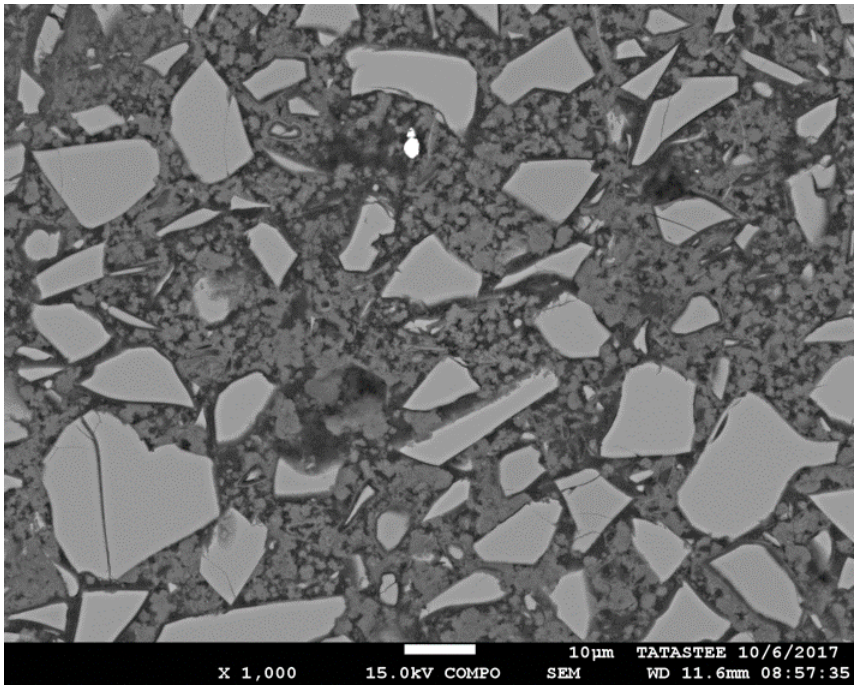


(b) carbonated S100 paste after 2 years carbonation at 1000 times magnification

Figure 7.9: SEM-BSE images of noncarbonated (sample core) area and carbonated (surface) area.

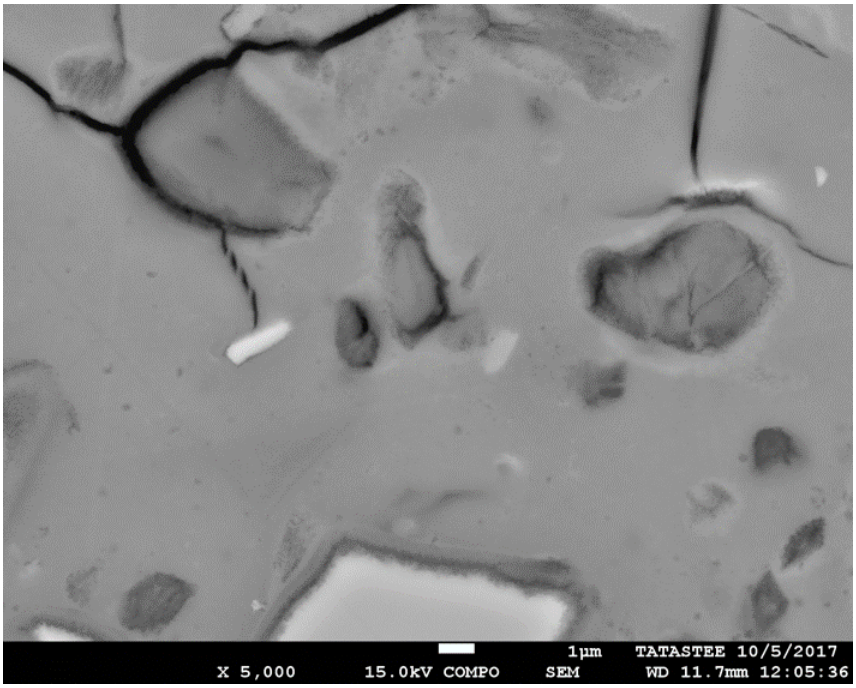


(c) reference noncarbonated S100 paste at 5000 times magnification



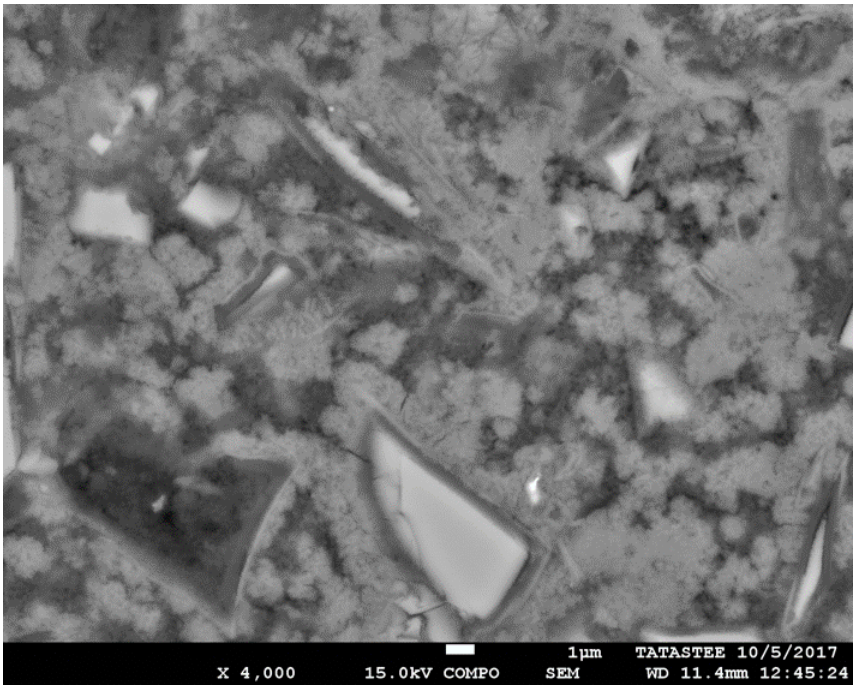


(d) carbonated S100 paste after 2 years carbonation at 4000 times magnification

Figure 7.9: SEM-BSE images of noncarbonated (sample core) area and carbonated (surface) area.

The area where carbonation occurs (Figure 7.8) reflect the behaviour of individual elements in these areas (Figure 7.10(a)) as presented by the change in colour intensity. In the greyscale image (Ref), an abrupt density change corresponds to the transition from the bright to the dark area, the noncarbonated area being denser than the carbonated. The image brightness profiles shown in Figure 7.10(b) result from a combination of two factors, the composition change and the material density change, together resulting in the chemical profiles for Ca, S, Na, Si. Looking at the Ca changes along the profile, the Ca intensity is reduced in the carbonated area compared to the noncarbonated area. Several distinct reaction fronts are observed, showing independent behaviour of Ca, Na and S in the carbonated area, oxidation area and noncarbonated area.

Figure 7.10(b) shows that S is accumulating just behind the local Na-peak in the Na profile (indicated by the two characteristic S-peaks), being enhanced in the entire oxidation area. Presumably, the pore solution in the oxidation area was saturated by sulphates which were intergrown with the microstructure. The S-depletion is from such a large area that it cannot be noticed here, while the S-enrichment in a specific layer is noticeable because the high levels it reached. It is not easy to explain why the sulphur concentration has the same apparent level before and after the enrichment zone. For Na it can be seen that it is strongly leached at the surface. However, it is enriched in the area where Ca is decreasing. Although Na- and S-peaks are close, they are not coinciding, with the Na-peak occurring shallower than S in the profiles (see Figure 7.10(b)).

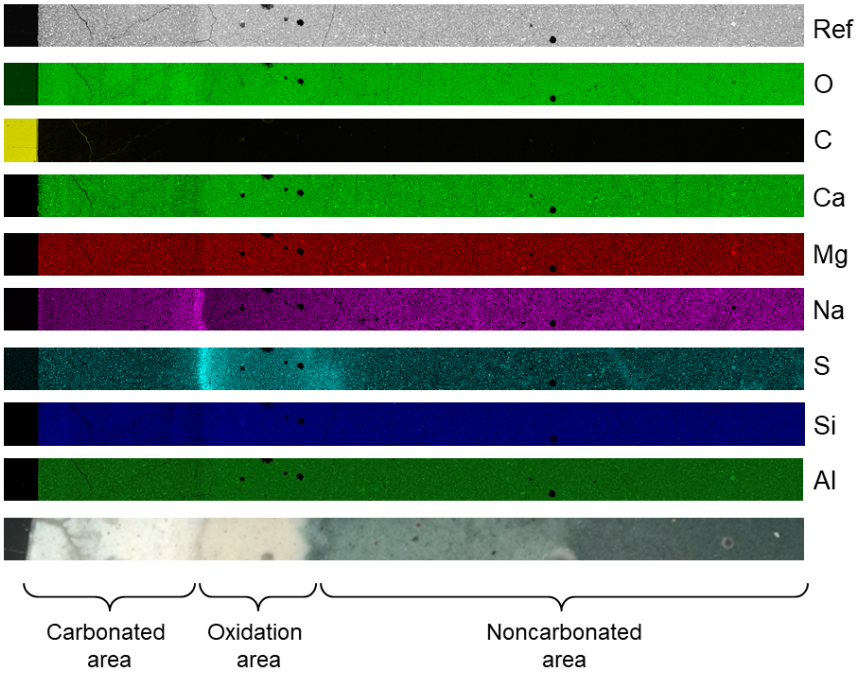


(a) Element zonation of paste S100 after 2 years of exposure to natural carbonation.

Figure 7.10: Element zonation and profiles of paste S100.

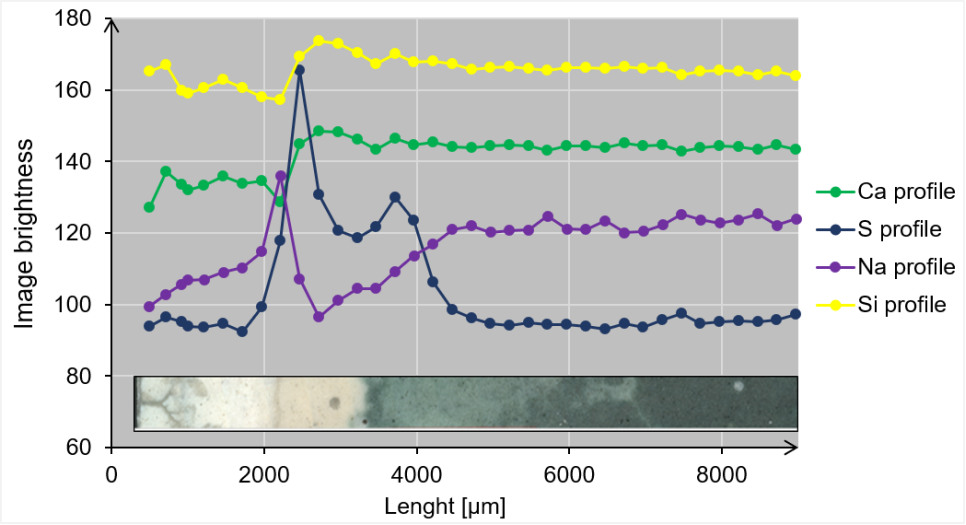


(b) Averaged brightness profiles of the EDS element maps.

Figure 7.10: Element zonation and profiles of paste S100.

In general, C is difficult to analyse with the SEM-EDX due to its low characteristic X-ray yield. It seems as if oxygen is less present in the surroundings of the microcracks. This is difficult to explain since its profile combines several effects (sulphur oxidation, carbonation, water loss). Si and Ca had similar behaviour along the profile, and they all were affected by carbonation. Both have a large drop in the dissolution front (between 2000 and 2800 $\mu$m) and in carbonated areas. Mg was concentrated in the rim of the GGBFS particle in the carbonated S100 paste as it was in the noncarbonated S100 paste, suggesting none or very small change after carbonation (see Figure A.1 and Figure A.2, Appendix A). The maps for Al and Mg reveal the smallest changes.

It is assumed that along the ribbon there is one primary material transition front, that is where all the element image brightnesses drop down, between 2200 and 2800 $\mu$m. At this front, the primary change is that material density in the matrix (not including the segmented-out unreacted grains) is significantly lowered. Taking the relatively immobile Al as a reference, compositional changes in other elements can be evaluated, but only within either the region below or above 2200 $\mu$m. Above and below this depth, the image intensities are offset by the material density change, as reflected in the comparison between image brightness. Thus, the profiles show two major horizons, one representing the beginning of mass leaching of Ca and Na, and second representing the beginning of the reprecipitation of these elements, i.e. the carbonation horizon, where the material density significantly decreases. The two horizons are coupled as a dissolution – precipitation pair, where elements are transported from the inner dissolution zone to the outer reprecipitation zone (carbonated area). The reduced material density in the carbonated area may have involved net material growth, i.e. expansion of the outwardly unconfined sample. Unfortunately, dimensional changes of the sample were not accurately recorded. In principle, a bulk volume expansion of the carbonated zone,

compared to the core, could be demonstrated by measuring the average interparticle distances between inert GGBFS grains assuming they are homogeneously distributed throughout the sample. However, there is a considerable difference in the degree of reaction of GGBFS grains in core and rim (Figure 7.9). Hence it is difficult to establish how distances between remaining grains should be compared and this concept has not been implemented.

**Discussion**

Based on the results of element zonation, for both pastes S50 and S100, it can be inferred that the gel dissolution was gradual under natural exposure conditions. The gel dissolution was initiated by lowering the pH due to the presence of carbonate ions in the pore solution. The dissolution front and carbonation front did not coincide. The main medium for carbonation reactions was the pore solution. The precipitation of $CaCO_3$ resulted from oversaturation of the pore solution. Therefore, the carbonation mechanism is not a simple transformation of CaO and $Na_2O$ to $CaCO_3$ and $Na_2CO_3$. If this would be the case, carbonation would be a reaction driven mechanism. That means that every slice would have nearly the same composition. Actually, the local bulk composition does not remain constant, as shown by element profiles in Figure 7.5 and Figure 7.10. Furthermore, the mass balance for carbonation is not possible, since it can be clearly seen that there are coupled reactions, where pore solution is mobilizing material at the point of dissolution and depositing it back to the carbonated area. This profile is gradually moving forward. It leaves in its wake a constant composition. That means that all peaks, which are measured in Figure 7.5, also move with profile forward.

Based on presented analysis, two length scales are distinguished in the reactions:

- the length scale of the surfaces of pores, grains and gels, at which actual reactions start. However, this is a very short local length scale. If the reactions occur only at this length scale then the bulk composition at larger length scale would not be affected when carbon and oxygen are added,
- the length scale of pore solution, where all reactions are taking place. This is a larger length scale at which the effect of carbonation is dominant.



## 7.3.2. CARBONATION PRODUCTS

### 7.3.2.1. OPTICAL MICROSCOPY

Figure 7.11 shows paste S50 under cross-polarized transmitted light, with a distinct carbonation front. Furthermore, the magnified carbonated and noncarbonated parts are given for closer distinction. In the noncarbonated part the amorphous phase is isotropic and black-coloured, while the crystalline phases show different colours. The phases are different from the surrounded microstructure which remains intact. These features are present all over the carbonated microstructure. The type of the carbonates could not be determined with optical microscopy. Therefore, XRD was used in the next section.

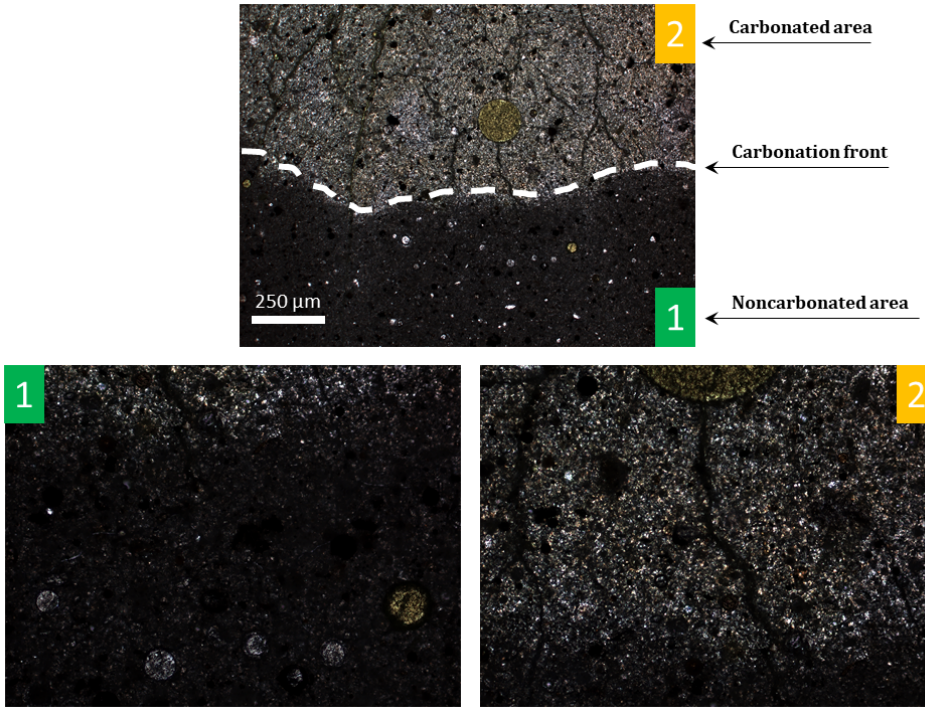


Figure 7.11: Noncarbonated (black) and carbonated alkali-activated paste S50 microstructure (bright). Image is obtained under cross-polarized transmitted (XPT) light at 25 times magnification. Close view of noncarbonated area (1) and carbonated area (2) at 100 times magnification, XPT, image width 0.75 mm. The exposure time was 1 year.



#### 7.3.2.2. CRYSTALLINE CARBONATION PRODUCTS

Identification of crystalline carbonation products was obtained with X-Ray diffraction. Figure 7.12 shows an example of the phase identification for reference paste S50 (sealed cured paste for 1 year, noncarbonated) and carbonated paste S50 in lab conditions. The major phases of reference paste S50 were the amorphous phase and crystalline phases such as quartz ($SiO_2$), mullite ($Al_{4.75}Si_{1.25}O_{9.63}$), hematite ($Fe_2O_3$), magnetite ($Fe_3O_4$) and traces of calcite ($CaCO_3$) (Figure 7.12). The presence of the amorphous phase in Figure 7.12 can be recognized by the broad hump beneath the diffraction peaks of the crystalline phases centred around 34 2theta (red magnified offset diffractogram visible in the same graph).

Table 7.1 compares the carbonation products and their quantities for carbonated pastes under different exposure conditions. In general, two different types of carbonates were identified in carbonated pastes, sodium-based (minor) and calcium-based carbonates. Nahcolite ($NaHCO_3$) and natron ($Na_2CO_3{\cdot}10H_2O$) were identified as sodium-based carbonates, which originated from the carbonation of $Na^+$ from the aqueous solution. On the other hand, calcium carbonates, i.e. vaterite, aragonite and calcite, were formed due to carbonation of Ca containing gel phases which were defined in Chapter 4.

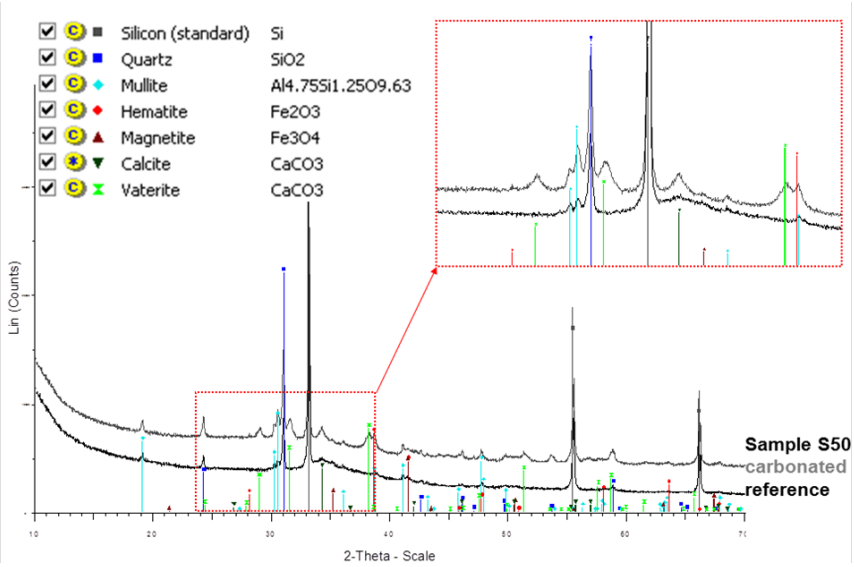


Figure 7.12: Comparison of the XRD diffractograms with respect to the phases in reference and natural carbonated pastes (sample age: 1 year).

The quantitative phase analysis shows that the dominant phase is amorphous (> 70 wt.%) for both the reference sample and samples exposed in different conditions (see Table 7.1). The amorphous phase content decreased for the carbonated samples compared to the reference samples. For paste S100, no other phases except minor traces of calcite (< 0.5 wt.%) were identified for both reference and exposed samples, indicating that reaction products (gels) were not carbonated. Similarly, analysis of paste S0 did not show a significant difference between carbonated and reference paste S0, except some traces of natron ($Na_2CO_3 \cdot 10H_2O$) (around 0.1 wt.%) in natural indoor conditions.

Vaterite was dominant in both accelerated and naturally indoor and outdoor carbonated S30, S50 and S70 pastes (see Table 7.1). Vaterite is well-known as unstable precipitate in supersaturated solutions caused by nonstoichiometric reaction conditions as shown by Jung et al. [242]. The nucleation of different calcium carbonates is reported to be dependent on the supersaturation level, ionic ratio of $[Ca^{2+}]/[CO_3^{2-}]$ in solution and the pH of the solution [199, 242, 243]. According to Hostomsky et al. [244], precipitation of vaterite in the reaction of calcium nitrate and sodium carbonate occurs at pH ≥ 9.5, but calcite is obtained at pH ≤ 8.5. In addition, Kralj et al. [199] reported precipitation of pure vaterite from the solution of calcium chloride and sodium carbonate at decreasing pH below 9.3, the unstable vaterite might recrystallize into stable calcite if there is a sufficient moisture [245]. The re-crystallization of vaterite in this study was not the case and it was most probably inhibited by the intermediate moisture content (50-60% RH), but also due to the pH level of the pore solution. The pH of the pore solution in pastes after carbonation was maintained above 9, as shown in Chapter 6.

In contrast to vaterite and low amount of calcite identified in this study, calcite is the main carbonate beside aragonite and vaterite, formed from the accelerated and nat-

ural indoor carbonation of OPC-based paste as found by Hidalgo et al. [246]. Accordingly, the formation of more vaterite than calcite in this study can be partially attributed to the nanostructural ordering and thermodynamic stability of the C-(N)-A-S-H gel in alkali-activated pastes, which is different from C-S-H gel in OPC-based pastes. White et al. [196] showed large intrinsic differences of nanoscale ordering between C–S–H derived from $C_3S$ and alkali-activated GGBFS pastes using X-ray total scattering. Authors showed that C-(N-)A-S-H gel is mostly amorphous and intrinsically less thermodynamically stable than (nano)crystalline $C_3S$-based gels. This implies a different phase dissolution mechanism of carbonation of AAMs compared to OPC-based materials. This leads to precipitation of different $CaCO_3$ polymorphs as shown in Chapter 5.

#### 7.3.2.3. AMORPHOUS CARBONATION PRODUCTS AND $CO_2$ BINDING CAPACITY

The GGBFS-rich pastes S30, S50, S70 and S100 predominantly form a Ca-Na-Al-Si-H gel with different Ca/Si ratio, while paste S0 consists of Na-Al-Si-H type gel (see Chapter 4). Depending on the Ca/Si ratio of the reaction products, the actual type and quantity of carbonate will differ. For that reason, different quantities of different carbonates are found with XRD analysis (Table 7.1). Otherwise than XRD analysis, thermogravimetric (TG) analysis helps to quantify the $CO_2$ binding capacity of alkali activated pastes and distinguish the amorphous carbonates from crystalline carbonates (vaterite, aragonite, calcite, natron and nahcolite). Based on TG curves, the first derivative of TG curves (DTG curves) and mass spectroscopy (MS) curves, all plotted in Figure 7.13, the cut-off temperatures for decomposition of water and $CO_2$ were determined accordingly:

- mass loss from 45 °C to 105 °C is mainly attributed to the evaporable water from the pastes;
- mass loss from 105 °C to 245 °C is mainly due to the loss of bound water in Ca-Mg-Na-Al-Si-H/Ca-Na-Al-Si-H/Ca-Al-Si-H/Na-Al-Si-H gels;
- mass loss between 105 °C and 180 °C: dissolved carbonates in the pore solution (with lower release temperature in TG-MS, such as sodium bicarbonates/carbonates);
- $CO_2$ emission between 245 °C and 950 °C: $CO_2$ in low-crystalline and high-crystalline $CaCO_3$.

According to aforementioned distinction and results presented in Figure 7.13, it can be seen that the release of $H_2O$ and $CO_2$ are two independent processes. This demonstrates that the gel phases and carbonation products are not structurally bound as one compound, but rather physically intergrown as independent phases. Furthermore, MS curves for $CO_2$ show that $CO_2$ starts releasing in the temperature range around 245 °C. This is the characteristic temperature for decomposition of amorphous carbonates in the structure of the carbonated pastes.

The decomposition of crystalline $CaCO_3$, such as vaterite, aragonite and calcite occurs at temperatures higher than 500 °C, as shown by Kralj et al. [199]. For most of the pastes, except paste S0, both amorphous and crystalline carbonates were identified.

Table 7.1: Quantitative phase analysis by Rietveld method for reference pastes and for the pastes exposed in the natural laboratory, natural outdoor and accelerated carbonation for 1 year. For comparison to bulk samples minerology, the results for minerology of the carbonated crushed pastes from Chapter 5 are presented.

| **Phases** | **Amorphous** | **Quartz** | **Mulite** | **Magnetite** | **Hematite** | **Hydrotalcite** | **Vaterite** | **Aragonite** | **Calcite** | **Natron** | **Nahcolite** |
|---|---|---|---|---|---|---|---|---|---|---|---|
| *Reference* | *Bulk paste samples* | | | | | | | | | | |
| S0 | 75.2 | 8.6 | 12.7 | 2.3 | 0.6 | | - | | 0.6 | | |
| S30 | 82.8 | 5.9 | 8.7 | 1.6 | 0.6 | | 0.1 | | 0.3 | | |
| S50 | 91.7 | 3.0 | 4.2 | 0.8 | 0.2 | | - | | 0.1 | | |
| S70 | 94.1 | 2.1 | 3.1 | 0.4 | 0.1 | | - | | 0.2 | | |
| S100 | 99.8 | 0.0 | 0.0 | 0.0 | 0.0 | | - | | 0.2 | | |
| *Natural laboratory* | *Bulk paste samples* | | | | | | | | | | |
| S0 | 71.1 | 10.0 | 15.5 | 1.9 | 0.7 | | 0.0 | | 0.7 | 0.1 | 0.0 |
| S30 | 72.7 | 6.8 | 10.3 | 1.1 | 0.8 | | 5.9 | | 1.9 | 0.5 | 0.0 |
| S50 | 77.2 | 5.0 | 8.2 | 0.7 | 0.8 | | 5.6 | | 2.0 | 0.4 | 0.1 |
| S70 | 82.9 | 3.3 | 4.7 | 0.3 | 0.6 | | 4.6 | | 3.2 | 0.3 | 0.1 |
| S100 | 99.9 | 0.0 | 0.0 | 0.0 | 0.0 | | 0.0 | | 0.1 | 0.0 | 0.0 |
| *Natural outdoor* | *Bulk paste samples* | | | | | | | | | | |
| S0 | 76.2 | 8.9 | 11.2 | 2.2 | 0.3 | - | 0.0 | | 1.2 | | |
| S30 | 77.0 | 6.5 | 7.5 | 1.5 | 0.5 | - | 2.4 | | 4.6 | | |
| S50 | 81.4 | 4.4 | 5.1 | 1.2 | 0.3 | - | 4.5 | | 3.1 | | |
| S70 | 85.5 | 2.8 | 3.9 | 0.6 | 0.2 | - | 4.9 | | 2.1 | | |
| S100 | 95.2 | 0.0 | 0.0 | 0.0 | 0.0 | 0.3 | 2.5 | | 2.0 | | |
| *Accelerated* | *Bulk paste samples* | | | | | | | | | | |
| S0 | 74.2 | 10.0 | 12.3 | 2.3 | 0.5 | - | 0.0 | | 0.7 | | - |
| S30 | 73.6 | 6.7 | 8.0 | 1.5 | 0.5 | - | 8.9 | | 0.8 | | - |
| S50 | 77.0 | 4.7 | 5.6 | 1.0 | 0.4 | - | 10.2 | | 1.1 | | - |
| S70 | 85.0 | 3.2 | 4.2 | 0.6 | 0.3 | - | 5.9 | | 0.5 | | 0.3 |
| S100 | 99.3 | 0.0 | 0.0 | 0.0 | 0.0 | 0.7 | 0.0 | | 0.0 | | - |
| *Accelerated* | *Crushed pastes (Ch. 5)* | | | | | | | | | | |
| S0 | 71.1 | 8.9 | 14.5 | 3.3 | 0.8 | | - | 0.0 | 0.4 | | 1.0 |
| S30 | 70.1 | 5.9 | 9.8 | 2.1 | 0.7 | | 0.1 | 3.2 | 7.8 | | 0.3 |
| S50 | 69.3 | 4.7 | 6.7 | 1.4 | 0.5 | | - | 14.6 | 2.7 | | 0.1 |
| S70 | 71.9 | 2.9 | 4.2 | 0.8 | 0.2 | | - | 18.8 | 1.0 | | 0.2 |
| S100 | 72.2 | 0.5 | 0.2 | 0.0 | 0.1 | | 0.6 | 25.3 | 1.0 | | 0.1 |

The temperature for $CO_2$ decomposition in carbonated paste S0 was 105-180 °C (see Figure 7.13). This narrow shoulder suggests the presence of nahcolite or natron. A similar observation was made by Bernal et al. [63] for carbonated alkali activated FA. The appearance of this shoulder in the MS curve indicates a rather low amount of these phases in carbonated paste S0 compared to MS curves for $CO_2$ of other pastes.

The TG-MS curves for pastes S100 exhibited a one-stage thermal degradation process during raising temperature, suggesting a homogeneous reaction product (Figure 7.13). The mass loss at 105–345 °C corresponds to the emission of chemically bound water in the Ca-Na-Al-Si-H/Ca-Mg-Na-Al-Si-H gels (with defined chemistry in Chapter 4) and hydrotalcite (found in traces, accelerated and outdoor conditions, Table 7.1). In natural outdoor conditions $CO_2$ was released from paste S100, suggesting slight paste carbonation.

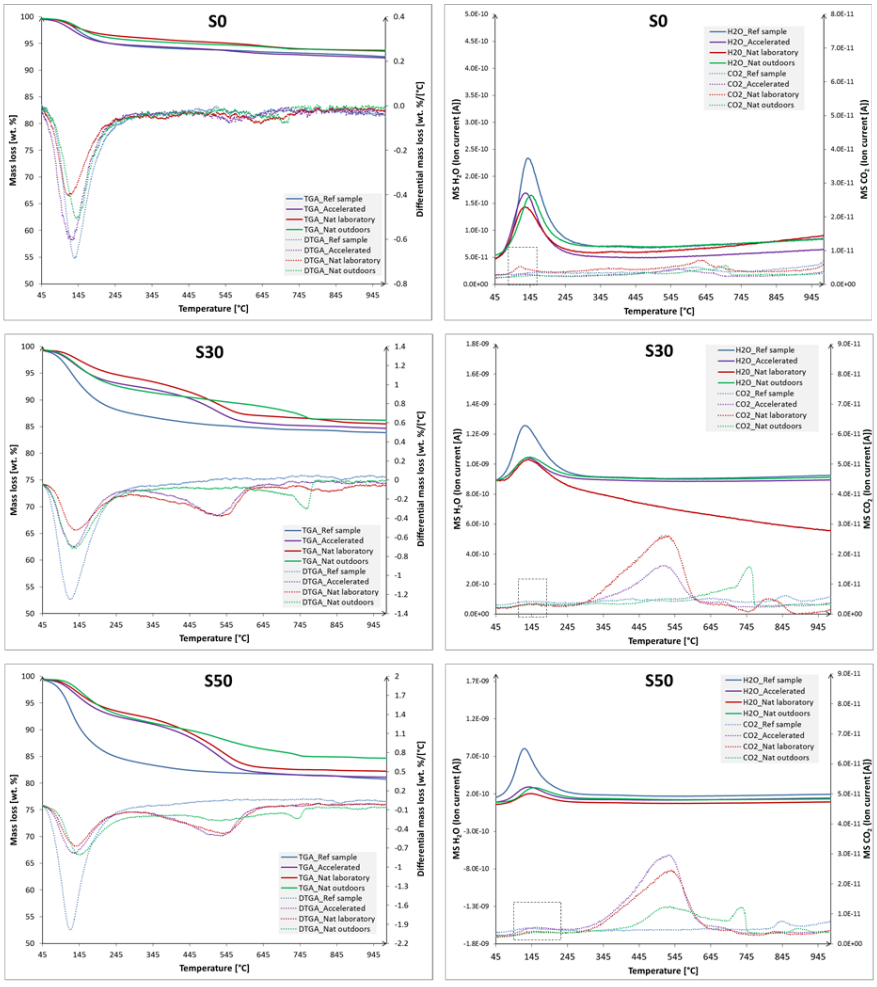


Figure 7.13: TG-DTG-MS curves for bulk paste samples after 1 year in different exposure conditions.

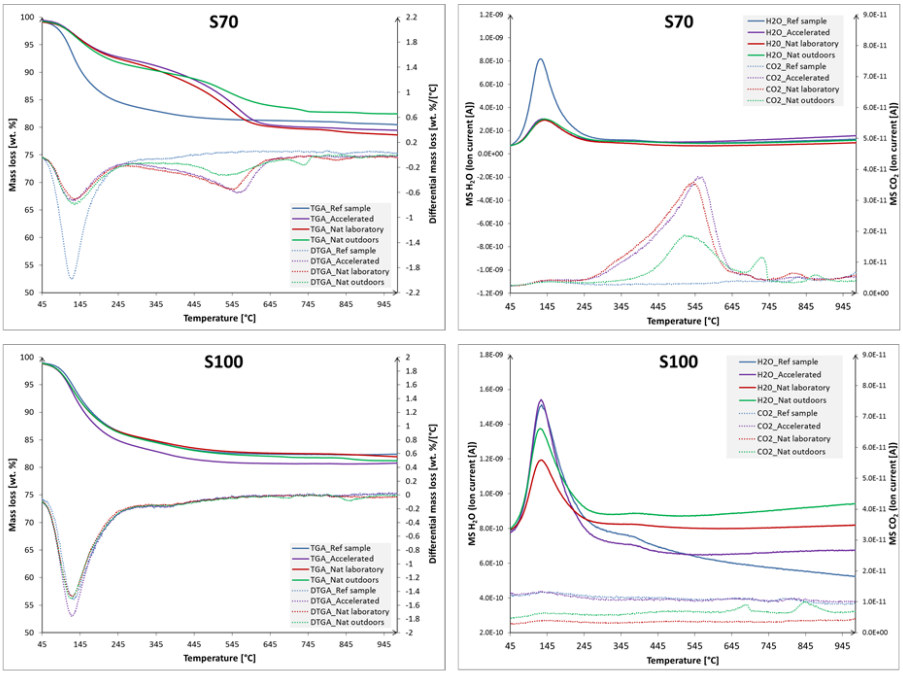


Figure 7.13: TG-DTG-MS curves for bulk paste samples after 1 year in different exposure conditions.

The maximum $CO_2$ binding capacity, according to Steinour [218], was determined from the total oxide content (Ca+Mg+Na+K) of raw FA and GGBFS powders. The real $CO_2$ binding capacity of alkali activated pastes is measured according to the procedure described in Chapter 5, Section 5.2.3.1. Overall, the measured $CO_2$ binding capacity of alkali activated pastes is much lower than the theoretical $CO_2$ binding capacity (see Table 7.2).

Table 7.2 also shows that the $CO_2$ binding capacity of alkali activated pastes is the lowest for natural outdoor conditions. This is attributed to outdoor weathering of the samples, where the average RH over the year is higher than 80% (for RH values, see Figure 6.3, Chapter 6). Moreover, the range for the temperature of $CO_2$ release for the samples which have been exposed in the natural outdoor conditions was different from the natural laboratory conditions. The difference in the conditions considered the RH, where for natural outdoor the RH was 80-99% and for indoor laboratory conditions it was around 50% RH. This demonstrates the role of RH on the type of $CaCO_3$ that is precipitating due to carbonation of alkali activated pastes. At low RH (50%, natural laboratory conditions) mainly low crystalline $CaCO_3$ was formed, while at high RH (80-90%, natural outdoor conditions) the high-crystalline $CaCO_3$ was formed, as shown by QXRD analysis (see Table 7.1, natural outdoor vs natural indoor conditions).

The $CO_2$ binding capacity of alkali activated pastes was different in accelerated and natural laboratory exposure conditions. Furthermore, the proportion of crystalline and amorphous $CaCO_3$ was different too. In accelerated exposure conditions, crystalline

$CaCO_3$ was dominant. When comparing the $CO_2$ binding capacity of carbonated bulk paste samples and carbonated powdered pastes under accelerated exposure conditions, powdered pastes have a higher $CO_2$ binding capacity. Hence, the pore structure plays an important role in the carbonation of bulk paste samples. It is likely that the bulk pastes have lower micropore volume or specific surface area than that of powdered pastes.

Table 7.2: The measured $CO_2$ binding capacity compared to the theoretical $CO_2$ binding capacity of water-free paste (expressed as values normalized to 100%).

| | $CO_2$ binding capacity Theoretical[a] [wt. %] | QXRD[b] (1 year) [wt. %] | TG-MS[c] (1 year) [wt. %] |
|---|---|---|---|
| Natural laboratory | | Bulk paste samples | |
| S0 | 11.36 | 0.32 | 7.14 |
| S30 | 17.33 | 3.51 | 10.79 |
| S50 | 21.59 | 3.46 | 11.89 |
| S70 | 24.05 | 3.53 | 16.34 |
| S100 | 28.34 | 0.04 | 5.78 |
| Natural outdoor | | Bulk paste samples | |
| S0 | 11.36 | 0.53 | 4.88 |
| S30 | 17.33 | 3.08 | 7.16 |
| S50 | 21.59 | 3.34 | 9.50 |
| S70 | 24.05 | 3.08 | 10.59 |
| S100 | 28.34 | 1.98 | 10.67 |
| Accelerated | | Bulk paste samples | |
| S0 | 11.36 | 0.31 | 4.72 |
| S30 | 17.33 | 4.27 | 8.27 |
| S50 | 21.59 | 4.97 | 13.80 |
| S70 | 24.05 | 4.97 | 16.30 |
| S100 | 28.34 | 0.00 | 1.31 |
| Accelerated | | Crushed powders (Ch. 5) | |
| S0 | 11.36 | 0.70 | 5.3 |
| S30 | 17.33 | 5.04 | 14.68 |
| S50 | 21.59 | 7.66 | 16.09 |
| S70 | 24.05 | 8.82 | 15.00 |
| S100 | 28.34 | 11.88 | 14.36 |

[a] The theoretical $CO_2$ binding capacity is the sum of the individual (earth) alkaline oxide $CO_2$ binding capacities (the amount of $CO_2$ bound as $CaCO_3$, $MgCO_3$, $NaHCO_3$, $KHCO_3$), calculated as shown in equation % $CO_2$ = 0.785(% CaO - 0.56% $CaCO_3$ - 0.7% $SO_3$) + 1.091% MgO + 1.42% $Na_2O$ + 0.94% $K_2O$ of Steinour [218]. The weight percent of oxides [%] was used from Table 3.1, Chapter 3. It should be noted that $Na_2O$ weight was accounted from both the raw material and from alkaline activator.
[b] $CO_2$ binding capacity from the quantitative phase analysis by Rietveld method for paste carbonated powders after 1 year of carbonation (Figure 7.12 and Table 7.1), i.e. the amount of $CO_2$ bound as crystalline $CaCO_3$ and $NaHCO_3$, which were detected with XRD analysis.
[c] $CO_2$ binding capacity from Figure 7.13, quantified with TG-DTG-MS method from the powders after 1 year of carbonation, i.e. the amount of $CO_2$ bound as amorphous and crystalline $CaCO_3$ and $NaHCO_3$, which were detected from the TG-DTG-MS analysis.

### 7.3.3. GEL MOLECULAR CHANGES WITH FTIR

It is well-known that carbonation changes the molecular structure of the C-S-H gel of the OPC-based pastes [212]. This change is a result of gel decalcification, silicate gel polymerization and formation of different types of carbonates in cement-based pastes. Since all alkali activated pastes in this study underwent carbonation, it is expected that their gel molecular structure has changed too. For that reason, FTIR is used to investigate these changes.

First, Figure 7.14 provides evidence of microscopic deterioration of the gel in paste S50. The carbonated paste consists of unreacted GGBFS and FA particles, silicate gel and remaining Ca-Na-Al-Si-H gel. Carbonation clearly modified the gel chemical composition by forming calcium carbonates as shown by QXRD (see Figure 7.12) and TG-MS (see Figure 7.13) and results in loss of the initial gel cohesion as shown in Figure 7.14.

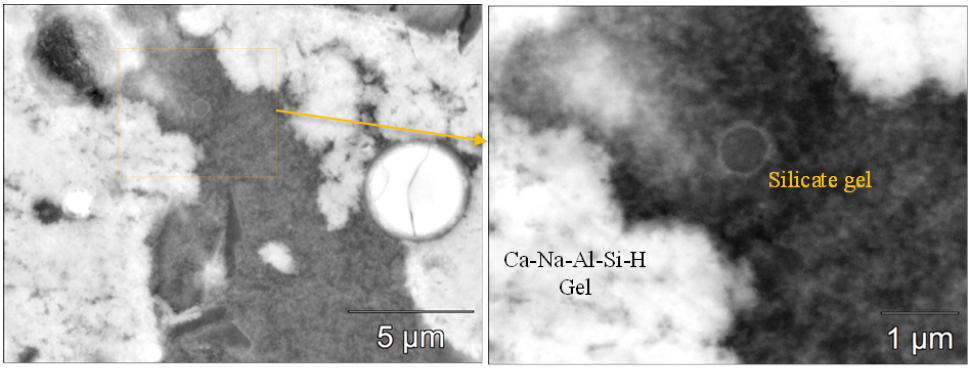


Figure 7.14: Gel morphology in carbonated paste S50 after 1 year of natural laboratory exposure. The right BSE image corresponds to the left image but magnified for observations of gel features.

To investigate gel molecular changes in depth, the FT-IR analysis focussed on difference between reference and carbonated alkali-activated pastes by following changes of silicate and carbonate groups. The Si-O stretching modes for the $SiQ^n$ units show infrared absorption bands localized around 1100, 1000, 950, 900 and 850 $cm^{-1}$ for n=4, 3, 2, 1 and 0, respectively [247]. These values shift to higher wavenumbers when the degree of silicon polymerization increases as shown in carbonated paste powders (see Chapter 5). In Figure 7.15 the change of primary bands due to carbonation were evaluated at 1 year of exposure, while reference spectra were recorded after 1 year of sealed curing.

The reference spectra of pastes S30, S50, S70 have the main band assigned to Si-O stretching vibrations of the $SiQ^2$ tetrahedra located at 960, 953, 947 $cm^{-1}$, which shifts to lower wavenumbers with increasing GGBFS content, i.e. with increasing Ca/Si ratio in the gel phases. This indicates depolymerisation of the silicate chains as shown by Yu et al. [204].

Figure 7.16 presents an overview of changes of the main Si-O-Si(Al) band position depending on the exposure conditions. For pastes S30, S50, S70 exposed to accelerated carbonation, the position for $SiQ^2$ appeared at higher wavenumber (1008 $cm^{-1}$, 1012 $cm^{-1}$, 1015 $cm^{-1}$) compared to reference spectra of pastes S30, S50, S70 (960 $cm^{-1}$, 953

$cm^{-1}$, 947 $cm^{-1}$) or to pastes which were exposed to natural conditions. The mechanism responsible for this change is polymerization of silicates due to water and calcium removal from the gel interlayer and surface spaces.

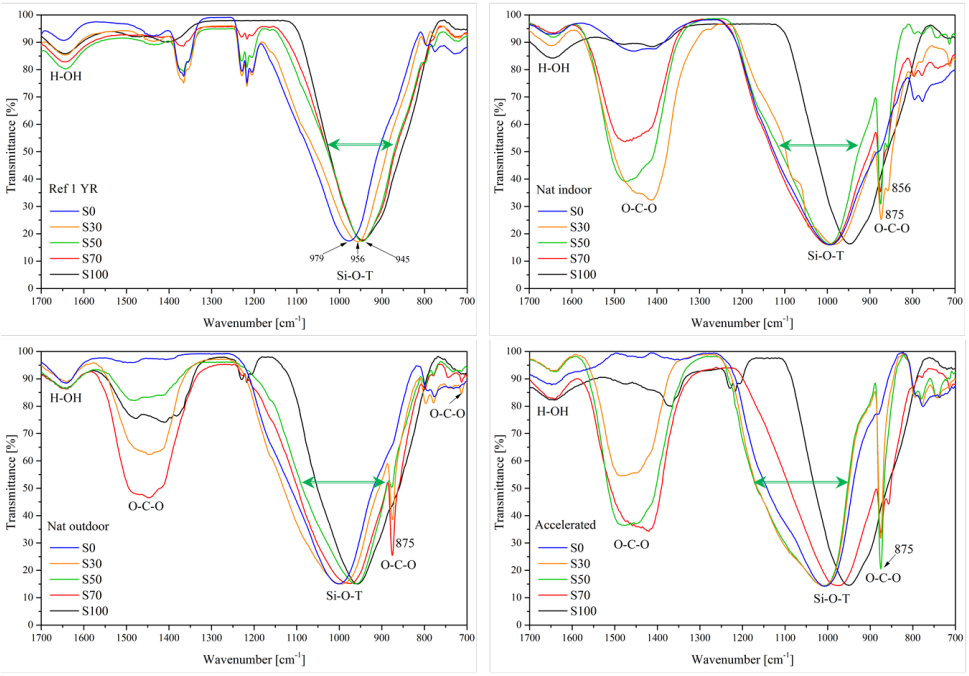


Figure 7.15: FT-IR spectra of alkali-activated pastes after 393 days of sealed curing (no carbonation) and FT-IR spectra of alkali-activated pastes subjected to different exposures for 1 year.

Subsequently, rearranging of the gel globules causes gel shrinking as demonstrated in Figure 7.14. The evidence of gel rearrangement is also inferred from nitrogen surface area measurements, which show variation of gel pore sizes and surface area with carbonation (see further Chapter 8). The excess of negative charge in the gel due to calcium removal is most likely balanced by adsorption of alkalis ($OH^-$, $Na^+$) in decalcified Ca-Na-Al-Si-H gel and formation of Si-OH or Si-ONa groups. Condensation of neighbouring groups Si-OH or Si-ONa into Si-O-Si moves the system towards the equilibrium, forming silicate gel following proposed reactions 5.4-5.6 in Chapter 5. The presence of Na can increase the content of non-bridging oxygen in the silicate structure. For that reason, polymerization of silicates gives broader Si-O-Si(Al) peak in the spectra of carbonated pastes compared to reference spectra in Figure 7.15 (indicated by green arrows for paste S50). This indicates the presence of molecularly coherent units of increasing size in the gel structure.

Spectra of the carbonated pastes S30, S50 and S70 contain also new features, which are associated with formation of carbonates with different intensities indicated by the presence of the large bands near 713, 856, 875, 1420 and 1490 $cm^{-1}$ (Figures 7.15). The intensity of the carbonate peaks varies depending on the exposure conditions. The same positions of the carbonate groups were identified for carbonated powdered pastes in Chapter 5 (Figure 5.10). Compared to standard FT-IR spectra for Ca-carbonates [202], bands at 713 $cm^{-1}$ and 875 $cm^{-1}$ are characteristic for vaterite and calcite, as found with XRD (Table 7.1). The bands at 1420 $cm^{-1}$ and 1490 $cm^{-1}$ correspond to amorphous $CaCO_3$. The amorphous $CaCO_3$ is identified in all pastes, which supports TG-MS results (Figure 7.13).

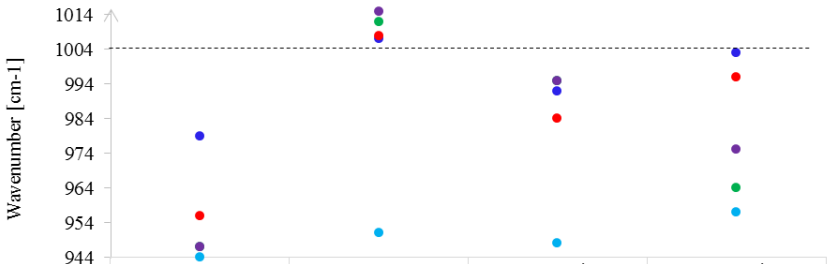


| | Ref samples_1 YR | Accelerated_1YR | Nat carb laboratory_1YR | Nat carb outdoors_1YR |
|---|---|---|---|---|
| S0 | 979 | 1007 | 992 | 1003 |
| S30 | 956 | 1008 | 984 | 996 |
| S50 | 947 | 1012 | 995 | 964 |
| S70 | 947 | 1015 | 995 | 975 |
| S100 | 944 | 951 | 948 | 957 |

Figure 7.16: Shift of the main Si-O-Si(Al) asymmetric stretching band of the alkali-activated pastes subjected to different exposures (1 year) compared to reference samples, which were sealed cured for 1 year.

In reference paste S0, the main band Si-O-Si(Al) is observed at 979 $cm^{-1}$ due to absence of calcium from the Na-Al-Si-H gel. In carbonated pastes S0 (accelerated and natural carbonation), this band is shifted to 1007 $cm^{-1}$ due to polymerization of the silicate gel. The increased extent of gel polymerization (979 $cm^{-1}$ → 1007 $cm^{-1}$) in pastes S0 under different exposure conditions is not due to carbonation of Na-Al-Si-H gel since Na-carbonates were not identified with XRD, consistent with findings of Bernal et al. [63]. It is believed that the pore solution carbonation of paste S0 can influence the extent of gel polymerization, i.e. rearrangement of the silicate units, but not in view of gel deterioration. This means that carbonation is less detrimental to the microstructure of paste S0, as observed later, and more detrimental to the pore solution of paste S0 as shown in Chapter 6.

Paste S100 did not carbonate under accelerated and natural indoor conditions as can be seen in Figure 7.15 (944 $cm^{-1}$ → 957 $cm^{-1}$). The absence of capillary pores and reduced gel porosity (supported by MIP and $N_2$ adsorption results in Chapter 4) did not allow $CO_2$ molecules to diffuse in paste S100. Only slight carbonation took place for paste S100 in natural outdoor carbonation in agreement with TG-MS results, due to microcracking of the samples under weathering.

Concerning the role of $CO_2$ concentration, it can be seen that the extent of gel polymerization increased with $CO_2$ concentration (from 0.04% v/v to 1% v/v $CO_2$, it increases from 995 $cm^{-1}$ → 1015 $cm^{-1}$, see Fig. 7.16). Comparing the extent of gel polymerization of alkali activated pastes from this study (1% v/v $CO_2$) and from Li et al. [209] (20% v/v $CO_2$) and Palacios et al. [59] (100% v/v $CO_2$), the extent of polymerization of alkali activated pastes is lower than in the latter two studies. This implies a much higher degree of deterioration of alkali activated pastes exposed to elevated concentrations of $CO_2$.

### 7.3.4. DISTRIBUTION AND CHEMICAL COMPOSITION OF GEL PHASES

Figure 7.17 shows the microstructure in both the core and the rim of S50 paste and corresponding domains separation with PARC (blue: mullite+AlSi glass; yellow: quartz; slag grain: purple; CaNaAlSi gel: green; NaMgAlSiCa gel: cyan; NaAlSi gel: light pink). The microcracking in Figure 7.17 originates from sample preparation, but also from carbonation (microstructure labelled as 2). The influence of carbonation on the domain proportions will be discussed by comparing microstructures in pastes S30 (Figure 7.18) and S50 (Figure 7.17).



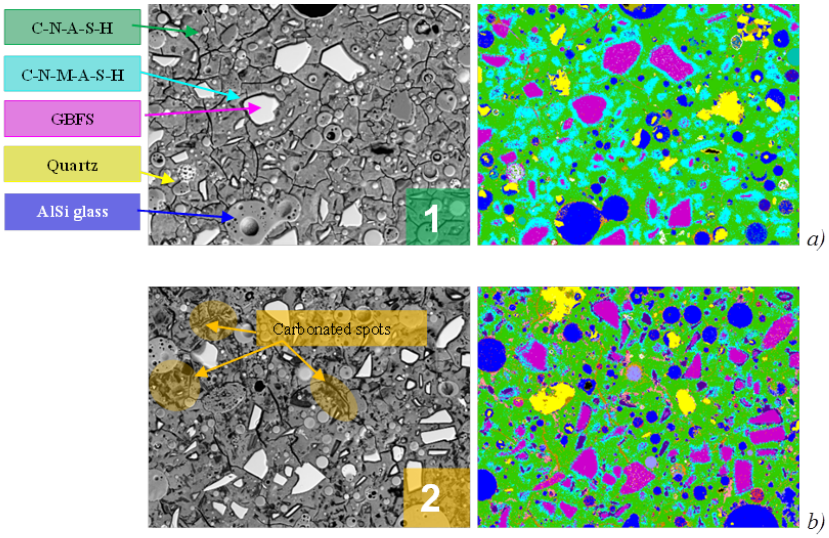


Figure 7.17: SEM-BSE images and compositional domains of S50 paste: core (a) and rim (b), obtained after 1 year of exposure to natural laboratory carbonation (0.04% v/v $CO_2$).

It was found that paste S30 was less resistant to carbonation compared to paste S50 (Chapter 6, see Figure 6.12). Both rim and core of paste S30 were carbonated (see Figure 7.18), and only the rim in paste S50 was deteriorated. Higher porosity of sample S30 as shown in Chapter 4 (Figure 4.30) and a lower Ca/Si ratio than in paste S50 explains the higher carbonation rate in this paste. Therefore, the pore structure turns out to be the governing factor which limits the propagation of the carbonation front.

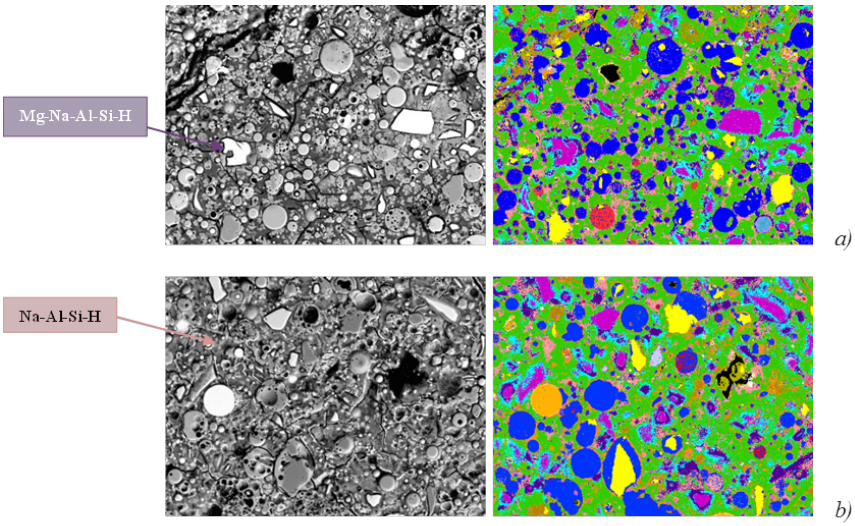


Figure 7.18: SEM-BSE images and compositional domains of S30 paste: core (a) and rim (b) obtained after 1 year of exposure to natural laboratory carbonation (0.04% v/v $CO_2$). Note that both core and rim of paste S30 were carbonated.

The carbonation of the pastes occurred predominantly around GGBFS particles (Figure 7.17 and Figure 7.18) (carbonation of Ca-Na-Mg-Al-Si-H gel) and throughout the gel (Ca-Na-Al-Si-H and Ca-Na-Si-H). The gel phases were partially decalcified. The carbonate phases were not detected with PARC, implying that the carbonates must be of nanometer size and intergrown with the gel (see Figure 7.14). This is consistent with optical microscopy observations and TG-MS results. The difference in gel contents (Ca-Na-Al-Si-H, Ca-Na-Mg-Al-Si-H) in Figure 7.19 between rim and core of S50 paste is apparently due to both a higher degree of reaction in the core compared to rim and an increase of the gel porosity after carbonation in the rim (because the total measured area remains 100%). Furthermore, a different reaction degree is also a reason for a higher fraction of AlSi grains in the rim than in the core. The result of gel decalcification in pastes S30 and S50 was formation of vaterite and calcite as shown with QXRD (Table 7.1).

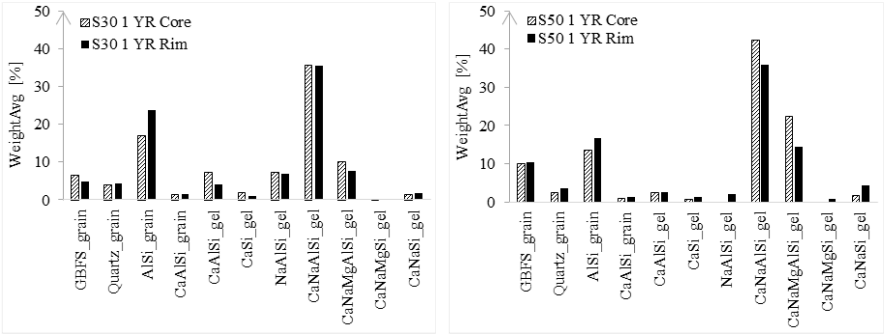


Figure 7.19: Weight proportions of compositional domains in core and rim of pastes S30 and S50, obtained after 1 year of exposure to natural laboratory carbonation (0.04% v/v $CO_2$).

## 7.3.5. OBSERVATIONS OF MICROSTRUCTURE

### 7.3.5.1. MORPHOLOGY

The change of the microstructure morphology of the pastes due to carbonation is presented in Figure 7.20. The difference between microstructures of reference pastes (1 year) and pastes exposed to indoor laboratory and accelerated carbonation conditions is clearly visible in blended pastes S30, S50 and S70. In reference pastes (1 year), a more uniform and denser microstructure is formed with a higher GGBFS content.

The difference of gel greyscale levels in backscattered electron (BSE) images between noncarbonated and carbonated areas can be seen in Figure 7.20. This difference is attributed to their different nanoporosities in carbonated specimens (see Chapter 8) and, therefore, to different densities and backscattered electron coefficients as found by Famy et al. [169] in carbonated cement pastes. This is in agreement with a previous study of Sisomphon et al. [248], who observed a similar morhology of the carbonated microstructure in GGBFS mortars (made by CEM III/B 42,5 N and CEM I 42,5 N) after 1 year of carbonation in the natural atmospheric conditions.

The microstructure of pastes S0 and S100 was not deteriorated under carbonation. This can be seen when the $CO_2$ exposed microstructures are compared to the corresponding reference microstructures. Paste S100 was very dense and hence it did not carbonate. This is in agreement with XRD and FT-IR analyses, which showed that the morhology of paste S100 is slightly or not at all altered. In contrast, paste S0 was carbonated only by pore solution carbonation. The reaction products in paste S0 were not altered, as confirmed by FTIR and XRD results. Therefore, blended pastes S30, S50 and S70 have been further studied with SEM-EDX for degree of decalcification.

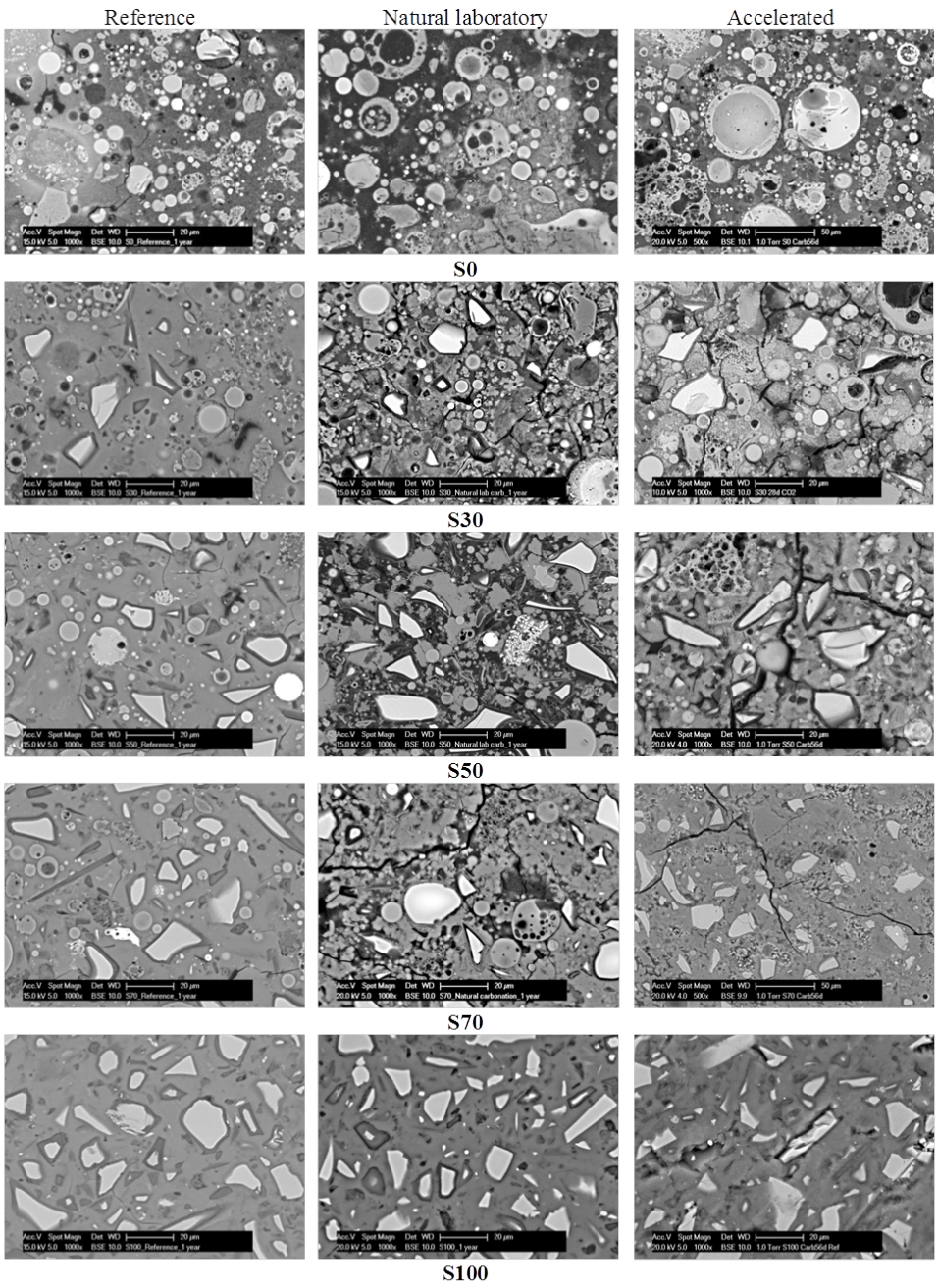


Figure 7.20: SEM-BSE images of the microstructures of reference samples (1 year), and the microstructures of samples after 1 year of exposure in the natural laboratory and accelerated conditions.

#### 7.3.5.2. CHEMICAL CHANGES

The atomic ratios Al/Si, Ca/Si, Na/Si, Mg/Si of the noncarbonated and carbonated areas in pastes S30, S50 and S70 determined by SEM-EDX analysis are presented in Table 7.3. An example of distinction between carbonated and noncarbonated areas is given in Figure 7.21. The corresponding map of decalcified spots in the microstructure S50 was extracted (cyan colour, see Figure 7.21). The map was used for point measurements. The spot analysis was done in such a way that unreacted FA and GGBFS particles or the rims between single particle and surrounding matrix were excluded from the analyses. However, due to possible cross-contamination of the EDS spectra, the lowest atomic ratios indicated by the extremity of the data cluster are reported in Table 7.3. Regardless of the GGBFS amount, the Na/Si ratio in the carbonated gel did not change significantly compared to the noncarbonated gel (Figure 7.22). The Mg/Si ratio showed significant variations in the distribution for pastes S50 and S70 compared to the paste S30. Paste S30 has the same Mg/Si ratio for both measured areas, i.e. carbonated and noncarbonated, because its composition consisted of only 30 wt.% of GGBFS and the results suggest that Mg has not formed other reaction products except being distributed in the gel. The results of Mg/Si ratio for pastes S50 and S70 suggest that the Mg is sporadically distributed throughout the gel and that some other reaction products consisting Mg, such as hydrotalcite showed by Haha et al. [185], are intermixed with the gel, causing the data scattering.

Table 7.3: Atomic ratios determined for the two areas of samples in natural laboratory conditions by SEM-EDX analyses.

| Sample | EDX area | Na/Si | Mg/Si | Ca/Si |
|---|---|---|---|---|
| S30 | Noncarbonated | 0.1 | 0.05 | 0.7 |
| | Carbonated nat. lab | 0.1 | 0.05 | 0.2 |
| S50 | Noncarbonated | 0.25 | 0.03 | 0.9 |
| | Carbonated nat. lab | 0.25 | 0.03 | 0.1 |
| S70 | Noncarbonated | - | 0.07 | 0.8 |
| | Carbonated nat. lab | - | 0.07 | 0.2 |

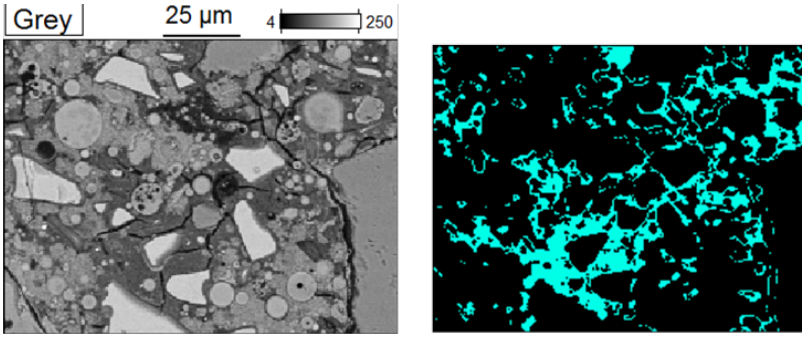


Figure 7.21: SEM-BSE image of carbonated paste microstructure S50 and the corresponding map of decalcified spots in the microstructure after 1 year of exposure in natural laboratory conditions.

Substantial decalcification (the last column in Table 7.3) have occurred in all blended pastes. The Ca/Si ratio has been reduced for the carbonated areas compared to the non-carbonated areas, but the gel was not completely decalcified. Instead, carbonation lowered the Ca/Si ratio. Although it was expected that the sample S70 has a higher decalcification than S50 since it has a higher Ca amount, the findings show that the decalcification degree was lower. This is most likely due to the finer pore structure of S70 sample compared to S50 sample, which hinders the $CO_2$ diffusion.

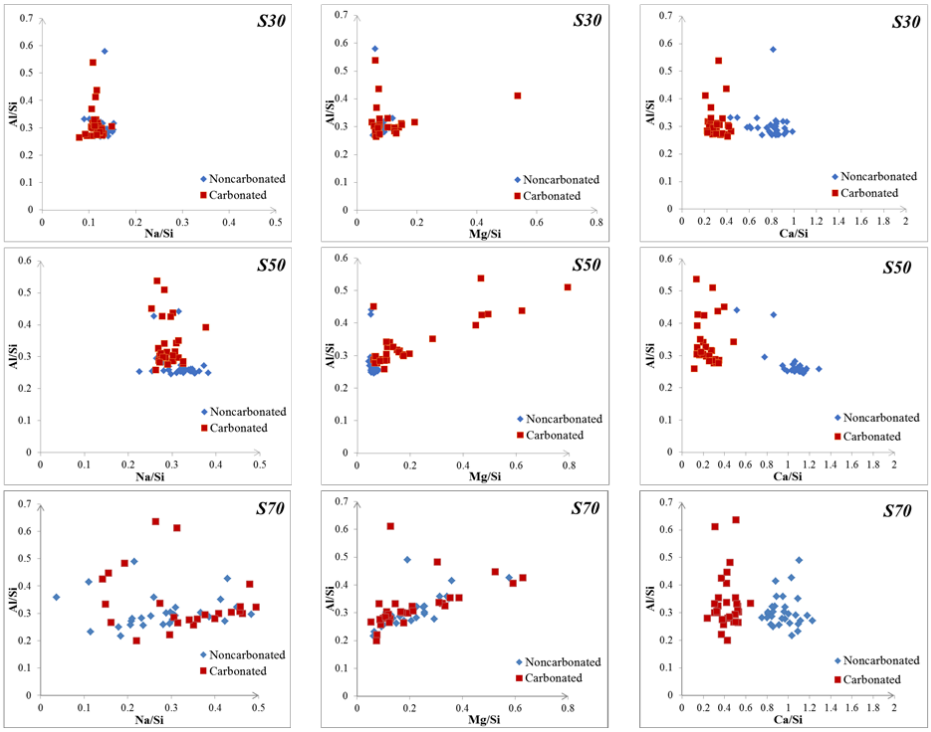


Figure 7.22: 2D scatter plots of EDX point analyses with different element atomic ratios in the carbonated and noncarbonated areas of the samples that were exposed in the natural laboratory conditions.

## 7.4. CONCLUDING REMARKS

In this chapter, the effect of carbonation on the gel element composition and gel phases distribution in the microstructure of alkali activated pastes has been investigated. The following conclusions can be drawn:

- *Element changes.* Element profiles (Figure 7.4 and Figure 7.10) indicated that Ca, S and Na show the most distinct spatial distributions in pastes S50 and S100 due to carbonation. From sample surface towards the noncarbonated core, several fronts were identified: carbonation, dissolution and sulfurization fronts. The carbonation front does not exactly coincide with dissolution front. The sulfurization front depends on oxidation extent, which in turn strongly depends on alkalinity of pore solution.

- *Distribution, identification and quantification of carbonation products.* From optical observations carbonates were present all over the paste microstructure. The carbonate phases were intergrown with gel phases and hence their identification was only possible with XRD/QXRD and TG-MS techniques. Based on XRD/QXRD and TG-MS results, two types of carbonates in carbonated bulk pastes were identified:

  1. crystalline carbonates (quantified with XRD, with known release temperatures in TG-MS),
  2. amorphous carbonates (quantified with TG-MS).

  The amount of amorphous carbonates was higher than of crystalline carbonates. $CO_2$ binding capacity of carbonated bulk pastes was lower than of the carbonated powdered pastes investigated in Chapter 5. Obviously, the pore structure plays an important role in the rate of carbonation of bulk alkali activated pastes. Additionally, $CO_2$ binding capacity of bulk alkali activated pastes is dependent on the amount of GGBFS and hence amount of gel phases.

- *Gel molecular structure.* Pastes S30, S50 and S70 have similar polymerization degree. In contrast, results showed that the alkali-activated FA (S0) was not carbonated in the studied conditions except its pore solution. The higher degree of polymerization in paste S0 was mainly due to rearrangement of the sodium aluminosilicate gel. Na-based carbonates were identified in very small amount. Hence, it is believed that major amount of Na was consumed for balancing the excess of negative charges in the gel due to $Ca^{2+}$-removal through formation of Si-OH or Si-ONa groups. Condensation of neighbouring Si-OH or Si-ONa groups into Si-O-Si formed silicate gel as confirmed with FT-IR.

- *Phase distribution and chemical composition.* Gel phases (Ca-Na-Al-Si-H/ Ca-Mg-Na-Al-Si-H/Ca-Al-Si-H, Ca-Si-H) were decalcified to varying degrees in pastes S30 and S50. The gel phases have a variable stoichiometry. That makes the kinetics of the gel dissolution difficult to constitute since the process most likely becomes diffusion-controlled at the microscopic level. The carbonation reaction

likely proceeds via interface pores 10-100 nm in size. Hence, the carbonation-induced chemical deterioration mechanism in pastes is a multiscale process, i.e. from nanoscale to microscale. Local microanalysis shows that carbonation of the alkali-activated GGBFS pastes was occurring predominantly around GGBFS particles (carbonation of Ca-Mg-Na-Al-Si-H gel). The gel decalcification was the main consequence of carbonation in studied pastes, accompanied by the microcracking.

- *Microstructure deterioration.* Finally, the effect of carbonation on the microstructure in alkali activated materials is different from that in the OPC-based materials. In OPC-based materials, carbonation densifies the microstructure and deterioration is not of concern. Hence, the existing engineering models for carbonation process assume implicitly that microstructure does not change after carbonation in OPC-based materials. The proposed models use carbonation coefficients to predict the propagation rate of carbonation front and focus only on the changes of the transport properties. However, in AAMs, the carbonation process as such modifies the gel phases and chemical deterioration is explicitly shown to be critical for mixtures S30 and S50. Based on the obtained effects of the carbonation on the microstructure of alkali activated FA/GGBFS pastes, the microstructure changes are necessary to be considered in the future predictive models for carbonation.

# 8

# EFFECT OF CARBONATION ON PORE STRUCTURE AND MODULUS OF ELASTICITY OF PASTES

*"For scientific explanations we need right indicators not currently used standards."*

Marija Nedeljković

*In Chapter 7, carbonation of the gel phases was investigated. The extent of chemical deterioration of the microstructure of alkali-activated pastes due to carbonation is shown to be significant and dependent on the binder composition. In this chapter, the effect of microstructure changes on the pore structure and modulus of elasticity is presented. The changes of the pore structure are relevant for long-term performance of alkali activated pastes. The pore structure and modulus of elasticity of the carbonated pastes were determined with mercury intrusion porosimetry (MIP), nitrogen ($N_2$) adsorption and nanoindentation. The results showed an increase of gel porosity of the pastes after carbonation. Furthermore, the increase of pore volume and pore size in the samples resulted in the weakening of cohesion within the paste. Consequently, the modulus of elasticity of carbonated blended pastes (S30, S50) was reduced. It is demonstrated that in addition to testing the alkalinity of the pore solution, the deterioration of alkali-activated fly ash (FA) and ground granulated blast furnace slag (GGBFS) pastes due to carbonation needs to be evaluated also by considering changes of modulus of elasticity.*

Parts of this chapter have been published in:
Nedeljković, M., Savija, B., Zuo, Y., Luković, M., Ye, G. (2017) Effect of natural carbonation on the pore structure and elastic modulus of the alkali-activated fly ash and slag pastes, Construction and Building materials.

## 8.1. INTRODUCTION

CARBONATION creates changes in the microstructure of pastes as shown in Chapter 7, which consequently can result in different pore size distributions and pore volume of carbonated and noncarbonated parts of the samples. These differences can significantly affect the transport and mechanical properties. Depending on the binder composition, the effect of carbonation on the pore structure can vary. For instance, carbonation of the $Ca(OH)_2$ in OPC-based pastes leads to a reduction in porosity of the pastes due to the positive difference between the molar volumes of $Ca(OH)_2$ and $CaCO_3$. Consequently, hardness and modulus of elasticity in cement paste increase [249, 250]. On the other hand, micro-mechanical properties of blended OPC and GGBFS (such as CEM III-B) pastes decrease due to carbonation, since they contain less $Ca(OH)_2$ and have a lower Ca/Si ratio in the C-S-H gel [219].

So far only a few studies have discussed pore structure changes and mechanical behavior of carbonated AAMs. For instance, Bakharev et al. [58] found that the alkali activated slag (AAS) concrete had higher strength loss than OPC concrete in two investigated exposure conditions, i.e. immersion in 0.352 molar (M) sodium bicarbonate solution and exposure to an atmosphere with 10–20% v/v $CO_2$ at 70% RH. Nevertheless, both conditions were highly aggressive and the results cannot be used directly to predict in-service behavior of AAS concrete subjected to natural carbonation.

Bernal et al. investigated accelerated carbonation of alkali silicate-activated GGBFS mortars exposed to 3.0±0.2% v/v $CO_2$, temperature of 20±2 °C and 65±5% RH [61]. Noncarbonated specimens had compressive strengths of up to 63 MPa after 28 days of curing when granulated GGBFS was used as a sole binder. The strength decreased by 40-50% due to carbonation.

Puertas et al. [60] studied the effect of carbonation on the compressive strength of AAS mortars. The carbonation tests were performed in $CO_2$ saturated chamber. The alkaline activator was varied among the mortars. When sodium waterglass was used as an activator, decalcification of the C-S-H gel prompted by carbonation led to a loss of cohesion of the microstructure, increase in total porosity and reduction of the compressive strength. On the other hand, when NaOH was used as activator, carbonation enhanced the compressive strength of the mortar. The authors assumed that this was due to precipitation of calcium carbonates in the pores, causing a decline in the total porosity and average pore size. In contrast, Li et al. [209] reported that the porosity of alkali activated GGBFS pastes after accelerated carbonation (RH of 65 ± 5%, temperature of 20±2 °C, 20±0.2% v/v $CO_2$) increased by 28.46%, 41.04%, 50.79%, and 60.20% when the modulus (MS=$SiO_2/Na_2O$) of sodium silicate solution in pastes was 0, 0.5, 1.0 and 1.5, respectively.

Since the effect of carbonation in the previous studies was mainly investigated on macro-mechanical properties of alkali-activated mortars or concretes, it is difficult to understand its effects on the pore structure and local micro-mechanical properties of the binder. Several parameters should be considered in order to come to correct interpretation of the results. The most important are the material scale, sample size and testing method.

- Effect of the material scale: For studying carbonation, pastes are more suitable than concrete. The presence of aggregates in the concrete encompasses the paste-aggregate interface. This interface can carbonate faster due to its higher porosity compared to the bulk paste. Therefore, the carbonation study on the paste samples is needed first for understanding the more complex carbonation mechanism at the concrete scale.
- Effect of the sample size: Carbonation reaction is dominant at the concrete surface and in the first millimeters from the surface. Testing the standard 150×150×150 $mm^3$ concrete cubes [NEN 12390-3:2009] will be useless for evaluating the effect of natural carbonation on the compressive strength if the carbonated concrete depth is only a few millimeters. Therefore, testing of the micromechanical properties provides a more reliable evaluation on local chemical deterioration of the paste, compared to a bulk test such as the compressive strength test of a standard concrete cube. Moreover, with a local analysis on the same sample, testing of both carbonated and noncarbonated areas is possible.

Considering these effects, the influence of carbonation on the pore structure and micromechanical properties at the paste level is the first step towards understanding the properties of carbonated concrete. Therefore, assessment of the micro-mechanical properties, such as modulus of elasticity, is needed. This might be of great importance for predicting the long-term performance and deterioration degree of AAMs under carbonation. Hence, the aim of this chapter is to evaluate the effect of carbonation reactions in the alkali-activated FA and GGBFS pastes on their pore structure properties and modulus of elasticity. MIP, $N_2$ adsorption, and nanoindentation were used to study the changes of pore structure and of modulus of elasticity of carbonated alkali activated pastes.

## 8.2. MATERIALS AND METHODS



### 8.2.1. MATERIALS

The material and mixture compositions were shown in Chapter 3.

### 8.2.2. METHODS AND SAMPLE PREPARATION

An overview of the exposure conditions and testing methods in this chapter is given in Table 8.1. The testing methods are described in following sections.

#### 8.2.2.1. COMPRESSIVE STRENGTH

Compressive strength tests for alkali activated pastes were performed on cubes 40×40×40 $mm^3$, according to NEN-EN-196-1. After demoulding, the samples were cured in unsealed conditions (at 20°C and ~99% RH) for 28 days. The evolution of strength was monitored during 62 days in accelerated carbonation conditions (20°C, 60% RH, 1% v/v $CO_2$) and in the laboratory conditions (20°C, 55% RH, 0.04% v/v $CO_2$). Then the mean values and standard deviations were calculated for each set of the data. Compressive strength results of reference samples (no $CO_2$) were presented in Chapter 3, Figure 3.14.

#### 8.2.2.2. PORE STRUCTURE CHARACTERIZATION - MIP AND $N_2$

Porosity and pore size distribution were investigated with MIP measurements combined with $N_2$ adsorption. The procedure for sample preparation was described in Chapter 4. The cylindrical samples were cured under sealed conditions for 28 days. After 28 days the samples were demolded and exposed to accelerated carbonation (20 °C, 60% RH, 1% v/v $CO_2$) and natural conditions (20 °C, 55% RH, 0.04% $CO_2$) for 1 year. In addition, reference samples were kept in sealed conditions (i.e. without $CO_2$) until the characterization of the pore structure was carried out.

Table 8.1: Exposure conditions and testing methods considered in this chapter.

| Exposure conditions | Compressive strength | Mercury intrusion porosimetry | $N_2$ adsorption | Nano-indentation |
|---|---|---|---|---|
| | Unsealed cured | Sealed cured | Sealed cured | Sealed cured |
| Reference (no $CO_2$) | √ | √ | √ | √ |
| Natural laboratory | √ | √ | √ | √ |
| Natural outdoor | | | √ | |
| Accelerated carbonation | √ | √ | √ | |

√ stands for studied type of samples

#### 8.2.2.3. MICROMECHANICAL PROPERTIES-NANOINDENTATION

Nanoindentation is a widely used technique for testing nano or micro-mechanical properties of cementitious materials [251–255] and also of AAMs [33, 85, 197, 256, 257]. It consists of indenting a sample surface with a diamond indenter, followed by a loading-unloading cycle while continuously recording the load and indentation depth. From the load-displacement slope and calibrated contact area, the modulus of elasticity of the material at the microscale can be determined. Here, nanoindentation was used to examine the modulus of elasticity for carbonated and noncarbonated areas. The cylindrical samples were cured under sealed conditions for 28 days. After 28 days the samples were demolded and exposed to laboratory conditions (20 °C, 55% RH, 0.04% v/v $CO_2$) for 1 year. In addition, reference samples were kept in sealed conditions (i.e. without $CO_2$) until the characterization of the micromechanical properties was carried out.

Nanoindentation testing was conducted using Agilent Nano Indenter G200, equipped with a Berkovich indenter. The samples for nanoindentation testing were first cut into slices of approximately 10 mm thickness. Then they were ground and polished manually following the procedure described in Table 8.2, to obtain a very flat and smooth ("mirror-like") surface. The tests were set in such a way that the loading was applied when the indenter comes into contact with the surface of the sample until a specified maximum penetration depth is reached. Afterwards, the load was maintained for 10 seconds followed by the unloading cycle. A typical example of an indentation curve is shown in Figure 8.1. A series of load-indentation depth curves were obtained. The indentation depth was 2000 nm. This depth was chosen because the scale of SEM analysis was ~2000 nm. This allows investigating correlation between chemical and micro-mechanical results, as reported by Ulm et al. [258, 259].

The measurements of the modulus of elasticity were performed on the top surface of the specimens. The measurements were obtained from a matrix of 15×15 indents, with a distance of 40 $\mu$m between individual indents. The indentation mesh for the noncarbonated sample S50 is visualized in Figure 8.2.

The modulus of elasticity of the selected points was determined based on the Continuous Stiffness Method developed by Oliver and Pharr [260]. The effect of non-rigid indenter on the load-displacement behavior must also be taken in account. This is achieved by defining a reduced modulus, $E_r$, which is calculated from the experimentally measured load-displacement slope (S=dP/dh) and calibrated contact area ($A_c$):

$$S = \frac{dP}{dh} = \frac{2}{\sqrt{\pi}} = E_r \sqrt{A_c} \tag{8.1}$$

$$S = \frac{\sqrt{\pi}}{2} \frac{\sqrt{S}}{\sqrt{A_c}} \tag{8.2}$$

Finally, the modulus of elasticity of the sample, $E_s$ (GPa) is calculated from the Equation 8.3:

$$\frac{1}{E_r} = \frac{(1-\upsilon_s)^2}{E_s} + \frac{(1-\upsilon_i)^2}{E_i} \tag{8.3}$$

where $\upsilon_s$ is the Poisson's ratio of the sample, which was assumed to be 0.18 for all measurements. $E_i$ is the modulus of elasticity of the diamond indenter, and $\upsilon_i$ is the Poisson's ratio of the diamond indenter ($E_i$ = 1141 GPa, $\upsilon_i$ = 0.07).

This method makes it possible that the modulus of elasticity is obtained as a continuous function of the indentation depth. For each indent, the average modulus of elasticity was determined from the loading range between 1000 and 1800 nm depth.

Table 8.2: Polishing procedure of the samples adopted in this study for SEM and Nanoindentation.

| Step | Sandpaper | Grit ($\mu$m) | Methods | Duration (min) |
|---|---|---|---|---|
| 1 | P-grade 120 | 12.5 | With ethanol | 5 |
| 2 | P-grade 320 | 46.2 | With ethanol | 5 |
| 3 | P-grade 500 | 30.2 | With ethanol | 5 |
| 4 | P-grade 800 | 25.8 | With ethanol | 5 |
| 5 | P-grade 1200 | 15.3 | With ethanol | 5 |
| 6 | Diamond paste | 6 | Ultrasonic bath with ethanol, air gun dry | 5 |
| 7 | Diamond paste | 3 | Ultrasonic bath with ethanol, air gun dry | 5 |
| 8 | Diamond paste | 1 | Ultrasonic bath with ethanol, air gun dry | 5 |
| 9 | Diamond paste | 0.25 | Ultrasonic bath with ethanol, air gun dry | 5 |

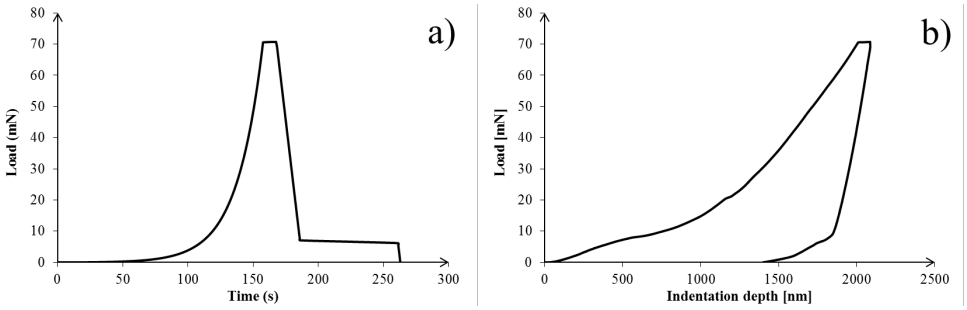


(a) (b)

Figure 8.1: Example of (a) load-time and (b) load-indentation depth curves by nanoindentation.

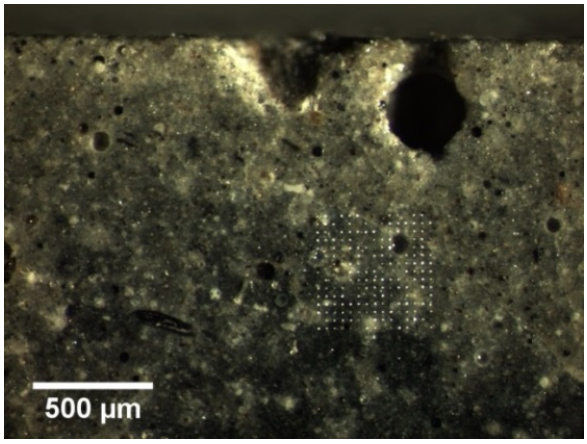


Figure 8.2: Light microscope photo of the area of indents in noncarbonated S50 sample.

## 8.3. RESULTS

### 8.3.1. COMPARISON OF THE PORE STRUCTURE BETWEEN THE NONCARBONATED AND CARBONATED ALKALI ACTIVATED PASTES MEASURED WITH MIP

MIP results for cumulative intrusion and corresponding pore size distributions obtained for carbonated and reference samples are presented in Figure 8.3. The results show that the incorporation of GGBFS in the pastes results in a refined microstructure with lower threshold pore size, as observed for pastes at 28 days (Figure 4.31, Chapter 4). There are two peaks in the differential curve for reference paste S30. The first peak at 10 nm is representative for gel pores. The second peak at 200 nm is typical for capillary pores.

Due to carbonation the peaks corresponding to gel and capillary pores of paste S30 were shifted toward larger pore sizes, suggesting coarsening of the pore structure. This

increase is due to carbonation-induced decalcification of C-(N-)A-S-H gel. The same tendency is observed for pastes S50 and S70. This implies that the pore structure of blended pastes becomes coarser after carbonation. Nevertheless, the peaks are not equal: it seems that with higher amount of GGBFS (S50 and S100), pastes are less deteriorated and, therefore, the pore size distribution is less changed than in paste S30. During 1 year of exposure, pore structure of the paste S100 was not changed at all, suggesting that the $CO_2$ could not diffuse in this paste.

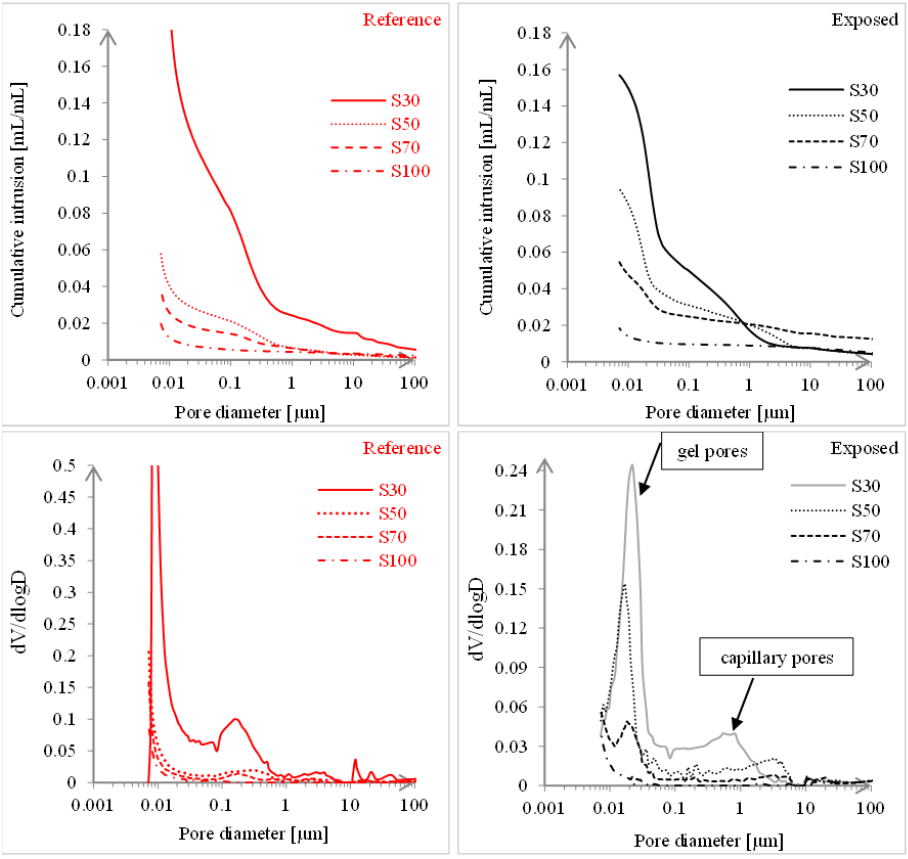


Figure 8.3: MIP capillary pore volume and pore size distribution (reference and exposed samples (natural laboratory) after 1 year).

The determined pore structure properties of reference and exposed pastes are compared in Table 8.3. Pastes with higher GGBFS content have low total porosity and threshold pore diameter. The threshold pore size could not be determined for reference samples S30, S50, S70 and S100 due to their dense microstructures. However, paste S0 exhibited an increase in total porosity, most probably due to reorganization of the gel molecular structure during carbonation.

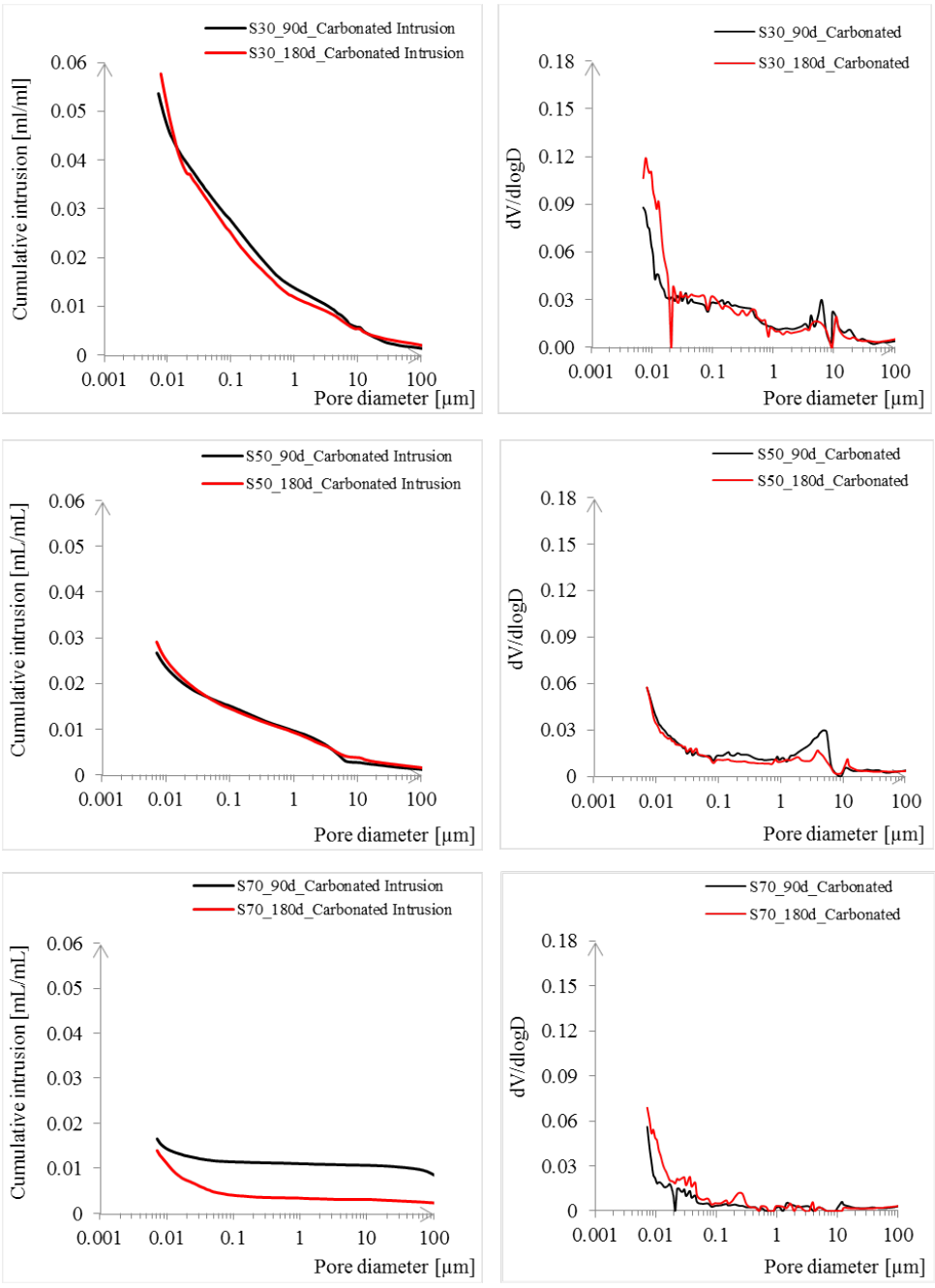


Figure 8.4: Pore volume and pore size distribution of pastes S30, S50 and S70 after accelerated carbonation.

Table 8.3: Capillary pore structure properties of reference and carbonated samples after 1 year determined with MIP.

| | Threshold pore access diameter [$\mu$m] | | Total porosity [%] | |
|---|---|---|---|---|
| Paste | Reference | Exposed | Reference | Exposed |
| S0 | 0.11 | 0.134 | 37.40 | 43.72 |
| S30 | - | 0.030 | 15.73 | 26.22 |
| S50 | - | 0.028 | 7.50 | 17.09 |
| S70 | - | 0.026 | 3.50 | 9.66 |
| S100 | - | - | 2.01 | 3.38 |

In Figure 8.4, the change of capillary porosity due to accelerated carbonation is shown for samples S30, S50 and S70. Only carbonated pastes S30 have a distinct peaks in the curves. These peaks are absent in the curves for pastes S50 and S70. This is because the main change for these samples occurs at the pore size smaller than the testing limits of MIP, as will be shown with $N_2$ adsorption tests. MIP results showed that the pore structure of pastes S0 and S100 was not affected by the carbonation and, therefore, results are not presented.

### 8.3.2. COMPARISON OF THE PORE STRUCTURE BETWEEN THE NONCARBONATED AND CARBONATED ALKALI ACTIVATED PASTES MEASURED WITH $N_2$

In order to study the effect of carbonation on the gel pore structure, the $N_2$ adsorption method was used. In general, the shape of a $N_2$ adsorption isotherm can be used to determine whether the pores present in the sample are micropores (below 2 nm), mesopores (between 2 and 50 nm) or macropores (above 50 nm) [178, 191].

Based on Jennings' colloid C-S-H model [261], there are two types of gel pores within C-S-H that can be identified with $N_2$ adsorption: the small gel pores (SGP, 1-3 nm) and large gel pores (LGP, 3-12 nm). Figure 8.5 presents the gel pore size distribution and differential curves of the studied pastes (S0-S100) as a function of exposure conditions:

- Sealed conditions (reference, no carbonation),
- Natural laboratory carbonation (0.04% v/v $CO_2$, 55% RH),
- Natural outdoor carbonation (0.04% v/v $CO_2$, 80% RH),
- Accelerated carbonation (1% v/v $CO_2$, 60% RH).

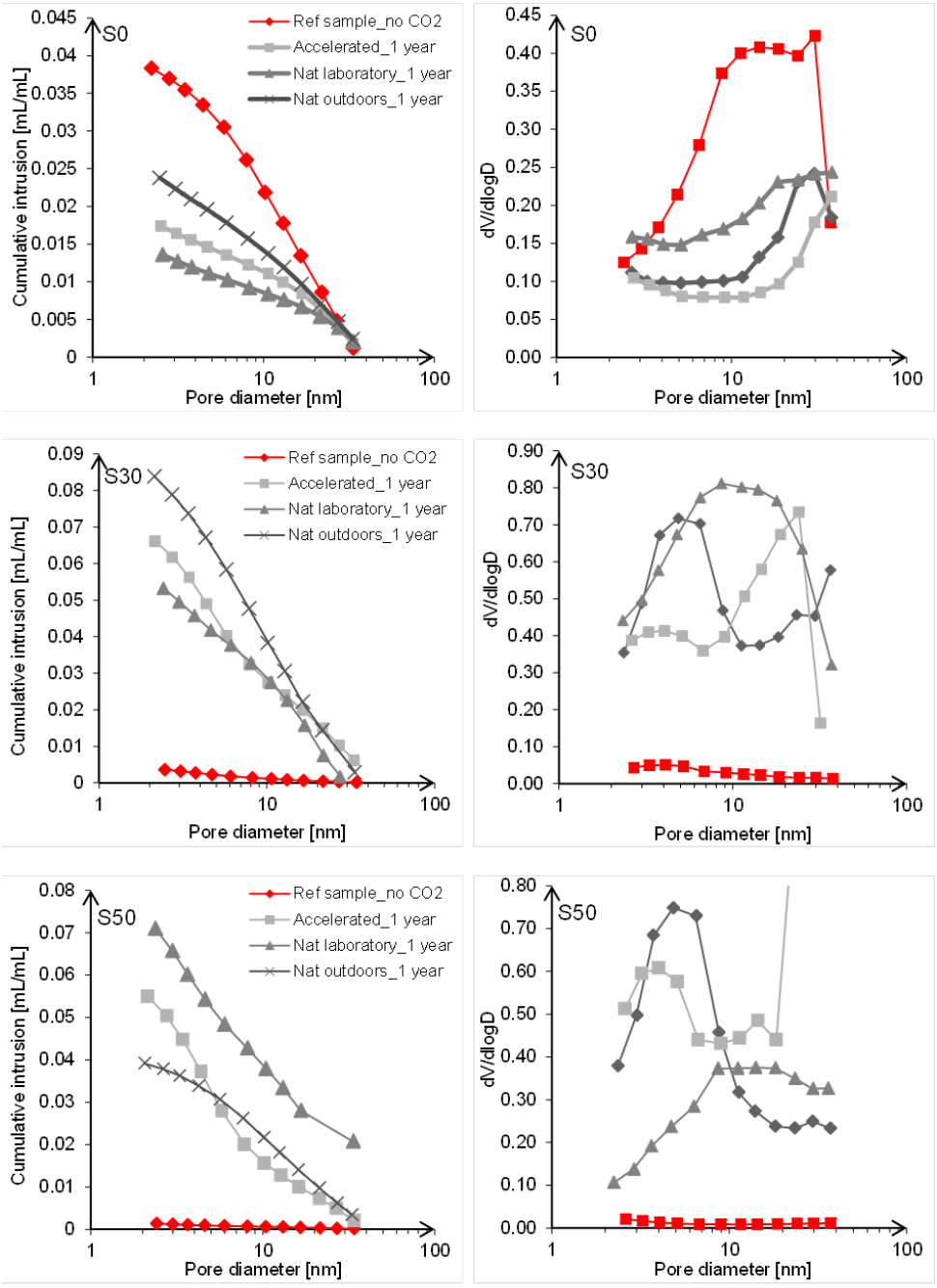


Figure 8.5: Pore size distributions determined with (Nitrogen adsorption) of pastes under different exposure conditions. Age: 1 year. Note different values on Y-scale for cumulative intrusion.

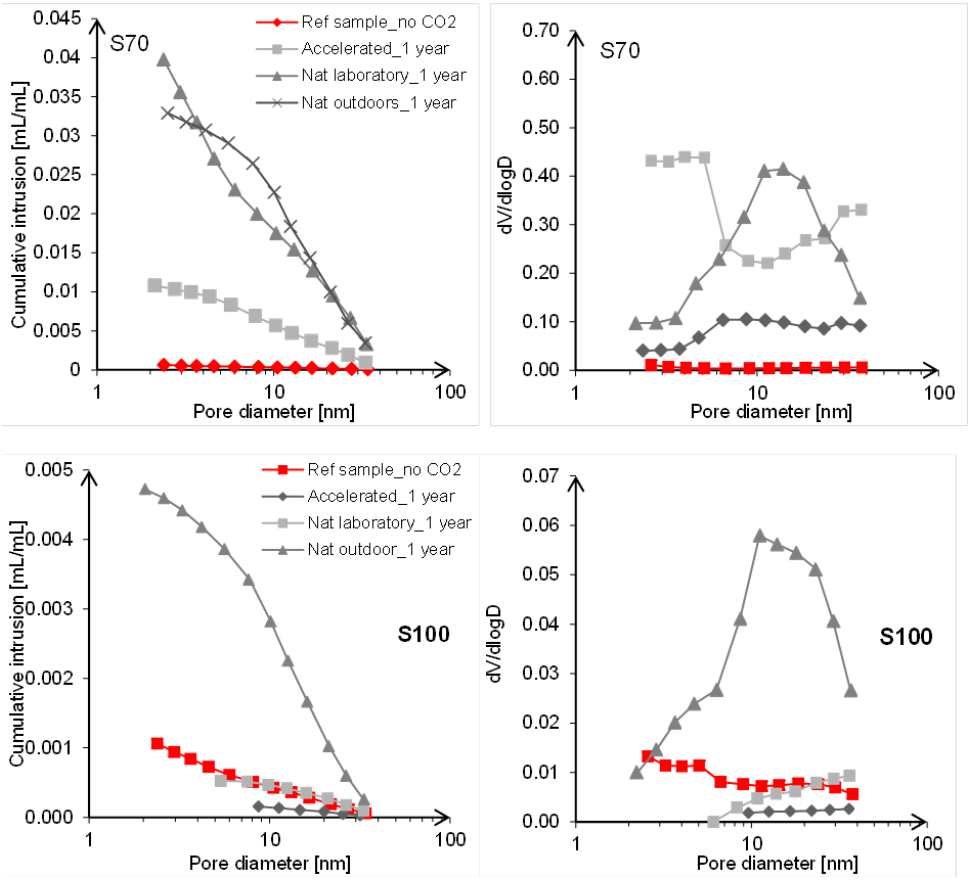


Figure 8.5: Pore size distributions determined with (Nitrogen adsorption) of pastes under different exposure conditions. Age: 1 year. Note different values on Y-scale for cumulative intrusion.



Figure 8.5 shows no distinct peak in the red differential curves for pores of reference pastes S30, S50, S70 and S100. This suggests a large reduction of pores during 1 year of sealed curing (between 2 and 50 nm) compared to their volume in pastes at 28 days (Chapter 4, Figure 4.33). Most likely the volume of pores (< 2 nm) contributes to a great extent to pore volume in these samples. The pores < 2nm can not be detected with $N_2$ adsorption, since they are intraglobule pores inside the Ca-Na-Al-Si-H gel structure [261]. These pores are not of interest because $CO_2$ diffusion takes place mainly in connected mesopores and macropores.

The changes during 1 year of BET surface area, i.e. the increase of the gel pore surfaces of alkali activated pastes in different exposure conditions, is presented in Table 8.4. The largest differences between reference and $CO_2$ exposed samples were found for pastes S30 and S50. The results showed that the carbonated paste S50 has more than 20 times higher BET surface area after exposure to natural carbonation conditions compared to the reference sample. The BET surface area is linked to the surface area of pores

with diameter between 2-50 nm. This increase is attributed to the negative difference between the molar volumes of Ca-Na-Al-Si-H gel and $CaCO_3$.

Table 8.4: Evolution of BET surface area of pores with diameter 2-50 nm in alkali activated pastes in different exposure conditions, at age of 1 year.

| | $BET_{N2}$ surface area ($m^2/g$) | | | | |
|---|---|---|---|---|---|
| Exposure conditions | S0 | S30 | S50 | S70 | S100 |
| Reference (no $CO_2$) | 15.85 | 2.58 | 1.58 | 0.89 | 0.78 |
| Accelerated (1% $CO_2$) | 7.95 | 33.42 | 32.45 | 4.94 | 0.03 |
| Natural laboratory | 6.71 | 27.91 | 34.89 | 25.00 | 0.25 |
| Natural outdoor | 11.76 | 41.71 | 16.65 | 12.99 | 1.72 |

For an explanation of the extremely low intrusion volume of paste S100, $N_2$ adsorption isotherms are considered. Figure 8.6 shows $N_2$ adsorption isotherms for four samples of S100 paste. The isotherm for the sample in the natural *outdoor* conditions has a steady increase in the adsorbed volume at approximately $p/p_0$=0.4 and a sharp increase in adsorbed volume from 0.7 to around $p/p_0$=0.96. This increase can be due to more severe *outdoor* weathering of the material. Still, the comparison of the quantities of adsorbed $N_2$ between paste S100 in *outdoor* conditions (0.138 mmol/g) and of the pure $C_3S$ paste which is supposed to be very dense (~2 mmol/g) [262], indicated a much denser microstructure of paste S100. Other curves in Figure 8.6 indicated almost nonporous material, since the quantity of adsorbed $N_2$ hardly exceeded 0.02 mmol/g. Furthermore, Figure 8.5 shows that the pore size distribution (PSD) is in the range of pores with diameter of 2 nm and maximum pore diameter of 15 nm. The transport mode for this range of pores sizes conforms Knudsen diffusion, according to Houst and Wittmann [263]. This means that the pore sizes are smaller than the mean free path of the gas molecules ($O_2$ or $CO_2$). Therefore, it is believed that this low accessibility of the gel pores for $O_2$ or $CO_2$ is the main reason for carbonation resistance of S100 bulk paste samples.



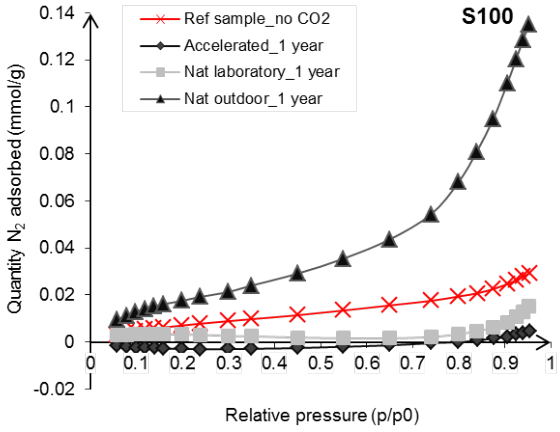


Figure 8.6: $N_2$ adsorption isotherms for pastes S100. Age: 1 year.

### 8.3.3. EFFECT OF CARBONATION ON THE COMPRESSIVE STRENGTH OF PASTES

The carbonation-induced coarsening of the microstructure, as demonstrated with pore structure measurements, is also addressed from the point of view of mechanical performance. The effect of accelerated carbonation (1% v/v $CO_2$) on compressive strength of alkali-activated fly ash and slag pastes cured in unsealed conditions shown in Figure 8.7 was evaluated by comparing the strength of these samples with those exposed to natural carbonation (0.04% v/v $CO_2$, Figure 8.8). Compressive strength results of reference cubic samples (no $CO_2$) were presented in Chapter 3, Figure 3.14. Complete carbonation of the pastes exposed to accelerated carbonation leads to dramatic reduction of compressive strength of pastes S30, S50, S70, as shown in Figures 8.7.

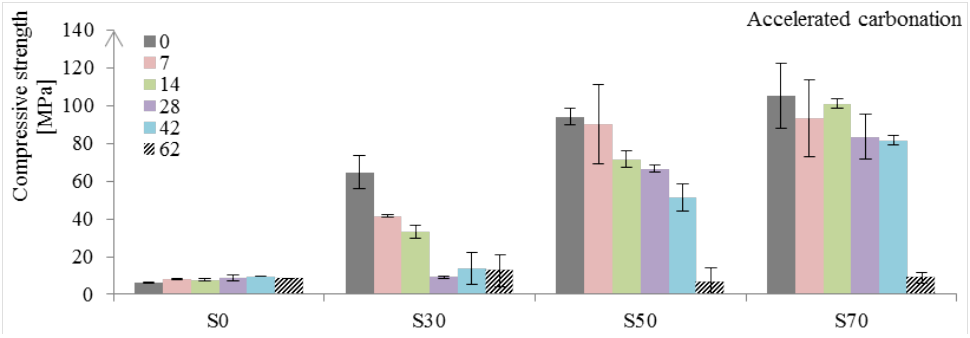


Figure 8.7: Effect of accelerated carbonation (1% v/v $CO_2$) on the compressive strength of pastes S0, S30, S50, S70. Samples (40×40×40 $mm^3$) were unsealed cured for 28 days in fog room (at 20°C and 99% RH) and after that preconditioned for additional 28 days in laboratory conditions at 20°C and 55% RH. Subsequently, samples were exposed to accelerated carbonation for 62 days.

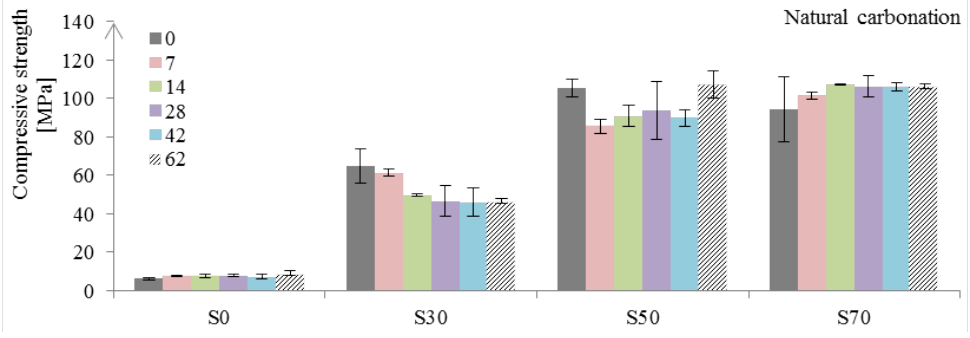


Figure 8.8: Effect of natural carbonation (0.04% v/v $CO_2$) on the compressive strength of pastes S0, S30, S50, S70. Samples (40×40×40 $mm^3$) were unsealed cured for 28 days in fog room (at 20°C and 99% RH) and after that preconditioned for additional 28 days in laboratory conditions at 20°C and 55% RH. Subsequently, samples were kept exposed to natural laboratory carbonation for 62 days.

The compressive strength of pastes exposed to accelerated carbonation declines rapidly with increasing time of exposure (see Figure 8.7). This decline is attributed to the deterioration of Ca-Na-Al-Si-H gel. The decomposition of Ca-Na-Al-Si-H gel content was

observed with TG-MS measurements presented in Chapter 7. Furthermore, the eroded pastes shown in Figure 8.9 and Figure 8.10, left, marks several physical discontinuities in the sample and results in weakening of the cohesion within the paste under accelerated carbonation. Here, it is demonstrated that accelerated carbonation conditions are not appropriate for investigating carbonation effects on the compressive strength. The samples crumble under hand pressure. Hence, testing bulk strength of the samples in order to see the difference between carbonated and noncarbonated parts is not the most appropriate way. Therefore, the local measurement of the mechanical properties, such as with nanoidentation, would be more appropriate so that clear difference between properties of carbonated and noncarbonated part of the sample can be obtained and not their average strengths. In addition, nanoidentation tests were done only for natural carbonation conditions.

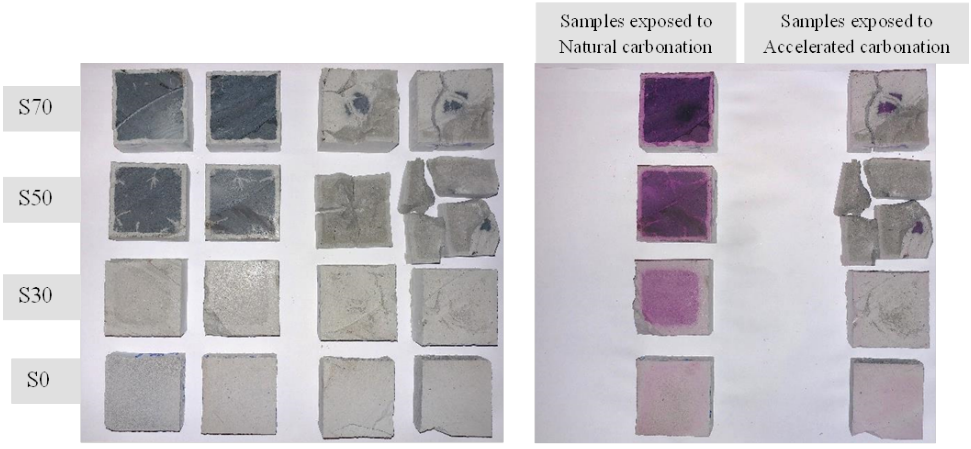


Figure 8.9: Cubic paste samples (40×40×40 mm$^3$) splitted and tested for carbonation depth (on the left are the samples before applying phenolphthalein indicator and on the right after applying the indicator).


Figure 8.10: Appearance of the sample S30 after compressive stength tests. Left: sample surface eroded by accelerated carbonation, right: sample's surface exposed to natural laboratory carbonation.

Figure 8.11 presents compressive strength development in S100 during 56 days of curing and preconditioning. The strengths are higher than those reported in previous

studies [159, 185]. This is mainly due to the difference in alkaline solution composition (% $Na_2O$, $SiO_2/Na_2O$ modulus ratio). The relatively low $Na_2O$ concentration used in this work (4.8% $Na_2O$/100g of GGBFS compared to the 5, 10, 15 wt.% $Na_2O$ in [132]) favored effective dissolution of GGBFS and formation of C-(N-)A-S-H gel, which is responsible for the strength gain.

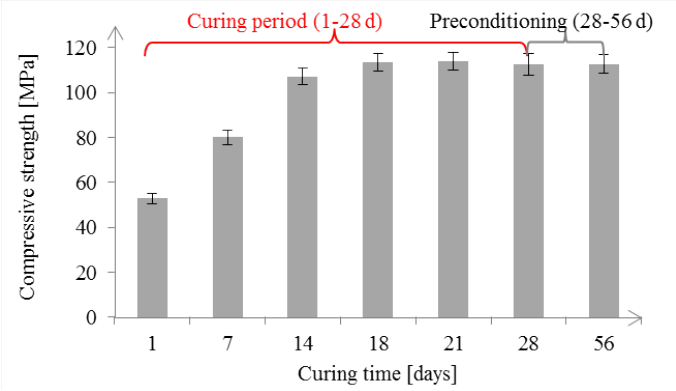


Figure 8.11: Compressive strength of pastes S100 during curing and preconditioning.

In Figure 8.12, the compressive strengths of pastes S100 exposed to natural laboratory and accelerated carbonation conditions are shown. There is no significant difference in strength results from two different exposure conditions. This is consistent with $N_2$ adsorption results, where it was shown that the pore size distribution stays unmodified regardless the exposure conditions.

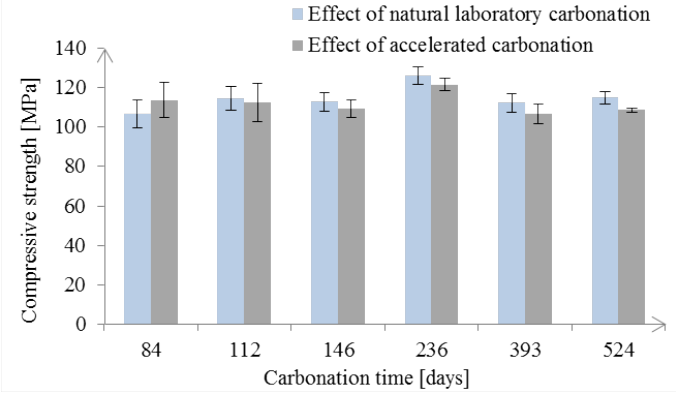


Figure 8.12: Compressive strength of pastes S100 during carbonation exposure.

### 8.3.4. MODULUS OF ELASTICITY OF ALKALI ACTIVATED PASTES BY NANOIDENTATION

In OPC-based materials, carbonation mainly affects the alkalinity of the pore solution. The change of (compressive) strength and modulus of elasticity upon carbonation of OPC-based materials and CEM III/B were never a concern for material and structural performance, although it was reported that the compressive strength of CEM III/B systems is decreasing under carbonation [219, 248]. It was demonstrated in previous study [209] and in this study that the compressive strength of alkali activated FA/GGBFS pastes, except paste S100, is substantially reduced due to accelerated carbonation. Given this information, it is of high importance also to know potential changes of modulus of elasticity of pastes under carbonation. A reduction of the modulus of elasticity of the paste can seriously affect stiffness of the concrete structure and structural reliability, specifically because the carbonation is faster in alkali activated FA/GGBFS materials than in OPC-based material as will be shown in Chapter 10 (see Figure 10.17). For that reason, this section deals with investigation of modulus of elasticity at micro level.

The samples used for microscopic examination and measurements of modulus of elasticity are shown in Figure 8.13. The carbonation depth was determined with a polarized light microscope (PLM) under cross polarized light as discussed in Chapter 7, see Figure 7.3. The carbonation depths after 1 year exposure are presented in Figure 8.14.


Figure 8.13: Cross-sections of representative samples after natural laboratory carbonation of 1 year, clearly showing the outer (carbonated) and the inner (noncarbonated) zone. Reference samples are of smaller diameter, placed beneath the exposed samples.

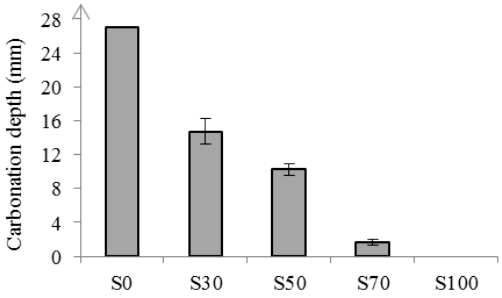


Figure 8.14: Carbonation depth after 1 year exposure in the natural laboratory conditions, determined with PLM in the alkali-activated pastes as a function of the GGBFS content.

The area of indents is visualized with the optical microscope for the samples S50 (Figure 8.15) and S100 (Figure 8.16). Both pastes have the grey/brownish background, which is the gel phase. The brightest irregular shaped particles are the unreacted GGBFS particles and the slightly bright/white particles are partially reacted FA and GGBFS particles.

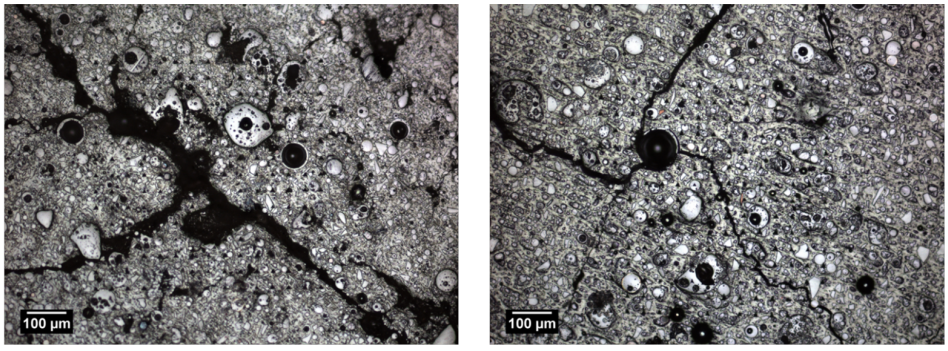


Figure 8.15: Optical microscope photo of sample S50 in the natural laboratory conditions. Left: edge and right: core. Age: 1 year.

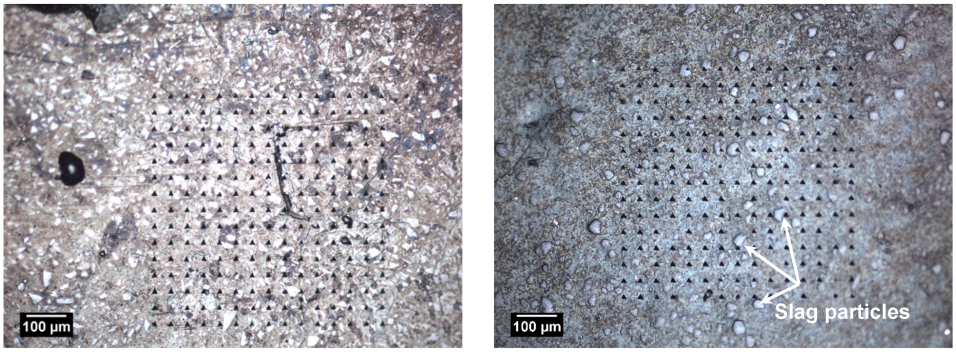


Figure 8.16: Optical microscope photo of sample S100 in the natural laboratory conditions. Left: edge and right: core. Age: 1 year.

The intermixing of the phases can be expected in the measurements due to inherent heterogenous nature of the studied material. However, the number of indents (200 in this study) was assumed to be statistically representative of the regions of interest, i.e. noncarbonated and carbonated, similar to [251]. For instance, Figure 8.16 shows noncarbonated areas of indents in the sample S100. It can be seen clearly that the proportion of the indents printed on the rims between large GGBFS particles and the gel, is much less compared to the proportion of the indents printed solely in the gel. When the effect of carbonation on the mechanical properties is tested in a standard way, such as sample bulk testing of compressive strength of concrete [NEN 12390-3:2009], the intermixing of the phases is far worse, since such a bulk analysis cannot separate the modulus of elasticity values for different phases in the system. The representative SEM images of indents

in the noncarbonated area (blue triangles) in sample S50 are shown in Figure 8.17 (1, 2). In contrast, Figure 8.17 (3, 4) show loss of microstructure cohesion (microcracks) in the carbonated areas. The change of the microstructure due to carbonation is visible in the vicinity and around the indents (red triangles).

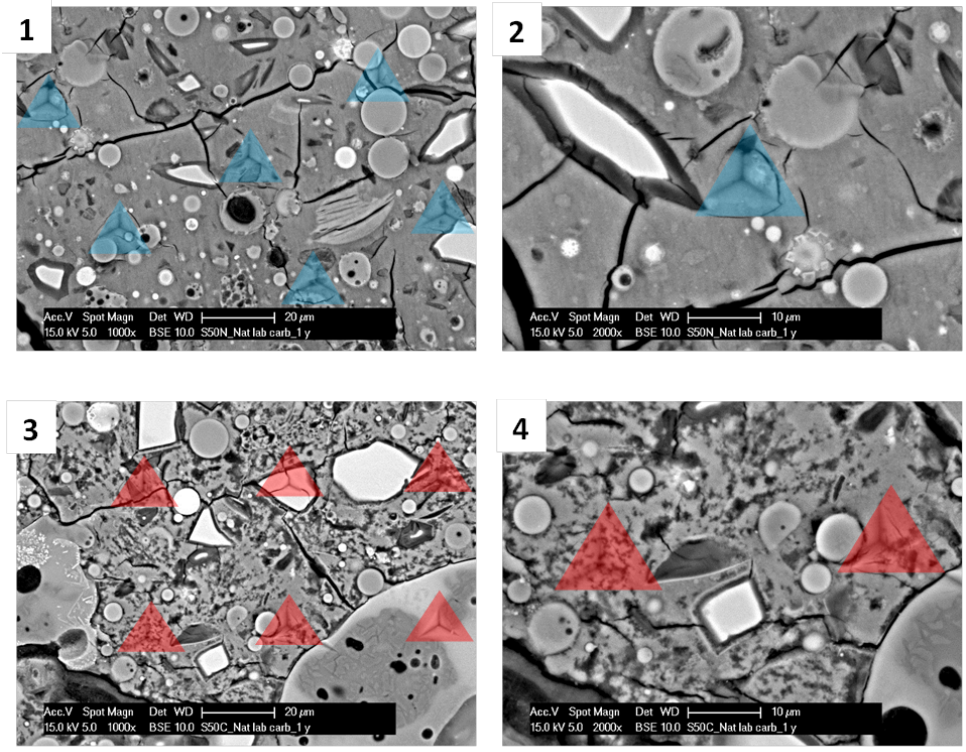


Figure 8.17: Visualization of an indentation size for nanoindentation of the noncarbonated (1, 2) and carbonated (3,4) microstructure morphology observed under the SEM. Age: 1 year.

Figure 8.18 shows a comparison between the results for modulus of elasticity in the carbonated and noncarbonated indented areas in the form of a histogram. Every histogram represents approximately 200 indents from the sample.

Four intervals of modulus of elasticity were defined and linked to the modulus of elasticity value of four features in the samples:

- pores, $E_m$<4 GPa,
- carbonated C-(N-)A-S-H gel, 4<$E_m$<21 GPa,
- noncarbonated C-(N-)A-S-H gel, 21<$E_m$<45 GPa,
- unreacted FA and GGBFS particles, $E_m$>46 GPa.

The definition of the four intervals defined in this work is based on the results from the literature [197, 251, 264]. Ma [197] has reported modulus of elasticity for different types of unreacted FA particles. The FA type used in this study was the same as in Ma's study. The modulus of elasticity of the Ca-rich FA particles was in the range of 75.7-91.2 GPa, the Fe-rich FA particles was 71.0-137.7 GPa, for Al-rich FA particles was between 33.3-65.4 GPa, and Si-rich FA particle presented the modulus of elasticity of 82.9 GPa. The modulus of elasticity for GGBFS particles and alkali-activated GGBFS was found in the study of Puertas et al. [264]. Constantinides and Ulm reported the modulus of elasticity of C-S-H, and decalcified C-S-H, ranging between 19.5 and 31.8 GPa, 2.2 and 13.2 GPa, respectively [251].

Due to the uniform and dense microstructure, the modulus of elasticity of the paste S100 was not altered under natural carbonation compared to the reference sample. Figure 8.18 shows one range of the modulus of elasticity for sample S100, which indicates its uniform phase composition. Unlike the mixture S100, the blended pastes were carbonated. The results were compared with those of equivalent noncarbonated parts of the samples, except for the paste S0. Due to low reactivity of FA in the S0 paste and consequently its low strength after 1 year (Chapter 3, Figure 3.14), the preparation of this sample for nanoindentation test was not possible.

The significant reduction of the modulus of elasticity was identified in the carbonated pastes S30 and S50, while the reduction of the modulus of elasticity was lower in paste S70. This can be explained by the lower CaO content in S30 and S50 pastes which results in faster carbonation of the reaction products in S30 and S50 compared to S70 or S100 pastes. On the other hand, pastes S30 and S50 are more porous (Table 8.4) compared to the paste S70 or S100 and, therefore, faster $CO_2$ diffusion occurs in the former. Carbonation mainly causes reduction of the modulus of elasticity in the 5-45 GPa range. These values correspond to the modulus of elasticity of the gel (Figure 8.18). These values shift to lower modulus of elasticity values after carbonation, as found by Çopuroglu et al. [219] in the carbonated blended OPC and GGBFS cement paste. Previous evidences of the pore structure modification (Figure 8.3 and Figure 8.5) due to the gel decalcification are the main support to reduction of the modulus of elasticity.

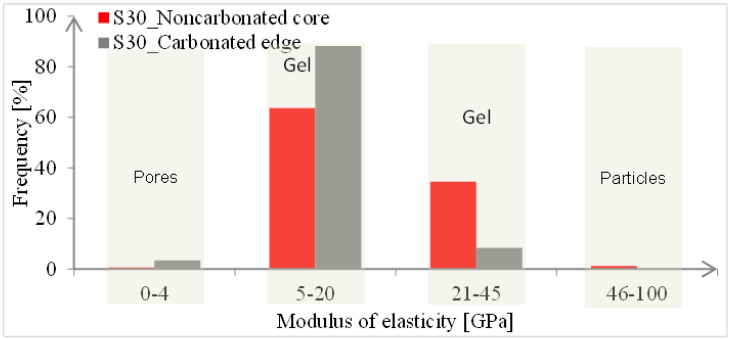


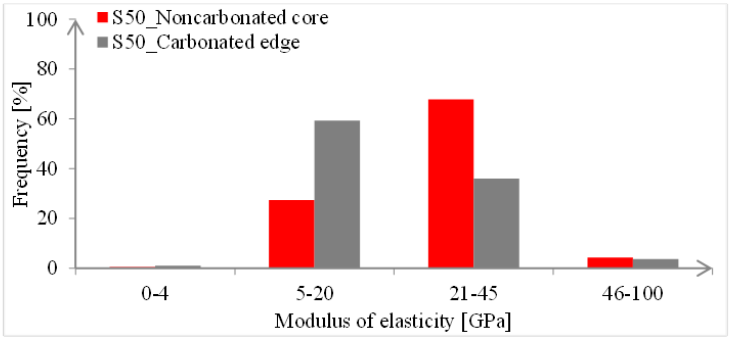


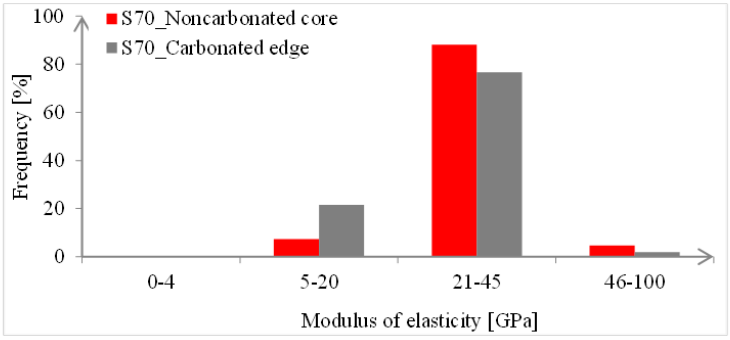


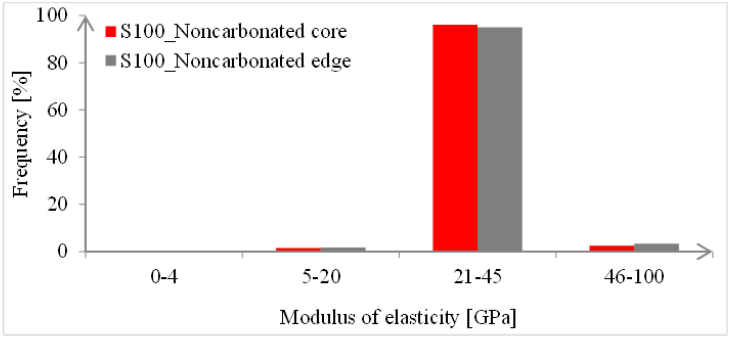


Figure 8.18: Effect of natural carbonation on modulus of elasticity of alkali activated pastes S30, S50, S70 and S100. Age: 1 year.

## 8.3.5. DISCUSSION

### 8.3.5.1. CA/SI VS MODULUS OF ELASTICITY OF THE GEL PHASES IN NONCARBONATED AND CARBONATED ALKALI ACTIVATED PASTES

Figure 8.19 shows a relationship between Ca/Si ratio and modulus of elasticity for samples S30, S50, S70 and S100. The noncarbonated samples have similar modulus of elasticity of the gel. This suggests that a similar type of gel, i.e. Ca-Na-Si-Al-H, is formed in all pastes. However, the Ca/Si ratio varied depending on GGBFS content as shown in Figure 8.19.

After carbonation, the modulus of elasticity decreases with Ca/Si reduction of the Ca-Na-Si-Al-H gel, except for paste S100. The main reasons for reduction of the modulus of elasticity in carbonated blended pastes are changes of the gel chemical composition due to decalcification, molecular structure and increase of nanoporosity. In all blended pastes the Ca/Si decreased to 0.2. The reduction of Ca/Si ratio favours polymerization of the Ca-Na-Si-Al-H chains leading to a continuous structure as shown for gels with low Ca/Si ratio with Al incorporation [265].

The reduction of modulus of elasticity was larger for pastes with lower GGBFS. The most significant change was observed for paste S30. Due to carbonation, the modulus of elasticity decreased from 26.8 GPa to 11.4 GPa. This finding is consistent with a study of Constantinides and Ulm [251]. They showed that a modulus of elasticity below 13 GPa is a result of large macroporosity. The change of BET surface area of pastes S30, S50, S70 and S100 in relation to the modulus of elasticity of the gel phases is discussed next.

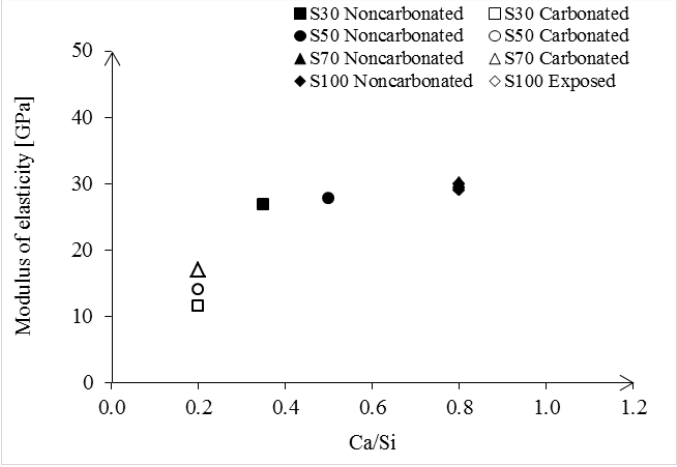


Figure 8.19: Ca/Si vs modulus of elasticity of gels in noncarbonated and carbonated alkali activated pastes.

### 8.3.5.2. BET PORE SURFACE AREA VS MODULUS OF ELASTICITY OF THE GEL PHASES IN NONCARBONATED AND CARBONATED ALKALI ACTIVATED PASTES

Figure 8.20 shows a relationship between the BET surface area and modulus of elasticity. The modulus of elasticity for all noncarbonated pastes S30, S50, S70 and S100 is in the range of 25-30 GPa. After carbonation, the modulus of elasticity for carbonated pastes is reduced by 42.7%, 50.5%, 56.5%, 0% for samples S30, S50, S70 and S100, respectively. The

reduction of the modulus of elasticity correlates with the increase of BET surface area. In hardened pastes, the increase of the number of gel pores, and hence BET surface area, is due to deterioration of the gel phases upon carbonation.

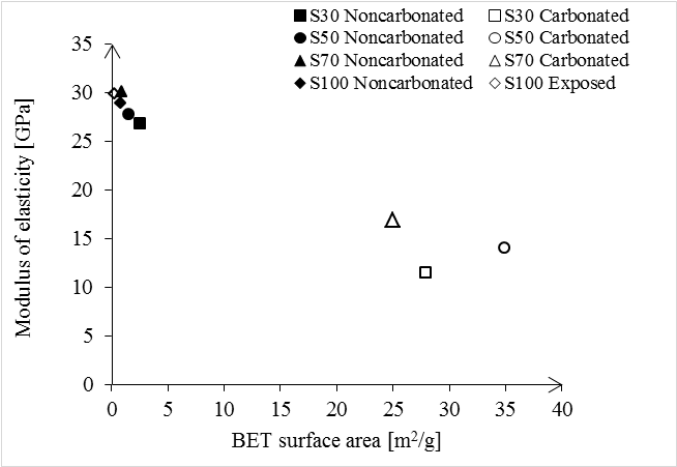


Figure 8.20: BET surface area vs modulus of elasticity of gels in noncarbonated and carbonated alkali activated pastes.

Locally, Figure 8.17 shows the surface of noncarbonated Ca-Na-Al-Si-H gel and decalcified (Ca)-Na-Al-Si-H. The noncarbonated gel has more tightly packed structure and low nanoporosity (Figure 8.17 (2)). The decalcified gel appears darker than the original Ca-Na-Al-Si-H gel (Figure 8.17 (4)). Their global redistribution leads to a loss of cohesion within the paste. The mechanism of loss of cohesion and evolution of the gel pore structure will be explained in Chapter 9.

8

## 8.4. CONCLUDING REMARKS

The main objective of this chapter was to study the effect of carbonation on the pore structure, compressive strength and modulus of elasticity. Based on the presented findings, the following conclusions can be drawn:

- Accelerated carbonation is not suitable for investigation of the effect of carbonation reactions on the compressive strength of alkali activated pastes. Accelerated carbonation of the samples led to substantial reduction of compressive strength of pastes S30, S50, S70, while in pastes S0 and S100 no significant change was observed. The series of “paleofronts” induced physical discontinuities in the sample and led to weakening of cohesion within the paste. For that reason, natural carbonation of the pastes was investigated.

- Significant differences were found between noncarbonated and carbonated microstructures of the pastes S30, S50 and S70 upon natural carbonation. This implies that carbonation is detrimental for the long-term performance of these mix-

tures. The major change in the pore size distribution occurred at the level of the nanometer pores. This is consistent with the observed increase of the BET surface area. The BET surface area increased up to 50% due to carbonation of blended alkali activated pastes, implying that the Ca-Na-Al-Si-H gel carbonation is favoured resulting in larger gel pore surface area.

- The nanoindentation measurements were more proper for evaluation of mechanical properties of pastes than measurements of compressive strength. Nanoindentation was used for evaluation of modulus of elasticity. The modulus of elasticity decreased significantly in the carbonated samples S30 and S50 compared to the corresponding noncarbonated samples, whereas no significant change of the modulus of elasticity was found in pastes with 70 and 100 wt.% of GGBFS. The main reasons for reduction of modulus of elasticity of carbonated blended pastes is the increase of nanoporosity due to volume reduction of the gel phases.

- Pastes S100 were highly resistant to carbonation, regardless the exposure conditions. Carbonation of pastes S100 was inhibited due to their dense microstructure, presence of extremely small pores with sizes ranging from sub-nm to tens of nm. Nitrogen adsorption tests identified the gel pores (<15 nm) to be dominant in the system. This blocked $CO_2$ to diffuse into the pastes within the exposure period. The modulus of elasticity of samples S100 was not altered either. The results of this chapter shed light on the importance and the effect of the physical properties (density, pore size distribution) on durability of paste S100 and also of other pastes.

- The nanoindentation measurements with $N_2$ adsorption tests and SEM/EDX analysis of noncarbonated and carbonated pastes demonstrate the existence of two gel structures with different values of the modulus of elasticity, nanoporosity, Ca/Si ratio and gel morphology. These experimental results are used to describe the mechanism of the reorganization of Ca-Na-Al-Si-H nanoparticles according to the colloid model of Ca-Na-Al-Si-H gel in Chapter 9, resulting in better understanding of the microstructural changes due to carbonation.

# 9

# CARBONATION MECHANISM

*"Scientific theories need reconstruction every now and then. If they didn't need reconstruction they would be facts, not theories."*

Charles Proteus Steinmetz

*In this chapter the carbonation mechanism for alkali-activated fly ash (FA) and ground granulated blast furnace slag (GGBFS) pastes is proposed based on the findings from Chapters 5, 6, 7 and 8. An attempt has been made (1) to correlate the gained information and (2) to formulate carbonation mechanism. Carbonation of alkali activated pastes is a complex process consisting of multiple changes in the pore solution and in the microstructure of the pastes. In alkali activated GGBFS-rich pastes, the $CO_2$ apparent diffusion (reactive transport of $CO_2$ in porous media) takes place mainly through the connected gel pores and small capillary pores. In some of the pastes carbonation occurs also in the close vicinity of the microcracks. The alkalinity was reduced in all pastes due to two reasons: ongoing gel formation and carbonation of the pore solution. In alkali activated FA/GGBFS pastes, the carbonation of C-N-A-S-H gel was the main contributor to the evolution of total porosity. With increase of GGBFS content in the pastes the deterioration of pastes due to carbonation decreased significantly.*

## 9.1. INTRODUCTION

COMPARED to the immense efforts to study how both the type of precursor and the exposure conditions influence the carbonation mechanism of alkali activated materials (AAMs) [61, 198], there is almost no information about the combined effect of GGBFS content, curing conditions and exposure conditions on the carbonation mechanism of AAMs. In practice, it is usually of high importance to know these combined effects. For different systems (i.e. S0, S50 and S100), Figure 9.1 presents phases involved in the carbonation mechanism, which were studied in the previous chapters. In paste S0 only the pore solution was carbonated. This resulted in the pH reduction of the paste. In blended paste S50, both pore solution and gel phases were carbonated, leading to the pH reduction of the paste and microstructure deterioration. In contrast, carbonation resistance of the paste S100 was high because of its high density.

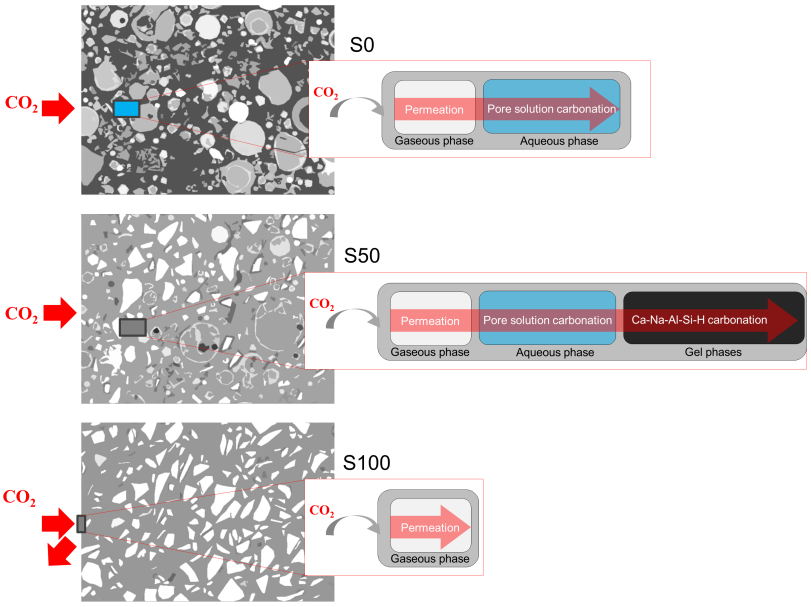


Figure 9.1: Schematic representation of carbonation mechanisms in different alkali activated pastes: S0, S50 and S100.

As schematically indicated in Figure 9.1, the deterioration of alkali activated pastes due to carbonation can appear as a single change or as a combination of different changes of material properties. They are characterized as chemical, physical and mechanical changes. Hence, complexity of deterioration of alkali activated pastes under carbonation is due to the sequence of elementary reactions (reactive transport of $CO_2$ in porous media) by which an overall change occurs. To elucidate the sequence of steps in a carbonation mechanism the findings from previous chapters are systematically highlighted in this chapter. For that purpose, the changes of chemical properties, such as $CO_2$ binding capacity, pore solution and gel phases, of physical properties, such as pore structure

and of micromechanical property as modulus of elasticity, were shown. These aspects of carbonation mechanisms in alkali activated pastes are discussed for different GGBFS content, curing conditions and exposure conditions (see Table 9.1).

Table 9.1: Parameters for consideration in carbonation mechanisms in alkali activated materials.

| | $CO_2$ binding capacity | | Pore solution | Gel phases | Pore structure, modulus of elasticity |
|---|---|---|---|---|---|
| | Powder paste | Bulk paste | Bulk paste | | |
| Slag content | √ | √ | √ | √ | √ |
| Curing conditions | x | x | √ | √ | √ |
| Exposure conditions | x | √ | √ | √ | √ |

## 9.2. $CO_2$ BINDING CAPACITY

In Chapter 5, a mineralogical assessment of crushed, powdered alkali activated pastes under 1% v/v $CO_2$ was performed. The study showed a lower $CO_2$ binding capacity for alkali activated materials compared to cement-based materials when exposed to 1% v/v $CO_2$. The bound $CO_2$ content amongst the alkali activated pastes (S30, S50, S70, S100) was very similar. With X-Ray Diffraction (XRD) and thermogravimetric (TG)-mass spectrometry (MS) both crystalline and amorphous carbonates were detected in the pastes. The crystalline fraction of carbonates increased linearly with increase of GGBFS, hence with the increase of CaO (Figure 9.2).

The $CO_2$ binding capacity was also studied for bulk paste samples. The bulk paste samples were sealed cured prior to carbonation. The mechanism of $CO_2$ binding capacity was investigated for different GGBFS content, i.e. different GGBFS/FA ratios in the pastes and different exposure conditions. In the following subsections these effects are discussed separately.

### 9.2.1. SLAG CONTENT

The theoretical $CO_2$ binding capacity of alkali activated pastes increases linearly with increasing GGBFS content, as shown in Figure 9.3. The theoretical $CO_2$ binding capacity was determined according to a study of Steinour [218]. The content of crystalline carbonates was determined with XRD, while the total $CO_2$ content was determined with TG-MS. Carbonation of the *bulk paste samples* resulted in not more than 17 wt.% $CO_2$ uptake with variations among the pastes and exposure conditions (Figure 9.3). For instance, the $CO_2$ uptake of paste S0 was the same for all exposure conditions, i.e. 4.7 wt.% $CO_2$. The $CO_2$ uptake increased linearly with increase of GGBFS content for all exposure conditions, except for paste S100. This paste underwent weathering and microcracking under exposure to outdoor conditions. This caused carbonation of the gel phases (see carbonation products in Chapter 7, Table 7.1) and $CO_2$ uptake of 5.78 wt.%. The same $CO_2$ uptake was measured in natural laboratory conditions.

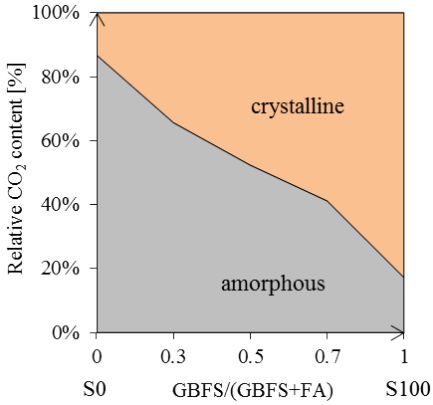


Figure 9.2: The contribution of $CO_2$ content in amorphous and crystalline carbonates to the total $CO_2$ content in the carbonated powders. The crushed paste samples (powders) were exposed to accelerated conditions. Before exposure, samples were sealed cured for 28 days. The exposure time was 180 days. The content of crystalline carbonates was determined with XRD, while the total $CO_2$ content was determined with TG-MS.

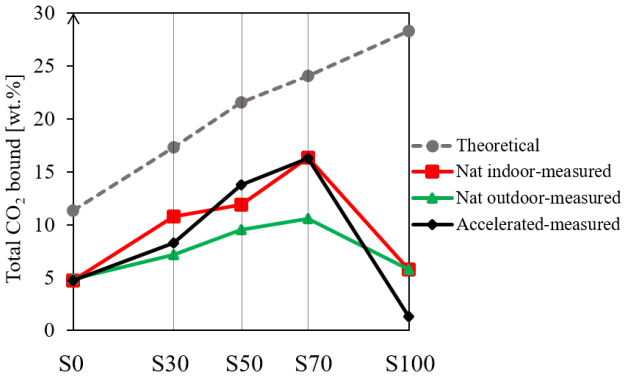


Figure 9.3: The measured $CO_2$ binding capacity of alkali activated pastes in different exposure conditions compared to theoretical binding capacity. The exposure time was 1 year.

### 9.2.2. EXPOSURE CONDITIONS

The total $CO_2$ uptake (from both amorphous and crystalline carbonates) is plotted in Figure 9.4 for bulk paste samples exposed for 1 year to natural indoor, natural outdoor and accelerated carbonation. As can be seen, the $CO_2$ uptake did not vary amongst different exposure conditions. The paste S100 has the lowest $CO_2$ uptake, implying that the apparent diffusion of $CO_2$ was largely hindered in this paste. Hence, the pore structure turns out to be the governing factor that limits carbonation in paste S100. Nevertheless, Figure 9.4 shows that the exposure conditions affect the ratio between amorphous and crystalline carbonates. The content of amorphous carbonates is dominant regardless the exposure conditions.

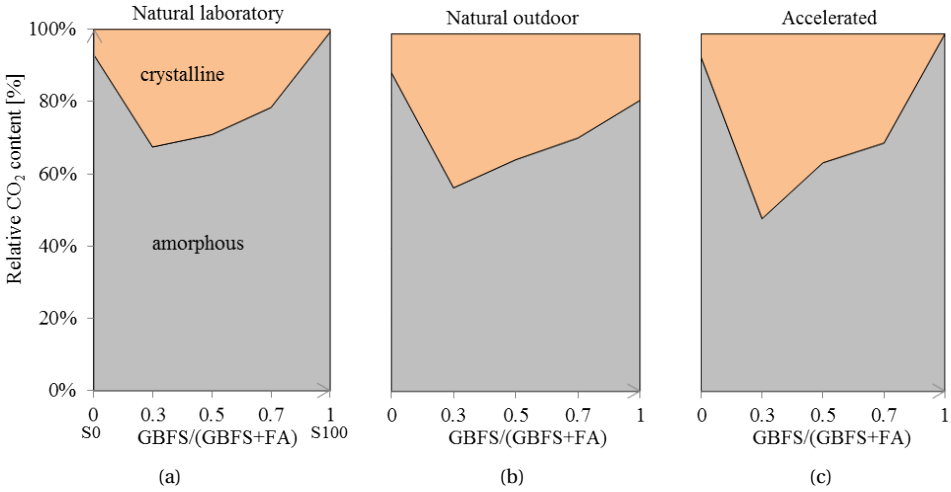


Figure 9.4: The contribution of amorphous and crystalline carbonates to the total $CO_2$ content in the alkali activated bulk pastes. The tests were done on the bulk pastes which were sealed cured for 28 days before exposure. The exposure time was 1 year. The total $CO_2$ content was determined with TG-MS. The content of crystalline carbonates was determined with QXRD.

The fraction of the crystalline carbonates in pastes which were ground to a *powder* and subsequently exposed to accelerated carbonation (Crushed pastes (Chapter 5), see Table 7.1) was larger than the fraction of the crystalline carbonates in *bulk paste samples* (Bulk paste samples, see Table 7.1) exposed to accelerated carbonation. This is mainly due to the different content of the moisture in the *paste powders* and in the *bulk paste samples*. In the carbonation reactions of the paste powders, the constant supply of water and $CO_2$ to the surface of the particles was possible, since the exposure was well controlled in the carbonation chamber (60% RH, 1% v/v $CO_2$) (see Figure 9.5). On the other hand, in the carbonation reactions of the bulk paste samples, the effect of drying must be taken into consideration. The increased $CO_2$ concentration results in the evaporation of the water at the reaction site [266] and, moreover, from the sample (Figure 9.5). The evaporated water is free water which cannot be compensated simply by the water flow inside the sample. The water which flows inside the sample is rather auto-dissociated water (reaction 9.9), which becomes instantaneously part of the pore solution as it flows inside the sample. Hence, bulk paste samples might undergo drying due to carbonation reactions as shown in Figure 9.5. Drying of the bulk pastes is governed by both liquid transport due to a capillary pressure gradient and by the gas diffusion due to a $CO_2$ pressure gradient. Schmidt et al. [267] showed that the decreasing amount of $H_2O$ plays a key role in transformation of amorphous calcium $CaCO_3$ to more stable forms of $CaCO_3$ (vaterite, aragonite, calcite). Namely, the drying reduces the liquid content in the pores of the bulk pastes. With reduced content of water the mobility of ions is dramatically reduced as shown by Zou et al. [268]. Consequently, the small particles of amorphous $CaCO_3$ are stabilized.

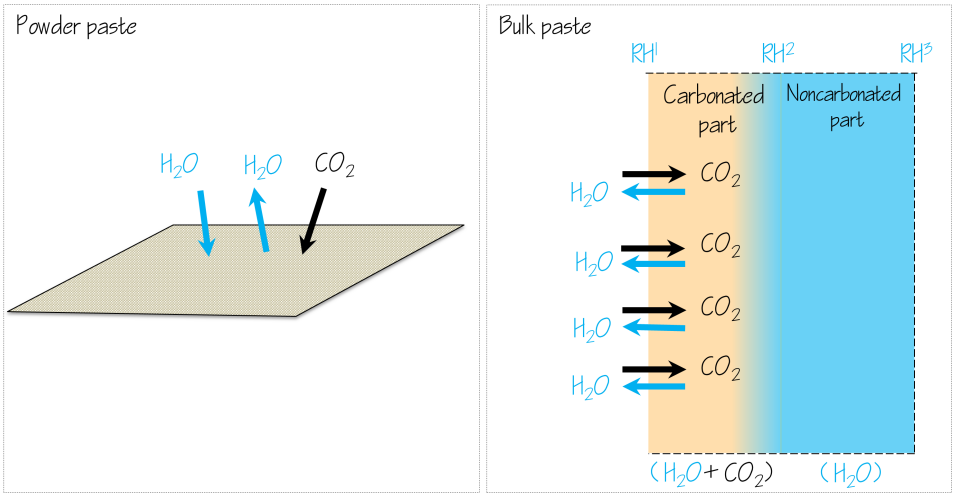


Figure 9.5: Carbonation of powder and bulk paste samples. The water has constant access to the surface of the powder's particles. In the bulk paste sample, water is consumed for $CO_2$ dissolution and additionally it is released in carbonation reactions at carbonation sites in the pores. The released water from carbonation reactions tends to evaporate from the sample since it is free water. The evaporation of water takes place due to the moisture gradient between the noncarbonated and carbonated part. Therefore, drying occurs as long as diffusion of $CO_2$ in the sample takes place.

Furthermore, under all exposure conditions different forms of $CaCO_3$ were observed. The nucleation of different calcium carbonates is reported to be dependent on the ionic ratio of $Ca^{2+}/CO_3^{2-}$ in solution, MgO-ions [269], concentrations/supersaturation levels of the starting solutions and the pH of the final solution once equilibrium with respect to $CaCO_3$ has been reached [199, 242, 243, 270]. In the bulk paste samples, Rietveld quantification of phases revealed that vaterite was the dominant carbonate phase (Table 7.1). The low ionic ratio of $Ca^{2+}/CO_3^{2-}$ in the solution may favour its formation [242]. The increase of $CO_2$ concentration (case of accelerated carbonation) elevates the $CO_2$ dissolution and accumulation of $H^+$, $HCO_3^-$, $CO_3^{2-}$ ions, hence increased the supersaturation of the solution. As a result of supersaturation of the solution, quick nucleation and precipitation take place [271]. This hinders the transformation of vaterite to calcite. This also explains the dominant presence of vaterite in the studied conditions. The pH of carbonated pastes could also have an influence on the type and size of the critical $CaCO_3$ nuclei [272]. Gebauer et al. [270] demonstrated the effect of the pH of the solution on the local coordination structure of nucleated particles, i.e. on the type of amorphous $CaCO_3$ or crystalline polymorph of $CaCO_3$, using carbon-13 nuclear magnetic resonance and X-ray absorption spectroscopy. They found that vaterite precipitated from more alkaline solutions (at pH 9.75-10) and calcite at less alkaline solutions (at pH 9.00-9.50). Since the pH of carbonated alkali activated pastes was largely preserved up to pH 10 (Chapter 6, Figure 6.12), the pH values can indeed justify the formation of mainly vaterite.

## 9.3. PORE SOLUTION CARBONATION

### 9.3.1. GENERAL REACTION MECHANISM

The absorbed $CO_2$ gas is mainly controlled by the gas/liquid exchange surface, the concentrations in the gas (partial pressure) and liquid phase [273]. Pore solution is the main liquid phase for carbonation reactions in bulk paste samples. The carbonation reactions can occur within a liquid film as long as the pores are partially dry [91]. The carbonation of the pore solution in the alkali activated pastes can be divided into two principal steps: (1) $CO_2$ gas dissolution (9.1-9.9) and (2) NaOH and KOH carbonation (9.10-9.17).

For highly alkaline pore solution, as in alkali activated paste (pH > 12) [74], there are two paths (blue and red arrows (downwards arrow left of upwards arrow), see Figure 9.6) along which carbonation begins: hydroxylation (red arrow) and hydration of $CO_2$ (blue arrow), depending on the pH value of the pore solution.

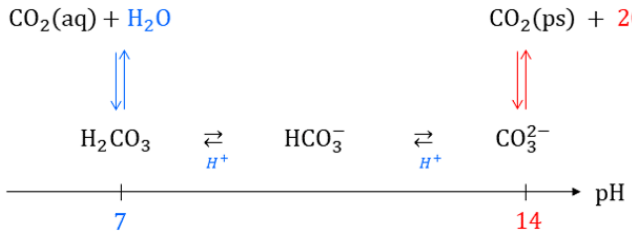


Figure 9.6: Reaction mechanism of $CO_{2_{(aq)}}$ in aqueous solution, adopted from [274].

When gaseous $CO_2$ diffuses in the pore solution of the alkali activated pastes (where pH is higher than 12, such that $[OH^-] \gg [H^+]$), the $CO_2$ is first physically absorbed as shown in reaction 9.1[1]. Subsequently, the *hydroxylation of* $CO_2$ involves two reactions 9.2 and 9.3:

$$CO_2(g) \rightarrow CO_2(ps) \tag{9.1}$$

$$CO_2(ps) + OH^-(ps) \rightleftharpoons HCO_3^-(ps) \tag{9.2}$$

$$HCO_3^-(ps) + OH^-(ps) \rightleftharpoons CO_3^{2-}(ps) + H_2O \tag{9.3}$$

If the equilibrium of the reaction 9.3 lies far to the right of the pH scale, which may be expected in the initial stage of the chemisorption process due to the high pH values, this process can be described by a single irreversible overall reaction 9.4 (similar to [275]):

$$CO_2(ps) + 2OH^-(ps) \rightleftharpoons CO_3^{2-}(ps) + H_2O \tag{9.4}$$

The $OH^-$ decreases rapidly via reaction 9.4. Hence, the pH decreases fast during the initial reaction period, while the $CO_3^{2-}$ concentration increases.

[1] "ps" stands for pore solution.

If the $CO_2$ dissolves in water (*hydration path*), it forms carbonic acid ($H_2CO_3$), following reactions 9.5 and 9.6. Subsequently, carbonic acid donates a proton (hydrogen ion, $H^+$) and forms a bicarbonate ion ($HCO_3^-$), reaction 9.7. The bicarbonate ion donates a proton and generates a carbonate ion ($CO_3^{2-}$), reaction 9.8.

$$CO_2(g) \rightarrow CO_2(aq) \tag{9.5}$$

$$CO_2(aq) + H_2O \rightleftharpoons H_2CO_3 \tag{9.6}$$

$$H_2CO_3 \rightleftharpoons HCO_3^- + H^+ \tag{9.7}$$

$$HCO_3^- \rightleftharpoons CO_3^{2-} + H^+ \tag{9.8}$$

Both *hydroxylation* and *hydration* of $CO_2$ are coupled by the auto-dissociation of water as reported by Eigen [276]:

$$H_2O \rightleftharpoons OH^- + H^+ \tag{9.9}$$

The pore solution of alkali activated pastes contains essentially NaOH and KOH as seen in Chapter 6. Hence, after $CO_2$ gas dissolution (reactions 9.1-9.9), the carbonation of NaOH and KOH gives bicarbonates (reactions 9.11, 9.13) and carbonates (reactions 9.10, 9.12). Alkali (bi)carbonates, however, are highly mobile and soluble in water, which results in releasing $CO_2$ back into the solution [221]. Consequently, carbonate ions react with $Ca^{2+}$ provided to the solution, forming insoluble calcium carbonates (reactions 9.14-9.17). Additionally, the regeneration of hydroxides (NaOH, KOH) is induced (reactions 9.14-9.17). To demonstrate the effect of the carbonation (reactions 9.1-9.17) on the pore solution properties, samples with different GGBFS content in the pastes, different curing and different exposure conditions were studied.

$$CO_3^{2-}(ps) + 2NaOH \rightarrow Na_2CO_3 + 2OH^-(ps) \tag{9.10}$$

$$HCO_3^-(ps) + NaOH \rightarrow NaHCO_3 + OH^-(ps) \tag{9.11}$$

$$CO_3^{2-}(ps) + 2KOH \rightarrow K_2CO_3 + 2OH^-(ps) \tag{9.12}$$

$$HCO_3^-(ps) + KOH \rightarrow KHCO_3 + OH^-(ps) \tag{9.13}$$

$$Na_2CO_3 + Ca^{2+}(ps) + 2OH^-(ps) \rightarrow CaCO_3(s) + 2NaOH \tag{9.14}$$

$$NaHCO_3 + Ca^{2+}(ps) + 2OH^-(ps) \rightarrow CaCO_3(s) + NaOH + H_2O \tag{9.15}$$

$$K_2CO_3 + Ca^{2+}(ps) + 2OH^-(ps) \rightarrow CaCO_3(s) + 2KOH \tag{9.16}$$

$$KHCO_3 + Ca^{2+}(ps) + 2OH^-(ps) \rightarrow CaCO_3(s) + KOH + H_2O \tag{9.17}$$

#### 9.3.1.1. SLAG CONTENT

The increase of the GGBFS content in the pastes increased the [$Na^+$] of the pore solution as seen in Chapter 6 (see Table 6.3). Similarly, the pH increased with increasing GGBFS in the pastes. This is due to lower $Na^+$ binding capacity by gel phases in GGBFS-rich pastes. Consequently, the carbonated pastes with higher GGBFS content contained higher content of $Na^+$ in the pore solution than FA-rich pastes, therefore higher pH was measured after carbonation in GGBFS-rich pastes.

#### 9.3.1.2. CURING CONDITIONS

Two curing conditions are considered: sealed and unsealed. To evaluate the effect of the curing conditions on the pH and propagation of the carbonation front, the carbonation resistance of sealed cured and unsealed cured specimens under accelerated conditions (1% v/v $CO_2$, 60% RH) was compared. The pH is primarily dependent on the proton activity, such as $OH^-$ activity, in the pore solution. A substantial lower concentration of $OH^-$ and $Na^+$ in the pore solution was observed in the unsealed cured samples compared to the samples that were sealed cured prior to exposure. Consequently, unsealed curing of the samples resulted in faster carbonation. Hence, sealed curing of the samples contributed to higher carbonation resistance of the alkali activated pastes.

#### 9.3.1.3. EXPOSURE CONDITIONS

The pH of the reference alkali activated pastes after 28 days was 13.45-13.97 (see Table 6.3), while the pH of the reference alkali activated pastes after 1 year (noncarbonated) was 11.5-12.6. The difference in pH between 28 days and 1 year is attributed to the dissolution of the remaining unreacted materials (FA and GGBFS) in the pastes. Their dissolution consumed the NaOH for the gel formation.

The pH of the carbonated alkali activated pastes depended on the exposure conditions. The reaction between atmospheric $CO_2$ and alkalis from the pore solution resulted in the pH decrease to 10.1-12.6. The relatively high alkalinity values (12.6) imply that these pastes did not carbonate at all (such as paste S100). The pH decreased more under accelerated carbonation (to 9.2) than under natural conditions (~10). Higher decrease of pH under accelerated conditions (1% v/v $CO_2$) is only due to higher $CO_2$ concentration than under natural conditions (0.04% v/v $CO_2$), consistent with literature [62, 225].

The phase analyses with Fourier Transformed Infrared spectroscopy (FT-IR) and quantitative X-ray diffraction (QXRD) in Chapter 7 did not show Na-carbonates, i.e. nahcolite or natron (reactions 9.10-9.13) in any of the exposure conditions. This was expected due to high solubility of Na-carbonates [221].



### 9.3.2. SUMMARY

Three influential factors above were selected to describe the effect of carbonation on the pore solution of alkali activated pastes. Curing conditions have the major effect on the pore solution composition prior to carbonation and the carbonation resistance of the pastes. Next, the GGBFS content also contributes to a higher pH of the pore solution. However, its effect is less significant than that of curing conditions. The pH of carbonated pastes did not drop below 9.2, regardless the exposure conditions. The reduction of the alkalinity of the pore solution, during carbonation, reduced the stability

of gel phases (Ca-Mg-Na-Al-Si-H, Ca-Na-Al-Si-H, Ca-Al-Si-H). The interaction between carbonated pore solution and gel phases caused changes of the gel nanostructure and hence of the whole paste microstructure. This is studied in the following section.

## 9.4. GEL CARBONATION IN PASTES

### 9.4.1. GENERAL REACTION MECHANISM

Calcium-(magnesium)-sodium aluminosilicate hydrate type gels (Ca-(Mg)-Na-Al-Si-H) and sodium aluminosilicate hydrate gel (Na-Al-Si-H) play an important role in transport of $CO_2$ in alkali activated pastes. The apparent diffusion of $CO_2$ is mainly controlled by the $CO_2$ transport through connected large gel pores (3-12 nm) confined by gel globules and $CO_2$ binding capacity. Based on experimental results and conceptual illustration of carbonation-induced chemical and physical changes at different gel scales (*atomic* (Figure 9.7), *molecular* (Figure 9.8), *nano* (Figure 9.9)), the carbonation mechanism of pastes is explained and effects of carbonation on *micro* scale properties are discussed. It should be noted that the gels in pastes are not pure gels (solid solutions with one chemistry), rather they have chemical domains which are defined with PARC in Chapter 4. These chemical domains of the gels are dependent on the the chemical composition of the FA and GGBFS, and the type of the activator. For that reason, the microstructure of the pastes contains rather intermixed phases, which may carbonate simultaneously.

#### 9.4.1.1. ATOMIC SCALE (GEL DECALCIFCATION)

The gel structure in alkali activated GGBFS systems was described as cross-linked substituted tobermorite with varying Ca/Si ratio, Al and Na content [167]. The chemical composition of gel phases vary with the GGBFS content as shown in Chapter 4. The reduction of the pH of the pore solution, during carbonation, results in dissolution of identified gel phases and precipitation of carbonation products. The mechanism develops according to reactions 9.1-9.17 and in addition reactions 9.18-9.20. According to these elementary carbonation reactions, the dissolution-precipitation process can be summarized:

1. The carbonation starts with dissolution of $CO_2$ into the alkaline pore solution of alkali activated pastes. By consumption of the $OH^-$ the pH decreases (reaction 9.4). This step occurs in all pastes. For paste S0, this is the only carbonation step.

2. Gel dissolution (Ca-Mg-Na-Al-Si-H, Ca-Na-Al-Si-H, Ca-Al-Si-H) takes place in pastes S30, S50, S70 and S100 at the pH below which the gel phases become unstable. The composition of the pore solution then changes in response to the dissolution of $CO_2$ and to the gel dissolution. The solubility of gels increases with further decrease of pH of the pore solution. The gel dissolution starts at the lowest scale, i.e. atomistic level of gels by gradual decalcification of the gel and release of chemically bound water as illustrated in Figure 9.7. The initial gel structure is replaced by a thermodynamically less stable molecular structure of the -(Mg)-(Na)-Al-Si-H gel due to loss of Ca and water from the gel interlayers (see Figure 9.7). The decalcification process of the gel phases is described by reactions 9.18-9.20. The main reaction products, as shown in Section 9.2, were amorphous calcium $CaCO_3$, vaterite and calcite.

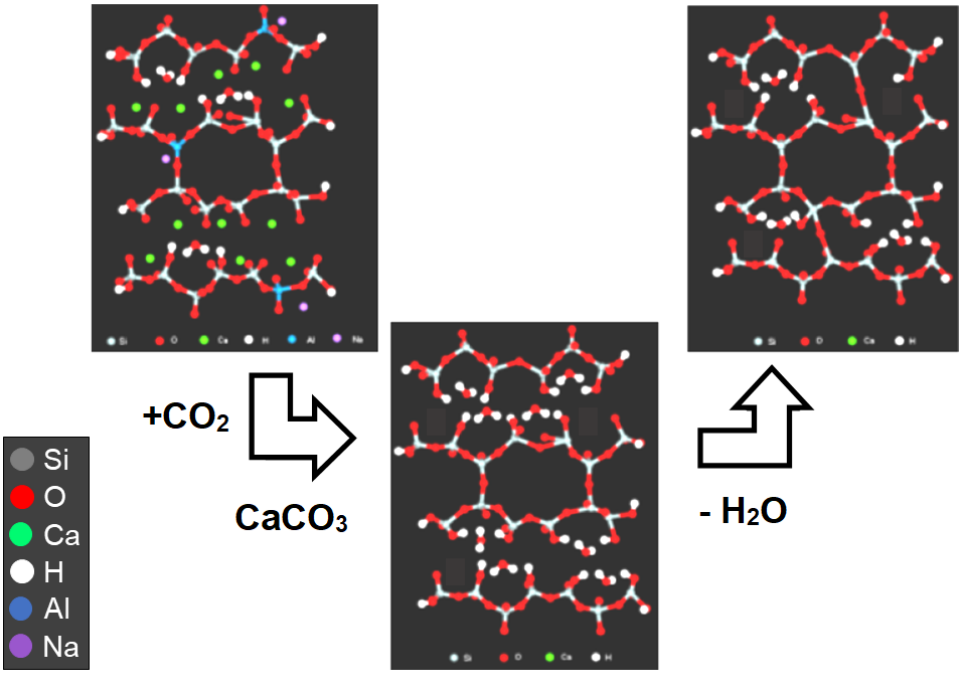


Figure 9.7: Conceptual illustration of the gel decalcification. The image is adapted from [59]. The C-N-A-S-H gel is described as cross-linked substituted tobermorite with varying Ca/Si ratio, Al and Na uptake [167].

Carbonation of Ca-Na-Al-Si-H gel produces:

$$aNa_2CO_3 + (CaO)a(Na_2O)b(Al_2O_3)c(SiO_2)d(H_2O)e \rightarrow$$

$$aCaCO_3 + (Na_2O)b(Al_2O_3)c(SiO_2)d(H_2O)f + 2aNaOH + (e-f)H_2O \quad (9.18)$$

Carbonation of Ca-Mg-Na-Al-Si-H gel produces:

$$aNa_2CO_3 + (CaO)a(MgO)b(Na_2O)c(Al_2O_3)d(SiO_2)e(H_2O)f \rightarrow$$

$$aCaCO_3 + (MgO)b(Na_2O)c(Al_2O_3)d(SiO_2)e(H_2O)g + 2aNaOH + (f-g)H_2O \quad (9.19)$$

Carbonation of Ca-Al-Si-H gel produces:

$$aNa_2CO_3 + (CaO)a(Al_2O_3)b(SiO_2)c(H_2O)d \rightarrow$$

$$aCaCO_3 + (Al_2O_3)b(SiO_2)c(H_2O)e + 2aNaOH + (d-e)H_2O \quad (9.20)$$

where a, b, c, d, e, f and g are the stoichiometric coefficients for the respective oxide components CaO, MgO, $Na_2O$, $Al_2O_3$, $SiO_2$ and $H_2O$. The coefficients are different for each of the studied mixtures and for each of exposure conditions.

#### 9.4.1.2. MOLECULAR SCALE (GEL POLYMERIZATION)

The removal of Ca from the structure of the gel occurs along with polymerization of remaining gel. The original structure of the C-N-A-S-H gel (before carbonation) with modified gel structure during carbonation are schematically illustrated in Figure 9.8.

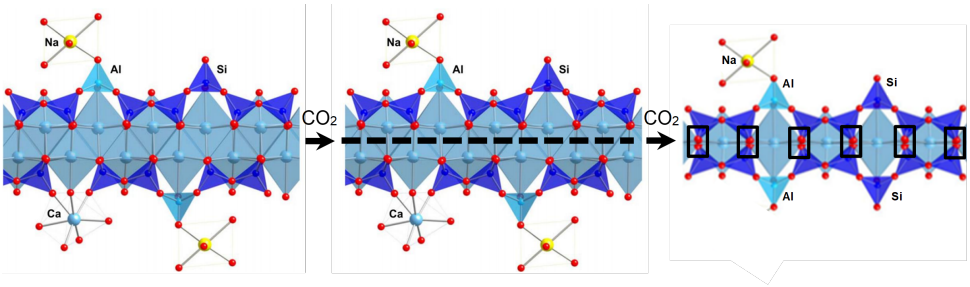


Figure 9.8: Conceptual illustration of the gel polymerization. The left image is an original structure of the C-N-A-S-H gel (before carbonation). The middle image presents a gradual removal of Ca from the gel structure during carbonation. The right image illustrate polymerization of (alumino)silicate chains during carbonation. The representation of the gel structure is adapted from Richardson [277]. The C-N-A-S-H gel is described as cross-linked substituted tobermorite with varying Ca/Si ratio, Al and Na uptake [167].

The polymerization of (alumino)silicates proceeds as long as carbonation of the gel phases (reactions 9.18-9.20) releases $OH^-$ and $Ca^{2+}$ ions which react with $HCO_3^-$ and/or $CO_3^{2-}$ ions. This means that for each studied paste (S30, S50, S70, S100), the carbonation kinetics will be different due to their different CaO content and, therefore, different $CO_2$ binding capacity. Based on alkalinity measurements (Figure 6.18) and FT-IR analysis of the pastes after carbonation (Figure 7.15), which suggest that the polymerization proceeds with presence of alkalis, the polymerization mechanism can be described with reactions 9.21-9.23. Furthermore, the formation of (alumino)silicate gel can be explained based on the fundamental study of Iler [181] on the polymerization of silica in aqueous systems where pH has an important role on the whole mechanism. The original mechanism that Iler [181] developed was based on the condensation reaction between the silicic acid anions themselves (Si-O-Si (Al) bonds), leaving the $OH^-$-groups on the outside. Besides $OH^-$-groups, water and bicarbonates are likely to be generated here.

$$\equiv Si-OH+HO-Si(Al) \equiv \rightarrow \equiv Si-O-Si(Al) \equiv +H_2O \tag{9.21}$$

$$\equiv Si-ONa+HO-Si(Al) \equiv \rightarrow \equiv Si-O-Si(Al) \equiv +NaOH \tag{9.22}$$

$$\equiv Si-ONa+HCO_3-Si(Al) \equiv \rightarrow \equiv Si-O-Si(Al) \equiv +NaHCO_3 \tag{9.23}$$

#### 9.4.1.3. NANO SCALE (EVOLUTION OF THE GEL POROSITY)

The previous analyses of gel deterioration at atomic and molecular scale due to carbonation were used to explain the reorganization of Ca-Na-Al-Si-H globules and evolution of gel porosity according to the colloid model [261]. By assuming that the basic building

blocks of Ca-Na-Al-Si-H can be represented as globules, the change of specific surface area and evolution of the gel pore structure can be represented by Figure 9.9.

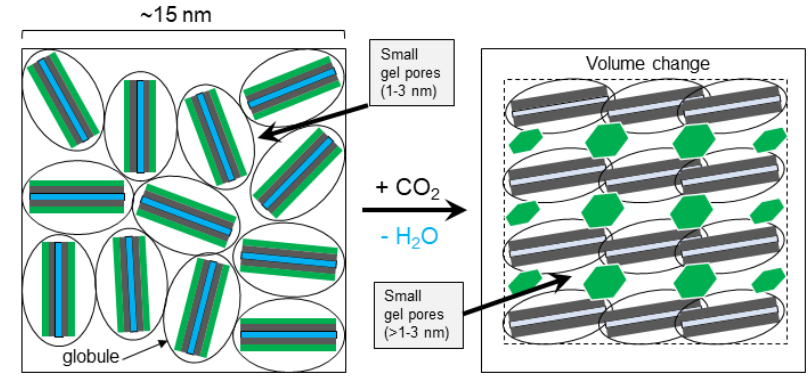


(I) Modification of the globules due to gel decalcification, polymerization and water loss.

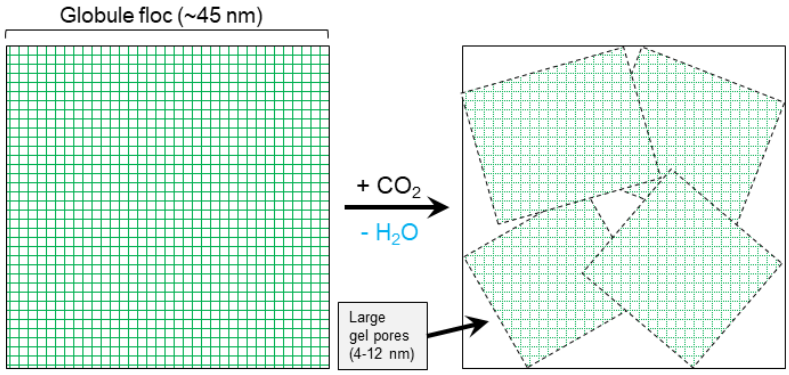


(II) Modification of the globule floc due to reorganization of the globules.

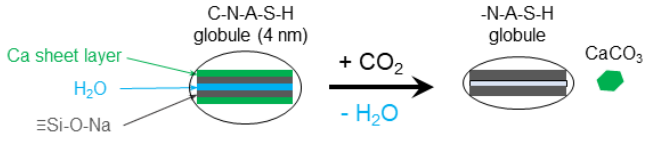


Figure 9.9: Schematic representation of the gel porosity evolution in pastes (S30, S50, S70) due to volume changes of the gel.

The basic building block (i.e. globule) is a unit of Ca-Na-Al-Si-H that is roughly spherical and, on average, 5 nm wide. These building blocks flocculate after carbonation to form larger units, i.e. new globules (see Figure 9.9). The reorganization of the globules generates the overlaps of silicate chains from the neighboring globules. This generates more small gel pores (Na-Al-Si-H gel compared to Ca-Na-Al-Si-H gel, Figure 9.10) and increases the size of the new globule (>5 nm). Consequently, the volume of pores between globules increases and contributes to the increase of surface area of the pores (Table 8.4, Chapter 8). At the same time, the polymerization of the silicate chains causes shrinkage (see Figure 9.10) and it decreases the size of the globule floc (see Figure 9.9). This increases the volume and diameter of large gel pores (4-12 nm) of pastes S30, S50 and S70 and generates the capillary pores (~30 nm) as shown in Table 8.3, Chapter 8. Effect of changes of the gel properties due to carbonation were discussed in relation to the GGBFS content in pastes, curing and exposure conditions in the following section.

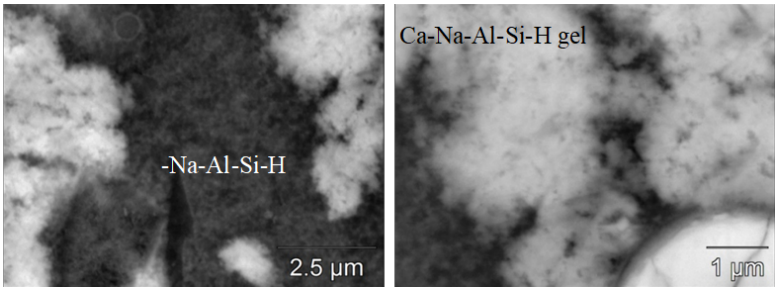


Figure 9.10: The visualization of the loss of the gel cohesion in paste S50 due to natural carbonation.

### 9.4.2. MICRO SCALE (MICROSTRUCTURE AND MICROMECHANICAL PROPERTIES OF THE PASTE)

#### 9.4.2.1. SLAG CONTENT

Based on PARC analysis of the chemistry of the gel phases, Ca was not identified in the composition of the gel of the alkali activated FA paste (S0, where GGBFS=0), and only Na, Si and Al were present (Chapter 4, Figure 4.17). The gel in alkali-activated FA did not carbonate as demonstrated with FT-IR and QXRD (Chapter 7). Similar results have been reported by Bernal et al. [63]. Hence, carbonation of alkali-activated FA is limited only to the pore solution.

The highest Ca content was measured in paste S100, but its microstructure was not carbonated at all. Paste S100 has the lowest porosity (~3.68%) amongst the pastes as shown in Chapter 4. In such fine microstructure, $CO_2$ could not diffuse. Since diffusion of dissolved gases only occurs through the nitrogen accessible gel pores and capillary pores [278] it is assumed that the contribution to the $CO_2$ diffusion of gel pores in C-N-A-S-H with sizes below 2 nm is negligible. The $CO_2$ apparent diffusion in the pastes S30, S50 and S70 took place mainly through the connected gel pores and small capillary pores, decalcifying the Ca-rich gel phases. It is assumed that the gel pore size distribution has wider range in blended pastes than in the paste S100. Furthermore, the gel in alkali-activated paste S50 had lower Ca/Si=0.50 compared to paste S100 with Ca/Si=0.83, as

shown by PARC. Therefore, the removal of the calcium from the gel took shorter time for FA-rich pastes (S30, S50). This is supported by the results on the rate of carbonation as presented in Chapter 6, Figure 6.12. With increase of GGBFS content in the pastes, the $CO_2$ diffusion slowed down due to refinement of the pore structure.

Beside gel and capillary pores, the microcracks were also a path for carbonation as demonstrated in naturally carbonated pastes. The microcracks were developed due to drying shrinkage. Figure 9.11 shows general patterns in cross-sections of (non)carbonated samples in the low magnification images obtained by fluorescent microscope. The existing defects can be clearly observed, due to the impregnation with resin. The microcrack patterns for alkali activated pastes show single and branched microcracking, as also observed for cement paste [279]. Shiotani et al. [279] showed that microracking perpendicular to the drying surface of cement paste was pure tensile cracking, while branching microcracks had a shear component. A single microcrack formation is observed in paste S100, compared to binary alkali activated FA/GGBFS pastes where more microcrack branching and bridging took place (see Figure 9.11). This is due to much more brittle behaviour and homogeneous microstructure of paste S100.

In paste S0, no particular carbonation front was observed. No defects such as voids and microcracks can be observed. The resin uniformly filled the section indicating the high porosity of the sample S0. In sample S30, continuous microcracks can be observed along the cross-section. These cracks are induced by the drying shrinkage during preconditioning of the samples. They start from the top surface and proceed toward the core of the sample. The S50 sample also demonstrated an uniform carbonation depth. In this sample, the noncarbonated zone did not show any defects or voids. The carbonated zone, however, presented extensive microcracking. The deteriorated area was clearly separated (carbonation front) from the noncarbonated zone. Paste S70 contained multiple microcracks perpendicular to the edge of the sample, which start from the edge towards the centre of the sample. The carbonation in paste S70 is dominant in the vicinity of the observed microcracks. The carbonation depth of the surface layer of paste S70 is smaller than the carbonation depth induced left or right from the axis of the microcrack. This can be explained by the difference in moisture content at the top of the surface and in depth of the sample. The carbonation reactions will be restricted by absence of the moisture or its very low content (less than 50% RH). In the crack, the RH is higher and thus carbonation can occur. Although microcracking was also present in paste S100, propagation of $CO_2$ was inhibited in natural laboratory conditions due to the dense microstructure of this paste.

The micromechanical properties of carbonated blended pastes, S30, S50 and S70 changed compared to the corresponding noncarbonated pastes. The largest decrease of modulus of elasticity was in paste S30 after carbonation. This is due to the progressive polymerization of aluminosilicate gel as a consequence of the gel decalcification as shown in Chapter 5, Figure 5.7. With increase of GGBFS content in the pastes, the decrease of modulus of elasticity was lower.

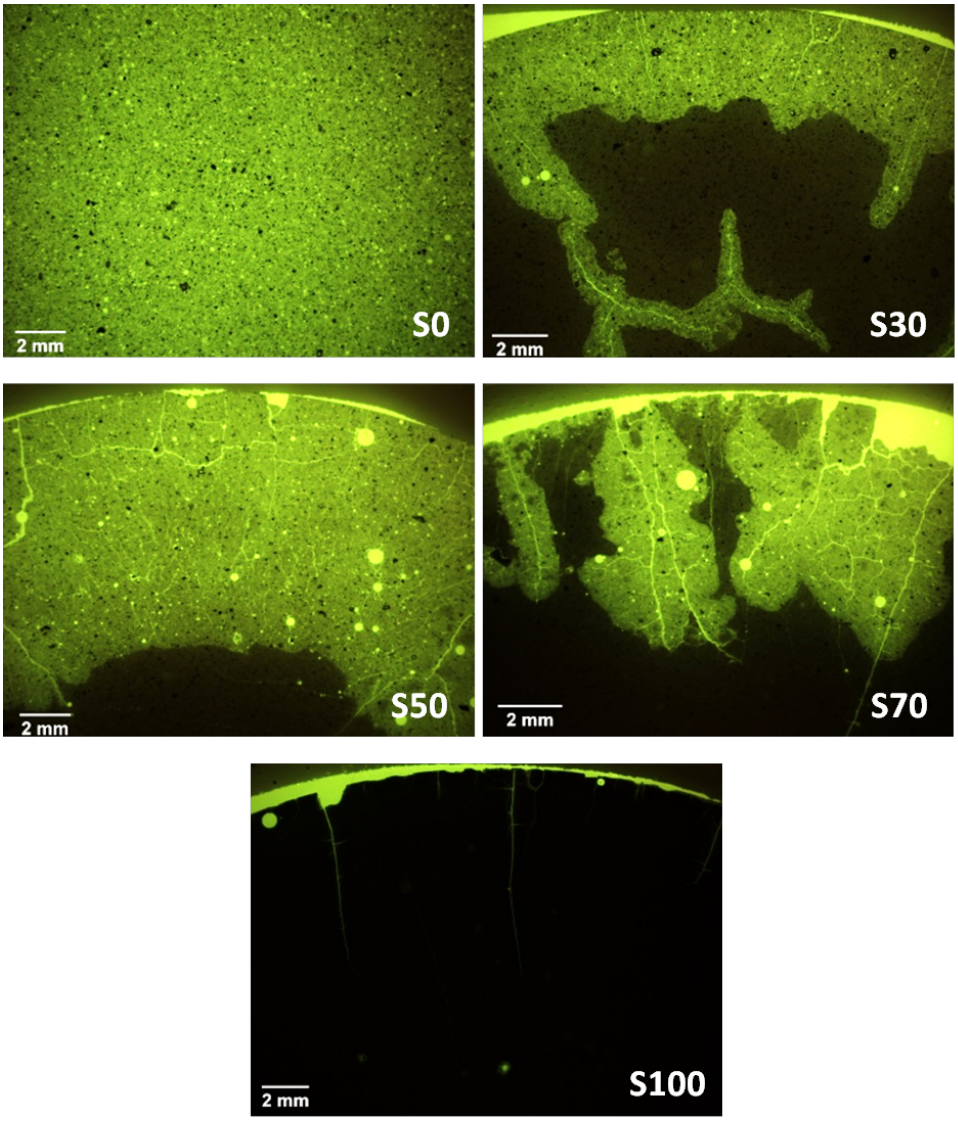


Figure 9.11: Fluorescent yellow resin impregnated thin-section paste samples viewed in reflected fluorescent light, showing the carbonation depth from the top surface toward the core of the samples; noncarbonated matrix is dark grey to black; carbonated matrix, microcracks, voids and pores are light green (the samples were sealed cured for 28 days and then demoulded and exposed to laboratory conditions for 1 year).

#### 9.4.2.2. CURING CONDITIONS

The role of the preconditioning and l/b ratio on the pore structure is demonstrated for the paste S50, Figure 9.12. One set of pastes was cured unsealed for 28 days (a) and an other set was unsealed cured for 28 days and then preconditioned for additional 28 days prior the exposure to carbonation (in total 56 days) (b). When comparing pore size distribution between the two sets of pastes, it is clear that the preconditioning leads to coarser pore structure independent of the l/b ratio. The difference can be attributed to the drying of the pastes during preconditioning. This suggests that carbonation can be accelerated not only by alkali loss from unsealed cured samples as shown in Chapter 6, but also by the change of the pore structure of these samples due to their preconditioning (from 28 to 56 days). The drying magnitude of unsealed cured samples was higher than that of sealed cured samples (see Figure 6.5 and Table 6.2). The different magnitude of drying of pastes is an indicator for different pore size distributions, as shown by Collins et al. [280]. This observation (Figure 9.12) together with results from Chapter 4, demonstrate that under different curing conditions, different gels are formed and different pore size distributions are obtained in the pastes. Therefore, the carbonation reactions are expected to proceed differently for sealed and unsealed cured pastes.

Paste S30 has similar behaviour as paste S50. Pastes S70 and S100 did not exhibited any change in the pore range that can be assessed with MIP.

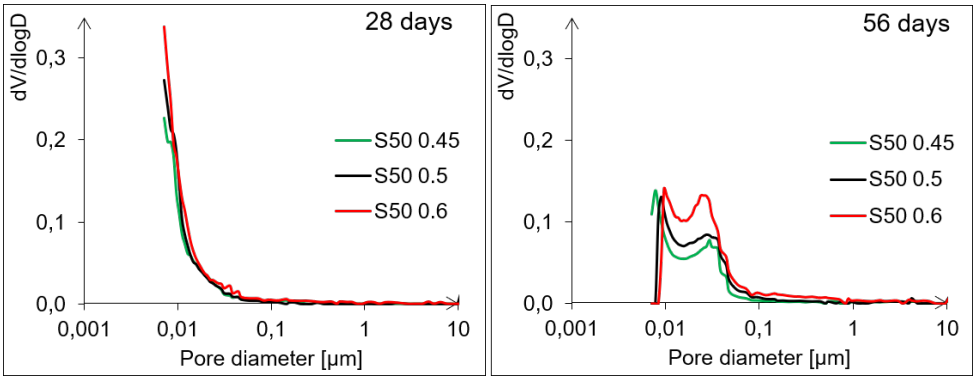


(a) unsealed cured pastes S50 for 28 days at 99%RH

(b) unsealed cured pastes S50 for 28 days at 99%RH and preconditioned for additional 28 days at 55%RH

Figure 9.12: MIP pore size distribution of the unsealed cured pastes S50. The pastes were produced with three different liquid-to-binder ratios, 0.45, 0.5, 0.6. These liquid-to-binder ratios are used in concretes S50 in Chapter 10.

#### 9.4.2.3. EXPOSURE CONDITIONS

In carbonated bulk paste samples, the carbonation products were amorphous $CaCO_3$, vaterite and calcite in all exposure conditions. Regardless the exposure conditions, the shifts of Si-O-Si (Al) (1000 $cm^{-1}$, Q2 silicon units) in alkali activated pastes were lower than that detected in cement-based materials (1080 $cm^{-1}$, Q3 silicon units) after carbonation, according to FT-IR measurements. For that reason, it is believed that the aluminosilicate and carbonate phases are closely intergrown to allow larger polymerization

of silicate units than observed in carbonated cement-based pastes.

The change of the pore structure due to carbonation is similar under both accelerated and natural exposure conditions. However, microcracking of the pastes was more dominant under accelerated exposure conditions due to '*drying*' effect (see Figure 9.5). For this reason, the compressive strength of alkali activated pastes was reduced significantly under accelerated carbonation, Figure 8.7. Under the natural exposure conditions (0.04% v/v $CO_2$, 55-60% RH, 20°C) this effect was not observed.

## 9.5. CONCLUDING REMARKS

Carbonation mechanism in this chapter is discussed regarding driving forces, carbonation reactions, carbonation products and effects of carbonation in relation to different paste compositions, curing and $CO_2$ concentration. Based on the experimental findings, carbonation is driven by the $CO_2$ concentration gradient. The $CO_2$ gas diffuses in the paste mainly through the connected gel pores or microcracks. Subsequently, $CO_2$ gas dissolves into the partially liquid-filled pores. Afterwards, the pore solution presents the main domain for carbonation reactions. Carbonation reactions follow then two steps, whereas the first step is characteristic for paste S0 and both steps are characteristic for pastes S30, S50, S70, S100:

1. the consumption of NaOH/KOH by the dissolution of $CO_2$ decreases the pH of the pore solution of the alkali activated paste,

2. the reduced pH initiates the dissolution of gel phases (Ca-Na-Al-Si-H, Ca-Na-Mg-Al-Si-H, Ca-Al-Si-H) and loss of calcium ions into the pore solution. Subsequently, calcium ions react with the soluble sodium/potassium carbonates forming calcium carbonates and NaOH/KOH. Subsequently, an excess of negative charges in the gel due to Ca removal, is balanced through formation of Si(Al)-OH or Si(Al)-O-Na groups. Condensation of neighbouring Si(Al)-OH or Si(Al)-O-Na results into Si-O-Si(Al), i.e. aluminosilicate gel. Carbonation products were predominantly amorphous calcium carbonates, vaterite and calcite.

Concerning the effect of carbonation on the pore solution of pastes, the critical parameter was curing. Sealed curing conditions prevented alkali loss from the paste during early stage of the gel formation and hence provided an enriched buffer for alkalinity of the pore solution. The coarsening of the pore structure

Concerning the effect of carbonation on the chemical changes of the gel phases, the GGBFS content had critical influence. In GGBFS-rich pastes, microstructure was less deteriorated. The paste S100 did not carbonate even after longer exposure (2 years) in accelerated and natural laboratory conditions, while it was carbonated in natural outdoor conditions due to microcracking.

Concerning the effect of carbonation on the physical properties, the GGBFS content had also the critical influence. The higher the GGBFS content in the mixture, the denser the microstructure is of the alkali activated pastes. Hence, $CO_2$ could hardly diffuse in the pastes S70 and S100. Chemical deterioration of the gel phases in blended FA/GGBFS alkali activated pastes resulted in an increase of gel pore size and the gel porosity. Additionally, physical discontinuities, such as microcracks and paste erosion, resulted in

the loss of cohesion within the blended pastes. Consequently, the modulus of elasticity decreased.

Regarding exposure conditions, both accelerated and natural carbonation resulted in similar carbonation products and increase of pore sizes and pore volume. However, pH of the alkali activated pastes was reduced more under accelerated than under natural carbonation. Beside pH difference, the change of microstructure is important to be taken into account for correlation between accelerated and natural carbonation. Gel formation is continuous under natural carbonation while it is not under accelerated carbonation due to short exposure time. For AAMs, this is of higher importance than for cement-based materials when it comes to carbonation. In AAMs, $Na^+$ and $OH^-$ are consumed continuously for gel formation, and at the same time they play role of buffer mechanism for carbonation reactions. Therefore, use of accelerated carbonation for predicting pH of AAMs under natural carbonation is not fully appropriate.

Finally, it is shown that the correct description of the microstructure evolution and evolution of the pore solution composition (primarily free $Na^+$) are crucial for long-term predictions of the propagation rate of carbonation in AAMs.

# 10

# CARBONATION RATES OF ALKALI-ACTIVATED AND CEMENT-BASED CONCRETES

*"The farther backward you can look, the farther forward you are likely to see."*

Winston Spencer Churchill

*The reduction of alkalinity from ~ 13 to ~ 9 by carbonation of the pore solution of reinforced cement-based concrete structures results in the reinforcement corrosion. The rate of carbonation is an important input for design of the concrete cover depth and the service life prediction of reinforced concrete structures because the initiation of reinforcement corrosion is usually considered as the end of service life of concrete infrastructure. The information from the field carbonation of alkali activated concrete is in most cases limited and related to exposure shorter than 30 years. In this chapter, a comparative study regarding carbonation of alkali-activated concretes and cement-based concretes in different environmental conditions has been carried out. The pH and carbonation depths are periodically measured. The chemical and physical changes of material constituents were also investigated. The interpretation of the findings at the concrete scale are based on the results presented in Chapters 5 and 9 and our understanding of the carbonation mechanism at the paste level. The results show that, despite the low porosity of alkali-activated concrete, these concretes must have an appropriate curing in order to be used in structural applications due to their lower carbonation resistance compared to cement-based concrete. Regardless the exposure conditions, the pH of carbonated alkali-activated concrete was maintained above 9. Finally, recommendations for alkali activated concrete applications and their improved carbonation resistance are given.*

## 10.1. INTRODUCTION

STRUCTURAL application of alkali activated concrete is still argued worldwide due to lack of data regarding long-term performance [40]. Additionally, the prediction of the service life of structures made with alkali activated concrete is still not considered in the literature. This largely impedes the standardization process of alkali activated concrete for the building industry. Furthermore, it is still unknown whether the carbonation is responsible for corrosion of reinforcing steel in alkali-activated concretes or some other carbonation-induced structural deterioration of the alkali-activated binder has to be envisaged.

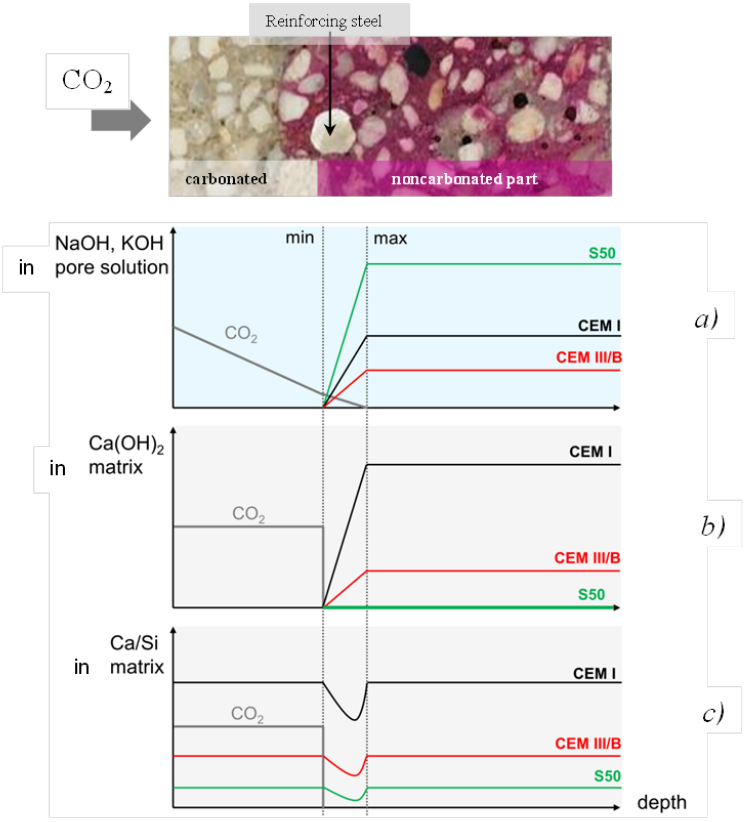


Figure 10.1: Domains (pore solution, microstructure) and parameters (NaOH/KOH, $Ca(OH)_2$ content, Ca/Si ratio) for comparative study between cement and alkali activated concretes (properties indicated in Table 10.3). The comparison includes the following:

a) Pore solution (NaOH/KOH). Carbonation initially occurs in the pore solution of the concrete. Therefore, NaOH/KOH as a dominant species in the pore solution plays a buffer role for the carbonation reactions. Concrete S50 has the highest concentration of the alkali amongst the studied concretes.
b) $Ca(OH)_2$ in microstructure. Concrete CEM I has the highest content of $Ca(OH)_2$.
c) Ca/Si in the microstructure. Concrete CEM I has the highest Ca/Si ratio.

As mentioned in Chapter 2, carbonation of cement-based concrete results in a decrease of the pH of the pore solution below values that cause steel depassivation; hence carbonation may initiate corrosion of reinforcing steel. Beside carbonation of the pore solution, the carbonation of $Ca(OH)_2$ and C-S-H gel results in the formation of $CaCO_3$ and amorphous silica gel, respectively. In alkali-activated slag paste, the absence of $Ca(OH)_2$ may account for faster carbonation compared to the rate of carbonation in cement-based pastes (Puertas et al. [60]). Furthermore, at concrete level, the presence of aggregate leads to the formation of Interfacial Transition Zone (ITZ). The ITZ contributes to a faster propagation rate of the carbonation front in cement based concrete [281]. Often the ITZ is a highly porous zone due to the non-optimized packing of the cement particles in the close vicinity of aggregate surfaces. However, the influence of ITZ on carbonation progress is unknown in alkali activated concrete.

Figure 10.1 demonstrates influence of key parameters on the carbonation mechanism for two concrete domains, i.e. pore solution and microstructure. The comparative study of cement and alkali activated concretes includes the following parameters:

- pore solution (NaOH/KOH). Carbonation initially occurs in the pore solution of the concrete. Hence, NaOH/KOH as a dominant species in the pore solution plays a buffer role for the carbonation reactions;
- $Ca(OH)_2$ in the microstructure;
- Ca/Si in the microstructure.

A full understanding of the effects of these parameters on deterioration of concrete is a key step in modelling of the carbonation rate in alkali activated materials, as shown in Chapter 9. To evaluate the effects of these parameters, the pH and carbonation depths are periodically measured in alkali activated concrete. The chemical and physical changes of material constituents (paste and ITZ) of alkali activated concrete were also investigated and compared to cement-based concretes. The interpretation of the findings at the concrete level are based on the results presented in Chapters 5 and 9 and our acquired understanding of the carbonation mechanism at the paste level. Finally, recommendations for alkali activated concrete applications and their improved carbonation resistance in practice are given. In addition, a model for the propagation rate of the carbonation front in alkali activated concrete is presented in Appendix B. The model is used for calculating the time to depassivation of reinforcing steel in alkali activated concrete.

## 10.2. EXPERIMENT DESIGN



### 10.2.1. MIXTURE PROPORTIONING AND EXPERIMENT SET UP

In Chapters 6 and 8 it was shown that pastes S100 have a high resistance to carbonation due to their dense microstructures. It remains of interest to study binders and concretes with lower slag content in the binder than 100 wt.%. For that purpose, the concretes labelled as S30 (l/b=0.5), S50 (l/b=0.5), S70 (l/b=0.5) and S50 (l/b=0.6) were cast. Although concrete mixture S100 was not considered in detail in this carbonation study, its carbonation rate and $Cl^-$ resistance are reported in Appendix B (Figure B.4 and Table B.3, together with concrete mixtures S30, S50 and S70.

In the absence of European standards for performance testing of alkali activated concrete, requirements for carbonation resistance are followed from the EN 206-1. In this standard, requirements for design of cement concrete mixtures are given (Appendix B, Table B.1). The assessment of carbonation resistance of alkali activated concrete with 260 kg/m$^3$ of FA+GGBFS was performed to investigate conformity of an alkali activated concrete with minimum binder content for exposure class XC1. In contrast, the assessment of carbonation resistance of alkali activated concrete with 400 kg/m$^3$ of FA+GGBFS was performed to investigate conformity of an alkali activated concrete with binder content as prescribed for XC3.

As discussed in Chapter 8, alkali activated pastes are prone to microcracking. In order to reduce the impact of microcracking, fibres were used in one of the concrete mixtures. The fibre reinforced geopolymer (FRG) mortar was designed with the same GGBFS:FA proportion as in alkali-activated concrete (Table 10.1, Mix 8: FRG S50). Polyvinyl alcohol (PVA) fibres and river aggregates (fine [0-4mm] and coarse [4-16mm]) were used. The amount of fibres added to the mixture is 2% by the total volume of the composite. Cement-based concretes were prepared with CEM I and CEM III/B. The details of mixtures proportion are listed in Table 10.1.

Table 10.1: Mixture designs for alkali activated concretes, cement-based concretes, fibre reinforced alkali activated (FRG) mortar and plain mortar S50 [m$^3$].

| | FA [kg] | GGBFS [kg] | OPC [kg] | Sand [0-4 mm] | Aggregate [4-8 mm] | Aggregate [8-16 mm] | Activator [kg] | Liquid/ binder |
|---|---|---|---|---|---|---|---|---|
| Density [kg/m$^3$] | 2440 | 2900 | 3000 | 2640 | 2650 | 2650 | 1250 | [-] |
| Mix 1 S30 | 280 | 120 | 0 | 789 | 439 | 524 | 200 | 0.5 |
| Mix 2 S50 | 200 | 200 | 0 | 789 | 439 | 524 | 200 | 0.5 |
| Mix 3 S70 | 120 | 280 | 0 | 789 | 439 | 524 | 200 | 0.5 |
| Mix 4 S100 | 0 | 400 | 0 | 789 | 439 | 524 | 200 | 0.5 |
| Mix 5 S50 | 130 | 130 | 0 | 789 | 439 | 524 | 156 | 0.6 |
| Mix 6 CEM I | 0 | 0 | 400 | 789 | 439 | 524 | 200 (water) | 0.5 |
| Mix 7 CEM III/B | 0 | 280 | 120 | 789 | 439 | 524 | 200 (water) | 0.5 |
| Mix 8 FRG S50* | 437 | 437 | 0 | 775 | | | 393 | 0.45 |
| Mix 9 plain mortar S50** | 373 | 373 | 0 | 1119 | | | 373 | 0.5 |

* Mixture 8, FRG S50, has in addition to primary constituents, also:
- Superplasticizer (type: sodium naphthalene formaldehyde sulphonate-based superplasticizer of 0.14 wt.% by binder. The density is 1070 kg/m$^3$.)
- PVA fibres (PVA fibres with a length of 8 mm and a diameter of 40 $\mu$m were used. The tensile strength of the PVA fibre is 1600 MPa and the density is 1300 kg/m$^3$.)

** Mixture 9, plain mortar S50, has sand fraction 0-2 mm, as used in standard cement mortar.



The concrete samples were beams (1500×100×150 mm$^3$), which were cured in unsealed conditions (in curing room with 99% RH) for 28 days. After 28 days curing, the beams were sawn into 187.5 mm-wide samples (see Figure 10.2), sealed at the lateral sides and preconditioned for additional 28 days under laboratory conditions (55% RH, 20 °C, 0.04% v/v $CO_2$). After preconditioning, samples were exposed to different carbonation conditions (Table 10.2). The concrete samples in natural outdoor conditions (TU Delft-CITG) are shown in Figure 10.3. In addition to concrete samples, cement (CEM I

and CEM III/B) and alkali-activated pastes with the same binder content and l/b were also made for microstructure and pore structure analyses.

Table 10.2: Exposure conditions for carbonation of concretes.

| | Natural laboratory | Natural outdoor | Accelerated carbonation |
|---|---|---|---|
| $CO_2$ concentration | 0.04% v/v | 0.04% v/v | 1.00% v/v |
| Relative humidity | 55% | 80-98% | 60% |
| Temperature | 20°C | 0-20°C | 20°C |

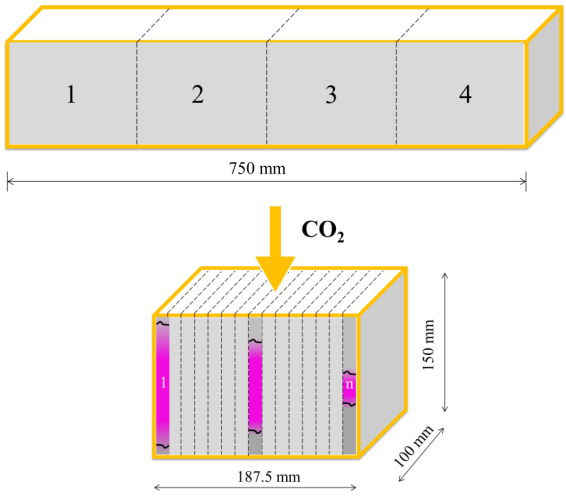


Figure 10.2: Geometry of the prepared concrete samples for each of the mixtures. After a certain period of exposure, a slice (width equal to 1 cm) of each of the prisms was cut (slices denoted as 1, . . . , n). Subsequently, the slice surface was sprayed with phenolphthalein for measurement of the carbonation depth. The noncarbonated part is indicated by the pink colour.

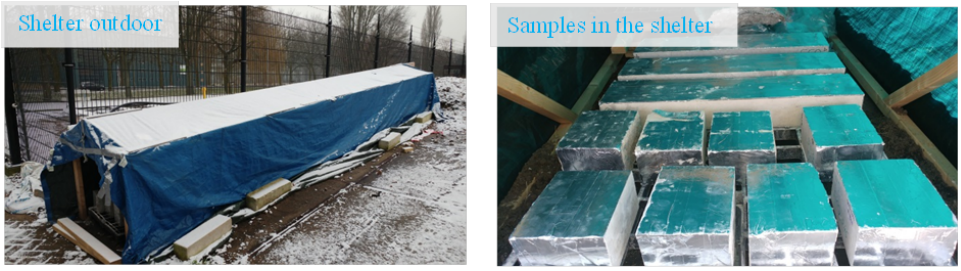


Figure 10.3: Concrete samples in natural outdoor conditions (TU Delft-CITG) sealed at the lateral sides, while bottom and top side were exposed to unidimensional carbonation as indicated in Figure 10.2 on the single prism.

## 10.2.2. METHODS

### 10.2.2.1. COMPRESSIVE STRENGTH

Compressive strength was measured for each concrete mixture at 1 day, 7, 28, 56, 180, 365, 548 days according to the [NEN 12390-3:2009] on three cubes with dimension of 150×150×150 $mm^3$. Then the mean values and standard deviations were calculated for each set of the data.

### 10.2.2.2. CARBONATION DEPTH TESTED WITH PHENOLPHTHALEIN

Carbonation depths were measured after 0, 14, 28, 42, 56, 114, 193, 236, 365, 548 days of exposure in accelerated conditions. In natural indoor and outdoor conditions, the carbonation depths were measured after 0, 28, 240, 365, 548. Slices with a thickness of 10-15 mm were cut from the concrete prisms by sawing (Figure 10.2). The fresh surface was sprayed with a 1 wt.% phenolphthalein aqueous solution. On average, 10 to 15 measurements were made per slice. Then the standard deviations were calculated for each set of the data.

### 10.2.2.3. CARBONATION FRONT TESTED WITH POLARIZED LIGHT MICROSCOPE (PLM) AND ELECTRON MICROSCOPE (ESEM)

In addition to the phenolphthalein spray method, the carbonation front was also assessed by PLM under cross-polarized transmitted (XPT) light, following the procedure discussed in Chapter 7, Section 7.2.2.2. Furthermore, samples were examined with ESEM, in order to show microstructural features of the material before and after carbonation. The microstructures of paste and ITZ in concrete were characterized with Philips-XL30-ESEM microscope. Element changes were studied with energy dispersive X-ray spectroscopy (EDS, NSS 3.3).

### 10.2.2.4. PORE STRUCTURE CHARACTERIZATION WITH MIP

Porosity and pore size distribution of the pastes were investigated with MIP measurements. For sample preparation the procedure is described in Chapter 4.

### 10.2.2.5. pH OF THE PORE SOLUTION

Direct extraction of the pore fluid from carbonated concrete samples was not possible due to the presence of aggregates and sample size that is needed for pore solution extraction. Therefore, pH measurements were carried out on the powder suspension, similar to [225]. The suspension was obtained by equilibrating 1 g of powdered sample with 10 ml of de-ionized water during 15 minutes at ambient temperature while stirring with a magnetic bar. Subsequently, the pH of the suspension was measured with a pH meter 827 Metrohm.



# 10.3. RESULTS

## 10.3.1. COMPRESSIVE STRENGTH

The compressive strength results and standard deviations for alkali activated concretes S50 (l/b=0.5), S50 (l/b=0.6), cement-based concretes made of CEM I (w/c=0.5) and CEM III/B (w/c=0.5) are shown in Figure 10.4. The compressive strength of concretes was

measured during curing, preconditioning and exposure. Afterwards, the concrete samples were placed in outdoor sheltered conditions, where development of the compressive strength was monitored from 56 days to 548 days. The compressive strength of mixtures S30, S50, S70, S100 are shown in [282]. The strength increased with increasing GGBFS content.

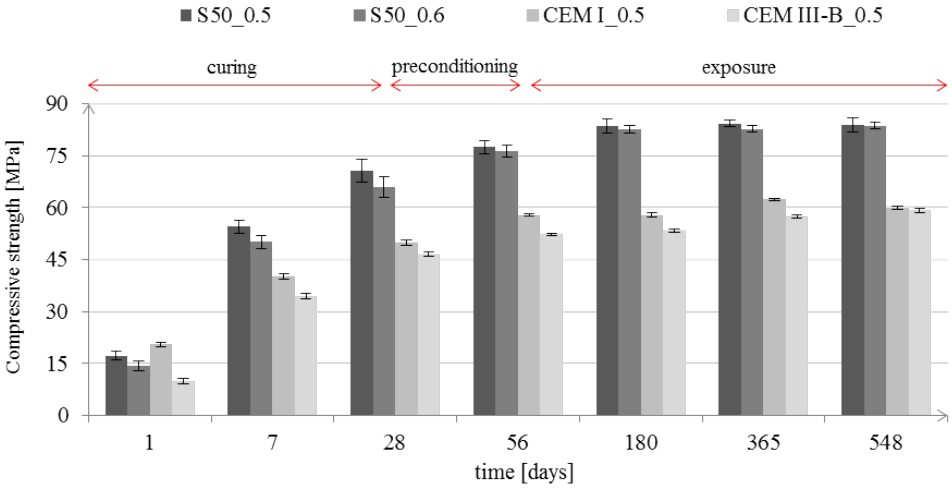


Figure 10.4: Compressive strength development in cement-based and alkali-activated concretes (samples (150×150×150 mm$^3$) were cured in the curing room for 28 days, preconditioned for additional 28 days (28-56 days) at 55% RH and then exposed to natural outdoor sheltered conditions (56-548 days)).

Figure 10.4 shows that the strength of alkali-activated concrete samples is higher than that of cement-based concrete samples. Furthermore, when comparing compressive strength of S50 mixture with precursor content (GGBFS+FA) of 400 kg/m$^3$ (l/b=0.5) with S50 mixture with precursor content of 260 kg/m$^3$ (l/b=0.6), there is no significant difference, specifically at the later ages (180, 365, 548 days). This suggests that for reaching high strength in alkali-activated concrete, the binder content can be optimized, i.e. reduced. Regardless the binder content, the failure in compression is determined by the aggregate strength, as illustrated in Figure 10.5.

Figure 10.6 shows compressive strength for paste compared to the strength of plain mortar, fibre-reinforced mortar and plain concrete S50. The activator to binder ratio for paste, mortar and concrete was 0.5. As for fibre-reinforced mortar S50, the activator to binder ratio was 0.45. Compressive strength of the plain mortar is slightly lower than the paste for all testing ages (Figure 10.6). This is due to the presence of ITZ around sand particles. The phenomenon of relatively weaker ITZ zone in OPC-based materials arises, at least in part, due to the spatial distribution of cement grains against the larger aggregate grains (the so-called wall effect) [283]. Such packing leads to a more porous area around the aggregates, leading to reduction of the overall mortar strength compared to the strength of the corresponding pastes. Similar phenomenon is observed in this study regarding the difference in strength between alkali-activated paste, mortar and concrete samples.

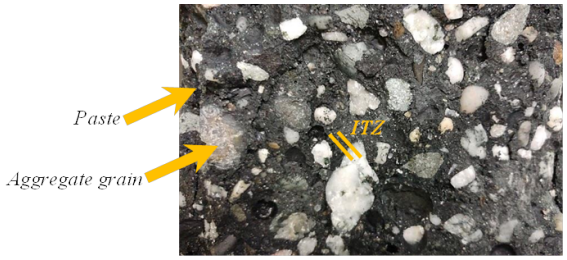


Figure 10.5: Photograph of concrete cube (sample S50) after compressive strength test (at 548 days). It can be seen that most of the aggregates were split. This implies that the paste and the bond between the paste and aggregate grains is stronger than the strength of the aggregate grains (maximum aggregate size 16 mm).

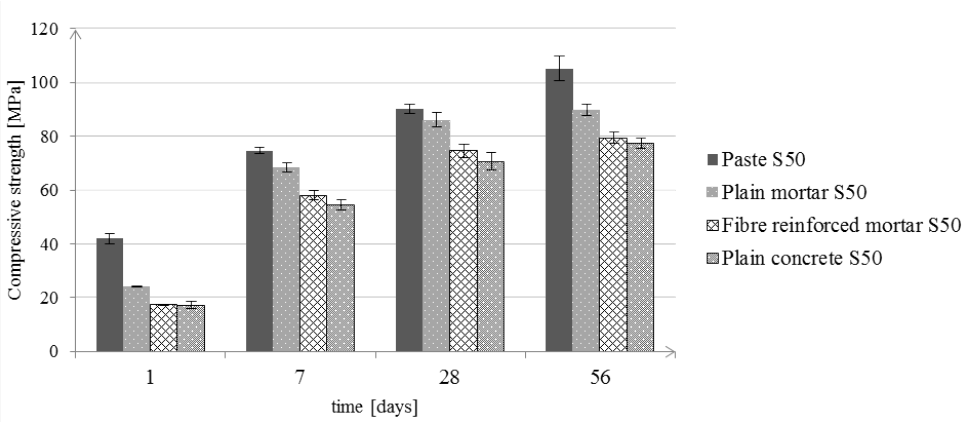


Figure 10.6: Compressive strength development in alkali-activated paste S50, alkali-activated plain mortar S50 (Mix 9, Table 10.1), alkali-activated fibre reinforced mortar S50 (Mix 8) and plain alkali-activated concrete S50 (Mix 2).

The difference in strength between alkali-activated and cement-based concretes (Figure 10.4) is explained by the microstructure of the pastes. The total porosity and pore size distributions were determined at 7, 28 and 56 days (Figure 10.7). In addition, images of microstructures of the pastes at 7, 28 and 56 days are given in Figure 10.8.



The peaks for capillary pores were identified in cement-based pastes at all ages. This was not the case in alkali activated pastes. Capillary pores were observed in tests at 56 days in alkali activated pastes S50, as a consequence of drying. Exposure of the specimens to laboratory conditions (at 55% RH and 20 °C) caused microstructure coarsening between 28 and 56 days as can be observed from Figure 10.7. Although the pore size distribution of pastes S50 is changed at 56 days compared to 28 days, the morphology of the microstructure did not change between 28 and 56 days. SEM images (Figure 10.8) indicate an evolution of the microstructure between 7 and 56 days of all pastes.

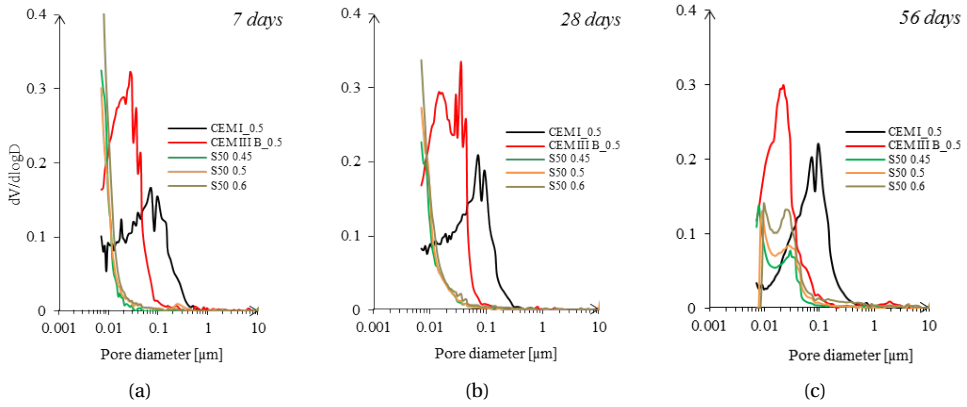


Figure 10.7: Evolution of the pore structure in alkali-activated paste S50 and cement-based pastes. Pastes were unsealed cured for 28 days (99% RH, 20 °C). Subsequently, they were preconditioned from 28 days until 56 days in natural laboratory conditions (55% RH, 20 °C).

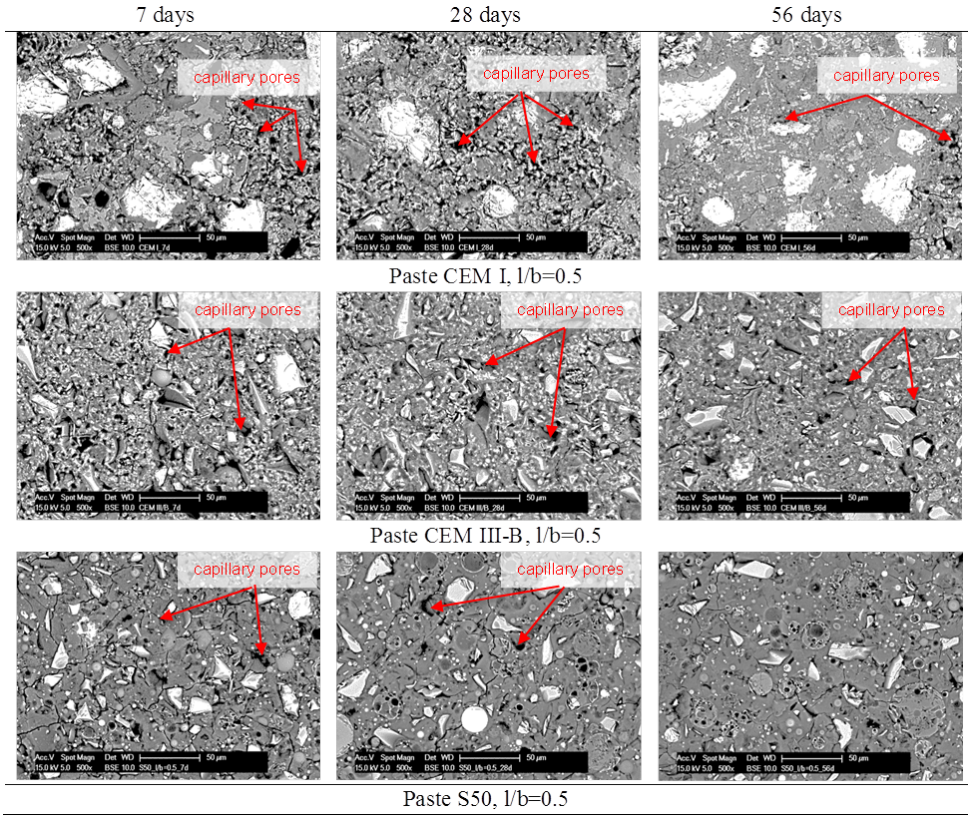


Figure 10.8: Microstructure of paste CEM I, paste CEM III/B and alkali-activated paste S50 at 7, 28 and 56 days. Pastes were cured unsealed for 28 days in the curing room (99% RH, 20 °C). Subsequently, pastes were preconditioned in laboratory conditions (55% RH, 20 °C) for additional 28 days.

In contrast to cement-based pastes, the dense microstructure of paste S50 was already observed after 7 days. This implies that alkali activated pastes have a very dense microstructure that is comparable to those of cement paste after 210 days of curing [284] (based on the same w/c ratio). This is a result of continuous volume growth of the reaction products [74]. Moreover, the reaction products of alkali activated GGBFS have a higher pore space filling capacity than that in the cement pastes, as shown by Zuo and Ye [74]. For that reason, the dense microstructure of paste S50 (Figure 10.8) is responsible for high strength of alkali-activated concretes (Figure 10.4) already at the early age. Due to refined and strong microstructure and strong ITZ, the final failure in compression is mainly through the aggregate and much less through the paste (see Figure 10.5).

### 10.3.2. CHARACTERIZATION OF THE INTERFACIAL TRANSITION ZONE (ITZ) IN NONCARBONATED CONCRETE

The ITZ of concrete is an important feature for the carbonation process. Therefore, its characterization is a basis for understanding its changes after carbonation. For a fair comparison of the microstructure and ITZ of different concrete mixtures, they were compared at 180 days. At that time, also slowly hydrating mixtures have reached their final microstructure. This is supported by compressive strength development of the concretes (see Figure 10.4): after 180 days the compressive strength did not show much change in both cement and alkali activated concretes. Figure 10.9 shows ESEM-BSE images of non-carbonated cement-based and alkali-activated S50 concrete and FRG S50 samples.

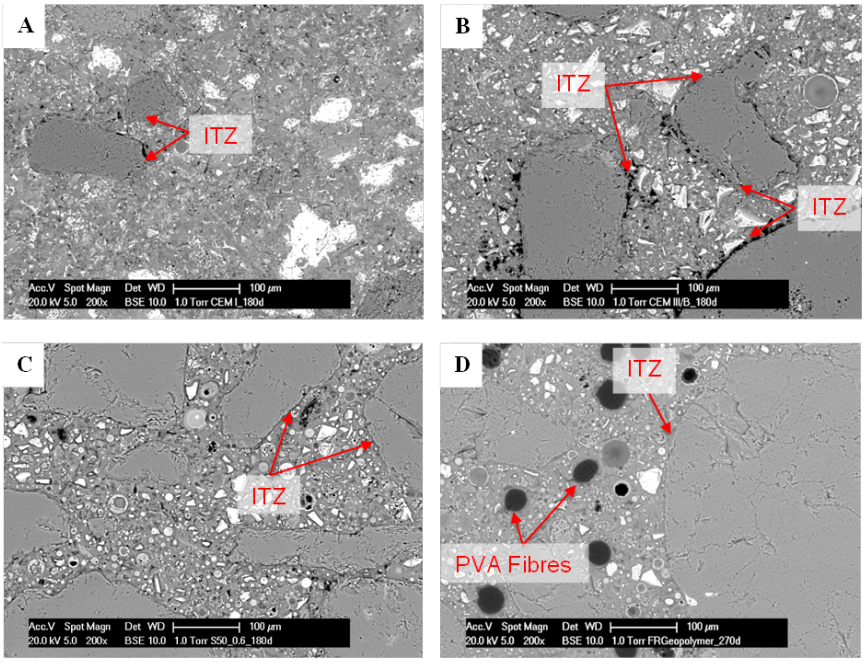


Figure 10.9: Visualization of the interfacial transition zone (ITZ) in CEM I (A), CEM-III B (400 kg/m$^3$) (B), S50-0.6 (260 kg/m$^3$) (C), FRG S50-0.45 (D).

In CEM I and CEM III/B concrete (Figure 10.9A, B), the heterogeneity within the interface between sand grains and paste is due to the presence of the unreacted cement particles, a higher concentration of calcium hydroxide and ettringite [285], less calcium-silicate-hydrate (C-S-H) and large capillary porosity [283]. In CEM III/B concrete (Figure 10.9 B), there were large voids adjacent to a sand grain. This indicates, together with MIP porosity results, a more porous ITZ in cement-based concrete than in alkali activated concrete. In alkali-activated concrete samples, there is no clear porous ITZ (Figure 10.9 C, D). SEM images show that adjacent to a sand grain, the gel is denser compared to reaction products in cement-based concrete (Figure 10.9A, B, C, Figure 10.10A, B, C), consistent with the observations from the literature [286]. The reason for this is that the C-(N-)A-S-H gel has a much denser atomic structure than C-S-H gel [149]. Although, the alkali activated concrete has more homogeneous and denser ITZ than cement-based concrete, the Ca/Si ratio of reaction products near the ITZ is observed to be lower than in the bulk paste [286].

Since only gel type reaction products (as shown in Chapter 4) form in the ITZ and in the matrix of alkali activated concretes (Figure 10.11) compared to cement-based concrete (calcium hydroxide, ettringite, C-S-H [283]) it is hypothesized that the carbonation will be favoured evenly in both the ITZ and the surrounding matrix of alkali-activated concrete.

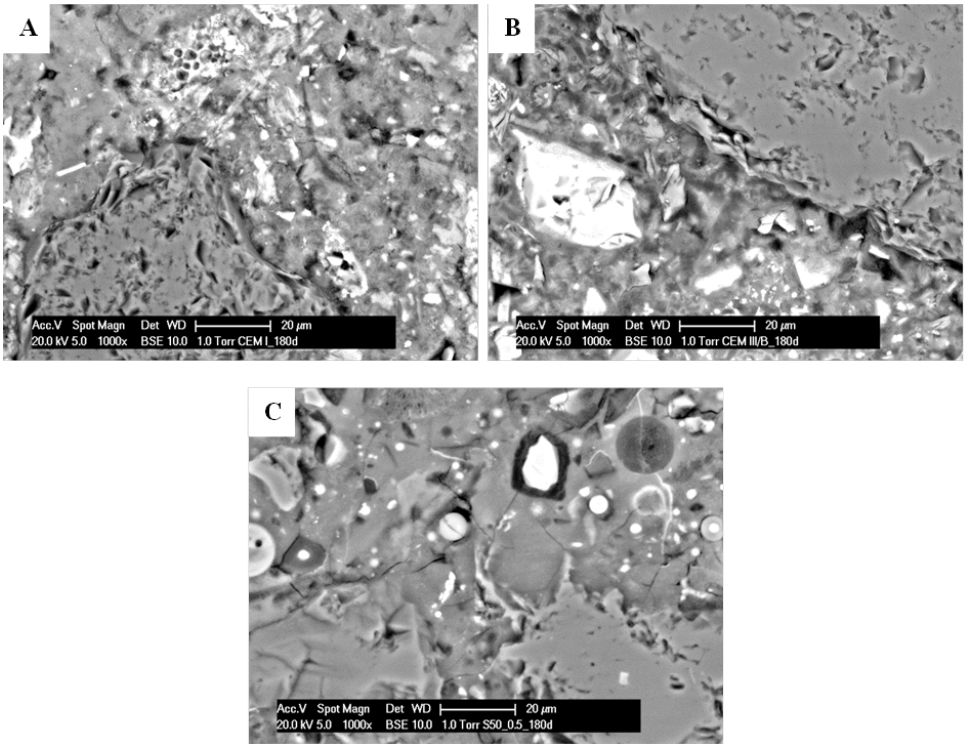


Figure 10.10: SEM-BSE images of the magnified interfacial transition zone (ITZ) in CEM I, CEM/III B (400 kg/m$^3$), S50-0.5 (400 kg/m$^3$).

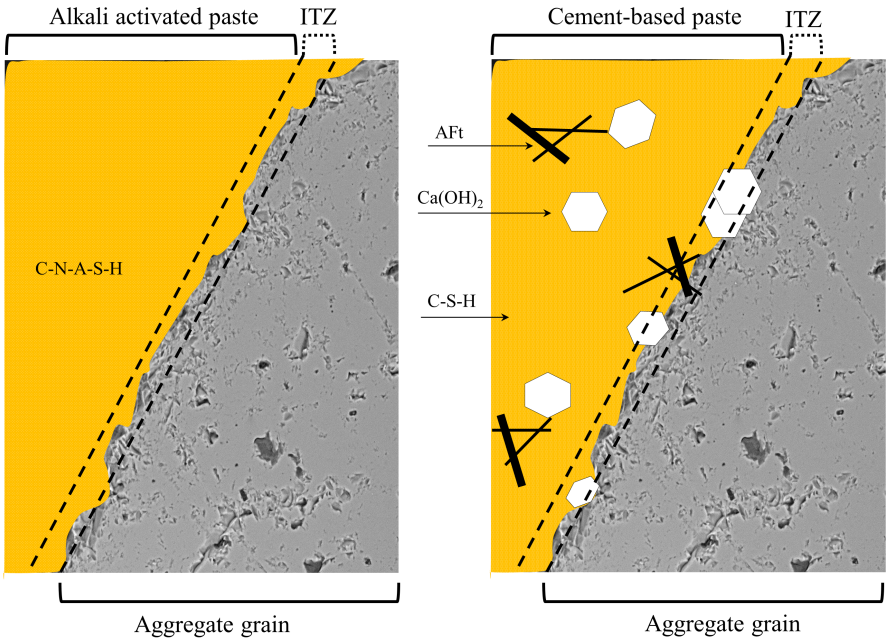


Figure 10.11: Schematic illustration of the ITZ in the alkali activated concrete and cement-based concrete. The ITZ of alkali activated concrete is homogeneous due to precipitation of only C-N-A-S-H gel in this zone. The ITZ of cement-based concrete is heterogeneous, it consists of different reaction products such as ettringite (AFt), $Ca(OH)_2$ and C-S-H gel.

### 10.3.3. CHARACTERIZATION OF THE CARBONATION FRONT

Figure 10.12 presents the cross sections of cement-based and alkali-activated concrete samples exposed for 548 days to laboratory and accelerated carbonation before and after spraying phenolphthalein indicator. The noncarbonated zone is pink coloured while the carbonated zone is colourless. It is clear that the propagation rate of carbonation front in alkali activated concretes is faster compared to that in cement-based concretes. The carbonation proceeds slower in cement-based concrete than in alkali activated concrete due to the presence of $Ca(OH)_2$ and higher Ca/Si ratio of reaction products of cement-based concretes. For studying the geometry of the carbonation front and distribution of carbonates, the carbonation front in alkali-activated concrete (S50-0.5) was assessed with PLM (see Figure 10.13).

When using appropriate modes of illumination of a polarizing microscope, the zones which underwent carbonation can be identified as presented in Figure 10.13. Similar to *paste* S50, as shown in Chapter 7, the carbonation front in alkali activated *concrete* S50 has been detected by a clear front line between carbonated (white/brown) and non-carbonated zone (black). Figures 10.14a,b show distribution of carbonates all over the microstructure of concrete. The identification of the carbonates is discussed next.

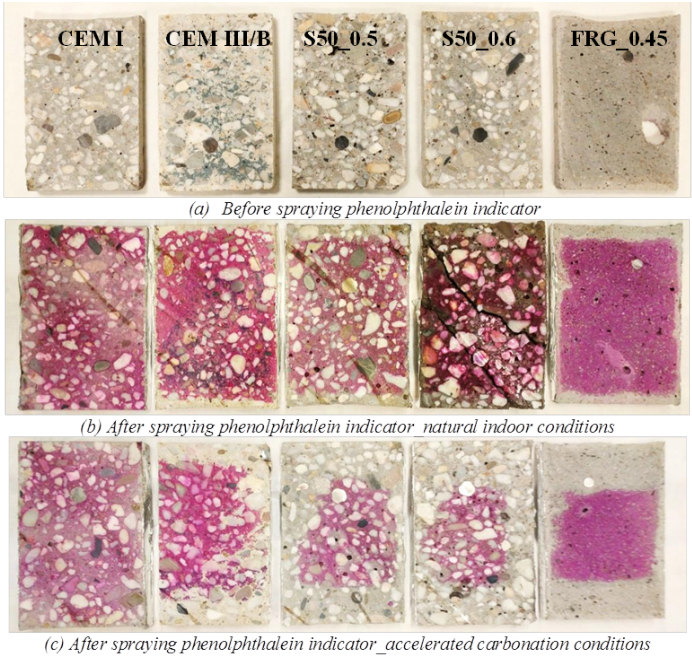


(a) Before spraying phenolphthalein indicator

(b) After spraying phenolphthalein indicator_natural indoor conditions

(c) After spraying phenolphthalein indicator_accelerated carbonation conditions

Figure 10.12: The cross sections of concrete samples exposed to natural laboratory and accelerated carbonation before and after spraying phenolphthalein indicator, comparison of the cement-based and alkali-activated concretes. Exposure time: 548 days.

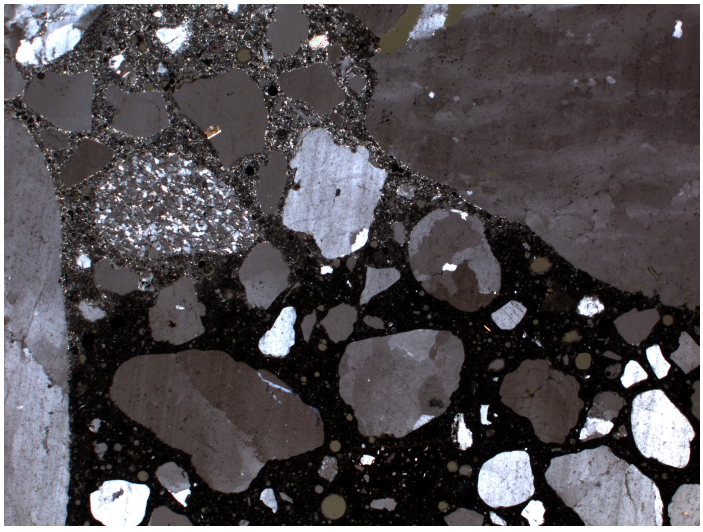

Figure 10.13: Noncarbonated (black) and carbonated concrete S50 microstructure (characterised by a light brown-yellowish paste matrix when viewed in plane-polarized transmitted light, not shown here). Image is obtained under cross-polarized transmitted (XPT) light at 25 times magnification, image width 2.5 mm.

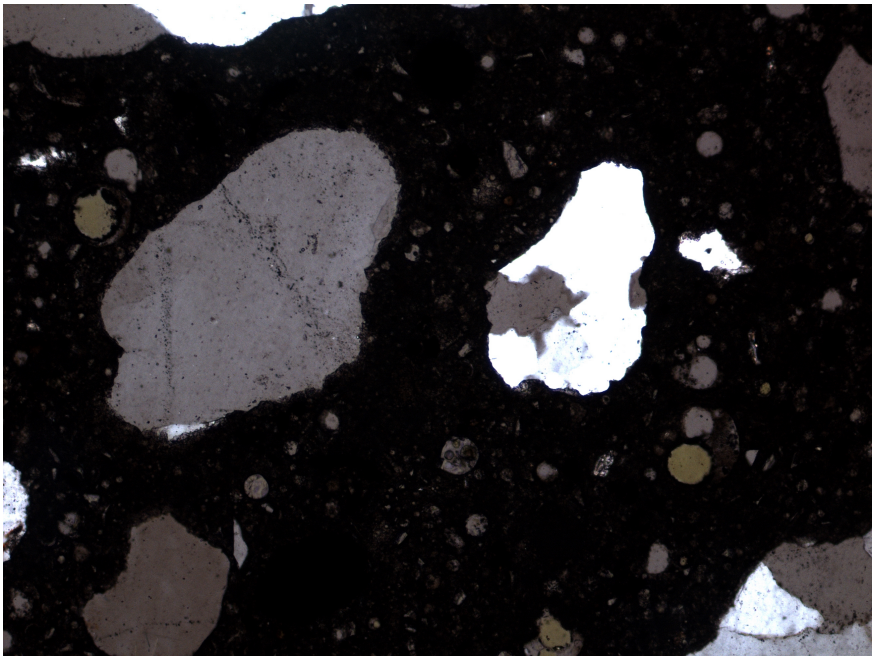

(a) Close view of noncarbonated area at 100 times magnification, XPT, image width 0.75 mm.

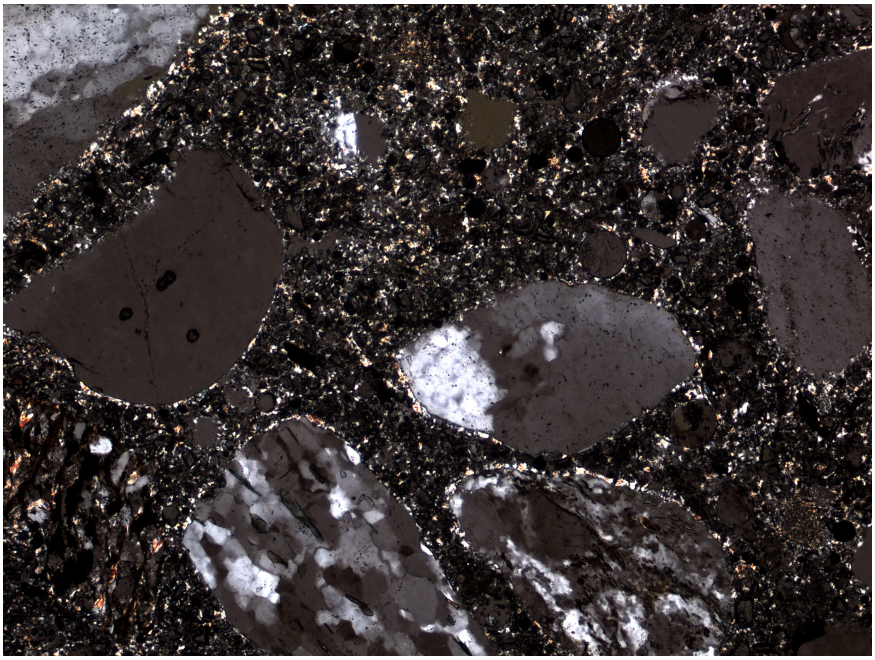

(b) Close view of carbonated area at 100 times magnification, XPT, image width 0.75 mm.

Figure 10.14: Alkali-activated concrete S50 with magnified noncarbonated and carbonated areas. In carbonated area, carbonates are distinguished from matrix based on their whitish appearance.

### 10.3.4. CHARACTERIZATION OF THE MICROSTRUCTURE OF CARBONATED CONCRETE

Figure 10.15 shows deterioration of the microstructure in carbonated concrete S50. It can be seen that microcracks (Figure 10.15) and decalcification (Figure 10.16) are the two main effects of natural carbonation. The occurrence of decalcification is supported by EDS observations. EDS-spectrum of carbonated concrete is presented by pattern (1) (Figure 10.16) with high silicon, carbon and low calcium peaks. The EDS spectrum (pattern (2)) shows that partially carbonated concrete contains a large amount of calcium.

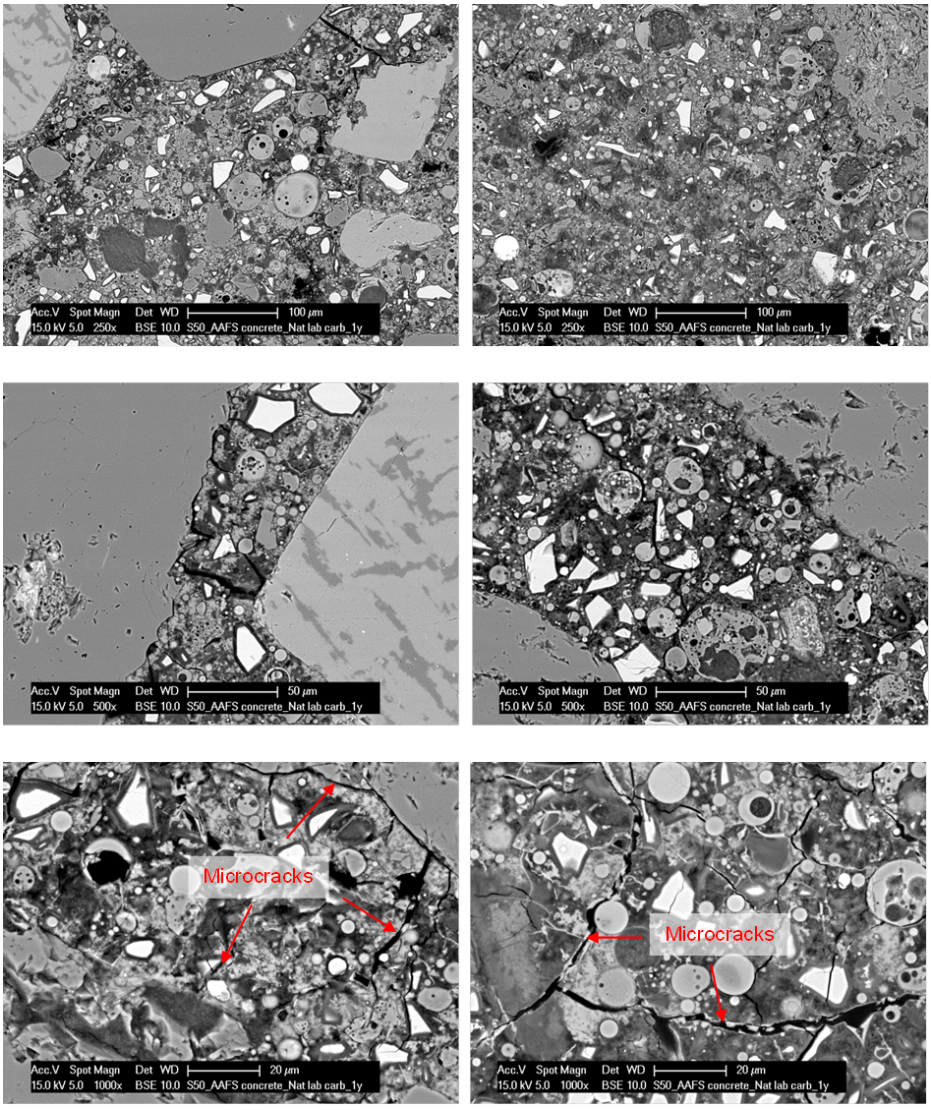


Figure 10.15: Carbonated alkali-activated concrete in natural laboratory conditions (S50-0.5).

The carbonation mechanism at concrete level is the same as found at paste level, accompanied by a chemically impure silica gel, depleted of calcium. Regarding carbonation of the ITZ between paste and aggregate, PLM and ESEM image analysis do not reveal a significant difference in degree of carbonation between carbonated matrix and carbonated ITZ (Figures 10.14 and 10.15) in agreement with the findings from Bernal et al. [65]. The Mg/Si ratio and Na/Si ratio of the gel did not change after carbonation. This means that only Ca is reacting with $CO_3^{2-}$ forming calcium carbonates, as shown for alkali activated pastes in Chapter 7.

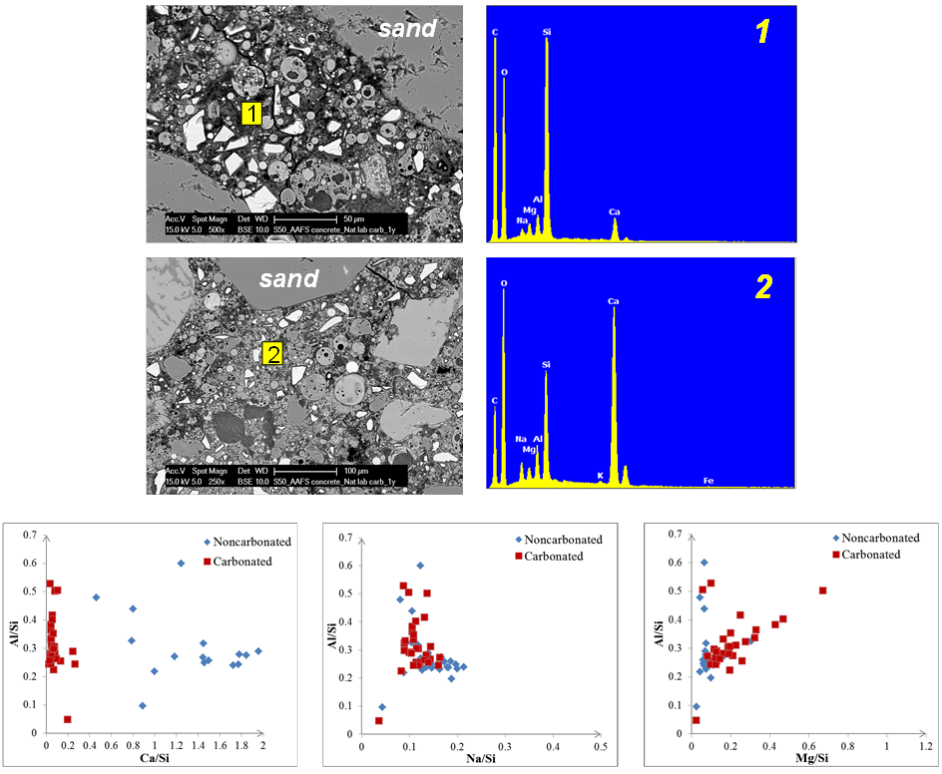


Figure 10.16: ESEM micrographs and EDS spectra of different zones in alkali-activated concrete; complete carbonated concrete (1), partially carbonated concrete (2).

10

### 10.3.5. EXPERIMENTAL INVESTIGATION OF THE CARBONATION RATE

The propagation rate of the carbonation front was monitored for three different exposure conditions: natural (outdoor (sheltered) and indoor) and accelerated carbonation conditions (Figure 10.17 (A), (B), (C)). Propagation of the carbonation front in concrete samples was monitored from the age of 56 days. Figure 10.17 (A) demonstrates that carbonation did not proceed in the CEM I concrete in natural outdoor (sheltered) conditions. This is due to the large hydroxide alkalinity of the CEM I concrete. In contrast, the carbonation proceeds in CEM III/B and alkali activated concretes.

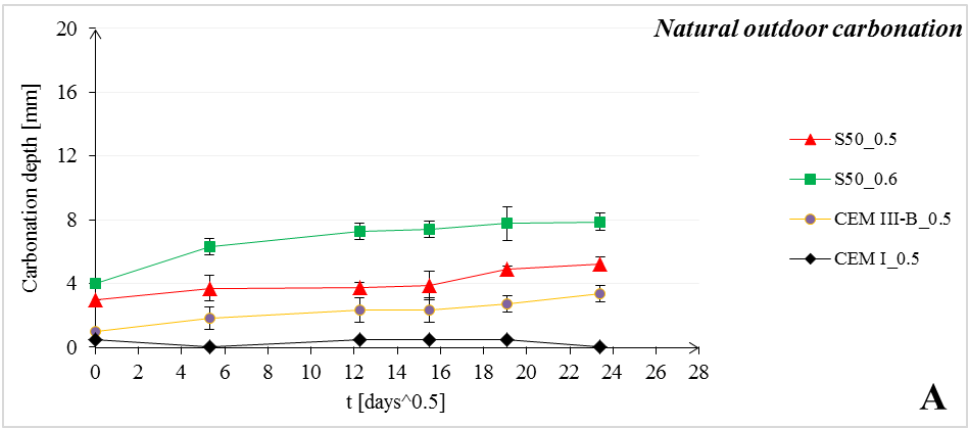


(a) Natural outdoor conditions

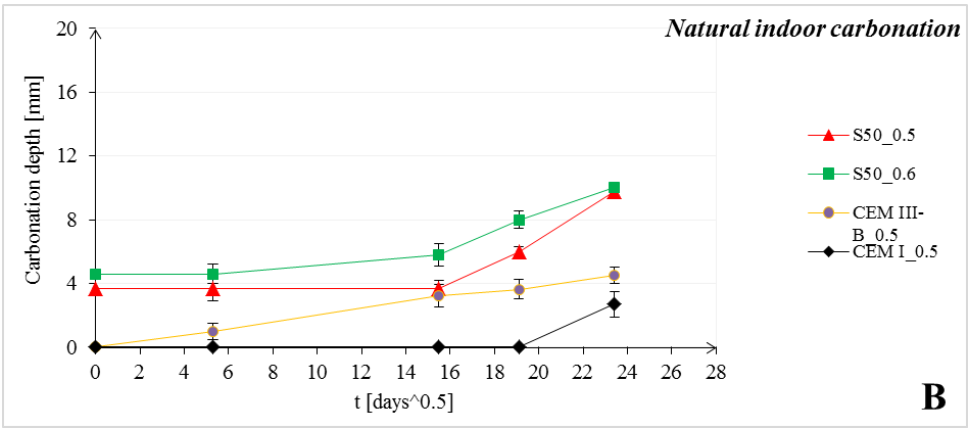


(b) Natural indoor conditions

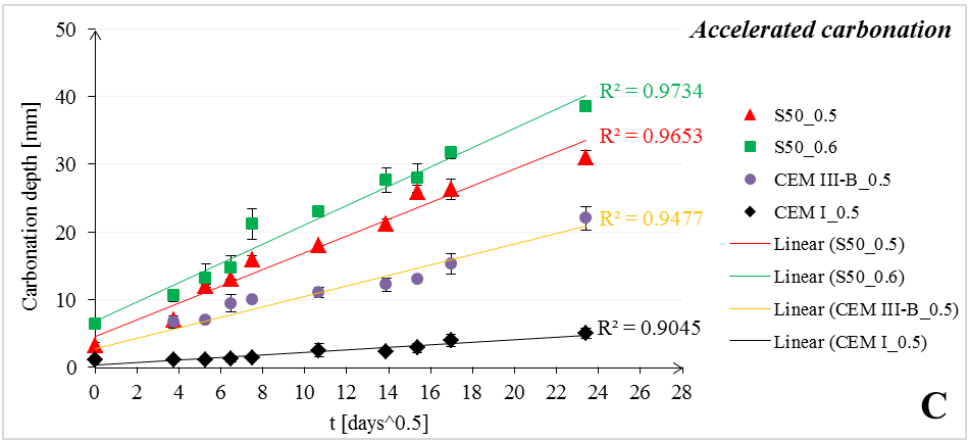


(c) Accelerated indoor conditions

Figure 10.17: Carbonation depth versus time in natural outdoor (sheltered), indoor and accelerated carbonation conditions. At 56 days measurements of the carbonation depth in concretes started and, therefore $56^{th}$ day is regarded as t=0. Since at 56 days carbonation depth was already measured, the fitted curves do not pass through the origin of the plots.

For natural indoor conditions, sudden increase of carbonation depths can be seen after an age of 240 days (Figure 10.17(B)). The internal RH gradient over the cross section of the concrete sample at earlier stages can be an explanation for delayed carbonation of internal layers of the samples (4-12 mm).

Figure 10.17(C) indicates that in case of accelerated carbonation conditions, the propagation of the carbonation front is fastest for the S50 (l/b=0.6) mixture, followed by the S50 (l/b=0.5), CEM III/B and CEM I. The carbonation is faster for S50 0.6 concrete, as l/b ratio is higher and the binder content is lower. CEM I 42.5 N concrete shows a high resistance to carbonation. Carbonation resistance decreases with decreasing clinker content, i.e. for CEM III/B 42.5 N concrete due to lower $Ca(OH)_2$ content, as shown in Chapter 5.

### 10.3.6. pH OF THE CARBONATED CONCRETES

The pH was also monitored for three different exposure conditions: natural (outdoor (sheltered) and indoor) and accelerated carbonation conditions (Figure 10.18 (A), (B), (C)). The pH of the pore solution in carbonated alkali-activated concrete reaches around 10 earlier than in cement-based concrete due to the absence of $Ca(OH)_2$. However, the phenolphthalein indicator shows that a gradual color change of phenolphthalein from fuchsia to colorless upon pH changes from 10 to 8.2 (see Figure 10.12b,c). Therefore, it cannot be stated that the pore solution of alkali-activated concrete is neutralized to 8.2, since it can also be reduced to maximum pH 10 and again it appears as colourless. This is demonstrated in Figure 10.18, where the pH of the carbonated concrete (accelerated carbonation) depth in alkali-activated concretes is found to be higher than 9. Due to the absence of $Ca(OH)_2$ in alkali-activated concretes, the $CO_2$ diffusion and $CO_2$ binding capacity of the mixture S50, as shown in Chapter 5, are the subsequent mechanisms for faster propagation of the carbonation front compared to the cement-based concretes. In the case of natural carbonation (indoor and outdoor), the pH values are very close for all concretes (see Figure 10.18 (A), (B)).

According to the pH values, after 548 days of exposure, three stages can be distinguished for alkali activated concretes in case of accelerated carbonation (see Figure 10.18 (C)):

- stage (1) from 0 mm to 15 mm, the pH of concrete surface decreases to 9.2, where the alkalis are fully depleted. This zone is fully carbonated;
- stage (2) from 30 mm to 15 mm, the pH of concrete decreases from 10.20 to 9.6. This suggests that the alkalis are partially depleted. This zone is partially carbonated;
- stage (3) from 30 mm to 40 mm, the pH of concrete is above 10. This zone is non-carbonated.

In case of natural carbonation, only stages (1) and (3) are observed. This indicates slow progress of the carbonation process in natural conditions. Nevertheless, the pH in stage (1) in natural conditions is similar to stage (1) for accelerated carbonation. The pH in stage (1) and (2) of carbonated alkali activated concrete corresponds well with the pH of alkali activated pastes after 500 days of accelerated carbonation, as shown in Chapter 6, Figure 6.15.

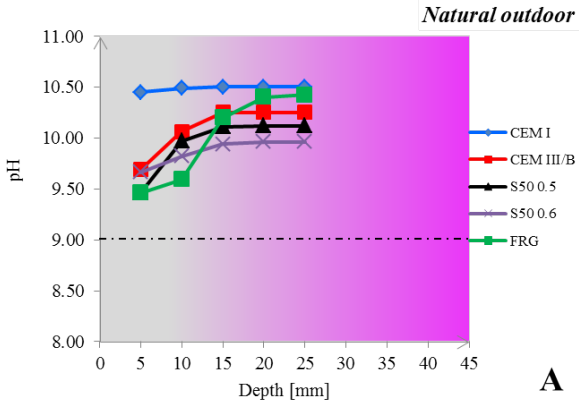


(a) Natural outdoor conditions

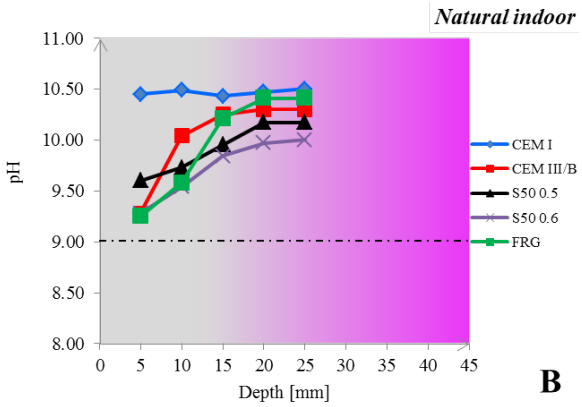


(b) Natural indoor conditions

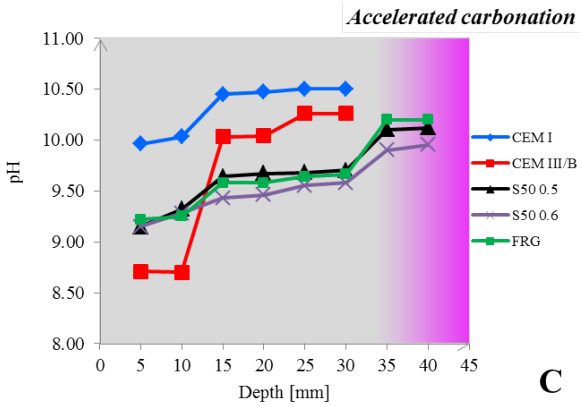


(c) Accelerated indoor conditions

Figure 10.18: pH along carbonation path measured after 548 days of exposure in natural (indoor and outdoor (sheltered)) and accelerated carbonation conditions. (In the graphs, pink colour indicates noncarbonated zone and grey colour indicates the carbonated zone.)

The pH of the CEM I concrete is maintained around 10.5. This value, however, is not a true pH especially not for the carbonated cement-based concrete (Figure 10.18 (C)). Some $Ca(OH)_2$ remains after carbonation and it dissolves when the suspension is made. Therefore, the pH evaluation using suspension method is not appropriate for CEM I concrete.

For CEM III/B concrete, the results reflect the real reduction of the pH under carbonation. $Ca(OH)_2$ in CEM III/B concrete is mainly consumed by the pozzolanic reaction of GGBFS. Therefore, the only source of alkalis after carbonation of this type of concrete are $Na^+$ and $K^+$. Under accelerated carbonation conditions, the carbonated CEM III/B concrete has a pH below 9, while in the noncarbonated part a pH >10 is measured. In natural indoor and outdoor conditions of exposure, the pH of carbonated CEM III/B concrete is above 9.

The pH of all carbonated alkali-activated S50 concretes was above the pH 9, which is reported as a threshold value for an initiation of the carbonation induced reinforcement corrosion in the OPC-based binders [47]. The pH of the noncarbonated alkali-activated concretes S50 was above 10.

### 10.3.7. PORE STRUCTURE CHARACTERIZATION OF PASTES DETERMINED WITH MIP

Figure 10.19 shows the changes of the pore structure of the pastes after accelerated carbonation (1% v/v $CO_2$). The results are compared to the reference sample at an age of 6 months. The total intruded mercury volume represents 17.5-20% of the volume of the noncarbonated cement-paste samples volume (A1, B1), while only 4.33% of the volume of alkali-activated paste S50 (C1). In contrast, the total intruded mercury volume represents 14.2-17.1% of the carbonated cement-paste samples volume (A1, B1), and 6.5% of the alkali-activated paste S50 (C1). It can be seen that for alkali-activated pastes there is an increase in the total percolated pore volume after carbonation, although no obvious change of the pore size is distinguished after carbonation of S50 paste sample (C2). In the graph (C2) it can be seen that there is a wide peak in the range 3-15 $\mu$m, representing microcracks rather than large capillary pores. Microcracking was also observed with ESEM in the carbonated pastes S50 in Chapter 7. Microcracking can be caused by carbonation shrinkage, in particular in the carbonated pastes where C-S-H gel has low Ca/Si ratio (< 1.2) [287].

Compared to the cement-based pastes, the paste S50 has a significantly lower total percolated pore volume (connected pores). This was also observed in S50 pastes after 28 days of curing in Chapter 4. Considering that the PoreSizer® 9500 is a 207 MPa mercury intrusion porosimeter, the pore sizes in the range of 7 nm to 500 $\mu$m can be determined according to the Washburn equation [173]. As a consequence, pores below this size (7 nm) cannot be measured. With $N_2$ adsorption was observed that the main change of the pore size distribution and pore volume under carbonation of the paste S50 occur in the range of the gel pores (see also Chapter 8). Consequently, the gel porosity increases under carbonation of the sample S50.

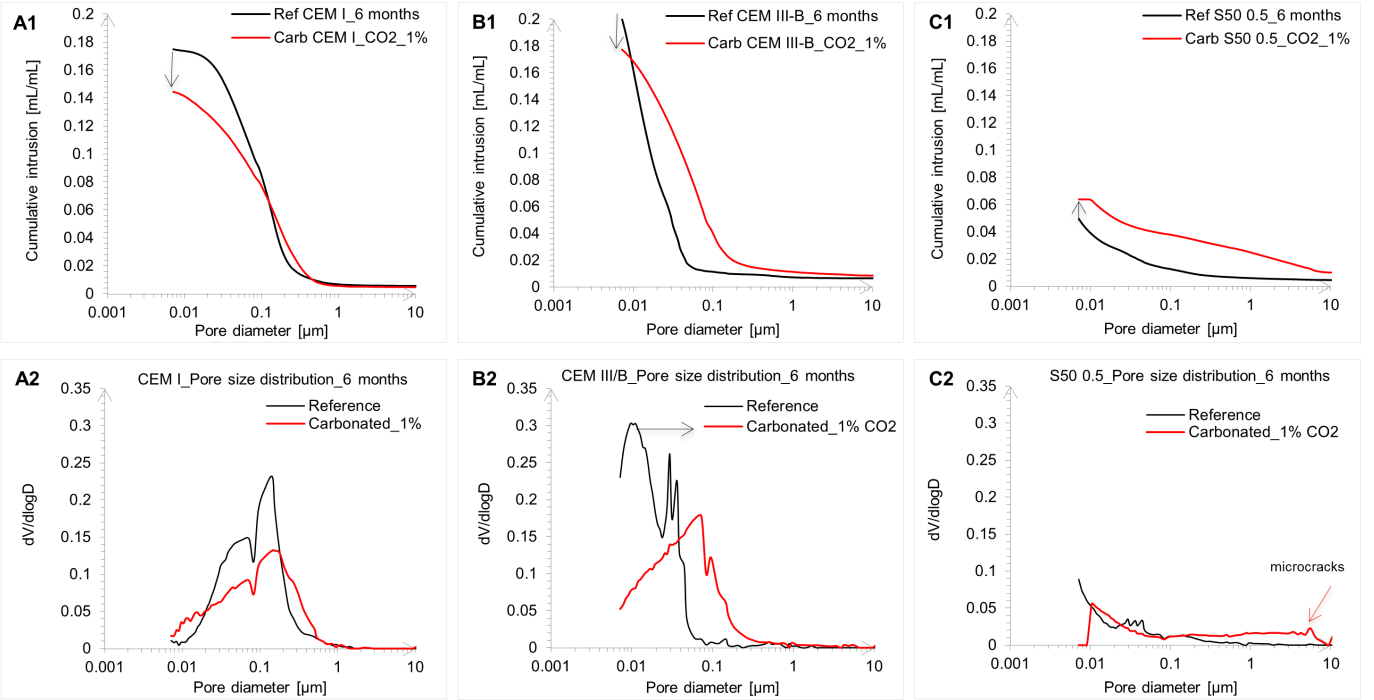


Figure 10.19: MIP cumulative and derivative curves of the cement and alkali-activated pastes after 6 months of exposure to accelerated carbonation. The reference samples were extracted from the noncarbonated core of the corresponding carbonated pastes. The two main characteristic values of MIP results are identified as the total percolated pore volume (A1, B1, C1) and the critical pore entry radius (A2, B2, C2).

For CEM I paste, the intensity of the first and the second critical pore entry radius decreases after carbonation due to the precipitation of calcium carbonates in the capillary pores of the sample. Carbonation of the CEM I paste resulted in densification of the microstructure and reduced porosity as reported by Wu et al. [117]. On the other hand, carbonation of the CEM III/B paste resulted in coarsening of the pore structure and increase of the pore volume [117, 288]. The larger critical pore entry diameter in CEM III/B paste is due to carbonation of mainly C-S-H gel with lower Ca/Si ratio compared to CEM I paste. Carbonation of C-S-H gel in cement pastes leads to volume reduction [116]. The same conclusion holds for paste S50, since the only reaction products affected by carbonation is C-N-A-S-H gel. The larger carbonation shrinkage (volume reduction) of alkali-activated paste is expected since the Ca/Si ratio of the gel in paste S50 (Ca/Si=0.50, Chapter 4) is lower than the Ca/Si ratio of the gel in CEM III/B paste (Ca/Si=1.2, [289]).

### 10.3.8. CARBONATION MECHANISM IN ALKALI ACTIVATED CONCRETE

Table 10.3 gives an overview of parameters for a comparative study of cement and alkali activated concretes in view of carbonation mechanisms. Furthermore, with knowledge of the carbonation mechanism in alkali activated pastes discussed in Chapter 9, the carbonation mechanism in alkali activated concrete is clarified.

Carbonation of alkali activated concretes is a two simultaneous steps mechanism:

1. carbonation of the pore solution by consumption of the alkalis and
2. carbonation of the reaction products in the concrete paste microstructure and ITZ microstructure by decalcification of the reaction products.

Once initiated, the carbonation will depend on both the internal reservoir of alkalis and the Ca-content of the reaction products (Figure 10.1, Table 10.3). Besides that, the pore structure also plays an important role. Considering the two steps mechanism of carbonation, the lower carbonation resistance of alkali activated S30 and S50 concretes compared to concretes S70 and S100, as shown in more detail in Appendix B (Figure B.4), results from a lower GGBFS-content of the former. This is attributed to three effects: coarser pore structure of pastes S30 and S50 compared to pastes S70 and S100 (Chapter 8, Figures 8.3 and 8.4), faster consumption of $[Na^+]$ from the pore solution for FA and GGBFS reactions in paste S50 compared to paste S100, and lower Ca/Si ratio of paste S50 (0.50) compared to paste S100 (0.83).

The results from previous sections also showed that the carbonation is faster for alkali activated concretes S50 compared to cement-based concretes CEM I and CEM III/B. It should be noted that all concretes were unsealed cured before carbonation tests. Faster propagation of the $CO_2$ in the samples S50-0.5 and S50-0.6 than in CEM I and CEM III/B is due to:

- the absence of $Ca(OH)_2$ in concretes S50.
- similar amount of $Na^+$ in all concretes;
- lower amount of $K^+$ in concrete S50 compared to CEM I and CEM III/B concretes;

- lower Ca/Si ratio in the reaction products than in cement-based concrete samples (CEM I and CEM III/B) as can be seen in Table 10.3. This statement is supported by lower $CO_2$ binding capacity of alkali activated pastes compared to cement-based pastes;
- in concrete S50, uniform carbonation is observed of reaction products in paste microstructure and ITZ microstructure (Figure 10.15).

A full understanding of the effects of the studied parameters on deterioration of alkali activated concrete will allow prediction of the carbonation rate in alkali activated concrete, as partially presented in Appendix B.

Table 10.3: Comparison between cement and alkali activated pastes pore solution and microstructure properties (tendencies indicated in Figure 10.1).

| | **CEM I 42.5 N** | **CEM III/B 42.5 N** | **S50_0.5** |
|---|---|---|---|
| | | Pore solution (28 days) | |
| Unsealed cured samples [Na] | 190 mmol/L | 100 mmol/L | 215 mmol/L |
| Sealed cured samples [Na] | 400 mmol/L | 120 mmol/L | 1100 mmol/L |
| Unsealed cured samples [K] | 85 mmol/L | 45 mmol/L | 4 mmol/L |
| Sealed cured samples [K] | 230 mmol/L | 58 mmol/L | 26 mmol/L |
| pH | >13 | | |
| Noncarbonated area (1.5 year, core) | | | |
| pH (natural indoor) | 10.50 | 10.30 | 10.17 |
| pH (natural outdoor) | 10.50 | 10.25 | 10.12 |
| pH (accelerated) | 10.50 | 10.26 | 10.12 |
| Carbonated area (1.5 year, surface) | | | |
| pH (natural indoor) | 10.45 | 9.28 | 9.60 |
| pH (natural outdoor) | 10.45 | 9.69 | 9.46 |
| pH (accelerated) | 9.96 | 8.71 | 9.15 |
| | | Microstructure (28 days) | |
| Compressive strength | 49.9 MPa ± 5.7 | 46.6 MPa ± 2.1 | 70.7 MPa ± 2.5 |
| Pore structure of paste | Capillary + gel pores | Capillary + gel pores | Capillary + gel pores |
| Porosity (unsealed samples) | 46.7 % | 48.9 % | 9.4 % |
| ITZ | heterogeneous | heterogeneous | homogeneous |
| $Ca(OH)_2$ | high | low | none |
| Ca/Si | high (1.7-1.8) [187] | medium (1.2) [289] | low (0.5), Ch. 4 |
| $CO_2$ binding capacity | 35.95 wt. % | 26.87 wt. % | 16.09 wt. % (TG-MS) |

## 10.4. CONCLUDING REMARKS

In this chapter, carbonation rates and carbonation-induced deterioration of the microstructure of unsealed cured cement-based and alkali activated concretes were studied. Based on the presented results, the following conclusions can be drawn:

- The propagation of the carbonation front in concrete mixtures S50 was faster compared to the cement-based concretes (CEM I 42.5 N and CEM III/B 42.5 N) in both accelerated and natural exposure conditions.
- The higher propagation rate of the carbonation front in the alkali-activated concretes (Appendix B, concrete mixtures S30, S50), despite their higher compressive strength and finer pore structure compared to cement-based concrete, is due to:
  - Absence of $Ca(OH)_2$ as shown in Chapter 5;
  - Different pore solution chemistry (alkalinity buffer) as shown in Chapter 6;
  - Lower calcium content in the gel phases as shown in Chapter 4, hence lower content of the carbonatable phases.
  - Different ITZ. Since the same type of the gel (Ca-(Mg)-Na-Al-Si-H gel, as shown in Chapter 4) forms in the ITZ and in the matrix of alkali activated concretes (Figure 10.11) compared to cement-based concrete (calcium hydroxide, ettringite, CSH) the carbonation is favoured evenly in both the ITZ and the surrounding matrix of alkali-activated concrete.
- From all above factors, the carbonation rate is the most influenced by the alkalinity of the alkali activated concretes and $CO_2$ binding capacity. It should be noted that the carbonation depth for alkali activated concrete is the domain where alkalinity is reduced and microstructure is deteriorated.
- As demonstrated in this Chapter, the phenolphthalein measurements in combination with optical microscope observations (under cross-polarized transmitted light), provide a method to determine the progress of the pH drop and microstructure deterioration under carbonation in alkali activated concrete.
- As it was seen in Chapter 8, the carbonation caused deterioration of the paste microstructure through decrease of micromechanical properties, beside decrease of alkalinity. Hence, service life of alkali activated materials should be examined not only considering the decrease of pH, but also taking other parameters in consideration, such as stiffness reduction of the deteriorated concrete. This is in contrast with standard predictions of carbonation rate for cement-based concrete, where the models use permeability/diffusion as their constitutive property.
- The carbonation predictions are confronted with shortage or lack of data for long-term exposures over several decades for alkali activated concrete structures. However, for engineering practice, probabilistic performance-based models (DuraCrete, CEB) can be used as it was shown in this thesis, if the $CO_2$ diffusion is a rate limiting step in the entire process. More discussion about carbonation predictions can be found in Appendix B.

- The expected life time of concrete S50-0.5 in outdoor sheltered conditions is shown to be around 50 years (Appendix B), which corresponds to a concrete cover thickness of 40 mm. Although, predictions of the carbonation rate are based on extrapolations of empirical data, the validation was not possible due to short exposure (2 years). However, the most important factor in justifying long-term predictions is to demonstrate a sound mechanistic understanding of the underlying carbonation mechanism, as presented in Section 10.3.8. Further modeling studies are needed to consider the synergy between reduced alkalinity and deterioration of mechanical properties under different exposure conditions.
- Based on recommendations given in Chapter 6 and results from this chapter, improved carbonation resistance of the alkali-activated concretes can be achieved by using mixtures with high GGBFS content (S70, S100) (Appendix B, Figure B.2) and by applying the sealed curing for studied alkali activated concrete mixtures.

# 11

# CONCLUSIONS, CONTRIBUTIONS AND FURTHER RESEARCH

*"One never notices what has been done; one can only see what remains to be done."*

Marie Skłodowska Curie

*This chapter summarises conclusions and contributions of the research and gives the recommendations for further studies.*

## 11.1. CONCLUSIONS

THE MAIN aim of this thesis was to understand the carbonation mechanism of alkali-activated materials and to propose strategies for improvement of their performance in view of carbonation. For this reason, the carbonation mechanism was studied at different length scales, from gel to concrete level, while the effects of carbonation on chemical, physical and mechanical properties were captured. The relationship between carbonation rate, pore solution chemistry and microstructure was investigated. In general, alkali activated pastes have lower $CO_2$ binding capacity than cement-based pastes. However, that does not mean that alkali activated pastes would carbonate faster. In the study, it turns out that although alkali activated pastes have much lower potential to bind $CO_2$, their pore structure and pore solution composition play critical roles when it comes to propagation of $CO_2$. Finally, a summary of the key findings and conclusions of this thesis is given below.

- **Alkali activated pastes and concrete mixtures were developed with an adequate workability, setting time and mechanical properties for carbonation study.** Fresh properties and mechanical performance of the pastes have been studied for different liquid-to-binder ratios, different FA-to-GGBFS ratios and a constant alkaline activator composition. The properties of pastes and concretes were mainly dependent on the GGBFS content. The pure GGBFS (S100) has the highest rate of heat release, subsequently developing higher compressive strength than other mixtures. In contrast, none or very little amount of reaction products were formed in paste S0. The reason of the unreactivity of FA is the composition of the amorphous phase being a glass too high in alumina and silica to react, despite being amorphous. To this end, carbonation mechanism was expected to be dependent on the paste mixture composition.

- **Carbonation mechanism in alkali activated pastes.**

  - The elementary carbonation reactions in the pore solution (reactive transport of $CO_2$ in a porous medium) and of the reaction products (chemical reactions) under prevailing exposure conditions determine the carbonation mechanism in the alkali activated paste.
  - Two length scales are distinguished in the reactions:
    - the length scale of the surfaces of pores, grains and gels, at which actual reactions start. However, this is a very short local length scale. If the reactions occur only at this length scale then the bulk composition at larger length scale would not be affected when carbon and oxygen are added,
    - the length scale of pore solution, where all reactions are taking place. This is a larger length scale at which the effect of carbonation is dominant.
  - Carbonation reactions affected initially the pore solution alkalinity and then the gel structure and composition. The extent of the reduction of the alkalinity was dependent on the curing conditions. The removal of the elements

from the gel caused the gel molecular structure to change which gives rise to deterioration of the microstructure. The gel dissolution starts at the lowest scale, i.e. atomistic level of the Ca-Mg-Na-Al-Si-H, Ca-Na-Al-Si-H, Ca-Al-Si-H gels by gradual decalcification of the gel and release of chemically bound water as illustrated in Figures 9.7. The release of chemically bound water is assumed to be a consequence of decalcification (reactions 9.18-9.20) and polymerization (reactions 9.21-9.23) processes.

- $CO_2$ apparent diffusion in FA/GGBFS pastes with more than 50 wt.% GGBFS proceeds through the connected network of the gel pores and microcracks. In pastes with lower GGBFS content than 50 wt.%, the $CO_2$ transport is through the gel pores, capillary pores and microcracks.
- Carbonation causes deterioration of C-N-A-S-H gel in alkali-activated FA/GGBFS pastes. The N-A-S-H gel in paste S0, alkali activated FA, did not carbonate (Chapter 5, Section 5.3.2). For pastes with 100 wt.% GGBFS carbonation was almost negligible, due to their dense microstructure (Chapter 8, Section 8.3.2). In cement-based pastes, carbonation causes loss of CH and deterioration of C-S-H.
- Unsealed curing in ~99% RH environment is known as the most suitable for cement-based materials in view of hydration. However, unsealed curing of alkali activated concrete leads to significant alkali loss. The alkalinity of the pore solution was reduced by alkali loss before carbonation took place. For longer periods of exposure (1 year) the pH of the pore solution is lowered even more due to both continuous dissolution of the unreacted material and carbonation. Because of the continuous dissolution of the unreacted material, carbonation proceeds faster, since then there is a lower amount of alkalis. Hence, sealed curing conditions are recommended for curing of alkali activated FA and GGBFS materials.
- Carbonation of alkali activated concrete was found not to reduce the pH below a value that is considered as a threshold for initiation of reinforcing steel corrosion. However, passivity of the reinforcing steel is influenced not only by the overall pH, but also by the percentage of various anions present in pore solution, such as sulphides and sulphates. It is assumed that the mechanism and consequences of carbonation-induced corrosion in alkali activated FA/GGBFS concrete are different from those in cement-based concrete.
- In alkali activated GGBFS-based pastes, the carbonation products were similar in both accelerated and natural carbonation, however their quantities varied. The pH level of the medium has had a crucial influence on the crystallization mechanism of carbonates. Calcium carbonates were the main carbonation products, regardless of the exposure conditions (natural or accelerated). Although it was expected that part of carbonation products would be Na-carbonates, their content was very low (< 1.0 wt.%). This indicated that most of the sodium was bound by the gel or remained in the pore solution, maintaining the pH above 9 after carbonation.

  - Calcium carbonates were clearly distinguished in the carbonated matrix in thin sections under optical microscope. Based on the optical observations, the carbonates were found to be intergrown with the gel phases. For that reason, carbonates could not be resolved with the resolution of SEM imaging. The carbonates were identified with XRD.

- **Carbonation of alkali-activated fly ash and slag pastes causes an increase of gel porosity and the shrinkage of the paste.**
  Carbonation alters the microstructure of GGBFS-containing pastes. This is associated with a reduction in sample volume, caused by decalcification of C-N-A-S-H/C-A-S-H gels, loss of chemically bound water and polymerization of remaining gels (Chapter 9, Reactions 9.18-9.23). The main difference in the pore size distribution after carbonation was observed at the level of the gel pore sizes in pastes with less than 50 wt.% of GGBFS content. The change of the volume and size of the capillary pores was negligible.

- **Carbonation of alkali-activated fly ash and slag pastes causes a reduction in modulus of elasticity.**
  The modulus of elasticity of the gel was reduced due to gel density change under carbonation. The modulus of elasticity decreased by half in carbonated paste S50 compared to noncarbonated paste (Chapter 8, Section 8.3.4). No significant change of the modulus of elasticity was found in mixtures with more than 50 wt.% of GGBFS.

- **Accelerated carbonation is not fully representative for natural carbonation.**
  Accelerated carbonation is found not to be representative for performance of pastes under natural carbonation from the aspect of compressive strength of pastes. The compressive strength of pastes substantially decreased after accelerated carbonation (1% v/v $CO_2$) as shown in Chapter 8, Section 8.3.3. The series of "paleofronts" had induced physical discontinuities in the samples which were unsealed cured and subsequently carbonated under accelerated conditions. The alkalinity due to accelerated carbonation was reduced more than under natural exposure conditions.

- **Alkali-activated fly ash and slag concretes carbonate faster than cement-based concretes, despite their denser microstructure and ITZ.**
  As a result of no $Ca(OH)_2$, lower Ca/Si ratio and consequently lower $CO_2$ binding capacity in alkali activated FA/GGBFS concretes compared to the cement-based concretes, alkali-activated concretes carbonated faster. They were affected more by carbonation and drying, which tends to stop hydration and deteriorates the concrete's external layer. It is assumed that carbonation and shrinkage-induced microcracking may yield continuous pores and an increase in permeability. By proper choice of curing conditions and $Na_2O$ alkaline activator concentration, the binder can be tailored to improve the carbonation resistance of alkali activated concrete as recommended in the next Section.

## 11.2. CONTRIBUTION TO SCIENCE AND ENGINEERING

**Science**

This PhD thesis contributes to the science of alkaline activated fly ash and ground granulated blast furnace slag as an environment friendly alternative to Ordinary Portland cement (OPC). In particular, it contributes to the systematic assessment and understanding of the carbonation mechanism in alkali activated pastes and concretes. Some of the most important highlights of the thesis are:

- In contrast to the traditional approach of studying carbonation in cementitious materials by numerical prediction of the carbonation rate based on experimental measurements of carbonation kinetics, this thesis used a multiscale approach to explain the deterioration of alkali-activated concrete. This approach provides the basis for understanding the carbonation mechanism and its effects on physical, chemical and mechanical properties of alkali-activated pastes and concretes. Emphasis is placed on the assessment of the performance of alkali-activated FA and GGBFS in terms of their $CO_2$ binding capacity and stability. Detailed material characterization is carried out aiming at decoupling of the effects of pore solution and microstructure carbonation.

- It is shown first that powders react with $CO_2$, regardless the type of binder. Further, the carbonation rate of the bulk samples is strongly dependent on the curing conditions, $Na^+$ concentration in the pore solution and type of reaction products within the paste and ITZ. Each system (S0, S30, S50, S70, S100) generates different reaction products as a function of the chemical composition of the raw materials and type of curing conditions. The study on $Na^+$-loss and Na binding capacity (higher in FA-rich pastes than in GGBFS-rich pastes) (Chapter 6, Section 6.3.1.3) is of great importance for the rate of carbonation, because reduction of the free $Na^+$ in the pore solution of the paste reduces the pH. This has been clearly overlooked in all experimental carbonation studies up to now.

- Microstructure deterioration due to carbonation of OPC-based materials is not a point of concern unless there is leaching of $Ca(OH)_2$ from the pore solution. In contrast, it is demonstrated that carbonation of microstructure is one of the most critical aspects in alkali activated pastes. The interaction of pore solution and microstructure carbonation and physico-chemical description of their mechanisms is shown to be crucial for understanding the long-term deterioration of alkali activated pastes under carbonation. In this respect, two essential observations were made:

    1. Carbonation of the pore solution leads to reduction of alkalinity. This alkalinity is important for initiation of dissolution of reaction products and potential corrosion of reinforcing steel in alkali activated concrete.
    2. Carbonation of the microstructure leads to reduction of the modulus of elasticity. This can reduce the stiffness of carbonated alkali activated concrete.

- The fundamental description of the carbonation mechanism and prediction of the carbonation rate in alkali-activated concrete was a result of the following steps:

| Step | Description | Aim |
|---|---|---|
| **1** | Raw material characterization | Primary phases |
| **2** | Characterization of the pore solution of pastes | Concentration of different ions |
| **3** | Internal relative humidity of the pastes and $Na^+$ loss from the pore solution | Preconditioning, Influence of curing conditions |
| **4** | Microstructure characterization of pastes (reaction products, pore structure) | Evolution of the gel phases, reaction degree and pore structure |
| **5** | $Na^+$ binding capacity of the pastes | Effective $Na^+$ concentration in the pore solution |
| **6** | $CO_2$ binding capacity of powdered pastes | Maximum carbonation degree |
| **7** | Carbonation of the pore solution | pH, carbonation rate |
| **8** | Carbonation of the gel phases | Element changes<br>Gel molecular structure change of carbonated pastes<br>Distribution, identification and quantification of carbonation products<br>Distribution and chemical composition of the gel phases<br>$CO_2$ binding capacity of the pastes |
| **9** | Effect of carbonation on the physical and mechanical properties of the microstructure | Change of the pore size, porosity and change of modulus of elasticity |
| **10** | Carbonation mechanism of alkali-activated paste | (Correlation between steps 2-8) |
| **11** | Carbonation rate of alkali-activated concrete | Comparative study with cement-based concretes |
| **12** | Preliminary modelling | Prediction of the carbonation rate in alkali-activated concrete |

- The thorough microstructure characterization with PARC provides for the very first time spatial distribution and proportions of the different reaction products (gels). This distribution could not be identified with XRD, since gel in AAMs is mainly amorphous. The PARC results can be applied for studying other deterioration mechanisms than carbonation, such as chloride attack and alkali silica reaction in AAMs. The study on the pore solution and microstructure changes due to carbonation, and the effect of these changes on the pore structure and mechanical properties, provides indispensable experimental data for understanding of the carbonation and its influencing factors. The analyses of changes of reaction products and identification of carbonation products provided valuable information about the reactions involved. The actual sequence of the elementary carbonation reactions (in the pore solution and of the reaction products) is proposed as carbona-

tion mechanism (Chapter 9, Sections 9.3.1 and 9.4.1). The presented findings are of great significance for further modeling studies of carbonation in AAMs.

**Engineering**

The scientific explanations of *paste* carbonation provided the basis for clarifying carbonation of alkali activated *concrete*. Carbonation resistance of alkali-activated concrete in engineering applications will strongly depend on the mixture design, curing conditions and type of exposure conditions (RH). Therefore, if the concrete mixtures from this thesis are to be applied in engineering practice where carbonation is dominant durability issue, following recommendations should be considered:

- Mixture design. Using higher content of GGBFS than 50 wt.% results in an increase of the carbonation resistance of the alkali activated concrete. Using higher $Na_2O$ alkaline activator concentration than 4.8 wt.% is assumed to contribute to better carbonation resistance of the alkali activated concrete.

- Curing conditions. There are optimal conditions under which carbonation can be delayed in the AAMs. Curing at lower RH than 80% would hinder alkali loss from the alkali activated concretes. Curing at higher RH leads inevitably to alkali loss and, therefore, lower alkalinity of the pore solution of the concrete.

- Exposure conditions. For concrete structures outside, carbonation would not be an issue if the RH is higher than 85% (Chapter 6, Addition to Table 6.2). However, sheltered concrete elements, with an average RH of 60%, can be carbonated since the environmental conditions are optimal for carbonation [NEN-EN 13295].

In contrast to OPC-based materials, carbonation has a significant effect on the mechanical properties, i.e. modulus of elasticity, of alkali activated materials. The deterioration of the outer layers of concrete structures due to carbonation combined with a decrease in modulus of elasticity leads, consequently, to a decrease of the stiffness. Engineers often reduce the stiffness of uncracked concrete structures when modeling concrete structures and designing the reinforcement in view of second order effects (shrinkage, expansion) [EN 1992-1-1: 2005]. In the design procedure (structural modeling) of alkali activated reinforced concrete structures, the effect of carbonation on the stiffness should be considered as well when carrying out the second order effect calculations. Compatibility must be ensured and maintained between all parts of the structure (limitation of deformations).

In the absence of European standards for performance testing of alkali activated concrete, requirements for design of cement concrete mixtures with respect to carbonation (EN 206-1, Table F.1-Recommended limiting values for composition and properties of concrete) should be adapted for alkali activated concrete. For each exposure class (XC1, XC2, XC3, XC4) the minimum alkali content ($Na_2O$) should be specified for design of alkali activated concrete mixtures rather than limiting minimum binder content as prescribed for cement-based concrete. Some restrictions should be applied also to exposure conditions within exposure classes. The exposure of alkali activated concrete to permanently wet or long-term water contact should be avoided due to alkali loss as explained in Chapter 6.

## 11.3. FURTHER RESEARCH

With respect to the scope of this thesis, several extensions of the presented study could be taken into account in further research regarding:

- **Carbonation-induced corrosion of the reinforcing steel.**
  Although the pH was not reduced below a value that is considered as a threshold for initiation of reinforcing steel corrosion, it could potentially be an issue since the passivity of the reinforcing steel is influenced not only by the overall pH, but also by the percentage of various anions present in the pore solution, such as sulphides and sulphates.

  It is recommended to take into account the influence of these anions, since their content in the pore solution is markedly high as shown in Table 6.3.

- **Carbonation-induced deterioration of the mechanical properties.**
  Since the modulus of elasticity of carbonated alkali activated FA/GGBFS pastes was reduced compared to noncarbonated pastes, the changes of the modulus of elasticity and tensile strength of carbonated alkali activated concretes needs further study. Serviceability limit state in terms of deformations, which can be caused by carbonation, must be defined for alkali activated concrete.

- **Microcracking potential.**
  The combined effect of autogeneous shrinkage, drying shrinkage and creep on the microcracking potential of alkali activated FA/GGBFS systems needs to be studied because this combined effect is considered to be essential for service life prediction of alkali-activated concrete. Microcracks, if connected, can form preferential continuous pathways for $CO_2$ mass transport and faster propagation of the carbonation front.

- **Coupled deterioration.**
  Based on the observations of the concrete microstructure deterioration by carbonation, the testing of chloride resistance or frost salt scaling of carbonated alkali activated concrete could be taken into account, as these coupled mechanisms might be detrimental.

- **Modeling of carbonation.**
  In the literature consulted so far, the models for the carbonation of OPC-based materials did not consider parameters such as the potential microcracking, curing conditions, preconditioning, $Na^+$ loss and $Na^+$ binding. These parameters should be considered in any multiscale carbonation model for alkali-activated materials.

- **Monitoring of the structural elements made by alkali activated concrete in this thesis.**
  Monitoring of the propagation rate of the carbonation front in developed alkali-activated concretes[1] [282, 290, 291] should be continued in order to relate long-term behaviour of alkali activated concrete in lab conditions to behaviour under outdoor exposure conditions.

- **Inspection of the long-term performance of existing alkali activated concrete structures worldwide.**
  Characterization and monitoring of the long-term exposed structures would be one of the main contributions to the research of carbonation in alkali activated materials, e.g. to the modeling of their long-term performance (some of the buildings are more than 30 years in service, as in Ukraine (Mariupol, 1960), Poland (Kraków, 1974), Russia (Lipeck, built between 1986 and 1994), China (Yinshan County, Hubei Province, 1988)). The ultimate aim would be to answer questions regarding the composition of field alkali-activated concrete, (mixture design) and to assess the deterioration of the concrete in the region of interest (cover depth, ITZ, microcracking, combination of the deterioration mechanisms).

[1] Canoes, plain alkali activated concrete beams and fiber-reinforced beams ($750 \times 100 \times 150$ mm$^3$ (location: Cornelis Drebbelweg 3, Delft) and alkali activated concrete bench (location: G.J. de Jonghweg, Rotterdam, corresponding to the exposure class for carbonation XC4.)

# A

# ELEMENT ZONATION IN PASTE S100

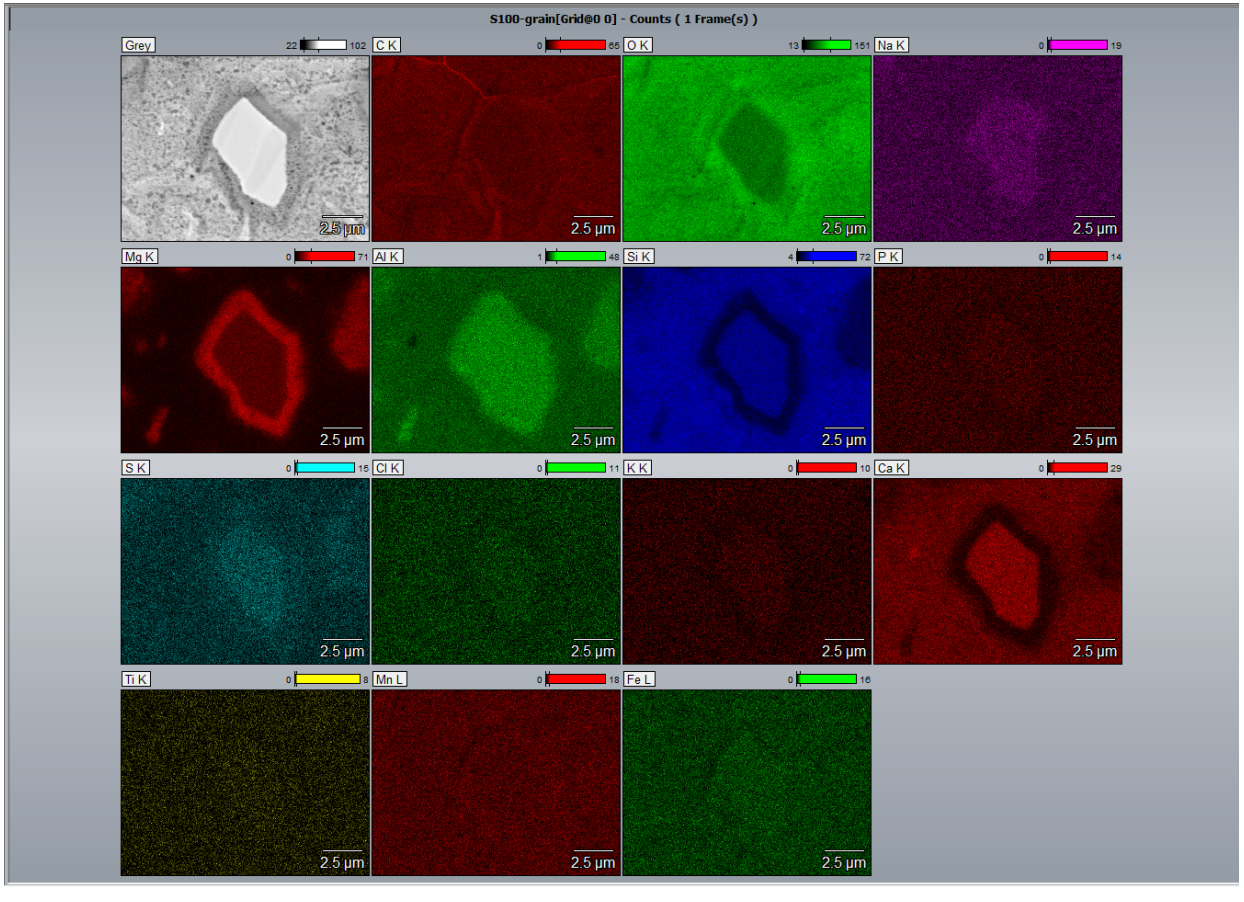


Figure A.1: X-ray element maps showing element zonation in noncarbonated paste S100 (exposure for 2 years), at 8000 times magnification with a beam voltage of 7.0 kV).

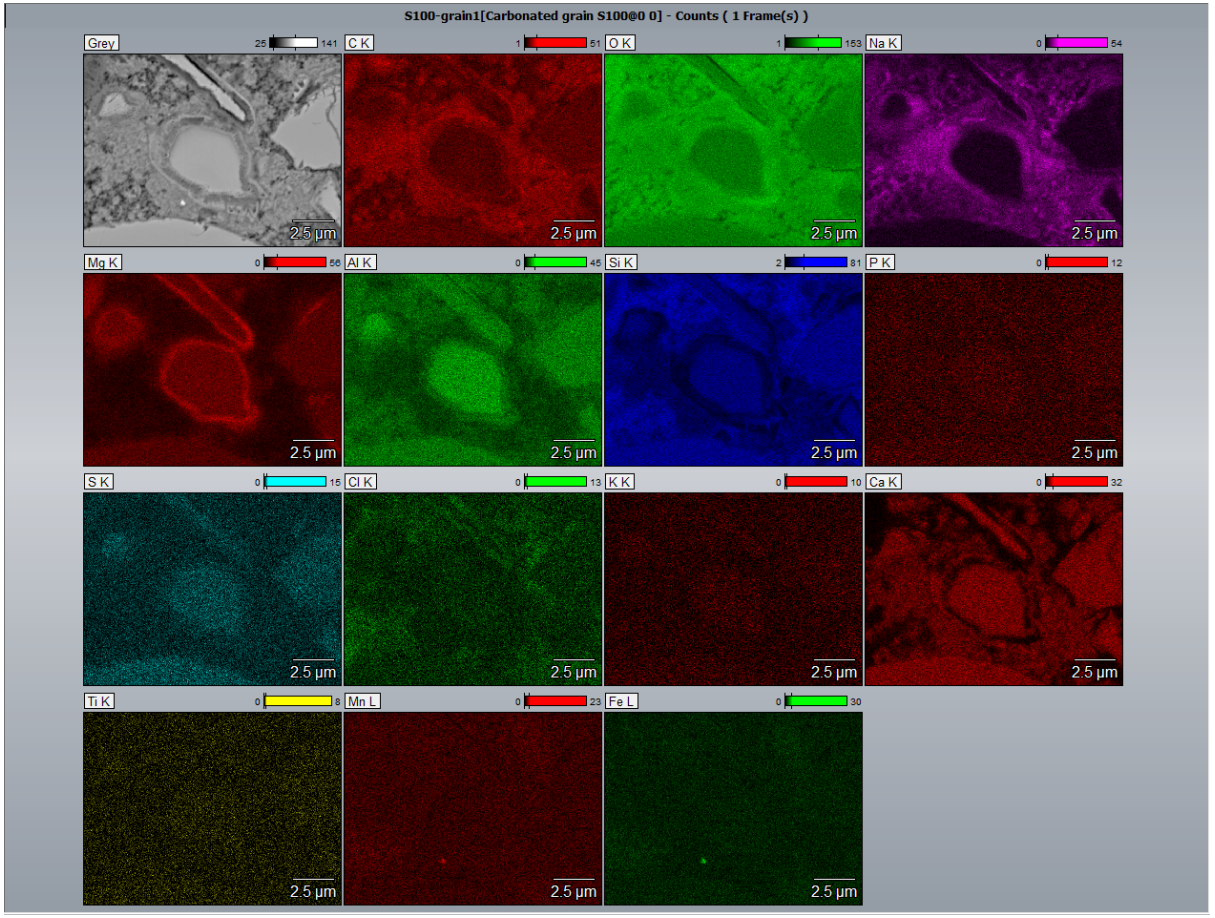


Figure A.2: X-ray element maps showing element zonation in carbonated paste S100 (exposure for 2 years), at 8000 times magnification with a beam voltage of 7.0 kV).

# B

# SERVICE LIFE PREDICTIONS OF ALKALI-ACTIVATED CONCRETE STRUCTURES

*"We must remember that everything depends on how we use a material, not on the material itself... New materials are not necessarily superior. Each material is only what we make it."*

Ludwig Mies van der Rohe

*Widespread use of alkali-activated concrete in engineering applications is limited by lack of standards and understanding of their long-term performance. Furthermore, the lack of data on long-term performance (evolution of transport and mechanical properties) of alkali-activated concretes makes it challenging to support the predictive models of the service life of alkali activated concretes. In this Appendix, the service life of alkali activated concrete structures with regard to carbonation is estimated by application of the DuraCrete model. This model estimates the time to corrosion initiation of reinforcing steel due to pH drop caused by carbonation. Based on experimental results that have been obtained in this thesis, the deterioration of mechanical properties might have an impact on the service life predictions. Therefore, a more advanced model for predicting the service life of alkali-activated concrete structures might be necessary.*

## B.1. SERVICE LIFE DESIGN OF CONCRETE STRUCTURES

Service life of a concrete structure is a period of time for which a structure performance complies with reliability requirements with or without periodic inspection and maintenance and without unexpected high costs for maintenance and repair [107]. The service life predictions of concrete structures are affected by the uncertainties associated with material properties, mechanical and environmental loads. Therefore, service life predictions require probabilistic models and methods to account for the uncertainties that govern the deterioration processes. For service life design of reinforced cement-based concrete structures, corrosion of reinforcing steel is usually a governing factor. Corrosion of reinforcing steel in cement-based concrete is mostly a result of chloride ingress and/or carbonation [45–47] and it consists of two phases: the inititation of corrosion and corrosion propagation (Figure B.1). Carbonation reduces the pH of the concrete pore solution to values where passivation of reinforcing steel disappears [47]. The rate of carbonation is an important input for service life design of reinforced cement-based concrete structures, because the corrosion initiation of reinforcing steel is usually considered as the end of service life of concrete infrastructure (Figure B.1).

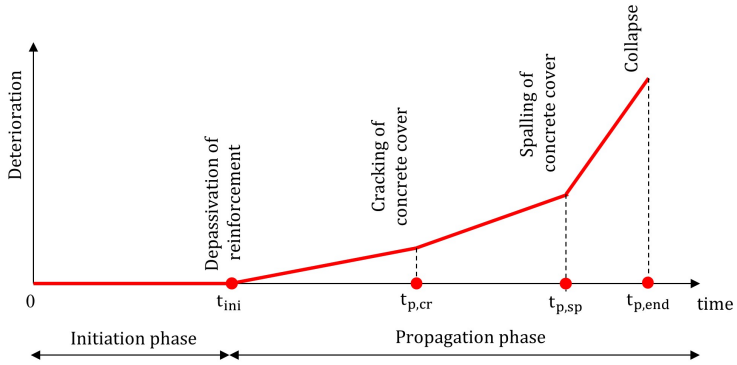


Figure B.1: Initiation and propagation phase, adopted from [107].

Generally, the service life of concrete structures can be designed using different approaches according to the fib Model Code [292]:

1. Prescriptive approach or deemed-to-satisfy rules.

   The prescriptive methodology determines the range of cement-based concrete constituents, the minimum compressive strength, the concrete cover depth and these are dependent on the exposure class. EN-206-1 defines four exposure classes XC1, XC2, XC3 and XC4 for carbonation-induced corrosion in reinforced cement-based concrete (Table B.1) [48]. It gives for each exposure condition standard minimum binder content and maximum content of mineral addition, ensuring the appropriate durability of cement-based concrete structures. This approach is based on long-term practical experience with cement-based concrete mixtures, and not on a fundamental scientific study [293].

2. Full probabilistic approach. Full probabilistic approach for carbonation-induced corrosion is based on the limit state equation, in which the concrete cover depth is compared to the carbonation depth at a certain point of time. The equation is based on Fick's $1^{st}$ law of diffusion, assuming that the $CO_2$ diffusion is the prevailing mechansim of $CO_2$ transport in concrete. The input parameters need to be quantified in a full probabilistic approach.

3. Semi-probabilistic approach (partial factor design). This approach provides a service life design for carbonation-induced corrosion that can be carried out as a simplified calculation without considering the probabilistic distributions of input parameters.

4. Avoidance of deterioration.

Table B.1: Exposure classes for carbonation-induced corrosion of reinforced cement-based concrete structures [48] (EN 206-1, the provisions valid in the place of use of the concrete should include requirements under the assumption of an intended service life of at least 50 years under the anticipated maintenance conditions).

| **Exposure class** | **Description of the exposure conditions** | **Exposure examples** | **Minimum binder content [kg/m$^3$]** | **Maximum w/b ratio** | **Minimum strength class** |
|---|---|---|---|---|---|
| XC1 | Dry or permanently wet | Concrete inside buildings with low air humidity; Concrete permanently submerged in water | 260 | 0.65 | C20/25 |
| XC2 | Wet, rarely dry | Concrete surface subject to long-term water contact Foundations | 280 | 0.60 | C25/30 |
| XC3 | Moderate humidity | Concrete inside buildings with moderate or high air humidity; External concrete sheltered from rain | 280 | 0.55 | C30/37 |
| XC4 | Cyclic wet and dry | Concrete surfaces subject to water contact, not within exposure class XC2 | 300 | 0.50 | C30/37 |

Currently, a prescriptive approach that determines the range of cement-based concrete constituents depending on the exposure conditions is a common practice. For concrete mixtures where alternative cements are used, the service life of concrete is usually assessed through a performance-based approach. In fact, the alkali activated concretes, as alternative to cement-based concrete, do not comply with the prescriptive requirements of the EN 206-1 [48]. However, a concrete mixture may be used even if it does not comply with the prescriptive requirements, using equivalent performance concept [294]. According to the equivalent performance concept, potential durability of a concrete has to be proved through comparison with reference concrete mixtures complying with prescriptive standard requirements.

## B.2. SERVICE LIFE PREDICTIONS OF CONCRETE STRUCTURES



Probabilistic performance-based durability design of concrete structures has been developed within the research project DuraCrete [107] for the modelling of most common durability issues, among others, carbonation induced corrosion of uncracked concrete. According to DuraCrete concept, the end of the service life is specified by the chosen limit-state. The design limit state is usually initiation of the corrosion of reinforcing steel in concrete. The protective passivating layer around the reinforcing steel might be lost if the alkalinity level at the surface of the reinforcing steel drops due to the carbonation to a level sufficient for initiation of the reinforcing steel corrosion in concrete. Aiming to estimate the time to corrosion initiation of reinforcing steel in an alkali activated concrete, a DuraCrete model was applied assuming that the corrosion is a governing factor. However, for assessment of the service life of alkali activated concrete, it is necessary to have data on performance of this material. Since the structural application of concrete from this thesis is done 2 years ago, the data (material properties, exposure condition, former monitoring) are available only from these 2 years. Because no actual long-term measurement of the evolution of transport and mechanical properties of alkali activated concrete is available, the results for alkali activated concrete are compared with results for cement-based concretes, all obtained by the DuraCrete model.

As shown in Chapter 10, carbonation rate was faster for alkali activated concrete S50 compared to cement-based concretes, and the driving force for the propagation rate of the carbonation front in alkali activated concrete was diffusion of $CO_2$ (see Figure 10.17). The DuraCrete model uses the diffusion theory (Fick's $1^{st}$ law of diffusion) and considers ageing for calculation of the carbonation depth. Furthermore, this model is presumed to be applicable for alkali activated concrete as the exposure conditions (relative humidity, sheltering, $CO_2$ concentration in the atmosphere, curing time) are in the range of conditions used in the DuraCrete approach for estimation of the service life of cement-based or cement and GGBFS blended concretes for exposure class XC4 (see Table B.1). The range of each parameter typical for the exposure conditions in the Netherlands was adopted from the DuraCrete. The characteristic values for the ageing factor are modified to suit the alkali activated concrete since this concrete has different microstructure development compared to cement-based concretes. The calculation of the propagation rate of carbonation front according to DuraCrete [107] is as follows:

$$X_c^d(t) = \sqrt{\frac{2 \cdot c_{s,ca}^d \cdot t}{R_{ca}^d}} \tag{B.1}$$

$X_c^d$(t) - design value of the penetration depth of the carbonation [mm],
$c_{s,ca}^d$ - design value of the surface $CO_2$ concentration $[\frac{kg}{m^3}]$,
t - time [years],
$R_{ca}^d$ - design value of the carbonation resistance $[\frac{year \cdot \frac{kg}{m^3}}{mm^2}]$.

The design equation for initiation of carbonation-induced corrosion in reinforced cement-based concrete is:

$$g = x^d - x_c^d(t) = x^d - \sqrt{\frac{2 \cdot c_{s,ca}^d \cdot t}{R_{ca}^d}} \tag{B.2}$$

where $x^d$– design value of the cover thickness [mm], g = 0 stands for the point in time of corrosion initiation.

To take in account the $CO_2$ binding capacity of the concrete, DuraCrete [107] proposed an expression for the carbonation resistance according to:

$$R_{ca} = \frac{B}{D_{eff}} = \frac{1}{D_{ca}} \tag{B.3}$$

B – the $CO_2$ binding capacity $[\frac{kg}{m^3}]$,

$D_{eff}$ – effective diffusion coefficient $[\frac{m^2}{s}]$,

$D_{ca}$ – the carbonation rate $[\frac{m^2}{s \cdot \frac{kg}{m^3}}]$.

The formulae for calculation of the design value of the cover thickness $x^d$ and the effective carbonation resistance $R_{ca}^d$ are given by:

$$x^d = x^c - \Delta x \tag{B.4}$$

$$R_{ca}^d = \frac{R_{0,ca}^d}{k_{e,ca}^c \cdot k_{c,ca}^c \cdot (\frac{t_0}{t})^{2n_{ca}^c} \cdot \gamma_{R_{ca}}} \tag{B.5}$$

with Δx – the safety margin for the cover thickness [mm] (Δx=20 mm),
$x^c$ – the characteristic value of the cover thickness [mm],
$R_{0,ca}^c$ – characteristic value of the carbonation resistance determined on the basis of compliance tests $[\frac{year \cdot \frac{kg}{m^3}}{mm^2}]$,
$k_{e,ca}^c$ – characteristic value of the environment factor [-],
$k_{c,ca}^c$ – characteristic value of the curing factor [-],
$t_0$ – the age of the concrete when the compliance test is performed [years],
$n_{ca}^c$ – characteristic value of the age factor [-],
$\gamma_{R_{ca}}$ – partial factor for the resistance with respect to carbonation [-].

The safety margin for the cover thickness of 20 mm is chosen in this study. However, lower safety margins can be adopted depending on the cost of mitigation of risk relative to the cost of repair.

Finally, for the boundary conditions $x^d = x_c^d(t)$, the time to carbonation-induced corrosion innitiation or the service life time $t_i^d$ is given by:

$$t_i^d = \left(\frac{(x^c - \Delta x)^2 \cdot R_{0,ca}^c}{2 \cdot c_{s,ca}^c \cdot k_{e,ca}^c \cdot k_{c,ca}^c \cdot (t_0)^{2n_{ca}^c} \cdot \gamma_{R_{ca}}}\right) \frac{1}{1-2n_{ca}^c} \tag{B.6}$$

### B.2.1. DETERMINATION OF THE CARBONATION RATE ($D_{ca}$)

The carbonation rate ($D_{ca}$) was calculated based on recorded carbonation depths during 2 years of exposure of alkali activated concrete to accelerated conditions. The phenolphthalein indicator was used to measure the depth of carbonation. Based on time-series measurements in Chapter 10 (see Figure 10.17), $D_{ca}$ was calculated. Subsequently, it was considered that $D_{ca}$ is the same in both accelerated and natural conditions and it was used for calculation of the service life time $t_i^d$ under outdoor sheltered conditions (Equation B.7 and Equation B.8). It should be noted that although it is assumed that the $CO_2$ diffusion coefficient is a constant material property, the $CO_2$ diffusion coefficient may vary largely during service life of concrete as emphasized in fib Model Code [292].

### B.2.2. DETERMINATION OF THE AGEING FACTOR N

Regarding concrete age t and microstructure development, a power function for diffusion coefficient is usually adopted to account for the densification of the microstructure. The time dependent diffusion coefficient D(t) is given with the formula $D(t)=k_e k_c D_0 (t_0/t)^n$, where D(t) is the chloride diffusion coefficient for concrete at age $t_0$ (reference time). The n stands for an ageing factor in DuraCrete model [107] and it is a mathematical way to consider concrete ageing effect. It describes the decrease of diffusion coefficient with time. In reality, the chloride diffusion coefficient D(t) is directly determined by the microstructure of concrete (not considering here the effect of drying and non-saturated conditions). This means that, once hydration stops and the microstructure does not densify further, we cannot expect a continuous decrease of the diffusion coefficient.

The alkali activated pastes mainly consist of gel pores and disconnected capillary pores, representing a dense microstructure already after 28 days of curing, as shown in Chapter 4 (Figures 4.31, 4.33). These facts are in accordance with very low chloride migration coefficients for concretes S50, S70 and S100, presented in Table B.4. For this reason, the compressive strength data of alkali activated concrete S50 are used to account for the densification of the microstructure in the calculation of the ageing factor as follows: $f_c(t)=\frac{f_o}{k_e k_c (\frac{t}{t_0})^n}$. It is proposed that for alkali activated concretes strength data are more proper indicator for ageing than their chloride diffusion coefficient. Because compressive strength is increasing with time and is not limited by the pore structure development as chloride diffusion coefficient.

### B.2.3. MODEL RESULTS AND DISCUSSION

The carbonation depth of concrete samples was calculated for a given time to carbonation-induced corrosion initiation of 50 years. It is assumed that at that depth the pH decreases to 9 and reinforcing steel is no longer passivated and becomes susceptible to corrosion (design limit state). Based on the previously described parameters and characteristic values shown in Table B.2, calculations of the time to carbonation-induced corrosion initiation (see Figure B.2) are made according to Equation B.6 and Equation B.7:

$$t_i^d = \left(\frac{(x^c)^2}{2 \cdot c_{s,ca}^c \cdot k_{e,ca}^c \cdot k_{c,ca}^c \cdot (t_0)^{2n_{ca}^c} \cdot \gamma_{R_{ca}} \cdot D_{0,ca}^c}\right)^{\frac{1}{1-2n_{ca}^c}} \tag{B.7}$$

where:

$c_{s,ca}^c$ - design value of the surface $CO_2$ concentration $[\frac{kg}{m^3}]$,

$k_{e,ca}^c$ – characteristic value of the environment factor,

$k_{c,ca}^c$ – characteristic value of the curing factor,

$t_0$ – the age of the concrete when the compliance test is performed,

$n_{ca}^c$ – characteristic value of the ageing factor $0<n_{ca}^c<1$

$\gamma_{R_{ca}} = 1$

The characteristic values were adopted for the natural carbonation predictions based on the suggested values within DuraCrete [107].

Table B.2: Summary of different factors for concrete mixtures [107].

| | $\mathbf{c}_{s,ca}^c$ $\frac{kg}{m^3}$ | $\mathbf{k}_{c,ca}^c$ [-] | $\mathbf{k}_{e,ca}^c$ [-] | $\mathbf{t}_0$ [days] | $\mathbf{n}_{ca}^c$ [-] | $\gamma_{R_{ca}}$ [-] |
|---|---|---|---|---|---|---|
| CEM I | | | 0.86 | | 0.098* | |
| CEM III/B | $4 \times 10^{-4}$ | 0.76 | 0.86 | 28 | 0.132* | 1.00 |
| S50 | | | 0.85 | | 0.144** | |

* The ageing factors for CEM I and CEM III/B concretes used for the calculations were the values adopted from the DuraCrete [107], for concrete structures exposed to outdoor sheltered conditions (81% RH).

** In this study, calculated ageing factor is 0.144 for alkali activated concrete S50 in natural outdoor sheltered conditions according to strength data $f_c(t)=\frac{f_o}{k_e k_c (\frac{t}{t_0})^n}$, where $f_c(t)$ is the compressive strength at 180 days (Figure 10.4), since the $f_c(t)$ did not change after 180 days, and $f_o$ is the compressive strength at 28 days.

The Fick's $1^{st}$ law of diffusion was also used to predict the time to carbonation-induced corrosion innitiation. The diffusion model is the same as the DuraCrete model, except for the ageing factor (Equation B.8):

$$t_i^d = \frac{(x^c)^2}{2 \cdot c_{s,ca}^c \cdot D_{ca}^c} \tag{B.8}$$

Figure B.2 shows the predicted carbonation rate in outdoor sheltered conditions for reinforced alkali activated concrete S50-0.5, CEM I and CEM III/B concretes by DuraCrete

model according to Equation B.7. The dashed lines for reinforced alkali activated concrete S50-0.5, CEM I, CEM III/B take into account the safety margin for the concrete cover Δx=20 mm for which $\gamma_{R_{ca}}$=3 in Equation B.6. The results in Figure B.3 show good agreement for longer ages between the pure diffusion model with DuraCrete model which takes into account the cover concrete safety margin of 20 mm. For 50 years, the highest cover depth i.e., 50 mm is required for concrete S50-0.5, if the safety margin of 20 mm is applied. Otherwise, it is 18 mm. The concrete CEM III/B has also a lower carbonation resistance and hence shorter time to carbonation-induced corrosion initiation than concrete CEM I. Sisomphon and Franke [93] found similar carbonation depth after 50 years of natural exposure for CEM III/B concrete with fly ash.

Finally, the use of concrete S50-0.5 in the practice seems less attractive. However, there are no data from practice to validate predicted values of the carbonation depth in Figure B.3, except data from the period of 548 days in Figure 10.17 (A). Furthermore, the calculations are deterministic and give the mean time to carbonation-induced corrosion initiation. For this reason, the probability of corrosion time initiation is 50%, which is unacceptable for concrete structures design in practice. Such a high probability would mean that weak spots suffer corrosion much earlier and interventions may already be needed before the intended end of the service life [295]. To obtain lower probability of failure than 50%, concrete cover depth can be increased or the rate of diffusion should decrease. In this study, a minimum cover depth (safety margin Δx=20 mm) was considered based on suggestions from DuraCrete, to lower the probability of corrosion time initiation. Contrary to this suggestion where intended service life is achieved by increasing the concrete cover, the attention could be rather drawn to proper design, curing method, and curing time of alkali-activated concrete. Further research is also needed on how to include the effect of microstructure deterioration (modulus of elasticity change, carbonation shrinkage) on alkali activated concrete structural reliability.

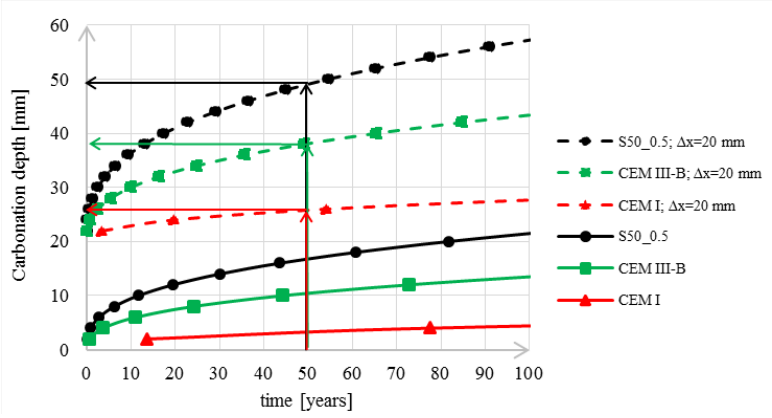


Figure B.2: Predicted carbonation depth development for alkali activated concrete S50, CEM I, CEM III/B by DuraCrete model. The dashed line for reinforced alkali activated concrete S50-0.5, CEM I, CEM III/B takes into account the safety margin for the concrete cover Δx=20 mm, for which $\gamma_{R_{ca}}$ =3 [107]. (Note: Carbonation depth for concrete S50-0.5 is the domain where pH is reduced and microstructure is deteriorated).

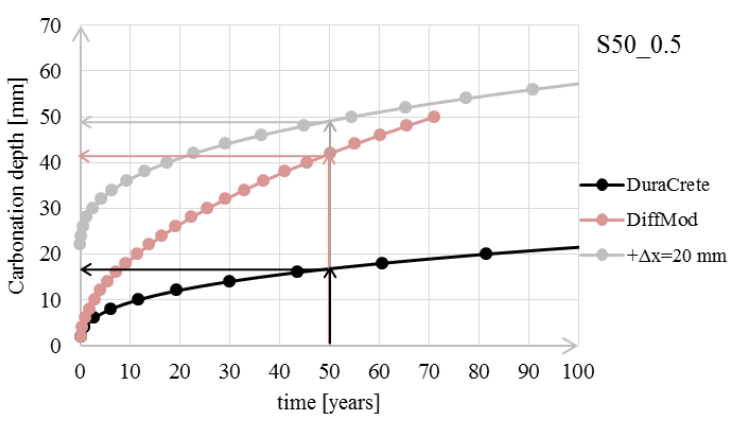


Figure B.3: Predicted carbonation depth development for alkali activated concrete S50-0.5:
- black line shows result of DuraCrete concept with ageing factor 0.144,
- light red line presents pure Diffusion model,
- grey line considers the safety margin for the concrete cover Δx=20 mm, for which $\gamma_{R_{ca}} = 3$ [107].

## B.3. CARBONATION RESISTANCE OF ALKALI ACTIVATED CONCRETES IN ACCELERATED CONDITIONS

Accelerated carbonation test is widely employed test for assessment of the carbonation resistance of a concrete mixture. According to fib Model Code [292], the benefit of the accelerated carbonation test in cement-based concrete is that "short duration is important to get as early as possible information about the material performance", while the $CO_2$ binding capacity of a concrete does not have to considered additionally. As for alkali activated concrete, the $CO_2$ binding capacity and microstructure deterioration might have a significant impact on the interpretation results of accelerated carbonation and their correlation to data from natural carbonation conditions.

The results reported here are obtained by Arbi [282] under the project S81.1.13498. These results provide further insight in carbonation performance of mixtures which were not tested in this thesis. In this research [282], a comparative study is performed regarding carbonation resistance of different alkali activated concrete mixtures in accelerated conditions (1% $CO_2$, 20°C, 60% RH). For each mixture (S30, S50, S70, S100), four cylindric specimens (∅76mm, h=150 mm) were drilled from cubic samples. Specimens have been cured at different ages (7, 14, 21 and 28 days) and then exposed to 1% $CO_2$ during 7, 14, 21 and 28 days. A preconditioning for 24 hours before starting the carbonation test was applied for all mixtures. Through a visual inspection, no cracks have been detected during the preconditioning. The carbonation depth was measured by applying phenolphthalein indicator on freshly broken specimens. The effects of curing time and exposure time on carbonation resistance of studied concretes were investigated.

### B.3.1. EFFECT OF CURING TIME AND EXPOSURE TIME

Figure B.4 presents the carbonation rate measured in four mixtures for different curing ages and exposure times. At early age curing (7 days and 14 days), all mixtures have been carbonated in accelerated carbonation conditions. When the curing time increased to 21 days or 28 days, a decrease of carbonation rate was observed. The concrete S100 cured for 28 days was not carbonated after 7 days of exposure. After 14 days to 28 days of exposure a carbonation depth of about 4-5 mm was measured. The same mixture shows high carbonation resistance when cured for 28 days (not carbonated even after 21 days exposure, while only 3-4 mm carbonation depth was measured after 28 days of exposure). It can be concluded that longer curing time results in improved carbonation resistance of alkali activated concretes, particularly of GGBFS-rich concrete mixtures.

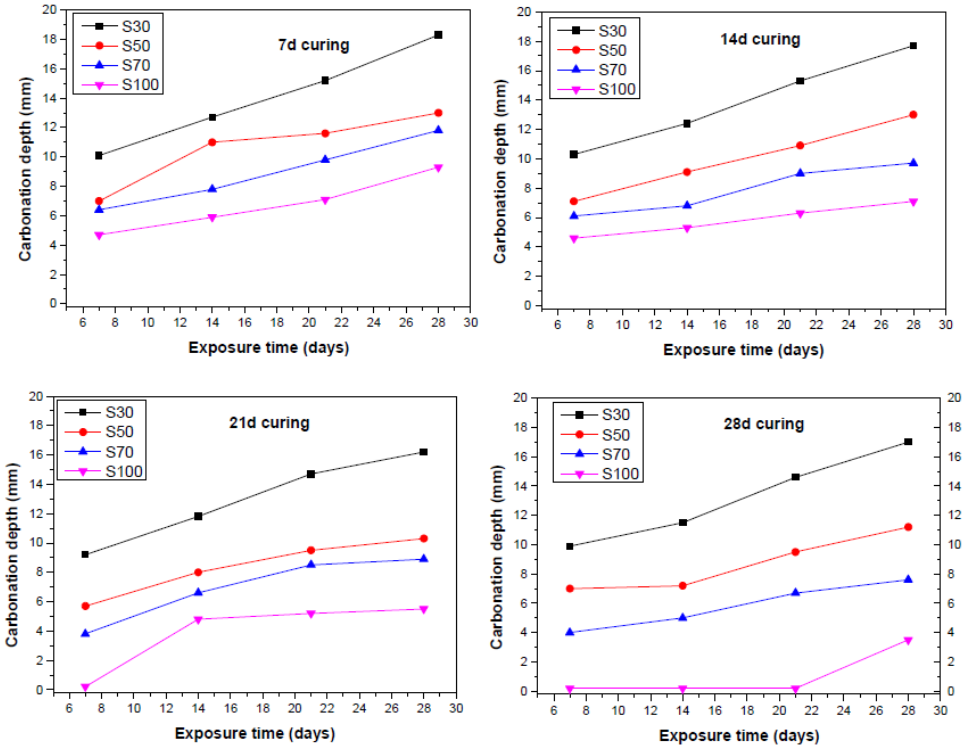


Figure B.4: Carbonation depths of concretes S30, S50, S70, S100 as a function of curing/exposure time [282].

### B.3.2. EFFECT OF FA-TO-GGBFS RATIO

In all investigated mixtures, the carbonation rate increases when increasing the FA content (see Figure B.4). The highest carbonation rate was measured in concrete S30 regardless the curing time. This is due to a higher porosity of FA-rich concrete compared to concretes containing high amount of GGBFS. In the case of concretes S70 and S100, the dense microstructure explains their high carbonation resistance.

### B.3.3. EFFECT OF ACCELERATED CARBONATION ON COMPRESSIVE STRENGTH

The compressive strengths of alkali activated concretes as well as those of OPC-based concrete (CEM I) are given in Table B.3. The strength of noncarbonated samples was compared with strength of carbonated samples. Note that *noncarbonated* and *carbonated* samples have been stored in the laboratory under the same conditions (temperature and relative humidity) with the only difference in the $CO_2$ concentration for carbonated samples. The results from the Table B.3 show that CEM I did not undergo any change in the compressive strength either after 28 days or 56 days of accelerated carbonation. These values are also similar to those of noncarbonated samples. This behaviour is expected considering that CEM I was not carbonated even after 56 days of $CO_2$ exposure.

For alkali activated concretes, the compressive strength of carbonated samples was lower compared to the compressive strength of noncarbonated samples indicating that the concrete microstructure is changing after carbonation. These results are in agreement with those reported by Bernal et al. [198] where a strength reduction due to accelerated carbonation was up to 15% in alkali-activated slag/metakaolin blended concretes.

Table B.3: Comparison of compressive strength of concretes CEM I, S30, S50 and S70 after 28 and 56 days of accelerated carbonation with compressive strength of concretes with no carbonation (Three standard $150\times150\times150$ mm$^3$ concrete cubes per concrete mixture were tested in compression test [NEN 12390-3:2009]).

| | **CEM I** | **S30** | **S50** | **S70** |
|---|---|---|---|---|
| 28 days carbonated | 58.0 ± 1.0 | 57.7 ± 1.0 | 87.6 ± 1.4 | 96.5 ± 1.9 |
| 28 days noncarbonated | 57.6 ± 1.2 | 61.9 ± 1.2 | 89.7 ± 1.8 | 99.1 ± 3.7 |
| 56 days carbonated | 57.5 ± 1.7 | 56.3 ± 3.2 | 88.9 ± 3.2 | 98.8 ± 2.6 |
| 56 days noncarbonated | 56.3 ± 2.5 | 60.6 ± 3.5 | 91.7 ± 4.8 | 103.5 ± 2.5 |

## B.4. CHLORIDE RESISTANCE OF ALKALI ACTIVATED CONCRETES BY NT BUILD 492

Besides carbonation resistance of alkali activated concretes in accelerated carbonation conditions, the resistance to chloride ingress was determined according to NT Build 492 (Rapid Chloride Migration test) by Arbi [282]. Cylindric specimens (∅=100mm, h=50mm) were drilled from cubic samples. The tests started after preconditioning of the specimens. During preconditioning, the specimens were placed in a vacuum container for 3 h. Subsequently, a saturated $Ca(OH)_2$ solution was added. The specimens were kept in the solution for 18 h. After saturation, specimens were placed in the test container. A voltage of 30 V was applied between the anode/anolyte solution (0.3 M NaOH) and the cathode/catholyte solution (10% NaCl solution). Experimental conditions as well as the chloride penetration depth and the non-steady state migration coefficient of investigated mixtures are given in Table B.4.

Table B.4 shows that the initial current (measured at 30 V) in concrete S30 is the highest value and that of S70 is the lowest. This is directly correlated with the chloride penetration depth and the migration coefficient values where for concrete S30 the highest values were obtained. The lowest values measured for S70 indicate that this concrete is very dense making difficult the ingress and/or mobility of any specie such as $Cl^-$ ions in its microstructure. Therefore, this mixture has an excellent chloride resistance.

Table B.4: Experimental conditions and test results on chloride penetration in alkali activated concretes [282].

| **Mixture** | **$I_0$ (30V)** | **App. Volt** | **$I_0$ (App. Volt)** | **Test duration** | **Samples size (0/h)** | **Chloride pentration depth** | **Chloride migration coefficient** |
|---|---|---|---|---|---|---|---|
| | [mA] | [V] | [mA] | [h] | [mm] | [mm] | [$10^{-12}$ $m^2/s$ |
| S30 | 162.3 | 15 | 80.3 | | 50.8/ 99.8 | 18.2 | 17.12 |
| S50 | 52.3 | 30 | 52.3 | | 49.5/ 102.4 | 10.1 | 4.40 |
| S70 | 33.8 | 35 | 39.4 | 24 | 49.9/ 100.0 | 5.3 | 1.91 |
| S100 | 41.3 | 30 | 41.3 | | 51.1/ 99.5 | 5.7 | 2.43 |
| OPC* | | | | | | 25 | |

* Data from study of Ismail et al. [296].

Based on the chloride penetration depth, concretes S50 and S100 have a good chloride resistance. However, results obtained for S100 are unexpected as this mixture should have lower chloride penetration depth in comparison with concrete S70. In contrast, Ismail et al. [296] reported a lower chloride penetration depth (1 mm) for GGBFS concrete (100% GGBFS) in comparison with 5 mm chloride penetration depth found for the concrete containing 75% GGBFS+25% FA. Further research should address the influence of the preconditioning regime and possible microcracking of the surface of concrete S100, which could explain the faster $Cl^-$ migration in this mixture.

# REFERENCES

## REFERENCES


[1] D. N. Huntzinger, T. D. Eatmon, A life-cycle assessment of portland cement manufacturing: comparing the traditional process with alternative technologies, Journal of Cleaner Production 17 (7) (2009) 668–675.

[2] Cement Technology Roadmap 2009 carbon emissions reductions up to 2050, https://www.iea.org/publications/freepublications/publication/Cement.pdf., accessed: 2018-10-13.

[3] B. C. McLellan, R. P. Williams, J. Lay, A. Van Riessen, G. D. Corder, Costs and carbon emissions for geopolymer pastes in comparison to ordinary portland cement, Journal of cleaner production 19 (9-10) (2011) 1080–1090.

[4] G. Habert, C. Ouellet-Plamondon, Recent update on the environmental impact of geopolymers, RILEM technical Letters 1 (2016) 17–23.

[5] M. Schneider, M. Romer, M. Tschudin, H. Bolio, Sustainable cement production—present and future, Cement and Concrete Research 41 (7) (2011) 642–650.

[6] E. Worrell, L. Price, N. Martin, C. Hendriks, L. O. Meida, Carbon dioxide emissions from the global cement industry, Annual review of energy and the environment 26 (1) (2001) 303–329.

[7] S. A. Miller, A. Horvath, P. J. Monteiro, Readily implementable techniques can cut annual co2 emissions from the production of concrete by over 20%, Environmental Research Letters 11 (7) (2016) 074029.

[8] H. Scharff, Landfill reduction experience in the netherlands, Waste management 34 (11) (2014) 2218–2224.

[9] B. Lothenbach, K. Scrivener, R. Hooton, Supplementary cementitious materials, Cement and Concrete Research 41 (12) (2011) 1244–1256.

[10] R. Siddique, M. I. Khan, Supplementary cementing materials, Springer Science & Business Media, 2011.

[11] J. S. Van Deventer, J. L. Provis, P. Duxson, D. G. Brice, Chemical research and climate change as drivers in the commercial adoption of alkali activated materials, Waste and Biomass Valorization 1 (1) (2010) 145–155.

[12] P. Duxson, A. Fernández-Jiménez, J. L. Provis, G. C. Lukey, A. Palomo, J. S. van Deventer, Geopolymer technology: the current state of the art, Journal of materials science 42 (9) (2007) 2917–2933.

[13] F. Škvára, L. Kopecký, V. Šmilauer, Z. Bittnar, Material and structural characterization of alkali activated low-calcium brown coal fly ash, Journal of hazardous materials 168 (2-3) (2009) 711–720.

[14] M. Van Lieshout, S. Nusselder, Update prioritering handelingsperspectieven verduurzaming betonketen 2016 (2016).

[15] J. Davidovits, Geopolymers: inorganic polymeric new materials, Journal of Thermal Analysis and calorimetry 37 (8) (1991) 1633–1656.

[16] A. Palomo, M. Grutzeck, M. Blanco, Alkali-activated fly ashes: a cement for the future, Cement and concrete research 29 (8) (1999) 1323–1329.

[17] D. Krizan, B. Zivanovic, Effects of dosage and modulus of water glass on early hydration of alkali–slag cements, Cement and Concrete Research 32 (8) (2002) 1181–1188.

[18] J. Van Jaarsveld, J. Van Deventer, G. Lukey, The characterisation of source materials in fly ash-based geopolymers, Materials Letters 57 (7) (2003) 1272–1280.

[19] M. Criado, A. Palomo, A. Fernández-Jiménez, Alkali activation of fly ashes. part 1: Effect of curing conditions on the carbonation of the reaction products, Fuel 84 (16) (2005) 2048–2054.

[20] F. Škvára, T. Jílek, L. Kopecký, Geopolymer materials based on fly ash, Ceram.-Silik 49 (3) (2005) 195–204.

[21] R. T. Chancey, P. Stutzman, M. C. Juenger, D. W. Fowler, Comprehensive phase characterization of crystalline and amorphous phases of a class f fly ash, Cement and Concrete Research 40 (1) (2010) 146–156.

[22] P. T. Durdziński, C. F. Dunant, M. B. Haha, K. L. Scrivener, A new quantification method based on semeds to assess fly ash composition and study the reaction of its individual components in hydrating cement paste, Cement and Concrete Research 73 (2015) 111–122.

[23] J. L. Provis, A. Hajimohammadi, C. E. White, S. A. Bernal, R. J. Myers, R. P. Winarski, V. Rose, T. E. Proffen, A. Llobet, J. S. van Deventer, Nanostructural characterization of geopolymers by advanced beamline techniques, Cement and Concrete Composites 36 (2013) 56–64.

[24] V. Glukhovsky, Soil silicates. kiev, USSR: Gostroiizdat Publish.

[25] V. Glukhovskij, Y. Zaitsev, V. Pakhomov, Slag-alkaline cements and concretes-structure, properties, technological and economical aspects of the use, Silicates industriels 48 (10) (1983) 197–200.

[26] I. Richardson, A. Brough, G. Groves, C. Dobson, The characterization of hardened alkali-activated blast-furnace slag pastes and the nature of the calcium silicate hydrate (csh) phase, Cement and Concrete Research 24 (5) (1994) 813–829.

[27] A. Brough, M. Holloway, J. Sykes, A. Atkinson, Sodium silicate-based alkali-activated slag mortars: Part ii. the retarding effect of additions of sodium chloride or malic acid, Cement and Concrete Research 30 (9) (2000) 1375–1379.

[28] H. Xu, J. Van Deventer, The geopolymerisation of alumino-silicate minerals, International journal of mineral processing 59 (3) (2000) 247–266.

[29] J. Phair, J. Van Deventer, Effect of silicate activator ph on the leaching and material characteristics of waste-based inorganic polymers, Minerals Engineering 14 (3) (2001) 289–304.

[30] A. Brough, A. Atkinson, Sodium silicate-based, alkali-activated slag mortars: Part i. strength, hydration and microstructure, Cement and concrete research 32 (6) (2002) 865–879.

[31] F. Puertas, A. Fernández-Jiménez, M. T. Blanco-Varela, Pore solution in alkali-activated slag cement pastes. relation to the composition and structure of calcium silicate hydrate, Cement and Concrete Research 34 (1) (2004) 139–148.

[32] I. García-Lodeiro, A. Palomo, A. Fernández-Jiménez, D. Macphee, Compatibility studies between nash and cash gels. study in the ternary diagram na2o–cao–al2o3–sio2–h2o, Cement and Concrete Research 41 (9) (2011) 923–931.

[33] J. Němeček, V. Šmilauer, L. Kopecký, Nanoindentation characteristics of alkali-activated aluminosilicate materials, Cement and Concrete Composites 33 (2) (2011) 163–170.

[34] J. L. Provis, V. Rose, R. P. Winarski, J. S. van Deventer, Hard x-ray nanotomography of amorphous aluminosilicate cements, Scripta Materialia 65 (4) (2011) 316–319.

[35] P. Rovnaník, Effect of curing temperature on the development of hard structure of metakaolin-based geopolymer, Construction and Building Materials 24 (7) (2010) 1176–1183.

[36] Y. Ma, Microstructure and engineering properties of alkali activated fly ash-as an environment friendly alternative to portland cement.

[37] J. L. Provis, P. Duxson, J. S. van Deventer, The role of particle technology in developing sustainable construction materials, Advanced Powder Technology 21 (1) (2010) 2–7.

[38] J. S. Van Deventer, J. L. Provis, P. Duxson, Technical and commercial progress in the adoption of geopolymer cement, Minerals Engineering 29 (2012) 89–104.

[39] K. Arbi, M. Nedeljkovic, Y. Zuo, G. Ye, A review on the durability of alkali-activated fly ash/slag systems: advances, issues, and perspectives, Industrial & Engineering Chemistry Research 55 (19) (2016) 5439–5453.

[40] C. Shi, D. Roy, P. Krivenko, Alkali-activated cements and concretes, CRC press, 2003.

[41] F. Pacheco-Torgal, Introduction to handbook of alkali-activated cements, mortars and concretes, in: Handbook of alkali-activated cements, mortars and concretes, Elsevier, 2015, pp. 1–16.

[42] T. RILEM, 224-aam, Alkali-Activated Materials: State-of-the-Art Report (2014) 396.

[43] M. Soutsos, Concrete durability: a practical guide to the design of durable concrete structures, Thomas Telford Ltd, 2010.

[44] L. Bertolini, B. Elsener, P. Pedeferri, E. Redaelli, R. B. Polder, Corrosion of steel in concrete: prevention, diagnosis, repair, Degradation of Concrete, p. 49-69, John Wiley & Sons, 2013.

[45] L. Parrott, Damage caused by carbonation of reinforced concrete, Materials and structures 23 (3) (1990) 230–234.

[46] L. Bertolini, B. Elsener, P. Pedeferri, E. Redaelli, R. B. Polder, Corrosion of steel in concrete: prevention, diagnosis, repair, Carbonation-Induced Corrosion, p. 79-92, John Wiley & Sons, 2013.

[47] L. Bertolini, B. Elsener, P. Pedeferri, E. Redaelli, R. B. Polder, Corrosion of steel in concrete: prevention, diagnosis, repair, Chloride-Induced Corrosion, p. 93-112, John Wiley & Sons, 2013.

[48] C. E. de Normalisation, En 206-1 "concrete—part 1: Specification, performance, production and conformity,", Brussels: CEN.

[49] 247-DTA durability-testing-of-alkali-activated-materials-290, https://www.rilem.net/groupe/247-dta-durability-testing-of-alkali-activated-materials-290, accessed: 2018-10-13.

[50] CEN, En 13295:2004, products and systems for the protection and repair of concrete structures. test methods. determination of resistance to carbonation (2004).

[51] ISO 1920-12:2015, Testing of concrete - Part 12: Determination of the carbonation resistance of concrete. Accelerated carbonation method,ISO.

[52] EN 14630:2006, Products and systems for the protection and repair of concrete structures. Test methods. Determination of carbonation depth in hardened concrete by the phenolphthalein method,CEN.

[53] R. DE LA RILEM, Cpc-18 measurement of hardened concrete carbonation depth, Mater Struct 21 (1988) 453–455.

[54] NT Build 357, Nordtest method, concrete, repairing materials and protective coating: carbonation resistance,Espoo (Finland).

[55] LNEC E 391:2003,Lisboa: Laboratório Nacional de Engenharia Civil.

[56] P. Rougeau, Les résultats d'essais croisés afrem «essai de carbonatation accéléré», dans compte-rendu des journées techniques afpc-afrem durabilité des bétons,«méthodes recommandées pour la mesure des grandeurs associées à la durabilité» (1997).

[57] S.-D. Wang, K. L. Scrivener, P. Pratt, Factors affecting the strength of alkali-activated slag, Cement and concrete research 24 (6) (1994) 1033–1043.

[58] T. Bakharev, J. Sanjayan, Y.-B. Cheng, Resistance of alkali-activated slag concrete to carbonation, Cement and Concrete Research 31 (9) (2001) 1277–1283.

[59] M. Palacios, F. Puertas, Effect of carbonation on alkali-activated slag paste, Journal of the American Ceramic Society 89 (10) (2006) 3211–3221.

[60] F. Puertas, M. Palacios, T. Vázquez, Carbonation process of alkali-activated slag mortars, Journal of Materials Science 41 (10) (2006) 3071–3082.

[61] S. A. Bernal, R. M. de Gutierrez, J. L. Provis, V. Rose, Effect of silicate modulus and metakaolin incorporation on the carbonation of alkali silicate-activated slags, Cement and Concrete Research 40 (6) (2010) 898–907.

[62] S. A. Bernal, J. L. Provis, D. G. Brice, A. Kilcullen, P. Duxson, J. S. van Deventer, Accelerated carbonation testing of alkali-activated binders significantly underestimates service life: the role of pore solution chemistry, Cement and Concrete Research 42 (10) (2012) 1317–1326.

[63] S. A. Bernal, J. L. Provis, B. Walkley, R. San Nicolas, J. D. Gehman, D. G. Brice, A. R. Kilcullen, P. Duxson, J. S. van Deventer, Gel nanostructure in alkali-activated binders based on slag and fly ash, and effects of accelerated carbonation, Cement and Concrete Research 53 (2013) 127–144.

[64] M. S. Badar, K. Kupwade-Patil, S. A. Bernal, J. L. Provis, E. N. Allouche, Corrosion of steel bars induced by accelerated carbonation in low and high calcium fly ash geopolymer concretes, Construction and Building Materials 61 (2014) 79–89.

[65] S. A. Bernal, R. San Nicolas, J. L. Provis, R. M. De Gutiérrez, J. S. Van Deventer, Natural carbonation of aged alkali-activated slag concretes, Materials and structures 47 (4) (2014) 693–707.

[66] A. E. Morandeau, C. E. White, Role of magnesium-stabilized amorphous calcium carbonate in mitigating the extent of carbonation in alkali-activated slag, Chemistry of Materials 27 (19) (2015) 6625–6634.

[67] A. E. Morandeau, C. E. White, In situ x-ray pair distribution function analysis of accelerated carbonation of a synthetic calcium–silicate–hydrate gel, Journal of Materials Chemistry A 3 (16) (2015) 8597–8605.

[68] S. A. Bernal, R. San Nicolas, R. J. Myers, R. M. De Gutiérrez, F. Puertas, J. S. Van Deventer, J. L. Provis, Mgo content of slag controls phase evolution and structural changes induced by accelerated carbonation in alkali-activated binders, Cement and Concrete Research 57 (2014) 33–43.

[69] K. Pasupathy, M. Berndt, A. Castel, J. Sanjayan, R. Pathmanathan, Carbonation of a blended slag-fly ash geopolymer concrete in field conditions after 8 years, Construction and Building Materials 125 (2016) 661–669.

[70] M. Nedeljković, Y. Zuo, K. Arbi, G. Ye, Natural carbonation of alkali-activated fly ash and slag pastes, in: High Tech Concrete: Where Technology and Engineering Meet, Springer, 2018, pp. 2213–2223.

[71] S. Sawada, C. Page, M. Page, Electrochemical injection of organic corrosion inhibitors into concrete, Corrosion Science 47 (8) (2005) 2063–2078.

[72] C. van Hoek, J. Small, S. van der Laan, Large-area phase mapping using phase recognition and characterization (parc) software, Microscopy Today 24 (5) (2016) 12–21.

[73] E. J. Berryman, A. E. Williams-Jones, A. A. Migdisov, Steel slag carbonation in a flow-through reactor system: The role of fluid-flux, Journal of Environmental Sciences 27 (2015) 266–275.

[74] Y. B. Zuo, M. Nedeljković, G. Ye, Pore solution composition and solubility of alkali-activated fly ash, in: Key Engineering Materials, Vol. 761, Trans Tech Publ, 2018, pp. 65–68.

[75] S. A. Bernal, E. D. Rodríguez, A. P. Kirchheim, J. L. Provis, Management and valorisation of wastes through use in producing alkali-activated cement materials, Journal of Chemical Technology & Biotechnology 91 (9) (2016) 2365–2388.

[76] Sindhunata, J. Van Deventer, G. Lukey, H. Xu, Effect of curing temperature and silicate concentration on fly-ash-based geopolymerization, Industrial & Engineering Chemistry Research 45 (10) (2006) 3559–3568.

[77] A. Fernández-Jiménez, A. Palomo, Composition and microstructure of alkali activated fly ash binder: Effect of the activator, Cement and concrete research 35 (10) (2005) 1984–1992.

[78] J. Chang, A study on the setting characteristics of sodium silicate-activated slag pastes, Cement and Concrete Research 33 (7) (2003) 1005–1011.

[79] J. L. Provis, A. Fernández-Jiménez, E. Kamseu, C. Leonelli, A. Palomo, Binder chemistry–low-calcium alkali-activated materials, in: Alkali Activated Materials, Springer, 2014, pp. 93–123.

[80] V. Glukhovsky, G. Rostovskaja, G. Rumyna, High strength slag-alkaline cements, in: Proceedings of the 7th international congress on the chemistry of cement, Paris, 1980, pp. 164–168.

[81] B. Talling, J. Brandstetr, Present state and future of alkali-activated slag concretes, Special Publication 114 (1989) 1519–1546.

[82] F. Collins, J. Sanjayan, Early age strength and workability of slag pastes activated by naoh and na2co3, Cement and Concrete Research 28 (5) (1998) 655–664.

[83] Y. Li, Y. Sun, Preliminary study on combined-alkali–slag paste materials, Cement and concrete research 30 (6) (2000) 963–966.

[84] T. Bakharev, Geopolymeric materials prepared using class f fly ash and elevated temperature curing, Cement and concrete research 35 (6) (2005) 1224–1232.

[85] V. Šmilauer, P. Hlaváček, F. Škvára, R. Šulc, L. Kopecký, J. Němeček, Micromechanical multiscale model for alkali activation of fly ash and metakaolin, Journal of Materials Science 46 (20) (2011) 6545–6555.

[86] A. Fernández-Jiménez, F. Puertas, Alkali-activated slag cements: kinetic studies, Cement and Concrete Research 27 (3) (1997) 359–368.

[87] Z. Yang, Modified hydrotalcites as smart additives for improved corrosion protection of reinforced concrete, Ph.D. thesis, TU Delft, Delft University of Technology (2015).

[88] N. Berke, A. Bentur, S. Diamond, Steel corrosion in concrete: fundamentals and civil engineering practice, CRC Press, 2014.

[89] D. Ho, R. Lewis, Carbonation of concrete and its prediction, Cement and Concrete Research 17 (3) (1987) 489–504.

[90] V. G. Papadakis, C. G. Vayenas, M. N. Fardis, Experimental investigation and mathematical modeling of the concrete carbonation problem, Chemical Engineering Science 46 (5-6) (1991) 1333–1338.

[91] A. V. Saetta, B. A. Schrefler, R. V. Vitaliani, The carbonation of concrete and the mechanism of moisture, heat and carbon dioxide flow through porous materials, Cement and Concrete Research 23 (4) (1993) 761–772.

[92] S. Roy, K. Poh, D. Northwood, Durability of concrete—accelerated carbonation and weathering studies, Building and environment 34 (5) (1999) 597–606.

[93] K. Sisomphon, L. Franke, Carbonation rates of concretes containing high volume of pozzolanic materials, Cement and Concrete Research 37 (12) (2007) 1647–1653.

[94] C. Pade, M. Guimaraes, The co2 uptake of concrete in a 100 year perspective, Cement and Concrete research 37 (9) (2007) 1348–1356.

[95] M. Castellote, C. Andrade, Modelling the carbonation of cementitious matrixes by means of the unreacted-core model, ur-core, Cement and concrete research 38 (12) (2008) 1374–1384.

[96] F. Duprat, N. T. Vu, A. Sellier, Accelerated carbonation tests for the probabilistic prediction of the durability of concrete structures, Construction and Building Materials 66 (2014) 597–605.

[97] T. P. Hills, F. Gordon, N. H. Florin, P. S. Fennell, Statistical analysis of the carbonation rate of concrete, Cement and Concrete Research 72 (2015) 98–107.

[98] A. Köliö, P. J. Niemelä, J. Lahdensivu, Evaluation of a carbonation model for existing concrete facades and balconies by consecutive field measurements, Cement and Concrete Composites 65 (2016) 29–40.

[99] V.-L. Ta, S. Bonnet, T. S. Kiesse, A. Ventura, A new meta-model to calculate carbonation front depth within concrete structures, Construction and Building Materials 129 (2016) 172–181.

[100] J. L. Provis, A. Palomo, C. Shi, Advances in understanding alkali-activated materials, Cement and Concrete Research 78 (2015) 110–125.

[101] J. Pacheco Farias, Corrosion of steel in cracked concrete: Chloride microanalysis and service life predictions, Ph.D. thesis, TU Delft, Delft University of Technology (2015).

[102] B. Bary, A. Sellier, Coupled moisture—carbon dioxide–calcium transfer model for carbonation of concrete, Cement and concrete research 34 (10) (2004) 1859–1872.

[103] M. Thiery, G. Villain, P. Dangla, G. Platret, Investigation of the carbonation front shape on cementitious materials: effects of the chemical kinetics, Cement and Concrete Research 37 (7) (2007) 1047–1058.

[104] T. Ishida, K. Maekawa, M. Soltani, Theoretically identified strong coupling of carbonation rate and thermodynamic moisture states in micropores of concrete, Journal of Advanced Concrete Technology 2 (2) (2004) 213–222.

[105] N. Hyvert, A. Sellier, F. Duprat, P. Rougeau, P. Francisco, Dependency of c–s–h carbonation rate on co2 pressure to explain transition from accelerated tests to natural carbonation, Cement and Concrete Research 40 (11) (2010) 1582–1589.

[106] I.-S. Yoon, O. Çopuroğlu, K.-B. Park, Effect of global climatic change on carbonation progress of concrete, Atmospheric environment 41 (34) (2007) 7274–7285.

[107] P. Goctermann, et al., Dura crete probabilistic performance based durability design of concrete structure: general guidelines for durability design and redesign, BE95 1347 (2000) R14.

[108] V. G. Papadakis, C. G. Vayenas, M. N. Fardis, Fundamental modeling and experimental investigation of concrete carbonation, Materials Journal 88 (4) (1991) 363–373.

[109] CEB, New Approach to Durability Design, CEB Bulletin No 238, Lausanne, 1997.

[110] Y. F. Houst, F. H. Wittmann, Depth profiles of carbonates formed during natural carbonation, Cement and concrete research 32 (12) (2002) 1923–1930.

[111] Y. F. Houst, P. E. Roelfstra, F. Wittmann, A model to predict service life of concrete structures, in: Proceedings of the International Conference" Materials Science and Restoration", no. LTP-CONF-2008-002, Edition Lack+ Chemie, 1983, pp. 181–186.

[112] A. V. Saetta, R. V. Vitaliani, Experimental investigation and numerical modeling of carbonation process in reinforced concrete structures: Part i: Theoretical formulation, Cement and concrete research 34 (4) (2004) 571–579.

[113] A. Steffens, D. Dinkler, H. Ahrens, Modeling carbonation for corrosion risk prediction of concrete structures, Cement and Concrete Research 32 (6) (2002) 935–941.

[114] K. Tutti, Corrosion of steel in concrete. swedish cement and concrete institute, Tech. rep., CIB, Research Report (1982).

[115] S. A. Bernal, R. M. De Gutiérrez, A. L. Pedraza, J. L. Provis, E. D. Rodriguez, S. Delvasto, Effect of binder content on the performance of alkali-activated slag concretes, Cement and Concrete Research 41 (1) (2011) 1–8.

[116] A. Morandeau, M. Thiery, P. Dangla, Investigation of the carbonation mechanism of ch and csh in terms of kinetics, microstructure changes and moisture properties, Cement and Concrete Research 56 (2014) 153–170.

[117] B. Wu, G. Ye, Development of porosity of cement paste blended with supplementary cementitious materials after carbonation, Construction and Building Materials 145 (2017) 52–61.

[118] S. Hamid, The crystal structure of the 11 ä natural tobermorite ca2. 25 [si3o7. 5 (oh) 1.5]· 1h2o, Zeitschrift für Kristallographie-Crystalline Materials 154 (1-4) (1981) 189–198.

[119] G. Renaudin, J. Russias, F. Leroux, F. Frizon, C. Cau-dit Coumes, Structural characterization of c–s–h and c–a–s–h samples—part i: long-range order investigated by rietveld analyses, Journal of Solid State Chemistry 182 (12) (2009) 3312–3319.

[120] M. B. Haha, G. Le Saout, F. Winnefeld, B. Lothenbach, Influence of activator type on hydration kinetics, hydrate assemblage and microstructural development of alkali activated blast-furnace slags, Cement and Concrete Research 41 (3) (2011) 301–310.

[121] A. M. F. Jiménez, Cementos de escorias activadas alcalinamente influencia de las variables y modelización del proceso, Ph.D. thesis, Universidad Autónoma de Madrid (2000).

[122] A. A. M. Neto, M. A. Cincotto, W. Repette, Drying and autogenous shrinkage of pastes and mortars with activated slag cement, Cement and Concrete Research 38 (4) (2008) 565–574.

[123] R. R. Lloyd, J. L. Provis, J. S. Van Deventer, Pore solution composition and alkali diffusion in inorganic polymer cement, Cement and Concrete Research 40 (9) (2010) 1386–1392.

[124] A. Fernández-Jiménez, I. García-Lodeiro, A. Palomo, Durability of alkali-activated fly ash cementitious materials, Journal of Materials Science 42 (9) (2007) 3055–3065.

[125] J. Bijen, H. Waltje, Alkali-activated slag–fly ash cements, Special Publication 114 (1989) 1565–1578.

[126] M. Nedeljković, Z. Li, G. Ye, Setting, strength, and autogenous shrinkage of alkali-activated fly ash and slag pastes: effect of slag content, Materials 11 (11) (2018) 2121.

[127] H. Wan, Z. Shui, Z. Lin, Analysis of geometric characteristics of ggbs particles and their influences on cement properties, Cement and concrete research 34 (1) (2004) 133–137.

[128] P. Wang, R. Trettin, V. Rudert, Effect of fineness and particle size distribution of granulated blast-furnace slag on the hydraulic reactivity in cement systems, Advances in cement research 17 (4) (2005) 161–167.

[129] S. B. Marinković, I. S. Ignjatović, J. S. Dragaš, N. D. Tošić, M. R. Nedeljković, Experimental study of alkali activated fly ash concrete with fly ash from one serbian power plant, in: Proc. of the Int. Conference on Sustainable Structural Concrete, La Plata Sept 15-18, 2015, pp. 22–33.

[130] D. Panias, I. P. Giannopoulou, T. Perraki, Effect of synthesis parameters on the mechanical properties of fly ash-based geopolymers, Colloids and Surfaces A: Physicochemical and Engineering Aspects 301 (1-3) (2007) 246–254.

[131] E. Douglas, A. Bilodeau, J. Brandstetr, V. Malhotra, Alkali activated ground granulated blast-furnace slag concrete: preliminary investigation, Cement and concrete research 21 (1) (1991) 101–108.

[132] O. Burciaga-Díaz, J. I. Escalante-García, R. Arellano-Aguilar, A. Gorokhovsky, Statistical analysis of strength development as a function of various parameters on activated metakaolin/slag cements, Journal of the American Ceramic Society 93 (2) (2010) 541–547.

[133] P. Nath, P. K. Sarker, Effect of ggbfs on setting, workability and early strength properties of fly ash geopolymer concrete cured in ambient condition, Construction and Building Materials 66 (2014) 163–171.

[134] M. Palacios, P. F. Banfill, F. Puertas, Rheology and setting of alkali-activated slag pastes and mortars: effect of organic admixture, ACI Materials Journal 105 (2) (2008) 140.

[135] Z. Tan, S. A. Bernal, J. L. Provis, Reproducible mini-slump test procedure for measuring the yield stress of cementitious pastes, Materials and Structures 50 (6) (2017) 235.

[136] S. Jiang, J. Mutin, A. Nonat, Studies on mechanism and physico-chemical parameters at the origin of the cement setting. i. the fundamental processes involved during the cement setting, Cement and Concrete Research 25 (4) (1995) 779–789.

[137] D. P. Bentz, Cement hydration: building bridges and dams at the microstructure level, Materials and Structures 40 (4) (2007) 397–404.

[138] NEN-EN 196-3:2005+A1:2009 en, Methods of testing cement – Part 3: Determination of setting times and soundness, CEN.

[139] M.-H. Zhang, K. Sisomphon, T. S. Ng, D. J. Sun, Effect of superplasticizers on workability retention and initial setting time of cement pastes, Construction and Building Materials 24 (9) (2010) 1700–1707.

[140] ASTM C1679-14, Standard Practice for Measuring Hydration Kinetics of Hydraulic Cementitious Mixtures Using Isothermal Calorimetry, American Society of Testing and Materials: West Conshohocken, PA, USA.

[141] NEN-EN 196-1:2005 en, Methods of testing cement. Determination of strength, CEN.

[142] D. Jiao, C. Shi, Q. Yuan, X. An, Y. Liu, H. Li, Effect of constituents on rheological properties of fresh concrete-a review, Cement and Concrete Composites 83 (2017) 146–159.

[143] G. Pólya, G. Pólya, G. Szegő, Isoperimetric inequalities in mathematical physics, Princeton University Press, 1951.

[144] H. F. Taylor, Cement chemistry, Thomas Telford, 1997.

[145] A. M. Fernandez-Jimenez, A. Palomo, C. Lopez-Hombrados, Engineering properties of alkali-activated fly ash concrete, ACI Materials Journal 103 (2) (2006) 106.

[146] S. Li, F. Sha, R. Liu, Q. Zhang, Z. Li, Investigation on fundamental properties of microfine cement and cement-slag grouts, Construction and Building Materials 153 (2017) 965–974.

[147] P. Chindaprasirt, C. Jaturapitakkul, T. Sinsiri, Effect of fly ash fineness on compressive strength and pore size of blended cement paste, Cement and Concrete Composites 27 (4) (2005) 425–428.

[148] J. L. Provis, R. J. Myers, C. E. White, V. Rose, J. S. van Deventer, X-ray microtomography shows pore structure and tortuosity in alkali-activated binders, Cement and Concrete Research 42 (6) (2012) 855–864.

[149] J. J. Thomas, A. J. Allen, H. M. Jennings, Density and water content of nanoscale solid c–s–h formed in alkali-activated slag (aas) paste and implications for chemical shrinkage, Cement and Concrete Research 42 (2) (2012) 377–383.

[150] F. Knudsen, Dependence of mechanical strength of brittle polycrystalline specimens on porosity and grain size, Journal of the American Ceramic Society 42 (8) (1959) 376–387.

[151] D. E. Macphee, K. Luke, F. P. Glasser, E. E. Lachowski, Solubility and aging of calcium silicate hydrates in alkaline solutions at 25 c, Journal of the American Ceramic Society 72 (4) (1989) 646–654.

[152] H. Ye, A. Radlińska, Effect of alkalis on cementitious materials: Understanding the relationship between composition, structure, and volume change mechanism, Journal of Advanced Concrete Technology 15 (4) (2017) 165–177.

[153] N. M. Z. Y. Y. G. Li, Zhenming, Autogenous shrinkage of alkali-activated slag-fly ash pastes.

[154] F. Collins, J. Sanjayan, Microcracking and strength development of alkali activated slag concrete, Cement and Concrete Composites 23 (4-5) (2001) 345–352.

[155] M. H. Hubler, J. J. Thomas, H. M. Jennings, Influence of nucleation seeding on the hydration kinetics and compressive strength of alkali activated slag paste, Cement and Concrete Research 41 (8) (2011) 842–846.

[156] P. Duxson, J. L. Provis, G. C. Lukey, S. W. Mallicoat, W. M. Kriven, J. S. Van Deventer, Understanding the relationship between geopolymer composition, microstructure and mechanical properties, Colloids and Surfaces A: Physicochemical and Engineering Aspects 269 (1-3) (2005) 47–58.

[157] H. M. Jennings, J. W. Bullard, J. J. Thomas, J. E. Andrade, J. J. Chen, G. W. Scherer, Characterization and modeling of pores and surfaces in cement paste, Journal of Advanced Concrete Technology 6 (1) (2008) 5–29.

[158] A. Gharzouni, L. Ouamara, I. Sobrados, S. Rossignol, Alkali-activated materials from different aluminosilicate sources: Effect of aluminum and calcium availability, Journal of Non-Crystalline Solids 484 (2018) 14–25.

[159] S. A. Bernal, J. L. Provis, V. Rose, R. M. De Gutierrez, Evolution of binder structure in sodium silicate-activated slag-metakaolin blends, Cement and Concrete Composites 33 (1) (2011) 46–54.

[160] S. A. Bernal, Effect of the activator dose on the compressive strength and accelerated carbonation resistance of alkali silicate-activated slag/metakaolin blended materials, Construction and Building Materials 98 (2015) 217–226.

[161] B. Lothenbach, A. Gruskovnjak, Hydration of alkali-activated slag: thermodynamic modelling, Advances in cement research 19 (2) (2007) 81–92.

[162] S. A. Bernal, J. L. Provis, V. Rose, R. M. De Gutiérrez, High-resolution x-ray diffraction and fluorescence microscopy characterization of alkali-activated slag-metakaolin binders, Journal of the american ceramic society 96 (6) (2013) 1951–1957.

[163] J. L. Bell, P. Sarin, P. E. Driemeyer, R. P. Haggerty, P. J. Chupas, W. M. Kriven, X-ray pair distribution function analysis of a metakaolin-based, kalsi 2 o 6· 5.5 h 2 o inorganic polymer (geopolymer), Journal of Materials Chemistry 18 (48) (2008) 5974–5981.

[164] I. Ismail, S. A. Bernal, J. L. Provis, R. San Nicolas, S. Hamdan, J. S. van Deventer, Modification of phase evolution in alkali-activated blast furnace slag by the incorporation of fly ash, Cement and Concrete Composites 45 (2014) 125–135.

[165] J. E. Oh, P. J. Monteiro, S. S. Jun, S. Choi, S. M. Clark, The evolution of strength and crystalline phases for alkali-activated ground blast furnace slag and fly ash-based geopolymers, Cement and Concrete Research 40 (2) (2010) 189–196.

[166] H. Ye, A. Radlińska, Fly ash-slag interaction during alkaline activation: Influence of activators on phase assemblage and microstructure formation, Construction and building materials 122 (2016) 594–606.

[167] R. J. Myers, S. A. Bernal, R. San Nicolas, J. L. Provis, Generalized structural description of calcium–sodium aluminosilicate hydrate gels: the cross-linked substituted tobermorite model, Langmuir 29 (17) (2013) 5294–5306.

[168] C. Shi, On the state and role of alkalis during the activation of alkali-activated slag cement, in: Proceedings of the 11th International Congress on the Chemistry of Cement. Durban (South Africa), 2003, pp. 2097–2105.

[169] C. Famy, K. Scrivener, A. Crumbie, What causes differences of csh gel grey levels in backscattered electron images?, Cement and Concrete Research 32 (9) (2002) 1465–1471.

[170] K. L. Scrivener, Backscattered electron imaging of cementitious microstructures: understanding and quantification, Cement and Concrete Composites 26 (8) (2004) 935–945.

[171] C. J. Van Hoek, M. de Roo, G. van der Veer, S. R. van der Laan, A sem-eds study of cultural heritage objects with interpretation of constituents and their distribution using parc data analysis, Microscopy and Microanalysis 17 (5) (2011) 656–660.

[172] C. van Hoek, How to process zillions of spectra from spectral imaging datasets? from phase-mapping to bulk-chemistry on micron-to centimeter scale using parc, Microscopy and Microanalysis 20 (S3) (2014) 660–661.

[173] K. Scrivener, R. Snellings, B. Lothenbach, A practical guide to microstructural analysis of cementitious materials, Crc Press, 2016.

[174] M. Nedeljkovic, K. Arbi, Y. Zuo, G. Ye, Physical properties and pore solution analysis of alkali-activated fly ash-slag pastes, in: Proceedings pro113: International RILEM Conference Materials Systems and Structures in Civil Engineering (MSSCE 2016) on Concrete with Supplementary Cementitious Materials, 2016.

[175] E. Underwood, 1970. quantitative stereology, Reading, lVIass., Addison-Wesley Publishing Co.

[176] J. Kaufmann, Pore space analysis of cement-based materials by combined nitrogen sorption–wood's metal impregnation and multi-cycle mercury intrusion, Cement and Concrete Composites 32 (7) (2010) 514–522.

[177] G. Ye, Experimental study and numerical simulation of the development of the microstructure and permeability of cementitious materials.

[178] K. S. Sing, Reporting physisorption data for gas/solid systems with special reference to the determination of surface area and porosity (recommendations 1984), Pure and applied chemistry 57 (4) (1985) 603–619.

[179] A. Katz, A. Thompson, Quantitative prediction of permeability in porous rock, Physical review B 34 (11) (1986) 8179.

[180] S. Brunauer, P. H. Emmett, E. Teller, Adsorption of gases in multimolecular layers, Journal of the American chemical society 60 (2) (1938) 309–319.

[181] R. K. Iler, Chemistry of silica–solubility, polymerization, colloid and surface properties, and biochemistry.

[182] W. D. Rickard, R. Williams, J. Temuujin, A. Van Riessen, Assessing the suitability of three australian fly ashes as an aluminosilicate source for geopolymers in high temperature applications, Materials Science and Engineering: A 528 (9) (2011) 3390–3397.

[183] R. R. Lloyd, J. L. Provis, J. S. van Deventer, Microscopy and microanalysis of inorganic polymer cements. 1: remnant fly ash particles, Journal of materials science 44 (2) (2009) 608–619.

[184] S. L. Valcke, A. J. Sarabèr, P. Pipilikaki, H. R. Fischer, H. W. Nugteren, Screening coal combustion fly ashes for application in geopolymers, Fuel 106 (2013) 490–497.

[185] M. B. Haha, B. Lothenbach, G. Le Saout, F. Winnefeld, Influence of slag chemistry on the hydration of alkali-activated blast-furnace slag—part i: Effect of mgo, Cement and Concrete Research 41 (9) (2011) 955–963.

[186] M. B. Haha, B. Lothenbach, G. Le Saout, F. Winnefeld, Influence of slag chemistry on the hydration of alkali-activated blast-furnace slag—part ii: Effect of al2o3, Cement and Concrete Research 42 (1) (2012) 74–83.

[187] I. Richardson, The nature of the hydration products in hardened cement pastes, Cement and Concrete Composites 22 (2) (2000) 97–113.

[188] R. J. Myers, S. A. Bernal, J. L. Provis, Phase diagrams for alkali-activated slag binders, Cement and Concrete Research 95 (2017) 30–38.

[189] M. Nedeljković, Y. Zuo, K. Arbi, G. Ye, Carbonation resistance of alkali-activated slag under natural and accelerated conditions, Journal of Sustainable Metallurgy 4 (1) (2018) 33–49.

[190] R. R. Lloyd, J. L. Provis, K. J. Smeaton, J. S. van Deventer, Spatial distribution of pores in fly ash-based inorganic polymer gels visualised by wood's metal intrusion, Microporous and Mesoporous Materials 126 (1-2) (2009) 32–39.

[191] K. K. Aligizaki, Pore structure of cement-based materials: testing, interpretation and requirements, CRC Press, 2014.

[192] P. Schneider, Adsorption isotherms of microporous-mesoporous solids revisited, Applied Catalysis A: General 129 (2) (1995) 157–165.

[193] Y. Ma, J. Hu, G. Ye, The pore structure and permeability of alkali activated fly ash, Fuel 104 (2013) 771–780.

[194] A. Korpa, T. Reinhard, Ultra high performance cement-based composites with advanced properties containing nanoscale pozzolans, in: Ultra High Performance Concrete (UHPC): Proceedings of the Second International Symposium on Ultra High Performance Concrete, Kassel, Germany, no. 10, 2008, p. 391.

[195] M. Nedeljković, B. Ghiassi, S. Melzer, C. Kooij, S. van der Laan, G. Ye, Co2 binding capacity of alkali-activated fly ash and slag pastes, Ceramics International 44 (16) (2018) 19646–19660.

[196] C. E. White, L. L. Daemen, M. Hartl, K. Page, Intrinsic differences in atomic ordering of calcium (alumino) silicate hydrates in conventional and alkali-activated cements, Cement and Concrete Research 67 (2015) 66–73.

[197] Y. Ma, G. Ye, J. Hu, Micro-mechanical properties of alkali-activated fly ash evaluated by nanoindentation, Construction and Building Materials 147 (2017) 407–416.

[198] S. A. Bernal, J. L. Provis, R. M. De Gutiérrez, J. S. van Deventer, Accelerated carbonation testing of alkali-activated slag/metakaolin blended concretes: effect of exposure conditions, Materials and Structures 48 (3) (2015) 653–669.

[199] D. Kralj, L. Brečević, A. E. Nielsen, Vaterite growth and dissolution in aqueous solution i. kinetics of crystal growth, Journal of Crystal Growth 104 (4) (1990) 793–800.

[200] J. G. Carmona, J. G. Morales, R. R. Clemente, Rhombohedral–scalenohedral calcite transition produced by adjusting the solution electrical conductivity in the system ca (oh) 2–co2–h2o, Journal of colloid and interface science 261 (2) (2003) 434–440.

[201] T. F. Sevelsted, J. Skibsted, Carbonation of c–s–h and c–a–s–h samples studied by 13c, 27al and 29si mas nmr spectroscopy, Cement and Concrete Research 71 (2015) 56–65.

[202] F. A. Andersen, D. Kralj, Determination of the composition of calcite-vaterite mixtures by infrared spectrophotometry, Applied spectroscopy 45 (10) (1991) 1748–1751.

[203] F. A. Andersen, L. Brecevic, et al., Infrared spectra of amorphous and crystalline calcium carbonate, Acta Chem. Scand 45 (10) (1991) 1018–1024.

[204] P. Yu, R. J. Kirkpatrick, B. Poe, P. F. McMillan, X. Cong, Structure of calcium silicate hydrate (c-s-h): Near-, mid-, and far-infrared spectroscopy, Journal of the American Ceramic Society 82 (3) (1999) 742–748.

[205] D. Dimas, I. Giannopoulou, D. Panias, Polymerization in sodium silicate solutions: a fundamental process in geopolymerization technology, Journal of materials science 44 (14) (2009) 3719–3730.

[206] W. Lee, J. Van Deventer, Structural reorganisation of class f fly ash in alkaline silicate solutions, Colloids and Surfaces A: Physicochemical and Engineering Aspects 211 (1) (2002) 49–66.

[207] D. Anstice, C. Page, M. Page, The pore solution phase of carbonated cement pastes, Cement and Concrete Research 35 (2) (2005) 377–383.

[208] M. Yousuf, A. Mollah, T. R. Hess, Y.-N. Tsai, D. L. Cocke, An ftir and xps investigations of the effects of carbonation on the solidification/stabilization of cement based systems-portland type v with zinc, Cement and Concrete Research 23 (4) (1993) 773–784.

[209] N. Li, N. Farzadnia, C. Shi, Microstructural changes in alkali-activated slag mortars induced by accelerated carbonation, Cement and Concrete Research 100 (2017) 214–226.

[210] M. Castellote, L. Fernandez, C. Andrade, C. Alonso, Chemical changes and phase analysis of opc pastes carbonated at different co 2 concentrations, Materials and Structures 42 (4) (2009) 515–525.

[211] E. Reardon, B. James, J. Abouchar, High pressure carbonation of cementitious grout, Cement and concrete research 19 (3) (1989) 385–399.

[212] L. Black, C. Breen, J. Yarwood, K. Garbev, P. Stemmermann, B. Gasharova, Structural features of c–s–h (i) and its carbonation in air—a raman spectroscopic study. part ii: carbonated phases, Journal of the American Ceramic Society 90 (3) (2007) 908–917.

[213] N. Rafai, R. Letolle, P. Blanc, A. Person, P. Gegout, Isotope geochemistry (13c, 18o) of carbonation processes in concretes, Cement and concrete research 21 (2-3) (1991) 368–377.

[214] D. Chakraborty, S. K. Bhatia, Formation and aggregation of polymorphs in continuous precipitation. 2. kinetics of caco3 precipitation, Industrial & engineering chemistry research 35 (6) (1996) 1995–2006.

[215] B. Johannesson, P. Utgenannt, Microstructural changes caused by carbonation of cement mortar, Cement and concrete Research 31 (6) (2001) 925–931.

[216] J. McConnell, Vaterite from ballycraigy, lame, northern ireland, Mineral. Mag 32 (1960) 534–544.

[217] K. Sawada, The mechanisms of crystallization and transformation of calcium carbonates, Pure and Applied Chemistry 69 (5) (1997) 921–928.

[218] H. H. Steinour, Some effects of carbon dioxide on mortars and concrete-discussion, J. Am. Concr. Inst 30 (2) (1959) 905–907.

[219] O. Çopuroğlu, E. Schlangen, Modeling of frost salt scaling, Cement and Concrete Research 38 (1) (2008) 27–39.

[220] M. Nedeljković, B. Ghiassi, S. van der Laan, Z. Li, G. Ye, Effect of curing conditions on the pore solution and carbonation resistance of alkali-activated fly ash and slag pastes, Cement and Concrete Research 116 (2019) 146–158.

[221] F. Škvára, V. Šmilauer, P. Hlaváček, L. Kopeckỳ, Z. Cilova, A weak alkali bond in (n, k)–a–s–h gels: evidence from leaching and modeling, Ceramics–Silikáty 56 (4) (2012) 374–382.

[222] N. Ukrainczyk, O. Vogt, E. A. Koenders, Reactive transport numerical model for durability of geopolymer materials, Advances in Chemical Engineering and Science 6 (04) (2016) 355.

[223] H. Huang, G. Ye, Examining the “time-zero” of autogenous shrinkage in high/ultra-high performance cement pastes, Cement and Concrete Research 97 (2017) 107–114.

[224] J. Kempl, O. Çopuroğlu, Eh-ph-and main element analyses of blast furnace slag cement paste pore solutions activated with sodium monofluorophosphate–implications for carbonation and self-healing, Cement and Concrete Composites 71 (2016) 63–76.

[225] M. Babaee, M. Khan, A. Castel, Passivity of embedded reinforcement in carbonated low-calcium fly ash-based geopolymer concrete, Cement and Concrete Composites 85 (2018) 32–43.

[226] C. Dow, F. P. Glasser, Calcium carbonate efflorescence on portland cement and building materials, Cement and Concrete Research 33 (1) (2003) 147–154.

[227] Z. Jiang, Z. Sun, P. Wang, Internal relative humidity distribution in high-performance cement paste due to moisture diffusion and self-desiccation, Cement and concrete research 36 (2) (2006) 320–325.

[228] Z. Zhang, J. L. Provis, A. Reid, H. Wang, Fly ash-based geopolymers: the relationship between composition, pore structure and efflorescence, Cement and concrete research 64 (2014) 30–41.

[229] B. Jones, X. Peng, Hot spring deposits on a cliff face: a case study from jifei, yunnan province, china, Sedimentary Geology 302 (2014) 1–28.

[230] R. Pouhet, M. Cyr, Carbonation in the pore solution of metakaolin-based geopolymer, Cement and Concrete Research 88 (2016) 227–235.

[231] Y. Zuo, M. Nedeljković, G. Ye, Coupled thermodynamic modelling and experimental study of sodium hydroxide activated slag, Construction and Building Materials 188 (2018) 262–279.

[232] J. Visser, Influence of the carbon dioxide concentration on the resistance to carbonation of concrete, Construction and Building Materials 67 (2014) 8–13.

[233] S.-Y. Hong, F. Glasser, Alkali binding in cement pastes: Part i. the csh phase, Cement and Concrete Research 29 (12) (1999) 1893–1903.

[234] S.-Y. Hong, F. P. Glasser, Alkali sorption by csh and cash gels: Part ii. role of alumina, Cement and Concrete Research 32 (7) (2002) 1101–1111.

[235] R. J. Myers, J. L. Provis, B. Lothenbach, et al., Composition–solubility–structure relationships in calcium (alkali) aluminosilicate hydrate (c-(n, k-) ash), Dalton Transactions 44 (30) (2015) 13530–13544.

[236] G. L. Kalousek, Studies of portions of the quaternary system soda-lime-silica-water at 25 c, J. Res. Natl. Bur. Stand 32 (1944) 285–302.

[237] P. Longuet, L. Burglen, A. Zelwer, The liquid phase of hydrated cement, Rev. Matér. Constr. Trav. Publics 676 (1973) 35–41.

[238] Y. Guang, Numerical simulation of connectivity of individual phases in hardening cement-based systems made of blended cement with and without admixtures (2006).

[239] G. Faure, Principles and applications of inorganic geochemistry: a comprehensive textbook for geology students, Macmillan Publ., 1991.

[240] K. Y. Chen, J. C. Morris, Kinetics of oxidation of aqueous sulfide by oxygen, Environmental Science & Technology 6 (6) (1972) 529–537.

[241] A. Scott, M. Alexander, Effect of supplementary cementitious materials (binder type) on the pore solution chemistry and the corrosion of steel in alkaline environments, Cement and Concrete Research 89 (2016) 45–55.

[242] W. M. Jung, S. H. Kang, W.-S. Kim, C. K. Choi, Particle morphology of calcium carbonate precipitated by gas–liquid reaction in a couette–taylor reactor, Chemical engineering science 55 (4) (2000) 733–747.

[243] C. Y. Tai, P.-C. Chen, Nucleation, agglomeration and crystal morphology of calcium carbonate, AIChE Journal 41 (1) (1995) 68–77.

[244] J. Hostomsky, A. Jones, Calcium carbonate crystallization, agglomeration and form during continuous precipitation from solution, Journal of Physics D: Applied Physics 24 (2) (1991) 165.

[245] Z. S˘auman, et al., Long-term carbonization of the phases 3cao. al2o3. 6h2o and 3cao. al2o3. sio2. 4h2, Cement and Concrete Research 2 (4) (1972) 435–446.

[246] A. Hidalgo, C. Domingo, C. Garcia, S. Petit, C. Andrade, C. Alonso, Microstructural changes induced in portland cement-based materials due to natural and supercritical carbonation, Journal of Materials Science 43 (9) (2008) 3101–3111.

[247] N. Clayden, S. Esposito, A. Aronne, P. Pernice, Solid state 27al nmr and ftir study of lanthanum aluminosilicate glasses, Journal of non-crystalline solids 258 (1-3) (1999) 11–19.

[248] K. Sisomphon, O. Copuroglu, A. Fraaij, Development of blast furnace slag mixtures against frost salt attack, Cement and Concrete Composites 32 (8) (2010) 630–638.

[249] B. Šavija, M. Luković, Carbonation of cement paste: understanding, challenges, and opportunities, Construction and Building Materials 117 (2016) 285–301.

[250] J. Han, G. Pan, W. Sun, C. Wang, D. Cui, Application of nanoindentation to investigate chemomechanical properties change of cement paste in the carbonation reaction, Science China Technological Sciences 55 (3) (2012) 616–622.

[251] G. Constantinides, F.-J. Ulm, The effect of two types of csh on the elasticity of cement-based materials: Results from nanoindentation and micromechanical modeling, Cement and concrete research 34 (1) (2004) 67–80.

[252] O. Bernard, F.-J. Ulm, E. Lemarchand, A multiscale micromechanics-hydration model for the early-age elastic properties of cement-based materials, Cement and Concrete Research 33 (9) (2003) 1293–1309.

[253] J. J. Hughes, P. Trtik, Micro-mechanical properties of cement paste measured by depth-sensing nanoindentation: a preliminary correlation of physical properties with phase type, Materials characterization 53 (2-4) (2004) 223–231.

[254] M. Luković, E. Schlangen, G. Ye, Combined experimental and numerical study of fracture behaviour of cement paste at the microlevel, Cement and Concrete Research 73 (2015) 123–135.

[255] B. Šavija, M. Luković, S. A. S. Hosseini, J. Pacheco, E. Schlangen, Corrosion induced cover cracking studied by x-ray computed tomography, nanoindentation, and energy dispersive x-ray spectrometry (eds), Materials and Structures 48 (7) (2015) 2043–2062.

[256] I. Beleña, W. Zhu, Nanoindentation study of na-geopolymers exposed to high temperatures, in: Nanotechnology in Construction 3, Springer, 2009, pp. 169–174.

[257] S. Das, P. Yang, S. S. Singh, J. C. Mertens, X. Xiao, N. Chawla, N. Neithalath, Effective properties of a fly ash geopolymer: Synergistic application of x-ray synchrotron tomography, nanoindentation, and homogenization models, Cement and Concrete Research 78 (2015) 252–262.

[258] F.-J. Ulm, M. Vandamme, H. M. Jennings, J. Vanzo, M. Bentivegna, K. J. Krakowiak, G. Constantinides, C. P. Bobko, K. J. Van Vliet, Does microstructure matter for statistical nanoindentation techniques?, Cement and Concrete Composites 32 (1) (2010) 92–99.

[259] J. J. Chen, L. Sorelli, M. Vandamme, F.-J. Ulm, G. Chanvillard, A coupled nanoindentation/sem-eds study on low water/cement ratio portland cement paste: evidence for c–s–h/ca (oh) 2 nanocomposites, Journal of the American Ceramic Society 93 (5) (2010) 1484–1493.

[260] W. C. Oliver, G. M. Pharr, Measurement of hardness and elastic modulus by instrumented indentation: Advances in understanding and refinements to methodology, Journal of materials research 19 (1) (2004) 3–20.

[261] H. M. Jennings, Colloid model of c- s- h and implications to the problem of creep and shrinkage, Materials and Structures 37 (1) (2004) 59–70.

[262] M. M. Costoya Fernández, Effect of particle size on the hydration kinetics and microstructural development of tricalcium silicate.

[263] Y. F. Houst, F. H. Wittmann, Influence of porosity and water content on the diffusivity of co2 and o2 through hydrated cement paste, Cement and Concrete Research 24 (6) (1994) 1165–1176.

[264] F. Puertas, M. Palacios, H. Manzano, J. Dolado, A. Rico, J. Rodríguez, A model for the cash gel formed in alkali-activated slag cements, Journal of the European Ceramic Society 31 (12) (2011) 2043–2056.

[265] P. Faucon, A. Delagrave, J. Petit, C. Richet, J. Marchand, H. Zanni, Aluminum incorporation in calcium silicate hydrates (c- s- h) depending on their ca/si ratio, The Journal of Physical Chemistry B 103 (37) (1999) 7796–7802.

[266] D. Moorehead, Cementation by the carbonation of hydrated lime, Cement and Concrete Research 16 (5) (1986) 700–708.

[267] M. P. Schmidt, A. J. Ilott, B. L. Phillips, R. J. Reeder, Structural changes upon dehydration of amorphous calcium carbonate, Crystal Growth & Design 14 (3) (2014) 938–951.

[268] Z. Zou, L. Bertinetti, Y. Politi, A. C. Jensen, S. Weiner, L. Addadi, P. Fratzl, W. J. Habraken, Opposite particle size effect on amorphous calcium carbonate crystallization in water and during heating in air, Chemistry of Materials 27 (12) (2015) 4237–4246.

[269] E. T. Stepkowska, J. Perez-Rodriguez, M. Sayagues, J. Martinez-Blanes, Calcite, vaterite and aragonite forming on cement hydration from liquid and gaseous phase, Journal of thermal analysis and calorimetry 73 (1) (2003) 247–269.

[270] D. Gebauer, H. Cölfen, A. Verch, M. Antonietti, The multiple roles of additives in caco3 crystallization: A quantitative case study, Advanced Materials 21 (4) (2009) 435–439.

[271] N. Spanos, P. G. Koutsoukos, The transformation of vaterite to calcite: effect of the conditions of the solutions in contact with the mineral phase, Journal of crystal growth 191 (4) (1998) 783–790.

[272] D. Daval, I. Martinez, J.-M. Guigner, R. Hellmann, J. Corvisier, N. Findling, C. Dominici, B. Goffé, F. Guyot, Mechanism of wollastonite carbonation deduced from micro-to nanometer length scale observations, American Mineralogist 94 (11-12) (2009) 1707–1726.

[273] P. V. Danckwerts, A. Lannus, Gas-liquid reactions, Journal of The Electrochemical Society 117 (10) (1970) 369C–370C.

[274] X. Wang, W. Conway, R. Burns, N. McCann, M. Maeder, Comprehensive study of the hydration and dehydration reactions of carbon dioxide in aqueous solution, The journal of physical chemistry A 114 (4) (2009) 1734–1740.

[275] D. Darmana, R. Henket, N. Deen, J. Kuipers, Detailed modelling of hydrodynamics, mass transfer and chemical reactions in a bubble column using a discrete bubble model: Chemisorption of co2 into naoh solution, numerical and experimental study, Chemical engineering science 62 (9) (2007) 2556–2575.

[276] M. Eigen, Proton transfer, acid-base catalysis, and enzymatic hydrolysis. part i: Elementary processes, Angewandte Chemie International Edition in English 3 (1) (1964) 1–19.

[277] I. Richardson, Tobermorite/jennite-and tobermorite/calcium hydroxide-based models for the structure of csh: applicability to hardened pastes of tricalcium silicate, $\beta$-dicalcium silicate, portland cement, and blends of portland cement with blast-furnace slag, metakaolin, or silica fume, Cement and Concrete Research 34 (9) (2004) 1733–1777.

[278] R. A. Patel, J. Perko, D. Jacques, G. De Schutter, G. Ye, K. Van Bruegel, Effective diffusivity of cement pastes from virtual microstructures: Role of gel porosity and capillary pore percolation, Construction and Building Materials 165 (2018) 833–845.

[279] T. Shiotani, J. Bisschop, J. Van Mier, Temporal and spatial development of drying shrinkage cracking in cement-based materials, Engineering Fracture Mechanics 70 (12) (2003) 1509–1525.

[280] F. Collins, J. Sanjayan, Effect of pore size distribution on drying shrinking of alkali-activated slag concrete, Cement and Concrete Research 30 (9) (2000) 1401–1406.

[281] E. Gruyaert, P. Van den Heede, N. De Belie, Carbonation of slag concrete: Effect of the cement replacement level and curing on the carbonation coefficient–effect of carbonation on the pore structure, Cement and concrete composites 35 (1) (2013) 39–48.

[282] K. Arbi, Long-term performance of geopolymer concrete systems for production of environment friendly building materials, s81.1.13498a; biannual project report: H01-2016 (2016).

[283] K. L. Scrivener, A. K. Crumbie, P. Laugesen, The interfacial transition zone (itz) between cement paste and aggregate in concrete, Interface science 12 (4) (2004) 411–421.

[284] L. Cui, J. H. Cahyadi, Permeability and pore structure of opc paste, Cement and Concrete Research 31 (2) (2001) 277–282.

[285] J. Monteiro, P. K. Mehta, Ettringite formation on the aggregate—cement paste interface, Cement and concrete research 15 (2) (1985) 378–380.

[286] R. San Nicolas, S. A. Bernal, R. M. De Gutiérrez, J. S. Van Deventer, J. L. Provis, Distinctive microstructural features of aged sodium silicate-activated slag concretes, Cement and Concrete Research 65 (2014) 41–51.

[287] J. J. Chen, J. J. Thomas, H. M. Jennings, Decalcification shrinkage of cement paste, Cement and concrete research 36 (5) (2006) 801–809.

[288] P. E. Holthuizen, O. Çopuroğlu, R. B. Polder, Chloride ingress of carbonated blast furnace slag cement mortars, in: High Tech Concrete: Where Technology and Engineering Meet, Springer, 2018, pp. 73–82.

[289] A. Gruskovnjak, B. Lothenbach, L. Holzer, R. Figi, F. Winnefeld, Hydration of alkali-activated slag: comparison with ordinary portland cement, Advances in cement research 18 (3) (2006) 119–128.

[290] M. Nedeljković, M. Luković, K. van Breugel, D. Hordijk, G. Ye, Development and application of an environmentally friendly ductile alkali-activated composite, Journal of Cleaner Production 180 (2018) 524–538.

[291] Z. Aldin, M. Nedeljkovic, M. Lukovic, J. Liu, K. Blom, G. Ye, Optimization of a geopolymer mixture for a reinforced cantilever concrete bench.

[292] F. I. du Beton, Model code for service life design, Bulletin 34.

[293] G. De Schutter, Durability of concrete: prescribing composition or requiring performance?, in: International Conference on the Regeneration and Conservation of Concrete Structures (RCCS), 2015, pp. 1–6.

[294] A. Younsi, P. Turcry, E. Rozière, A. Aït-Mokhtar, A. Loukili, Performance-based design and carbonation of concrete with high fly ash content, Cement and Concrete Composites 33 (10) (2011) 993–1000.

[295] G. van der Wegen, R. B. Polder, K. van Breugel, Guideline for service life design of structural concrete–a performance based approach with regard to chloride induced corrosion, Heron 57 (3) (2012) 153–167.

[296] I. Ismail, S. A. Bernal, J. L. Provis, R. San Nicolas, D. G. Brice, A. R. Kilcullen, S. Hamdan, J. S. van Deventer, Influence of fly ash on the water and chloride permeability of alkali-activated slag mortars and concretes, Construction and Building Materials 48 (2013) 1187–1201.

# SUMMARY

Concretes with ordinary Portland cement (OPC)-based binders have a high environmental impact. These materials are unfavourable in terms of $CO_2$ emission, energy and natural resources consumption. It is estimated that concrete production is responsible for about 8.6% of the global $CO_2$ output. Large $CO_2$ emission of concrete industry can be overcome through the replacement of OPC by various industrial by-products, such as fly ash (FA) from coal-fired electricity production and ground granulated blast furnace slag (GGBFS) from steel production. Alkali-activated materials (AAMs) are one of the most environmentally friendly alternatives to OPC-based materials. So far, AAMs are increasingly used for non-structural applications. Currently, widespread use of AAMs for structural applications is limited by lack of standards and understanding of their long-term behaviour in engineering practice.

Deterioration of reinforced OPC-based concrete structures is often caused by the corrosion of reinforcing steel. Corrosion of reinforcing steel in concrete is mostly a result of chloride ingress and/or carbonation. Compared to OPC-based concrete, carbonation of AAMs is less understood despite many studies on the effect of various parameters on carbonation resistance of AAMs. Furthermore, the lack of data on long-term performance of alkali-activated concretes makes it challenging to assist the predictive models of the service life of alkali activated concretes. Other parameters, such as curing conditions and binder compositions further complicate the understanding of the carbonation mechanism of AAMs. There is almost no information that deals with the combined effect of binder composition, curing conditions and exposure conditions on the carbonation of AAMs.

This thesis concentrates on understanding the carbonation mechanism of alkali-activated materials and on strategies to improve their performance in view of carbonation. A three level concept was applied. The information with respect to carbonation at the gel level (Level I) and paste level (Level II) has been used for studying carbonation at the concrete level (Level III). The carbonation mechanism was studied from two aspects: (1) pore solution carbonation and (2) carbonation of gel phases. The combined effect of GGBFS content, curing conditions (sealed/unsealed) and exposure conditions (natural indoor/outdoor and accelerated carbonation) was considered.

First, paste mixtures were developed for studying the carbonation mechanism. Their properties, such as workability and strength, were tested in order to determine their suitability for making concretes. The chemical compositions of phases in the raw materials, GGBFS and FA, were assessed. Next, a PhAse Recognition and Characterization (PARC) software was - for the first time - used to determine the spatial distribution of the dominant reaction products and their chemical composition as a function of different curing conditions. While pure alkali-activated GGBFS paste consists of mainly three phases (GGBFS, CaMgNaAlSi, CaNaAlSi), paste with GGBFS and FA exhibited compositionally different gel domains due to heterogeneity of raw FA. The phase characterization provided stoichiometry of the phases and rate of reaction, which were necessary for assessment of the carbonated pastes.

Second, the $CO_2$ binding capacity of pastes was investigated. Direct carbonation has enabled time-series measurements of the gel molecular changes. The $CO_2$ binding capacity, carbonate phases, gel molecular changes of crushed alkali activated pastes have been tested with TG-MS, QXRD and FTIR. Gel decalcification was the main consequence of carbonation in alkali activated FA/GGBFS pastes. The carbonate phases were intergrown with the gel, hence their identification was only possible with XRD. The most dominant carbonate phases were amorphous calcium carbonates. Other carbonate phases were vaterite and calcite. The study showed that AAMs had lower $CO_2$ binding capacity compared to cement-based materials under 1% v/v $CO_2$.

Third, the pore solution carbonation was studied. It was found that the pH was in the of range 13-14 at 28 days, depending on the composition of the mixture and curing conditions. These pH values guarantee the presence of a passive layer around the reinforcing steel. The major effect of unsealed curing of the samples on their pore solution is loss of $Na^+$ due to the condensation of water on the surface and diffusive movement of ions from the interior towards the surface of the samples. The substantial decrease of $Na^+$ concentration in the pore solution in unsealed cured samples resulted in a faster propagation rate of the carbonation front in these specimens. Furthermore, pH was lower for unsealed cured samples compared to the sealed cured samples after carbonation. Additionally, higher reduction in alkalinity was seen in pastes containing 0, 30, 50

wt.% GGBFS in comparison to the specimen which contained 70 and 100 wt.% GGBFS. The main reason is higher consumption of [$Na^+$] and [$OH^-$] in pastes containing 0, 30, 50 wt.% GGBFS for dissolution of FA. The binding of $Na^+$ by the gel phases of the alkali activated paste reduces the effective $Na^+$ concentration in the pore solution, therefore the alkalinity of the pore solution becomes lower. The pH of carbonated pastes did not drop below 9.2 regardless the exposure conditions.

Fourth, the effect of carbonation on the pore structure of pastes was investigated. The removal of calcium from the C-N-A-S-H gel caused the polymerization of the remaining gel and loss of chemically bound water. This resulted in an increase of pore volume and pore size in the samples. This weakened the cohesion within the alkali-activated FA/ GGBFS pastes. Consequently, the modulus of elasticity of carbonated blended pastes (S30, S50) was reduced. With increase of GGBFS content in the pastes, the deterioration of pastes due to carbonation was significantly reduced.

Fifth, based on previous steps, a carbonation mechanism was proposed that can be applied for analysis of carbonation of any alkali activated concrete mixture. The apparent diffusion of $CO_2$ is controlled by the $CO_2$ transport through connected large gel pores (3-12 nm) and $CO_2$ binding capacity of the gels. Carbonation reactions affected initially the pore solution alkalinity and then the gel structure and composition. Regarding the exposure conditions, both accelerated and natural carbonation resulted in similar carbonation products and increase of porosity. However, the pH of alkali activated pastes was reduced more under accelerated than under natural carbonation conditions. Beside pH difference, the change of microstructure has to be taken into account for correlation between accelerated and natural exposure conditions. Gel formation is continuous under natural carbonation conditions while it is not under accelerated carbonation conditions due to short exposure time. For AAMs, this is of higher importance than for cement-based materials when it comes to carbonation. Compared to cement-based materials where $Ca(OH)_2$ and C-S-H gel are the main reaction products, in AAMs the main reaction products are the gel-type products. In AAMs, $Na^+$ and $OH^-$ are consumed continuously for gel formation. At the same time they are the main buffer for alkalinity of the pore solution of the pastes when carbonation starts. Therefore, use of accelerated carbonation for predicting change of pH of AAMs under natural carbonation conditions is not fully appropriate.

Despite low porosity of alkali-activated concrete, these concretes must have an appropriate curing in order to be used in structural applications due to their lower carbonation resistance compared to cement-based concrete. Their low $CO_2$ binding capacity correlates with their lower carbonation resistance. Depending on the exposure class and the application, service life of alkali activated materials should be examined not only considering the decrease of pH, but also taking other parameters in consideration such as stiffness of the deteriorated concrete.

In summary, in this thesis knowledge has been generated of the carbonation mechanism at the paste level and has been used for understanding carbonation of alkali activated concrete. Based on the parameter studies (GGBFS content, curing, exposure conditions), recommendations for the design of alkali activated concrete for engineering practice are given in view of carbonation resistance. With respect to the scope of this thesis, several extensions of the presented study are proposed.

# SAMENVATTING

Beton met Portland cement (OPC) als bindmiddel heeft een hoge impact op het milieu. Dit type beton is zeer ongunstig in termen van $CO_2$-uitstoot, energie en het verbruik van natuurlijke bronnen. Naar schatting is de productie van beton verantwoordelijk voor ongeveer 8,6% van de wereldwijde $CO_2$-uitstoot, waarbij OPC klinkerproductie het grootste aandeel heeft. Een groot aandeel van de $CO_2$-uitstoot van de betonindustrie kan worden overwonnen door de vervanging van OPC voor verschillende industriële bijproducten, zoals vliegas (FA) uit kolengestookte elektriciteitsproductie en gegranuleerde hoogovenslakken (GGBFS) van de staalproductie. Alkali-geactiveerde materialen (AAM's) zijn één van de meest milieuvriendelijke alternatieven voor OPC-gebaseerde materialen. Tot dusverre worden AAM's in toenemende mate gebruikt voor niet constructieve toepassingen. Momenteel wordt algemeen gebruik van AAM's voor constructieve toepassingen beperkt door een gebrek aan normen en kennis van hun langetermijngedrag in de praktijk.

Degradatie van gewapende betonconstructies wordt vaak veroorzaakt door wapeningscorrosie. Corrosie van wapeningsstaal in beton is meestal een gevolg van indringing van chloride en/of ten gevolge van carbonatatie. Vergeleken met traditioneel beton, is carbonatatie van AAM's minder begrepen ondanks vele studies over het effect van verschillende parameters op de carbonatatieweerstand van AAM's. Bovendien maakt het gebrek aan gegevens over de prestaties op lange termijn van alkali-geactiveerd beton het een uitdaging om levensduur voorspellende modellen van alkali-geactiveerd beton te ondersteunen. Andere parameters, zoals nabehandeling en bindmiddelsamenstellingen bemoeilijken verder het begrip van het carbonatatiemechanisme van AAM's. Er is bijna geen informatie over het gecombineerde effecten van bindmiddelsamenstelling, nabehandelingswijze en omgevingscondities op de carbonatatie van AAM's.

Dit proefschrift concentreert zich op het begrijpen van het carbonatatiemechanisme van alkali-geactiveerde materialen en op strategieën om hun prestaties te verbeteren met het oog op carbonatatie. Een concept met drie niveaus is toegepast. De informatie met betrekking tot carbonatatie op gelniveau (niveau I) en pasta niveau (niveau II) is gebruikt voor het bestuderen van carbonatatie op beton niveau (niveau III). Het carbonatatiemechanisme is bestudeerd vanuit twee aspecten: (1) carbonatatie van poriënoplossing en (2) carbonatatie van gelfasen. Het gecombineerde effect van het slakgehalte, nabehandeling (gesealed/ongesealed) en omgevingscondities (binnenklimaat/buitenklimaat en versnelde carbonatatie) werd overwogen.

Eerst werden er pasta mengsels ontwikkeld om het carbonatatiemechanisme te bestuderen. Hun eigenschappen, zoals verwerkbaarheid en sterkte, werden getest om hun geschiktheid voor het maken van beton te bepalen. De chemische samenstellingen van de grondstoffen, GGBFS en FA werden beoordeeld. Vervolgens werd een PhAse Recognition and Characterization (PARC) software - voor de eerste keer - gebruikt om de ruimtelijke verdeling van de dominante reactieproducten en hun chemische samenstelling te bepalen als een functie van verschillende nabehandelingswijzen. Hoewel pure alkali-geactiveerde GGBFS-pasta uit voornamelijk drie producten bestaat (GGBFS, CaMgNaAlSi, CaNaAlSi), vertoonde de compositie van pasta met GGBFS en FA verschillende gelproducten vanwege de heterogeniteit van ruwe FA. De karakterisering van de gelproducten verschafte de stoichiometrie en reactiesnelheid van de fasen, die noodzakelijk waren voor de beoordeling van de gecarbonateerde pasta's.

Hierna werd de $CO_2$-bindingscapaciteit van pasta's onderzocht. Directe carbonatatie heeft metingen van de moleculaire veranderingen door de tijd van de gel mogelijk gemaakt. De $CO_2$-bindingscapaciteit, carbonaatfasen en gel-moleculaire veranderingen van gemalen alkali-geactiveerde pasta's zijn getest met TG-MS, QXRD en FTIR. Ontkalking van gel was de belangrijkste consequentie van carbonatatie in alkali-geactiveerde FA/GGBFS-pasta's. De carbonaatfasen werden met de gel vergroeid, waardoor hun identificatie alleen met XRD mogelijk was. De meest dominante carbonaatfasen waren amorfe calciumcarbonaten. Andere carbonaatfasen in gecarbonateerde alkali-geactiveerde pasta's waren vaterite en calciet. De studie toont aan dat AAM's een lagere $CO_2$-bindingscapaciteit hebben vergeleken met materialen op cementbasis onder 1% v/v $CO_2$.

Vervolgens is de carbonatatie van de poriënoplossingen onderzocht. pH-waarden binnen het bereik 13-14 werd gevonden na 28 dagen, afhankelijk van de samenstelling van het mengsel en de nabehandeling. Deze pH-waarden garanderen de aanwezigheid van een passieve laag rondom het wapeningsstaal. Het belangrijkste effect van ongesealde nabehandeling van de proefstukken op hun poriënoplossing is het verlies van $Na^+$ ionen ten gevolg van de condensatie van water op het oppervlak en diffuse bewegingen van ionen van binnenuit

naar het oppervlak van de proefstukken. De aanzienlijke afname van de $Na^+$ concentratie in de poriënoplossing in niet-afgedichte verharde proefstukken resulteerde in een snellere voortplantingssnelheid van het carbonatatiefront in deze proefstukken. Tevens was de pH na carbonatatie lager voor niet-afgedichte verharde proefstukken vergeleken met gesealde proefstukken. Bovendien werd een grotere vermindering van de alkaliniteit waargenomen in pasta's die 0, 30, 50% GGBFS bevatten in vergelijking met het monster dat 70 en 100% GGBFS bevatte. De belangrijkste reden is een groter verbruik van $[Na^+]$ en $[OH^-]$ in pasta's met 0, 30, 50% GGBFS voor het oplossen van FA. De binding van $Na^+$ door de gelfasen van alkali-geactiveerde pasta's verlaagt de effectieve $Na^+$-concentratie in de poriënoplossing, daarom is de alkaliniteit van de poriënoplossing lager. De pH van gecarbonateerde pasta's daalde niet onder 9.2, ongeacht de omgevingscondities.

Verder werd het effect van carbonatatie op de poriënstructuur van pasta's onderzocht. De verwijdering van calcium uit de C-N-A-S-H-gel veroorzaakte de polymerisatie van de overblijvende gel en het verlies van chemisch gebonden water. Dit resulteerde in een toename van het poriënvolume en de poriegrootte in de proefstukken, waardoor de cohesie binnen de alkali-geactiveerde FA/GGBFS-pasta's verzwakte. Een bijgevolg hiervan was de vermindering van de elasticiteitsmodulus van gecarbonateerde pasta's (S30, S50). Met een verhoging van het GGBFS-gehalte werd de aantasting van pasta's door carbonatatie aanzienlijk verminderd.

Tenslotte, gebaseerd op voorgaande stappen, werd een carbonatiemechanisme voorgesteld dat kan worden toegepast voor de beoordeling van carbonatatie van elk alkali-geactiveerd betonmengsel. De schijnbare diffusie van $CO_2$ wordt gecontroleerd door het $CO_2$-transport door verbonden gelporiën (3-12 nm) en de $CO_2$-bindingscapaciteit van de gel. Carbonatatiereacties beïnvloedden aanvankelijk de alkaliniteit van de porieoplossing en vervolgens de gelstructuur en samenstelling. Met betrekking tot de omgevingscondities resulteerde zowel versnelde als natuurlijke carbonatatie in vergelijkbare carbonatatieproducten en een toename van porositeit. Daarentegen werd de pH van alkali-geactiveerde pasta's onder versnelde carbonatatie meer verminderd dan onder natuurlijke carbonatatie. Naast het verschil in pH moet de verandering van de microstructuur in overweging worden genomen voor de correlatie tussen versnelde en natuurlijke carbonatatie. Onder natuurlijke carbonatatie is er een doorgaande gelvorming, in tegenstelling tot versnelde carbonatatie waarbij de testtijd dusdanig wordt verkort waardoor er geen additionele gelformatie optreedt. Voor carbonatatie van AAM's is dit van groter belang dan voor op cement gebaseerde materiale. In AAM's worden $Na^+$ en $OH^-$ continu verbruikt voor gelvorming. Tegelijkertijd zijn dit ook de belangrijkste buffer voor de alkaliniteit van de poriënoplossing van de pasta's wanneer carbonatatie optreedt. Daarom is het gebruik van versnelde carbonatatie voor het voorspellen van de pH verandering van AAM's onder natuurlijke carbonatatie niet volledig geschikt.

Ondanks de lage porositeit van alkali-geactiveerd beton moet deze betonsoort, in verband met hun lagere carbonatatieweerstand in vergelijking met cementbeton, een geschikte nabehandeling hebben om te kunnen worden gebruikt in constructieve toepassingen. De lagere $CO_2$-bindingscapaciteit heeft een correlatie met de carbonatatieweerstand. Afhankelijk van de milieuklasse en de toepassing, moet de levensduur van alkali-geactiveerde materialen worden onderzocht. Niet alleen de daling van de pH beschouwend, maar ook rekening houdend met andere parameters zoals stijfheid van het aangetaste beton.

Samenvattend, is in dit proefschrift kennis gegenereerd met betrekking tot het carbonatiemechanisme op het niveau van de pasta's en is het gebruikt voor het begrijpen van carbonatatie van met alkali geactiveerd beton. Op basis van de parameterstudies (GGBFS-gehalte, nabehandeling, omgevingscondities) worden aanbevelingen gegeven voor het ontwerp van alkali-geactiveerd beton voor de praktijk met het oog op carbonatatieweerstand. Met betrekking tot de scope van dit proefschrift worden verschillende uitbreidingen van het gepresenteerde onderzoek voorgesteld.

# CURRICULUM VITÆ

## PERSONAL INFORMATION

| | |
|---|---|
| Name | **Marija Nedeljković** |
| Nationality | Serbian |
| Date of birth | 21 August 1990 |
| Email | marijanedeljkovic90@gmail.com |

## EDUCATION AND WORK EXPERIENCE

| | |
|---|---|
| September 2005–June 2009 | "1300 kaplara" Gymnasium, Ljig, Serbia |
| September 2009–August 2014 | B.Sc. and M.Sc. in Civil Engineering,<br>Faculty of Civil Engineering,<br>University of Belgrade, Serbia |
| June 2013–August 2013 | Intern, Afrique Travaux,<br>Tunis, Tunisia |
| September 2014–September 2018 | Ph.D. Researcher,<br>Faculty of Civil Engineering and Geosciences<br>Delft University of Technology, The Netherlands |
| March 2017–September 2018 | Visiting Researcher,<br>Internship in Ceramic Research Center,<br>TATA STEEL IJmuiden,The Netherlands |
| December 2018–present | Post-doctoral Researcher,<br>TNO and Delft University of Technology,<br>The Netherlands |

# LIST OF PUBLICATIONS

JOURNAL PUBLICATIONS

1. **M. Nedeljković**, B. Ghiassi, S. van der Laan, Z. Li, G. Ye, *Effect of curing conditions on the pore solution and carbonation resistance of alkali-activated fly ash and slag pastes*, Cement and Concrete Research, 116, 146-158, 2019.

2. **M. Nedeljković**, B. Ghiassi, S. Melzer, C. Kooij, S. van der Laan, G. Ye, *$CO_2$ binding capacity of alkali-activated fly ash and slag pastes*, Ceramics International, 44, 19646-19660 (2018).

3. **M. Nedeljković**, Y. Zuo, K. Arbi, G. Ye, *New test method for assessing the carbonation front in alkali-activated fly ash and slag binders: microscopic complementary techniques*, Key engineering materials, 761, 148-151 (2018).

4. **M. Nedeljković**, Y. Zuo, K. Arbi, G. Ye, *Carbonation Resistance of Alkali-activated Slag under Natural and Accelerated Conditions*, Journal of Sustainable Metallurgy, 4, 33-49 (2018).

5. **M. Nedeljković**, Z. Li, G. Ye, *Setting, Strength, and Autogenous Shrinkage of Alkali-Activated Fly Ash and Slag Pastes: Effect of Slag Content*, Materials, 11, 2121 (2018).

6. **M. Nedeljković**, M. Luković, K. Van Breugel, D. Hordijk, G. Ye, *Development and application of an environmentally friendly ductile alkali-activated composite*, Journal of cleaner production, 180, 524-538 (2018).

7. **M. Nedeljković**, B. Savija, Y. Zuo, M. Luković, G. Ye, *Effect of natural carbonation on the pore structure and elastic modulus of the alkali-activated fly ash and slag pastes*, Construction and Building Materials, 161, 687-704 (2018).

8. Y. Zuo, **M. Nedeljković**, G. Ye, *Pore solution composition of alkali-activated slag/fly ash pastes*, Cement and Concrete Research, 115, 230-250 (2019).

9. Y. Zuo, **M. Nedeljković**, G. Ye, *Coupled thermodynamic modelling and experimental study of sodium hydroxide activated slag*, Construction and Building Materials, 188, 262-279 (2018).

10. Y. Zuo, **M. Nedeljković**, G. Ye, *Pore Solution Composition and Solubility of Alkali-Activated Fly Ash*, Key engineering materials, 761, 65-68 (2018).

11. K. Arbi, **M. Nedeljković**, Y. Zuo, G. Ye, *A Review on the Durability of Alkali-Activated Fly Ash/Slag Systems: Advances, Issues, and Perspectives*, Industrial and Engineering Chemistry Research, 55, 5439-5453 (2016).

12. Z. Li, **M. Nedeljković**, B. Chen, G. Ye, *Mitigating the autogenous shrinkage of alkali-activated slag by metakaolin*, Cement and Concrete Research, under review.

CONFERENCE PUBLICATIONS

1. **M. Nedeljković**, C. van Hoek, S. Melzer, S. van der Laan, G. Ye, *Assessment of the slag reactivity in alkali-activated fly ash and slag pastes*, Proceedings of the Workshop on Concrete Modelling and Materials Behaviour in honor of Professor Klaas van Breugel, Delft, the Netherlands, Edited by Guang Ye, RILEM Publications S.A.R.L. (27-28 August 2018).

2. **M. Nedeljković**, C. van Hoek, E. Zinngrebe, S. van der Laan, G. Ye, *Gel deterioration in alkali-activated fly ash and slag pastes subjected to natural carbonation*, In the Proceedings of the 4th International Conference on Service Life Design for Infrastructures (SLD4), Delft, the Netherlands, Edited by Guang Ye, Yong Yuan, Claudia Romero Rodriguez, Hongzhi Zhang, Branko Savija, RILEM Publications S.A.R.L. (27-30 August 2018).

3. **M. Nedeljković**, E. Zinngrebe, S. van der Laan, C. van Hoek, B. Ghiassi, S. Melzer, G. Ye, *Element zonation in carbonated alkali-activated slag paste.*, Conference in honor of the Centennial Laboratory of Construction Materials (EPFL) and Karen Scrivener 60th Birthday, Lausanne, Switzerland (19-22 August 2018).

4. **M. Nedeljković**, Y. Zuo, K. Arbi, G. Ye, *New test method for assessing the carbonation front in alkali-activated fly ash and slag binders: microscopic complementary techniques*, In the 6th International Conference, Non-Traditional Cement and Concrete, Brno, Czech Republic, Edited by Sarka Nenadalova, Vlastimil Bilek, Zbynek Kersner, Stanislav Seitl and Dr. Hana Simonova, (19–22 June 2017).

5. **M. Nedeljković**, Y. Zuo, K. Arbi, G. Ye, *Natural carbonation of alkali-activated fly ash and slag pastes*, In: Hordijk D., Luković M. (eds) High Tech Concrete: Where Technology and Engineering Meet, Maastricht, the Netherlands, p. 2213-2223, Springer, Cham (12–14 June 2017).

6. **M. Nedeljković**, Y. Zuo, K. Arbi, G. Ye, *Carbonation Resistance of Alkali-Activated Slag Under Natural and Accelerated Conditions*, In Proceedings of the 5th International Slag Valorisation Symposium, From fundamentals to applications, Leuven, Belgium, Edited by Dr. Ir. Remus Ion Iacobescu, Dr. Ir. Annelies Malfliet (3-5 April 2017).

7. **M. Nedeljković**, K. Arbi, Y. Zuo, G. Ye, *Microstructural and mineralogical analysis of alkali activated fly ash-slag pastes*, In Proceedings of the 3rd International RILEM Conference on Microstructure Related Durability of Cementitious Composites, Nanjing, China, Edited by Changwen Miao, Wei Sun, Jiaping Liu, Huisu Chen, Guang Ye and Klaas van Breugel, RILEM Publications S.A.R.L. (24-26 October 2016).

8. **M. Nedeljković**, K. Arbi, Y. Zuo, G. Ye, *Physical properties and pore solution analysis of alkali activated fly ash-slag pastes*, In Proceedings of the International RILEM Conference on Materials, Systems and Structures in Civil Engineering, Conference segment on Concrete with Supplementary Cementitious Materials, Technical University of Denmark, Lyngby, Denmark, Edited by Ole M. Jensen, Konstantin Kovler and Nele De Belie, RILEM Publications S.A.R.L. (22-24 August 2016).

9. Z. Aldin, **M. Nedeljković**, M. Luković, J. Liyu, K. Blom, G. Ye, *Optimization of a geopolymer mixture design for a reinforced cantilever concrete bench*, In Proceedings of the 9th International Symposium on Cement and Concrete (ISCC 2017), Wuhan University, China (1-3 November 2017).

10. S. Zhang, **M. Nedeljković**, B. Ghiassi, G. Ye, *A Comparative Study on Deflection-hardening Behaviour of Ductile Alkali-activated Composite*, In: Mechtcherine V., Slowik V., Kabele P. (eds) Strain-Hardening Cement-Based Composites. SHCC 2017. RILEM Bookseries, vol 15. Springer, Dordrecht (18-20 September 2017).

11. Y. Zuo, **M. Nedeljković**, G. Ye, *Pore Solution Composition and Solubility of Alkali-Activated Fly Ash*, In the 6th International Conference, Non-Traditional Cement and Concrete, Brno, Czech Republic, Edited by Sarka Nenadalova, Vlastimil Bilek, Zbynek Kersner, Stanislav Seitl and Dr. Hana Simonova, (19–22 June 2017).

12. Z. Li, **M. Nedeljković**, Y. Zuo, G. Ye, *Autogenous shrinkage of alkali-activated slag-fly ash pastes*, In Proceedings of the 5th International Slag Valorisation Symposium, From fundamentals to applications, Leuven, Belgium, Edited by Dr. Ir. Remus Ion Iacobescu, Dr. Ir. Annelies Malfliet (3-5 April 2017).

13. Y. Zuo, **M. Nedeljković**, G. Ye, *Pore structure characterisation of sodium hydroxide activated slag paste*, In Proceedings of the 5th International Slag Valorisation Symposium, From fundamentals to applications, Leuven, Belgium, Edited by Dr. Ir. Remus Ion Iacobescu, Dr. Ir. Annelies Malfliet (3-5 April 2017).

14. Y. Zuo, **M. Nedeljković**, G. Ye, *Reaction kinetics and thermodynamic modelling of sodium hydroxide activated slag paste*, In Proceedings of the 3rd International RILEM Conference on Microstructure Related Durability of Cementitious Composites, Nanjing, China, Edited by Changwen Miao, Wei Sun, Jiaping Liu, Huisu Chen, Guang Ye and Klaas van Breugel, RILEM Publications S.A.R.L. (24-26 October 2016).

15. Y. Zuo, **M. Nedeljković**, K. Arbi, G. Ye, *Aqueous of alkali-activated blast furnace slag paste*, In Proceedings of the 2nd International Conference on the Chemistry of Construction Materials, Munchen, Germany, Edited by the GDCh Division of Construction Chemistry (10-12 October 2016).

16. K. Arbi, **M. Nedeljković**, Y. Zuo, G. Ye, *Durability of alkali-activated fly ash and slag concrete*, In Proceedings of the 9th International Concrete Conference 2016-Environment, Efficiency and Economic Challenges for Concrete, Dundee, Scotland (4-6 July 2016).

17. Y. Zuo, **M. Nedeljković**, K. Arbi, G. Ye, *Thermodynamic modeling and experimental study of alkali-activated slag paste*, In Proceedings of HiPerMat 2016, 4th International Symposium on Ultra-High Performance Concrete and High Performance Construction Materials, Kassel, Germany, Edited by E. Fehling, B. Middendorf, J. Thiemicke (9-11 March 2016).

18. S. Marinković, I. Ignjatović, J. Dragas, N. Tosić, **M. Nedeljković**, *Experimental study of alkali activated fly ash concrete with fly ash from one Serbian power plant*, In Proceedings of the International Conference on Sustainable Structural Concrete, La Plata, Argentina (15-18 September 2015).

19. K. Arbi, **M. Nedeljković**, Y. Zuo, S. Grunewald, A. Keulen, G. Ye, *Experimental study on workability of alkali activated fly ash and slag-based geopolymer concretes*, In Proceedings of the Engineering Conferences International (ECI) Geopolymers: The route to eliminate waste and emissions in ceramic and cement manufacturing, Hernstein, Austria (24-29 May 2015).

# Propositions

accompanying the dissertation

**CARBONATION MECHANISM OF ALKALI-ACTIVATED FLY ASH AND SLAG MATERIALS**

- IN VIEW OF LONG-TERM PERFORMANCE PREDICTIONS

by

**Marija NEDELJKOVIĆ**

1. The evolution of $Na^+$ in the pore solution and microstructure development (gel phases) are crucial for understanding the degradation mechanism of carbonation in alkali activated materials.
2. Sealed curing is the first preventive measure against carbonation of alkali activated concrete.
3. For prediction of carbonation of reinforced alkali activated concrete it might be more important to evaluate the mechanical properties than to measure the initiation of the steel bar corrosion.
4. For a reliable design of future concrete structures, reinforced concrete must be durable in the first place and sustainable in the second place.
5. The people who study and apply innovative materials are ignorant.
6. Unlike in science, in music a new generation shall not destroy the works of its predecessors.
7. Ph.D. research is like a Gordian knot. Instead of untying, it can be cut.
8. To grow, it is better to follow ideas of young and spirited students than to listen to mature minds. The experiences of mature minds will always be comfortable.
9. With regard to performance, commitment, effort, dedication, there is no middle ground. Or you do something very well or not at all. (Ayrton Senna)
10. The Ph.D. research is like an Olympic sport: a good coach does not guarantee achieving the best result. What you learn during the process and how you apply it determines whether your participation has had particular value.
11. Long-term consistency beats short-term intensity. (Xiǎolóng Lǐ)

These propositions are regarded as opposable and defendable, and have been approved as such by the promotors prof. dr. ir. K. van Breugel and dr. G. Ye.

# Stellingen

behorende bij het proefschrift

**CARBONATION MECHANISM OF ALKALI-ACTIVATED FLY ASH AND SLAG MATERIALS**

- IN VIEW OF LONG-TERM PERFORMANCE PREDICTIONS

door

**Marija NEDELJKOVIĆ**

1. De verandering van $Na^+$ ionen in de poriënoplossing en de ontwikkeling van de microstructuur (gelfasen) zijn cruciaal om het degradatiemechanisme van carbonatatie in alkali geactiveerde materialen te begrijpen.
2. Afgesloten curing is de eerste preventieve maatregel tegen carbonatatie van alkali geactiveerd beton.
3. Voor het voorspellen van carbonatatie van gewapend alkalisch geactiveerd beton kan het belangrijker zijn om de mechanische eigenschappen te beoordelen, dan om de initiatie van de corrosie van de wapening te meten.
4. Voor het betrouwbaar ontwerpen van toekomstige betonconstructies moet gewapend beton in de eerste plaats de levensduur garanderen en op de tweede plaats duurzaam zijn.
5. De mensen die innovatieve materialen bestuderen en toepassen zijn onwetend.
6. Anders dan in de wetenschap, zal een nieuwe generatie in de muziek de werken van haar voorgangers niet vernietigen.
7. Ph.D. onderzoek is als een Gordiaanse knoop. In plaats van los te maken, kan deze worden doorgehakt.
8. Om te groeien, is het beter om ideeën van jonge en bezielde studenten te volgen dan naar volwassen gedachten te luisteren. De ervaringen van volwassen gedachten zullen altijd comfortabel zijn.
9. Met betrekking tot prestaties, inzet, inspanning, toewijding is er geen middenweg. Of je doet iets heel goed of helemaal niet. (Ayrton Senna)
10. Een Ph.D. onderzoek is als een Olympische sport: een goede coach is geen garantie voor het bereiken van het beste resultaat. Wat je tijdens het proces leert en hoe je het toepast, bepaalt of jouw deelname een bijzondere waarde heeft gehad.
11. Consistentie op lange termijn verslaat korte termijn intensiteit. (Xiǎolóng Lǐ)

Deze stellingen worden opponeerbaar en verdedigbaar geacht en zijn als zodanig goedgekeurd door de promotors prof. dr. ir. K. van Breugel and dr. G. Ye.

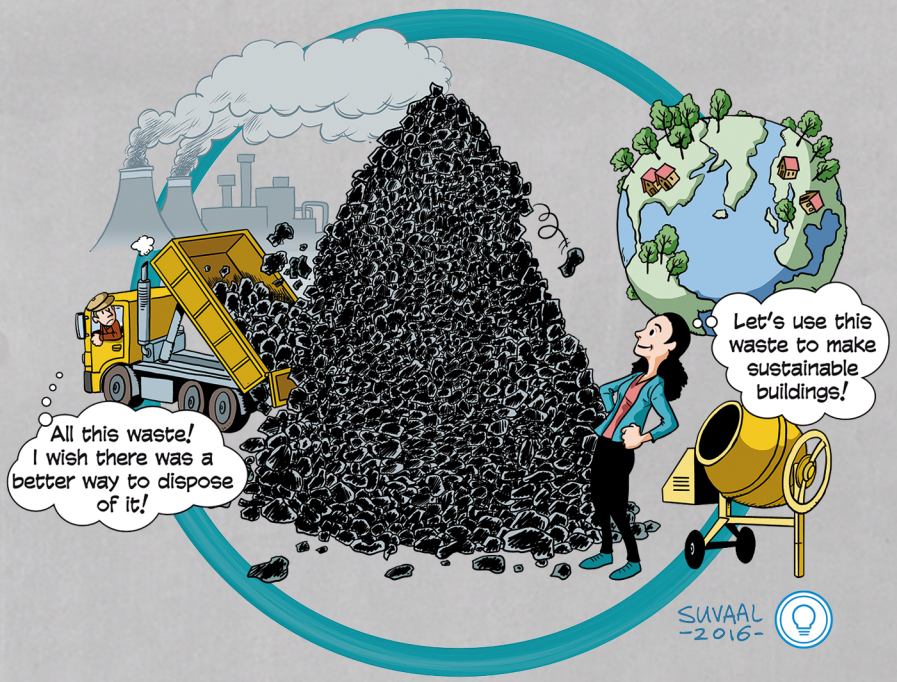


ISBN 978-94-6384-020-0

TU Delft Delft University of Technology